materials

Obtaining and Characterization of New Materials, Volume II

Edited by
Andrei Victor Sandu

www.mdpi.com/journal/materials

MDPI

Obtaining and Characterization of New Materials, Volume II

Obtaining and Characterization of New Materials, Volume II

Editor

Andrei Victor Sandu

MDPI • Basel • Beijing • Wuhan • Barcelona • Belgrade • Manchester • Tokyo • Cluj • Tianjin

MDPI

Editor
Andrei Victor Sandu
Faculty of Materials Science
and Engineering
Gheorghe Asachi Technical
University of Iasi
Iasi
Romania

This is a reprint of articles from the Special Issue published online in the open access journal *Materials* (ISSN 1996-1944) (available at: www.mdpi.com/journal/materials/special_issues/Obtain_Charact_Mater_II).

For citation purposes, cite each article independently as indicated on the article page online and as indicated below:

LastName, A.A.; LastName, B.B.; LastName, C.C. Article Title. *Journal Name* **Year**, *Volume Number*, Page Range.

Contents

Editorial

Obtaining and Characterizing New Advanced Materials

Andrei Victor Sandu [1,2,3]

1   Department of Technologies and Equipment for Materials Processing, Faculty of Materials Science and
     Engineering, Gheorghe Asachi Technical University of Iasi, 41 D. Mangeron Blvd., 700050 Iasi, Romania;
     sav@tuiasi.ro
2   Romanian Inventors Forum, St. P. Movila 3, 700089 Iasi, Romania
3   National Institute for Research and Development in Environmental Protection INCDPM,
     Splaiul Independentei 294, 060031 Bucharest, Romania

Abstract: This editorial highlights the results presented in the second Special Issue dedicated to obtaining and characterizing new materials, wherein one review paper and 13 research articles have been published. The most important field covered is that of materials involved in civil engineering, focusing on geopolymers and insulating materials alongside developing new methods for enhancing the characteristics of different systems. Another important field is that of the materials used for environmental issues, and finally, those involved in human health.

Keywords: geopolymers; fly ash; thermal insulation; laser sintering; chia seed oil

Introduction

The development of new materials opens up more and more opportunities day by day, and after a successful first Special Issue "Obtaining and Characterizing New Materials", with the support of editors, we have created a second Special Issue to highlight the latest trends in the broad field of materials engineering.

This second collection, much like the first one, covers a large range of topics. We discuss obtaining and characterizing new materials, from nano- to macro-scale, involving new alloys, ceramics, composites, biomaterials, and polymers, as well as procedures and technologies for enhancing their structures, properties, and functions. In order to choose the future applications of these new materials, we first must understand their structures and know their characteristics by involving modern techniques such as microscopy (SEM, TEM, AFM, STM, etc.), spectroscopy (EDX, XRD, XRF, FTIR, XPS, etc.), mechanical tests (tensile, hardness, elastic modulus, toughness, etc.), and understand their behavior (corrosion, thermal, DSC, STA, DMA, magnetic properties, biocompatibility, in vitro and in vivo).

The most represented of the domains included here is that of construction materials, in which we seek to create sustainable materials with low costs and effective characteristics.

Geopolymers are a type of inorganic polymer that can be made from a wide range of materials and also from industrial wastes. In order to produce cementitious products inside treated soils and improve the mechanical and physical qualities of clayey soils, alkaline activation of industrial waste was posited. This way, the use of geopolymers based on fly ash and ground-granulated blast furnace slag (GGBFS) for soil stabilization increased their strength. S.R. Abdila et al. [1] involved two different types of precursors, performing unconfined compressive strength (UCS) and concluding that GGBFS and fly ash-based geopolymers can successfully be used for soil stabilization [1].

Due to its improved acid resistance compared to regular Portland cement and lower CO_2 emissions during the synthesis process, a fly ash geopolymer is suggested as a material for rigid pavement applications. In order to manufacture a fly ash-based geopolymer with the best compressive strength, the authors have sought to improve its formulation. The findings indicate that for fly ash-based geopolymers, the ideal sodium hydroxide

concentration, sodium silicate to sodium hydroxide ratio, and solid-to-liquid ratio are, respectively, 10 M, 2.0, and 2.5, with a maximum compressive strength of 47 MPa. With a higher percentage of compressive strength than OPC concrete, the geopolymer is a more durable material for rigid pavement applications because it is based on fly ash, with a percentage of compressive strength loss of 7.38% to 21.94% for OPC concrete [2].

Another study [3] focused on developing a geopolymer based on fly ash; in this study, ladle furnace slag was combined with foam created by pre-foaming polyoxyethylene alkyether sulphate (PAS). At temperatures between 29 and 1000 °C, the performance of a fly ash-slag geopolymer blend with and without PAS foam was examined using a PAS foam-to-paste ratio of 1 and 2. (G-1 and G-2). At 29–1000 °C, the compressive strength of the foamed geopolymer was lower than that of G-0 (36.9–43.1 MPa) (25.1–32.0 MPa for G-1 and 21.5–36.2 MPa for G-2). Heating G-0 decreased its compressive strength by 8.7%, up to 1000 °C compared to unheated samples; however, foamed geopolymer gained compressive strength by 68.5% up to 1000 °C.

In a highly sought after area, that of the road concrete development, L.M. Nicula et al. [4] involved nuclear magnetic resonance (NMR) relaxometry to compare the porosity of three combinations of road concrete that contain blast furnace slag to two mixtures created with conventional ingredients. The samples involved were maintained for 300 freeze–thaw cycles and then compared to control samples. The investigations allowed for the identification of the ideal composition of blast furnace slag to be added to road concrete mixtures. Additionally, using this non-invasive method, it is possible to evaluate the porosity and the development of interior cracks during the freeze–thaw test.

In other aspect of civil engineering, the involvement of wood is crucial. P. Mania et al. [5] managed to densify samples of paulownia clone wood and hornbeam (*Carpinus betulus* L.). The specimens underwent plastic treatment in an ammonia solution before being densified. Following densification, it was possible to measure the wood's Brinell hardness in each of the three anatomical directions, and its compressive strength in the radial direction. The extent to which wood would swell in water that was liquid and humid (98% RH) was also determined. The densities of hornbeam and paulownia wood increased by 40% and approximately 280%, respectively. For hornbeam and paulownia, the Brinell hardness parallel to the fibers increased by 49 and 390%, and perpendicularly by 80 and 388%. Additionally, it was discovered that the woods' compressive strength significantly increased in the radial direction. Paulownia wood exhibited 107% swelling, compared to 153% for densified hornbeam wood exposed to water.

For many years, multi-beam box girder bridges have been used extensively worldwide. For this issue, a method for reinforcing embedded steel plate (ESP) was proposed by adding carbon-A/-B glue to the longitudinal joints of old multi-beam box girder bridges [6]. We can conclude that the proposed strengthening method can be used to enhance the mechanical performance of multi-beam box girder bridges and serve as a guide for such bridge reinforcement. Analysis results of the actual bridge and finite element model show that the structural stiffness and load lateral transferring performance between the box girders were improved after ESP strengthening.

Given the current situation, it is necessary to find sustainable and cutting-edge ways of improving the thermal efficiency of projects. An intriguing study [7] shows experimental findings from the testing of a variety of composite thermal insulation materials made from a blend of sheep wool, cellulose, rPET, and rPES fibers. The study's findings highlight the advantages of utilizing such materials for improving indoor air quality, while also demonstrating their qualities of thermal insulation (the ability to adjust to humidity and reduce concentrations of harmful substances). When compared to conventional thermal insulation materials, the benefits of employing sheep wool composite mattresses in terms of their resistance to insect attack are also shown.

Some researchers [8] discuss the capacity of sheep wool heat-insulating mattresses to simultaneously meet the real need for high-quality air inside living spaces and thermally efficient buildings by cumulatively analyzing efficiency indicators for thermal insulation and indicators of improved air quality. As a result, the results for the coefficient of thermal conductivity and its resistance to heat transfer show that these mattresses are appropriate for use as thermal insulation. The discovered features of permeability to water vapor and the sorption/desorption of water and air show their ability to control the humidity of indoor air, and the resulting decrease in formaldehyde content show their contribution to the improvement of air quality.

On the subject of materials and sustainability, we need to focus on environmental issues and materials' impact on human health.

In this vein, investigations were conducted on soil samples to perform a quality status assessment, determining pH, texture, structure, and metal concentration, as well as carrying out an assessment of anthropogenic activity by determining the pollution indices of CF (contamination factor). These investigations aimed to determine soil quality, soil environmental risk, and extraction of metals from polluted soils by bioleaching, and aimed to identify influential factors in achieving high remediation yields (potential ecological risk index). Though optimistic, the depollution yield after 12 h of treatment is Cu 29–76%, Pb 10–32%, Cr 39–72%, and Ni 44–68%. The best exposure duration for the bioleaching extraction process can be determined using yield–time correlation equations [9].

Many other parts of the industry are seeking new technologies and materials. To investigate the effects of the powder's physical characteristics and operating conditions on the bed quality—which is determined by density characteristics, density uniformity, and the flatness of the powder layer—powder spreading in realistic SLS settings was simulated using the discrete element method (DEM) [10]. Based on the response surface methodology, a regression model of the powdering quality was created (RSM). The non-dominated sorting genetic algorithm II (NSGA-II) was utilized to optimize the nylon powder laying quality in the SLS process using an improved multi-objective optimization approach. We offered various optimization plans in accordance with the various process needs. Experiments were used to confirm the validity of multi-objective optimization outcomes for powdering quality.

In another of this publication's articles [11], the influence of isothermal annealing on the mechanical and microstructural properties of Sn-0.7Cu-1.5Bi solder junctions is discussed. The intermetallic layer thickness at the solder/Cu interface increased by 0.042 m/h for Sn-0.7Cu and 0.037 m/h for Sn-0.7Cu-1.5Bi, according to the results, as the solder/Cu interface cured. With a 1.5 weight percent Bi addition in the reflowed condition and after isothermal annealing, the hardness and shear strength of Sn-0.7Cu dramatically increased.

Innovative materials known as shear thickening fluids (STFs) can be used in smart body armor. The objective of the published paper [12] was to examine how UV light affects STF aging. Artificial aging was used in the experimental inquiry to look into how UV light affects the characteristics of STFs. The highest viscosity of the STFs based on PPG425, PPG2700, and KE-P10 reached 580.7 PaS for the STF425 and 3313 PaS for the STF2700, respectively. Our findings show that STFs are UV light-sensitive and can lose some of their characteristics while being stored.

Building on our knowledge of coatings, J.J.K.Ngouoko et al. [13] studied a glassy carbon electrode (GCE) coated with a sheet of hydroxy-apatite (HA)/L-lysine (Lys) composite material to create an amperometric sensor for the detection of Nile blue A. (NBA). Electrochemical research revealed an increase in the GCE/Lys/HA sensor's sensitivity to the detection of NBA in solution. Investigations were carried out to elucidate how the pH, scan rate and NBA concentration affected the peak current and potential. The GCE/Lys/HA sensor demonstrated excellent repeatability, selectivity, and an NBA low detection limit of 5.07 108 mol L1 under ideal circumstances. NBA in several water samples was successfully detected using the developed HA/Lys-modified electrode.

In the field of organic chemistry, a novel epoxidized vegetable oil (EVO) from chia seed oil (CSO) has been produced with the intention of use as a plasticizer and compatibilizer in a wide range of eco-friendly goods related to the polymeric industry [14]. Analysis of various parameters revealed that 75 °C and an H_2O_2:DB (1.50:1) ratio produced the best epoxidation results. These high values demonstrate that the potential of chia seed oil's chemical modification to be exploited in the creation of biopolymers is much greater than that of commercially available epoxidized oils such as soybean or linseed oil.

Finally, the last article [15] examined the ways in which hydrochloric acid and brushing affected the surface quality of three flowable composite resins used for direct restoration, concluding that brushing with firm bristles straight after an acidic challenge causes two of the three flowable composite resins to have increased surface roughness. Thirty minutes after acidic aggression, brushing teeth with medium or stiff brushes had no effect on the flowable composite resins' surface quality.

In conclusion, the published articles under this Special Issue represent an excellent collection of research and review articles, with cutting-edge results that promote sustainable development in the field of materials engineering.

Conflicts of Interest: The authors declare no conflict of interest.

References

1. Abdila, S.R.; Abdullah, M.M.A.B.; Ahmad, R.; Burduhos Nergis, D.D.; Rahim, S.Z.A.; Omar, M.F.; Sandu, A.V.; Vizureanu, P.; Syafwandi. Potential of Soil Stabilization Using Ground Granulated Blast Furnace Slag (GGBFS) and Fly Ash via Geopolymerization Method: A Review. *Materials* **2022**, *15*, 375. [CrossRef] [PubMed]
2. Tahir, M.F.M.; Abdullah, M.M.A.B.; Rahim, S.Z.A.; Mohd Hasan, M.R.; Sandu, A.V.; Vizureanu, P.; Ghazali, C.M.R.; Kadir, A.A. Mechanical and Durability Analysis of Fly Ash Based Geopolymer with Various Compositions for Rigid Pavement Applications. *Materials* **2022**, *15*, 3458. [CrossRef] [PubMed]
3. Hui-Teng, N.; Cheng-Yong, H.; Yun-Ming, L.; Abdullah, M.M.A.B.; Rojviriya, C.; Razi, H.M.; Garus, S.; Nabiałek, M.; Sochacki, W.; Abidin, I.M.Z.; et al. Preparation of Fly Ash-Ladle Furnace Slag Blended Geopolymer Foam via Pre-Foaming Method with Polyoxyethylene Alkyether Sulphate Incorporation. *Materials* **2022**, *15*, 4085. [CrossRef] [PubMed]
4. Nicula, L.M.; Corbu, O.; Ardelean, I.; Sandu, A.V.; Iliescu, M.; Simedru, D. Freeze–Thaw Effect on Road Concrete Containing Blast Furnace Slag: NMR Relaxometry Investigations. *Materials* **2021**, *14*, 3288. [CrossRef] [PubMed]
5. Mania, P.; Hartlieb, K.; Mruk, G.; Roszyk, E. Selected Properties of Densified Hornbeam and Paulownia Wood Plasticised in Ammonia Solution. *Materials* **2022**, *15*, 4984. [CrossRef]
6. He, Y.; Wang, K.; Cao, Z.; Zheng, P.; Xiang, Y. Reinforcement Analysis of an Old Multi-Beam Box Girder Based on a New Embedded Steel Plate (ESP) Strengthening Method. *Materials* **2022**, *15*, 4353. [CrossRef]
7. Hegyi, A.; Vermeșan, H.; Lăzărescu, A.-V.; Petcu, C.; Bulacu, C. Thermal Insulation Mattresses Based on Textile Waste and Recycled Plastic Waste Fibres, Integrating Natural Fibres of Vegetable or Animal Origin. *Materials* **2022**, *15*, 1348. [CrossRef] [PubMed]
8. Hegyi, A.; Bulacu, C.; Szilagyi, H.; Lăzărescu, A.-V.; Meiță, V.; Vizureanu, P.; Sandu, M. Improving Indoor Air Quality by Using Sheep Wool Thermal Insulation. *Materials* **2021**, *14*, 2443. [CrossRef]
9. Sur, I.M.; Micle, V.; Hegyi, A.; Lăzărescu, A.-V. Extraction of Metals from Polluted Soils by Bioleaching in Relation to Environmental Risk Assessment. *Materials* **2022**, *15*, 3973. [CrossRef]
10. Xiao, X.; Jin, Y.; Tan, Y.; Gao, W.; Jiang, S.; Liu, S.; Chen, M. Investigation of the Effects of Roller Spreading Parameters on Powder Bed Quality in Selective Laser Sintering. *Materials* **2022**, *15*, 3849. [CrossRef] [PubMed]
11. Ramli, M.I.I.; Salleh, M.A.A.M.; Sandu, A.V.; Amli, S.F.M.; Said, R.M.; Saud, N.; Abdullah, M.M.A.B.; Vizureanu, P.; Rylski, A.; Chaiprapa, J.; et al. Influence of 1.5 wt.% Bi on the Microstructure, Hardness, and Shear Strength of Sn-0.7Cu Solder Joints after Isothermal Annealing. *Materials* **2021**, *14*, 5134. [CrossRef] [PubMed]
12. Żurowski, R.; Tryznowski, M.; Gürgen, S.; Szafran, M.; Świderska, A. The Influence of UV Radiation Aging on Degradation of Shear Thickening Fluids. *Materials* **2022**, *15*, 3269. [CrossRef] [PubMed]

13. Ngouoko, J.J.K.; Tajeu, K.Y.; Temgoua, R.C.T.; Doungmo, G.; Doench, I.; Tamo, A.K.; Kamgaing, T.; Osorio-Madrazo, A.; Tonle, I.K. Hydroxyapatite/L-Lysine Composite Coating as Glassy Carbon Electrode Modifier for the Analysis and Detection of Nile Blue A. *Materials* **2022**, *15*, 4262. [CrossRef] [PubMed]

14. Dominguez-Candela, I.; Lerma-Canto, A.; Cardona, S.C.; Lora, J.; Fombuena, V. Physicochemical Characterization of Novel Epoxidized Vegetable Oil from Chia Seed Oil. *Materials* **2022**, *15*, 3250. [CrossRef] [PubMed]

15. Tărăboanță, I.; Stoleriu, S.; Gurlui, S.; Nica, I.; Tărăboanță-Gamen, A.C.; Iovan, A.; Andrian, S. The Influence of Abrasive and Acidic Aggressions on the Surface Condition of Flowable Composite Resin. *Materials* **2022**, *15*, 1000. [CrossRef] [PubMed]

Potential of Soil Stabilization Using Ground Granulated Blast Furnace Slag (GGBFS) and Fly Ash via Geopolymerization Method: A Review

Syafiadi Rizki Abdila [1,*], Mohd Mustafa Al Bakri Abdullah [1,2,*], Romisuhani Ahmad [1,2], Dumitru Doru Burduhos Nergis [3,*], Shayfull Zamree Abd Rahim [1,4], Mohd Firdaus Omar [1,2], Andrei Victor Sandu [3,5], Petrica Vizureanu [3,6] and Syafwandi [7]

1 Centre of Excellence Geopolymer and Green Technology (CEGeoGTech), Universiti Malaysia Perlis, Kangar 01000, Perlis, Malaysia; romisuhani@unimap.edu.my (R.A.); shayfull@unimap.edu.my (S.Z.A.R.); firdausomar@unimap.edu.my (M.F.O.)
2 Faculty of Chemical Engineering Technology, Universiti Malaysia Perlis (UniMAP), Kangar 01000, Perlis, Malaysia
3 Faculty of Materials Science and Engineering, Gheorghe Asachi Technical University of Iaşi, Boulevard D. Mangeron, No. 51, 700050 Iasi, Romania; sav@tuiasi.ro (A.V.S.); peviz@tuiasi.ro (P.V.)
4 Faculty of Mechanical Engineering Technology, Universiti Malaysia Perlis, Arau 02600, Perlis, Malaysia
5 Romanian Inventors Forum, Str. P. Movila 3, 700089 Iasi, Romania
6 Technical Sciences Academy of Romania, Dacia Blvd 26, 030167 Bucharest, Romania
7 Faculty of Civil Engineering, Mercu Buana Universiti, Jakarta 11650, Indonesia; syafwandi@mercubuana.ac.id
* Correspondence: rizkisyafiadi@gmail.com (S.R.A.); mustafa_albakri@unimap.edu.my (M.M.A.B.A.); doru.burduhos@tuiasi.ro (D.D.B.N.)

Abstract: Geopolymers, or also known as alkali-activated binders, have recently emerged as a viable alternative to conventional binders (cement) for soil stabilization. Geopolymers employ alkaline activation of industrial waste to create cementitious products inside treated soils, increasing the clayey soils' mechanical and physical qualities. This paper aims to review the utilization of fly ash and ground granulated blast furnace slag (GGBFS)-based geopolymers for soil stabilization by enhancing strength. Previous research only used one type of precursor: fly ash or GGBFS, but the strength value obtained did not meet the ASTM D 4609 (<0.8 Mpa) standard required for soil-stabilizing criteria of road construction applications. This current research focused on the combination of two types of precursors, which are fly ash and GGBFS. The findings of an unconfined compressive strength (UCS) test on stabilized soil samples were discussed. Finally, the paper concludes that GGBFS and fly-ash-based geo-polymers for soil stabilization techniques can be successfully used as a binder for soil stabilization. However, additional research is required to meet the requirement of ASTM D 4609 standard in road construction applications, particularly in subgrade layers.

Keywords: geopolymer; fly ash; GGBFS; compressive strength; soil stabilization

1. Introduction

Low-strength soil layers are frequently encountered in road construction, and they have a significant impact on various phases of construction design [1–3]. Another issue in civil engineering is clayey soil [4,5]. Clayey soil is a global issue, causing several difficulties for civil engineers, building enterprises, and property owners [6–8]. Clayey soils are seen as a potential natural hazard capable of wreaking havoc on engineering buildings [9,10]. Additionally, structures constructed on clayey soils have incurred significant damage as a result of the clayey soil's undesirable and unpredictable characteristics [11–13].

According to ASTM D 2487 [14], the soil is commonly considered to have clay tendencies (the soil as to be classified as clay soil with high plasticity) when its liquid limit is greater than 50% and plasticity index is higher than 17%. Clays or soft soils primarily

belong to the fine-grained group of soils and are classified as "clays" having the ability to change in volume when they come in contact with water [14]. Generally, the soil shrinks as the water content decreases and expands as the water content increases, due to the fact that the primary clay minerals have the potential to interact and absorb water [13–15]. This results in a high liquid limit and plasticity index [9,10,13,15]. Thus, clayey soil exhibits high swelling, shrinkage, and plasticity characteristics [14,15]. However, fine-grained soils were considered suitable applicants for stabilization [13–15].

In order to stabilize soil, the most common or usual approach was by removing the soft soil first [3,16–18]. More substantial materials, such as crushed rock, will replace soft soil [4,19]. Various researchers found another method to encounter this problem since the cost involved in replacing the materials was relatively high [18,20,21]. The mechanical and chemical stabilization alteration of one or more soil properties has been termed as soil stabilization [21,22]. Most researchers studied to improve the engineering properties by increasing the compressive strength of the soil [6,8,12,16,17,23] according to the ASTM D 4609 standard [24] (>0.8 Mpa). Soil stabilization can be described as a collective term for any physical, chemical, or combination of those approaches used to enhance certain features of natural soil in order for it to meet the engineering requirements [3,4,9–11,15,21,24].

Mechanical stabilization involves a physical process in altering the soil's physical nature [25,26]. It entails compacting the soil in order to change its resistance, compressibility, permeability, and porosity [27,28]. Mechanical stabilization of a material is typically accomplished by adding another substance, which is fly ash or GGBFS, that enhances the grading or reduces the plasticity of the original material [28–30]. The original material's physical qualities will be altered, but no chemical reaction will occur [26,31]. This method could increase the density of soil due to the elimination of maximum air. The material was not affected due to the particle size distribution [25,30,32]. However, the redistribution of the particles changes the structure [27,31]. Mechanical stabilization is frequently the most cost-effective method of enhancing the quality of low-grade materials (problematic soil) [26,27,29,33]. The stiffness and strength of the material will typically be less than those obtained through chemical stabilization and will frequently be unsuitable for heavy traffic pavements [33–35]. Additionally, a stabilizing agent may be required to improve the final qualities of the blended substance [30,34].

Other than mechanical soil stabilization, chemical soil stabilization is the most popular technique for remediation of poor ground conditions [19,36–38]. It is possible to alter the compressive strength, swelling potential, and volume change properties of soil through chemical stabilization processes such as mixing with ground granulated blast furnace slag (GGBFS) and fly ash by-products, as well as mixes of any of these materials [39–43]. The chemical substances work as compaction aids, binders, and water repellents and modify the soil behavior [44,45]. Stabilization of soils using chemical additives displays the usefulness of this technique, in engineering, such as road constructions and foundation substructure development [34–36,38,46].

The manufacturing of conventional soil stabilizers such as cement and lime results in considerable CO_2 and energy emissions [47–49]. Therefore, civil engineering firms are continuously on the search for the new soil stabilizer, a low-carbon, sustainable substance, to be employed to replace cement as a soil stabilizer [47,50–55]. Geopolymerization is the process of polymerizing inorganic natural materials to form geopolymers [43,56,57]. Geopolymers have recently been shown to be a viable alternative to Portland cement for reinforcing degraded soils [52–55]. Geopolymers have outstanding engineering properties, such as increased strength and improved soil adhesion [36,40,56]. Materials containing high proportion of alumina (Al) and silica (Si) are required to manufacture this geopolymer material [47,48,57]. The Si and Al minerals found in industrial by-products such as fly ash from coal combustion and GGBFS from iron combustion are employed in geopolymer processes for soil stabilization [57–60]. In order to produce geopolymer, the sources of alumina and silica (fly ash and GGBFS) act as precursors that are easily dissolved in alkaline solutions resulted from alkaline activation, making geopolymerization possible [47,49,57,58,60–68].

In this paper, the usage of a GGBFS and fly ash Class-C-based geopolymer for soil stabilization by means of an unconfined compressive strength (UCS) test is reviewed and discussed.

2. Soil Stabilization by Conventional Method

2.1. Soil Stabilization Using Fly Ash

Fly ash is a material that is increasingly being used as a cement alternative in concrete mixtures and for soil stabilization [25,27,29,36,38,40,42,54]. The addition of fly ash is one of the methods to stabilize soil because fly ash is a pozzolan, in which it can bind to minerals in soil and make the soil stable, so as to reduce the swell shrinkage of the soil and improve soil strength [41,42,44,46,54,69–73]. The morphology of fly ash can be seen in Figure 1.
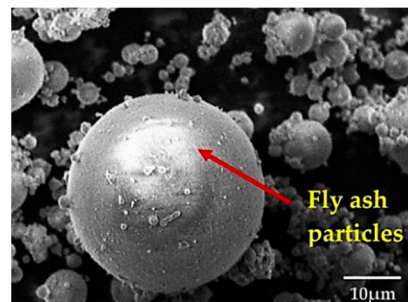
Figure 1. The microstructure image at 2000× magnification of fly ash [74].

2.2. Soil Stabilization Using Ground Granulated Blast Furnace Slag (GGBFS)

Ground granulated blast furnace slag (GGBFS) is a by-product the manufacture of iron [27,35,36,40–43,47,54,64]. It is composed primarily of lime, alumina, and silicate [48,54,65–67]. GGBFS material is also used as a substitute for cement in concrete mixtures and as a material for soil stabilization [42,48,54,59,65,66]. Mixing GGBFS with soil improves compressive strength, permeability, and durability [39,54,65–69]. The morphology of GGBFS can be seen in Figure 2.
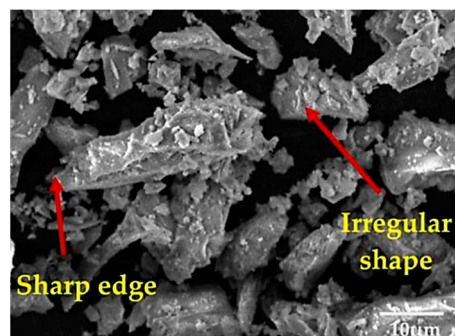
Figure 2. The microstructure image at 2000× magnification of GGBFS [74].

2.3. Strength of Soils after Stabilization with Fly Ash and Ground Granulated Blast Furnace Slag (GGBFS)

The strength of soil is a measure of its ability to absorb forces without collapsing [6,7]. A soil's ability to bear normal and shear pressures can be used to determine its strength [65,71,72]. Apart from the primary reaction products generated, additional factors may impact the rate of rising in soil strength [51,73]. The presence of soil-borne accelerating or retarding chemical components may result in an increase in soil strength [65,66,68,74,75]. The summary of previous studies on soil stabilization application is presented in Table 1.

Research by Simatupang et al. [68] investigated the stability of soil with the addition of fly ash. Fly ash percentages range from 5–25% by dry weight of soil. By increasing the fly ash content in the samples and the curing time, the compressive strength value for fly

ash increased. However, a long curing time is required to reach the optimum strength. To shorten the curing period, adding other materials such as GGBFS may be necessary.

Another study in 2016 by Dayalan et al. [65] investigated soil stabilization with ground granulated blast furnace slag (GGBFS). Different percentages of GGBFS 5–25% by dry weight of soil were used to stabilize the clayey soil. Based on the strength performance test, the optimum amount of GGBFS was determined to be 20%. Moreover, the result indicates that the inclusion of GGBFS increases the strength of clayey soils but the acquired properties do not meet the ASTM D 4609 soil-stabilizing criteria for road construction applications [76].

Another study in the same year by Mandal et al. [54] investigated soil stabilization using ground granulated blast furnace slag (GGBFS) and fly ash. Different samples were prepared with different proportions of soil, GGBFS, and fly ash. Based on the result, the best compressive strength values were obtained in a 10% GGBFS and 10% fly ash mixture. This provides proof that the addition of GGBFS and fly ash can improve the clayey soil's mechanical properties. However, the soil strength value still does not comply the ASTM D 4609 standard [76], which requires a value greater than 0.8 MPa. To comply with the requirement, increasing the percentage of fly ash and GGBFS mixture proportions may be required.

Research performed in 2019 by Neeladharan et al. [39] investigated the possibility of stabilizing expansive soils through the use of a binder comprising of fly ash and ground granulated blast furnace slag (GGBFS).The clayey soil was mixed with different percentages fly ash of 5–25% and GGBFS of 2.5–10% by dry weight of soil. According to the results of the unconfined compressive strength test, a binder percentage of 20% is recommended as the optimal. However, the unconfined compressive strength value did not fulfill the ASTM D 4609 standard [76], which must be greater than 0.8 MPa. To fulfill the standard, increasing the percentage of fly ash mixture proportions and adding other ingredients such as GGBFS may be required.

Another study in 2014 by Oormila et al. [66] investigated the potential of using GGBFS as a stabilizer for the clay/soft soil. The soft soil was mixed with GGBFS at different percentages (15–25% by dry weight of soil) with curing times of 7, 14, and 21 days. The result indicates that the use of GGBFS increased the strength characteristics of the soil. Based on compressive strength, the optimum amount of GGBFS was 20%, as it increased the strength by about 73.79% of clayey soil. This provides proof that the GGBFS can improve the strength of the clayey soil. However, a long curing time is required to reach optimum strength. To reduce the curing time and increase strength, it may be essential to combine two types of precursors (fly ash and GGBFS) and increase the percentage of fly ash mixture proportions.

Research performed by Sharma et al. [67] investigated the possibility of utilizing a binder composed of fly ash and powdered granulated blast furnace slag to stabilize expansive soils (GGBFS). The expansive soil was mixed at different percentages of fly ash 70% and GGBFS 30% with curing times of 7, 14, and 28 days. Based on the strength result, the strongest soil was achieved after 28 days of curing time, with a compressive strength value of 0.45 MPa. However, the unconfined compressive strength value does not fulfill the ASTM D 4609 standard [76], which must be more than 0.8 MPa. Furthermore, a long curing time is required to reach optimum strength. To shorten the curing period and increase compressive strength, increasing the percentage of fly ash and GGBFS mixture proportions may be required.

Table 1. The summary of previous studies on soil stabilization application.

No	Author	Testing	Raw Materials	Percentage of Blended Mix Proportion (%)	Curing Condition	Finding
1.	Simatupang et al. [68]	• Unconfined compressive strength (ASTM D 2166) [77]	• Fly ash	Fly ash: 5%, 10%, 15%, 20%, and 25%	7, 14, 28, and 56 days curing at room temperature	• By increasing the fly ash quantity in the specimen and curing period, the strength of fly ash increased.
2.	Dayalan J et al. [65]	• Unconfined compressive strength (ASTM D 2166) [77]	• GGBFS • Fly ash	Fly ash: 5%, 10%, 15%, 20%, and 25% GGBFS: 5%, 10%, 15%, 20%, and 25%	1 day curing	• The optimum compressive strength value for fly ash is 15% and GGBFS is 20%, respectively.
3.	Neeladharan et al. [39]	• Unconfined compressive strength (ASTM D 2166) [77]	• GGBFS • Fly ash	Fly ash: 5%, 10%, 15%, and 20%, GGBFS: 2.5%, 5%, 7.5%, and 10%,	1 day curing	• The strength value increases with an increase in amount of fly ash and GGBFS, which attained maximum value at 15% and 10%, respectively.
4.	Oormila et al. [66]	• Unconfined compressive strength (ASTM D 2166) [77]	• GGBFS • Fly ash	Fly ash: 5%, 10%, 15%, and 20%, GGBFS: 15%,20%, and 25%,	7, 14, and 21 days curing at room temperature	• The optimum compressive value for fly ash is 10% and GGBFS is 20%, respectively.
5.	Sharma et al. [67]	• Unconfined compressive strength (ASTM D 2166) [77]	• Fly ash • GGBFS	Fly ash: 70% GGBFS: 30%	7, 14, and 28 days curing at room temperature	• The optimum soil strength value is 0.45 MPa.
6.	Mandal et al. [54]	• Unconfined compressive strength (ASTM D 2166) [77]	• GGBFS • Fly ash	Fly ash: 5%, 10%, 15%, 20%, and 25% GGBFS: 10%	1 day curing	• The maximum value was found at 10% GGBFS and 10% fly ash, which is 4.51 kg/cm²
7.	Tyagi et al. [69]	• Unconfined compressive strength (ASTM D 2166) [77]	• GGBFS • Fly ash	Fly ash: 0%, 3%, 6% 9%, 12% 15%, and 18%, GGBFS: 0%, 5%, 10%, 15%,20%, 25% and 30%	7 and 14 day curing	• The strength value increases with increases in amount of fly ash and GGBFS, which attained maximum value at 18% and 30%, respectively.
8.	Mujtaba et al. [70]	• Unconfined compressive strength (ASTM D 2166) [77]	• GGBFS	GGBFS: 5%, 10%, 15%, 20%, 30%, 40%, 50%, and 55%	0, 3, 7, 14, and 28 days curing at room temperature	• The optimum compressive strength value for GGBFS is 30%.

Another study by Tyagi et al. [69] investigated soil stabilization with GGBFS and fly ash. Fly ash and GGBFS were utilized in amounts of 0%, 5%, 10%, 15%, 20%, 25%, and 30%, respectively, by weight of the soil sample. The strength value increases as the amounts of fly ash and GGBFS reach their maximum values of 18% and 30%, respectively. However, the unconfined compressive strength value does not fulfill the ASTM D 4609 standard [76], which must be greater than 0.8 MPa. To reduce the curing time and increase strength, it may be essential to combine two types of precursors (fly ash and GGBFS) and increase the percentage of fly ash mixture proportions.

Research performed by Mujtajab et al. [70] investigated the enhancement of expansive soils' engineering qualities with the addition of GGBFS. The impact of GGBFS in stabilizing these expansive soils was examined by applying various amounts of GGBFS between 0% and 55% to these soil samples. The strength of a remolded sample after 28 days was increased by approximately 35% with the addition of 30% GGBFS. Although, the compressive strength of the soil fulfils the ASTM D 4609 [76] standard, it requires a long curing time to get the optimum strength value. To reduce the curing time and increase strength, adding other materials such as fly ash may be necessary.

Therefore, additional research is necessary to determine the possibility of employing GGBFS and fly ash as soil stabilizers in increasing soil compression strength and shortening the curing time in order to maximize soil power. Geopolymers have recently been shown to be an effective replacement to Portland cement for reinforcing degraded soils; hence, geopolymers can be pushed for their suitability for use as a concrete substitute [52–55].

3. Geopolymer

Geopolymers can usually be synthesized from many materials with high concentration of aluminosilicates. Geopolymer precursors that are high in silica (Si) and alumina (Al) minerals, such as fly ash and GGBFS, are highly suggested for geopolymerization in soil stabilization applications [48,51,54,66]. All the aluminosilicate materials must be activated by a second raw material known as alkali activator solution [56].

Geopolymerization is an integrated process for synthesizing geopolymers, which involves leaching, diffusion, reorientation, polymerization, and condensation [56]. Three stages of polymerization occur: (1) dissolution of oxide minerals from source materials (typically silica and alumina) under extreme alkaline conditions; (2) orientation of dissolved oxide minerals followed by gelation; and (3) polycondensation to form a three-dimensional network of silico-aluminates structures [56]. Duxson et al. [56], proposed a polymerization that process involves several steps proposed in the conceptual model. A general mechanism of geopolymerization is shown in Figure 3.

This model assumes that geopolymerization starts with the dissolution of the source materials by the alkali solution, which causes the breaking of the aluminosilicate bond and releases silica and alumina, mainly in the source materials [78,79]. The aluminosilicate chain's negative charge is balanced by alkali cations such as potassium, sodium, or calcium. Thus, the silica and alumina content in the source material has a significant effect that governs geopolymer performance [73].

Furthermore, the dissolution rate increases as the solution alkalinity increases. This rate controls the time required to reach saturation, after which a supersaturated aluminosilicate solution is reached. Then, the main condensation process begins, and the aluminosilicate gel in the form of oligomers precipitates to produce larger and more stable networks [56].

The first polymer (Gel 1) is formed when the solution contains a higher Si and Al concentration. As the reaction continues, more Si enters the solution, resulting in gels containing higher amounts of Si (Gel 2). The initial setting starts when the condensation rate of the aluminosilicate species exceeds the dissolution rate. Finally, polycondensation and rearrangement processes continue to produce more connected 3D networks, forming the final geopolymer matrix [56].
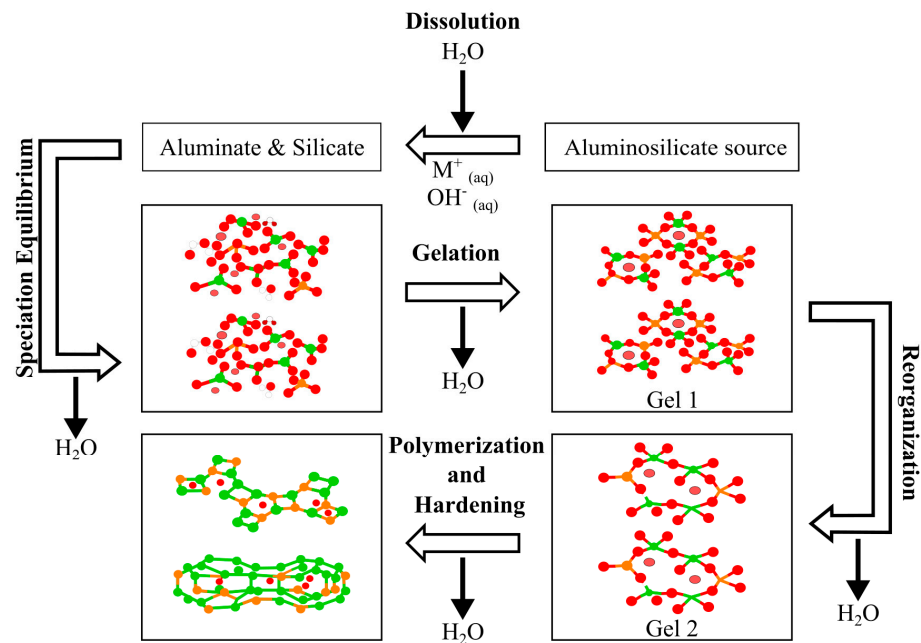
Figure 3. Geopolymerization mechanism.

3.1. Source of Raw Materials

The most common source material to produce geopolymers is fly ash [51,72,80–85]. High-strength geopolymers generally could be obtained from Class F fly ash (low calcium mineral) [48,54,66,86,87]. However, Class C fly ash (high calcium) has shown that it can also be used to produce geopolymer [11,50,87–90]. The fly ash from different sources could affect the final properties since they have different levels of reactivity under specific geopolymer synthesis conditions [48,51,76]. The chemical content, quantity of fly ash, and activator solution will influence fly-ash-based geopolymer properties in the fresh and hardened state [51,72,73].

In 1957, the first method to utilize a slag-based geopolymer as a binder in building was created [91]. Ground granulated blast furnace slag (GGBFS) is a granular glass composed primarily of calcium oxide (CaO), silicon dioxide (SiO_2), aluminium oxide (Al_2O_3), and magnesium oxide (MgO) [76–79]. It is an amorphous by-product of the production of pig iron from iron ore, coke combustion residue, and fluxes such as limestone [48,54,75]. The existence of calcium (CaO) content in GGBFS contributed to the shortened setting time and development of the compressive strength of the clay soil [48,54,66,73,82,83,85,88]. The reaction between GGBFS and alkali activator solution forms a calcium–aluminate–silicate–hydrate (C–A–S–H) gel-forming within the geopolymer matrix. These hydration products, along with aluminosilicate structure in the GGBFS samples, contributed to significantly gaining high strength [78].

3.2. Alkali Activator

The most common alkali solution used in geopolymerization is a mixture of sodium silicate (Na_2SiO_3), and sodium hydroxide (NaOH) [48,51,72,82]. The sodium hydroxide (NaOH) solution concentration has a significant effect on the physical and mechanical properties of soil-stabilization-based geopolymer [48,51,72,75,82]. This solution contains hydroxide ions (OH-) and sodium ions (Na+), which initiate the reaction between the internal silicate (Si) and aluminate (Al) components, initiating the dissolving process [48,51,75,82]. Using a mixture of both sodium silicate (Na_2SiO_3) and sodium hydroxide (NaOH) as an alkali activator will give better strength than using a sodium hydroxide (NaOH) solution only [51,74,80,83]. The reaction of sodium silicate (Na_2SiO_3) to process polymerization is crucial in dissolving Si, and the mixing ratio of sodium hydroxide (NaOH) concentration is also crucial in producing good strength of the product from geopolymer [48,51,75,82].

Generally, higher strength could be obtained by using higher contents of NaOH and sodium silicate [48,75]. However, there will be an adverse effect on strength if there was too much alkali in the composition [51,82,83]. In order to control the compressive strength, various alkali activator compositions were usually used [48,51,72,82]. The use of a higher molar concentration of alkali ions could accelerate the reactants in the chain reaction [48,51,72,75,82]. Nevertheless, it might lead to the rapid loss inconsistency during the mixing process due to the faster reaction of the polymer [51,81,82]. Then, to provide the maximum mechanical properties, there should be an optimum alkali activator content [51,81,84].

3.3. Strength of Soil after Stabilization with Fly Ash and Ground Granulated Blast Furnace Slag (GGBFS) Geopolymer

Numerous investigations on geopolymers have been undertaken, which are used to make ceramics, earth bricks, mortar, and concrete. Stabilizing soil with geopolymer binders is a relatively recent concept. The use of ground granulated blast furnace slag and fly-ash-based geopolymers to stabilise clayey soil showed promising results. The summary of previous studies on soil stabilization with fly ash and GGBFS-based geopolymer is presented in Table 2.

Research by Anne et al. [72] investigated the use of fly ash in the synthesis of geopolymer for soil stabilization. Fly ash was used in proportions of 15% and 25% and ratio of alkali activator Sodium Silicate: Sodium Hydroxide:Sodium Aluminate of 50:50:0, 33:33:33, 50:20:30. According to the findings, strength increased as the amount of fly ash increased. However, the strength value still does not comply with the ASTM D 4609 standard [76], which requires a value greater than 0.8 MPa. Furthermore, a longer curing time is required to reach the optimum strength. To shorten the curing period and increase compressive strength, adding other materials such as GGBFS may be necessary.

In 2017, Abdullah et al. [51] investigated the effect of the alkaline activator/fly ash ratio on the stability of geopolymer-stabilized soil. A variety of mix designs were made and cured for 7 and 28 days at varied fly ash/alkaline activator ratios and Na_2SiO_3/NaOH ratios. The molecular weight of the geopolymer and the proportion of geopolymer in the soil were set to 10 molar and 8%, respectively. The maximum strength was attained with a fly ash/alkaline activator ratio of 2.5 and a Na_2SiO_3/NaOH ratio of 2.0 after 28 days of curing period. Additionally, the mixture of fly ash geopolymers contributed to filling the large surface area of the voids between the clay particles and controlling the moisture content of the clay. This can cause the clay to become stable and compact and increase the compressive strength of the clay. However, the results are not in accordance with the ASTM D 4609 [76] soil stabilization criteria for road construction applications. The strength of the soil should be greater than 0.8 MPa [76,91]. To comply with the standard, additional chemicals such as GGBFS may be required, as well as an increase in the percentage of fly ash mixture proportions.

In 2018, Parhi et al. [75] investigated the stabilization of soil with the use of an alkali-activated fly-ash-based geopolymer. The fly ash is activated using concentrations of sodium hydroxide of 10, 12.5, and 15 molars. The various percentages of fly ash (20–40%) relative to the expanding soil's total solids are employed. The ratios of activator to ash (liquid to solid mass ratio) were maintained between 1 and 2.5. The 10 molal samples have a greater three- and seven-day strength than the 12.5 and 15 molar samples, which make them more cost effective than the 12.5 and 15 molal samples. However, the strength results do not adhere to the ASTM D 4609 [76] standard soil stabilization criteria for road construction applications. To comply with the requirement, increasing the percentage of fly ash mixture proportions and adding other ingredients such as GGBFS may be required.

Table 2. The summary of previous studies on soil stabilization with fly ash and ground granulated blast furnace slag (GGBFS)-based geopolymer.

No	Author	Testing	Raw Materials	Activator Chemical	Molarity NaOH (M)	Percentage of Blended Mix Proportion (%)	Curing Condition	Finding
1.	Anne et al. [72]	• Unconfined compressive strength (ASTM D 2166) [77]	• Fly ash	• Sodium silicate (Na$_2$SiO$_3$) • Sodium hydroxide (NaOH)	Na/Al: 2.05 Si/Al: 2.64 Na/Si: 0.78	Fly ash: 15% and 25%	7, 14, and 28 days of curing at room temperature	• Adding more fly ash increased compressive strength.
2.	Thomas et al. [73]	• Unconfined compressive strength (ASTM D 2166) [77]	• GGBFS	• Sodium silicate (Na$_2$SiO$_3$) • Sodium hydroxide (NaOH)	1 M	GGBFS: 6%, 9%, 12%, 15%, 20%, and 30%	7 and 28 days of curing at room temperature	• The optimal dose for GGBFS is 20%.
3.	Abdullah et al. [51]	• Unconfined compressive strength (ASTM D 2166) [77]	• Fly ash	• Sodium silicate (Na$_2$SiO$_3$) • Sodium hydroxide (NaOH)	10 M	Fly ash: 8%	7 and 28 days of curing at room temperature	• The optimum strength obtained at the fly ash/alkaline activator ratio 2.5 and Na$_2$SiO$_3$/NaOH ratio 2.0 at 28 days of the curing period.
4.	Parhi et al. [75]	• Unconfined compressive strength (ASTM D 2166) [77]	• Fly ash	• Sodium silicate (Na$_2$SiO$_3$) • Sodium hydroxide (NaOH)	10 M, 12.5 M and 15 M	Fly ash: 20%, 30%, and 40%	3 and 7 days of curing at room temperature	• 10 molal samples provide greater 3 and 7 strength than 12.5 and 15 molal samples.
5.	Phummiphan et al. [88]	• Unconfined compressive strength (ASTM D 2166) [77]	• Fly ash • GGBFS	• Sodium silicate (Na$_2$SiO$_3$) • Sodium hydroxide (NaOH)	5 M	Fly ash: 30% GGBFS: 10%, 20%, and 30%,	7, 28, and 60 days of curing	• The optimal dosage is 20% for GGBFS and 30% for fly ash.
6.	Leong et al. [81]	• Unconfined compressive strength (ASTM D 2166) [77]	• Fly ash	• Sodium silicate (Na$_2$SiO$_3$) • Sodium hydroxide (NaOH)	8 M	Ratio Fly ash/Soil: 0.3, 0.6, 0.8, and 0.9	1 day of curing at 100 °C temperature	• The compressive strength improves as fly ash/soil ratio increases.
7.	Shihab et al. [80]	• Unconfined compressive strength (ASTM D 2166) [77]	• Fly ash	• Sodium silicate (Na$_2$SiO$_3$) • Sodium hydroxide (NaOH)	10 M, 12M, and 14M	Fly ash: 8%, 10%, 12%, and 14%	1 day of curing at 70 °C temperature	• The optimum molar concentration is 12 M.

In the same year, Leong et al. [81] investigated the strength improvement of soil stabilization with fly-ash-based geopolymer: an appraisal of soil, fly ash, alkali activators, and water. Molarity was fixed at 8 molars and the ratios of fly ash/soil were 0.3, 0.6, 0.8, and 0.9. According to the results, strength increases as the fly ash/soil ratio increases. Although the compressive strength of the soil fulfils the ASTM D 4609 [76] standard, it required a long curing time to obtain the optimum strength value. To shorten the curing period, increasing the percentage of fly ash mixture proportions and molarity and adding other materials such as GGBFS may be necessary.

In another study, Shihab et al. [80] investigated the influence of NaOH molar concentration on the mechanical strength of a soft clayey soil stabilized with a fly-ash-based geopolymer after initial heating. The fly ash was activated with 8, 10, 12 and 14 molars. Dosages of fly ash were selected as 8%, 10%, 12%, and 14% of dry weight of soil. Based on the result, the optimum molar concentration is 12 M. Although the compressive strength of the soil fulfils the ASTM D 4609 [76] standard, it requires a high molarity to obtain the optimum compressive strength value.

Another study conducted by Thomas et al. [73] investigated the stabilization of soils through the use of alkali-activated GGBFS. The GGBFS doses of 6%, 9%, 12%, 15%, and 20% of dry weight of soil were chosen. The optimal dosage for GGBFS can be set as 20% based on the strength. However, the strength results do not fulfill the ASTM D 4609 [76] standard soil stabilization criteria for road construction applications. To comply with the requirement, increasing the molarity and adding other ingredients such as fly ash may be required.

Another research performed by Phummiphan et al. [88] examined the use of geopolymer stabilized soil, fly ash, and GGBFS blends as a pavement base material. Molarity was fixed at 5 molars. Dosages of fly ash were selected as 30% and GGBFS of 10%, 20%, and 30%. The soil sample was prepared by mixing it with fly ash and GGBFS and curing it for 7, 28, and 60 days. Based on unconfined compressive strength (UCS) result, the optimum dosage can be selected as 20% for GGBFS and 30% for fly ash. However, the compressive strength value still did not comply with the ASTM D 4609 standard [76], which requires a value greater than 0.8 MPa. Furthermore, a long curing time is required to reach optimum strength. To shorten the curing period and increase compressive strength, increasing the percentage of fly ash mixture proportions and molarity may be necessary. Additionally, the existence of calcium (CaO) content in GGBFS contributed to the shortened setting time and development of the compressive strength of the clay soil. This finding was supported by a previous study by Aziz et al. [78] where the reaction between GGBFS and alkali activator solution formed a calcium–aluminate–silicate–hydrate (C–A–S–H) and calcite ($CaCO_3$) within the geopolymer matrix. These hydration products, along with aluminosilicate structure in the GGBFS samples, contributed significantly to high strength gain.

In addition, a few crucial factors influencing the properties of geopolymer so as to contribute to achieving a good mix of design and formulation of geopolymer include solid-to-liquid (S/L) ratio, sodium hydroxide molarity, and sodium silicate (Na_2SiO_3)/sodium hydroxide (NaOH) ratio, which will be explained in the next section.

4. Factors Affecting the Geopolymer Properties

Commonly, in soil stabilization-based geopolymer, fly ash Class C and GGBFS are used as the primary source material containing mostly high content in silica (Si) and alumina (Al) that dissolve in alkali solution for geopolymerization in soil stabilization application [51,65,72–74]. A few crucial factors influencing the properties of geopolymer so as to contribute to achieving a good mix of design and formulation of geopolymer include solid-to-liquid (S/L) ratio, sodium hydroxide molarity, and sodium silicate (Na_2SiO_3)/sodium hydroxide (NaOH) ratio [51,74,92–94].

4.1. Effect of Solid to Liquid Ratio on Geopolymer

The solid-to-liquid (S/L) ratio corresponds to the aluminosilicate source to activator solution ratio [72,73,88,92,95,96]. The aluminosilicate source's alkali activator is a blend of solid and liquid. The liquid is extremely alkaline, and the solid contains an appropriate amount of highly reactive silicate aluminate [40,48,50,51,57,78]. Based on a previous study by Alonso et al. [97], it is said that the initial solid content highly influences the rate of geopolymer formation; it was evident that a large number of precipitates was observed with an increasing solid-to-liquid ratio. This is said to be due to high dissolved reactant species.

As the solid-to-liquid ratio rose, the geopolymers sample became less homogeneous due to the limited amount of alkali activator [48,51,72,74,78,93,94,98]. At this solid-to-liquid (S/L) ratio, the liquid content was negligible in comparison to the solid content [51,74]. Thus, it resulted in a soil-based geopolymer with low compressive strength. Abdullah et al. [51] also analyzed the influence of solid-to-liquid (2.0, 2.5, and 3.0) ratio to soil stabilization using fly-ash-based geopolymer, observing a lower extent of binder formation, which resulted in a soil and fly-ash-based geopolymer sample with a solid-to-liquid ratio higher than 2.5. This is due to the high degree of supersaturation of the aluminosilicate phase, so as to produce a less connected geopolymer structure [51,74].

4.2. Effect of Sodium Hydroxide Molarity on Geopolymer

The concentration of sodium hydroxide (NaOH) solution is a critical parameter that influences the geopolymer's properties. This solution is one of the alkali activators used in the production of geopolymer [9,40,48,50,51,57,74,78,99]. It contains and provides hydroxide ion (OH-) and sodium ion (Na+), mainly responsible for the dissolution of aluminosilicate source materials and the polymerization process of geopolymer [74,78,82,83,99–101]. The molarity of NaOH solution is reported to significantly affect the workability, geopolymerization reaction, and strength development of the final product [74,87,102,103]. The obstacle of using NaOH solution in the geopolymer synthesis is the low strength development if the molarity used is too high or too low [71,72,74,80,92,94].

There were a few studies on the effect of NaOH molarity on the geopolymer [72,74,75,80,104]. According to Malkawi et al. [105], a strong alkali is needed due to the alkali activator's function, which is required to partially or entirely dissolve the silica and alumina available in the source materials as explained in details in the polymerization mechanism [74,78,101,106]. The researcher found that 10 M NaOH solution is suitable for Class F and Class C fly-ash-based geopolymer, respectively [51,74,101,107,108].

4.3. Effect of Sodium Silicate to Sodium Hydroxide Ratio on Geopolymer

Previous research has employed the merger of sodium hydroxide and sodium silicate as an alkali activator [48,51,74,83,88,106–110]. As reported by Tempest et al. [111], the degree of reactivity of raw geopolymer material decreases when the sodium silicate (Na_2SiO_3)/sodium hydroxide (NaOH) ratio is too high. This is because sodium hydroxide solution plays an essential role in dissolving the raw materials [111]. However, higher sodium silicate (Na_2SiO3)/sodium hydroxide (NaOH) ratios are encouraged to be studied for geopolymer systems due to commercial and marketing interest, lowering the workability and strength of the mixture [51,74,78,102,103,109,110]. This is supported by multiple another study, which also found that sodium silicate (Na_2SiO_3)/sodium hydroxide (NaOH) ratio at 2.0 in soil stabilization using fly-ash-based geopolymer process shows the best performance [51,74].

Much attention has been given to the utilization of stabilization materials for soil stabilization, but only a few scholars investigated the use of geopolymer for soil stabilization application. Instead of focusing on stabilizing soil with fly ash and GGBFS-based geopolymer, this paper investigated the soil stabilization using fly ash and GGBFS via the geopolymerization process, where the soil stabilization was performed by mixing the soil, fly ash, and GGBFS directly with alkali solutions. In other words, the soil, fly ash, and GGBFS act as the source materials for polymerization, producing soil-based geopolymers.

5. Summary and Future Works

This paper presents the clayey soil or problematic soil that can be stabilized and the strength improved by using a fly ash Class C and GGBFS-based geopolymerization process. The experimental results indicate that stabilization using stabilizers chemically and mechanically alters the majority of clayey soils, resulting in a significant increase (>0.8 Mpa) in unconfined compressive strength (UCS). Geopolymerization process is a relatively new approach for soil stabilization that has the potential to outperform previous treatments (conventional method).

Additionally, this paper discusses the factor that determines the geopolymer's properties. Two factors have been shown to have a major effect on the geopolymer's properties: the S/L ratio and the Ca concentration of the geopolymer. The S/L ratios vary according to the materials utilized. The majority of assessments of fly ash Class C and GGBFS utilized an S/L ratio between 1 and 3. Thus, analyzing prior research will aid in determining the optimum S/L ratio to be applied in future studies. On the other hand, the calcium concentration of a geopolymer can be connected to the materials employed. For instance, increasing the amount of fly ash Class C and GGBFS used will improve the calcium content.

While a wealth of literature is available on using fly ash Class C and GGBFS-based geopolymers, they nearly always refer to their use in building materials. Several researchers reported on the use of geopolymers for soil stabilization but did not discuss their applicability in road construction, particularly in the subgrade layer. Additionally, if the soil stabilization only uses geopolymers, it does not produce CO_2. Hence, it is impossible to evaluate and discuss the CO_2 emission reduction ratio of soil-based geopolymers. However, if soil stabilization involves the use of materials such as cement, it is possible to evaluate and discuss the CO_2 emission because one ton of cement is manufactured, accounting for approximately one ton of greenhouse gas CO_2 released into the atmosphere as a result of lime decarbonization in the kiln during cement manufacture. Moreover, the swell behavior, flexural strength, or abrasion resistance of soil stabilization-based geopolymer using GGBFS and fly ash Class C in road construction, particularly in the subgrade layer of the soil, have not been investigated. Thus, this article only discusses the performance of using geopolymer technology in soil stabilization based on compressive strength in road construction applications, especially in subgrade layers. In addition, the potential applications of GGBFS-FA geo-polymer are seen in soil stabilization operation with deep injection techniques, slope stabilization techniques, and in situ stabilization techniques. Based on the identified gaps, several future works are proposed in this study as listed below:

i.   Previous research has demonstrated that soil stabilization based on geopolymers using fly ash Class C and GGBFS as raw materials can increase the compressive strength of clayey soil. Thus, it is advised that future works concentrate on using fly ash Class C and GGBFS geopolymers as soil-stabilizing materials.

ii.   The mix design of soil stabilization-based geopolymer is critical in defining the mechanical and physical properties of soil stabilization-based geopolymer. Thus, the optimal solid-to-liquid ratio, sodium hydroxide to sodium silicate ratio, and sodium hydroxide molarity must be further researched in relation to soil-stabilizing requirements such as unconfined compressive strength and Atterberg limits test.

iii. The effects of various curing temperature on soil-based geopolymer need to be further investigated.

References

1. Pandey, A. Soil stabilization using cement. *Int. J. Civ. Eng. Technol.* **2017**, *8*, 316–322. [CrossRef]
2. Pereira, R.S.; Emmert, F.; Miguel, E.P.; Gatto, A. Soil Stabilization with Lime for the Construction of Forest Roads. *Floresta E Ambient.* **2018**, *25*. [CrossRef]
3. Emarah, D.A.; Seleem, S.A. Swelling soils treatment using lime and sea water for roads construction. *Alex. Eng. J.* **2018**, *57*, 2357–2365. [CrossRef]
4. Ural, N. *The Importance of Clay in Geotechnical Engineering*; Intech: London, UK, 2018; p. 13.
5. Cherif, M.M.; Amal, M.; Ramdane, B. Effect of swelling mineral on geotechnical characteristics of clayey soil. *MATEC Web. Conf.* **2018**, *149*, 02067. [CrossRef]
6. Seco, A.; Del Castillo, J.M.; Espuelas, S.; Marcelino-Sadaba, S.; Garcia, B. Stabilization of a clayey soil using cementing material from spent refractories and ground-granulated blast furnace slag. *Sustainability* **2021**, *13*, 3015. [CrossRef]
7. Cavalcante, F. Editorial for special issue clays, clay minerals, and geology. *Minerals* **2021**, *11*, 1057. [CrossRef]
8. Soból, E.; Gabryś, K.; Zabłocka, K.; Šadzevičius, R.; Skominas, R.; Sas, W. Laboratory studies of small strain stiffness and modulus degradation of Warsaw mineral cohesive soils. *Minerals* **2020**, *10*, 1127. [CrossRef]
9. Eberwein, J.R.; Oikawa, P.Y.; Allsman, L.A.; Jenerette, G.D. Carbon availability regulates soil respiration response to nitrogen and temperature. *Soil Biol. Biochem.* **2015**, *88*, 158–164. [CrossRef]
10. Davidson, E.A.; Verchot, L.V.; Henrique Cattânio, J.; Ackerman, I.L.; Carvalho, J.E.M. Effects of soil water content on soil respiration in forests and cattle pastures of eastern Amazonia. *Biogeochemistry* **2000**, *48*, 53–69. [CrossRef]
11. Khan, T.A.; Taha, M.R.; Khan, M.M.; Shah, S.A.R.; Aslam, M.A.; Waqar, A.; Khan, A.R.; Waseem, M. Strength, and volume change characteristics of clayey soils: Performance evaluation of enzymes. *Minerals* **2020**, *10*, 52. [CrossRef]
12. Di Sante, M.; Di Buò, B.; Fratalocchi, E.; Länsivaara, T. Lime treatment of a soft sensitive clay: A sustainable reuse option. *Geosciences* **2020**, *10*, 182. [CrossRef]
13. Vukićević, M.; Marjanović, M.; Pujević, V.; Jocković, S. The alternatives to traditional materials for subsoil stabilization and embankments. *Materials* **2019**, *12*, 3018. [CrossRef]
14. ASTM D 4287. *Standard Practice for Classification of Soils for Engineering Purposes (Unified Soil Classification System)*; ASTM International: West Conshohocken, PA, USA, 2017.
15. Won, J.; Park, J.; Kim, J.; Jang, J. Impact of Particle Sizes, Mineralogy and Pore Fluid Chemistry on the Plasticity of Clayey Soils. *Sustainability* **2021**, *13*, 11741. [CrossRef]
16. She, J.; Lu, Z.; Yao, H.; Fang, R.; Xian, S. Experimental Study on the Swelling Behavior of Expansive Soil at Different Depths under Unidirectional Seepage. *Appl. Sci.* **2019**, *9*, 1233. [CrossRef]
17. Tiwari, N.; Satyam, N. Experimental study on the influence of polypropylene fiber on the swelling pressure expansion attributes of silica fume stabilized clayey soil. *Geosciences* **2019**, *9*, 377. [CrossRef]
18. Long, Z.; Cheng, Y.; Yang, G.; Yang, D.; Xu, Y. Study on Triaxial Creep Test and Constitutive Model of Compacted Red Clay. *Int. J. Civ. Eng.* **2021**, *19*, 517–531. [CrossRef]
19. Ghadir, P.; Ranjbar, N. Clayey soil stabilization using geopolymer and Portland cement. *Constr. Build. Mater.* **2018**, *188*, 361–371. [CrossRef]
20. Gharib, M.; Saba, H.; Barazesh, A. Experimental Investigation of Impact of Adding Lime on Atterberg Limits in Golestan Province Soils. *Mater. Sci.* **2012**, *3*, 796–800.
21. Bahadori, H.; Hasheminezhad, A.; Taghizadeh, F. Experimental Study on Marl Soil Stabilization Using Natural Pozzolans. *J. Mater. Civ. Eng.* **2019**, *31*, 04018363. [CrossRef]
22. Salehi, M.; Bayat, M.; Saadat, M.; Nasri, M. Experimental Study on Mechanical Properties of Cement-Stabilized Soil Blended with Crushed Stone Waste. *KSCE J. Civ. Eng.* **2021**, *25*, 1974–1984. [CrossRef]
23. Geliga, E.A.; Salma, D.; Ismail, A. Geotechnical Properties of Fly Ash, and its Application on Soft Soil Stabilization. *UNIMAS E J. Civ. Eng.* **2010**, *1*, 1–6.

24. Amhadi, T.S.; Assaf, G.J. Improvement of Pavement Subgrade by Adding Cement and Fly Ash to Natural Desert Sand. *Infrastructures* **2021**, *6*, 151. [CrossRef]
25. Afrin, H. A Review on Different Types Soil Stabilization Techniques. *Int. J. Transp. Eng. Technol.* **2017**, *3*, 19. [CrossRef]
26. Lakhanpal, A.; Chopra, A. A Brief Review on Various Methods and Materials Used for. *Int. Res. J. Eng. Technol.* **2018**, *5*, 682–684.
27. Dhakar, S.; Jain, S.K. Stabilization of Soil: A Review. *J. Xidian Univ.* **2020**, *14*, 545–549. [CrossRef]
28. Utami, G.S. Clayey soil stabilization with lime effect the value CBR and swelling. *ARPN J. Eng. Appl. Sci.* **2014**, *9*, 1744–1748.
29. Baloochi, H.; Aponte, D.; Barra, M. Soil stabilization using wastepaper fly ash: Precautions for its correct use. *Appl. Sci.* **2020**, *10*, 8750. [CrossRef]
30. Mishra, S.; Sachdeva, S.N.; Manocha, R. Subgrade Soil Stabilization Using Stone Dust and Coarse Aggregate: A Cost-Effective Approach. *Int. J. Geosynth. Gr. Eng.* **2019**, *5*, 40891. [CrossRef]
31. Sagar Mali, S.K. Soil Stabilization by using Plastic Waste. *Int. Res. J. Eng. Technol.* **2019**, *6*, 4056–4060.
32. Mokhtar, M.; Hamid, N.B.; Nadia Mohd Yusoff, S.A.; Sani, S. An experimental study on dust shell as an admixture in soft soil stabilization. *ARPN J. Eng. Appl. Sci.* **2016**, *11*, 7254–7257.
33. Kharade, A.S. Waste Product Bagasse Ash from Sugar Industry Can Be Used as Stabilizing Material for Expansive Soils. *Int. J. Res. Eng. Technol.* **2014**, *3*, 506–512. [CrossRef]
34. Tavakol, M.; Hossain, M.; Tucker-Kulesza, S.E. Subgrade Soil Stabilization Using Low-Quality Recycled Concrete Aggregate. *J. Geotech.* **2019**, *1*, 235–244. [CrossRef]
35. Behiry, A.E.A.E.-M. Utilization of a New By-Product Material for Soft Subgrade Soil Stabilization. *OALib* **2014**, *1*, 1–22. [CrossRef]
36. Firoozi, A.A.; Guney Olgun, C.; Firoozi, A.A.; Baghini, M.S. Fundamentals of soil stabilization. *Int. J. Geo Eng.* **2017**, *8*, 26. [CrossRef]
37. Saneiyan, S.; Ntarlagiannis, D.; Werkema, D.D.; Ustra, A. Geophysical methods for monitoring soil stabilization processes. *J. Appl. Geophys.* **2018**, *148*, 234–244. [CrossRef]
38. Rahgozar, M.A.; Saberian, M.; Li, J. Soil stabilization with non-conventional eco-friendly agricultural waste materials: An experimental study. *Transp. Geotech.* **2018**, *14*, 52–60. [CrossRef]
39. Neeladharan, C. Stabilization of soil using Fly ash with ground granulated blast furnace slag (GGBS) as binder. *Suraj Punj. J.* **2019**, *9*, 23.
40. Amulya, S.; Ravi Shankar, A.U.; Praveen, M. Stabilization of lithomargic clay using alkali activated fly ash and ground granulated blast furnace slag. *Int. J. Pavement Eng.* **2020**, *21*, 1114–1121. [CrossRef]
41. Sihag, P.; Suthar, M.; Mohanty, S. Estimation of UCS-FT of Dispersive Soil Stabilized with Fly Ash, Cement Clinker and GGBS by Artificial Intelligence. *Iran. J. Sci. Technol. Trans. Civ. Eng.* **2021**, *45*, 901–912. [CrossRef]
42. Ghaffoori, F.K.; Arbili, M.M. Effects of Fly Ash and Granulated Ground Blast Furnace Slag on Stabilization of Crude Oil Contamination Sandy Soil. *Polytech. J.* **2019**, *9*, 80–85. [CrossRef]
43. Miraki, H.; Shariatmadari, N.; Ghadir, P.; Jahandari, S.; Tao, Z.; Siddique, R. Clayey soil stabilization using alkali-activated volcanic ash and slag. *J. Rock Mech. Geotech. Eng.* **2021**. [CrossRef]
44. Kumar, P.G.; Harika, S. Stabilization of expansive subgrade soil by using fly ash. *Materials* **2020**, *45*, 6558–6562. [CrossRef]
45. Chethan, B.A.; Ravi Shankar, A.U. Strength and Durability Characteristics of Cement and Class F Fly Ash-Treated Black Cotton Soil. *Indian Geotech. J.* **2021**, *51*, 1121–1133. [CrossRef]
46. Prasad, S. Experimental Investigation of Soil Behaviour Using Industrial Fly Ash. *Am. J. Eng. Technol. Manag.* **2021**, *6*, 24. [CrossRef]
47. Hamzah, H.N.; Al Bakri Abdullah, M.M.; Yong, H.C.; Zainol, M.R.R.A.; Hussin, K. Review of soil stabilization techniques: Geopolymerization method one of the new technique. *Key Eng. Mater.* **2015**, *660*, 298–304. [CrossRef]
48. Singhi, B.; Laskar, A.I.; Ahmed, M.A. Investigation on Soil–Geopolymer with Slag, Fly Ash and Their Blending. *Arab. J. Sci. Eng.* **2016**, *41*, 393–400. [CrossRef]
49. Hanegbi, N.; Katra, I. A clay-based geopolymer in loess soil stabilization. *Appl. Sci.* **2020**, *10*, 2608. [CrossRef]
50. Murmu, A.L.; Dhole, N.; Patel, A. Stabilization of black cotton soil for subgrade application using fly ash geopolymer. *Road Mater. Pavement Des.* **2020**, *21*, 867–885. [CrossRef]
51. Abdullah, M.S.; Ahmad, F. Effect of Alkaline Activator to Fly Ash Ratio for Geopolymer Stabilized Soil. *MATEC Web Conf.* **2017**, *97*, 01012. [CrossRef]
52. Teerawattanasuk, C.; Voottipruex, P. Comparison between cement and fly ash geopolymer for stabilized marginal lateritic soil as road material. *Int. J. Pavement Eng.* **2019**, *20*, 1264–1274. [CrossRef]
53. Pathak, A.K.; Pandey, V.; Murari, K.; Singh, J.P. Soil Stabilization Using Ground Granulated Blast Furnace Slag. *J. Eng. Res. Appl.* **2014**, *4*, 164. [CrossRef]
54. Mandal, S.; Singh, J.P. Stabilization of Soil using Ground Granulated Blast Furnace Slag and Fly Ash. *IJIRSET* **2016**, *5*, 21121–21126. [CrossRef]
55. Yankwa Djobo, J.N.; Elimbi, A.; Kouamo Tchakouté, H.; Kumar, S. Mechanical properties and durability of volcanic ash based geopolymer mortars. *Constr. Build. Mater.* **2016**, *124*, 606–614. [CrossRef]
56. Duxson, P.; Fernández-Jiménez, A.; Provis, J.L.; Lukey, G.C.; Palomo, A.; Van Deventer, J.S.J. Geopolymer technology: The current state of the art. *J. Mater. Sci.* **2007**, *42*, 2917–2933. [CrossRef]

57. Javdanian, H. The effect of geopolymerization on the unconfined compressive strength of stabilized fine-grained soils. *Int. J. Eng. Trans. B Appl.* **2017**, *30*, 1673–1680. [CrossRef]

58. Sukprasert, S.; Hoy, M.; Horpibulsuk, S.; Arulrajah, A.; Rashid, A.S.A.; Nazir, R. Fly ash-based geopolymer stabilization of silty clay/blast furnace slag for subgrade applications. *Road Mater. Pavement Des.* **2021**, *22*, 357–371. [CrossRef]

59. Noolu, V.; Mallikarjuna Rao, G.; Sudheer Kumar Reddy, B.; Chavali, R.V.P. Strength, and durability characteristics of GGBS geopolymer stabilized black cotton soil. *Mater. Today Proc.* **2020**, *43*, 2373–2376. [CrossRef]

60. Samuel, R.; Puppala, A.J.; Banerjee, A.; Huang, O.; Radovic, M.; Chakraborty, S. Improvement of Strength and Volume-Change Properties of Expansive Clays with Geopolymer Treatment. *Transp. Res. Rec. J. Transp. Res. Board* **2021**, *2675*, 308–320. [CrossRef]

61. Ravi, K.; Gopal, V. Effect of Ground Granulated Blast Furnace Slag and Metakaolin on Geotechnical Properties of Clayey Soil. *ICSWMD* **2019**, *21*, 386–392. [CrossRef]

62. Abdullah, H.H.; Shahin, M.A.; Walske, M.L.; Karrech, A. Systematic approach to assessing the applicability of fly-ash-based geopolymer for clay stabilization. *Can. Geotech. J.* **2020**, *57*, 1356–1368. [CrossRef]

63. Alam, S.; Das, S.K.; Rao, B.H. Strength and durability characteristic of alkali activated GGBS stabilized red mud as geo-material. *Constr. Build. Mater.* **2019**, *211*, 932–942. [CrossRef]

64. Toryila, T.M. Expansive Soil Stabilization Using Industrial Solid Wastes an Expansive Soil Stabilization Using Industrial Solid Wastes a Review. *Int. J. Adv. Technol. Eng. Sci.* **2016**, *4*, 636–646.

65. Dayalan, J. Comparative Study on Stabilization of Soil with Ground Granulated Blast Furnace Slag (GGBS) and Fly Ash. *Int. Res. J. Eng. Technol.* **2016**, *3*, 2198–2204.

66. Oormila, T.R.; Preethi, T.V. Effect of Stabilization Using Flyash and GGBS in Soil Characteristics. *Int. J. Eng. Trends Technol.* **2014**, *11*, 284–289. [CrossRef]

67. Sharma, A.K.; Sivapullaiah, P.V. Ground granulated blast furnace slag amended fly ash as an expansive soil stabilizer. *Soils Found.* **2016**, *56*, 205–212. [CrossRef]

68. Simatupang, M.; Mangalla, L.K.; Edwin, R.S.; Putra, A.A.; Azikin, M.T.; Aswad, N.H.; Mustika, W. The mechanical properties of fly-ash-stabilized sands. *Geosciences* **2020**, *10*, 132. [CrossRef]

69. Tyagi, A.; Soni, D.K. *Effects of Granulated Ground Blast Furnace Slag and Fly Ash on Stabilization of Soil*; Springer: Singapore, 2019.

70. Mujtaba, H.; Aziz, T.; Farooq, K.; Sivakugan, N.; Das, B.M. Improvement in Engineering Properties of Expansive Soils using Ground Granulated Blast Furnace Slag. *J. Geol. Soc. India* **2018**, *92*, 357–362. [CrossRef]

71. Tigue, A.A.S.; Malenab, R.A.J.; Dungca, J.R.; Yu, D.E.C.; Promentilla, M.A.B. Chemical stability and leaching behavior of one-part geopolymer from soil and coal fly ash mixtures. *Minerals* **2018**, *8*, 411. [CrossRef]

72. Tigue, A.A.S.; Dungca, J.R.; Hinode, H.; Kurniawan, W.; Promentilla, M.A.B. Synthesis of a one-part geopolymer system for soil stabilizer using fly ash and volcanic ash. *Minerals* **2018**, *156*, 05017. [CrossRef]

73. Thomas, A.; Tripathi, R.K.; Yadu, L.K. A Laboratory Investigation of Soil Stabilization Using Enzyme and Alkali-Activated Ground Granulated Blast-Furnace Slag. *Arab. J. Sci. Eng.* **2018**, *43*, 5193–5202. [CrossRef]

74. Abdila, S.R.; Mustafa, M.; Bakri, A.; Ahmad, R.; Zamree, S.; Rahim, A.; Rychta, M.; Wnuk, I.; Nabiałek, M.; Muskalski, K.; et al. Evaluation on the Mechanical Properties of Ground Granulated Blast Slag (GGBS) and Fly Ash Stabilized Soil via. *Materials* **2021**, *14*, 2833. [CrossRef]

75. Parhi, P.S.; Garanayak, L.; Mahamaya, M.; Das, S.K. Stabilization of an Expansive Soil Using Alkali Activated Fly ash based Geopolymer. *Sustain. Civ. Infrastruct.* **2018**, *1*, 36–50. [CrossRef]

76. 4609 AD. *Standard Guide for Evaluating Effectiveness of Admixtures for Soil Stabilization*; ASTM International: West Conshohocken, PA, USA, 2017; Volume 4, p. 5.

77. 2166 AD. *Standard Test Method for Unconfined Compressive Strength of Cohesive Soil*; ASTM International: West Conshohocken, PA, USA, 2000; Volume 4, pp. 1–9.

78. Aziz, I.H. Behaviour changes of ground granulated blast furnace slag geopolymers at high temperature. *Adv. Cem. Res.* **2019**, *32*, 465–475. [CrossRef]

79. Taylor, P.; Journal, A.I.; Rao, F.; Liu, Q. Geopolymerization and Its Potential Application in Mine Tailings Consolidation: A Review Geopolymerization and Its Potential Application in Mine Tailings Consolidation: A Review. *Miner. Process. Extr. Metall. Rev.* **2015**, *36*, 399–409. [CrossRef]

80. Ibrahim, A.; Abbas, J.M.; Shihab, A.M. Effect of NaOH molar concentration to soft clayey soil stabilized by fly ash-based geopolymer mechanical strength subjected to initial heating. *Int. J. Eng. Res. Sci. Technol.* **2018**, *7*, 1–9.

81. Leong, H.Y.; Ong, D.E.L.; Sanjayan, J.G.; Nazari, A. Strength Development of Soil–Fly Ash Geopolymer: Assessment of Soil, Fly Ash, Alkali Activators, and Water. *J. Mater. Civ. Eng.* **2018**, *30*, 04018171. [CrossRef]

82. Sharma, K.; Kumar, A. Utilization of industrial waste—Based geopolymers as a soil stabilizer—A review. *Innov. Infrastruct. Solut.* **2020**, *5*, 97. [CrossRef]

83. Wang, Z.; Lu, D.; Process, G.; Nwonu, D.C. A review on geopolymerisation in soil stabilization A review on geopolymerisation in soil stabilization. *Mater. Sci. Eng.* **2019**, *495*, 012070. [CrossRef]

84. Khadka, S.D.; Jayawickrama, P.W.; Senadheera, S.; Segvic, B. Transportation Geotechnics Stabilization of highly expansive soils containing sulfate using metakaolin and fly ash based geopolymer modified with lime and gypsum. *Transp. Geotech.* **2020**, *23*, 100327. [CrossRef]

85. Disu, A.A.; Kolay, P.K. A Critical Appraisal of Soil Stabilization Using Geopolymers: The Past, Present and Future. *Int. J. Geosynth. Gr. Eng.* **2021**, *7*, 23. [CrossRef]

86. Parikshith, M.V.; Sekhar, D.C. Feasibility of Flyash based Geopolymer for Soil Stabilization. *Int. J. Innov. Technol. Explor. Eng.* **2019**, *9*, 4348–4351. [CrossRef]

87. Xie, J.; Kayali, O. Effect of superplasticiser on workability enhancement of Class F and Class C fly ash-based geopolymers. *Constr. Build. Mater.* **2016**, *122*, 36–42. [CrossRef]

88. Phummiphan, I.; Horpibulsuk, S.; Rachan, R.; Arulrajah, A.; Shen, S.; Chindaprasirt, P. Revised manuscript HAZMAT-D-17-00478R2 High Calcium Fly Ash Geopolymer Stabilized Lateritic Soil and Granulated Blast Furnace Slag Blends as a Pavement Base Material. *J. Hazard. Mater.* **2017**, *341*, 257–267. [CrossRef]

89. Khasib, I.A.; Norsyahariati, N.; Daud, N. Physical and Mechanical Study of Palm Oil Fuel Ash (POFA) based Geopolymer as a Stabilizer for Soft Soil. *Sci. Technol.* **2020**, *28*, 149–160.

90. Priyadharshini, P.; Ramamurthy, K.; Robinson, R.G. Applied Clay Science Excavated soil waste as fi ne aggregate in fly ash based geopolymer mortar. *Appl. Clay Sci.* **2017**, *146*, 81–91. [CrossRef]

91. Provis, J.L. Alkali-activated materials. *Cem. Concr. Res.* **2018**, *114*, 40–48. [CrossRef]

92. Aziz, I.H.; Zulkifly, K.; Sakkas, K.; Panias, D.; Tsaousi, G.M.; Bakri, M.M.A.; Al Yong, H.C. The Characterization of Steel Slag by Alkali Activation. *OALib* **2017**, *4*, 1–13. [CrossRef]

93. Zaliha, S.; Zuber, S.; Mustafa, M.; Bakri, A.; Hussin, K.; Ahmad, F.; Binhussain, M. The Influence of Geopolymerization Process on Liquid and Plastic Limits of The Influence of Geopolymerization Process on Liquid and Plastic Limits of Soils. *Appl. Mech. Mater.* **2015**, *754*, 886–891. [CrossRef]

94. Zaliha, S.Z.S.; Al Bakri, A.M.M.; Kamarudin, H.; Fauziah, A. Characterization of soils as potential raw materials for soil stabilization application using geopolymerization method. *Mater. Sci. Forum* **2015**, *803*, 135–143. [CrossRef]

95. Wazien, W. Strength and Density of Geopolymer Mortar Cured at Ambient Temperature for Use as Repair Material Strength and Density of Geopolymer Mortar Cured at Ambient Temperature for Use as Repair Material. *Mater. Sci. Eng.* **2016**, *133*, 012042. [CrossRef]

96. Department, P.W. Development of Design Guidelines for Rural Low Volume Roads in Malaysia. In Proceedings of the ARRB Conference—Shaping the Future: Linking Policy, Research and Outcomes, Perth, Australia, 23–26 September 2012; Volume 1, pp. 1–12.

97. Alonso, S.; Palomo, A. Calorimetric study of alkaline activation of calcium hydroxide-metakaolin solid mixtures. *Cem. Concr. Res.* **2001**, *31*, 25–30. [CrossRef]

98. Aizat, E.A. Dolomite/fly ash alkali activated geopolymer strengths with the influence of solid/liquid ratio Dolomite/Fly Ash Alkali Activated Geopolymer Strengths with the Influence of Solid/Liquid Ratio. *MATEC Web Conf.* **2018**, *78*, 020274. [CrossRef]

99. Zhang, M.; Guo, H.; El-Korchi, T.; Zhang, G.; Tao, M. Experimental feasibility study of geopolymer as the next-generation soil stabilizer. *Constr. Build. Mater.* **2013**, *47*, 1468–1478. [CrossRef]

100. Ayyappan, A. Influence of Geopolymers in the Stabilization of Clayey soil. *Int. J. Emerg. Technol. Eng. Res.* **2017**, *5*, 108–120.

101. Dheyab, W.; Ismael, Z.T.; Hussein, M.A.; Bin, B.; Huat, K. Soil Stabilization with Geopolymers for Low Cost and Environmentally Friendly Construction. *Int. J. GEOMATE* **2019**, *17*, 271–280. [CrossRef]

102. Trinh, S.H.; Anh, Q.; Bui, T. Influencing of Clay, and Binder Content on Compression Strength of Soft Soil Stabilized by Geopolymer Based Fly Ash. *Int. J. Appl. Eng. Res.* **2018**, *13*, 7954–7958.

103. Ghugal, Y.M. Effect of Fineness of Fly Ash on Flow and Compressive Strength of Geopolymer Concrete Effect of fly ash fineness on workability and compressive strength of geopolymer concrete. *Indian Concr. J.* **2013**, *1*, 57–62.

104. Liu, Z.; Asce, S.M.; Cai, C.S.; Ph, D.; Asce, F.; Liu, F.; Fan, F.; Ash, F. Feasibility Study of Loess Stabilization with Fly Ash—Based Geopolymer. *J. Mater. Civ. Eng.* **2016**, *28*, 04016003. [CrossRef]

105. Malkawi, A.B.; Fadhil, M.; Fauzi, A.; Almattarneh, H. Effects of Alkaline Solution on Properties of the HCFA Geopolymer Mortars. *Procedia Eng.* **2016**, *148*, 710–717. [CrossRef]

106. Phetchuay, C.; Horpibulsuk, S.; Arulrajah, A. Applied Clay Science Strength development in soft marine clay stabilized by fly ash and calcium carbide residue based geopolymer. *Appl. Clay Sci.* **2016**, *127*, 134–142. [CrossRef]

107. Burduhos Nergis, D.D.; Vizureanu, P.; Corbu, O. Synthesis and characteristics of local fly ash-based geopolymers mixed with natural aggregates. *Rev. Chim.* **2019**, *70*, 1262–1267. [CrossRef]

108. Burduhos Nergis, D.D.; Vizureanu, P.; Ardelean, I.; Sandu, A.V.; Corbu, O.C.; Matei, E. Revealing the Influence of Microparticles on Geopolymers' Synthesis and Porosity. *Materials* **2020**, *13*, 3211. [CrossRef]

109. Kwek, S.Y. Influence of Liquid-to-Solid and Alkaline Activator (Sodium Silicate to Sodium Hydroxide) Ratios on Fresh and Hardened. *Materials* **2021**, *14*, 4253. [CrossRef] [PubMed]

110. Zaliha, S. Review on Soil Stabilization Techniques Review on Soil Stabilization Techniques. *Aust. J. Basic Appl. Sci.* **2013**, *7*, 258–265.

111. Tempest, B.; Sanusi, O.; Gergely, J.; Ogunro, V.; Weggel, D. Compressive Strength and Embodied Energy Optimization of Fly Ash-Based Geopolymer Concrete. In Proceedings of the 3rd World Coal Ash, WOCA Conference, Lexington, KY, USA, 4–7 May 2009; Volume 1, pp. 1–17.

Article

Mechanical and Durability Analysis of Fly Ash Based Geopolymer with Various Compositions for Rigid Pavement Applications

Muhammad Faheem Mohd Tahir [1,2,*], Mohd Mustafa Al Bakri Abdullah [1,2,*], Shayfull Zamree Abd Rahim [1,3], Mohd Rosli Mohd Hasan [4], Andrei Victor Sandu [5,6,*], Petrica Vizureanu [5,7,*], Che Mohd Ruzaidi Ghazali [8] and Aeslina Abdul Kadir [9]

1 Centre of Excellence Geopolymer and Green Technology, (CEGeoGTech), Universiti Malaysia Perlis, Perlis 01000, Malaysia; shayfull@unimap.edu.my
2 Faculty of Chemical Engineering Technology, Universiti Malaysia Perlis, Perlis 01000, Malaysia
3 Faculty of Mechanical Engineering Technology, Universiti Malaysia Perlis, Perlis 01000, Malaysia
4 School of Civil Engineering, Universiti Sains Malaysia, Pulau Pinang 14300, Malaysia; cerosli@usm.my
5 Faculty of Material Science and Engineering, Gheorghe Asachi Technical University of Iasi, 41 D. Mangeron St., 700050 Iasi, Romania
6 Romanian Inventors Forum, St. P. Movila 3, 700089 Iasi, Romania
7 Technical Sciences Academy of Romania, Dacia Blvd 26, 030167 Bucharest, Romania
8 Faculty of Ocean Engineering Technology and Informatic, Universiti Malaysia Terengganu, Kuala Terengganu 21030, Malaysia; ruzaidi@umt.edu.my
9 Faculty of Civil Engineering and Built Environment, Universiti Tun Hussein Onn Malaysia, Parit Raja 86400, Malaysia; aeslina@uthm.edu.my
* Correspondence: faheem@unimap.edu.my (M.F.M.T.); mustafa_albakri@unimap.edu.my (M.M.A.B.A.); sav@tuiasi.ro (A.V.S.); peviz@tuiasi.ro (P.V.)

Abstract: Ordinary Portland cement (OPC) is a conventional material used to construct rigid pavement that emits large amounts of carbon dioxide (CO_2) during its manufacturing process, which is bad for the environment. It is also claimed that OPC is susceptible to acid attack, which increases the maintenance cost of rigid pavement. Therefore, a fly ash based geopolymer is proposed as a material for rigid pavement application as it releases lesser amounts of CO_2 during the synthesis process and has higher acid resistance compared to OPC. This current study optimizes the formulation to produce fly ash based geopolymer with the highest compressive strength. In addition, the durability of fly ash based geopolymer concrete and OPC concrete in an acidic environment is also determined and compared. The results show that the optimum value of sodium hydroxide concentration, the ratio of sodium silicate to sodium hydroxide, and the ratio of solid-to-liquid for fly ash based geopolymer are 10 M, 2.0, and 2.5, respectively, with a maximum compressive strength of 47 MPa. The results also highlight that the durability of fly ash based geopolymer is higher than that of OPC concrete, indicating that fly ash based geopolymer is a better material for rigid pavement applications, with a percentage of compressive strength loss of 7.38% to 21.94% for OPC concrete. This current study contributes to the field of knowledge by providing a reference for future development of fly ash based geopolymer for rigid pavement applications.

Keywords: rigid pavement; fly ash based geopolymer; compressive strength; acid resistance

1. Introduction

Pavements are an essential part of our life as we use them as roads, highways, driveways, and parking lots. Pavements are an important engineering structure for trading, commerce, and defence because they provide a smooth, flat, and durable all-weather travelling surface for a variety of vehicles and users. The construction of pavements will continue to be a major industry for both developing and developed countries. Pavements can be

divided into two types, asphalt (or flexible) pavements and concrete (or rigid) pavements, which are composed of different layers [1]. Binder or surface, base, subbase, and subgrade are the layers from top to bottom. The primary function of pavements is to distribute load from the surface to the sub-grade, allowing them to withstand the load applied by vehicles or users without deforming excessively.

The initial construction cost of flexible pavement is lower when compared to rigid pavement, as bituminous surfacing materials are cheap, and construction of flexible pavement does not require extra reinforcements such as joints and steel bars. Furthermore, thermal stress cannot be induced, as flexible pavement is free to contract and relax, thus it is more resistant to temperature changes [2]. Rutting, which is a permanent deformation or rut depth along the wheel load part on the movable asphalt surface over time, is a major distress mode for flexible pavement [3]. In addition, it is more susceptible to oil stains and chemical damages. However, among all types of road pavements, rigid pavements have the greatest advantages in terms of durability and ability to maintain shape under continuous traffic and harsh environmental conditions. Although rigid pavements are generally expensive, they require less maintenance and have a good design life [4]. However, the installation and maintenance process of rigid pavements, such as grouting and subgrade treatment are expensive. Table 1 summarises the major benefits and drawbacks of each type of pavements previously discussed.

Table 1. Basic characteristics of flexible and rigid road pavements [4].

Type of Pavement	Advantages	Disadvantages
Flexible Pavements	- Can be used in the pre-construction stage - Simple maintenance; can be opened and repaired - Inexpensive materials - Can easily repair frost swelling and sedimentation - Prevent ice glaze formation - Shorter management time means shorter traffic and business interruption - No connectors required during installation	- The service life is shorter than that of rigid pavements - Frequent maintenance is required, which increases costs - Easily damaged by oil stains and other chemicals - The edges are weak, so curb structures or edges are needed
Rigid Pavements	- Longer service life - Less maintenance - Allows future asphalt resurfacing - Allows for wider load distribution with fewer basic and sub-basic requirements - Can be installed on low-quality and high-quality soil - Does not require extra trimming work or firm edges of curbs - Oil spills and chemical damage resistant	- Expensive initial installation - Expensive maintenance cost - Riding quality is low and very rough - Concrete shrinkage and expansion under various conditions require support joints

Both flexible and rigid pavements are vital to the economic and social development of a country because they contribute to other sectors, namely, education, health, employment, and social services. The mechanical and durability characteristics of the road surface are equally important for providing resistance to degradation processes during the expected life of the road surface. The durability of concrete mainly depends on the characteristics of the pore structure of the pavement and the size of the cracks. Water penetration, chloride ions, CO_2, acids (including chlorides), and sulphates in the pavements are all related to its durability [2–4].

Rigid pavements are constructed by placing concrete slab on a stabilized subgrade, or base, or subbase if extra structural support is required. Most of the rigid pavements are made of Portland cement concrete (PCC), which has a high rigidity, flexural strength, and modulus of elasticity, allowing the load to be evenly distributed over a larger area of soil and providing a large portion of the structural capacity [5]. However, the production of

cement is an energy consuming and carbon-intensive process, and it is a main contributor to global CO_2 emission [6–9]. The cement industry is one of the largest sources of CO_2, where production of one ton of cement will release approximately 900 kg of carbon dioxide into the environment, causing global warming and depletion of the ozone layer [7]. Aside from emission of large amounts of CO_2, there are also other disadvantages found in rigid pavement constructed by ordinary Portland cement (OPC). PCC has a low resistance to chemical attack. Acid corrosion resistance of OPC is rather poor because of the nature of high pH and porous matrix. Acid can react with CH and C-S-H gel in cement concrete to form non-gelling or water-soluble substances, resulting in the destruction of the concrete. To overcome these disadvantages, fly ash based geopolymer is introduced as an alternative to OPC.

Fly ash based geopolymer can be produced by activating fly ash, which is rich in silica, and alumina material with alkaline solution [10], and it is defined as a binding phase comprising aluminosilicate gel where aluminium and silicon are linked into a three-dimensional tetrahedral gel framework [11]. It has several advantages compared to OPC. First, fly ash based geopolymer has higher durability than OPC, as it has denser layer of aluminosilicate gel, causing it to have low permeability and preventing it from corrosion by acid [9]. It is also proven that production of fly ash based geopolymer can emit 5 to 6 times less CO_2 when compared to OPC, as high temperature calcination is not required [12]. Fly ash based geopolymer also has higher workability than OPC due to its spherical shape [13].

In current studies [10–14], the potential role of geopolymers as a substitute for OPC in pavement production is being explored because of its significant positive impact on the environment, society, and economy. However, its performance as a rigid pavement material is limited, and there is no compelling evidence that it could replace typical OPC concrete firm pavements. Although many studies have been done on fly ash based geopolymer [9–16], the studies with regard to the optimization of mix design remain scarce. This study is an initiative in realizing that mechanical and durability properties are crucial aspects in applying fly ash based geopolymer as rigid pavements. In this research, the optimum ratio of fly ash/alkaline activator, sodium silicate/sodium hydroxide, and concentration of sodium hydroxide to yield fly ash based geopolymer concrete that has optimum strength for newly constructed rigid pavements are investigated. In addition, the durability of fly ash based geopolymer and OPC rigid concrete pavement in acidic environment are investigated and compared.

2. Materials and Method

2.1. Materials

In this study, class F fly ash based on ASTM C618 [17] was used as the raw material and source material for the geopolymer binder, aluminosilicates. Fly ash was collected from Manjung Power Station, located in Lumut, Perak, Malaysia. Sodium hydroxide and sodium silicate were used to produce an alkaline activator. Sodium hydroxide (NaOH) pellets were obtained from Formosa Plastic Corporation, Taiwan, and sodium silicate (Na_2SiO_3) solution was supplied by South Pacific Chemical Industries Sdn. Bhd. (SPCI), Perai, Penang, Malaysia. Coarse aggregates, which consist of crushed stone with particle size larger than 5 mm, and fine aggregates, which consist of sand obtained from the river, were used for making the concrete mixes. Five percent sulphuric acid solution was used to test the acid resistance of the concrete mixes.

2.2. Methodology

The investigation of fly ash based geopolymer for rigid pavement application is divided into four phases. Based on Figure 1a, Phase 1 is raw material characterization. In this stage, the morphology of class F fly ash is determined using scanning electron microscopy (SEM), JEOL Ltd., Tokyo, Japan, and the chemical composition of class F fly ash is determined using X-ray fluorescence (XRF), Bruker Malaysia Sdn. Bhd., Penang, Malaysia. The microstructure analysis of fly ash is in the form of powder that is spread onto

a carbon tape. The samples are then coated with palladium by using Auto Fine Coater JEOL JFC 1600 model prior to testing. Phase 2 is the synthesis of fly ash based geopolymer using different mix designs, and determination of density, water absorption, and compressive strength of the samples.
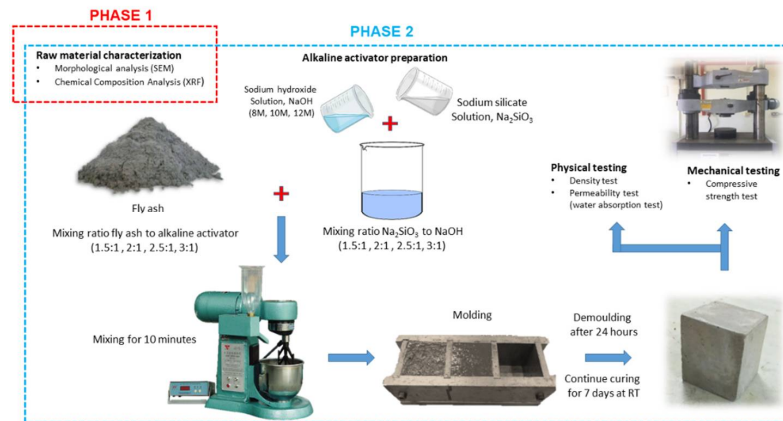
(**a**)

(**b**)

Figure 1. (**a**) Flow chart for fly ash based rigid pavements application process (Phase 1 and Phase 2). (**b**) Flow chart for fly ash based rigid pavement application process. (Phase 3 and Phase 4).

Fly ash based geopolymer is prepared by mixing class F fly ash with the alkaline activator. To achieve good solid–liquid homogeneity, sodium hydroxide was mixed with sodium silicate for a few minutes before fly ash is added, according to ASTM C305 [18]. After fly ash has been added, a scraper was used to tamp into the mould several times to release the air trapped in the geopolymer paste. Another way to release the trapped air is to vibrate the mould. The solution was mixed quickly to prevent it from curing before casting. In this study, the effects of concentration of NaOH, ratio of solid-to-liquid, and ratio of sodium silicate to sodium hydroxide on density, water absorption, and compressive strength were investigated. The best mix design that produces fly ash based geopolymer with optimum compressive strength required for rigid pavement application was determined.

Based on Figure 1b, Phase 3 includes the synthesis of OPC concrete and fly ash based geopolymer concrete using the optimum mix design determined from Phase 2. Both types of concrete were made using the same mix design. There was no addition of water during synthesis of geopolymer concrete as it has already obtained water from the alkaline solution. Table 2 shows the ratio of material based on M40 mix design.

Table 2. Mix design for grade M40 design.

Cement/Binder	Fine Aggregates	Coarse Aggregates	Water/Cement Ratio
1	1.84	2.65	0.4

The fourth phase is the durability testing of fly ash based geopolymer concrete and OPC concrete exposed in an acidic environment in accordance with ASTM C267 [19]. An acid immersion test was carried out, and the percentage of compressive strength loss and weight loss was calculated to determine the durability of both concretes after immersing in 5% sulphuric acid. Next, visual inspection was done on both concrete samples.

3. Result and Discussion

3.1. Chemical Composition of Fly Ash

The most abundant chemical content in fly ash is silicon dioxide (SiO_2), which accounts for 52.11% according to the XRF analysis. Silica in silicon dioxide is the source material for the geopolymer, as the product of geopolymer synthesis is an aluminosilicate gel that requires silica to be formed [13]. The gel undergoes further geopolymerisation by eliminating water and converting it into strong and durable material with excellent mechanical strength [20]. The second most abundant chemical content is alumina (Al_2O_3), which accounts for 23.59% in fly ash. Al_2O_3 is also the main component of geopolymer, as it is a polymeric chain made up of silica and alumina that shares the oxygen ion. Al_2O_3 and SiO_2 react with alkaline activators, namely, NaOH and Na_2SiO_3, in the geopolymerisation process.

Iron oxide (Fe_2O_3) is one of the main chemical constituents, which accounts for 7.39% in fly ash. It contributes to the dark colour of fly ash. Aside from appearance, it also increases the specific gravity value of fly ash. The percentage of calcium oxide (CaO) content in fly ash is 2.61%. During the geopolymerisation process, calcium oxide forms CSH and CASH gels within geopolymer binder, and these gels are responsible for the increase in strength and reduction in setting time [21]. The calcium content in the raw material is considered as low, resulting in the geopolymer having longer setting time. Loss of ignition (LOI) content in fly ash is 9.59%, which is considered high, as ASTM C618 [12] prescribes a maximum of LOI content of 6% by weight. LOI quantifies the total content of unburned coal residue. High LOI causes detrimental effects that include high water demand, leading to high porosity and reducing the compressive strength of prepared geopolymers. There were also other chemical compounds found in fly ash. Table 3 tabulates the chemical composition of fly ash collected from Manjung Power Station, which is located in Lumut, Perak, Malaysia.

Table 3. Fly ash chemical composition by X-ray fluorescence (XRF).

Chemical Composition	Percentage (%)
SiO_2	52.11
Al_2O_3	23.59
Fe_2O_3	7.39
TiO_2	0.88
CaO	2.61
MgO	0.78
Na_2O	0.42
K_2O	0.80
P_2O_5	1.31
SO_3	0.49
MnO	0.03
LOI	9.59

For class F fly ash, ASTM C618 [17] specifies a total composition of silicon oxide (SiO_2), alumina (Al_2O_3), and iron oxide (Fe_2O_3) of at least 70%, and less than 10% calcium oxide (CaO). As the total content of SiO_2, Al_2O_3, and Fe_2O_3 is 83.09% and CaO content is 2.61%, it is classified as Class F fly ash.

3.2. Morphological Analysis of Fly Ash

Using ImageJ Ver. 1.5 software, the fly ash particle was shown to have a mean particle size of 4.543 μm with a minimum of 1.903 μm and a maximum of 11.534 μm. It can be seen that fly ash consists of series of cenosphere particles of different sizes. Cenospheres are hollow spherical particles filled with gas that is mostly CO_2 and nitrogen (N_2). When undergoing alkaline attack, the wall of cenospheres will dissolve and release Si and Al ions as supported by Rahman [22]. There were also some irregularly shaped particles observed. This is because the original mineral in coal is not sufficiently fired. The coarse particles that appear to consist of a cluster of fine particles are possibly formed by aggregation of molten aluminosilicate droplets during cooling, where fine droplets could minimize surface free energy. Figure 2 illustrates the morphological characteristics of Class F fly ash using SEM analysis.
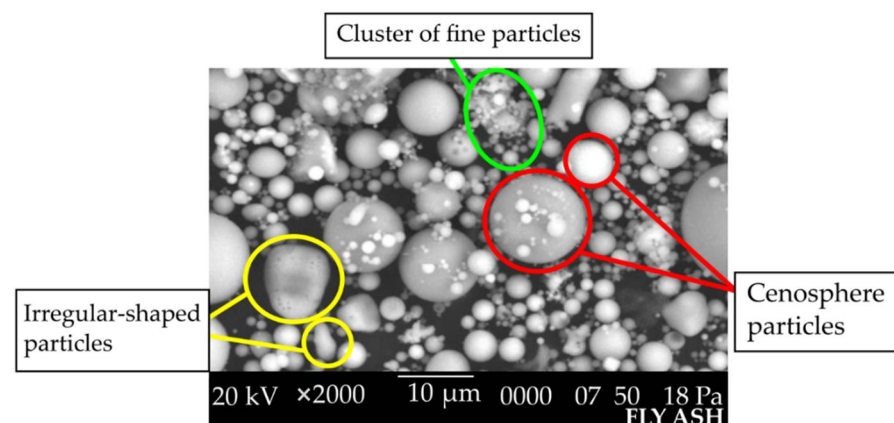
Figure 2. SEM micrograph of fly ash.

Geopolymer synthesis starts with the leaching of silica and alumina on the surface of fly ash. The spherical shape and fine size of fly ash particles allows a large surface area to be exposed to the alkaline activator and increases the dissolution rate. The higher the surface area and the higher the number of particles, the better the aluminosilicate gel formation. The fine particle size of fly ash also helps to increase compressive strength and accelerate initial setting time of geopolymer. The spherical shape also causes the sliding between particles to be easier, resulting in high flowability geopolymer paste. Therefore, the amount

of liquid required to produce geopolymer paste would be lower. This is crucial because the less water used, the lower the porosity, as previous studies have shown [22–25].

3.3. Optimization of Fly Ash Based Geopolymer for Rigid Pavement Application

3.3.1. Effect of Molarity of NaOH on Density of Fly Ash Based Geopolymer

Figure 3 illustrates the density values of geopolymer paste with different molarities of sodium hydroxides after 7 days curing period at room temperature. Based on Figure 3, the density increases when NaOH molarity increases from 8 M to 10 M, which is from 1861.33 kg/m^3 to 1908.00 kg/m^3, respectively. However, the density then decreases to 1896.00 kg/m^3 when NaOH molarity is further increased to 12 M. The density of geopolymer is the lowest at 8 M, which is 1861.33 kg/m^3, and highest at 10 M, which is 1908.00 kg/m^3.
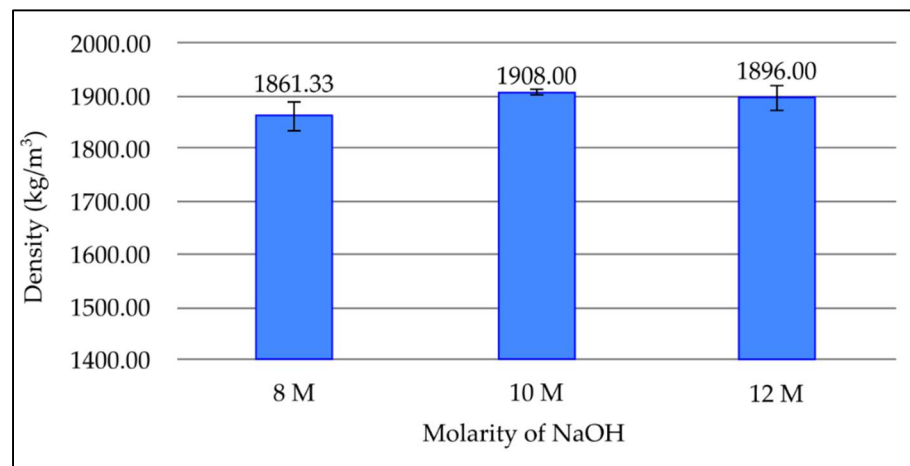
Figure 3. Density of fly ash based geopolymer with different molarities of NaOH.

It can be seen that NaOH concentration does not have a significant effect on density. The density of fly ash based geopolymer increased slightly when NaOH concentration increases to 10 M. This is because at this concentration, there are enough Na$^+$ and OH$^-$ ions to complete the geopolymerisation process and form dense aluminosilicate gel. At high concentration, fly ash undergoes a greater dissolution process from the leaching of silica and alumina [24]. However, the density reduces as molarity increased to 12 M. Due to fast setting, increasing the NaOH concentration may result in paste with lower density due to a mixing problem. The higher concentration of NaOH limits the flow of geopolymer and reduces the setting time. This causes poor compaction and increases the porosity of the geopolymer, resulting in low density.

3.3.2. Effect of Molarity of NaOH on Water Absorption of Fly Ash Based Geopolymer

Figure 4 shows the effect of different molarities of sodium hydroxides on water absorption in geopolymer paste after 7 days curing period at room temperature. Based on Figure 4, the water absorption percentage decreases when molarity increases to 10 M, which is 15.54% at 8 M and 15.36% at 10 M. Furthermore, the water absorption percentage increases to 15.52% when the molarity further increased to 12 M. The maximum water absorption percentage is recorded at a molarity of 8 M, which is 15.54%, whereas the minimum value is recorded at 10 M, which is 15.36%.
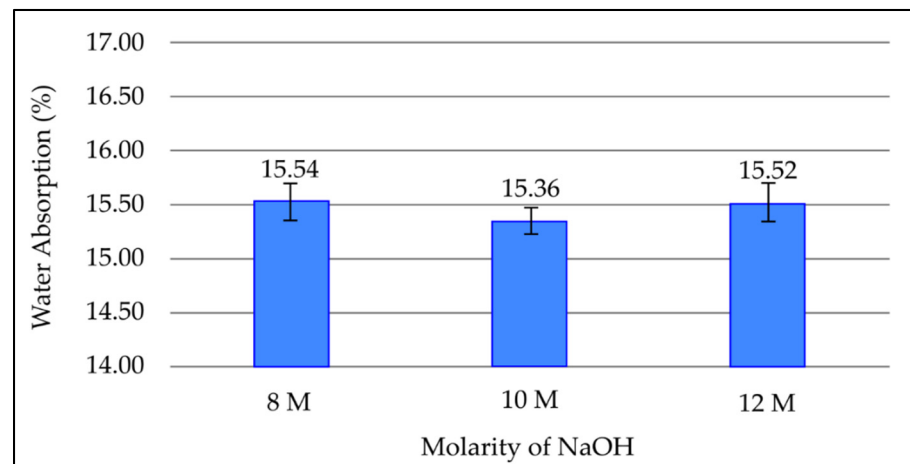
Figure 4. Water absorption of fly ash based geopolymer with different molarities of NaOH.

The effect of NaOH concentration on water absorption of fly ash based geopolymer is not significant. Water absorption of the geopolymer decreases a little when molarity increases to 10 M. This is because as concentration of NaOH solution increases, the leaching of silica and alumina ion increases as well. Sufficient amounts of Si^{4+} and Al^{3+} ions allow more aluminosilicate gel to form and reduce the pores in the geopolymer, thus reducing water absorption of the material. Water absorption then increases again at a molarity of 12 M. This is due to excess concentration of sodium hydroxide that causes unreactive alkali solution, which weakens the binding of sodium components in the geopolymer structure. Similar results were obtained from another study where 10 M NaOH was found to be the optimum value for synthesis of fly ash based geopolymer [26].

3.3.3. Effect of Molarity of NaOH on Compressive Strength of Fly Ash Based Geopolymer

Figure 5 shows the effect of various sodium hydroxide molarities on compressive strength in geopolymer paste after 7 days curing period at room temperature. Based on Figure 5, the compressive strength of geopolymer increases when molarity of NaOH increases with values of 15.57 MPa and 31.48 MPa for molarities of 8 M and 10 M, respectively. The compressive strength then dropped to 18.59 MPa at a molarity of 12 M. The highest value of compressive strength was obtained at a molarity of 10 M, which is 31.48 MPa.
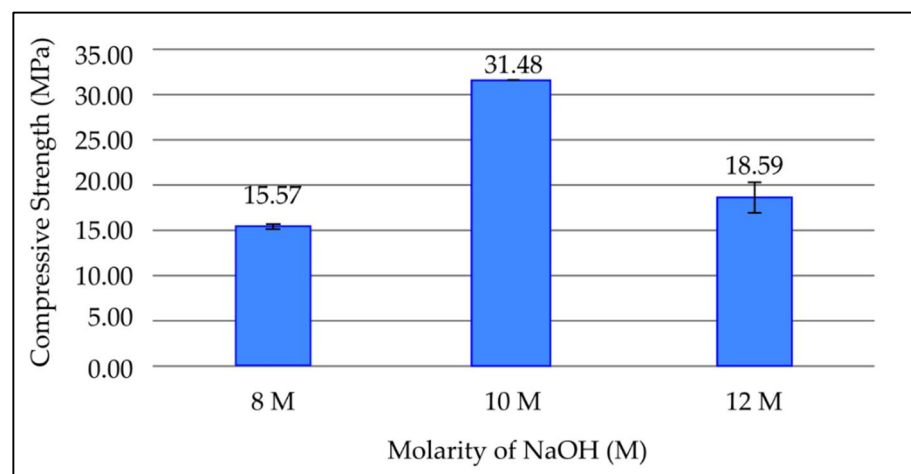
Figure 5. Compressive strength of fly ash based geopolymer with different molarities of NaOH.

The strength of the geopolymer paste is affected by the molarity of NaOH because it affects the dissolution of Si^{4+} and Al^{3+} ions in fly ash particles. The compressive strength

increases when molarity of NaOH increases due to the increase of OH$^-$ concentration, which accelerates the dissolution and hydrolysis processes. During the dissolution process, the leaching of Si^{4+} an Al^{3+} ion enhances the formation of aluminosilicate gel and contributes to high strength in the geopolymer. In addition, the amount of NaOH is high enough to maintain the charge balance for the substitution of tetrahedral Si by Al [27]. However, the compressive strength drops when the molarity of NaOH is further increased to 12 M. This is because excess hydroxide ion concentration causes aluminosilicate gel precipitation at an early age. The precipitation prevents further leaching of Si^{4+} and Al^{3+} ions, therefore lowering the compressive strength. This is supported by studies that found that 10 M is the optimum molarity of NaOH for the synthesis of fly ash based geopolymer [28].

3.3.4. Effect of NaOH to Na$_2$SiO$_3$ (SS/SH) Ratio on Density of Fly Ash Based Geopolymer

Figure 6 depicts the change in density of geopolymer samples with various SS/SH ratios after a 7-day room temperature curing period. It can be seen that the density increases until the SS/SH ratio reaches 2. However, as the SS/SH ratio increases beyond 2, the density decreases gradually to 1880 kg/m^3 and 1858 kg/m^3 at SS/SH ratios of 2.5 and 3, respectively. The lowest density obtained was 1828 kg/m^3 at an SS/SH ratio of 1.5. Density is the highest at an SS/SH ratio of 2, which is 1895 kg/m^3.
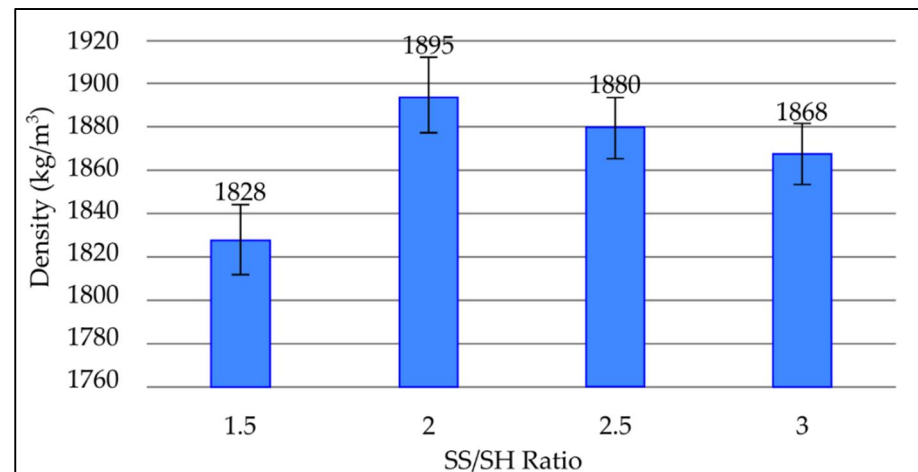
Figure 6. Density of fly ash based geopolymer with different SS/SH ratios.

As the SS/SH ratio increases to 2, the high silica content encourages the formation of N-A-S-H (sodium aluminosilicate) gel, which provides good compact structure, subsequently increasing the density of the geopolymer paste. Thus, the highest value of density is obtained at an SS/SH ratio of 2. The drop in density after the SS/SH ratio exceeds 2 is due to the excess sodium silicate, which hinders water evaporation and structure formation [29]. In addition, the excessive sodium silicate content retards the geopolymerisation process, as formation of Al-Si phase precipitation prevents interaction between reacting material and the alkaline activator [30,31]. These factors increase the porosity and reduce density of the geopolymer.

3.3.5. Effect of NaOH to Na$_2$SiO$_3$ (SS/SH) Ratio on Water Absorption of Fly Ash Based Geopolymer

Figure 7 portrays the effect of various SS/SH ratios on the water absorption percentage of a fly ash-based geopolymer after 7 days curing period at room temperature. Based on Figure 7, the water absorption percentage decreases from 17.23% at an SS/SH ratio of 1.5 to 13.65% at an SS/SH ratio of 2. The water absorption percentage then increases when the SS/SH ratio further increases from 2. The highest water absorption percentage recorded was at an SS/SH ratio of 1.5, which is 17.23%, whereas the lowest value is obtained at an SS/SH ratio of 2, which is 13.65%.
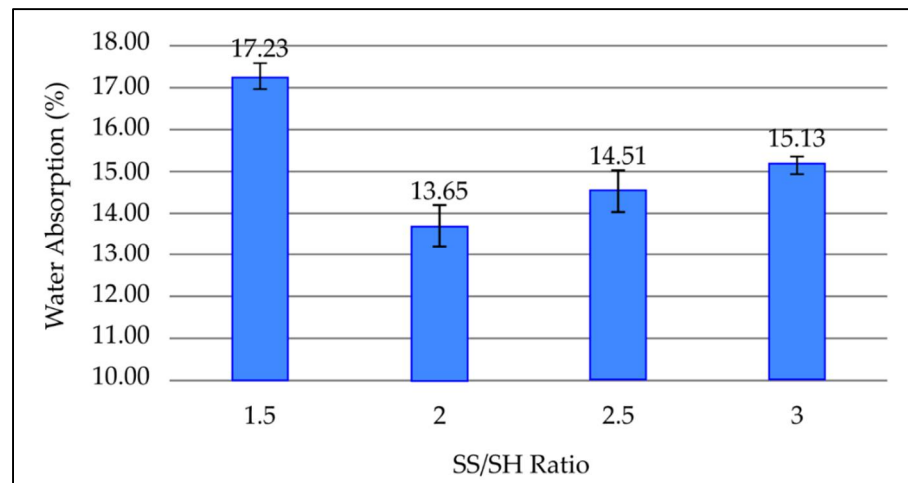
Figure 7. Water absorption percentage of fly ash based geopolymer with different SS/SH ratios.

By referring to Figure 7, the water absorption of geopolymer paste decreases as the SS/SH ratio increases to 2. As the SS/SH ratio increases, a higher ratio of sodium silicate increases the formation of N-A-S-H gel and reduces the pores in the geopolymer paste, consequently reducing water absorption. The water absorption then increases when the SS/SH ratio further increases from 2. This is because the coagulation of silica happens due to excessive amounts of sodium silicate. This coagulation separates the aluminosilicate source from the alkali activators and prevents further geopolymerisation, resulting in increased porosity and higher water absorption percentage. These findings are consistent with previous research [22,23,32].

3.3.6. Effect of NaOH to Na_2SiO_3 (SS/SH) Ratio on Water Absorption of Fly Ash Based Geopolymer

Figure 8 shows the compressive strength values for various SS/SH ratios in geopolymer paste after 7 days curing time at room temperature. Figure 8 highlights that when the SS/SH ratio increases to 2.5 and 3, the compressive strength of geopolymer steadily decreases. The maximum compressive is obtained at an SS/SH ratio of 2, which is 34.52 MPa, and the strength reduced to 32.31 MPa and 19.20 MPa at SS/SH ratios of 2.5 and 3, respectively. The lowest compressive strength obtained is 18.42 MPa at an SS/SH ratio of 1.5.
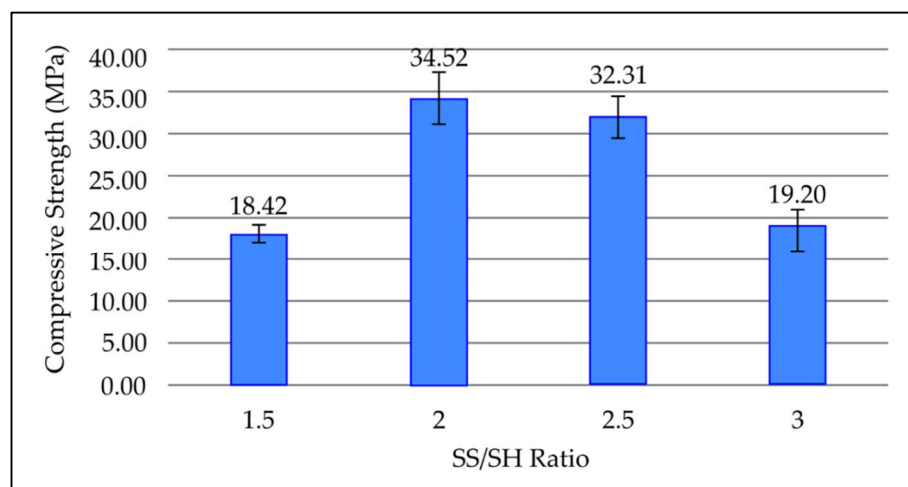
Figure 8. Compressive strength of fly ash based geopolymer with different SS/SH ratios.

Compressive strength increases when the SS/SH ratio reaches 2. As the amount of NaSiO$_3$ increases, the ratio of Si/Al increases. In comparison to aluminium, more silicon is required in the structure of geopolymers such as poly (sialate), poly (sialate-siloxo), and poly (sialate-disiloxo). In addition, high silica content promotes the formation of Si-O-Si bond, which makes materials stronger [33–35]. However, further increases in the SS/SH ratio will result in strength loss, because extra soluble silicate species hinders the reaction between silicate and aluminate species. Ultimately, the dissolution did not occur or was reduced, causing the material to lose strength and the majority of the silica to remain unreacted.

3.3.7. Effect of Solid-to-Liquid (S/L) Ratio on Density of Fly Ash Based Geopolymer

Figure 9 shows how adjusting the S/L ratio affects the density of fly ash-based geopolymer that has been cured for 7 days at room temperature. When the S/L ratio reaches 2.5, the density rises, as seen in Figure 9. However, when the S/L ratio increases to 3, the density reduces. The highest density value is found at an S/L ratio of 2.5, which is 2158.33 kg/m^3, whereas the lowest value is found at an S/L ratio of 1.5, which is 1845 kg/m^3.
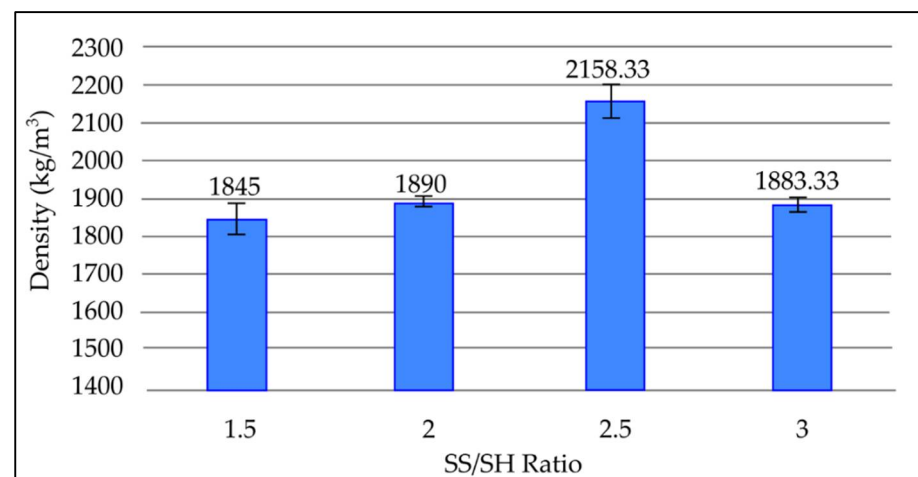
Figure 9. Density of fly ash based geopolymer with different S/L ratios.

Density increases as the S/L ratio increases until it reaches 2.5. This is due to the reduction of the alkaline activator content. High content of alkaline activator results in excessive OH$^-$ left in the system, which weakens the geopolymer structure. In addition, excess sodium content can form sodium carbonate by atmospheric carbonation and may disrupt the polymerization process [36,37]. Therefore, reduction of the alkaline activator allows denser geopolymer structure to form and increases the density of the geopolymer paste. However, density reduces as the S/L ratio increases further to 3, as high solid content reduces workability. The mixing becomes undesirable and undergoes a compaction problem during the moulding process. This increase in porosity reduces the density of geopolymer. Research conducted by Sing et al. [38] showed similar results that stated that an S/L ratio of 2.5 produced geopolymer with the highest density.

3.3.8. Effect of Solid-to-Liquid (S/L) Ratio on Water Absorption of Fly Ash Based Geopolymer

Figure 10 presents the effect of S/L ratio on water absorption of the geopolymer after being cured for 7 days at room temperature. As shown in Figure 10, the water absorption percentage of geopolymer decreases as the S/L ratio rises. When the S/L ratio exceeds 2.5, however, the percentage of water absorbed again increases. The minimum water absorption percentage is 10.81% at an S/L ratio of 2.5, whereas the highest water absorption percentage is 16.28% at an S/L ratio of 1.5.
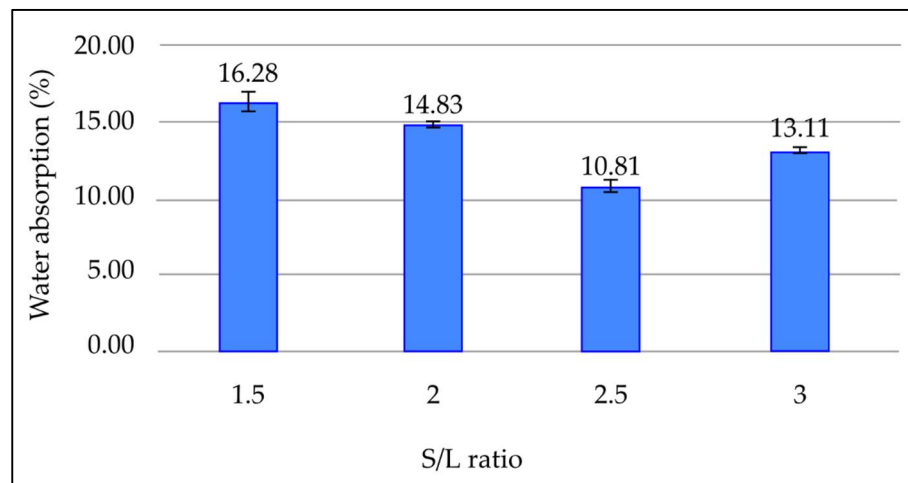
Figure 10. Water absorption percentage of fly ash based geopolymer with different S/L ratios.

The water absorption percentage decreases as the S/L ratio increases to 2.5. This is due to reduction of excessive OH⁻ contributed by the alkaline solution, which weakens the geopolymer structure. Furthermore, lowering the alkaline content prevents excess sodium from forming sodium carbonate, which stymies the geopolymerisation process. Therefore, as alkaline solution reduces and fly ash content increases to a certain extent, denser geopolymer structure could be formed, resulting in geopolymer with less porosity, and thus reduced water absorption. Water absorption percentage increases when the S/L ratio increases beyond 2.5. These results are in line with those reported by previous researchers [38]. This is because increasing the S/L ratio will increase the setting time. This reduces workability and causes difficulty in mixing and compaction, consequently resulting in more pore formation and increased water absorption percentage in geopolymer paste.

3.3.9. Effect of Solid-to-Liquid (S/L) Ratio on Compressive Strength of Fly Ash Based Geopolymer

Figure 11 shows the effect of various S/L ratios on compressive strength in geopolymer paste after 7 days curing time at room temperature. Figure 11 highlights that when the S/L ratio approaches 2.5, the compressive strength of geopolymer rises. Compressive strength reduces as the S/L ratio exceeds 2.5. The highest compressive strength is 44.03 MPa at an S/L ratio of 2.5, whereas the minimum compressive strength is 21.37 MPa at an S/L ratio of 1.5.

Compressive strength of geopolymer paste increases as the S/L ratio increases to a certain point. As the S/L ratio increases, the rate of intermolecular contact between precursor material and alkaline activator increases as the volume of fluid medium reduces. This increases the rate of dissolution of aluminosilicate material and therefore causes the compressive strength of geopolymer to rise. Further increase of the S/L ratio will reduce the compressive strength of geopolymer. This is due to insufficient alkaline activator to activate the aluminosilicate source materials, causing less reaction product to form and reducing compressive strength. Moreover, the presence of a high amount of unreacted fly ash increases the roughness of the matrix and reduces the compressive strength of the material [39,40].
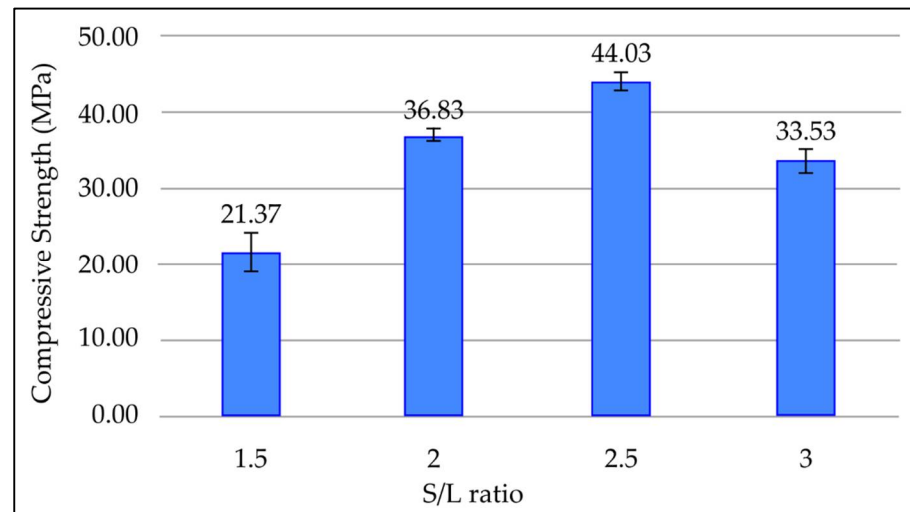
Figure 11. Compressive strength of fly ash based geopolymer with different S/L ratios.

3.4. Durability Analysis

3.4.1. Acid Resistance Test on Concrete

Figure 12 highlights the compressive strength of fly ash based geopolymer concrete and OPC concrete before and after immersing in 5% concentration of sulphuric acid for 28 days. Both concrete mixes were cured for 7 days prior to the acid immersion. According to Figure 12, the compressive strengths of fly ash based geopolymer concrete before and after exposure to acidic solution are 46.97 MPa and 43.50 MPa, respectively, whereas the compressive strengths of OPC concrete before and after exposure to acidic solution are 45.73 MPa and 35.70 MPa, respectively. The percentage of compressive strength loss for fly ash based geopolymer concrete is 7.38%, and the percentage of compressive strength loss for OPC concrete is 21.94%. The percentage of compressive strength loss for OPC concrete is higher compared to fly ash based geopolymer concrete.
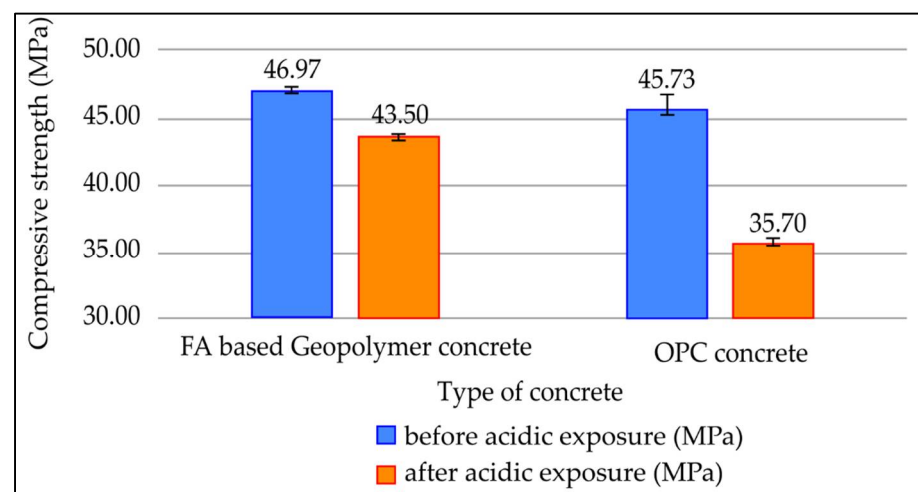
Figure 12. Compressive strength of concrete before and after acidic exposure for 28 days.

After 28 days of acidic exposure, OPC concrete had a larger percentage of compressive strength loss than fly ash based geopolymer. This is because OPC is vulnerable to acid assault due to its high calcium concentration, which raises the Ca/Si ratio. The presence of free calcium causes the cement paste to deteriorate and the creation of gypsum and ettringite, which can lead to a loss of mechanical performance. As fly ash-based geopolymers have low calcium content, the reaction produces less ettringite and gypsum after sulphuric

acid exposure, resulting in less mechanical degradation. Furthermore, due to the creation of a thick layer of aluminosilicate gel, fly ash-based geopolymers have lesser permeability, resulting in a longer decalcification process and less strength loss [41,42].

Figure 13 illustrates the weight loss of fly ash-based geopolymer concrete and OPC concrete after being cured for 7 days at room temperature and then immersed in a 5% sulphuric acid solution for 28 days. Based on the figure, OPC concrete loses 7.23% of its weight, whereas fly ash-based geopolymer loses 4.57% following acidic exposure. When compared to geopolymer concrete made with fly ash, OPC concrete lost more weight following acid immersion.
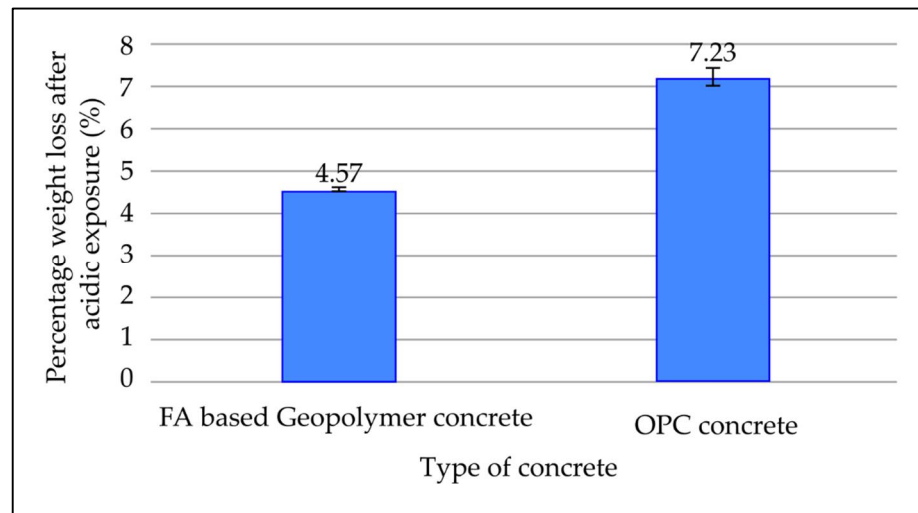
Figure 13. Percentage weight loss of concrete mixes after acidic exposure for 28 days.

OPC concrete exhibits high weight loss due to its higher calcium content. Its weight losses are mainly attributed to the reaction between calcium hydroxide, which is $Ca(OH)_2$, and sulphuric acid, which causes tensile stress and increases crack and delamination of concrete. Due to the reaction between sulphuric acid and calcium hydroxide, high calcium content in OPC concrete causes more gypsum and ettringite to form, leading to expansion, dimensional instability, cracking, spalling, softening, and mass loss. The low weight loss of fly ash based geopolymer is due to its lower content of calcium. The low calcium content causes lower formation of gypsum and ettringite [43]. The low weight loss of fly ash based geopolymer concrete is also due to its higher resistance to water penetration compared to OPC concrete. The pores in geopolymer are filled with alumino-silcates, which lower its permeability. There are more pores persisting in the OPC concrete to enable the hydration of the cement [44]. Due to low permeability, a lower amount of acid will penetrate into the structure to erode the interior.

3.4.2. Appearance of Exposed Concrete

Figure 14a shows the appearance of exposed fly ash based geopolymer concrete under an optical microscope after it is immersed in 5% sulphuric acid for 28 days, whereas Figure 14b illustrates the appearance of OPC concrete after immersion in 5% sulphuric acid for 28 days. Based on Figure 14a,b, it can be seen that the aggregates in OPC concrete are more visible after acidic exposure compared to aggregates from the surface of fly ash based geopolymer concrete. For OPC concrete, the surface erosions can be easily observed, whereas moderate surface erosions were observed in fly ash based geopolymer concrete. OPC concrete undergoes more deterioration in sulphuric acid solution compared to fly ash based geopolymer. Furthermore, the surface colour of OPC concrete changed from grey to white due to the existence of gypsum, which is white in colour, whereas the colour of fly ash geopolymer changed from grey to slightly brown due to the reaction of iron (II) oxide with sulphuric acid to produce iron (II) sulphate [45]. The yellowish line at the surface of

geopolymer is most probably the result of the reaction of ferum (II)oxide with sulfuric acid and produced ferum (II) sulfate, as shown in Figure 15.

(**a**)   (**b**)

Figure 14. Concrete sample after acidic exposure for 28 days: (**a**) geopolymer, (**b**) OPC.

$$Fe_2O_3 + 3H_2SO_4 \rightarrow \quad Fe_2(SO_4)_3 \quad + \quad 3H_2O$$
$$\text{(ferum(II)sulfate)}$$
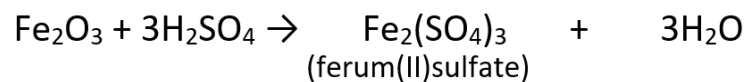
Figure 15. Chemical reaction of ferum(II)oxide with sulfuric acid.

OPC concrete is more susceptible to acid attack due to the presence of hydration products, namely $Ca(OH)_2$. The $Ca(OH)_2$ on the surface of OPC concrete is consumed by the reaction with acid and turned into gypsum, which is soft and porous and causes the surface of OPC concrete to deteriorate. Subsequently, gypsum would undergo distractive reaction with tricalcium aluminates within the cement matrix, resulting in the formation of calcium sulphoaluminate (ettringite), which has large volume and causes expansive deterioration mechanism. The reaction of OPC with sulfuric acid is presented in Figure 16.

$$Ca(OH)_2 + H_2SO_4 \rightarrow CaSO_4 \cdot 2H_2O$$
$$\text{(gypsum)}$$

$$3CaO \cdot 2SiO_2 \cdot 3H_2O + H_2SO_4 \rightarrow CaSO_4 \cdot 2H_2O + Si(OH)_4$$

$$3CaSO_4 + 3CaO \cdot Al_2O_3 \cdot 6H_2O + 25H_2O \rightarrow 3CaO \cdot Al_2O_3 \cdot 3CaSO_4 \cdot 31H_2O$$
$$\text{(ettringite)}$$
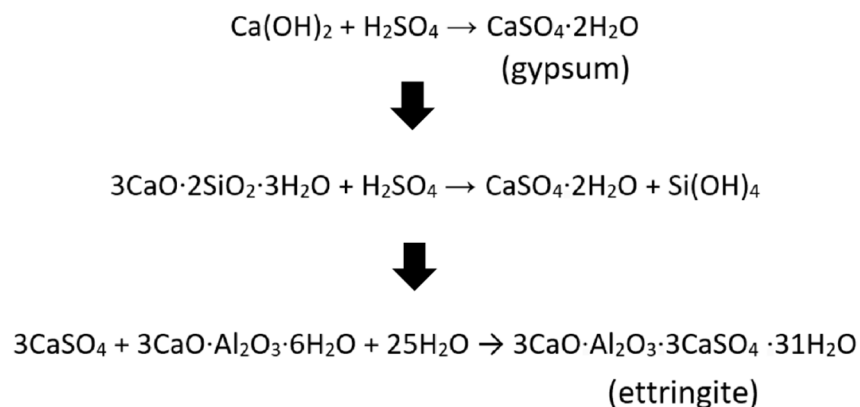
Figure 16. Chemical reaction of OPC with sulfuric acid.

Fly ash-based geopolymers do not contain hydration products; they produce N-A-S-H gel, which is acid resistant and has less surface deterioration. Fly ash also has low calcium content, resulting in the formation of less gypsum and ettringite that cause expansive deterioration mechanism. The change in colour of geopolymer from grey to slightly brown is due to the reaction of iron (II) oxide with sulphuric acid to produce iron (II) sulphate, as supported by previous researchers [46].

4. Conclusions and Future Work

In this study, the best formulation for synthesis of fly ash based geopolymer with highest compressive strength in terms of concentration of NaOH, SS/SH ratio, and S/L ratio was determined. In addition, the durability of both fly ash based geopolymer and OPC concrete in an acid environment were tested and compared. Based on the results obtained from the analysis and experimental data, the following conclusions can be drawn:

- The concentration of NaOH of 12 M, SS/SH ratio of 2.0, and S/L ratio of 2.5 are the optimum parameters to synthesize fly ash based geopolymer.
- The optimum ratio of sodium silicate to sodium hydroxide (SS/SH ratio) for synthesis of fly ash based geopolymer is 2.0, as geopolymer with an SS/SH ratio of 2.0 produced the best result compared to other the SS/SH ratios of 1.5, 2.5, and 3.0.
- The optimum solid to liquid (S/L) ratio for fly ash based geopolymer is 2.5. This S/L ratio yields fly ash based geopolymer with the highest compressive strength compared to ratios (1.5, 2.0, and 3.0).
- As the concentration of NaOH increases to 12 M, the OH^- concentration increases, which accelerates the dissolution and hydrolysis processes. As the ratio of SS/SH increases, the Si/Al ratio increases and favours the formation of strong bonds. As the S/L ratio increases to 2.5, the rate of intermolecular contact between precursor material and alkaline activator increases, consequently increasing the rate of dissolution of aluminosilicate material.
- The use of this formulation produces fly ash based geopolymer with compressive strength of 47 MPa, which exceeds the minimum compressive strength required for rigid pavement application based on Standard Specification for Road Work by Jabatan Kerja Raya (JKR).
- It is also found that the percentage of compressive strength loss and weight loss of fly ash based geopolymer concrete is lower compared to that of OPC concrete after acid immersion. Fly ash based geopolymer is less susceptible to acid attack due to low calcium content and low permeability. OPC concrete suffers from high surface erosion due to the presence of hydration product $Ca(OH)_2$. The acid reacts with $Ca(OH)_2$ to form gypsum and ettringite, which are soft and porous.

Because the mechanical properties and durability of fly ash based geopolymer concrete are higher compared to OPC based concrete, it is highly recommended to use this material for rigid pavement application, as it suffers from less deterioration under acid attack compared to OPC concrete, and this could lower the maintenance cost required. This demonstrates that fly-based geopolymer is more suitable for use in rigid pavement applications due to its high mechanical performance and durability, which could result in lower rigid pavement maintenance costs. It is beneficial to expand future research on the study of using fly ash based geopolymer as rigid pavements in terms of quality, effect of environment temperature, and long-term durability when exposed to harmful environmental conditions.

References

1. Hajj, E.Y.; Sebaaly, P.E.; Kandiah, P. Evaluation of the use of reclaimed asphalt pavement in airfield HMA pavements. *J. Transp. Eng.* **2010**, *136*, 181–189. [CrossRef]

2. Topini, D.; Toraldo, E.; Andena, L.; Mariani, E. Use of recycled fillers in bituminous mixtures for road pavements. *Constr. Build. Mater.* **2018**, *159*, 189–197. [CrossRef]

3. Shill, S.K.; Al-Deen, S.; Ashraf, M.; Rashed, M.G.; Hutchison, W. Consequences of aircraft operating conditions at military airbases: Degradation of ordinary mortar and resistance mechanism of acrylic and silica fume modified cement mortar. *Road Mater. Pavement Des.* **2022**, *23*, 98–111. [CrossRef]

4. Milind, V.M.; Kadam, K.N. A Comparative Study on Rigid and Flexible Pavement: A Review. *J. Mech. Civ. Eng.* **2016**, *13*, 84–88. [CrossRef]

5. Gautam, P.K.; Kalla, P.; Jethoo, A.S.; Agrawal, R.; Singh, H. Sustainable use of waste in flexible pavement: A review. *Constr. Build. Mater.* **2018**, *180*, 239–253. [CrossRef]

6. Chalangaran, N.; Farzampour, A.; Paslar, N.; Fatemi, H. Experimental Investigation of Sound Transmission Loss in Concrete Containing Recycled Rubber Crumbs. *Adv. Conc. Constr. Technopress* **2021**, *11*, 447–454. [CrossRef]

7. Farzampour, A. *Compressive Behavior of Concrete under Environmental Effects*; Intech Open: Rijeka, Croatia, 2019. [CrossRef]

8. Chalangaran, N.; Farzampour, A.; Paslar, N. Nano silica and metakaolin effects on the behavior of concrete containing rubber crumbs. *CivilEng* **2020**, *1*, 264–274. [CrossRef]

9. Wang, A.; Zheng, Y.; Zhang, Z.; Liu, K.; Li, Y.; Shi, L.; Sun, D. The Durability of Alkali-Activated Materials in Comparison with Ordinary Portland Cements and Concretes: A Review. *Engineering* **2020**, *6*, 695–706. [CrossRef]

10. Davidovits, J. *Geopolymer Chemistry and Application*, 4th ed.; Institut Geopolymere: Saint-Queentin, France, 2015.

11. Ahmed, S.F.U. Fibre-reinforced geopolymer composites (FRGCs) for structural applications. *Adv. Ceram. Matrix Compos.* **2014**, 471–495. [CrossRef]

12. Anuradha, P.; Thirumala, R.; John, P. Optimization of molarity on workable self-compacting geopolymer concrete and strength study on SCGC by replacing fly ash with silica fume and GGBFS. *Int. J. Adv. Struct. Geotech. Eng.* **2014**, *3*, 11–18.

13. Zailani, W.W.A.; Abdullah, M.M.A.B.; Arshad, M.F.; Razak, R.A.; Tahir, M.F.M.; Zainol, R.R.M.A.; Nabialek, M.; Sandu, A.V.; Wysłocki, J.J.; Błoch, K. Characterisation at the Bonding Zone between Fly Ash Based Geopolymer Repair Materials (GRM) and Ordinary Portland Cement Concrete (OPCC). *Materials* **2021**, *14*, 56. [CrossRef] [PubMed]

14. Azimi, E.A.; Abdullah, M.M.A.B.; Vizureanu, P.; Salleh, M.A.A.M.; Sandu, A.V.; Chaiprapa, J.; Yoriya, S.; Hussin, K.; Aziz, I.H. Strength Development and Elemental Distribution of Dolomite/Fly Ash Geopolymer Composite under Elevated Temperature. *Materials* **2020**, *13*, 1015. [CrossRef] [PubMed]

15. Tadesse, M.G.; Nagy, L.; Nierstrasz, V.; Loghin, C.; Chen, Y.; Wang, L. Low-Stress Mechanical Property Study of Various Functional Fabrics for Tactile Property Evaluation. *Materials* **2018**, *11*, 2018. [CrossRef] [PubMed]

16. Burduhos Nergis, D.D.; Vizureanu, P.; Ardelean, I.; Sandu, A.V.; Corbu, O.C.; Matei, E. Revealing the Influence of Microparticles on Geopolymers' Synthesis and Porosity. *Materials* **2020**, *13*, 3211. [CrossRef] [PubMed]

17. *ASTM C618-12a*; Standard Specification for Coal Fly Ash and Raw or Calcined Natural Pozzolan for Use in Concrete. ASTM International: West Conshohocken, PA, USA, 2012.

18. *ASTM C305-20*; Standard Practice for Mechanical Mixing of Hydraulic Cement Pastes and Mortars of Plastic Consistency. ASTM International: West Conshohocken, PA, USA, 2020.

19. *ASTM C267-20*; Standard Test Methods for Chemical Resistance of Mortars, Grouts, and Monolithic Surfacings and Polymer Concretes. ASTM International: West Conshohocken, PA, USA, 2020.

20. Nikoloutsopoulos, M.; Sotiropoulou, A.; Kakali, G.; Tsivilis, S. Physical and Mechanical Properties of Fly Ash Based Geopolymer Concrete Compared to Conventional Concrete. *Buildings* **2021**, *11*, 178. [CrossRef]

21. Wattimena, O.K.; Antoni; Hardjito, D. A review on the effect of fly ash characteristics and their variations on the synthesis of fly ash based geopolymer. *AIP Conf. Proc.* **2017**, *1887*, 020041. [CrossRef]

22. Rahman, S. Nanofiber Reinforcement of a Geopolymer Matrix for Improved Composite Materials Mechanical Performance. Ph.D. Thesis, Colorado State University, Fort Collins, CO, USA, 2015. Available online: https://www.researchgate.net/publication/282981109_Nanofiber_Reinforcement_of_a_Geopolymer_Matrix_for_Improved_Composite_Materials_Mechanical_Performance (accessed on 1 July 2015).

23. Zhang, Z. The Effects of Physical and Chemical Properties of Fly Ash on the Manufacture of Geopolymer Foam Concretes. Ph.D. Thesis, University of Southern Queensland, Darling Heights, Australia, 2014. Available online: https://core.ac.uk/download/pdf/211498587.pdf (accessed on 8 May 2022).

24. Abdullah, A.; Hussin, K.; Abdullah, M.M.A.B.; Yahya, Z.; Sochacki, W.; Razak, R.A.; Błoch, K.; Fansuri, H. The Effects of Various Concentrations of NaOH on the Inter-Particle Gelation of a Fly Ash Geopolymer Aggregate. *Materials* **2021**, *14*, 1111. [CrossRef]

25. Fatimah, A.A.S.; Ming, L.Y.; Bakri, M.M.A.; Yong, H.C.; Zulkifly, K.; Hussin, K. Effect of Alkali Concentration on Fly Ash Geopolymers. *IOP Conf. Ser. Mater. Sci. Eng.* **2018**, *343*, 012013. [CrossRef]

26. Ng, H.T.; Heah, C.Y.; Liew, Y.M.; Abdullah, M.M.A.B. The effect of various molarities of NaOH solution on fly ash geopolymer paste. *AIP Conf. Proc.* **2018**, *2045*, 020098. [CrossRef]

27. Chindaprasirt, P.; Jaturapitakkul, C.; Chalee, W.; Rattanasak, U. Comparative study on the characteristics of fly ash and bottom ash geopolymers. *Waste Manag.* **2009**, *29*, 539–543. [CrossRef]

28. Arafa, T.A.; Ali, A.Z.M.; Awal, A.S.M.A.; Loon, L.Y. Optimum mix of fly ash binder based on workability and compressive strength. *IOP Conf. Ser. Earth Environ. Sci.* **2018**, *140*, 012157. [CrossRef]

29. Ferdous, M.W.; Kayali, O.; Khennane, A. *A Detailed Procedure of Mix Design for Fly Ash Based Geopolymer Concrete*; International Institute for FRP in Construction: Melbourne, Australia, 2013.

30. Morsy, M.S.; Alsayed, S.H.; Al-Salloum, Y.; Almusallam, T. Effect of Sodium Silicate to Sodium Hydroxide Ratios on Strength and Microstructure of Fly Ash Geopolymer Binder. *Arab. J. Sci. Eng.* **2013**, *39*, 4333–4339. [CrossRef]

31. Leong, I.Y.; Ong, D.E.L.; Sanjayan, J.G.; Nazari, A. The effect of different Na_2O and K_2O ratios of alkali activator on compressive strength of fly ash based-geopolymer. *Constr. Build. Mater.* **2016**, *106*, 500–511. [CrossRef]

32. Wang, X.; Liu, X.; Zhang, W.; Li, Z.; Zhang, Y.; Li, Y.; Ren, Y. Effects of Si/Al ratio on the efflorescence and properties of fly ash based geopolymer. *J. Clean. Prod.* **2019**, *244*, 118852. [CrossRef]

33. Asif, A.; Man, Z.; Azizli, K.A.M.; Nuruddin, M.F.; Ismail, L. The Effect of Si/Al Ratio and Sodium Silicate on the Mechanical Properties of Fly Ash Based Geopolymer for Coating. *Mater. Sci. Forum* **2014**, *803*, 355–361. [CrossRef]

34. Doğan-Sağlamtimur, N.; Öz, H.Ö.; Bilgil, A.; Vural, T.; Süzgeç, E. The effect of alkali activation solutions with different water glass/NaOH solution ratios on geopolymer composite materials. *IOP Conf. Ser. Mater. Sci. Eng.* **2019**, *660*, 012003. [CrossRef]

35. Abdila, S.R.; Abdullah, M.M.A.B.; Ahmad, R.; Rahim, S.Z.A.; Rychta, M.; Wnuk, I.; Nabiałek, M.; Muskalski, K.; Tahir, M.F.M.; Syafwandi; et al. Evaluation on the Mechanical Properties of Ground Granulated Blast Slag (GGBS) and Fly Ash Stabilized Soil via Geopolymer Process. *Materials* **2021**, *14*, 2833. [CrossRef]

36. Hardjito, D.; Cheak, C.C.; Ing, C.H.L. Strength and Setting Times of Low Calcium Fly Ash-based Geopolymer Mortar. *Mod. Appl. Sci.* **2008**, *2*, 3–11. [CrossRef]

37. Tahir, M.F.M.; Abdullah, M.M.A.B.; Hasan, M.R.M.; Zailani, W.W.A. Optimization of fly ash based geopolymer mix design for rigid pavement application. *AIP Conf. Proc.* **2019**, *2129*, 020144. [CrossRef]

38. Sing, N.Y.; Ming, L.Y.; Abdullah, M.M.A.B.; Teng, N.H.; Hussin, K.; Yong, H.C.; Mortar, N.A.M.; Sandu, A.V. Effect of Solid-to-Liquid Ratio on Thin Fly Ash Geopolymer. *IOP Conf. Ser. Mater. Sci. Eng.* **2020**, *743*, 012006. [CrossRef]

39. Wang, Q.; Guo, H.; Yu, T.; Yuan, P.; Deng, L.; Zhang, B. Utilization of Calcium Carbide Residue as Solid Alkali for Preparing Fly Ash-Based Geopolymers: Dependence of Compressive Strength and Microstructure on Calcium Carbide Residue, Water Content and Curing Temperature. *Materials* **2022**, *15*, 973. [CrossRef] [PubMed]

40. Ahmad Zailani, W.W.; Bouaissi, A.; Abdullah, M.M.A.B.; Abd Razak, R.; Yoriya, S.; Mohd Salleh, M.A.A.; Rozainy MAZ, M.R.; Fansuri, H. Bonding Strength Characteristics of FA-Based Geopolymer Paste as a Repair Material When Applied on OPC Substrate. *Appl. Sci.* **2020**, *10*, 3321. [CrossRef]

41. Kurtoğlu, A.E.; Alzeebaree, R.; Aljumaili, O.; Gulsan, A.N.M.E.; Humur, G.; Cevik, A. Mechanical and durability properties of fly ash and slag based geopolymer concrete. *Adv. Conc. Constr.* **2018**, *6*, 345. [CrossRef]

42. Lloyd, R.R.; Provis, J.L.; van Deventer, J.S.J. Acid resistance of inorganic polymer binders. 1. Corrosion rate. *Mater. Struct.* **2011**, *45*, 1–14. [CrossRef]

43. Valencia-Saavedra, W.G.; de Gutiérrez, R.M.; Puertas, F. Performance of FA-based geopolymer concretes exposed to acetic and sulfuric acids. *Const. Build. Mater.* **2020**, *257*, 119503. [CrossRef]

44. Luhar, S.; Luhar, I.; Nicolaides, D.; Gupta, R. Durability Performance Evaluation of Rubberized Geopolymer Concrete. *Sustainability* **2021**, *13*, 5969. [CrossRef]

45. Izzat, M.; Bakri, A.M.M.A.; Kamarudin, H.; Moga, L.M.; Ruzaidi, G.C.M.; Faheem, M.T.M.; Sandu, A.V. Microstructural Analysis of Geopolymer and Ordinary Portland Cement Mortar Exposed to Sulfuric Acid. *Mater. Plast.* **2013**, *50*, 50.

46. Albitar, M.; Ali, M.S.M.; Visintin, P.; Drechsler, M. Durability evaluation of geopolymer and conventional concretes. *Const. Build. Mater.* **2017**, *136*, 374–385. [CrossRef]

Preparation of Fly Ash-Ladle Furnace Slag Blended Geopolymer Foam via Pre-Foaming Method with Polyoxyethylene Alkyether Sulphate Incorporation

Ng Hui-Teng [1,2], Heah Cheng-Yong [1,3,*], Liew Yun-Ming [1,2], Mohd Mustafa Al Bakri Abdullah [1,2], Catleya Rojviriya [4], Hasniyati Md Razi [5], Sebastian Garus [6], Marcin Nabiałek [7], Wojciech Sochacki [6], Ilham Mukriz Zainal Abidin [5], Ng Yong-Sing [1,2], Agata Śliwa [8] and Andrei Victor Sandu [9,10,*]

1   Geopolymer and Green Technology, Centre of Excellence (CEGeoGTech),
    Universiti Malaysia Perlis (UniMAP), Kangar 01000, Perlis, Malaysia; nghuiteng93@gmail.com (N.H.-T.);
    ymliew@unimap.edu.my (L.Y.-M.); mustafa_albakri@unimap.edu.my (M.M.A.B.A.);
    nicholas.zai.1130@gmail.com (N.Y.-S.)
2   Faculty of Chemical Engineering Technology, Universiti Malaysia Perlis (UniMAP),
    Kangar 01000, Perlis, Malaysia
3   Faculty of Mechanical Engineering Technology, Universiti Malaysia Perlis (UniMAP),
    Kangar 01000, Perlis, Malaysia
4   Synchrotron Light Research Institute, Muang, Nakhon Ratchasima 30000, Thailand; catleya@slri.or.th
5   Malaysian Nuclear Agency, Bangi, Kajang 43000, Selangor, Malaysia; hasniyati@nm.gov.my (H.M.R.);
    mukriz@nm.gov.my (I.M.Z.A.)
6   Faculty of Mechanical Engineering and Computer Science, Częstochowa University of Technology,
    42-201 Częstochowa, Poland; sebastian.garus@pcz.pl (S.G.); wojciech.sochacki@pcz.pl (W.S.)
7   Department of Physics, Częstochowa University of Technology, 42-201 Częstochowa, Poland;
    marcin.nabialek@pcz.pl
8   Division of Materials Processing Technology and Computer Techniques in Materials Science, Silesian
    University of Technology, 44-100 Gliwice, Poland; agata.sliwa@polsl.pl
9   Faculty of Materials Science and Engineering, "Gheorghe Asachi" Technical University of Iasi,
    41 "D. Mangeron" Street, 700050 Iasi, Romania
10 Romanian Inventors Forum, Str. Sf. P. Movila 3, 700089 Iasi, Romania
*   Correspondence: chengyongheah@hotmail.com (H.C.-Y.); sav@tuiasi.ro (A.V.S.)

Abstract: This paper uses polyoxyethylene alkyether sulphate (PAS) to form foam via pre-foaming method, which is then incorporated into geopolymer based on fly ash and ladle furnace slag. In the literature, only PAS-geopolymer foams made with single precursor were studied. Therefore, the performance of fly ash-slag blended geopolymer with and without PAS foam was investigated at 29–1000 °C. Unfoamed geopolymer (G-0) was prepared by a combination of sodium alkali, fly ash and slag. The PAS foam-to-paste ratio was set at 1.0 and 2.0 to prepare geopolymer foam (G-1 and G-2). Foamed geopolymer showed decreased compressive strength (25.1–32.0 MPa for G-1 and 21.5–36.2 MPa for G-2) compared to G-0 (36.9–43.1 MPa) at 29–1000 °C. Nevertheless, when compared to unheated samples, heated G-0 lost compressive strength by 8.7% up to 1000 °C, while the foamed geopolymer gained compressive strength by 68.5% up to 1000 °C. The thermal stability of foamed geopolymer was greatly improved due to the increased porosity, lower thermal conductivity, and incompact microstructure, which helped to reduce pressure during moisture evaporation and resulted in lessened deterioration.

Keywords: polyoxyethylene alkyether sulphate foam; blended geopolymer foam; high temperature; pre-foaming method

1. Introduction

Today, the excellent lightweight and mechanical properties, good thermal and chemical stability, and low environmental impact have led to the successful use of porous geopolymer

or geopolymer foam as a catalyst, thermal insulator, adsorbent and filter [1]. Geopolymer foam can be made by mixing aluminosilicate material (natural resource or industrial waste), foaming agent and alkali solution. There are numerous methods that can be used to prepare geopolymer foam, such as replica, sacrificial filler, pre-emulsification, solid impregnation, direct foaming and pre-foaming [1–3]. The pre-foaming method involves a two-step process, which is more complex compared to the commonly used direct foaming method, as it only involves a one-step process. In the direct foaming method, the foaming agent is directly added to the geopolymer mixture. In the pre-foaming method, the foaming agent is mixed with water to generate foam through a foam generator, and the generated foam is then added to the geopolymer mixture.

Several studies have been focused on the production of geopolymer foam by adopting the pre-foaming method, with the incorporation of polyoxyethylene alkyether sulphate (PAS) foaming agent. PAS is a brown liquid extracted from coconut oil, and it can be easily and quickly dissolved in water to generate foam [4]. Based on previous studies, Ibrahim et al. [5] produced fly ash geopolymer foam with PAS foam-to-paste ratios ranging from 0.5 to 2.0, revealing that the compressive strength of the foamed geopolymer (17.8–4.1 MPa) decreased with increasing foam-to-paste ratio. Mastura et al. [6] and Ibrahim et al. [4] produced fly ash geopolymer foam with a PAS foam-to-paste ratio of 1.0, reporting that the compressive strength of the foamed geopolymer was in the range of 9.0 MPa to 19.3 MPa. On the other hand, Tiong et al. [7] also produced concrete foam using PAS foam.

The past literature examined the influence of PAS foam addition on geopolymer at room temperature, as well as the influence of PAS foam addition on geopolymer at high temperatures. Mastura et al. [2] studied the effect of high temperature exposure on the strength performance of fly ash geopolymer foam with a PAS foam-to-paste ratio of 1.0. The results showed that the compressive strength of the foamed geopolymer reduced with the increase of temperature from 200 °C (33.3 MPa) to 800 °C (18.6 MPa).

Moreover, in previous studies [8,9], geopolymer foams were mainly based on a single precursor. Very little research has been investigated on geopolymer foams based on blended aluminosilicates. For instance, Zhang et al. [10] prepared fly ash-ground granulated blast furnace slag geopolymer foam via a pre-foaming method using diluted aqueous. They concluded that the geopolymer foam based on blended precursors outperformed those produced using single precursor in terms of thermo-mechanical properties. Thus far, there are no studies on the preparation of PAS-geopolymer foams using blended precursors to investigate their performance at room temperature and high temperatures.

Consequently, the PAS-geopolymer foams produced in this study were made from a mixed precursor of fly ash and ladle furnace slag. The physical, mechanical and thermal performance of fly ash-slag blended geopolymer foams were evaluated at room temperature (29 °C) and high temperatures (200–1000 °C). The microstructural, functional group and phase analyses of fly ash-slag blended geopolymer foams were also assessed. The PAS foam-to-paste ratio was fixed at 1.0 and 2.0 to prepare geopolymer foam. Unfoamed geopolymer was also prepared to compare with foamed geopolymer. Investigation of the influence of PAS foam addition on the thermal properties of fly ash-slag blended geopolymer foam is a worthwhile effort.

2. Materials and Methods

2.1. Raw Materials

Fly ash and ladle furnace slag were mixed as a blended precursor to prepare geopolymer foam. Table 1 demonstrates the chemical composition of fly ash and slag using X-ray fluorescence. Three bulks of fly ash and slag were analysed. SiO_2 and Al_2O_3 were the main compounds of fly ash, with a total amount of 84.30 wt.%, which was within the suitable composition range (83.70–87.21 wt.%) to produce geopolymers [2,11]. The low CaO content demonstrated that the fly ash was Class F fly ash based on ASTM C618. On the other hand, CaO, SiO_2 and Al_2O_3 were the main compounds of slag, with a total amount of 87.19 wt.%., which was similar to other studies (73.00–83.15 wt.%) for geopolymer preparation [12,13].

Table 1. Chemical composition of fly ash and slag.

Compound	Fly Ash (wt.%)	Slag (wt.%)
SiO_2	56.30 ± 0.15	21.30 ± 0.10
Al_2O_3	28.00 ± 0.30	2.30 ± 0.20
CaO	3.89 ± 0.16	63.59 ± 0.13
Fe_2O_3	6.86 ± 0.05	8.08 ± 0.12
K_2O	1.49 ± 0.04	-
MgO	-	2.60 ± 0.20
TiO_2	2.17 ± 0.04	0.50 ± 0.16
PdO	-	-
SO_3	-	-
Others	1.29 ± 0.16	1.63 ± 0.09

Polyoxyethylene alkyether sulphate (PAS) was utilised as a foaming agent to prepare geopolymer foam. The PAS consists mainly of 11.0 wt.% of PdO and 78.6 wt.% of SO_3. By using the pre-foaming method, the PAS was prepared in foam before being mixed with the geopolymer mixture, as in accordance with ASTM C796. The foam was produced by PAS and water through a foam generator with a constant pressure of 0.5 MPa, as shown in Figure 1. The mechanism of PAS foam can be divided into four stages, as illustrated in a schematic diagram in Figure 2. The PAS molecule had both hydrophilic (water soluble) and hydrophobic (water insoluble) substances [14]. When PAS was mixed with water, the head of the PAS molecule favoured water while its tail resisted water. As a result, micelles formed, causing bubbles to form in the water medium. Moreover, a bubble can form in the air medium as seen in Stage IV.
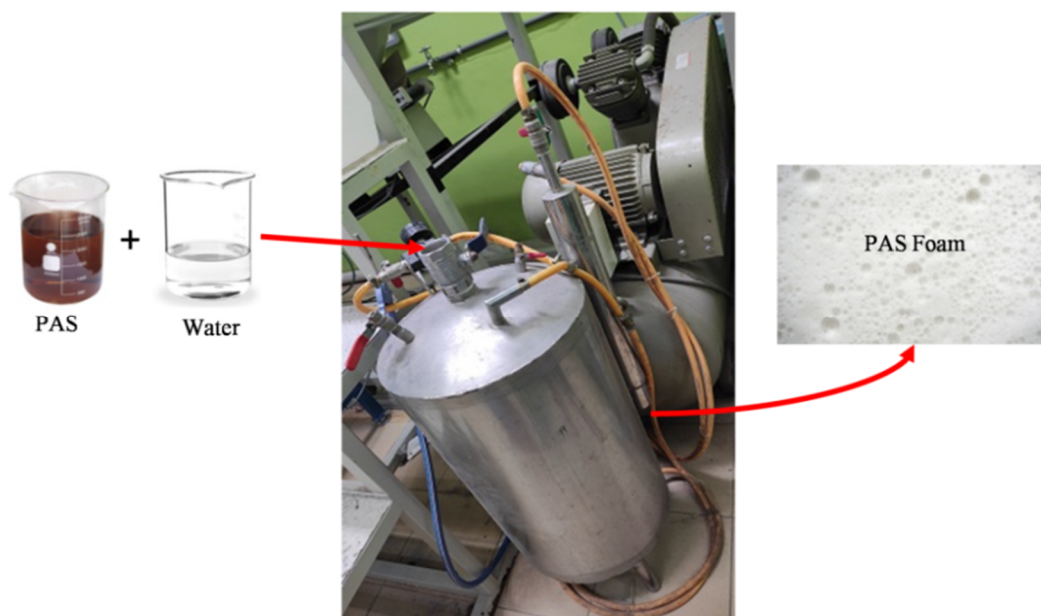
Figure 1. Preparation of PAS foam using a foam generator.
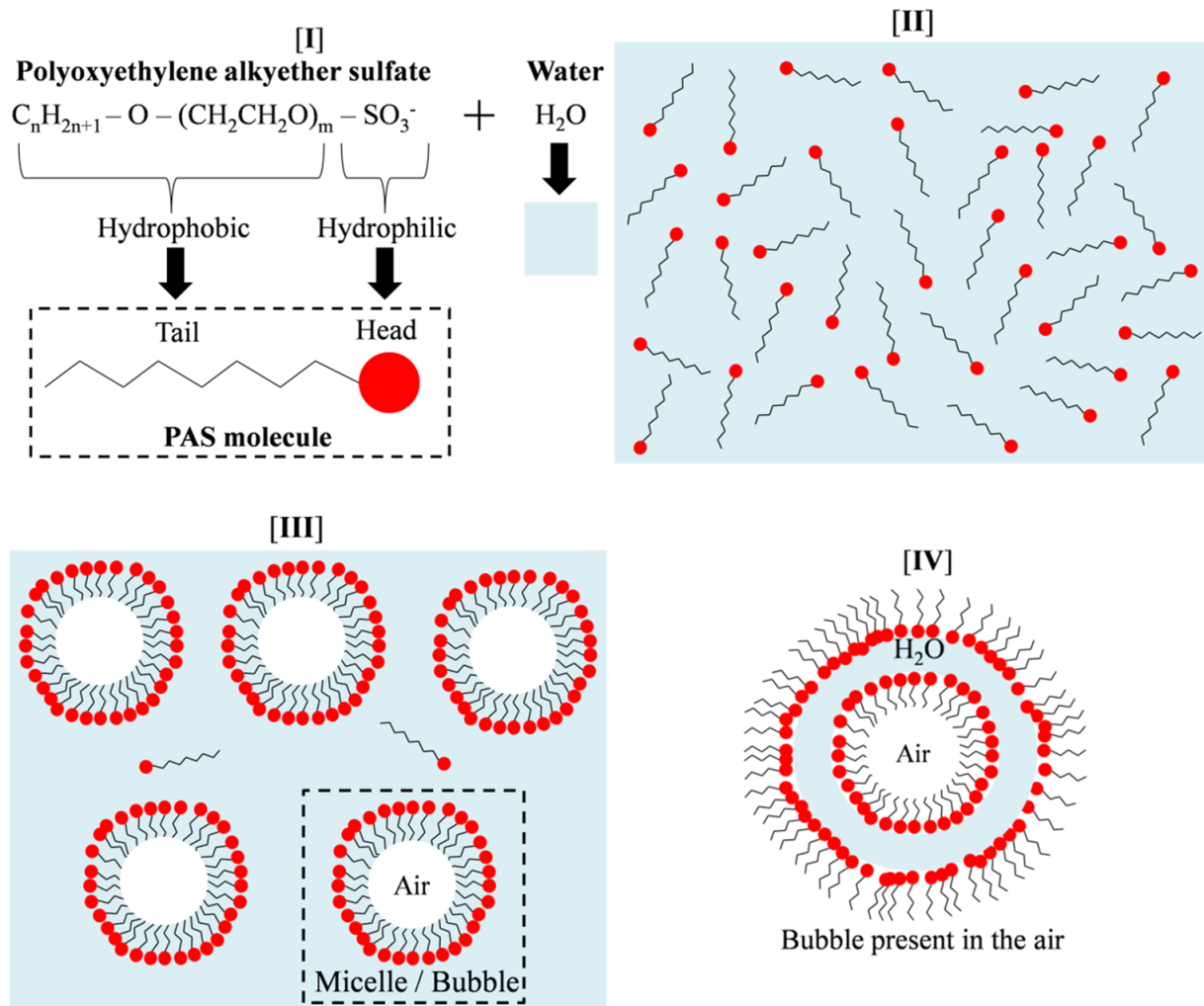
Figure 2. (**I**) Structural formulas of PAS and water, (**II**) PAS and water mixture, PAS foam formation in (**III**) water and (**IV**) air.

Sodium hydroxide pellets (HmbG®, Sigma-Aldrich, Taufkirchen，Germany) and distilled water were mixed together to prepare a sodium hydroxide solution. The main constituents of the sodium silicate solution (South Pacific Chemicals Industries Sdn. Bhd., Selangor, Malaysia) were 30.1% SiO_2, 9.4% Na_2O, and 60.5% H_2O. Sodium hydroxide and sodium silicate solutions were mixed to prepare an alkaline activator, and the mixed solution was placed at room temperature for 24 h before use.

2.2. Preparation of Unfoamed and Foamed Geopolymers

Fly ash, slag and alkaline solution were mixed together to prepare the unfoamed geopolymer, and the geopolymer was designated as G-0. The mixture was stirred with a blender (IKA-RW-20 digital, Taufkirchen，Germany) at a constant mixing speed of 1000 rpm for 15 min before being cast into a cubic (5 × 5 × 5 cm) plastic mould. The moulded mixture was placed at room temperature for 1 day, and it was further placed in an oven (60 °C) for another 1 day. The curing regime was selected in accordance to Bakharev [15], who stated that pre-curing 1 day before oven-curing for another day would lead to excellent compressive strength. The demoulded sample was stored at room temperature for 28 days before being subjected to high temperatures.

On the other hand, G-0 and PAS foam were mixed to prepare the geopolymer foam. The PAS foam-to-paste ratio was set at 1:1 and 2:1, and the PAS-to-water ratio was fixed at 1:10. The selection of these ratios was based on the optimal ratios obtained by Ibrahim

et al. [5]. The foam, PAS and water were measured in volume (ml). Based on the PAS foam-to-paste ratio of 1.0 and 2.0, the resulting geopolymer foam was designated as G-1 and G-2, respectively. The geopolymer foam also used the similar curing method as the unfoamed geopolymer. The constant formulations (sodium hydroxide concentration, solid:liquid, sodium silicate:sodium hydroxide and fly ash:slag ratios) were chosen as tabulated in Table 2, owing to the optimal ratios achieved in previous work [16].

Table 2. Details of sample preparation.

Category	Unfoamed Geopolymer	Foamed Geopolymer	
Abbreviation	G-0	G-1	G-2
PAS Foam:Paste Ratio	0:0	1:1	2:1
Fly ash:Slag Ratio	80:20		
Sodium Hydroxide Concentration (M)	8		
Solid:Liquid Ratio	3:1		
Sodium Silicate:Sodium Hydroxide Ratio	1.5:1		
PAS:Water Ratio	1:10		
Exposure Temperature (°C)	29, 200, 400, 600, 800 and 1000		

2.3. High Temperature Exposure

After 28 ambient-curing days, the unfoamed and foamed geopolymers were sintered to high temperatures (Table 2) in a Muffle furnace, with a heating rate of 10 °C/min and a soaking time of 2 h. The unheated geopolymer sample was also prepared as a control sample to compare with the heat-treated geopolymer sample.

2.4. Test and Characterisation Method

The water absorption (dry and immersion weights) and apparent porosity (dry, immersion and suspended weights) of geopolymer were measured based on ASTM C642. The bulk density (mass and volume) of geopolymer was measured in accordance with BS EN 12390-7. The volume and mass changes of geopolymer were measured before and after exposure to high temperatures.

The pore size distribution of geopolymer was determined by Synchrotron radiation X-ray tomographic microscopy, equipped with Drishti software and Octopus Reconstruction software. The specimen was prepared in a small piece (0.2 cm × 0.2 cm × 0.5 cm) for analysis.

The thermal conductivity of geopolymer was measured by a KD2 Pro Thermal Properties Analyser (Decagon Devices Inc., Pullman, WA, USA). The transient line heat source method was applied based on IEEE 442-1981 and ASTM D5334. The pre-calibration of the sensor was performed according to DB1175 before each measurement.

The compressive strength of geopolymer before and after exposure to high temperatures was tested using a mechanical tester (Instron Machine Series 5569). Three samples were tested at each exposure temperature.

The morphology of fly ash, slag and geopolymer can be visualised by a scanning electron microscope (SEM, JEOL JSM-6460 LA). Fly ash and slag were prepared in power form while geopolymer was prepared in a small piece (1 × 1 × 1 cm) for analysis. The specimens were coated with platinum using a coater (JEOL JFC 1600) before analysis.

The functional group of fly ash, slag and geopolymer was identified using Fourier transform infrared spectroscopy (FTIR, Perkin Elmer Spectrum RX1 Spectrometer), with a resolution of 4 cm^{-1} and a scan range of 650 cm^{-1} to 4000 cm^{-1}. The sample was prepared in powder form for analysis.

The crystalline phase of fly ash, slag and geopolymer was carried out using an X-ray diffractometer (XRD, D2-Phaser Bruker), with 10–80° 2θ, 2°/min scan rate and 0.02° scan

step. The phase patterns of specimens were analysed by X'Pert HighScore Plus software, and the specimens were prepared in powder form for analysis.

3. Results and Discussion

3.1. Effect of PAS Foam-to-Paste Ratio

The bulk density of geopolymer can be determined by the changes in water absorption and apparent porosity, as shown in Figure 3. Geopolymer with higher porosity was expected to exhibit higher water absorption but lower bulk density. G-0 had a bulk density of 2.09 g/cm^3, water absorption of 7.4% and apparent porosity of 17.3%. The inclusion of PAS foam increased the water absorption and porosity to 17.1–20.3% and 27.9–29.1%, respectively, while reducing the bulk density to 1.69–1.77 g/cm^3 in geopolymer foam. When the PAS foam was added to the geopolymer, the pores in the sample would increase directly due to the increased bubbles caused by the PAS foam addition (Figure 1), subsequently reducing the bulk density. A similar explanation was observed by Ibrahim et al. [5], who reported that the bulk density of fly ash geopolymer foam decreased from 1.65 g/cm^3 to 1.20 g/cm^3 with increasing PAS foam content. The bulk density of the fly ash-slag blended geopolymer foam achieved in this work was greater than in their work, which was due to the high-density slag addition [16].
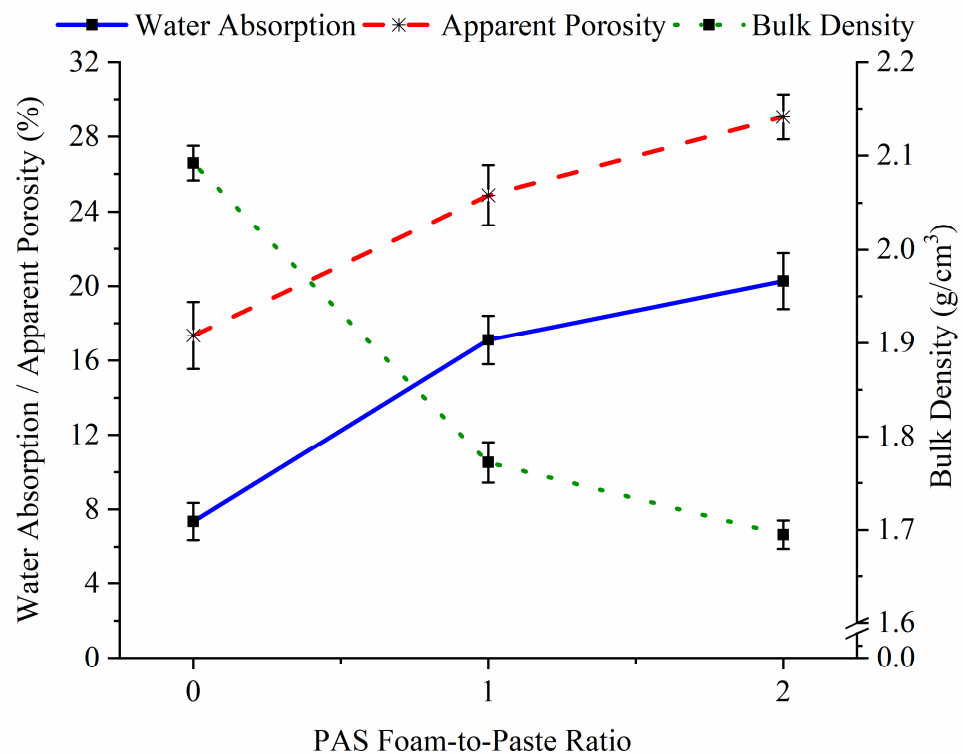
Figure 3. Bulk density, water absorption and apparent porosity of G-0, G-1 and G-2.

The pore size distribution and total porosity of G-0, G-1 and G-2 are plotted in Figure 4. G-0 (Figure 4a), G-1 (Figure 4b) and G-2 (Figure 4c) were mostly made up of open pores, while minorly made up of closed pores. However, foamed geopolymer (14.81% for G-1 and 15.94% for G-2) exhibited a greater total porosity than G-0 (10.45%), supporting the bulk density and apparent porosity results (Figure 3). This was because of the large pore diameter of 500–1000 μm (~78%) present in the foamed geopolymers but absent in G-0.
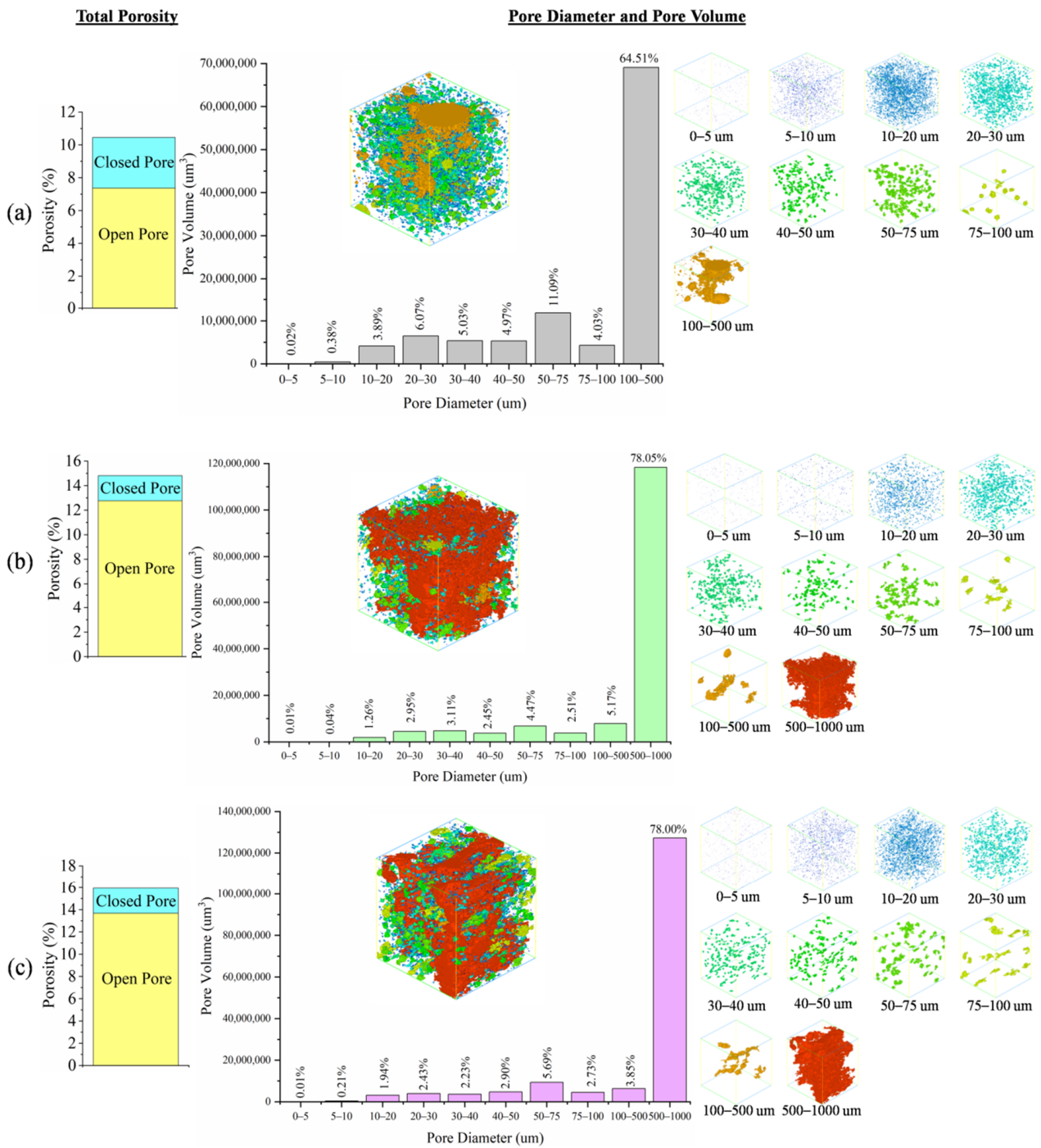
Figure 4. Total porosity and pore size distribution of (**a**) G-0, (**b**) G-1 and (**c**) G-2.

The addition of PAS foam decreased the thermal conductivity of G-0 from 1.05 W/(m·K) to 0.70–0.81 W/(m·K), as demonstrated in Figure 5. The results were complied with bulk density and apparent porosity values, as shown in Figure 3. When a geopolymer has a higher porosity and a lower density, its thermal conductivity is always lower [17]. The trend was further supported by pore size distribution results (Figure 4) as the foamed geopolymers had larger pore sizes up to 1000 μm but G-0 had lower pore sizes up to 500 μm.
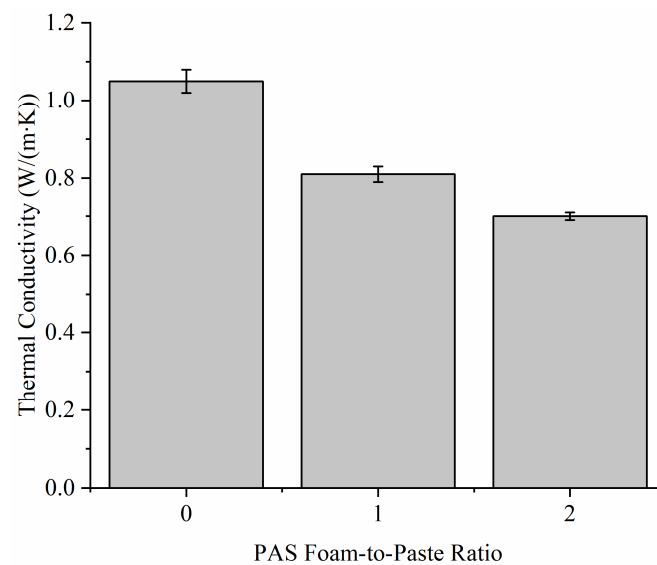
Figure 5. Thermal conductivity of G-0, G-1 and G-2.

The relationship between compressive strength, bulk density, apparent porosity and thermal conductivity of G-0, G-1 and G-2 is displayed in Figure 6. The addition of PAS foam decreased the compressive strength of G-0 from 40.5 MPa to 26.3 MPa (G-1) and 21.5 MPa (G-2), as shown in Figure 6a. As stated earlier, pores were induced in the geopolymer after adding PAS foam, thereby weakening the sample structure and resulting in poor strength. The explanation was further supported by Figure 6b, as the compressive strength had a strong correlation with apparent porosity, bulk density and thermal conductivity, with correlation coefficients (R^2) of 0.93881, 0.98106 and 0.97550, respectively.
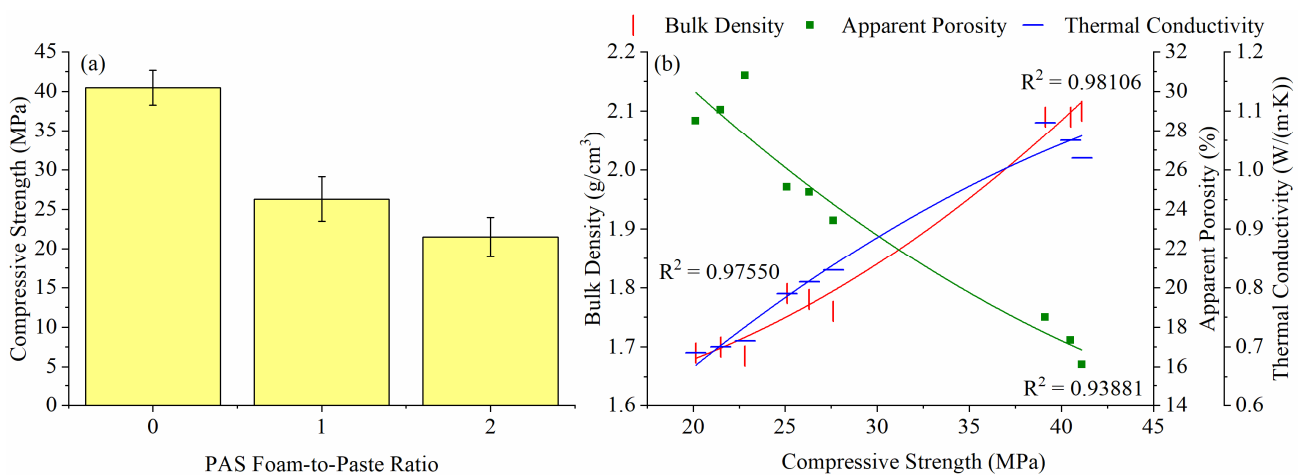
Figure 6. (**a**) Compressive strength and (**b**) correlation curve between compressive strength, bulk density, apparent porosity and thermal conductivity of G-0, G-1 and G-2.

According to the functional classification of International Union of Laboratories in Construction Materials, Systems and Structures (RILEM), a sample with a density of 1.44–1.84 g/cm^3, compressive strength of >17.0 MPa and thermal conductivity of 0.4–0.7 W/(m·K) can be used as a structural lightweight concrete [17]. Based on the compressive strength, density and thermal conductivity values achieved in this work, only G-2 (compressive strength of 21.5 MPa, density of 1.69 g/cm^3 and thermal conductivity of 0.7 W/(m·K)) met the RILEM requirements for the application.

The compressive strength of the fly ash-slag blended geopolymer foam achieved in this work (21.5–26.3 MPa) was higher than the work done by Ibrahim et al. [5], who adopted

the same mixing ratios of PAS foam-to-paste and PAS-to-water as in this work to produce fly ash geopolymer foam (10.2–15.8 MPa). The inclusion of slag promoted a combined matrix of calcium (CASH) and sodium (NASH) aluminosilicate hydrate in the blended geopolymer foam, while fly ash geopolymer foam only had a NASH matrix [10], thereby obtaining higher compressive strength in the blended geopolymer foam compared to the pure geopolymer foam.

3.2. High Temperature Performance

Figure 7 demonstrates the mass, volume and bulk density of G-0, G-1 and G-2 before and after exposure to high temperatures. Increasing temperature caused the bulk density of all geopolymers to gradually reduce up to 600 °C, and the bulk density was relatively stable between 600 °C and 1000 °C (Figure 7a). The changes in bulk density were varied by the mass and volume. The mass (Figure 7b) and volume (Figure 7c) of all geopolymers were reduced with increasing temperature up to 600 °C, and the mass and volume remained almost constant above 600 °C. The reduction in mass and volume at temperatures below 600 °C was affected by the loss of physically and chemically bonded water in the sample structure [11]. A geopolymer sample with a higher mass or lower volume was expected to have a higher bulk density.
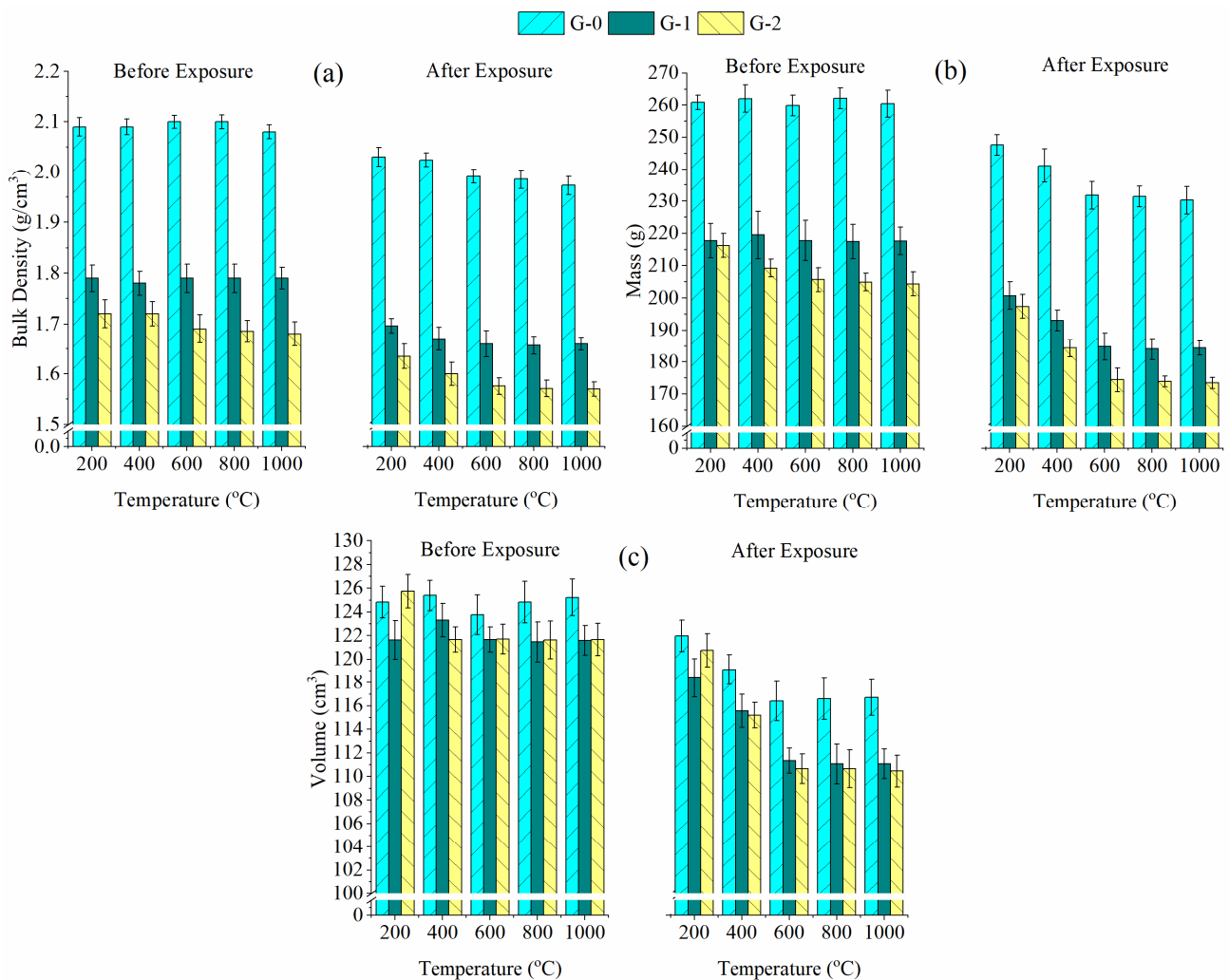
Figure 7. (**a**) Bulk density, (**b**) mass and (**c**) volume of G-0, G-1 and G-2 before and after exposure to high temperatures.

At high temperatures, G-0 (1.97–2.03 g/cm^3) had a higher bulk density than the foamed geopolymers (1.57–1.70 g/cm^3). This was due to G-0 obtaining a higher remaining mass (230.25–247.60 g) and volume (116.41–121.96 cm^3) after exposure to high temperatures compared to the foamed geopolymer (mass of 173.43–200.78 g and volume of 110.46–120.75 cm^3). The lower residual mass and volume of foamed geopolymer were due to the increased dehydration caused by the high-moisture PAS foam addition. In terms of bulk density loss, the density loss of the fly ash-slag blended geopolymer foam in this work (4.94–7.43%) was comparatively lower than that of the fly ash geopolymer foam (17.65–28.66%) produced by Mastura et al. [2], verifying that the blended geopolymer foam showed better structural stability than the pure geopolymer foam at high temperatures.

G-1 and G-2 also had greater water absorption and apparent porosity than G-0 at high temperatures, as plotted in Figure 8. The porosity and water absorption of G-0, G-1 and G-2 showed parallel and similar trends, increasing from 29 °C to 1000 °C. The increased porosity from 29 °C to 600 °C was associated with the abovementioned dehydration of the sample, leading to the formation of pores in G-0, G-1 and G-2. The slight increase in porosity between 600 °C and 1000 °C might be related to the recrystallisation effect, as described in the phase analysis below. The induced new crystals caused the geopolymer matrix to slightly open and form pores in the unfoamed and foamed geopolymers.
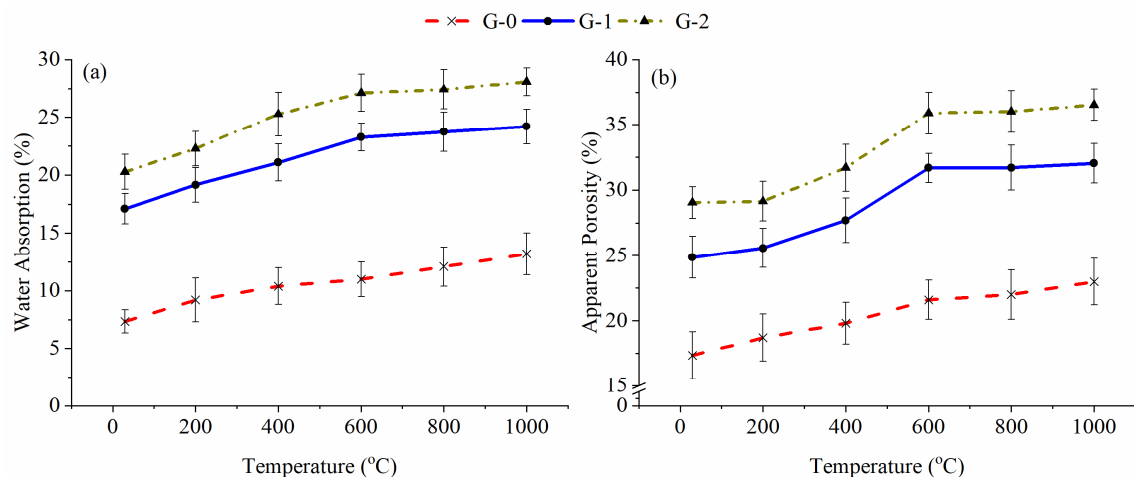
Figure 8. (**a**) Water absorption and (**b**) apparent porosity of G-0, G-1 and G-2 before and after being subjected to high temperatures.

Figure 9 depicts the compressive strength changes of G-0, G-1 and G-2 before and after being subjected to high temperatures. The compressive strength of all geopolymers was identical at below 600 °C, increasing from 29 °C to 200 °C and decreasing from 200 °C to 600 °C. The temperature of 200 °C caused better dissolution of slag, fly ash and alkali activator, thereby increasing the compressive strength [18]. The presence of pores (Figure 8) and bulk density loss (Figure 7) caused by the dehydration process resulted in a decrease in compressive strength at 200–600 °C. Beyond 600 °C, the trend in compressive strength of G-0 was different from that of G-1 and G-2. The strength of G-0 increased slightly at 800 °C due to the dense microstructure obtained, while the strength of G-1 and G-2 was continuously reduced at 800 °C due to the loose microstructure obtained, as shown in the following microstructural analysis. At 1000 °C, the strength of all geopolymers increased slightly was affected by phase change, as shown in the phase analysis below, which was attested by Murri et al. [13] for unfoamed geopolymer.
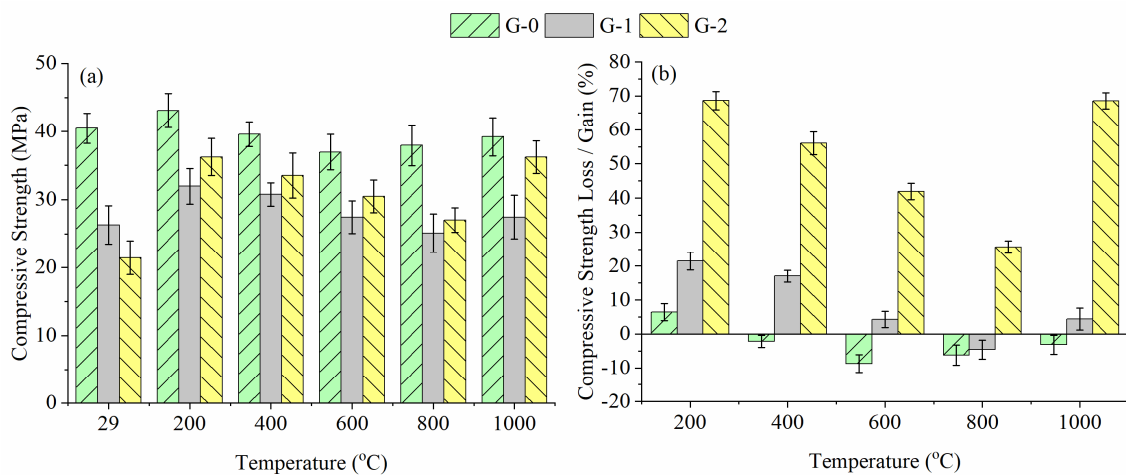
Figure 9. (**a**) Compressive strength and (**b**) strength changes of G-0, G-1 and G-2 with respect to unexposed samples.

At high temperatures, G-0 (36.9–43.1 MPa) had a greater compressive strength than the foamed geopolymers (25.1–36.2 MPa). The explanation was consistent with the higher residual bulk density, mass and volume (Figure 7) and lower porosity (Figure 8) obtained in G-0 compared to the foamed geopolymers. The addition of PAS foam degraded the compressive strength of the control sample, resulting in the unfoamed geopolymer possessing better heat resistance than the foamed geopolymer.

However, referring to Figure 9b, G-0 lost compressive strength (2.2–8.7%) between 400 °C and 1000 °C, while foamed geopolymer gained compressive strength (4.2–68.6%) at the same temperature exposure. An exception occurred in G-1 at 800 °C due to strength loss (4.6%). As stated earlier, foamed geopolymer had a higher porosity than the unfoamed geopolymer. High porosity allowed moisture to be removed during heating without deteriorating the structure of the foamed geopolymer, while pressure was generated in the unfoamed geopolymer during the moisture removal process and resulted in a loss of strength. Therefore, the compressive strength of the foamed geopolymer at high temperatures was greatly improved due to the increased pores, especially in the case of G-2. The increase in porosity improved the thermal resistance of geopolymer foam [19]. In addition, the lower thermal conductivity value (Figure 5) of foamed geopolymer, particularly G-2, facilitated the heat transfer and reduced the damaging effect of heat at elevated temperatures.

Mastura et al. [2] heated fly ash geopolymer foam at temperatures ranging from 200 °C to 800 °C, obtaining a compressive strength in the range of 18.6 MPa to 33.3 MPa and a strength loss in the range of 29.3% to 60.4%. The fly ash-slag blended geopolymer foam produced in this work achieved better compressive strength (25.1–36.2 MPa) than their work even at high temperatures up to 1000 °C. The strength in this work even increased (4.2–68.6%) at high temperatures instead of losing strength, which was also different from their work. Thus, the geopolymer foam made with blended precursors was more stable than the geopolymer foam made with a single precursor at high temperatures.

The influence of various foaming techniques and foaming agents on the thermo-mechanical performance of geopolymer foam has been widely investigated. Geopolymer foam prepared by varying foaming methods and foaming agents resulted in different thermo-mechanical properties. For instance, Bai et al. [8] added hydrogen peroxide (H_2O_2) into geopolymer by adopting the direct foaming method, obtaining a compressive strength in the range of 4.5 MPa to 20.4 MPa at high temperatures. Le-ping et al. [9] used the direct foaming method to incorporate alumina powder (AP) into geopolymer, obtaining compressive strengths ranging from 6.3 MPa to 13.8 MPa at high temperatures. This work and Mastura et al. [2] work used the pre-foaming method to add PAS foam into geopolymer, with compressive strength of 18.6–36.2 MPa at high temperatures, which

showed better strength and thermal performance than the geopolymer foam incorporated with H_2O_2 or AP. This was because PAS was an amphiprotic substance that was strongly hydrophilic and easily dissolved in water during the pre-foaming process, yielding and resulting in the formation of homogeneous air bubbles and pores [20]. However, when H_2O_2 or AP interacted with the geopolymer matrix, pores of varying sizes and shapes were formed during the hydrogen gas generation [3]. Thus, PAS-geopolymer foam prepared by the pre-foaming method achieved a more stable pore size and shape when compared to the H_2O_2- or AP-geopolymer foam prepared by the direct foaming method, resulting in PAS-geopolymer foam outperforming H_2O_2- or AP-geopolymer foam at high temperatures.

3.3. Microstructural Analysis

The SEM images of fly ash and slag were taken at a magnification of $\times 300$, as shown in Figure 10. The fly ash particles (Figure 10a) were spherical, while the slag particles (Figure 10b) were presented in block shape. On the other hand, the SEM images of unheated G-0 (Figure 10c) and G-2 (Figure 10d) were taken at a magnification of $\times 500$. G-0 and G-2 were chosen due to the greatest difference in compressive strength between G-0 and G-2 (Figure 6). Generally, the geopolymer matrix in G-0 and G-2 showed some pores, cracks, remaining fly ash and slag particles. A more compact microstructure was observed in G-0 as compared to G-2. The larger pores and cracks of G-2 were caused by the pores induced by PAS foam addition, as supported by bulk density and porosity results (Figures 3 and 4), thereby achieving a low compressive strength.
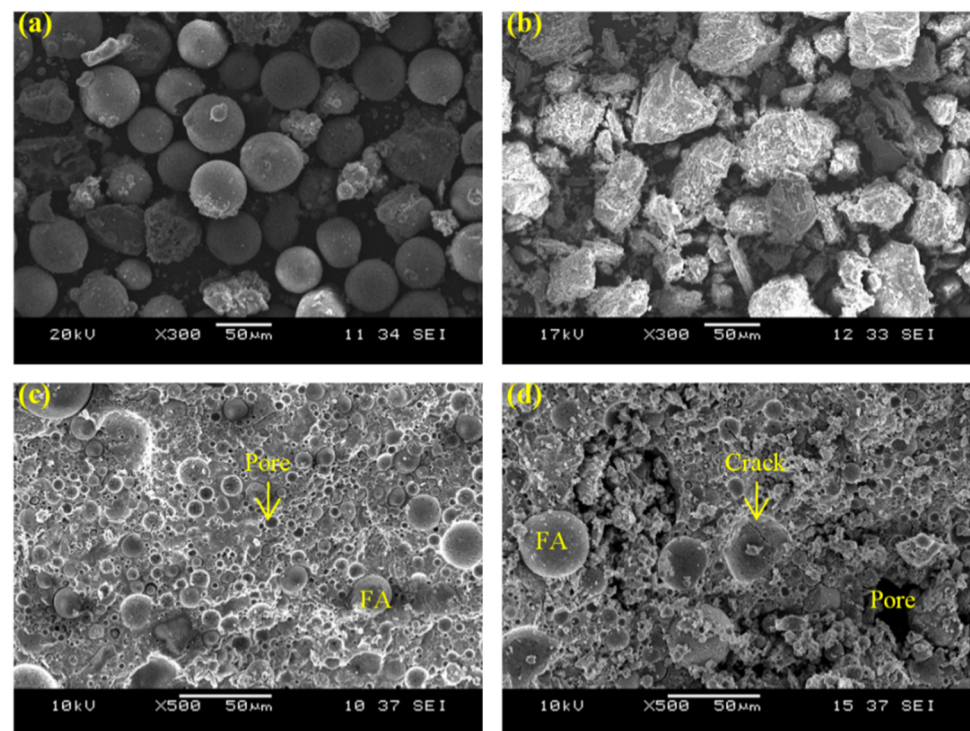
Figure 10. SEM images of (**a**) fly ash, (**b**) slag, unheated (**c**) G-0 and (**d**) G-2 (FA denoted fly ash).

Figure 11 depicts the SEM images of G-0 and G-2 after being heated to 800 °C and 1000 °C. The temperatures of 800 °C and 1000 °C were selected based on the different compressive strength trends of G-0 and G-2 at 800 °C (Figure 9). At 800 °C, the geopolymer matrix in G-0 was observed to be connected and smooth with a small number of pores and residual particles (Figure 11a), leading to a slight improvement in the compressive strength. However, the compressive strength of G-2 was further degraded at 800 °C due to the loose matrix obtained with a large number of pores (Figure 11b). At 1000 °C, the disappearance of residual particles and the appearance of the solidified melt in the geopolymer matrix [21]

most likely contributed to the increase in compressive strength of G-0 (Figure 11c) and G-2 (Figure 11d). The presence of rod and/or plate anorthite crystal (Figure 11c') was also expected to enhance the compressive strength of G-0 at 1000 °C. Anorthite was typically discovered in a high-calcium geopolymer system at 1000 °C [22].
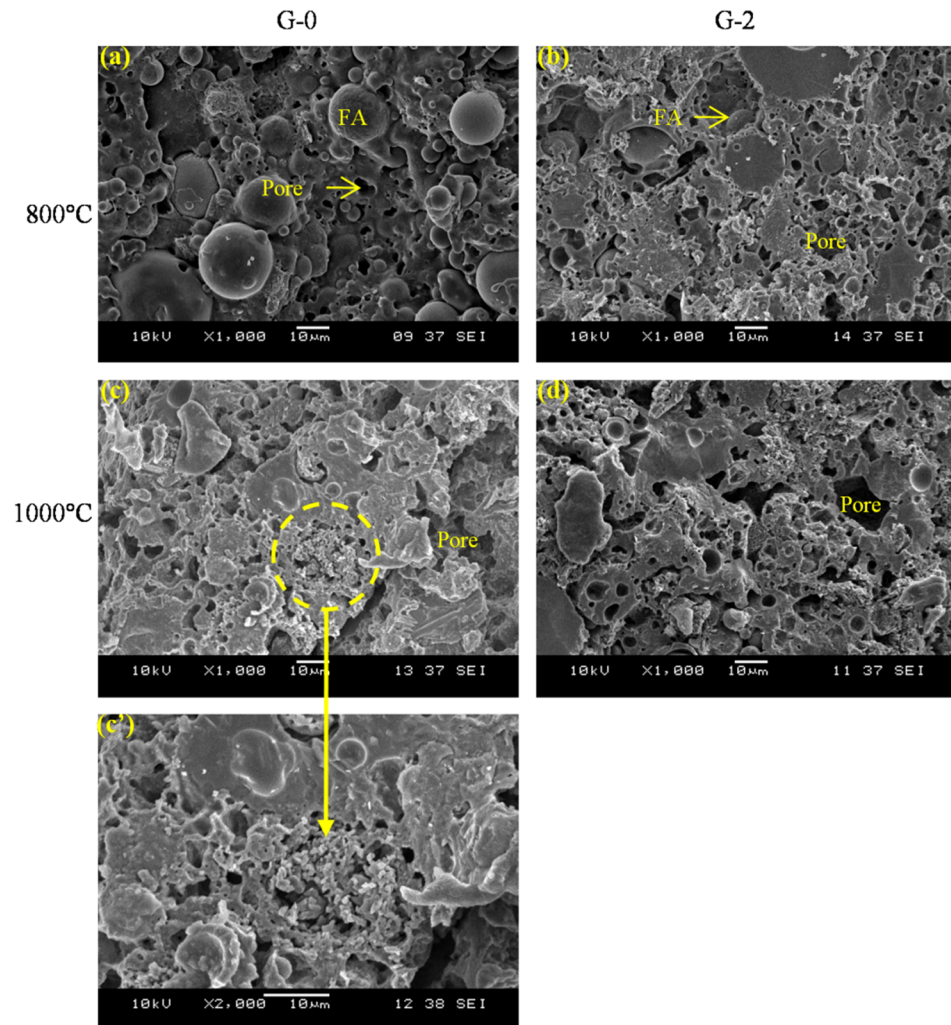
Figure 11. SEM images of G-0 and G-2 after exposed to (**a**,**b**) 800 °C and (**c**,**c'**,**d**) 1000 °C (FA denoted fly ash).

3.4. Phase Analysis

Figure 12 illustrates the phase patterns of fly ash, slag, unexposed, and temperature-exposed G-0 and G-2. Fly ash had an amorphous broad hump in the range of 15° to 35° 2θ, with some peaks of mullite, quartz and hematite. Slag was mainly crystalline with peaks of calcio-olivine, merwinite, magnetite and calcium aluminium oxide. Unheated G-0 and G-2 (Figure 12b,c) had an amorphous broad hump between 16–38° 2θ, also had some peaks of mullite, quartz, hematite, calcio-olivine and calcium aluminium oxide, which came from raw fly ash and slag. In addition, some new peaks of calcite and calcium silicate hydrate (CSH) appeared in the unheated samples, which were caused by alkali activation of fly ash and slag.
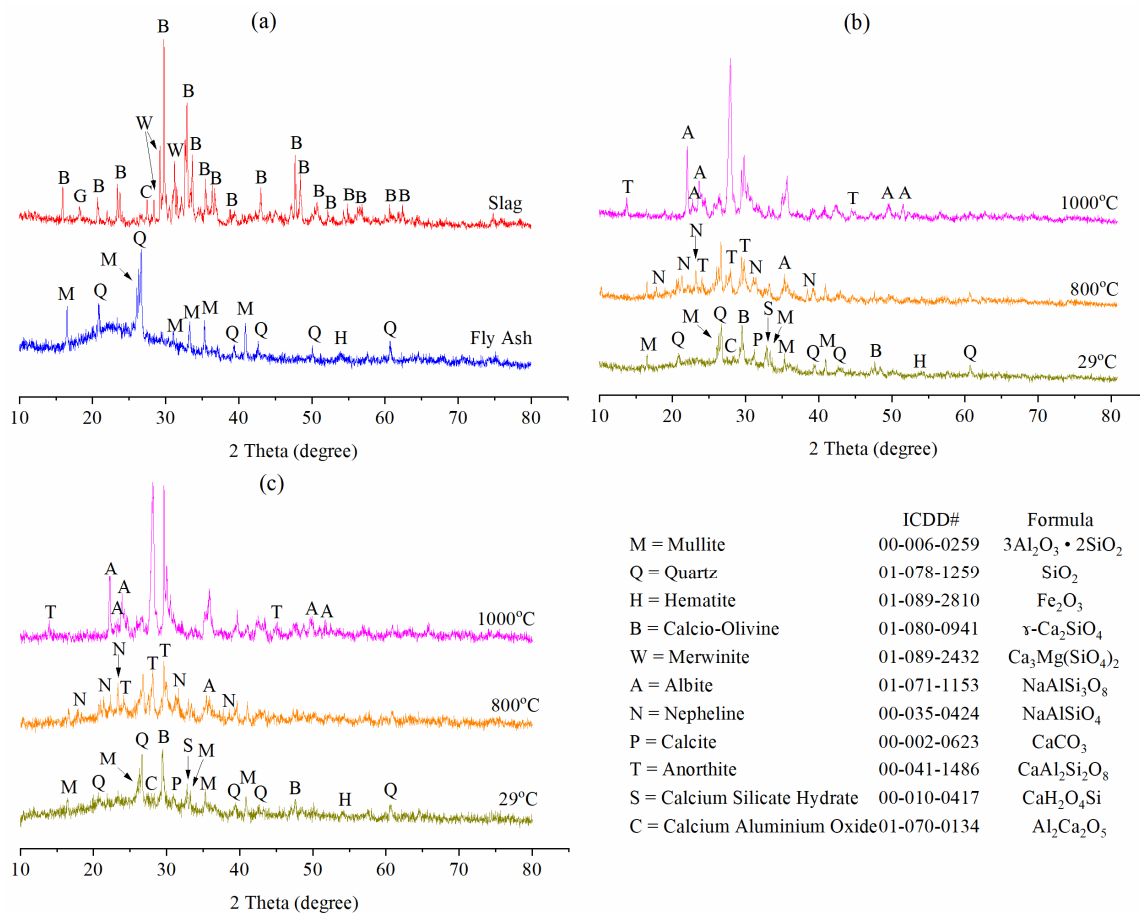
Figure 12. Phase patterns of (**a**) fly ash and slag, unexposed and temperature-exposed (**b**) G-0 and (**c**) G-2.

The rise in temperature caused the (i) crystalline peaks to change, increase, reduce, disappear and/or decompose and (ii) amorphous phase (geopolymer matrix) to reduce and/or decompose (Figure 12b,c). Calcite and CSH vanished and decomposed at 800 °C, as supported by Shaikh [23] for unfoamed geopolymer. The combined decomposition of the geopolymer matrix, calcite and CSH caused nepheline, albite and anorthite to form at 800 °C and 1000 °C. The presence of anorthite was also confirmed by the SEM image in Figure 11c'. The addition of PAS foam did not cause any changes to the phase patterns of geopolymer at room temperature and high temperatures.

3.5. Functional Group Identification

Figure 13 plots the IR spectra of fly ash, slag, unexposed and temperature-exposed G-0 and G-2. The main band of raw fly ash was located at 1031 cm^{-1}, corresponding to the asymmetric stretching vibration of Si-O-X (X = Si or Al) [24]. The band at 775 cm^{-1} was expressed as the symmetric stretching vibration of Si-O-Si [25]. Moreover, the main band of raw slag was located at 858 cm^{-1}, indicating the stretching vibration of Ca-O and Si-O [26]. The bands at 2168 cm^{-1}, 2025 cm^{-1} and 1418 cm^{-1} were verified as the stretching vibrations of O-C-O [27]. The bands at 2805 cm^{-1} and 3325 cm^{-1} were denoted as the stretching vibrations of OH and H-O-H [28].
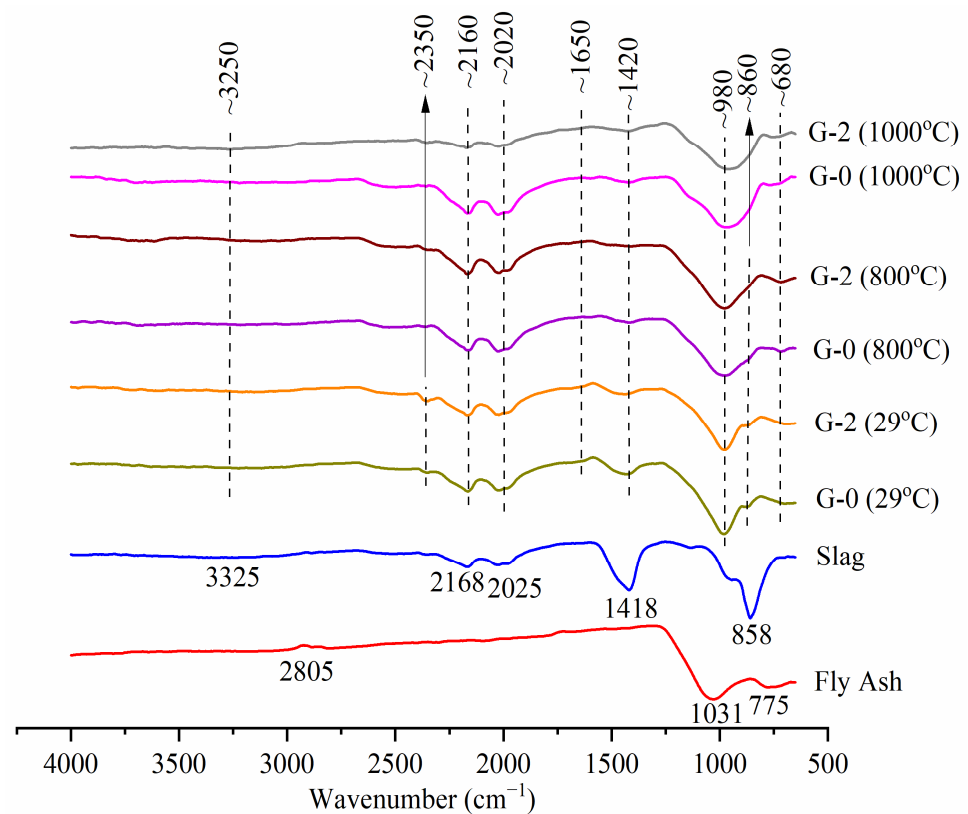
Figure 13. IR spectra of fly ash, slag, unexposed and temperature-exposed G-0 and G-2.

The presence of O-C-O (~2160, ~2020 and ~1420 cm^{-1}) and OH and H-O-H (~3250 cm^{-1}) stretching vibrations in the unheated G-0 and G-2 originated from raw fly ash and slag. New bands of calcite [29] and H-O-H bending vibration [30] appeared at ~2350 cm^{-1} and ~1650 cm^{-1}, respectively, in unheated G-0 and G-2. Calcite disappeared and decomposed at 800 °C, as proven by the phase analysis in Figure 12. The wavenumber of fly ash at 1031 cm^{-1} and 775 cm^{-1} shifted to ~980 cm^{-1} and ~680 cm^{-1}, respectively, in unheated G-0 and G-2, inferring the NASH matrix was formed [28,31]. The wavenumber of slag at 858 cm^{-1} shifted to a higher value in the unheated G-0 and G-2 (~860 cm^{-1}), implying the CASH matrix was formed [32].

The rise in temperature changed the intensity of the absorption bands of G-0 and G-2. The main band at ~980 cm^{-1} widened at high temperatures, especially at 1000 °C, indicating that the high temperatures led to the formation of structural disorder, as proven by the literature for unfoamed geopolymer [33,34]. The intensity of ~1650 cm^{-1} reduced at high temperatures, inferring that the geopolymer had dehydrated [19]. The intensity at ~860 cm^{-1} vanished at 1000 °C, implying that the cross-linking in the CASH matrix was lessened [35]. The addition of PAS foam did not create any new bands in the geopolymer at room temperature and high temperatures.

4. Conclusions

This paper compares the thermo-mechanical performance of fly ash-ladle furnace slag blended geopolymer with and without PAS foam addition at 29–1000 °C. The PAS foam-to-paste ratio of 1.0 and 2.0 was used to prepare geopolymer foam. The incorporation of PAS foam degraded the compressive strength of unheated G-0 (40.5 MPa) by 35.0–46.9%, and also decreased the heat-treated G-0 (36.9–43.1 MPa) by 7.6–33.9%. Nonetheless, when compared to unheated samples, the compressive strength of the heat-treated G-0 decreased by 2.2–8.7% at 400–1000 °C, whereas the compressive strength of the heat-treated G-1 and G-2 increased by 4.2–68.5% at the same temperature exposure. The higher porosity, lower thermal conductivity and lower connectivity of the geopolymer matrix aided dehydration

and reduced deterioration of the geopolymer structure, resulting in a significant improvement in the strength loss of foamed geopolymer.

References

1. Bai, C.; Colombo, P. Processing, properties and applications of highly porous geopolymers: A review. *Ceram. Int.* **2018**, *44*, 16103–16118. [CrossRef]
2. Mastura, W.I.; Mustafa, M.A.B.A.; Ahmad, R.; Naveed, A.; Ruzaidi, C.M.G.; Ibrahim, M. Effects of thermal resistance to fly ash-based lightweight geopolymer. *IOP Conf. Ser. Mater. Sci. Eng.* **2019**, *551*, 012082. [CrossRef]
3. Reeb, C.; Pierlot, C.; Davy, C.; Lambertin, D. Incorporation of organic liquids into geopolymer materials—A review of processing, properties and applications. *Ceram. Int.* **2021**, *47*, 7369–7385. [CrossRef]
4. Ibrahim, W.M.W.; Ahmad, R.; Coman, B.T.; Abdullah, M.M.A.B.; Puskas, A.; Jaganathan, V.S. The effects of solid to liquid ratio on fly ash based lightweight geopolymer. *IOP Conf. Ser. Mater. Sci. Eng.* **2020**, *877*, 012013. [CrossRef]
5. Ibrahim, W.M.W.; Hussin, K.; Abdullah, M.M.A.B.; Kadir, A.A.; Deraman, L.M.; Sandu, A.V. Influence of foaming agent/water ratio and foam/geopolymer paste ratio to the properties of fly ash-based lightweight geopolymer for brick application. *Rev. Chim.* **2017**, *68*, 1978–1982. [CrossRef]
6. Mastura, W.I.W.; Romisuhani, A.; Abdullah, M.M.A.B.; Faheem, M.T.M.; Ahmad, S.S.; Aida, M.M.N. Correlation between thermal insulation properties with compressive strength and density of lightweight geopolymer. *IOP Conf. Ser. Mater. Sci. Eng.* **2020**, *864*, 012040. [CrossRef]
7. Tiong, H.Y.; Lim, S.K.; Lee, Y.L.; Ong, C.F.; Yew, M.K. Environmental impact and quality assessment of using eggshell powder incorporated in lightweight foamed concrete. *Constr. Build. Mater.* **2020**, *244*, 118341. [CrossRef]
8. Bai, C.; Colombo, P. High-porosity geopolymer membrane supports by peroxide route with the addition of egg white as surfactant. *Ceram. Int.* **2017**, *43*, 2267–2273. [CrossRef]
9. Le-ping, L.; Xue-min, C.; Shu-heng, Q.; Jun-li, Y.; Lin, Z. Preparation of phosphoric acid-based porous geopolymers. *Appl. Clay Sci.* **2010**, *50*, 600–603. [CrossRef]
10. Zhang, Z.; Provis, J.L.; Reid, A.; Wang, H. Mechanical, thermal insulation, thermal resistance and acoustic absorption properties of geopolymer foam concrete. *Cem. Concr. Compos.* **2015**, *62*, 97–105. [CrossRef]
11. Yang, Z.; Mocadlo, R.; Zhao, M.; Sisson, R.D.; Tao, M.; Liang, J. Preparation of a geopolymer from red mud slurry and class F fly ash and its behavior at elevated temperatures. *Constr. Build. Mater.* **2019**, *221*, 308–317. [CrossRef]
12. Luo, Y.; Klima, K.M.; Brouwers, H.J.H.; Yu, Q. Effects of ladle slag on Class F fly ash geopolymer: Reaction mechanism and high temperature behavior. *Cem. Concr. Compos.* **2022**, *129*, 104468. [CrossRef]
13. Murri, A.N.; Rickard, W.D.A.; Bignozzi, M.C.; van Riessen, A. High temperature behaviour of ambient cured alkali-activated materials based on ladle slag. *Cem. Concr. Res.* **2013**, *43*, 51–61. [CrossRef]
14. Koyama, K.; Koyama, K.; Goto, K. Cardiovascular effects of a herbicide containing glufosinate and a surfactant: In vitroandin vivo analyses in rats. *Toxicol. Appl. Pharmacol.* **1997**, *145*, 409–414. [CrossRef]
15. Bakharev, T. Geopolymeric materials prepared using Class F fly ash and elevated temperature curing. *Cem. Concr. Res.* **2005**, *35*, 1224–1232. [CrossRef]
16. Hui-Teng, N.; Cheng-Yong, H.; Yun-Ming, L.; Abdullah, M.M.A.B.; Ern Hun, K.; Razi, H.M.; Yong-Sing, N. Formulation, mechanical properties and phase analysis of fly ash geopolymer with ladle furnace slag replacement. *J. Mater. Res. Technol.* **2021**, *12*, 1212–1226. [CrossRef]
17. Jaya, N.A.; Yun-Ming, L.; Cheng-Yong, H.; Abdullah, M.M.A.B.; Hussin, K. Correlation between pore structure, compressive strength and thermal conductivity of porous metakaolin geopolymer. *Constr. Build. Mater.* **2020**, *247*, 118641. [CrossRef]

18. Pan, Z.; Sanjayan, J.G.; Collins, F. Effect of transient creep on compressive strength of geopolymer concrete for elevated temperature exposure. *Cem. Concr. Res.* **2013**, *56*, 182–189. [CrossRef]

19. Cheng-Yong, H.; Yun-Ming, L.; Abdullah, M.M.A.B.; Kamarudin, H. Thermal resistance variations of fly ash geopolymers: Foaming responses. *Sci. Rep.* **2017**, *7*, 45355. [CrossRef]

20. Panesar, D.K. Cellular concrete properties and the effect of synthetic and protein foaming agents. *Constr. Build. Mater.* **2013**, *44*, 575–584. [CrossRef]

21. Škvára, F.; Jílek, T.; Kopecký, L. Geopolymer materials based on fly ash. *Ceram. Silik.* **2005**, *49*, 195–204.

22. Dombrowski, K.; Buchwald, A.; Weil, M. The influence of calcium content on the structure and thermal performance of fly ash based geopolymers. *J. Mater. Sci.* **2007**, *42*, 3033–3043. [CrossRef]

23. Shaikh, F.U.A. Effects of slag content on the residual mechanical properties of ambient air-cured geopolymers exposed to elevated temperatures. *J. Asian Ceram. Soc.* **2018**, *6*, 342–358. [CrossRef]

24. Liu, Y.; Zhu, W.; Yang, E.H. Alkali-activated ground granulated blast-furnace slag incorporating incinerator fly ash as a potential binder. *Constr. Build. Mater.* **2016**, *112*, 1005–1012. [CrossRef]

25. Peyne, J.; Gautron, J.; Doudeau, J.; Joussein, E.; Rossignol, S. Influence of calcium addition on calcined brick clay based geopolymers: A thermal and FTIR spectroscopy study. *Constr. Build. Mater.* **2017**, *152*, 794–803. [CrossRef]

26. Guetteche, M.; Abdesselam, Z.; Hannachi, S. Investigating the local granulated blast furnace slag. *Open J. Civ. Eng.* **2012**, *2*, 10–15. [CrossRef]

27. Aissa, B.; Long-yuan, L.; Abdullah, M.M.A.B.; Quoc-Bao, B. Mechanical properties and microstructure analysis of FA-GGBS-HMNS based geopolymer concrete. *Constr. Build. Mater.* **2019**, *210*, 198–209.

28. Prusty, J.K.; Pradhan, B. Multi-response optimization using Taguchi-Grey relational analysis for composition of fly ash-ground granulated blast furnace slag based geopolymer concrete. *Constr. Build. Mater.* **2020**, *241*, 118049. [CrossRef]

29. Pereira, A.P.; Silva, M.H.; Lima, É.P.; Paula, A.D.; Tommasini, F.J. Processing and characterization of PET composites reinforced with geopolymer concrete waste. *Mater. Res.* **2017**, *20*, 411–420. [CrossRef]

30. Ishwarya, G.; Singh, B.; Deshwal, S.; Bhattacharyya, S.K. Effect of sodium carbonate/sodium silicate activator on the rheology, geopolymerization and strength of fly ash/slag geopolymer pastes. *Cem. Concr. Compos.* **2019**, *97*, 226–238.

31. Khater, H.M. Effect of silica fume on the characterization of the geopolymer materials. *Int. J. Adv. Struct. Eng.* **2013**, *5*, 12. [CrossRef]

32. Criado, M.; Aperador, W.; Sobrados, I. Microstructural and mechanical properties of alkali activated colombian raw materials. *Materials* **2016**, *9*, 158. [CrossRef] [PubMed]

33. Lahoti, M.; Wong, K.K.; Tan, K.H.; Yang, E.H. Effect of alkali cation type on strength endurance of fly ash geopolymers subject to high temperature exposure. *Mater. Des.* **2018**, *154*, 8–19. [CrossRef]

34. Fernández-Jiménez, A.; Palomo, A.; Pastor, J.Y.; Martín, A. New cementitious materials based on alkali-activated fly ash: Performance at high temperatures. *J. Am. Ceram. Soc.* **2008**, *91*, 3308–3314. [CrossRef]

35. Bernal, S.A.; Rodríguez, E.D.; Mejía, R.d.G.; Provis, J.L. Performance at high temperature of alkali-activated slag pastes produced with silica fume and rice husk ash based activators. *Mater. Constr.* **2015**, *65*, e049. [CrossRef]

Article

Freeze–Thaw Effect on Road Concrete Containing Blast Furnace Slag: NMR Relaxometry Investigations

Liliana Maria Nicula [1], Ofelia Corbu [1,2,3,*], Ioan Ardelean [4], Andrei Victor Sandu [3,5,6,*], Mihai Iliescu [1] and Dorina Simedru [7]

1. Faculty of Civil Engineering, Technical University of Cluj-Napoca, 28 Memorandumului Street, 400114 Cluj-Napoca, Romania; Liliana.nicula@infra.utcluj.ro (L.M.N.); mihai.iliescu@staff.utcluj.ro (M.I.)
2. Research Institute for Construction Equipment and Technology, ICECON S.A. Bucharest, 266 Pantelimon Road, 2nd District, CP 3-33, 021652 Bucharest, Romania
3. Center of Excellence Geopolymer & Green Technology (CEGeoGTech), School of Materials Engineering, University Malaysia Perlis, Kangar 01000, Malaysia
4. Department of Physics and Chemistry, Technical University of Cluj-Napoca, 400114 Cluj-Napoca, Romania; ioan.ardelean@phys.utcluj.ro
5. Faculty of Materials Science and Engineering, "Gheorghe Asachi" Technical University of Iași, 67 Dimitrie Mangeron Street, 700050 Iași, Romania
6. Romanian Inventors Forum, Sf. P. Movila 3, 700089 Iasi, Romania
7. INCDO-INOE2000, Subsidiary Research Institute for Analytical Instrumentation, ICIA Cluj-Napoca, 67 Donath, 400293 Cluj-Napoca, Romania; dorina.simedru@icia.ro
* Correspondence: ofelia.corbu@staff.utcluj.ro (O.C.); sav@tuiasi.ro (A.V.S.)

Abstract: The present work investigates the effect of freeze–thaw cycles on the porosity of three mixtures of road concrete containing blast furnace slag in comparison with two mixtures made with conventional materials. The main technique used in our investigations is nuclear magnetic resonance (NMR) relaxometry. This permitted the extraction of information with respect to the freeze–thaw effect on pore-size distribution, which influences both the mechanical strength and the molecular transport through the material. Moreover, by using this technique, the structure of the air voids was analyzed for the entire pore system in the cement paste and the aggregate particles. The samples under study were first dried in a vacuum oven and then saturated with water or cyclohexane where the distribution of the transverse relaxation times of the protons was recorded. The NMR relaxation measurements were performed on samples extracted from specimens maintained at 300 freeze–thaw cycles and on control samples extracted from specimens kept in water during the freeze–thaw period. Scanning Electron Microscopy (SEM) was used to analyze the microstructure of concrete samples in order to obtain information about the pore sizes and the distance between them. The results from the NMR relaxation measurements were consistent with those obtained by using standard techniques for determining the porosity and the freeze–thaw resistances. The investigations made it possible to establish the optimal composition of blast furnace slag that can be incorporated into road concrete compositions. This non-invasive technique can also complete standard techniques for assessing the porosity and the progress of internal cracks during the freeze–thaw test.

Keywords: road concrete; porosity; (NMR) relaxometry; freeze–thaw; blast furnace slag

1. Introduction

The resistance to freezing is a factor that needs to be considered when designing road concrete structures because the freeze–thaw phenomenon produces deterioration of the internal structure and on the surface layer of the concrete. If the concrete is exposed to a dry environment the structure is not usually affected by the freeze–thaw phenomenon. However, due to the fact that the road concrete is in contact with water, the water is absorbed by the concrete in the structure of the pores and it generates a high internal

tension, which leads to internal structure damage and produces irreversible changes of its properties [1–3].

The most important factor influencing freeze–thaw resistance is the distribution and dimensions of the pores [1,4]. The free spaces filled with water in the fresh cement paste or the spaces resulting from the reaction of cement particles during the process of hydration of the cement paste represents the fraction of total volume unoccupied by solid matter and is known as porosity. By mixing components, the cement particles are spread in the total volume of materials and, upon contact with water, reaction takes place between the mineral components and the solution forming around the cement particles. The dispersion of cement particles as evenly as possible is improved by the superplasticizers used [5]. These particles are transformed in colloids by dispersing the solid substance in the liquid due to the forces of attraction at the molecular and atomic level, but the water continues to penetrate inside these colloids. The pore size does not change much during the mixing and dormancy stage in which the activity of the chemical compounds slows down, but there is a change in their size that commences during the hardening stage [6]. The hardened cement paste in the cooling and densifying stage consists of hydrates of different compounds in the form of a gel, calcium hydroxide crystals $Ca(OH)_2$, and other minor components, such as un-hydrated cement, and free spaces left in the hydration process [7]. Moreover, additional pores may result in the concrete application stage due to improper compaction. The free spaces that have not been filled with hydration products form capillary pores and the free spaces formed in gel as interconnected spaces define the gel pores. These gel pores can be classified into intra-C-S-H and inter-C-S-H pores [8].

The total volume of voids in concrete can occupy between 1% and 10% of the total volume and a porous concrete at the upper limit indicates low strength [7]. The capillary pores form an interconnected system spread irregularly throughout the mass of the paste [7,9], with sizes ranging from 50 nm and up to 5 μm [10]. The dimensions of the gel pores are much smaller than the capillary pores (approximately $1 \div 50$ nm) and, therefore, are classified as micropores. The gel pores absorb water even at very low values of ambient humidity [7,9] due to the hygroscopic property of the cement paste and the presence of submicroscopic pores. The spaces with larger dimensions of $5 \div 10$ μm are considered as entrained air [10].

The PN-EN 480-11 standard [11] describes the air-voids system in the hardened concrete by the following parameters: total air content A (%), specific surface α (mm^2), spacing factor L (mm) and the micropores content A_{300} (%). The spacing factor (L) of the air pores can be determined using the simplified Powers' model, which assumes that all air bubbles have the same diameter and are distributed in the corners of a cube. Another approach for determining the spacing factor (L) of the air pores is based on the Pilleo concept, which considers both the air voids system in the cement paste and in the aggregate particles; the principles of the method were described by Wawrzeńczyk J. and Kozak W. in their paper [12]. The sustainability requirements limit the spacing factor to 0.20 mm in Norway and Denmark and to 0.25 mm in Canada [13]. Yuan J. [14] experimented with the variation of concrete pores in the action of freeze–thaw cycles using X-ray tomography (CT). The results showed that there was no large variation in the amounts and volume of pores located in the range (0.5 mm^3–20 mm^3), but there were major changes for pores in another range. Tracz T. and Zdeb T. [15] studied the effects of hydration and carbonation on porosity and permeability at 90 days and up to 2 years of preservation on pastes made of ordinary Portland cement with different ratios of w/c. The results highlighted changes in capillary porosity caused by subsequent hydration advances and the carbonation phenomenon, while the depth of permeability did not change significantly during the monitored period.

Due to the pozzolanic and hydraulic properties, supplementary cementitious materials SCM may be used as a substitute for cement in the designed composition. They influence the properties of fresh concrete by their reaction with water or calcium hydroxide CH and forms additional hydrating compounds. Supplementary cementitious type materials may have pozzolanic properties by chemically reacting with calcium hydroxide to form

additional hydrated calcium silicate C-S-H, which is a hydrating compound that has the greatest contribution to the development of concrete strength [6].

In this context the granulated and ground blast furnace slag GGBS in combination with ultrafine silica SF are used in the concrete industry for different applications because they have strength, durability, economic and environmental benefits.

Rao S.K. et al. [16] investigated the effect of GGBS on mechanical properties and the abrasion resistance of RCC for a level of substitution of cement with GGBS from 10% to 60%. Roller compacted concrete (RCC) is a stiff mixture of traditional concrete components that is proportioned with higher aggregate content and lower cementitious material content than compared to conventional concrete [6]. The test results showed that after the age of 28 days the increase in GGBS content led to an increase in the abrasion resistance of RCC at all replacement levels. Aghaeipour A. et al. [17] investigated the effects of GGBS as a substitute for cement in different percentages (20%, 40% and 60%) regarding water absorption, permeability and freeze–thaw resistance in RCC, with applications in road infrastructures in mind. The results not only showed a reduction in water absorption but also in mechanical resistances of concretes with GGBS compared to those without GGBS content. The depth of water penetration under pressure was lower for substitution levels up to 40%, after which it was higher than the value obtained from the control mixture. The lowest losses of resistance after 300 freeze–thaw cycles were registered in mixture with 60% substitution of GGBS, which is lower than the control mixture. Limbachiya V. et al. [18] made concrete paving blocks using GGBS and silica fume SF to replace the ordinary Portland cement OPC. High content of SiO_2 in SF and of CaO in GGBS increased the durability properties of concrete paving blocks, which allowed the successful replacement of cement up to 40%. However, it was observed that the levigation properties of the blocks with GGBS and SF decreased, but within acceptable limits regarding the soil protection at levigation. In addition to improving the mechanical properties, the reduction in cracks developed in concrete during the different stages of hardening and densification is just as important for the durability of road pavements. Crack growth restriction has been studied in the works [19,20] by using hybrid fibers, such as steel-polyvinyl-polypropylene-calcium carbonate $CaCO_3$, in cementitious compositions. The research conducted by Lam M.N.-T. et al. [21,22] investigated the feasibility of using slag aggregate resulting from electric arc furnace (FEA) to partially replace natural coarse aggregates and fly ash to partially replace cement.

The investigation methods regarding the effect of the supplementary cementitious materials are varied and depends on the envisaged properties of the manufactured materials. Moreover, research aims to establish the links between microscopic and macroscopic properties [23]. Nedunuri S.S.S.A. et al. [24] used water saturation and mercury porosimetry to study the evolution of pore structure as a function of the hardening age of Portland cement and of those that are partially replaced with SCM, such as SF, GGBS and fly ash. Majhi R.K. et al. [25] determined the rate of water absorption by capillary pores using the sorptivity test on concrete with GGBS and aggregates recycled from concrete in its composition. The microstructural characteristics extracted from scanning electron microscopy and X-ray diffraction, confirmed the results obtained by such classical methods. Renato J. et al. [26] studied the porosity of concrete using two non-destructive methods, which are X-ray microtomography and digital scanning. The porosity results obtained through the non-destructive methods were compatible with those obtained through the standard mercury intrusion porosimetry MIP test. However, the study by Diamond S. [27] drew attention to the fact that the MIP method is inadequate for measuring the pore size due to the method's inability to penetrate the C-S-H gel pores; however, it is rather suitable for assessing the apparent porosity. The analysis of the pore structure was performed in the study [28] using the fractal theory, which allows a quantitative evaluation based on the fractal size of the pores. By the fractal model proposed by Jin S. et al. [29], a regression relationship was obtained between the fractal size and the durability factor. The characteristic parameters of the pore structure of the recycled concrete with residual fibers were

investigated in the study conducted by Zhou J. et al. [30] by using the mercury intrusion porosimetry test and fractal theory. The results showed that the pore structure was mainly influenced by the water–cement ratio. The morphology of the pores developed in the first 7 days of hardening of the concrete was analyzed in the paper [31] relative to two different compositions. The first is made of simple concrete (PC) and the second is a mixture of high-performance reinforced concrete (SFRC). The internal voids of the mixtures in combination with the geometric parameters were identified by computed tomography (CT) scanning and the data were analyzed using digital image processing software (DIP) [32].

Kowalczyk R.M. et al. [33] highlighted, via nuclear magnetic resonance NMR relaxometry technique, the mechanism of water–isopropanol exchange in cement pastes. The results showed that the isopropanol revealed the presence of capillary pores better than revealed in the experiments on samples saturated with water. On the other hand, isopropanol draws water out from the gel pores but does not replace it in the same amount. One of the non-destructive methods commonly used to assess internal cracks resulting from the freeze–thaw phenomenon is the method of measuring the ultrasonic pulse propagation time (UPTT) in compliance with the Technical Report CEN/TR 15177:2006 [34]. The increase in propagation time of the wave through concrete shows a greater number of voids and internal cracks.

The great advantage of the NMR techniques is that they are completely non-invasive and, in addition, they permit the study of materials without prior preparation of samples. In the present work, NMR relaxometry [5,8,35–41] is used, again, to determine the residual water within the pores of the material and the effects of the freeze–thaw cycles on the porous system. Using this technique, information can be obtained about the porous structure of concrete containing a mixture of cement paste and aggregates, which is similar to the approach of Wawrzeńczyk J. and Kozak W. [12] and based on the Philleo concept. The NRM investigations on the effects of the freeze–thaw cycles complement the results obtained by measuring the physical characteristics (density, water absorption and content of permeable pores) of hardened road concrete determined by standard methods. The porosity results obtained from this experiment were compared to the results obtained in a previous experiment [42] on the compressive strengths and the loss of compressive strength after 300 freeze–thaw cycles. The microstructure of the concrete (in this case the pore sizes and the distance between them) can be investigated and analyzed using Scanning Electron Microscopy (SEM). The porosity induced by freeze–thaw cycles was analyzed for three mixtures, prepared with blast furnace slag and compared with two conventional mixtures used in road pavements. The investigation methods aimed to obtain more accurate conclusions for the selection of the optimal mixture of the blast furnace slag that would ensure durability for road concrete.

2. Materials and Methods

2.1. Materials

The Portland cement used for preparing the samples is of the CEM I 42,5R type and it was supplied by Lafarge Holcim S.A. The performances stated by the manufacturer are in compliance with the technical specification from SR EN 197-1:2011 [43]. The specified cement surface is 4385 cm^2/g and the specific weight is 3.00 g/cm^3. The granulated blast furnace slag 0/12.5 mm obtained by sudden cooling in water was supplied by the company Liberty (Galați, Romania). After grounding to under 69 μm, the granulated and ground blast furnace slag GGBS reached the specific surface of 5770 cm^2/g and specific weight of 2.77 g/cm^3. The admissibility conditions of the GGBS blast furnace slag were in compliance with the technical specifications from SR EN 15167-1:2007 [44]. The high content of 95% vitreous mass and the 1.15 ratio between calcium oxide and silicon oxide demonstrates good activity. The value of the activity index at 28 days was 74.94%. The values obtained for the alkalis content of 1% and the 0% calcination loss show that the GGBS used does not generate expansion by its use in concrete mixtures. Table 1 demonstrates the oxide composition for cement and (GGBS).

Table 1. Oxide content for cement CEM I 42.5R and (GGBS) (%).

Oxides	SiO$_2$	Al$_2$O$_3$	MnO	MgO	CaO	Fe$_2$O$_3$	Na$_2$O	K$_2$O
CEM I 42.5R	18.57	3.09	3.72	0.70	63.93	4.84	0.12	0.74
GGBS	36.44	11.60	0.55	5.8	41.81	0.78	0.345	0.428

The aggregate proportions used in the preparation approach were 32% sand (sand dimension of 0/4 mm) and 68% coarse aggregate with a maximum grain dimension of 25 mm. The selection of aggregates was in compliance with the national standard NE 014:2002 [45] for road coating with role of wear and the physical properties were in compliance with SR EN 12620:2003 and SR EN 12620+A1:2008 [46]. The granulometric curve of the total aggregate mixture followed the framing within the granulometric area that is permitted by the standard NE 014-2002 [45]. The coarse aggregates were made of crushed river gravel (4/8) and crushed quarry rock (dacite from the category of igneous rocks) that were (8/16) and (16/25) mm, respectively. The use of crushed aggregates enables better adhesion between the aggregate and the cement paste due to the irregular surface, which is beneficial for the resistance to bending. The crushed strength of 14% (expressed by the Los Angeles coefficient) and the wear resistance of the aggregates of 6% (expressed by the micro-Deval coefficient) demonstrate superior performance compared to the standard SR EN 12,620 [46] result of tests performed by the manufacturer. The artificial aggregate from ungranulated blast furnace slag (ACBFS) is a crystalline by-product resulting from the solidification in air of molten blast furnace with applications in road pavements [47]. The characteristics of natural sand and aggregates (ACBFS) were determined by the manufacturer and are presented in Table 2.

Table 2. Characteristics of natural sand (NA) and of aggregates from blast furnace slag (ACBFS), 0/4 mm.

Technical Characteristics	Obtained Values ACBSF_0/4 mm	Obtained Values NA_0/4 mm	Limits SR EN 12620
Granularity	GF $_{85}$	GF $_{85}$	GF $_{85}$
Coefficient of water absorption	WA$_{24}$2	WA242	-
Content of fine particles <0.063 mm, %	f$_{3.5}$	f$_3$	(3 ÷ 22)
Sulphate soluble in acid, %	AS $_{0.52}$	-	≤1.0
Total sulphate, %	0.96	-	≤2.0
Disintegration of iron from blast furnace slag	Does not present cracks and disintegrate	-	Visual aspect
Disintegration of dicalcium silicate from blast furnace slag	Presents a uniform violet color, with shining stains in small quantities uniformly distributed	-	Visual aspect

The additives used here are commercially available from Badische Anilin und Soda Fabrik (BASF, Ludwigshafen, Germany). As a superplasticizer, we used MasterGlenium SKY 527 and air training additive Master Air 9060 (BASF, Germany) and both possess characteristics in compliance with SR EN 934-2+A1:2012 [48]. The water in the concrete mixture was taken from the water supply system of the city Cluj-Napoca in compliance with SR EN 1008:2003 [49].

2.2. Sample Preparation

The parameters of designing the road concrete complied with the minimum requirements for the severe exposure class (XF4) in accordance with SR EN 206-1:2002 and SR EN 206+A1:2017 [50]. The classification in conditions of exposure according to the XF4 class requires a minimum cement dosage of 350 kg/m^3, maximum w/c ratio of 0.45 and a minimum strength class of C35/45 with entrained air [50,51]. A number of five mix-

tures were prepared with different quantities of materials presented in Table 3. The first two control mixtures were prepared using Portland cement type CEM I 42,5R utilizing natural aggregates and the following three mixtures were prepared using granulated and crushed blast furnace slag, under 63 μm, and aggregates from crushed blast furnace slag at a dimension of 0/4 mm in different proportions. The below observations were used:

S 360, control mixture of 360 kg/m^3 Portland cement dosage and natural aggregates;

S 414, control mixture of 414 kg/m^3 Portland cement dosage and natural aggregates;

S 54/20, 360 kg/m^3 (cement) + 54 kg/m^3 (GGBS) and 20% (ACBFS)_0/4 mm + 80% (NA)_0/4;

S 54/40, 360 kg/m^3 (cement) + 54 kg/m^3 (GGBS) and 40% (ACBFS)_0/4 mm + 60% (NA)_0/4;

S 54/60, 360 kg/m^3 (cement) + 54 kg/m^3 (GGBS) and 60% (ACBFS)_0/4 mm + 40% (NA)_0/4.

Table 3. Material quantities in mixtures.

Quantities (kg/m^3)	Mixtures (kg/m^3)				
	S 360	S 414	S 54/20	S 54/40	S 54/60
Cement (C)	360	414	360	360	360
Blast furnace slag powder (GGBS)	-	-	54	54	54
Total binder (L)	360	414	414	414	414
Water (W)	156.60	169.74	167.67	178.02	178.02
W/L, (water/binder)	0.44	0.41	0.41	0.43	0.43
Natural sand (NA 0/4 mm)	596	586	477	347	232
Blast furnace slag aggregate (ACBFS 0/4 mm)	-	-	119	232	347
Coarse aggregate (CA 4/25 mm)	1268	1245	1267	1231	1231
Total aggregate	1864	1831	1863	1810	1810
Superplasticizer additive	3.60	4.14	4.14	4.97	4.97
Air training additive	1.08	2.07	2.07	2.07	2.07
Slump (mm)	14	15	13	16	15
Fresh state density	2380	2415	2444	2402	2402

Compared to the control mixture S 360, the blast furnace slag (GGBS) was brought as a contribution to the cement mass in a percentage of 15% and, compared to the control mixture S 414, the GGBS substituted the cement in a percentage of 13%. The ground granulated blast furnace slag was used in road concrete mixtures as a binder with supplementary constituents with cement characteristics similar to those described in the study [52]. Natural sand NA was substituted in percentages of 20%, 40% and 60% with crushed blast furnace slag aggregates ACBFS with dimensions of 0/4 mm. In this experiment the water content and additive content was adjusted to maintain the consistency of the concrete at the most appropriate values of 20 mm.

2.3. Methods

2.3.1. Sampling, Preservation and Preparation of Samples for Testing

For each mixture, 8 cubic specimens with a side of 150 mm and 3 specimens with a side of 71 ± 1.5 mm, as shown in Table 4, were prepared and kept in the air for 24 h after which they were stripped and immersed in water at a temperature of 20 ± 2 °C.

At the age of 7 days, all specimens were removed from water and stored in the climatic chamber at a temperature of 20 ± 2 °C and at a humidity of 65% ± 5% up to the age of 50 days. Next, the cubic specimen with the side of 71 mm was kept in water until the age of 100 days and the abrasion resistance was then determined; the values of are found in paper [53]. From the age of 100 days to the age of 150 days they were kept in the air in the climate chamber. The density, water absorption and content of permeable pores were determined from the average of the results for the 3 cubic specimens for each type of mixture with the side of 71 mm and at the age of 150 days in compliance with the standard

ASTM C642-2006 [54]. The nuclear magnetic resonance measurements were performed on concrete cores extracted from two intact 150 mm cubes for each mixture; one tested for 300 freeze–thaw cycles and one control specimen maintained in water until the age of 150 days. For the NMR measurements, the cubes with apparent density close to the average of the 3 cubes tested for the freeze–thaw in the study were selected [42] by the method of the loss of compressive strength according to SR 3518:2009 [55]. The thermostatic chamber was set to maintain a temperature of $(-17 \pm 2)\ °C$ for 4 h for the freeze cycle, up to $(20 \pm 2)\ °C$ for the thaw cycle for 4 h and the humidity of RH 95%. Four days before the commencement of the test, the specimens were placed in a water tank at a temperature of $(20 \pm 5)\ °C$ for saturation and the control specimens were kept in water. Those intended for the freeze–thaw cycles were introduced in the thermostatic chamber, such as in Figure 1.

Table 4. Number of samples prepared for testing in each composition.

Name of Tests (Test Method)	Number of Samples (Pieces)	Dimension (mm)	Trial Age (Days)
Dry density, density after immersion and boiling and content of permeable pores (ASTM C642: 2006)	3	71 mm	150
Control samples kept in water (w) (SR 3518: 2009)	3	150 mm	150
Tests tested at 300 cycles (f-t) (SR 3518: 2009)	3	150 mm	150
Control samples kept in water (w) (NMR relaxometry and SEM)	1	150 mm	150
Tests tested at 300 cycles (f-t) (NMR relaxometry)	1	150 mm	150

Figure 1. Control specimens kept in water and specimens underwent the freeze–thaw test (150 mm × 150 mm × 150 mm).

After 300 repeated freeze–thaw cycles, the specimens were tested for compression and the compressive strength losses were calculated, for the specimens tested with freeze–thaw cycles compared to the control specimens, with Equation (1) as follows:

$$\eta_n = \frac{f_{cmwater} - f_{cmfreez}}{f_{cmwater}} \times 100 \ (\%) \tag{1}$$

where:

η_n—the compressive strength loss after "n" freeze–thaw cycles;

$f_{cm\ water}$—the average compressive strength of the samples maintained in water during "n" freeze–thaw cycles;

$f_{cm\ freeze}$—the average compressive resistance of the samples maintained in the thermostat chamber during "n" freeze–thaw cycles.

Compressive strength at 150 days was determined by applying a uniform and continuous force increasing in increments of 0.5 MPa/s on a loading machine type Advantest 9

of 300 tf. in accordance with SR EN 12390-3:2002 [56] and is calculated as by Equation (2) as follows:

$$f_c = \frac{F}{A_c} \text{ (MPa)} \tag{2}$$

where:

f_c—compressive strength in N/mm^2,
F—the maximum load in N;
A_c—cross-sectional area of the section of rupture in mm^2.

2.3.2. NMR Relaxometry Approach for Determining the Pore Size Distribution

The NMR relaxometry techniques are completely non-invasive and allow the investigation of cement samples without special prior preparation. These have been used successfully in the recent years to extract information about the porous structure of cement-based materials and to extract information with respect to the evolution of water inside the pores during the hydration process [5,8,35–40]. In the NMR relaxometry of cement-based materials, both the longitudinal relaxation time and the transverse relaxation time can be monitored [5,8,35–40]. Due to the fact that longitudinal relaxation measurements are slower and are more difficult to apply to the systems that evolve during the measurement process, it is preferable for many applications to measure the transverse relaxation time. However, in the case of transverse relaxation measurements, it is important to take into account the effects that diffusion in internal gradients could have on the accuracy of the measurement and so it is preferable that they be performed in low magnetic fields and with pulse sequences that could minimize internal gradients effects [5,8,40].

A technique often used in NMR applications on cement-based materials is known as the Carr-Purcell-Meiboom-Gill (CPMG) technique [57]. This technique allows the rapid and robust measurement of the transverse relaxation rate ($1/T_2$) of the nuclear spins and if the time interval between radio frequency pulses is short, the influence of internal gradients can be neglected. Under these conditions, there is a relationship [5,8,37–39] between the transverse relaxation rate and the surface-volume (S/V) ratio of the pores that is described as follows.

$$\frac{1}{T_2} = \varepsilon \frac{S}{V} \tag{3}$$

In the above equation, ε represents the surface relaxivity, which is a constant that depends on the interaction of molecules with the surface, the intensity of the magnetic field in which the NMR experiment is performed and the content of magnetic impurities of the pore surface. Note that in Equation (3) we neglected the contribution of bulk relaxation to the phenomenon of nuclear relaxation because the bulk relaxation time is much longer than the one induced by the surface. Based on Equation (2) we can establish a direct proportionality between the relaxation time and the pore size. This proportionality allows us to discover the distribution of pore dimensions if we know the distribution of relaxation times and the relaxivity of the surface. Even if the relaxivity of the surface is not known, information can be obtained about the relative distribution of pore sizes. This distribution can be extracted from the CPMG echo series if a numeric Laplacian transformation is applied to this series [58,59].

In the present work, in order to highlight the effect of the freeze–thaw cycles on the relative distribution of pore sizes, the specimens were investigated by NMR relaxometry at the age of 150 days and after the completion of the 300 freeze–thaw cycles. The test period in the study was extended from the requirements of national standard NE014-2002 [45] from 100 to 300 freeze–thaw cycles and is similar to the number of freeze–thaw cycles provided by the standard ASTM C666/C666M-03 [60]. A laboratory exposure of concrete samples to an extended number of repeated freeze–thaw cycles can simulate, as closely as possible, the damage caused by the freeze–thaw phenomenon in concrete exposed to real weather, as experienced in the literature [61], where the samples were tested in a laboratory for up to 1000 freeze–thaw cycles. From the core of intact cubes kept in the

thermostatic chamber and the control cubes kept in water during this period, cylindrical samples with a length of 20 mm and a diameter of 9.5 mm were extracted, such as in Figure 2. To eliminate interpretation errors, the mass of the samples extracted from the cubes was the same for each mixture of 1.06 g. It was possible to take samples for testing at these small sizes because the proportion of maximum size aggregates has a relatively small volume of the total volume of aggregates. The samples were dried in an oven at $105 \pm 5\,°C$ for 24 h to eliminate water from the pores. They were then inserted into 10 mm NMR tubes which were sealed to prevent molecular exchange with water from atmospheric air. After measuring the dry samples, they were dried again and immersed in water for 48 h at $22 \pm 2\,°C$. After this interval, the samples were lightly buffered with filter paper, then inserted into the NMR tubes and sealed. The third set of measurements was performed on samples saturated with cyclohexane and follows the same procedure as in the case of samples saturated with water. The saturation with cyclohexane was performed to better highlight the inter-C-S-H pores and capillaries, as is demonstrated in the other study [8]. Note that the intra-C-S-H pores are highlighted by the presence of water molecules that cannot be removed without destroying the material [8].
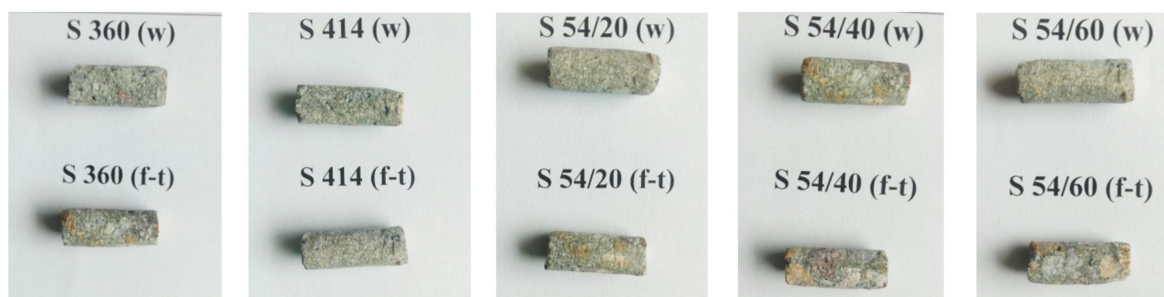
Figure 2. Samples ready for the NMR measurements.

The NMR measurements were performed with a low field instrument MinispecMQ20 (Bruker, Karlsruhe Germany) using the CPMG technique. Before each measurement, the samples were permitted to reach the thermal equilibrium at a temperature of 35 °C. A number of 2000 spin echoes were recorded in each experiment and the time between two echoes was maintained at 0.1 ms to reduce the effects of internal gradients on the measurements. Relaxation time distributions were extracted from the CPMG echo series using a Laplace numerical inversion [59].

2.3.3. Scanning Electron Microscopy (SEM)

Small pieces of samples were taken from the interior part of the crushed samples and analyzed at room temperature using a VEGA3 SBU electronic microscope with an Energy Dispersive Spectrometer Quantax EDS from Bruker in order to obtain information about the pore's sizes and the distance between the pores. Fragments from the 150 mm side cubes remaining after the NMR measurements were used from the control sample set, which was kept in water during the freeze–thaw test.

2.3.4. Density after Immersion and Boiling, Water Absorption and Proportion of Permeable Pores

The density after immersion and boiling, water absorption and permeable pore content were obtained by a method in accordance with ASTM C 642-2006 [54] that was used in another study [62]. The water-saturated samples with the dry saturated surface were weighted in air (*b*) and then dried in an oven at 100–110 °C until a constant mass (*a*) was reached. The samples were then placed in a suitable container, covered with tap water and boiled for 5 h. They were then allowed to cool to room temperature ($22 \pm 2\,°C$). The moisture from the surface was removed with a towel and the dry mass of the surface-dry sample suspended in air after immersion and boiling was determined (*c*), with the mass

measured in air. The apparent mass (*d*), after immersion and boiling, was measured in water with the hydrostatic balance, such as in Figure 3. The absorption after immersion (*m*$_1$) and absorption after immersion and boiling (*m*$_2$) were calculated with the following equations.

$$m_1 = [(b-a)/a] \times 100 \tag{4}$$

$$m_2 = [(c-a)/a] \times 100 \tag{5}$$

Figure 3. Hydrostatic weighing of cubes with 71 mm side.

Dry mass density, ρ_1, and density after saturation and boiling, ρ_2, were calculated with the following equations:

$$\rho_1 = [a/(c-d)] \times \rho_w \tag{6}$$

and

$$\rho_2 = [a/(a-d)] \times \rho_w \tag{7}$$

For water density, ρw, the value of 0.998 g/cm^3 was used. The permeable pore proportion was calculated with the equation:

$$P_0 = [(\rho_2 - \rho_1)/\rho_1] \times 100, \text{ specified in \%} \tag{8}$$

which is in accordance with ASTM C 642-2006 [54] standard.

3. Results and Discussion

3.1. Relative Distribution of Pore Sizes

The distribution of transverse relaxation times for the gel pores obtained from the Laplace numerical inversion, for each composition described in Table 3, is shown in Figures 4 and 5. Three peaks can be distinguished in all cases and the position of the peaks can be associated with the three types of pores. The values recorded on the horizontal axis for the transverse relaxation time T$_2$ are proportional to the pore size (see Equation (3)) and the values recorded on the vertical axis show the probability of having a certain pore dimension. The measuring unit on the y-axis is arbitrary (a.u. = arbitrary units). For a direct comparison of the curves, the same scale was used at each measurement performed.

Figure 4 depicts the samples dried according to the procedure described above, both control samples (Figure 4a) and those subjected to the freeze–thaw process (Figure 4b). A small amount of water (the first peak) was observed in the gel-like pores (intra C-S-H) with dimensions up to 2 nm [8], which could not be removed during drying process. In the mixture S 360, the distribution of transverse relaxation times corresponding to the gel pores (intra C-S-H) for the control samples, preserved in water (Figure 4a), shows a maximum placed in the range 0.02–0.3 ms and indicated a maximum probability density of 0.0045 for a value of T$_2$ of 0.08 ms. At T$_2$, the values slightly shifted to the right and

the maximum probability density decreased to 0.003 for the mixtures S 54/20 and S 54/40 followed by the mixtures S 414 and S 54/60, with an intensity inferior to 0.002. However, for the samples subjected to 300 freeze–thaw cycles (Figure 5b), the transverse relaxation time distribution interval shifted to the right (for S 414, S 54/20, S 54/40) at the higher pore size values between 0.02–0.6 ms and the most accentuated values were recorded in the mixtures S 360 and S 54/60 between 0.06–0.6. For all mixtures stored in the refrigerator (f-t), a maximum probability density close to the value recorded for the control mixtures, 0.003, was registered. The results of the experiment show that, after the freeze–thaw test, the pore size was higher compared to the control mixtures, which indicated the appearance of microcracks even in the intra C-S-H pores.
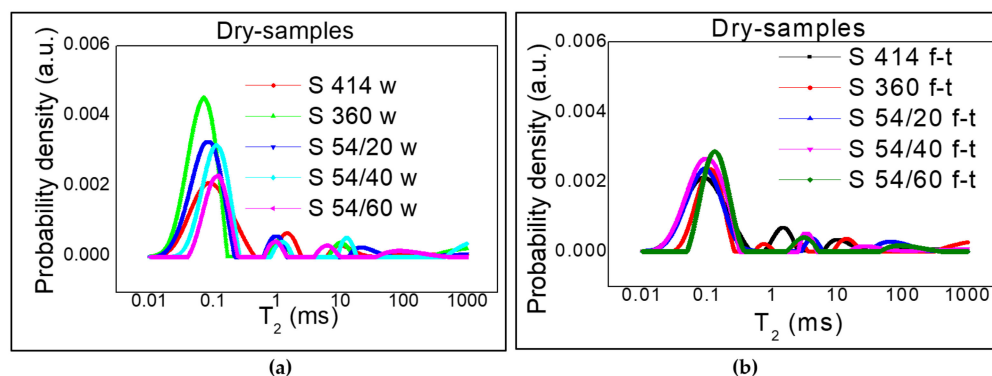
Figure 4. Distribution of the transverse relaxation time T_2 after drying: (**a**) control samples kept in water (w); (**b**) samples subjected to 300 freeze–thaw cycles (f-t).
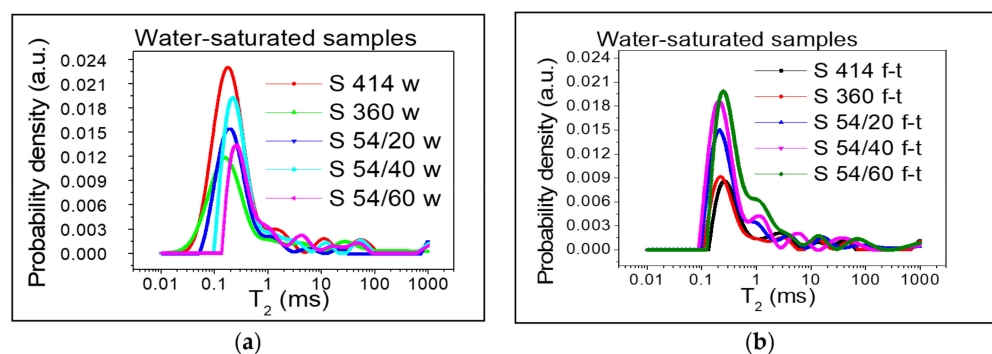
Figure 5. Distribution of the transverse relaxation time T_2 after water saturation: (**a**) control samples kept in water (w); (**b**) samples subjected to 300 freeze–thaw cycles (f-t).

By introducing the samples into the water, the clear increase in the area of the peaks corresponding to the gel pores (intra C-S-H and inter C-S-H) can be observed in Figure 5.

The pore distribution continues with several lower intensity peaks, which correspond to capillary pores, cracks or are artefacts of the numerical inverse Laplace. In the control samples (Figure 5a) the distribution of the transverse relaxation times was within the range 0.03–1.10 ms and for the mixtures tested for freeze–thaw (Figure 5b) the peak shift to the right was recorded at higher values, in the range 0.1–1.20 ms, as can be observed in Figure 6, which shows the starting and ending values for T_2 in each mixture corresponding to the gel pores as well as the position of the maximum (a.u.) (broken line).

The relative distribution of pore sizes in mixture S 54/20 and S 54/40 was kept close to the distribution in mixture S 360 and lower than the distribution in the control mixture S414 in both control samples and the samples tested for freeze–thaw. However, for the 54/60 mixture, the distribution range shifted to higher values compared to the two reference mixtures in both the control specimens and in the specimens that underwent the freeze–thaw text.
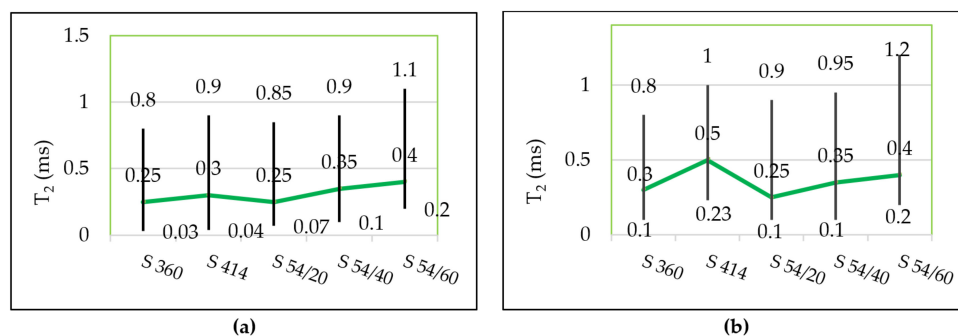
Figure 6. The distribution range of the gel pores for: (**a**) the control samples; (**b**) for samples subjected to freeze–thaw cycles. Both measurements are performed on water-saturated samples.

Figure 7a shows the maximum probability density recorded in both control samples kept in water (w) and in samples tested in water-saturated freeze–thaw (f-t). For the water-saturated control samples (Figure 7a), the maximum probability density with the highest value was registered in the mixture S 414 (of 0.023) and the lowest value (of 0.012) was obtained in the mixture S 360. In all blast furnace slag mixtures, the maximum probability density value corresponding to the gel pores is higher than the reference mixture S 360, but lower than in the control mixture S 414. For all water-saturated samples tested at 300 freeze–thaw cycles (Figure 7a), it was observed that the maximum value of the probability density corresponding to the peak of the gel pores increases with the increase in the percentage of substitution with blast furnace slag aggregate and it is above the level in the control mixtures S 360 and S 414. The largest difference in the maximum value of the probability density compared to the control sample was recorded in the mixture S 54/60 maintained at freeze–thaw.
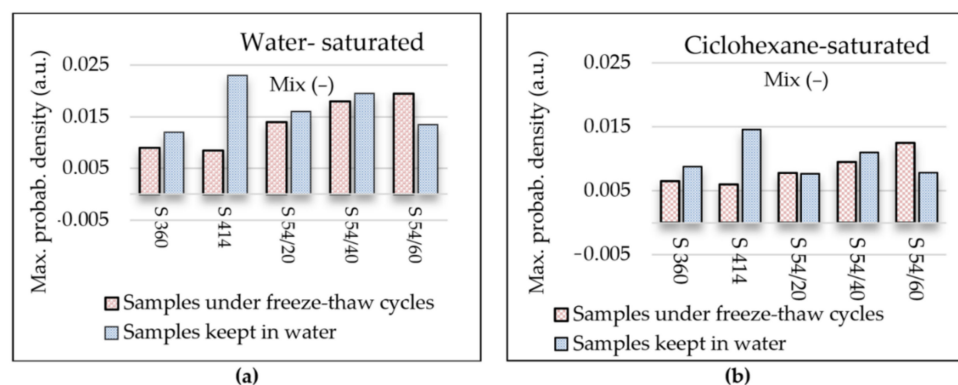
Figure 7. Maximum value of the probability density corresponding to the gel pores in the case of water saturated (**a**) and cyclohexane saturated (**b**) samples.

For the better monitoring of the capillary pores, it is preferable that they are saturated with cyclohexane because a higher degree of filling can be obtained in the case of cyclohexane than in the case of water [8]. This is due to the significantly lower contact angles in the case of cyclohexane than water relative to the mineral surfaces inside the cement paste [8,63]. Figure 8 shows the distribution of relaxation times and Figure 7b shows the maximum probability density corresponding to the peak of the capillary pores in the samples saturated with cyclohexane.

It is observed in Figure 7b that the evolution of the maximum probability density of the capillary pores has a tendency similar to that of the gel pores from the water-filled samples (Figure 7a); in all compositions with blast furnace slag, the intensity of the capillary pores increases with the increasing level of substitution of slag aggregate, respectively. In the control samples, the shortest range of distribution of capillary pores was recorded in

the mixture S 360 situated between 1.0–75 ms and the largest range was recorded in the mixture S 54/60 between 2.2–150 ms, according to Figure 9a.

(a)   (b)
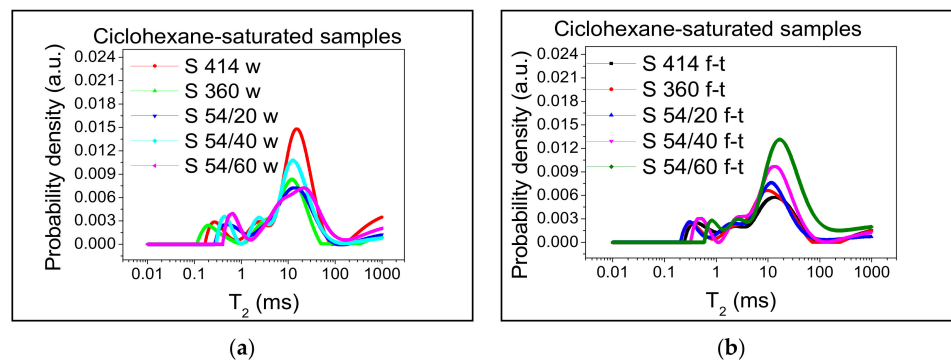
Figure 8. Transverse relaxation time distribution T_2 after cyclohexane saturation: (**a**) control samples kept in water (w); (**b**) samples subject to 300 freeze–thaw cycles (f-t).

(a)   (b)
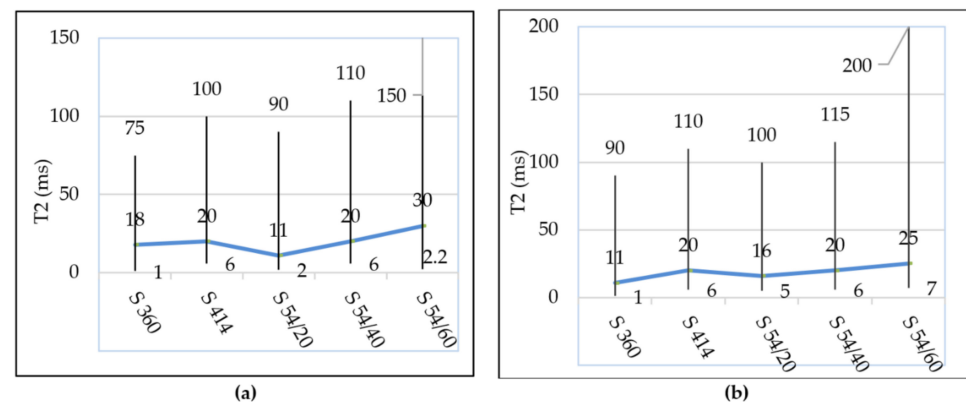
Figure 9. The capillary pores distribution range: (**a**) for the control samples (w); (**b**) for the samples tested in freeze–thaw (f-t). Both measurements were made on cyclohexane-saturated samples.

In samples subjected to 300 freeze–thaw cycles, the transverse relaxation time distribution T_2 is slightly shifted to the right in mixture S 360 between 1.0–90 ms and more accentuated in mixture S 54/60 between 7.0–200 ms, as can be seen in Figure 9b. In the S 54/60 mixture, the peak corresponding to the capillary pores does not tend towards the minimum intensity in the position of T_2 (200 ms), which indicated the presence of the larger capillary pores or internal cracks in concrete.

A longer relaxation time (Figure 9b) and a higher intensity (Figure 9b) in the S 54/60 mixture show an increase in the size and the proportion of capillary pores in the samples tested at freeze–thaw (f-t) compared to the control specimens kept in water (w).

This change in the dimension of capillary pores from the samples subjected to freeze–thaw (f-t) is explained by the fact that the phenomenon of frost water enters the structure of concrete capillary pores, freezes at about −0.5 °C and the resulting volume of the ice formed is approximately 9% higher compared to the water initially absorbed [1–3]. Thus, repeated freeze–thaw cycles lead to an increase in the size of the capillary pores and the appearance of cracks.

3.2. Pores Size

SEM images obtained for the investigated samples are presented in Figure 10. In order to obtain a better view of the pores, all samples were measured using the same parameters but at different magnifications. The pores radius and the distance between pores were measured automatically by SEM software after selecting the shape most appropriate (circle or ellipse) to the shape of the pores. It can be observed that the radius of the pores ranges

from ~33.84 µm for S 360 to ~2.95 µm for S 54/60. The distance between pores ranges from ~915.06 µm for S360 to ~63.64 µm for S 54/40. For S 54/60, no pores were found in the close vicinity of the selected pore to measure the distance. Pore radii with dimensions over ~2.95 µm indicate their framing at capillary pores in accordance with Reference [10]. The results obtained for the S 360 mixture suggest a lower pore density because the largest pore distance was identified. These results can be correlated with those obtained from the technique (NMR), which identified the lowest density of capillary pores on the control sample S 360 (Figure 7a). For the mixture S 54/20 and S 54/40 the distance between the pores was shorter compared to the mixture S 360, which suggests a higher pore density. It is observed that the measurements (NMR) show the same increase in the probability density in the compositions S 54/20 and S 54/40 compared to the mixture S 360 (Figure 7a).
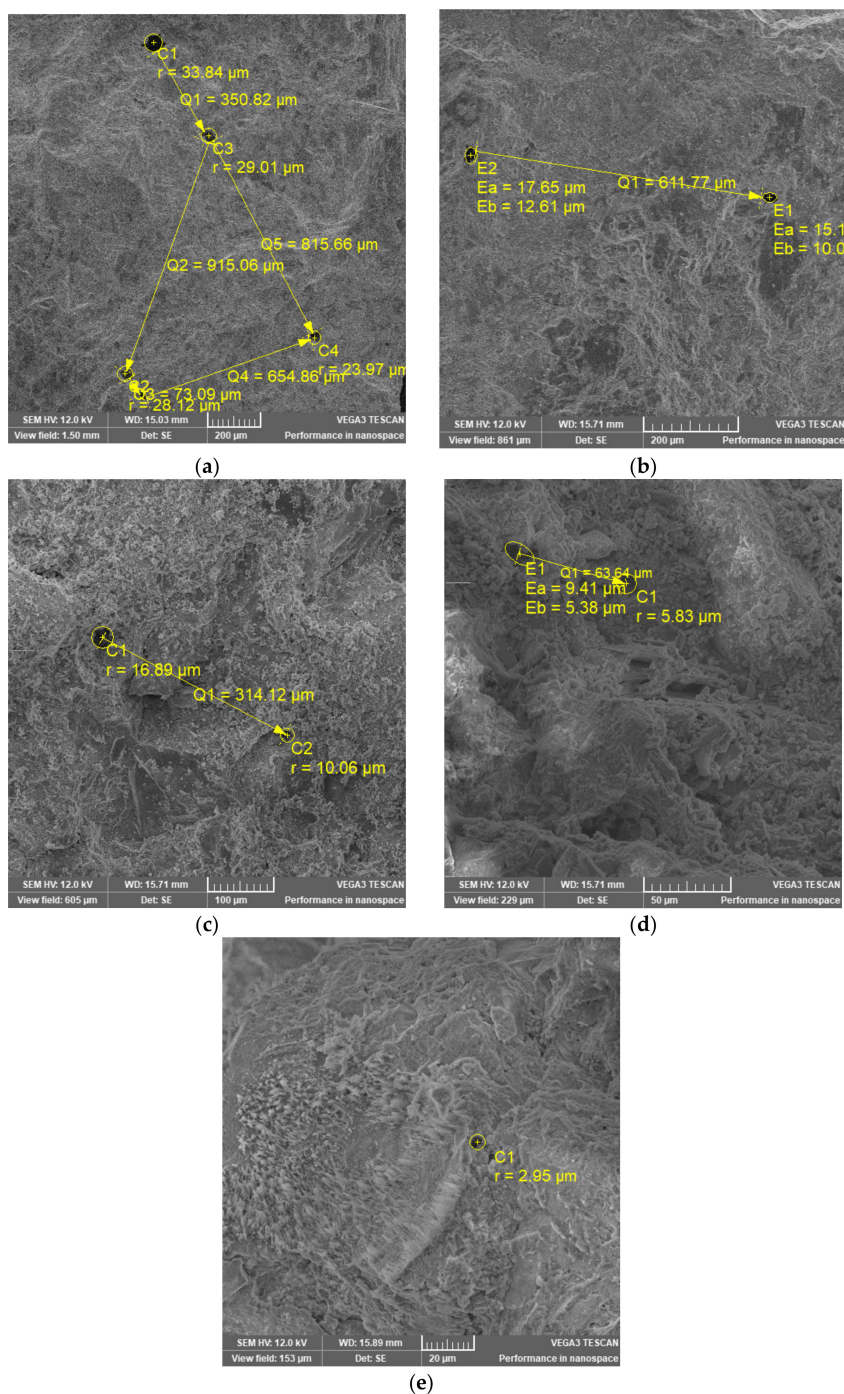
Figure 10. SEM images of S360 (**a**), S414 (**b**), S54/20 (**c**), S54/40 (**d**) and S54/60 (**e**).

3.3. Density, Water Absorption and Permeable Pores Content of Hardened Concrete

Following the determinations performed in compliance with [54] on cubes with side 71 mm, the proportion of permeable pores (P_0), dry density (ρ_1) and density after saturation and boiling (ρ_2) are illustrated in Figure 11a, respectively. The reported results represent the average of three samples tested in each mixture and the standard deviation (SD) and the coefficient of variation (CoV) are shown in Table 5.
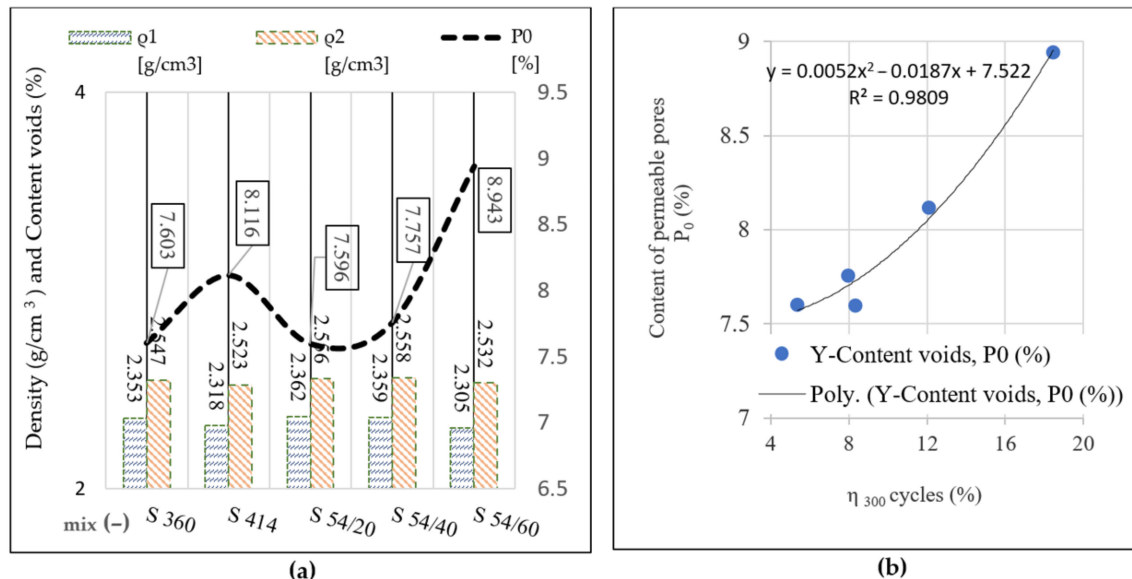
Figure 11. (**a**) Dry density (ρ_1), density after immersion and boiling (ρ_2) and content of permeable pores (P_0) at the age of 150 days; (**b**) the relationship between the loss of compressive strength after 300 freeze–thaw cycles (η_{300}) and the permeable pore content (P_0) of the control samples.

Table 5. Standard deviation (SD) and coefficient of variation (CoV) calculated for density and permeable pore content.

Mixture	S 360	S 414	S 54/20	S 54/40	S 54/60
SD-$\rho 1$ (g/cm^3)	0.005	0.019	0.007	0.001	0.013
CoV (%)	0.002	0.008	0.003	0.000	0.006
SD-$\rho 2$ (g/cm^3)	0.003	0.041	0.009	0.019	0.033
CoV (%)	0.001	0.016	0.004	0.008	0.013
SD-P_0 (g/cm^3)	0.195	1.425	0.763	0.730	1.717
CoV (%)	0.026	0.176	0.100	0.094	0.192

Evaluation of compressive strengths and loss of compressive strengths (η_{300}) after 300 freeze–thaw cycles determined on cubes with a 150 mm side, according to SR 3518:2009 [55], are found in the other studies [42] and included in Table 6. The compressive strengths for the control samples and for the samples tested at 300 freeze–thaw cycles recorded a standard deviation (SD) in the range (0.15–5.53) MPa and the coefficient of variation (CoV) between (0.2–9.1) %. It is observed that the scattering of results is below the accepted limit of 15%, while having a reasonable quality in the range of 5% to 10% as suggested in the study [64].

Analyzing the results from Table 6, it is observed that the compressive strengths determined on the control specimens have a similar evolution with the results of the densities presented in Figure 11a. Furthermore, the value of compressive strength losses after 300 freeze–thaw cycles tends to evolve similarly to that of the permeable pore content and develops a second order polynomial relation having a very good correlation coefficient (R value), shown in the diagram in Figure 11b.

Table 6. The average compressive strengths, resistance losses after 300 freeze–thaw cycles [42], standard deviation and coefficient of variation.

Mixture	S 360	S 414	S 54/20	S 54/40	S 54/60
fcm—water (MPa)	87.78	80.96	84.80	79.38	74.77
SD (MPa)	4.802	1.078	0.855	1.528	4.748
CoV (%)	0.055	1.300	0.010	0.019	0.064
fcm—300 cycles (f-t) (MPa)	83.06	71.15	77.82	73.06	60.95
SD (MPa)	0.492	2.630	0.147	4.040	5.525
CoV (%)	0.006	0.037	0.002	0.055	0.091
Reduction in compressive strength (η_{300})	5.38	12.10	8.32	7.96	18.47
SD (MPa)	4.633	2.078	1.089	3.325	2.220
CoV (%)	0.862	0.171	0.132	0.415	0.120

In Figure 12, it is observed that the compressive strengths determined on the control specimens and on specimens maintained at 300 freeze–thaw cycles maintain their evolution trend with the content of permeable pores (Figure 12a) with the relative size of the capillary pores evaluated by NMR technique (Figure 12b,c). With the reduction in the content of permeable pores (P_0) and the transverse relaxation time (T_2), for which the probability density (au) recorded the maximum value (broken line in Figure 9a,b), the result is the increase in mechanical strengths. The polynomial relation of order two, derived by regression, developed between the compressive strength and the content of permeable pores and the relative size of the capillary pores determined on the control samples, possesses a value of the correlation coefficient very close to 0.8779 and 0.8567 (Figure 12a,b), which confirms the concordance results obtained by standard methods and NMR technique. Moreover, the confirmation of the results obtained by the NMR technique can be appreciated from the correlation coefficient 0.9931 (having the standard error of only 6.9×10^{-3}) obtained from the polynomial relationship developed between the compressive strength and the transverse-room relaxation time (T_2) for the maximum (a.u.) capillary pores and are measured on samples maintained at 300 freeze–thaw cycles (Figure 12c).
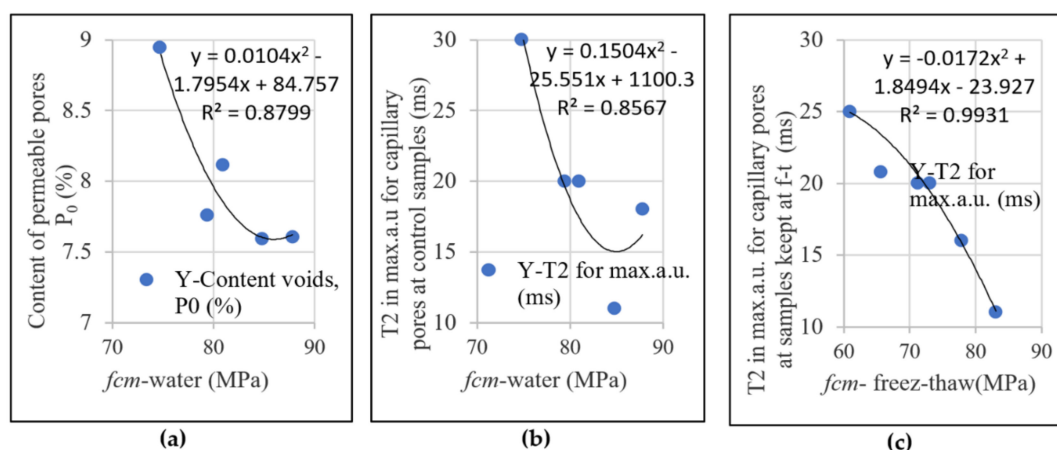
Figure 12. Relationship between compressive strength (*fcm*) and porosity: (**a**) relative to the permeable pore content (P_0) in the control samples; (**b**) relative to the relative pore size for the position in which the transverse relaxation time (T_2) records the maximum density in the control samples; (**c**) relative to (T_2) for the position in which it records the maximum density at the samples kept at freeze–thaw (f-t).

The permeable pore content obtained for the mixture S 54/20 is lower compared to the two control mixtures S 360 and S 414. The mixture S 54/40 is above the level of the control mixture S 360 and below the level of S 414. However, at mixture S 54/60, in which the substitution with artificial aggregates was 60% the porosity of the concrete increased the most, it was above the level of the two control mixtures. For blast furnace slag mixtures, the

mechanical strengths decreased as the level of substitution with slag aggregates increased and the lowest values were registered for the S 54/60 mixture. The cause that led to the decrease in the mechanical strengths was the increase in capillary porosity, which in turn was influenced by the amount of water used and by the increase in water/binder ratio; this is a fact shown in the specialty literature [6]. The increase in the specific surface of the ground furnace blast slag and the increase in the porosity of the slag aggregate led to the increase in the water requirement in the preparation of the mixtures S 54/40 and S 54/60 in order to obtain a similar consistency to the reference mixtures; the results are in compliance with the specialty literature [65]. The crushed slag aggregates have an angular shape, which reduces the workability of the concrete and have a higher porosity than natural sand [47]. Similarly, the grinding fineness of the blast furnace slag was higher than that of cement; the specific surface in furnace blast slag was 5770 cm^2/g and in cement it was 4385 cm^2/g. However, for the mixture S 54/20, the proportions of blast furnace slag used led to the increase in the mechanical resistances and to the decrease in the porosity, obtaining better performances than the control mixture S 414 at the same water/binder ratio. For this mixture, the use of slag as a binder (GGBS) and aggregates (ACBFS) in low dosages was advantageous.

4. Conclusions

The connectivity of gel (intra C-S-H and inter C-S-H) and capillary pore network was investigated for the first time on road concrete samples tested for repeated freeze–thaw cycles through low field NMR relaxometry. The experiments rely on monitoring the distribution of water and cyclohexane molecules saturating the pores. The relative distribution of gel and capillary pores, determined through NMR, was conducted on samples taken from control specimens kept in water during the freeze–thaw test period and on samples extracted from specimens tested at 300 freeze–thaw cycles. The content of permeable pores was obtained on cubes with a side of 71 mm, made of the same composition and tested at the same age. For the three blast furnace slag compositions, the same amount of (GGBS), 54 kg/m^3, but different percentages (20%, 40%, 60%) of crushed aggregates (ACFBS) were used. Different dosage of Portland cement, 360 and 414 kg/m^3, were used for the two compositions made with conventional materials. The conclusions of the experiments are summarized in the following:

I.   After the freeze–thaw cycles, the transverse relaxation time distribution interval, T_2, a of the intra C-S-H pores shifted towards higher values compared to the control mixtures, which indicates the appearance of microcracks even in the (intra C-S-H) pores. In addition, the maximum probability density was close to the value indicated for the control mixtures.

II.   From the diagrams of the distribution of inter C-S-H gel pores and of the capillary pores of the specimens tested at freeze–thaw, displacements are observed for higher values of T_2 in all compositions with blast furnace slag compared to the control samples, which indicates an increase in the relative size of the pores.

III.   Furthermore, the maximum probability density of samples maintained at freeze–thaw cycles, measured on the y-axis, increased with the increase in the substitution level of crushed aggregates, indicating the increase in the density of the pore distribution in concrete with the highest increase registered in the S 54/60 mixture.

IV.   For the S 54/40 and S 54/60 mixtures tested on freeze–thaw, the distribution range of the capillary pores was shifted to higher values compared to the control mixtures, which showed an increase in pore size due to the increase in the amount of water in the capillary pore mixtures.

V.   However, for the mixture S 54/20, the distribution range and the maximum intensity of the capillary pores were close to the control mixture S 360 and lower than the control mixture S 414, which indicates that this mixture contains the optimal dosages of slag built-in furnace.

VI.   The results obtained for the content of permeable pores and the mechanical strengths obtained through standard methods and of capillary pore distribution obtained through NMR technique were consistent.

VII.   The analysis of SEM images for slag mixtures shows that the pore density for S 54/20 mixture is the lowest, which confirms the highest compressive strength.

VIII. Using the CPMG technique, the distribution and relative size of gel pores and capillaries on concrete samples tested on freeze–thaw were revealed, which permits the additional extraction of gel pore information compared to the standard method in which only the content of permeable pores is extracted.

IX.   The CPMG technique can reflect the effect of freeze–thaw cycles on the total porosity of the concrete internal structure; however, the results must be correlated with standardized methods.

X.   An important advantage of this technique is that it allows the progressive and repeated evaluation of the distribution of gel pores and capillaries throughout the freeze–thaw test.

Conflicts of Interest: The authors declare no conflict of interest.

References

1. Kocáb, D.; Kucharczyková, B.; Daněk, P.; Vymazal, T.; Hanuš, P.; Halamová, R. Destructive and non-destructive assessment of the frost resistance of concrete with different aggregate. In Proceedings of the IOP Conference Series: Materials Science and Engineering, Moscow, Russia, 25–27 April 2018; Volume 379, p. 012022.
2. Aïtcin, P.C. *High-Performance Concrete*; Stern B 624; E. & F.N. Spon: New York, NY, USA, 1998.
3. Collepardi, M. *The New Concrete*; Grafiche Tintoretto: Lancenigo, Italy, 2006.
4. Neville, A.M. *Properties of Concrete*, 5th ed.; Longman: Harlow, UK, 2011.
5. Pop, A.; Badea, C.; Ardelean, I. The Effects of Different Superplasticizers and Water-to-Cement Ratios on the Hydration of Gray Cement Using T2-NMR. *Appl. Magn. Reson.* **2013**, *44*, 1223–1234. [CrossRef]
6. Taylor, P.; Van Dam, T.; Sutter, L.; Fick, G. *Integrated Materials and Construction Practices for Concrete Pavement: A State-of-the-Practice Manual*, 2nd ed.; Part of InTrans Project 13-482; National Concrete Pavement Technology Center at Iowa State University: Ames, IA, USA, 2019.
7. Verbeck, G.J. *Hardened Concrete—Pore Structure*; ASTM: West Conshohocken, PA, USA, 1955; pp. 136–142.
8. Bede, A.; Scurtu, A.; Ardelean, I. NMR relaxation of molecules confined inside the cement paste pores under partially saturated conditions. *Cem. Concr. Res.* **2016**, *89*, 56–62. [CrossRef]
9. Neville, A.M. *Properties of Concrete*; Bucharest Technical Publishing House: Bucharest, Romania, 1979.
10. Aligizaki, K.K. *Pore Structure of Cement-Based Materials: Testing, Interpretation and Requirements*; Taylor & Francis: London, UK; New York, NY, USA, 2006; p. 432.
11. Polish Committee for Standardization. *Standard for Admixtures for Concrete, Mortar and Grout—Test Methods—Part 11: Determination of Air Void Characteristics in Hardened Concrete*; PN-EN 480-11; Polish Committee for Standardization: Warsaw, Poland, 1998.
12. Wawrzeńczyk, J.; Kozak, W. A method of analyzing the porous microstructure in air-entrained concrete on the basis on 2D image analysis. *Procedia Eng.* **2015**, *108*, 102–107. [CrossRef]
13. Shpak, A.; Jacobsen, S. *Requirements and Recommendations for Frost Durable Concrete: Durable Advanced Concrete Structures (DaCS)*; Norwegian University of Science and Technology: Trondheim, Norway, 2019; ISBN 978-82-7482-116-3.

14. Yuan, J.; Liu, Y.; Li, H.; Yang, C. Experimental Investigation of the Variation of Concrete Pores under the Action of Freeze-thaw Cycles. *Procedia Eng.* **2016**, *161*, 583–588. [CrossRef]

15. Tracz, T.; Zdeb, T. Effect of hydration and carbonation progress on the porosity and permeability of cement pastes. *Materials* **2019**, *12*, 192. [CrossRef]

16. Rao, S.K.; Sravana, P.; Rao, T.C. Abrasion resistance and mechanical properties of Roller Compacted Concrete with GGBS. *Constr. Build. Mater.* **2016**, *114*, 925–933. [CrossRef]

17. Aghaeipour, A.; Madhkhan, M. Effect of ground granulated blast furnace slag (GGBFS) on RCCP durability. *Constr. Build. Mater.* **2017**, *141*, 533–541. [CrossRef]

18. Limbachiya, V.; Ganjian, E.; Claisse, P. Strength, durability and leaching properties of concrete paving blocks incorporating GGBS and SF. *Constr. Build. Mater.* **2016**, *113*, 273–279. [CrossRef]

19. Zhang, C.; Han, S.; Hua, Y. Flexural performance of reinforced self-consolidating concrete beams containing hybrid fibers. *Constr. Build. Mater.* **2018**, *174*, 11–23. [CrossRef]

20. Li, L.; Cao, M. Influence of calcium carbonate whisker and polyvinyl alcohol- steel hybrid fiber on ultrasonic velocity and resonant frequency of cementitious composites. *Constr. Build. Mater.* **2018**, *188*, 737–746. [CrossRef]

21. Lam, M.N.-T.; Jaritngam, S.; Le, D.-H. Roller-compacted concrete pavement made of Electric Arc Furnace slag aggregate: Mix design and mechanical properties. *Constr. Build. Mater.* **2017**, *154*, 482–495. [CrossRef]

22. Lam, M.N.-T.; Le, D.-H.; Jaritngam, S. Compressive strength and durability properties of roller-compacted concrete pavement containing electric arc furnace slag aggregate and fly ash. *Constr. Build. Mater.* **2018**, *191*, 912–922. [CrossRef]

23. Lei, D.; Guo, L.; Chen, B.; Curosu, I.; Mechtcherine, V. The connection between microscopic and macroscopic properties of ultra-high strength and ultra-high ductility cementitious composites (UHS-UHDCC). *Compos. B Eng.* **2019**, *164*, 144–157. [CrossRef]

24. Nedunuri, S.S.S.A.; Sertse, S.G.; Muhammad, S. Microstructural study of Portland cement partially replaced with fly ash, ground granulated blast furnace slag and silica fume as determined by pozzolanic activity. *Constr. Build. Mater.* **2020**, *238*, 117561. [CrossRef]

25. Majhi, R.K.; Nayak, A.N. Bond, durability and microstructural characteristics of ground granulated blast furnace slag based recycled aggregate concrete. *Constr. Build. Mater.* **2019**, *212*, 578–595. [CrossRef]

26. De Castro Pessoa, J.R.; Dominguez, J.S.; De Carvalho, G.; De Assis, J.T. Obtaining Porosity of Concrete Using X-ray Microtomography or Digital Scanner. *J. Chem. Chem. Eng.* **2014**, *8*, 371–377. [CrossRef]

27. Diamond, S. Mercury porosimetry. *Cem. Concr. Res.* **2000**, *30*, 1517–1525. [CrossRef]

28. Li, L.; Li, Z.; Cao, M.; Tang, Y.; Zhang, Z. Nanoindentation and Porosity Fractal Dimension of Calcium Carbonate Whisker Reinforced Cement Paste After Elevated Temperatures (up to 900 °C). *Fractals* **2021**, *29*, 2140001. [CrossRef]

29. Jin, S.; Zhang, J.; Huang, B. Fractal analysis of effect of air void on freeze–thaw resistance of concrete. *Constr. Build. Mater.* **2013**, *47*, 126–130. [CrossRef]

30. Zhou, J.; Kang, T.; Wang, F. Pore structure and strength of waste fiber recycled concrete. *J. Eng. Fibers Fabr.* **2019**, *14*, 1558925019874701. [CrossRef]

31. Kowalczyk, R.M.; Gajewicz, A.M.; McDonald, P.J. The mechanism of water\isopropanol exchange in cement pastes evidenced by NMR relaxometry. *RSC Adv.* **2014**, *4*, 20709–20715. [CrossRef]

32. Vicente, M.A.; Mínguez, J.; González, D.C. Variation of the Pore Morphology during the Early Age in Plain and Fiber-Reinforced High-Performance Concrete under Moisture-Saturated Curing. *Materials* **2019**, *12*, 975. [CrossRef]

33. Vicente, M.A.; Mínguez, J.; González, D.C. Recent advances in the use of computed tomography in concrete technology and other engineering fields. *Micron* **2019**, *118*, 22–34. [CrossRef]

34. European Committee for Standardization. *Testing the Freeze-Thaw Resistance of Concrete—Internal Structural Damage*; CEN/TR 15177; Committee for Standardization: Brussels, Belgium, 2006.

35. Badea, C.; Pop, A.; Mattea, C.; Stapf, S.; Ardelean, I. The Effect of Curing Temperature on Early Hydration of Gray Cement Via Fast Field Cycling-NMR Relaxometry. *Appl. Magn. Reson.* **2014**, *45*, 1299–1309. [CrossRef]

36. McDonald, P.J.; Korb, J.P.; Mitchell, J.; Monteilhet, L. Surface relaxation and chemical exchange in hydrating cement pastes: A two-dimensional NMR relaxation study. *Phys. Rev. E* **2005**, *72*, 011409. [CrossRef]

37. Holly, R.; Reardon, E.J.; Hansson, C.M.; Peemoeller, H. Proton Spin-Spin Relaxation Study of the Effect of Temperature on White Cement Hydration. *J. Am. Ceram. Soc.* **2007**, *90*, 570–577. [CrossRef]

38. Muller, A.C.A.; Scrivener, K.L.; Gajewicz, A.M.; McDonald, P.J. Use of bench-top NMR to measure the density, composition and desorption isotherm of CSH in cement paste. *Microporous Mesoporous Mater.* **2013**, *178*, 99–103. [CrossRef]

39. Faure, P.F.; Caré, S.; Magat, J.; Chaussadent, T. Drying effect on cement paste porosity at early age observed by NMR methods. *Constr. Build. Mater.* **2012**, *29*, 496–503. [CrossRef]

40. Pop, A.; Bede, A.; Dudescu, M.C.; Popa, F.; Ardelean, I. Monitoring the Influence of Aminosilane on Cement Hydration Via Low-field NMR Relaxometry. *Appl. Magn. Reson.* **2015**, *47*, 191–199. [CrossRef]

41. Burduhos Nergis, D.D.; Vizureanu, P.; Ardelean, I.; Sandu, A.V.; Corbu, O.C.; Matei, E. Revealing the influence of microparticles on geopolymers' synthesis and porosity. *Materials* **2020**, *13*, 3211. [CrossRef] [PubMed]

42. Nicula, L.M.; Corbu, O.; Iliescu, M. Methods for assessing the frost-thaw resistance of road concrete used in our country and at European level. In *IOP Conference Series: Materials Science and Engineering*; IOP Publishing: Bristol, UK, 2020; Volume 877, p. 012025.

43. Romanian Standards Association (ASRO). *Standard Cement—Part 1: Composition, Specification, and Conformity Criteria Common Cements*; Romanian Standard EN 197-1; Romanian Standards Association (ASRO): Bucharest, Romania, 2011.

44. Romanian Standards Association (ASRO). *Standard Ground Granulated Blast Furnace Slag for Use in Concrete, Mortar and Grout Part 1: Definitions, Specifications and Conformity Criteria*; Romanian Standard EN 15167/1; Romanian Standards Association (ASRO): Bucharest, Romania, 2007.

45. Romanian Standards Association (ASRO). *The Norm for the Execution of Cement Concrete Road Pavements in A Fixed and Sliding Formwork System*; Romanian Norms NE 014; Romanian Standards Association (ASRO): Bucharest, Romania, 2002.

46. Romanian Standards Association (ASRO). *Aggregates for Concrete*; Romanian Standard EN 12620; EN 12620+A1; Romanian Standards Association (ASRO): Bucharest, Romania, 2008.

47. Smith, K.D.; Morian, D.A.; Van Dam, T.J. *Use of Air-Cooled Blast Furnace Slag as Coarse Aggregate in Concrete Pavements—A Guide to Best Practice*; Quality Engineering Solutions; Federal Highway Administration: Washington, DC, USA, 2012.

48. Romanian Standards Association (ASRO). *Concrete Additives*; Romanian Standard EN 934-2; Romanian Standards Association (ASRO): Bucharest, Romania, 2010.

49. Romanian Standards Association (ASRO). *Standard for Mixing Water for Concrete*; Romanian Standard EN 1008; Romanian Standards Association (ASRO): Bucharest, Romania, 2003.

50. Romanian Standards Association (ASRO). *Standard for Concrete-Part 1: Specification, Performance, Production and Conformity*; Romanian Standard EN 206-1; EN 206+A1; Romanian Standards Association (ASRO): Bucharest, Romania, 2017.

51. Georgescu, D.P. *Design Guide for Concrete Durability in Accordance with the National Annex for the Application of SR EN 206-1, Durability Classes*; Romanian Standards Association (ASRO): Bucharest, Romania, 2001; Everest; ISBN 978-973-0-04914-5.

52. Corbu, O.; Ioani, A.; Al Bakri, A.M.; Meita, V.; Szilagyi, H.; Sandu, A.V. The Pozzoolanic Activity Level of Powder Waste Glass in Comparisons with other Powders. *Key Eng. Mater.* **2015**, *660*, 237–243. [CrossRef]

53. Nicula, L.M.; Corbu, O.; Iliescu, M. The Influence of Blast Furnace Slag on Abrasion Resistance for Road Concretes. In *IOP Conference Series: Materials Science and Engineering*; IOP Publishing: Bristol, UK, 2020; Volume 877, p. 012040.

54. American Society for Testing and Materials. C642 Standard test method for Density, Absorption and Voids in Hardened Concrete. In *American Society of Testing Materials*; American Society for Testing and Materials: Philadelphia, PA, USA, 2013.

55. Romanian Standards Association (ASRO). *Tests on Concrete: Determination of the Freeze-Tawing Resistance by Measuring the Variations of the Resistance Strength and/or of the Dynamic Relative Elastics Modulus*; Romanian Standard SR 3518; Romanian Standards Association (ASRO): Bucharest, Romania, 2009.

56. Romanian Standards Association (ASRO). *Testing Hardened Concrete—Compessive Strenght of Test Specimens*; SR EN 12390-3; Romanian Standards Association (ASRO): Bucharest, Romania, 2002.

57. Meiboom, S.; Gill, D. Modified spin-echo method for measuring nuclear relaxation times. *Rev. Sci. Instrum.* **1958**, *29*, 688–691. [CrossRef]

58. Venkataramanan, L.; Song, Y.-Q.; Hurlimann, M.D. Solving Fredholm integrals of the first kind with tensor product structure in 2 and 2.5 dimensions. *IEEE Trans. Signal Process.* **2002**, *50*, 1017–1026. [CrossRef]

59. Provencher, S.W. CONTIN: A general purpose constrained regularization program for inverting noisy linear algebraic and integral equations. *Comput. Phys. Commun.* **1982**, *27*, 229–242. [CrossRef]

60. American Society for Testing and Materials. Standard test method for resistance of concrete to rapid freezing and thawing. In *Annual Book of ASTM Standards*; ASTM-C666/C666M-03; American Society for Testing and Materials: Philadelphia, PA, USA, 2008.

61. Magureanu, C.; Sosa, I.; Negrutiu, C.; Heghes, B. Physical and mechanical properties of ultra high strength fiber reinforced cementitious composites. In *Fracture Mechanics of Concrete and Concrete Structures—High Performance, Fiber Reinforced Concrete, Special Loadings and Structural Application*; Korea Concrete Institute: Seoul, Korea, 2010; ISBN 978-89-5708-182-2.

62. Mardani-Aghabaglou, A.; Andiç-Çakir, Ö.; Ramyar, K. Freeze thaw resistance and transport properties of high-volume fly ash roller compacted concrete designed by maximum density method. *Cem. Concr. Compos.* **2013**, *37*, 259–266. [CrossRef]

63. Ethington, E.F. *Interfacial Contact Angle Measurements of Water, Mercury, and 20 Organic Liquids on Quartz, Calcite, Biotite, and Ca-Montmorillonite Substrates*; Open-File Report, No. 90–409; US Geological Survey: Golden, CO, USA, 1990.

64. Badr, A.; Ashour, A.F.; Platten, A.K. Statistical variations in impact resistance of polypropylene fibre-reinforced concrete. *Int. J. Impact Eng.* **2006**, *32*, 1907–1920. [CrossRef]

65. Ionescu, I.; Ispas, T. *Properties and Technology of Concrete*; Bucharest Technical Publishing House: Bucharest, Romania, 1997.

Article

Selected Properties of Densified Hornbeam and Paulownia Wood Plasticised in Ammonia Solution

Przemysław Mania *, Karol Hartlieb, Grzegorz Mruk and Edward Roszyk

Department of Wood Science and Thermal Techniques, Faculty of Forestry and Wood Technology,
Poznań University of Life Sciences, Wojska Polskiego 38/42, 60-627 Poznań, Poland;
karol.hartlieb@up.poznan.pl (K.H.); grzegorz.mruk@up.poznan.pl (G.M.); edward.roszyk@up.poznan.pl (E.R.)
* Correspondence: przemyslaw.mania@up.poznan.pl; Tel.: +48-618-487-448

Abstract: The aim of the study was to densify samples of Paulownia Clone wood in vitro 112 and hornbeam (*Carpinus betulus* L.) by compression in the radial direction. Before the specimens were densified, they were subjected to plastic treatment in an ammonia solution. After densification, the compressive strength in the radial direction and the determination of the Brinell hardness in all three anatomical directions of the wood were determined. The wood swelling in humid air (98% RH) and liquid water was also determined. Paulownia wood density increased by about 280% and hornbeam wood density by 40%. The Brinell hardness parallel to the fibres increased by 49 and 390%, perpendicular by 80 and 388% for hornbeam and Paulownia, respectively. A significant increase in the compressive strength of wood in the radial direction was also observed. Densified hornbeam wood exposed to water showed a high swelling value of 153, while Paulownia wood exhibited 107%.

Keywords: densified wood; ammonia; mechanical properties; Brinell hardness; Paulownia; hornbeam

1. Introduction

It is known that the density of wood is related to its mechanical properties, i.e., the strength of the wood increases proportionally with the increase in its density. Densification, i.e., the thickening of the wood structure, improves the mechanical properties of low-density species and replaces hard species. Wood species with high hardness can also be densified, and their properties are even more improved [1]. The first concept of wood compaction appeared in 1900, but it consisted only of wood compression and did not consider plasticising treatment. Research on increasing wood density has been carried out for many years. It is said that this effect is achieved by compressing the wood in the transverse direction, which improves its mechanical properties [2–6]. In the 20th Century, patents for densification through wood compression began to appear [1,7]. These ideas involved mechanically compressing the wood tissue after subjecting it to steam under high pressure. However, this method did not capture the "memory effect" of wood, i.e., the post-deformation effect [8,9], which led to the "desire" for the wood to return to its original dimensions. According to Jakes et al. [8], hemicelluloses are responsible for dimension stabilisation of lignocellulosic materials. Lignin is the substance responsible for the shape memory effect. Delignification, leading to a reduction in the content of the components that make up the matrix encrusting the cellulose skeleton (hemicellulose and lignin), causes a significant decrease in post-deformation recovery because the hemicellulose in the wood is responsible for shape stabilisation. Lignin plays a substantial role in the quasi-elastic recovery mechanism [6,10–13]. Wood subjected to densification treatment has better physical and mechanical properties, but the increase in density does not always go hand in hand with improving these properties. This is permanent damage to the cell wall during such significant deformation of the wood [3,14].

The thermo-hygro-mechanical (THM) wood thickening process depends on the type of wood, both in terms of the degree of densification and the properties of the modified

wood. This is due to the structural diversity and composition of the chemical cell walls of individual types of wood. Species with a lower density can be densified more easily than species with a higher value [15,16]. This is related to porosity and susceptibility to deformation. For this reason, when the timber is compressed in the radial direction, the earlywood zones first deform, and then the latewood zones. In this case, deformations of the early and latewood zones are inversely proportional to the value of their modulus of elasticity. Usually, the compaction of the wood tissue contributes to the improvement of the mechanical properties of the wood, even more than the increase in the density of the wood. Sometimes, however, the increase in the value of the mechanical parameters is smaller than the increase in wood density caused by its compaction.

One method that ensures plasticisation and fixation in one step is treatment with ammonia. Ammonia penetrates deeper into wood than water. This causes significant plasticisation of the wood, and the permanent displacement of particles becomes possible as the cellulose changes its morphology as new bonds are formed. The effect of ammonia is to swell the wood tissue, dissolve the low-molecular substances it contains, and split higher polymerised hemicelluloses, which is manifested by increasing the solubility of wood in water. Part of the ammonia is permanently bound to the lignin. Along with the destruction of hemicelluloses, some changes occur in the cellulose itself, and some of the bonds between lignin and carbohydrates are broken. Ammonia penetrates not only amorphous areas, but also, it can be assumed, partially in ordered areas. Due to the washing out of soluble substances and the deep penetration of ammonia and water particles into the cell membrane structure, an additional capillary system appears, and the inner surface of the wood is increased. Microfibrils gain greater freedom of movement from each other, manifested externally in the advanced plasticisation of the wood tissue [17–21].

Paulownia Clone in vitro, commonly known as Oxytree, is a new species that has appeared in Poland for several years. Apart from the tree's physical and mechanical properties and the environmental impact of the tree, the species has not been thoroughly researched. Furthermore, not many studies related to the compression of this wood structure have been carried out. The aim of the study was to densify wood after its plasticizing in ammonia solution and to determine its selected properties. It was decided to determine the hardness of the wood in all anatomical directions and the compressive strength in the direction of densification. The dimensional stability of the material in water and humid air was also determined. Therefore, it was decided to compare the densification process after the wood was plasticised with ammonia on two completely different types of wood: the heaviest type of wood naturally occurring in Poland and one of the lighter ones, which is popular in Poland. For this purpose, hornbeam and Paulownia wood were used.

2. Materials and Methods

The test samples were obtained from 10 Paulownia wood planks, 24 mm thick, purchased from a local seller, originating from Shantung Province (China). The boards were machined and cut into samples with lengths: of 22 mm in the tangential and longitudinal directions and 106 mm in the radial direction. The panels were selected so that the growth rings were as parallel as possible to the longer edge of the specimen. The moisture content (MC) of the samples obtained was about 12%. Hornbeam wood was the second experimental material, as hornbeam is the heaviest species that grows naturally in Poland. The material for the tests was taken from 60 mm-thick hornbeam logs. The log was cut into one-meter sections and mechanically processed to obtain samples of the exact dimensions as above. The drawing showing the model cut out with the dimensions marked is shown below (Figure 1). The densification process was applied to 70 samples of hornbeam and Paulownia wood. The exact number of samples was used as the reference material. Thirty samples were then used for the hardness determination, 30 for the compressive strength of the wood, and 10 for thickness swelling.
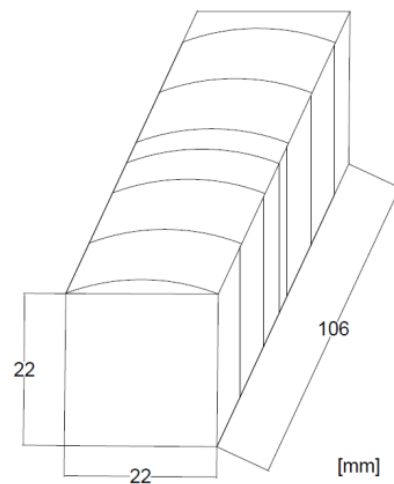
Figure 1. Sample shape and its dimensions.

The density of the samples was determined before densification and after the modifications made to measure the degree of compaction as a percentage. Density was determined using the ISO 13061-2 standard [22]. Rectangular samples were measured in three directions with a calliper with an accuracy of 0.01 mm and then weighed on a laboratory balance with a measurement accuracy of 0.001 g. Density was calculated as the ratio of its mass and volume.

The samples were plasticised in a 25% ammonia solution. It consisted of heating the pieces in a boiling aqueous 25% ammonia solution for seven hours. The samples were placed in 6 L round-bottomed flasks. The flasks containing 2.5 L of the ammonia solution and the pieces were connected to a reflux condenser and placed in a heating mantle to bring the solution to a boil. The boiling point of the solution was 110 °C. After 7 h, the samples were taken out of the solution and inserted into the clamps in a hot-plasticized state.

A particular device was designed to densify the wood. The device was designed in such a way as to limit the possibility of the sample buckling on either side (Figure 2). Therefore, the samples after densification had a rectangular shape. Compression took place in the radial direction of the wood on a Zwick ZO50TH (Zwick/Roell, Ulm, Germany) strength testing machine. The maximum deformation that the samples could withstand without cracking and failure was 85 mm for paulownia and 55 mm for hornbeam wood samples. This compression of the samples was achieved by applying a stress of 2.5 N/mm^2. This is the value beyond which the stress rapidly increased, as proven by preliminary tests. After pressing the specimens, the clamps were clamped by tightening the screws to prevent elastic recovery. The samples clamped in this way were left in the laboratory to dry.
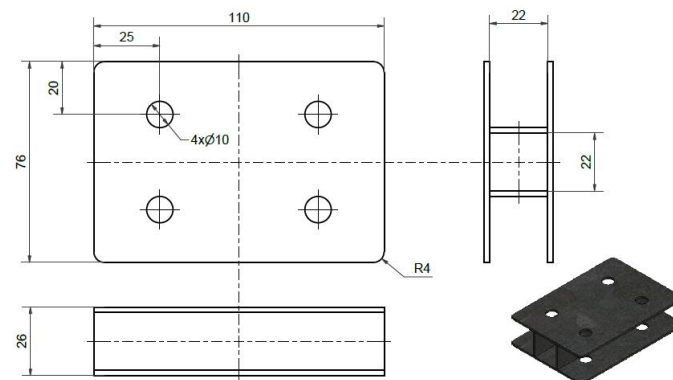
Figure 2. Drawing of the device for densification of wood samples.

After six weeks of conditioning, the densified wood samples were subjected to compression and a Brinell hardness test. The hardness of the tested materials was determined in three anatomical directions. A steel ball with a diameter of 10 mm was pressed into the surface of the samples with a force of 1000 N for densified and 500 N for control hornbeam samples and for paulownia wood, 500 N and 150 N, respectively. The maximum and minimum diameters of the residual indentation were measured with a Brinell magnifier to the accuracy of 0.1 mm. The hardness was calculated from the following formula:

$$HB = \frac{2F}{D\pi\left(D - \sqrt{D^2 - d^2}\right)} \; (MPa) \tag{1}$$

where *F* is the force acting on the ball (N), *D* is the diameter of the pressed ball (mm), and d is the average residual indentation (mm).

Compressive strength was determined in the direction of densification, so in the radial direction. The stress at the proportionality limit (so-called compressive strength perpendicular to the grain or relative strength (R_{cR} in the radial direction)) was determined. Compression tests were conducted using a numerically controlled test machine, Zwick Z050TH (Zwick/Roell, Ulm/Germany).

The maximum wood swelling degree was determined on five densified hornbeam and Paulownia wood samples. The maximum swelling was determined only in the radial direction. The oven-dried samples were measured in the radial direction with a calliper with an accuracy of 0.01 mm; then, the samples were placed in a desiccator above the water surface for 14 days (RH = 98%). After this time, the samples were again measured in this direction with an electronic calliper. Similar measurements were made on five consecutive samples, with the difference that the samples were placed in a beaker with distilled water for 14 days. Thanks to this, it is possible to evaluate the behaviour of such wood in humid air and water. The maximum swelling degree was calculated as the ratio of the increase in the size of the sample to its initial size.

The experimental data were analysed using the STATISTICA 13.3 software (TIBCO Software Inc., Palo Alto, CA, USA) with the analysis of variance (ANOVA). Significant differences between mean values of the parameters describing paulownia and hornbeam wood properties were determined using Tukey's HSD test. The comparison tests were performed at a 0.05 significance level. Identical superscripts, e.g., a, b, c, denote no significant difference between mean values of the investigated properties.

3. Results and Discussion

The results of the determined density of hornbeam and Paulownia wood before and after densification are presented in Table 1.

Table 1. Basic statistical parameters of the density of the studied wood species.

Material	Statistical Parameters				Coefficient of Variation, CV (%)
	ρ_{min}	ρ_{mean}	ρ_{max}	$\pm$**SD**	
		(kg $\times$ m^{-3})			
Control hornbeam	761	786 [a]	831	31.5	4.01
Densified hornbeam	1010	1102 [c]	1232	95.2	8.65
Control Paulownia	243	249 [b]	279	6.3	2.53
Densified Paulownia	643	705 [d]	784	59.2	8.39

[a–d] different superscripts denote a statistically significant ($p < 0.05$) difference between mean values according to Tukey's HSD test.

As shown in Table 1, the average measured density of the hornbeam with a moisture content of MC = 12% is 786 kg/m^3. This is a relatively low value for Poland's heaviest and hardest native species because, according to Wagenführ [23], the average density of hornbeam is about 830 kg/m^3 and the minimum is 530 kg/m^3. The density at 790 kg/m^3

was almost identical to [24,25]. The average density of the studied variety of Paulownia at 12% moisture is slightly lower than usual for this species. The density for Oxytree should be between 220 and 350 kg/m^3 with an average value of 270 kg/m^3 [26–29]. The average density for all densified samples of hornbeam wood increased by an average of about 320 kg/m^3. However, this is only an average value. The densification results of individual specimens differed significantly, as evidenced by the difference between the minimum and maximum obtained density. The higher coefficient of variation for non-densified samples and the standard deviation show that the spread of density is significant compared to the control, unmodified wood. The density of hornbeam wood after densification increased by nearly 40% compared to the reference samples. A lower increase in hornbeam wood density can be explained by a higher initial density and a significant recovery of this wood after deformation. The densification process was carried out in the radial direction, where the wood rays constituted a substantial obstacle in the compaction process. The presence of aggregate wood rays characterises the hornbeam. However, the microstructure of these rays looks different than, for example, those in beechwood. The aggregate rays present in hornbeam wood are made of narrow wood rays separated by layers of wood fibres. A much higher increase in wood density was observed in Paulownia. The average value increased by over 2.8-times. A similar values, 740 kg/m^3, was given by Li et al. [30] after densification. Although the increase in wood density is significant, it is still much lower than in the case of previously delignified wood [6,10]. It should be noted that the density of hornbeam and Paulownia samples was not the same. The initial height of hornbeam samples was reduced by 55 and Paulownia by 85 mm. The changes in wood density after the densification process were statistically significant for both types of wood.

Table 2 summarises the average values of the Brinell hardness for three anatomical directions (L—longitudinal, T—tangential, R—radial) of hornbeam wood and Paulownia wood before and after densification.

Table 2. Basic statistical parameters of the Brinell hardness (HB) of the studied material.

Material		Statistical Parameters		
		HB_L (MPa)	HB_T (MPa)	HB_R (MPa)
Control hornbeam	HB_{mean}	69.24 [d]	37.25 [b]	38.13 [b]
	±SD (MPa)	7.26	4.55	4.98
	CV (%)	10.48	12.21	12.82
Densified hornbeam	HB_{mean}	103.35 [c]	67.12 [a]	65.64 [e]
	±SD (MPa)	10.06	7.67	8.72
	CV (%)	9.73	11.42	13.28
Control Paulownia	HB_{mean}	10.61 [b]	5.63 [d]	5.46 [a]
	±SD (MPa)	1.22	1.06	1.10
	CV (%)	11.49	18.83	20.15
Densified Paulownia	HB_{mean}	41.55 [c]	22.51 [e]	20.51 [f]
	±SD (MPa)	5.49	2.39	2.63
	CV (%)	13.21	10.62	12.82

[a–f] different superscripts denote a statistically significant ($p < 0.05$) difference between mean values according to Tukey's HSD test.

The table above shows that the wood has the highest hardness in the longitudinal direction, despite compacting it in the radial direction. The wood's radial densification increases the wood's hardness in three anatomical directions. Likewise, a significant change in hardness due to densification has also been reported for different densification processes [31–33]. The presented data indicate that the hardness of the tested materials is in the range of 5.63 MPa for control Paulownia wood to 103.35 MPa for densified hornbeam.

The obtained results for the control hornbeam wood did not differ from the values given, for example, by [24,34]. Very similar results were also presented by Fodor et al. [35], where HB along the fibres was 67 and across the fibres 28 MPa. Comparing the hardness results for particular anatomical directions of hornbeam wood, a significant increase in this parameter can be noticed. The increase in hardness was about 80% perpendicular to the fibres and nearly 49% in the longitudinal direction in favour of densified wood. The lowest HB values characterised paulownia wood. In the longitudinal direction, it was only 10.6 MPa and across the fibres, only half of this value. There are no specific Brinell tests on Oxytree hardness in the literature. According to [26], the hardness determined by the Brinell method for the Paulownia tomentosa species is 19.7 MPa in the longitudinal direction, 9 MPa in the radial direction, and 8.2 MPa in the tangential direction, which is almost twice as high as in the Oxytree control samples. According to [36], HB parallel to fibres is about 27 and perpendicular 9.5 MPa. By densifying the Paulownia wood by 85 mm, the hardness increased nearly four-times in each anatomical direction. Li et al. obtained a minor increase in density with the densification of Paulownia wood, which amounted to 84 to 173%. The ANOVA analysis of variance confirmed that HB differed statistically after the densification process. Statistically insignificant differences occurred only in the hornbeam control wood, where the differences were statistically insignificant for both transverse directions.

Table 3 shows the average values and primary statistical data of the compressive strength of wood in the radial direction (R_{cR}) carried out before and after the densification process.

Table 3. Basic statistical parameters of the compressive strength of the studied material.

Material	Statistical Parameters				Coefficient of Variation, CV (%)
	$R_{C_R min}$	$R_{C_R mean}$ ($N \times mm^{-2}$)	$R_{C_R max}$	$\pm SD$	
Control hornbeam	10.11	11.75 [c]	15.32	2.11	17.96
Densified hornbeam	18.23	20.08 [a]	31.76	5.62	25.45
Control Paulownia	1.12	1.37 [b]	1.65	0.20	14.82
Densified Paulownia	3.81	4.38 [d]	5.45	0.75	17.05

[a–d] different superscripts denote a statistically significant ($p < 0.05$) difference between mean values according to Tukey's HSD test.

The compressive strength of wood perpendicular to the grain is low. It is also impossible to determine the maximum compressive stress in the radial direction. During compression, successive wood zones are destroyed, resulting in the wood's compaction. Therefore, stress at the limit of proportionality is most often taken as strength. Comparing the average values of the compressive strength of hornbeam wood samples before and after modification, a significant increase in this parameter can be noticed in the modified wood. On average, the compressive strength increased by almost 71%. The obtained results for the control hornbeam samples did not differ significantly from the results of other authors and fell within the given range of 9.7–11.5 MPa [25,37]. The Paulownia wood analysed had a very low compressive strength perpendicular to the fibres. During the densification of Paulownia wood and its shortening by 85 mm, the strength increased by over 320%. Such a large change may indicate significant changes in the structure of the wood. The force at the limit of proportionality was over 2100 N and was over three-times greater than the force in the control samples. The obtained differences are statistically significant at the significance level of 0.05.

A significant increase in the analysed mechanical parameters proves that ammonia is a suitable plasticiser. Its good plasticising properties have been described many times [17,19,21]. However, the biggest problem of mechanically densified wood is the post-deformation recovery associated with the discharge of the elastic energy previously accumulated and partially preserved in the drying process. Wood expansion deformations result from its elastic–viscous properties, exacerbated by moisture changes. In such a case,

apart from the elastic deformations (immediate and delayed) resulting from the partial return of the deformed cell walls to their original form, there are also deformations related to the swelling of the wood. As the value of wood swelling increases with the greater density of wood, the problem of the moisture deformation of the densified wood is still the subject of many studies to reduce this unfavourable feature of such modified wood [8,9,38]. Therefore, it was purposeful to answer the question: How does the tested wood swell in the radial direction, i.e., in the direction of densification? Figure 3 shows the values of the maximum degree of swelling for densified hornbeam and Paulownia wood after 14 days of exposure to various humidity conditions. Both analysed materials behave similarly in conditions of increased humidity or liquid water. Hornbeam (Hb) wood was characterised by higher swelling. This is due to its higher density and aggregate wood rays. The wood swelling in humid air shows lower values. The process is more relaxed and slower. The post-deformation recovery of Paulownia (P) was about 50% and of hornbeam almost 80%. While in water, these values were about twice as high and about 107 and 153%, respectively.
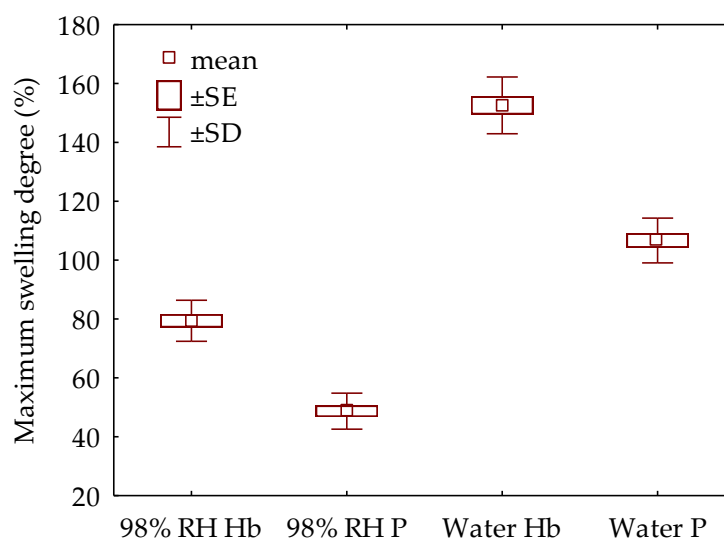
Figure 3. The maximum swelling degree of wood under various conditions (SE—standard error; SD—standard deviation).

Prior plasticisation of the wood in ammonia solution does not sufficiently stabilise the obtained material. Wood deformation recovery is significant. Jakes et al. [8] found that hemicelluloses are responsible for shape stabilisation and that lignin plays a significant role in the recovery mechanism. The chemical change in the wood after the action of ammonia is not substantial. Part of the ammonia is permanently bound to the lignin. Along with the destruction of hemicelluloses, some changes occur in the cellulose itself, and some of the bonds between lignin and carbohydrates are broken. Because lignin is not removed during the modification of ammonia, but is only combined with it, the recovery stabilisation effect is reduced. Partial removal of matrix components from the cell walls significantly reduces their relaxation effect. The above observation confirms the earlier results of [10].

4. Conclusions

The presented and discussed results led to the following conclusions:

1. Ammonia solution is a suitable wood plasticiser. The previously plasticised and mechanically densified hornbeam and Paulownia wood was characterised by a wood density higher than the control samples. This increase was approximately 40% and 280%, respectively.
2. Radial densification of wood contributed to a statistically significant increase in Brinell hardness in all anatomical directions of the wood. There was also a substantial increase in the compressive strength of wood in the radial direction.

3. The ammonia solution does not contribute to stabilising the shape of the obtained material in conditions of increased humidity. The recovery of samples immersed in water is essential.

References

1. Kutnar, A.; Šernek, M. Densification of wood. *Zb. Gozdarstva Lesar.* **2007**, *82*, 53–62.
2. Blomberg, J.; Persson, B. Plastic deformation in small clear pieces of Scots pine (*Pinus sylvestris*) during densification with the CaLignum process. *J. Wood Sci.* **2004**, *50*, 307–314. [CrossRef]
3. Blomberg, J. Elastic strain at semi-isostatic compression of Scots pine (*Pinus sylvestris*). *J. Wood Sci.* **2005**, *51*, 401–404. [CrossRef]
4. Blomberg, J.; Persson, B.; Blomberg, A. Effects of semi-isostatic densification of wood on the variation in strength properties with density. *Wood Sci. Technol.* **2005**, *39*, 339–350. [CrossRef]
5. Mania, P.; Majka, J.; Zborowska, M. The Effect of Thermo-Mechanical Treatment of Moso Bamboo (*Phyllostachys pubescens*) on Its Sorption and Physicomechanical Properties. *Drv. Ind.* **2019**, *70*, 265–272. [CrossRef]
6. Mania, P.; Wróblewski, M.; Wójciak, A.; Roszyk, E.; Moliński, W. Hardness of Densified Wood in Relation to Changed Chemical Composition. *Forests* **2020**, *11*, 506. [CrossRef]
7. Kollmann, F.; Kuenzi, E.; Stamm, A. Principles of wood science and technology. In *Wood Based Materials*; Springer: Berlin, Germany, 1975; Volume 2, pp. 139–149.
8. Jakes, J.E.; Nayomi, N.; Zelinka, S.; Stone, D. Water-activated, shape-memory twist effect in wood slivers as an inspiration for biomimetic smart materials. In Proceedings of the International Conference on Nanotechnology for Renewable Materials, Montreal, QC, Canada, 4–7 June 2012.
9. Gorbacheva, G.A.; Ugolev, B.N.; Sanaev, V.G.; Belkovskiy, S.Y. Methods of characterization of memory effect of wood. *Pro. Ligno.* **2015**, *11*, 65–72.
10. Song, J.; Chen, C.; Zhu, S.; Zhu, M.; Dai, J.; Ray, U.; Li, Y.; Kuang, Y.; Li, Y.; Quispe, N. Processing bulk natural wood into a high-performance structural material. *Nature* **2018**, *554*, 224–228. [CrossRef]
11. Frey, M.; Widner, D.; Segmehl, J.S.; Casdorff, K.; Keplinger, T.; Burgert, I. Delignified and densified cellulose bulk materials with excellent tensile properties for sustainable engineering. *ACS Appl. Mater. Interfaces* **2015**, *10*, 5030–5037. [CrossRef]
12. Jakob, M.; Stemmer, G.; Czabany, I.; Müller, U.; Gindl-Altmutter, W. Preparation of High Strength Plywood from Partially Delignified Densified Wood. *Polymers* **2020**, *12*, 1796. [CrossRef]
13. Wang, J.; Liu, J.; Li, J.; Zhu, J.Y. Characterization of Microstructure, Chemical, and Physical Properties of Delignified and Densified Poplar Wood. *Materials* **2021**, *14*, 5709. [CrossRef] [PubMed]
14. Perkitny, T.; Jablonski, W. Zur beurteilung der mechanischen eigenschaften von pressvollholz. *Holz Als Roh-Und Werkst.* **1984**, *42*, 81–84. [CrossRef]
15. Bao, M.; Huang, X.; Jiang, M.; Yu, W.; Yu, Y. Effect of thermos-hydro-mechanical densification on microstructure and properties of poplar wood (*Populus tomentosa*). *J. Wood Sci.* **2017**, *63*, 591–605. [CrossRef]
16. Kutnar, A.; O'Dell, J.; Hunt, C.; Frihart, C.; Kamke, F.; Schwarzkopf, M. Viscoelastic properties of thermo-hydro-mechanically treated beech (*Fagus sylvatica* L.) determined using dynamic mechanical analysis. *Eur. J. Wood Wood Prod.* **2021**, *79*, 263–271. [CrossRef]
17. Schuerch, C. Plasticizing wood with liquid ammonia. *Ind. Eng. Chem.* **1963**, *55*, 39. [CrossRef]
18. Bariska, M. Plastifizierung des Holzes mit Ammoniak in Theorie und Praxis. *Holz-Zentralblatt* **1969**, *84*, 1309–1311.
19. Rousek, R.; Rademacher, P.; Brabec, M.; Dejmal, A.; Horníček, S.; Baar, J.; Šprdlík, V. Beech wood modification with ammonia gas—Improved properties. *Pro. Ligno.* **2015**, *11*, 230–238.
20. Yamashita, D.; Kimura, S.; Wada, M.; Samejima, M.; Takabe, K. Effect of ammonia treatment on white birch wood. *Holzforschung* **2018**, *72*, 31–36. [CrossRef]

21. Hackenberg, H.; Zauer, M.; Dietrich, T.; Hackenberg, K.A.M.; Wagenführ, A. Alteration of Bending Properties of Wood Due to Ammonia Treatment and Additional Densification. *Forests* **2021**, *12*, 1110. [CrossRef]

22. ISO. *Physical and Mechanical Properties of Wood—Test Methods for Small Clear Wood Specimens—Part 2: Determination of Density for Physical and Mechanical Tests*; International Organization for Standardization: Geneva, Switzerland, 2014.

23. Wangenführ, R. *Holzatlas. 6., Bearbeitete und Erweiterte Auflage*; Fachbuchverlag: Leipzig, Germany, 2007.

24. Gunduz, G.; Korkut, S.; Aydemir, D.; Bekar, Í. The density, compression strength and surface hardness of heat-treated hornbeam (*Carpinus betulus* L.) wood. *Maderas. Cienc. Y Tecnol.* **2009**, *11*, 61–70. [CrossRef]

25. Kiaei, M.; Abadian, Z. Physical and Mechanical Properties of Hornbeam Wood from Dominant and Suppressed Trees. *Drv. Ind.* **2018**, *69*, 63–69. [CrossRef]

26. Akyildiz, M.H.; Kol Sahin, H. Some Technological Properties and Uses of Paulownia (*Paulownia tomentosa* Steud.) Wood. *J. Environ. Biol.* **2010**, *31*, 351–355.

27. Kaymakci, A.; Bektas, I.; Bal, B. Some Mechanical Properties of Paulownia (*Paulownia elongata*) Wood. In Proceedings of the International Caucasian Forestry Symposium, Artvin, Turkey, 24–26 September 2013; pp. 24–26.

28. Lachowicz, H.; Giedrowicz, A. Characteristics of the technical properties of Paulownia COTE- 2 wood. *Sylwan* **2020**, *164*, 414–423.

29. Jakubowski, M. Cultivation Potential and Uses of Paulownia Wood: A Review. *Forests* **2022**, *13*, 668. [CrossRef]

30. Li, H.; Jiang, X.; Ramaswamy, H.S.; Zhu, S.; Yu, Y. High-pressure treatment effects on density profile, surface roughness, hardness, and abrasion resistance of paulownia wood boards. *Trans. ASABE* **2018**, *61*, 1181–1188. [CrossRef]

31. Navi, P.; Heger, F. Combined densification and thermo-hydro-mechanical processing of wood. *MRS Bull.* **2004**, *29*, 332–336. [CrossRef]

32. Kamke, F.A. Densified radiate pine for structural composites. *Maderas. Ciencia y Tecnología* **2006**, *8*, 83–92. [CrossRef]

33. Laskowska, A. Density profile and hardness of thermo-mechanically modified beech, oak and pine wood. *Drewno* **2020**, *63*, 25–41.

34. Sedlar, T.; Sinković, T.; Perić, I.; Jarc, A.; Stojnić, S.; Šefc, B. Hardness of thermally modified beech wood and hornbeam wood. *Šumarski List* **2019**, *143*, 425–433.

35. Fodor, F.; Lankveld, C.; Németh, R. Testing common hornbeam (*Carpinus betulus* L.) acetylated with the Accoya method under industrial conditions. *iForest* **2017**, *10*, 948–954. [CrossRef]

36. Koman, S.; Feher, S.; Vityi, A. Physical and Mechanical Properties of *Paulownia tomentosa* Wood Planted in Hungaria. *Wood Res.* **2017**, *62*, 335–340.

37. Raczkowski, J. Relation between strength of wood parallel and perpendicular to the grain. *Folia For. Polonica Ser. B* **1995**, *25*, 57–63.

38. Navi, P.; Sandberg, D. *Thermo-Hydro-Mechanical Processing of Wood*, 1st ed.; EPFL Press: Lausanne, Switzerland; CRC Press: Lausanne, Switzerland; Boca Raton, FL, USA, 2012; ISBN 9781439860427.

Article

Reinforcement Analysis of an Old Multi-Beam Box Girder Based on a New Embedded Steel Plate (ESP) Strengthening Method

Yuliang He [1], Kai Wang [1], Zongyong Cao [2], Peijuan Zheng [1,*] and Yiqiang Xiang [3]

[1] College of Civil Engineering, Shaoxing University, 508 West Huangcheng Road, Shaoxing 312000, China; hyliang88888@163.com (Y.H.); wangkai1999622@163.com (K.W.)

[2] Hua Hui Group, Shaoxing University, 508 West Huangcheng Road, Shaoxing 312000, China; cao-zy@cnhh.com

[3] College of Civil Engineering and Architecture, Zijingang Campus, Zhejiang University, Anzhong Building B718, Yuhangtang Road 866, Hangzhou 310058, China; xiangyiq@126.com

[*] Correspondence: peijuanzheng1987@163.com

Abstract: Multi-beam box girder bridges have been applied widely throughout the world for many years. However, the cracking of longitudinal joints between the box girders always leads to reflective cracking of the bridge decks during the service period and thus finally affects the safety and durability of the actual bridges. An embedded steel plate (ESP) strengthening method was presented by introducing carbon-A/-B glue to reinforce the longitudinal joints of old multi-beam box girder bridges for this problem. In order to evaluate the feasibility of the proposed method for actual bridges, an old multi-beam box girder bridge was reinforced, and structural parameters including strain, frequency, and deflection were obtained by adopting field tests before and after strengthening. In addition, the corresponding finite element (FE) model of the background bridge was also set up using ANASYS 18.0 to analyze the strengthening process. Analysis results of the actual bridge and FE model indicate that structural stiffness and load lateral transferring performance between the box girders were enhanced after ESP strengthening. Therefore, this proposed strengthening method can be used to improve the mechanical performance of multi-beam box girder bridges and provide reference for such bridge reinforcement.

Keywords: multi-beam box girder bridge; ESP strengthening; field test; load lateral transferring performance; structural stiffness

1. Introduction

Multi-beam box girder bridges have always been applied in short- and medium-span bridges. Those bridges were longitudinally connected together through full-depth and partial-depth shear keys between adjacent girders to enhance the bridge's integrity [1]. Due to accelerated bridge construction, high torsional stiffness, favorable depth-to-span ratios, cost-effectiveness, and aesthetic appeal [2,3], multi-beam box girder bridges are one of the most popular bridges and have been applied widely for many years in the world. However, this type of bridge has lost attractiveness little by little because of the longitudinal cracks at the girder-key interface or in the shear key that are created under a combination of live loads and temperature [4]. These cracks can spread to the bridge slab surface and lead to salt and water leakage through the shear key, and they can accelerate the corrosion of the joint rebar. Lateral load transferring among the box girders can be lost, which leads to safety concerns [5]. Attanayake and Aktan [2] tried to apply a cast-in-place concrete slab, transverse post-tensioning, full-depth shear keys, and seven-day moist curing of the bridge slab to mitigate reflective cracks. The results showed that these methods failed to solve the longitudinal joint cracking of multi-beam box girder bridges.

In America, four types of keyway details (three generic partial-depth shear keys and a generic narrow full-depth shear key) are used. Conversely, the wide full-depth shear

key is applied in South Korea, Japan, and England [6–8]. El-Remaily et al. [9] indicated that longitudinal cracks were seldom found in multi-beam box girder bridges with wide full-depth shear keys. At present, four grouting materials (shrinkage-compensated concrete, fiber-reinforced concrete, cement-based construction grout, and epoxy grout) were applied in the shear key. It is easy to de-bond at the interface of the shear key, which is filled with cement-based construction grout, during the early-age period when the shear key is subjected to the heat of hydration and joint material expansion. Liu and Phares [10] showed that the wide full-depth joint filled with shrinkage-compensated concrete performed better than the narrow full-depth joint filled with epoxy grout. It was also found that the wide full-depth joint filled with shrinkage-compensated concrete would have cracks during the early-age period. However, the epoxy has a high thermal expansion relative to that of the concrete, and this may lead to cracking of the epoxy grout. Sang [11] found that longitudinal cracks have not occurred in the full-depth shear key but did occur in the partial-depth keyways using fiber-reinforced cementitious grout. This showed that it was very important to choose the grouting material and joint details to mitigate longitudinal cracking of the bridge slab. Yuan and Graybeal [12] reported a new shear key design for multi-beam box girder bridges using ultra-high performance concrete (UHPC). Hussein and Steinberg [13] found that UHPC might enhance the capacity of the shear key and mitigate reflective cracking of the bridge deck due to high adhesion and higher strength of the UHPC material, and the adhesive strength increased with surface roughness (adhesion/cohesion values of 3.01, 5.01, and 5.63 MPa for smooth, mid-rough, and rough surfaces). Shad et al. [14] and Ali et al. [15] showed that a UHPC joint with a smooth surface and minimum transverse rebar was sufficient for load transfer between the beams for the load level used in the Federal Highway Administration testing, and these research studies indicated that a UHPC joint with a mid-rough surface and minimum transverse rebar was capable of transferring the load up to failure of the girder system.

Multi-beam box girder bridges constitute one-sixth of all the bridges in America [5], and they account for the largest percentage (about 85%) of bridges built during the early years in China. About 73% of these bridges have partial-depth shear keys, about 80% have spans ranging between 12 m and 18 m, and more than 15% are replaced or built each year [16]. The cause for the replacement is that the shear key is ruptured, which leads to the loss of lateral load transfer between the box girders, and the capacity of the single box girder is further reduced under the action of overloaded vehicles and environmental variations, which creates safety concerns. If the shear key is reinforced to enhance the overall performance of box girder bridges, there is no need to rebuild or replace most of the multi-beam box girder bridges with the distress, which can avoid inconvenient vehicle traffic and economic loss. To the authors' knowledge, few studies were conducted to strengthen the longitudinal joints of multi-beam box girder bridges. Attanayake and Aktan [2] and Shi [17] tried to apply transverse post-tensioning and large diameter screws to reinforce the shear key of box girder bridges, and this required that the stress must be constant per unit length in the direction of the bridge span. In fact, the compressive stress is only limited to a slab width of 1.35 times in the direction of post-tensioning, and it varied with the bridge width, which made the reinforced effect of transverse post-tensioning ineffective. Fu et al. [18] also reported that the transverse post-tensioning had no effect on the load transfer between the girders before the cracking of the shear key.

Since the full-depth shear key with high adhesive strength of the grouting material might mitigate reflective cracking [11,12], the authors tried to propose a new method by introducing a new grouting material (carbon-A/-B glue) to strengthen the partial-depth keyways. Carbon-A/-B glue has outstanding advantages in adhesion/cohesion strength and shear strength, and it especially gives good mobility to grout, conveniently, in the narrow gaps between the box girders. To reduce the amount of carbon-A/-B glue, the steel plates are embedded in the shear key and the gaps between the girders as the skeleton. The box girders and steel plates are pasted by the carbon-A/-B glue in the full depth of the longitudinal joints, as the full-depth shear key, to make the box girder

bridge behave monolithically. In this study, an old multi-beam box girder bridge was strengthened using the ESP method. Then its corresponding structural performance before and after ESP strengthening were obtained and analyzed by adopting field tests. Finally, a three-dimensional finite element (FE) model was developed to further investigate the strengthening effect.

2. Experimental Program

2.1. Bridge Description

The background bridge, located in Shaoxing, China, was constructed in 1994 and was scheduled to be dismantled in 2021. Its three box girders of 1# span were selected as the experiment subject to evaluate the feasibility of the proposed ESP method. Figure 1 is composed of three figures, and these figures show the longitudinal section, girder section, and transverse section, respectively. It can be seen that the bridge consists of five spans and the total length is 86 m. The length of the 1# and 3# span is 13 m and other spans are 20 m. The width of the bridge slab is 23.3 m, and each girder of 1# span is 990 mm and 550 mm in width and depth, respectively, as shown in Figure 1b. Each span of the bridge is made up of twenty-one box girders. Each girder of 1# span is prestressed using nine 9.5-mm-diameter pre-tensioning strands and all these strands are stressed to 195 kN. The box girders are connected together by adopting partial-depth shear keys, which incorporate an on-site concrete slab (100 mm deep) with monolayer rebar mesh. In 2002, the reflective cracking of the bridge slab was observed in the longitudinal joints, and a few cracks were also found in the bottom surface of the box girders. In the following years, the reflective cracking of the bridge slab became worse with the increasing of traffic loads and the overloading of vehicles. In 2006, the partial-depth shear keys and bridge slab were removed, and the longitudinal joints were rebuilt using concrete with a compressive strength of 40 MPa. The bridge deck was replaced by a cast-in-place concrete slab (200 mm deep) with two-layer rebar mesh, and the designed compressive strength of the concrete is also 40 MPa. In 2018, the longitudinal reflective deck crack was observed again, and the damage degree was less than that in 2006. This showed that the increasing of the depth and reinforcement ratio of the bridge slab might relieve the development of reflective cracking. With the service time increasing, the reflective cracking of the bridge slab would become more and more severe, which was consistent with Attanayake and Aktan [2].
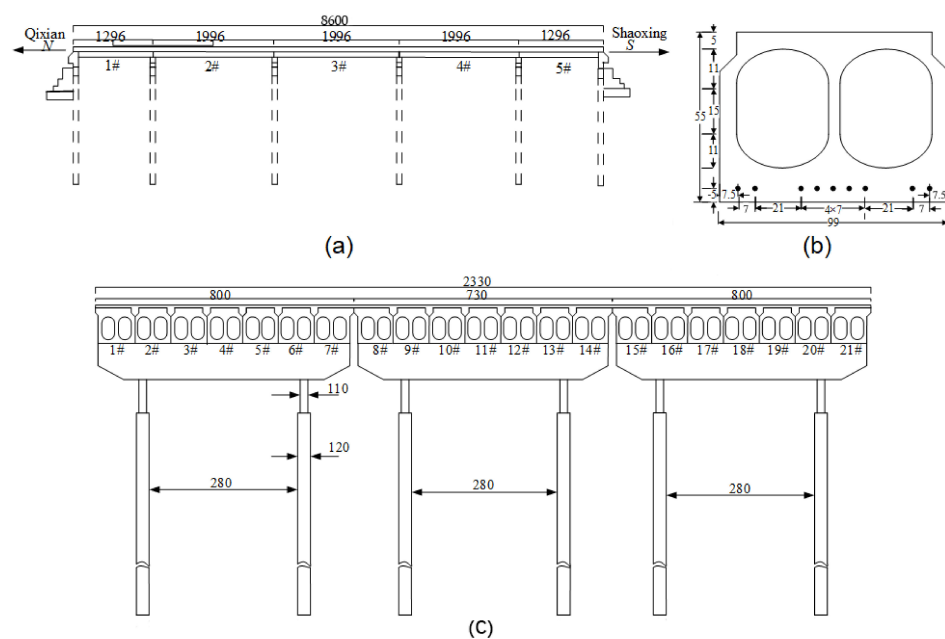
Figure 1. Background bridge (cm). (**a**) Longitudinal section. (**b**) Girder section. (**c**) Transverse section.

2.2. Material Properties

It can be seen in the introduction that the full-depth shear key with high adhesive strength of grouting material might mitigate reflective cracking. Since the carbon-A/-B glue, a kind of composite material, has high tensile and shear strength, high adhesion/cohesion strength, and good mobility, it is chosen in our work. The carbon-A/-B glue is shown in Figure 2. The carbon-A/-B glue is divided into an A-type and B-type in storage. When the two kinds of glues are mixed together, the solidification takes place after about six hours. The mixture ratio is A:B = 1:2. According to the product instructions, the adhesion strength of the concrete-concrete interface with a smooth surface is 4.2 MPa; this is larger than that of the HSC-UHPC interfaces with a smooth surface (3.5 MPa) [11], whereas the adhesion strength of the steel-steel interface is 35 MPa. The steel plate was embedded in the shear keys, and the gaps between the box girders might further improve the adhesion strength of the girder-key interface or the girder-girder interface. The elongation of the glue after the solidification is 2.1%, and the shear deformation is less than 0.2 mm. Huckelbridge et al. [15] reported that the shear key is fractured if the relative displacement value is between 0.08 and 0.5 mm, whereas a relative displacement value of 0.025 mm or less between box girders indicates that the shear key remains intact when the grouting material is concrete. This also shows that the carbon-A/-B glue endures a good shear deformation in comparison with concrete. The material properties of the steel plate and carbon-A/-B glue are listed in Table 1.

(a)   (b)
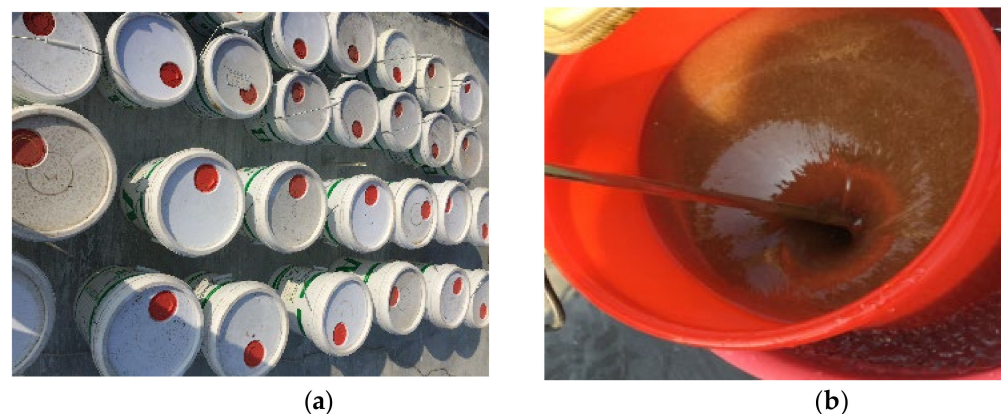
Figure 2. Carbon-A/-B glue and mixture. (**a**) Glue. (**b**) Mixture.

Table 1. Material properties of carbon-A/-B glue and the steel plate.

	Shear Strength (Mpa)	Yield Strength (Mpa)	Tensile Strength (Mpa)	Young's Modulus (Gpa)
Steel plate	265	435	540	210
Carbon-A/-B glue	≥15	≥65	≥30	≥2.5

2.3. Schematic Process

Figure 3 shows the details of the steel plate, which is embedded in the shear keys and gaps between the box girders. The steel plate is divided into two parts. One part is welded into the grooved section located in the shear keys, and another part is embedded directly into the gaps between the box girders, as shown in Figure 3a. The PVC pipes are inserted by drilling holes at the bottom of the grooved section to grout the carbon-A/-B glue. The length of the steel plate is more than 100 mm from the bottom surface of the box girder, and some holes were drilled at the exceeding part of steel plate, as shown in Figure 3b. Two angle irons are connected to the steel plates, using the bolts to resist the pressure caused by grouting the carbon-A/-B glue, as shown in Figure 3a. The sealing strips are pasted between the angle irons and the bottom surface of the box girder to prevent leakage

of the carbon-A/-B glue. The steel plate is divided into thirteen parts in the longitudinal of the box girder in order to be easily installed, as shown in Figure 3b.
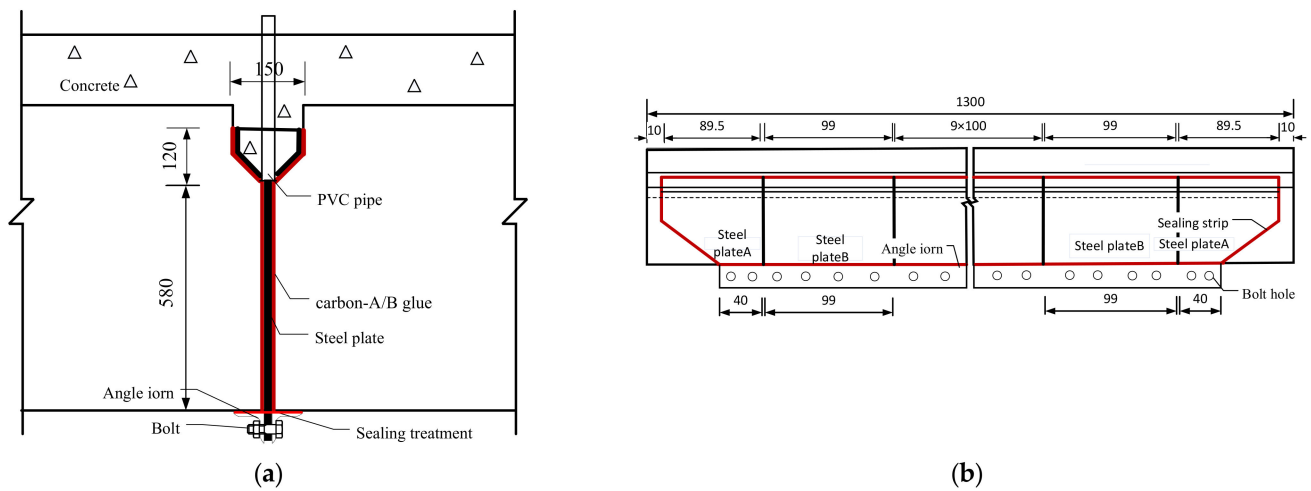
Figure 3. Details of inserting the steel plate. (**a**) Transverse section (mm). (**b**) Longitudinal section (cm).

Figure 4 shows the process of the ESP strengthening method. As the initial step, the bridge slab and shear keys of the old bridge are chipped away and then the girder-key interface and girder-girder interface are cleaned up (Figure 4a). The steel plates are embedded in the shear keys and gaps between the box girders, as shown in Figure 3. Two angle irons are placed flat and tight against the underside of the box girders at the gaps between the box bridges and are connected with the steel plate by the bolts, as shown in Figures 3a and 4b. The sealing strips are applied to plug the gaps between the angle irons and the underside of the box girders to prevent leakage of the carbon-A/-B glue (Figure 4b). Some holes need be reserved at the bottom of the grooved steel located in the partial-depth shear keys in order to install the PVC pipes, and the carbon-A/-B glue is injected into the spaces between the steel plate and box girders through the PVC pipes. The upper ends of the spaces between the grooved steel and the box girders are also sealed by the strips to prevent leakage of the concrete when the bridge deck and the shear keys are cast-in-situ (Figure 4c). The carbon-A/-B glue is injected into the spaces between the steel plates and box girders through the PVC pipes until the concrete strength reaches 40 Mpa (Figure 4d). The carbon-A/-B glue was grouted from the mid-span to the edge along the longitudinal joint.
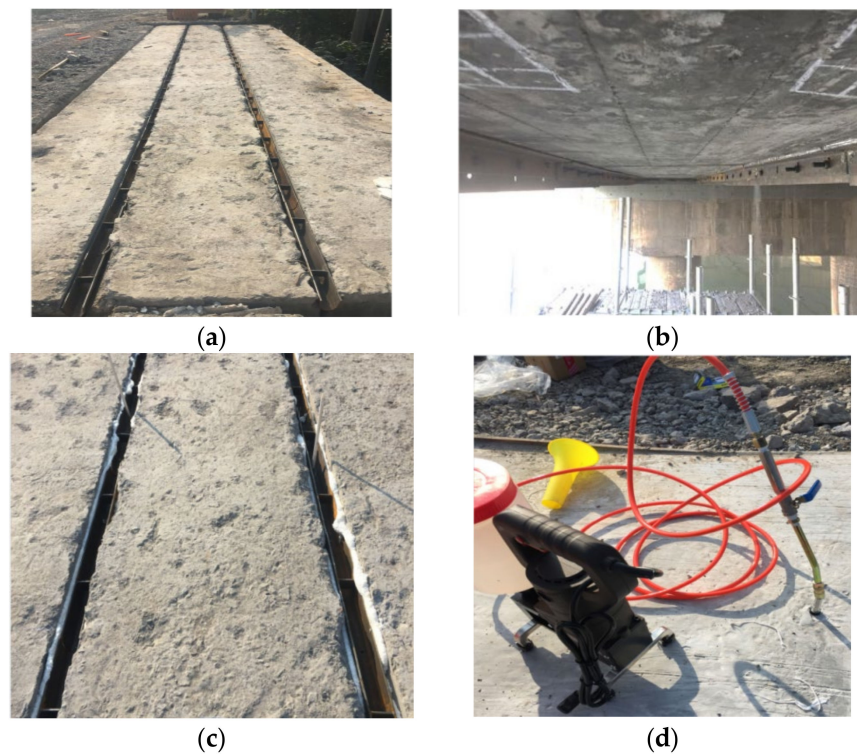
Figure 4. Process of the ESP strengthening method. (**a**) Cleanup and installation. (**b**) Sealing treatment. (**c**) Insertion of PVC pipe. (**d**) Cast-in-place and grout.

2.4. Field Test

A truck was applied to conduct field tests before and after ESP strengthening. Its parameters and configurations are listed in Table 2 and Figure 5, respectively. The tests were proceeded under three cases: the first was continuous loading and the truck was driven along the box bridge, the second was symmetrical loading at the mid-span (Figure 5a), and the third was partial loading at the mid-span (Figure 5b). Figure 6 shows the layout of the strain gauge and LVDTs for the three box girders. Three 1/1000-mm LVDTs were applied to measure the vertical displacements at the mid-span of the box girders (Figure 6), and four 1/1000-mm LVDTs were laid near the gaps to measure the relative displacements between the box girders. Strain gauges were also placed in the underside of the box girders at the mid-span to measure the concrete strain (Figure 6). The data acquisition instrument (DHDAS-3818Y) was used to collect the static experimental data, and all strain gauges and LVDTs were connected to the data acquisition instrument using extension lines (Figure 7). In addition, the dynamic test was also carried out to further verify the reinforcement effect of the ESP method. The frequencies of the box girder bridge were measured under ambient excitation before and after ESP strengthening, and the data logger was used to collect the dynamic test data (Figure 8). Both the dynamic and static loading tests were conducted twice, and the average values were selected as test results.

Table 2. Load Vehicle Parameters.

Axle	Axle Load (kN)	Left Tire (kN)	Right Tire (kN)	Distance between Axle (m)	Axle Width (m)	Truck Total Load (kN)
1	80	39	41	3.9	2.036	
2	111	55	56	1.3	1.860	300
3	109	53	56	/	1.860	

(**a**)

(**b**)
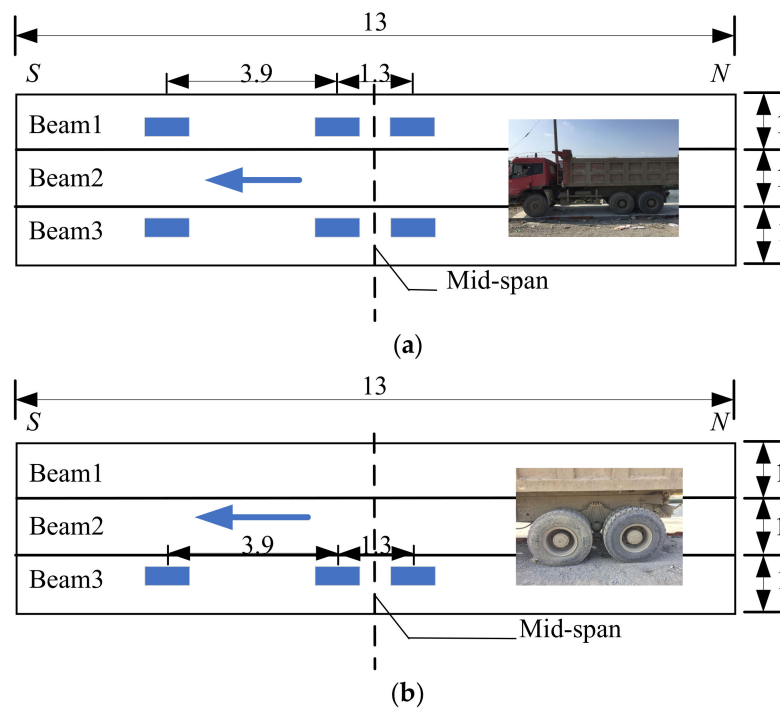
Figure 5. Truck load configuration (m). (**a**) Symmetrical loading. (**b**) Partial loading.
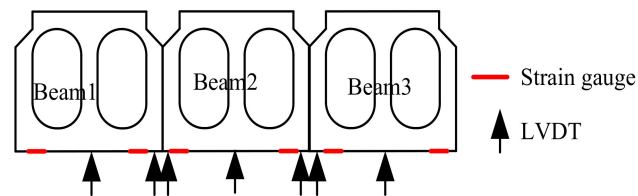
Figure 6. Layout of the strain gauge and LVDTs.

Figure 7. Static test.

Figure 8. Dynamic test.

3. Experimental Results

In this study, the ESP method was used to strengthen the longitudinal joint of an old multi-beam box girder bridge. Figure 9 shows the vertical deflections under the symmetrical and partial static loading test before and after ESP strengthening. Under the symmetrical static loading case (Figure 9a), the deflections for the 1#, 2#, and 3# girders were 4.834 mm, 1.085 mm, and 5.018 mm before strengthening, respectively, and 3.766 mm, 3.102 mm, and 3.85 mm after strengthening, respectively. The strengthening effect of the deflections was improved by 28.4%, 185.9%, and 30.3% for the 1#, 2#, and 3# girders, respectively. The relative displacement before strengthening was 0.75 mm between the 1# and 2# girders and 0.93 mm between the 2# and 3# girders. This indicates that the shear keys of the old box girder bridge have been fractured according to Huckelbridge et al. [15]. After strengthening, the relative displacement was 0.02 mm between the 1# and 2# girders and 0.023 mm between 2# and 3# girders. This indicates that the shear keys remain intact. Figure 9b displays the vertical displacements at the mid-span under partial loading before and after strengthening. The displacements were 0.446 mm, 1.553 mm, and 3.437 mm for the 1#, 2#, and 3# girders before strengthening, respectively, and the corresponding displacements were 1.65 mm, 1.692 mm, and 1.965 mm after strengthening, respectively. The displacement of the 3# girder was decreased by 43% and increased by 270% and 9% for the 1# and 2# girders, respectively. The relative displacements before strengthening were 0.51 mm between the 1# and 2# girders and 0.89mm between the 2# and 3# girders. After strengthening, the corresponding relative displacements were 0.012 mm and 0.018 mm. This shows that the whole performance of the box bridge after strengthening was better than that before strengthening.
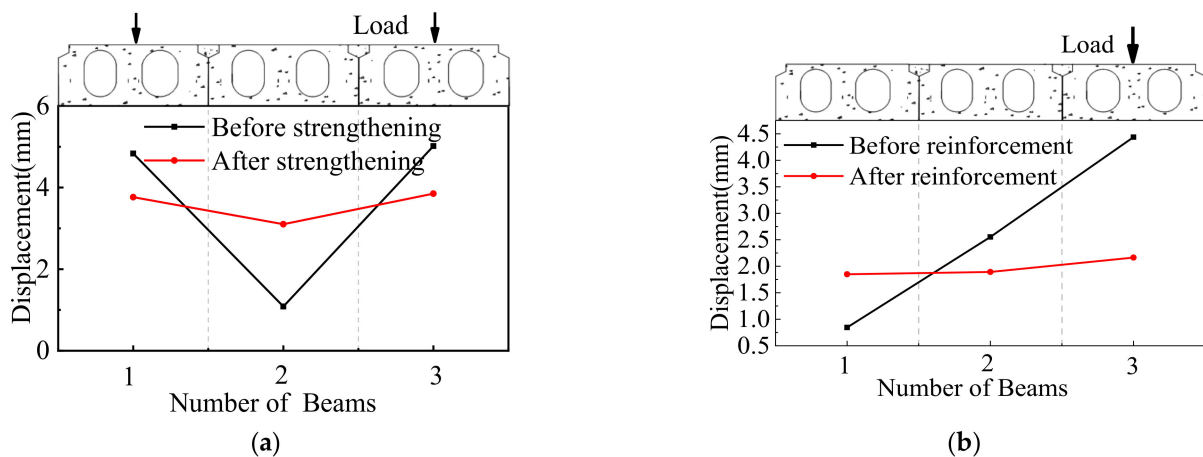
Figure 9. Displacement at the mid-span. (**a**) Symmetrical loading. (**b**) Partial loading.

Figure 10 displays the concrete strain values in the underside of the box girders at the mid-span under the symmetrical and static partial loading tests before and after ESP strengthening. The test results under symmetrical loading presented that the maximum and minimum concrete strain values at the mid-span were 1747 μɛ and 952 μɛ before strengthening, respectively. After strengthening, the corresponding strain values were 1413 μɛ and 1299 μɛ, respectively. Under the case, the maximum concrete strain value of the concrete was decreased by 23.6%, and the minimum concrete strain value was increased by 26.7%. Under the partial loading, the maximum and minimum concrete strain values in the underside of the box girders at the mid-span were 1244 μɛ and 248 μɛ before strengthening, respectively, and 763 μɛ and 637 μɛ after strengthening, respectively. Under the condition, the maximum and minimum concrete strain values were decreased by 63% and increased by 61%, respectively. In one word, the concrete strain values were improved obviously before and after strengthening.
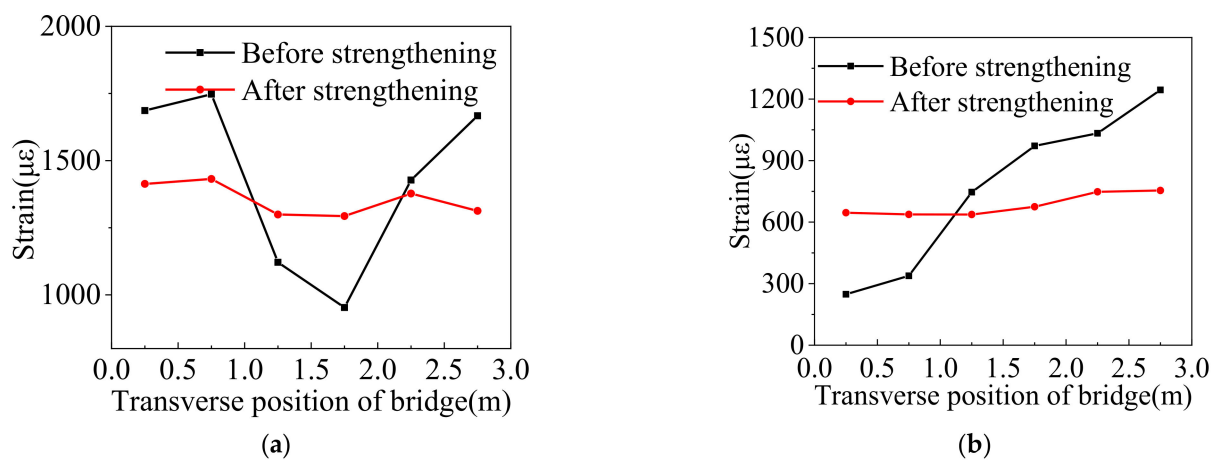
Figure 10. Concrete strains in the underside of the box girders at the mid-span. (**a**) Symmetrical loading. (**b**) Partial loading.

The truck was driven along the box bridge to present the variations in the deflection of the box girder at the mid-span under the symmetrical and partial continuous loading conditions. The deflection curves under the above cases are shown in Figure 11. Before strengthening, the maximum deflection was 5.17 mm under the symmetrical continuous loading case, and the big relative displacement was 0.75 mm. After strengthening, the maximum deflection was reduced to 3.8 mm, and the big relative displacement decreased to 0.021 mm. The maximum deflection was improved by 36%, and the relative displacement met the requirements that Huckelbridge et al. [15] proposed. Under the partial continuous loading case, the maximum deflection before strengthening was 4.44 mm, and the big relative displacement was 0.89 mm. After strengthening, the corresponding values were 2.2 mm and 0.02 mm, respectively. The maximum deflection was improved by 50%, and the relative displacement was less than 0.025 mm. The comparison of the deflections and the relative displacement before and after strengthening indicate that the box girder bridge behaves more monolithically after strengthening.

Figure 12 displays the concrete strain curves in the underside of the box girders at the mid-span under the symmetrical and partial continuous loading tests before and after the ESP strengthening. The test results under the symmetrical continuous loading case presented that the maximum concrete strain value was 1927 μɛ before strengthening, and the corresponding value was 1409 μɛ after strengthening. Under the partial continuous loading case, the maximum concrete strain value was 1542 μɛ before strengthening and 787 μɛ after strengthening. It can be seen that the maximum concrete strain value was decreased by 36.8% under the symmetrical continuous loading case and 49% under continuous partial loading.
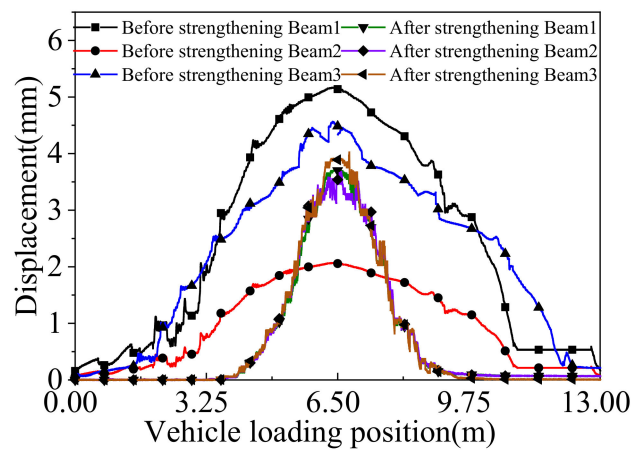
(a)
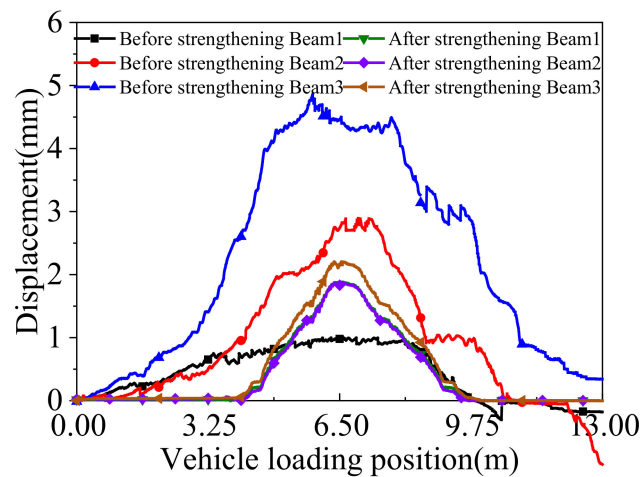
(b)

Figure 11. Deflections of the box girder at the mid-span under the continuous loading case. (**a**) Symmetrical loading. (**b**) Partial loading.

The collection time of the acceleration signal is not less than 30 min in order to get enough data under ambient excitation. Then the signals were used to obtain the Fast Fourier transform (FFT) spectrum of the box bridge (Figure 13). It can be seen that the first three order frequencies before strengthening were 8.875 Hz, 11.274 Hz, and 18.167 Hz, respectively, and the corresponding frequencies were 17.578 Hz, 25.282 Hz, and 30.416 Hz after strengthening, respectively. The fundamental frequency was increased by 46%, and this indicates the overall stiffness of the box girder bridge is improved by adopting the ESP method.
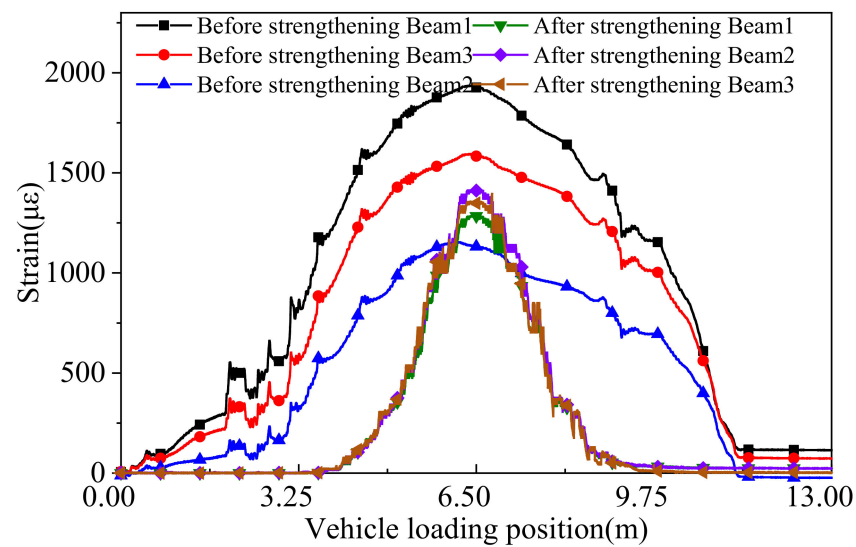
(a)
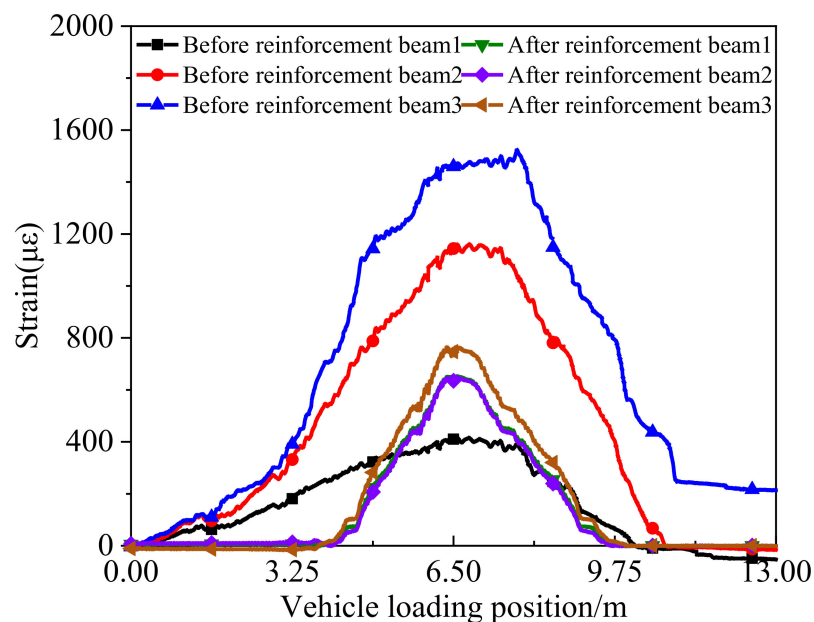
(b)

Figure 12. Concrete strain curves of the box girder at the mid-span under continuous loading. (**a**) Symmetrical loading. (**b**) Partial loading.

Multi-beam box girder bridges always consist of side-by-side prestressed or precast reinforced concrete box girders, which are then longitudinally connected together using the shear keys. The distribution factor of the vehicle axle load to each box girder is not always equal, as it is commonly characterized by a live load distribution factor. Some researchers have tried to explore the analytical approaches of lateral load distribution by adopting field tests. However, load effects cannot be directly measured in the field, whereas the deflection and strain can be measured. As a result, the distribution factor can alternatively be determined by taking the ratio of the response in a given member to the summation of

all primary load-carrying member responses and multiplying the number of trucks applied on the bridge [19], as follows:

$$g_i = \frac{R_{\mathrm{max},i}}{\sum_i^{\mathrm{NO}.girders} R_{\mathrm{max},i}} \cdot N_{trucks} = \frac{\Delta_{\mathrm{max},i}}{\sum_i^{\mathrm{NO}.girders} \Delta_{\mathrm{max},i}} \cdot N_{trucks}$$
$$= \frac{\varepsilon_{\mathrm{max},i}}{\sum_i^{\mathrm{NO}.girders} \varepsilon_{\mathrm{max},i}} \cdot N_{trucks} \tag{1}$$

where $R_{\mathrm{max},i}$ is the maximum reaction force in the ith girder; $\Delta_{\mathrm{max},i}$ is the maximum deflection in the ith girder; $\varepsilon_{\mathrm{max},i}$ is the maximum strain in the ith girder; and N_{trucks} is the number of trucks on the bridge for the given loading.
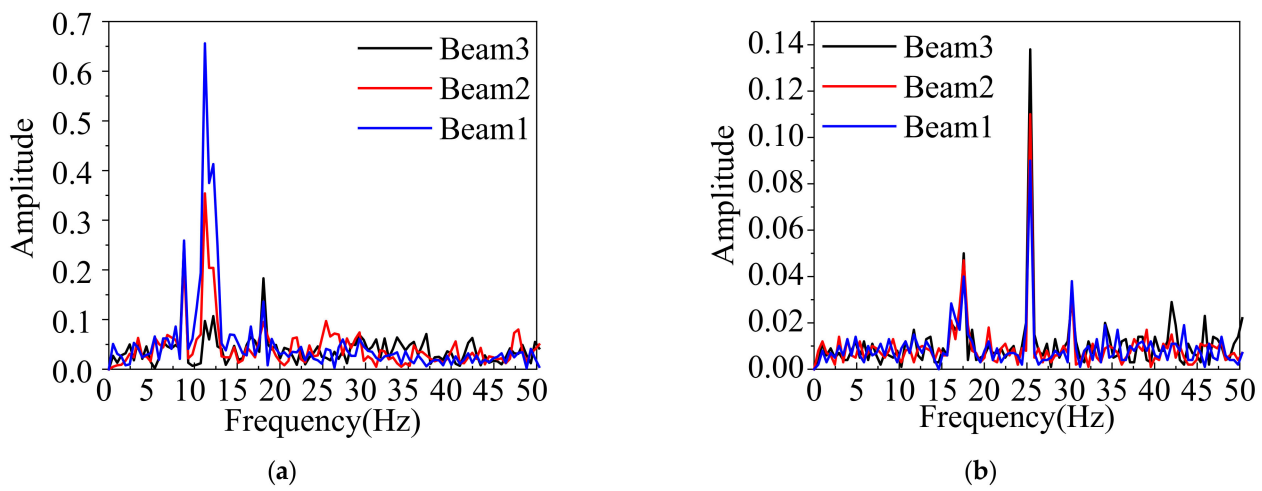
Figure 13. FFT Spectrum. (**a**) Before ESP strengthening. (**b**) After ESP strengthening.

Figure 14 shows the lateral load distribution factors under the symmetrical and static partial loading cases before and after ESP strengthening. Under the symmetrical static loading case, the deflection distribution factors obtained from Equation (1) before strengthening were 0.44, 0.1, and 0.46 for the 1#, 2#, and 3# girders, respectively, and the coefficient of variation was 0.036. The strain distribution factors were 0.4, 0.22, and 0.38 for the 1#, 2#, and 3# girders, respectively, and the coefficient of variation was 0.039. After strengthening, the corresponding deflection distribution factors were 0.35, 0.29, and 0.36, respectively, and the coefficient of variation was 0.017. The corresponding strain distribution factors were 0.35, 0.32, and 0.33, respectively, and the coefficient of variation was 0.018. Under the case, the coefficient of variation of the deflection and strain distribution factors was improved by 53% and 50% after strengthening, respectively. Under the static partial loading condition, the deflection distribution factors before strengthening were 0.08, 0.29, and 0.63 for the 1#, 2#, and 3# girders, respectively, and the coefficient of variation was 1.167. The strain distribution factors were 0.13, 0.38, and 0.49 for the 1#, 2#, and 3# girders, respectively, and the coefficient of variation was 0.752. After strengthening, the deflection distribution factors were 0.31, 0.32, and 0.37 in order, and the coefficient of variation was 0.126. The corresponding strain distribution factors were 0.31, 0.33, and 0.36, respectively, and the coefficient of variation was 0.12. Under the condition, the coefficient of variation of the deflection distribution factors was improved by 89% and 84% for the strain distribution factor. This indicates that the load lateral transferring performance between the box girders is improved under two cases.
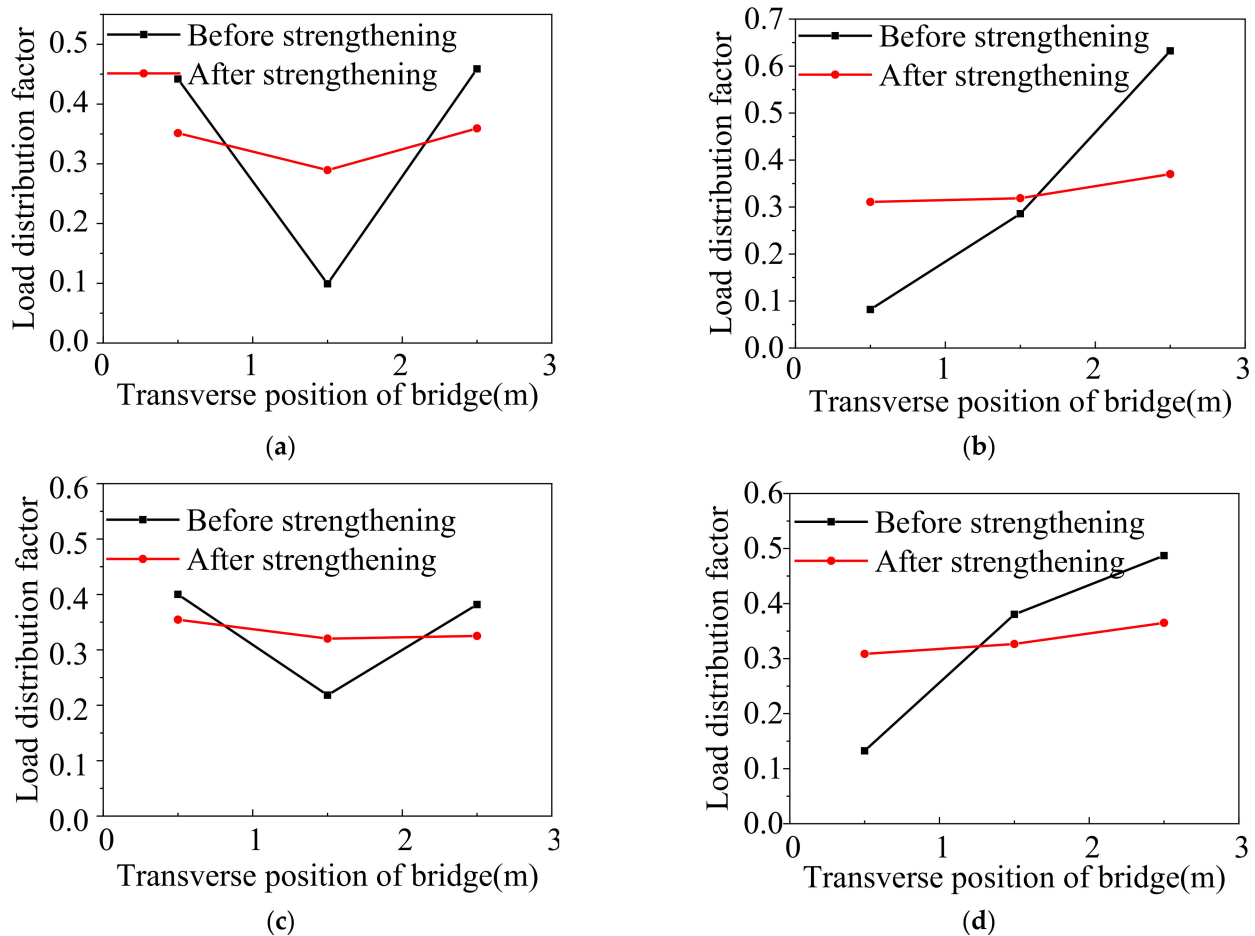
Figure 14. Lateral load distribution factor from field tests. (**a**) Deflection distribution factors under symmetrical load. (**b**) Deflection distribution factors under partial load. (**c**) Strain distribution factors under symmetrical loading. (**d**) Strain distribution factors under partial loading.

4. Finite Element Analysis

To further verify the strengthening effect of the ESP method, ANSYS 18.0 [20] was used to conduct a study based on the background bridge. Figure 15 shows the FE model of the bridge in Sections 2.3 and 2.4. Concrete box girders, the shear key, and bridge slabs were all simulated as 3-D element SOLID65. Reinforcing bars and pre-tensioning strands were modeled as link elements. Double cells with the irregular figure were converted into the double circular according to the equality of the area and inertia moment. The concrete properties came from Schmidt hammer tests. The elastic modulus of the steel rebar and concrete is 200 GPa and 32.5 Gpa, respectively. Poisson's ratio of the steel rebar and concrete is 0.3 and 0.18, respectively. The background bridge worked in the elastic behavior under the truck load, which was applied in the field tests, and the non- linearity behavior was not taken into consideration in the FE analysis. Before strengthening, the partial-depth shear key was fractured, and the girder-key interface was thought to be de-bonded in the FE model. After strengthening, because the adhesion strength of carbon-A/-B glue was more than the tensile strength of concrete, the girder-key interface strength of the concrete, the girder-key interface, and the girder-girder interface were thought to be bonded perfectly in the FE model. The loading process was divided into a loading step and a pre-tension step. In the pre-tension step, an initial stress, 195 kN, was applied to all strands. A roller and a hinge were applied as boundary conditions.
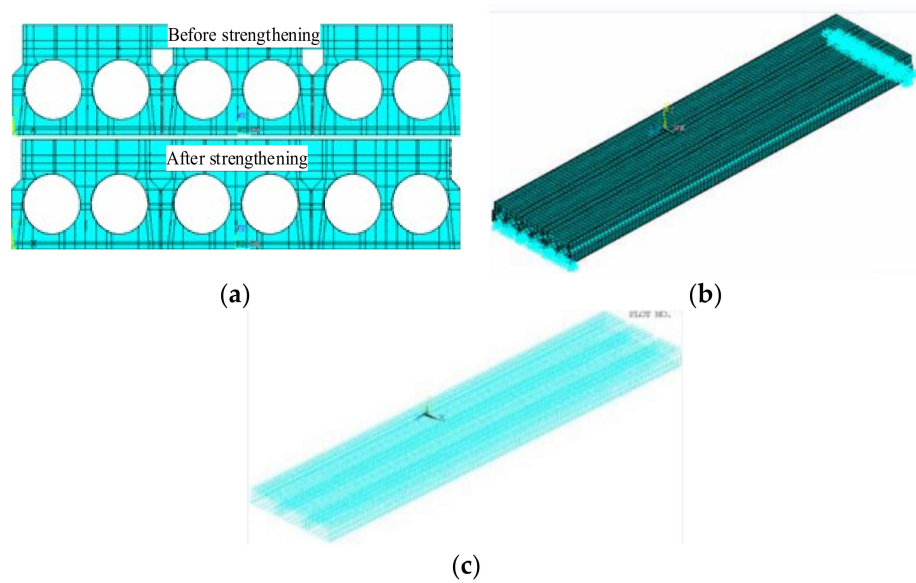
Figure 15. Finite element (FE) model. (**a**) Analysis model. (**b**) Boundary conditions. (**c**) Reinforcement.

In this paper, the Lanczos algorithm was applied for free vibration analysis. The fundamental frequency results are listed in Table 3. The fundamental frequency of the FE analysis was 8.76 Hz and 17.45 Hz before and after ESP strengthening, respectively. The FE analysis results were in good agreement with the test results, and the corresponding error was only 1.3% and 0.7%, respectively. Table 4 lists the comparison of the deflection of the 1# girder at the mid-span under the symmetrical loading test between the test results and the FE analysis. The deflections of the 1# girder at the mid-span from the FE analysis were 4.71 mm and 3.62 mm before and after strengthening, respectively, and they agreed well with the corresponding deflection of the test results.

Table 3. Fundamental frequency results.
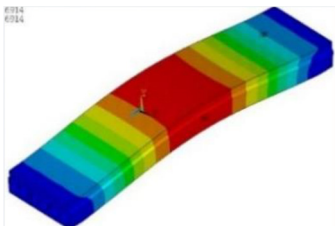
| Model Number | Fundamental Frequency (Hz) | | | | Model Shape |
| | Test | | FEA | | |
	Before	After	Before	After	
1	8.88	17.58	8.76	17.45	

Table 4. Comparison of the deflection of the 1# girder at the mid-span under the symmetrical load.

Deflection	Before Strengthening	After Strengthening	Before/After (%)
Test (mm)	4.83	3.77	128.1
FE analysis (mm)	4.71	3.62	130.1

Figure 16 shows the comparison of lateral load distribution factors between the test and FE analysis under the symmetrical and static partial loading cases before and after ESP strengthening. Under the symmetrical static loading case, the load distribution factors

from the FE analysis before strengthening were 0.37, 0.26, and 0.37 for the 1#, 2#, and 3# girders, respectively. After strengthening, the load distribution factors from the FE analysis were 0.345, 0.31, and 0.345 in order. Under the static partial loading condition, the load distribution factors from the FE analysis were 0.1, 0.32, and 0.58 for the 1#, 2#, and 3# girders before strengthening, respectively. After strengthening, the corresponding load distribution factors from the FE analysis were 0.32, 0.33, and 0.35, respectively. This indicates that the FE analysis results were consistent with the field tests' results.
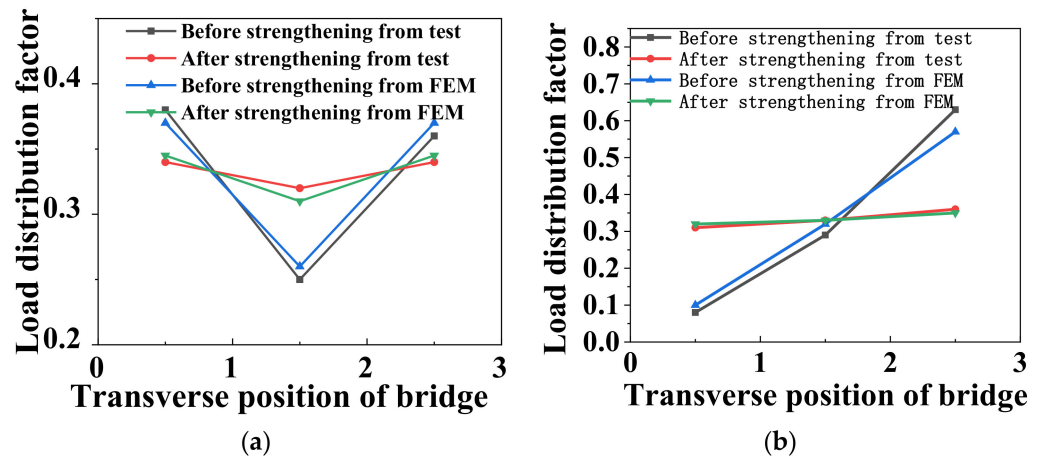
Figure 16. Comparison of load distribution factors between the test and FE analysis. (**a**) Symmetrical loading. (**b**) Partial loading.

Table 5 displays the stress contours of the 1# girder before and after ESP strengthening. The maximum longitudinal stress was located in the underside of box girder at the midspan. The girder strengthened based on the ESP method had a relatively low stress distribution at the same load condition, which indicated that ESP method could be used to improve the capacity of the box girder bridge.

Table 5. Stress contours of the 1# girder under the symmetrical loading condition.

Load Step	Before Strengthening	After Strengthening
100 kN		
200 kN		
300 kN		

5. Conclusions

In this paper, a 26-year-old multi-beam box girder bridge was reinforced by adopting the ESP method, and the strengthening results were investigated by adopting field tests before and after strengthening. The conclusions are drawn as follows.

(1) In comparison to the box girder bridge before strengthening, the field test results showed that the strengthening effect of the deflections and relative displacements under the symmetrical/partial loading case was improved greatly. The maximum concrete strain values under the symmetrical/partial load case were decreased by 23.6%/63% after strengthening, respectively. However, the minimum concrete strain values under the symmetrical/partial load case were increased by 26.7%/61%, respectively. This indicates that the box girder bridge behaves more monolithically after strengthening.

(2) The results showed that the first three order frequencies before strengthening were 8.875 Hz, 11.274 Hz, and 18.167 Hz, respectively, and the corresponding frequencies were 17.578 Hz, 25.282 Hz, and 30.416 Hz after strengthening for the background bridge, respectively. The fundamental frequency was increased by 46%, which shows the overall stiffness of the box girder bridge was enhanced.

(3) The coefficient of variation of the deflection and strain distribution factors was improved by 53% and 50% under the symmetrical load case for the actual bridge, respectively. The coefficient of variation of the deflection and strain distribution factors was improved by 89% and 84% under the partial load condition, respectively. This presents that the load lateral transferring performance between the box girders is enhanced under two cases.

(4) It was manifested that the FE analysis results had a good agreement with the test results for the fundamental frequency, load lateral distribution factor, and deflection. The FE analysis results further verified that the ESP method could be used to improve the mechanical performance of multi-beam box girder bridges.

Author Contributions: Project administration, data curation, Z.C.; resources, Y.X.; software, K.W.; validation, Y.H. and P.Z. All authors have read and agreed to the published version of the manuscript.

Data Availability Statement: Some or all data, models, or code that support the findings of this study are available from the corresponding author upon reasonable request.

Conflicts of Interest: The authors declare no conflict of interest.

References

1. PCI (Precast/Prestressed Concrete Institute). *The State of the Art of Precast/Prestressed Adjacent Box Beam Bridges*, 1st ed.; PCI: Chicago, IL, USA, 2012.
2. Attanayake, U.; Aktan, H. First-generation ABC system, evolving design, and half a century of performance: Michigan side-by-side box-beam bridges. *J. Perform. Constr. Facil.* **2015**, *29*, 04014090. [CrossRef]
3. Steinberg, E.P.; Semendary, A.A. Evaluation of transverse tie rods in a 50-year-old adjacent prestressed concrete box beam bridge. *J. Bridge Eng.* **2017**, *22*, 05016010. [CrossRef]
4. Grace, N.F.; Jensen, E.A.; Bebawy, M.R. Transverse post-tensioning arrangement for side-by-side box-beam bridges. *PCI J.* **2012**, *57*, 48–63. [CrossRef]
5. Russell, H.G. *Adjacent Precast Concrete Box Beam Bridges: Connection Details*; NCHRP Synthesis 393 Transportation Research Board: Washington, DC, USA, 2009.
6. Kim, J.H.J.; Nam, J.W.; Kim, H.J.; Kim, J.H.; Kim, S.B.; Byun, K.J. Overview and applications of precast, prestressed concrete adjacent box-beam bridges in south korea. *Precast./Prestress. Concr. Inst. J.* **2008**, *53*, 83–107. [CrossRef]
7. Liu, Z. Evaluation of An Innovative Joint Design for the Adjacent Box Beam Bridges. Ph.D. Thesis, Iowa State University, Ames, IA, USA, 2018.
8. Wang, L.; Tang, C. Experimental study of hollow plate beam reaming with anchor plate connection rebar. *Seism. Eng. Eng. Vib.* **2020**, *40*, 140–147. (In Chinese)
9. El-Remaily, A.; Krause, A.G. Transverse design of adjacent precast prestressed concrete box girder bridges. *PCI J.* **1996**, *41*, 96–113. [CrossRef]
10. Liu, Z.Y.; Phares, B.M. Small-scale investigation on wide longitudinal joints filled with shrinkage-compensated concrete for adjacent box beam bridges. *J. Bridge Eng.* **2019**, *24*, 04019114. [CrossRef]
11. Sang, Z. A numerical Analysis of the Shear key Cracking Problem in Adjacent Box Beam Bridges. Ph.D. Thesis, Pennsylvania State University, State College, PA, USA, 2010. Available online: https://etda.libraries.psu.edu/catalog/11283 (accessed on 20 May 2022).
12. Yuan, J.; Graybeal, B. Full-scale testing of shear key details for precast concrete box-beam bridges. *J. Bridge Eng.* **2016**, *21*, 04016043. [CrossRef]
13. Hussein, H.H.; Walsh, K.K.; Sargand, S.M.; Steinberg, E.P. Interfacial properties of ultrahigh-performance concrete and high-strength concrete bridge connections. *J. Mater. Civ. Eng.* **2016**, *28*, 04015208. [CrossRef]
14. Hussein, H.H.; Walsh, K.K.; Sargand, S.M.; Rikabi, F.T.A.; Steinberg, E.P. Modeling the shear connection in adjacent box-beam bridges with ultrahigh-performance concrete joints.ii: Load transfer mechanism. *J. Bridge Eng.* **2017**, *22*, 04017044. [CrossRef]

15. Semendary, A.A.; Steinberg, E.P.; Walsh, K.K.; Barnard, E. Live-Load Moment-Distribution Factors for an Adjacent Precast Prestressed Concrete Box Beam Bridge with Reinforced UHPC Shear Key Connections. *J. Bridge Eng.* **2017**, *22*, 1–18. [CrossRef]

16. Phares, L.G.Z.L.; Freeseman, B.K. *Context Sensitive Designs: Testing of Multi-Performance Level Box Beam Standards. Bridge Engineering Center Rep*; Institute for Transportation, Iowa State University: Ames, IA, USA, 2013.

17. Shi, H. Study on the performance of the large diameter screw method to reinforce the hinges of the hollow plate. *Wuhan Hua Zhong Univ. Sci. Technol.* **2018**. (In Chinese)

18. Fu, C.C.; Pan, Z.F.; Ahmed, M.S. Transverse posttensioning design of adjacent precast solid multibeam bridges. *J. Perform. Constr. Facil.* **2010**, *25*, 223–230. [CrossRef]

19. Amir Gheitasi, H.D.K. Overload flexural distribution behavior of composite steel girder bridges. *J. Bridge Eng.* **2015**, *20*, 04014076. [CrossRef]

20. ANSYS. *Software Documentation Release 18.0*; Ansys, Inc.: Canonsburg, PA, USA, 2018.

Thermal Insulation Mattresses Based on Textile Waste and Recycled Plastic Waste Fibres, Integrating Natural Fibres of Vegetable or Animal Origin

Andreea Hegyi [1], Horațiu Vermeșan [2,*], Adrian-Victor Lăzărescu [1,3,*], Cristian Petcu [4,*] and Cezar Bulacu [5,6]

1   NIRD URBAN-INCERC Cluj-Napoca Branch, 117 Calea Florești, 400524 Cluj-Napoca, Romania; andreea.hegyi@incerc-cluj.ro
2   Faculty of Materials and Environmental Engineering, Technical University of Cluj-Napoca, 103-105 Muncii Boulevard, 400641 Cluj-Napoca, Romania
3   IOSUD-UTCN Doctoral School, Technical University of Cluj-Napoca, 15 Daicoviciu Street, 400020 Cluj-Napoca, Romania
4   NIRD URBAN-INCERC Bucharest, 266 Șoseaua Pantelimon, 021652 Bucharest, Romania
5   MINET S.A., 12 Depozitelor Street, 240426 Ramnicu Valcea, Romania; cezar.bulacu@minet.ro
6   Faculty of Industrial Design and Business Management, "Gheorghe Asachi" Technical University of Iași, 29 Prof. Dr. Doc. Dimitrie Mangeron Street, 700050 Iasi, Romania
*   Correspondence: horatiu.vermesan@imadd.utcluj.ro (H.V.); adrian.lazarescu@incerc-cluj.ro (A.-V.L.); cristian.petcu@yahoo.com (C.P.)

Abstract: The current context provides, worldwide, the need to identify solutions for the thermal efficiency of constructions, through sustainable and innovative methods and products. A viable solution is to produce thermal insulating products by carding-folding technology, using natural fibres and recycled polyethylene terephthalate (rPET) and polyester (rPES) waste, converted to fibres. This paper presents experimental results obtained after testing several thermal insulation composite products produced using a mix of sheep wool, cellulose, rPET and rPES fibres. The results of the research demonstrate the thermal insulation properties but, at the same time, identify the benefits of using such materials on the quality of the air in the interior space (the ability to adjust humidity and reduce the concentration of harmful substances). At the same time, the advantages of using sheep wool composite mattresses concerning their resistance to insect attack is demonstrated when compared with ordinary thermal insulation materials. Finally, sensitivity elements of these composites are observed in terms of sensitivity to mould, and to contact with water or soil, drawing future research directions in the development of this type of materials.

1. Introduction

According to the Energy Performance Directive (EPBD recast, 2010/31/EU) and the Energy Efficiency Directive (2012/27/EU) [1,2], nowadays all new buildings should have been designed according to the principles of the lowest possible energy consumption, and old buildings are currently designed thermally efficient as much as possible. One of the key factors in this design is the possibility of thermal insulation. On the other hand, the principles of the Sustainable Development concept and the need to implement the defining guidelines of the Circular Economy oblige us to identify new possibilities for the development of sustainable thermal insulation materials. If by 2020 it was estimated that buildings represented 30–40% of the global primary energy consumption and more than 25% of the sources of greenhouse gas emissions [3–6], the current pandemic context changed this paradigm. It has required the migration of activities in individual or smaller indoor spaces, with a lower degree of occupancy, so the adverse effects have increased

substantially, leading to the increasing need to identify sustainable thermal envelope possibilities. Worldwide, various thermal insulation materials are currently used extensively, mainly expanded or extruded polystyrene or mineral wool. On the one hand, they offer satisfactory thermal performance but the impact of their production on the health of users and the environment cannot be neglected: most of the time, in addition to the polluting emissions that occur during the manufacturing process, these materials reduce the quality of the air in the living space by reducing the permeability of the walls to water vapour and various gaseous compounds. Consequently, there is an accumulation of indoor humidity leading to the development of moulds, the accumulation of volatile organic compounds or radon [7,8] and, finally, leading to the development of the so-called "sick building syndrome" [9–15]. Despite these disadvantages, thermal insulation based on expanded or extruded polystyrene, polyurethane foam, glass fibre or mineral wool accounts for about 87% of the market [16,17].

The use of plant and animal fibres and recycled waste in new bio-eco-innovative thermal insulation products, on the one hand, opens new possibilities for the development of such materials, but, on the other hand, brings new challenges, especially in terms of water and micro-organism behaviour [2,18]. The advantages of natural fibre-based thermal insulation materials are, above all, that they are relatively straightforward to obtain, from renewable resources, with low cost and environmental impact. Moreover, some characteristics that would appear to be disadvantages at first sight can easily be turned into benefits. For example, the feature of natural fibres to absorb moisture from the air can be seen as a benefit if viewed through the lens of sorption/desorption capacity, which will clearly contribute to the regulation of indoor air humidity [2,18–22]. A market share analysis [23] shows that growth in environmental awareness in the developed countries translates into the increased use of natural insulating materials, thus representing a growing market share in recent years. Correlated with market concerns, it is not surprising that research into the development of natural fibre-based thermal insulation materials has increased in scope over the last 20–25 years. Worldwide research has shown that insulation produced using natural plant or animal raw materials or recycled raw materials has lower greenhouse gas emissions than other insulation materials, e.g., mineral wool or polystyrene [24–29]. A comparative analysis of the impact of different types of insulation materials on global warming places sheep wool as having the lowest contribution (1.457 kg CO_{2eq}/functional unit), 9–10 times lower than, e.g., extruded polystyrene (13.22 kg CO_{2eq}/functional unit), and even half that of mineral wool insulation (2.77 kg CO_{2eq}/functional unit) [30]. A similar report also ranked the lifetime energy consumption, from production to disposal and recycling, and in terms of stored energy (MJ/functional$_{eq}$ unit)—much lower parameters for bio-eco-innovative thermal insulation [24–30]. Moreover, animal fibres, and especially sheep wool, due to the COOH-CHNH-R_2 structure of the proteins in the wool yarn, contribute to the reduction in environmental pollution by adsorption on the yarn of gases such as SO_2, NO_x, aldehydes, or VOC, this adsorption being in some cases reversible (VOC, phenols) or irreversible (NO_x, SO_x, formaldehyde). In the case of sheep wool fibres, some research has shown that under conditions of 2.32 ppm sulphur dioxide concentration, the adsorption capacity of wool was initially 0.012 mg/g wool/min, reaching 0.003 mg/g wool/min after 60 min of exposure. Regarding the toxic products from cigarette smoke, a retention capacity of 40 mg cigarette smoke/g of wool was demonstrated. Moreover, other studies showed the capacity to reduce Cu^{2+} concentration by 41% in 1 h, and As^{3+} content by 34–53% in 1 h [31–36].

In terms of the mechanisms underlying these unique properties, natural fibres of animal and plant origin are defined by their structural specificity. Thus, in the case of wool yarns, the genetic structure, of a proteinaceous nature, with hydrophobic cuticles due to the presence of fatty acids covalently bound to the protein substrate, with a cortex composed of elongated cells containing more than 93% keratin (mass percentage) and 18 other α-amino acids and with a specific medullary channel, allows the absorption of 15–18% of the water vapour mass under normal conditions, but can reach up to 40% under saturated

atmosphere conditions. The expansion of the medullary canal facilitates the absorption phenomenon, the diameter of the strand can increase by up to 18% and its length by 1%, and the formaldehyde neutralisation capacity is based on the keratin chemisorption reaction shown in Figure 1 [37–40]. In the case of fibres of plant origin, the absorption of atmospheric moisture is associated with the possibility of trapping hydroxyl (OH) groups and molecular water in the cell wall, which can be considered a cellulosic composite formed by crystalline microfibrils embedded in an amorphous lignin/hemicellulose/pectic matrix. Cellulose, consisting of linear chains of glucose grouped into units of microfibrils with high crystallinity, also has a paracrystalline component, favouring the binding of molecular water. Lignin is an amorphous cross-linked polymer composed of phenolic units; it has a lower (OH) group affinity compared with the polysaccharides characteristic of cellulose. Hemicellulose and the pectin component, predominantly amorphous polysaccharides, are very accessible for the addition of water molecules [22].
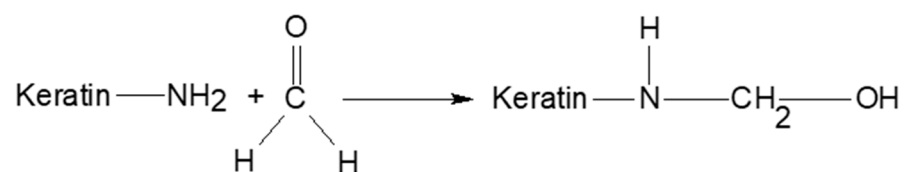
Figure 1. Keratin chemisorption reaction.

Unlike fibres of plant or animal nature, those from recycled waste plastics such as polyethylene terephthalate (PET) or polyester textile waste (PES) are relatively inert in terms of their chemical binding capacity to water or other compounds. Nonetheless, they offer different advantages, and the need to recycle and reuse them is imperative under the Waste Directive 2008/98/EC [41]. Their recycling successfully addresses the need to reduce the quantity of polymer waste and to obtain new products with reduced emissions and the sustainable use of non-renewable raw material and energy reserves. Polyethylene terephthalate (PET) is a material of great interest in the materials sector in general and, by extension, in the building materials sector as it is 100% recyclable, the only more easily recyclable material being aluminium. The cost of recycled polyethylene terephthalate (R-PET) is 20–60% lower than the cost of polyethylene terephthalate produced from virgin raw material (V-PET). Additionally, the reduction in energy consumption is 50–70% and the reduction in petroleum feedstock consumption is 50–60% [42–47]. Worldwide, the main use of R-PET is for fibre production, accounting for more than 70% of all polyethylene terephthalate fibres produced [29,42,44]. Studies have demonstrated the possibility of using polymeric fibres from recycled materials to produce non-woven thermal insulation materials for the construction sector, thus identifying the potential for conserving natural resources and reducing environmental impact. In the case of polyethylene terephthalate (PET) mattresses, thermal conductivity varies with increasing density. For the same thickness of non-woven thermal insulation product, a low density ensures a high thermal insulation potential, but for mechanical strength reasons this density must be increased. A balancing calculation of thermal and mechanical performance is necessary, also taking into account that around a density value of 60 kg/m^3, the phenomenon of heat transfer through conduction becomes dominant and thermal insulation performance decreases significantly [48–51]. Research has demonstrated the possibility of obtaining thermal insulation mattresses produced using R-PET fibres characterised by a thermal conductivity coefficient around values of 0.035 W/mK [29]. Based on the research, the quantifiable indicator TIV "Thermal Insulating Value" was identified, which indicates that the thermal insulating efficiency of a product depends on the thermal conductivity coefficient of the material, the thickness of the product and the thermal emission of the surface. For thermal insulation products produced using PET, the TIV coefficient ranges from 41.21% to 52.15% for thicknesses in the range 3.54–7.97 mm, increasing alongside increasing thickness [48–51].

At the same time, the advantage of this type of fibre is its reduced sensitivity to water and increased resistance to mould action.

Approximately 5.8 million tons of textile waste are produced annually in the EU, of which only 25% is recycled and reused, although the recycling potential is 95% [52–54]. One of the possibilities for recycling is the transformation into fibres which, although not fully suitable for reuse in the textile industry, can successfully become a raw material in the non-woven thermal insulation sector for the construction industry. Research results to date [55,56] have shown that recycled textiles have competitive thermal properties, thermal conductivity and thermal diffusivity, and can be used as an alternative to commercial thermal insulation materials (extruded polystyrene or mineral wool) in the construction sector. Danihelová et al. [55], in agreement with other reports [48] showed that recycled textile waste mattresses can be good thermal insulators, characterised by a thermal conductivity coefficient around 0.033 W/mK.

Therefore, producing thermal insulation mattresses from a mixture of recycled PET fibres, recycled PES, fibres of plant origin and fibres of animal origin makes it possible to exploit the basic principle of composite materials: the accumulation of benefits.

This paper aims to present the possibility of producing composite materials, of the non-woven type (mattresses), intended for use as thermal insulation materials in the construction sector, and through the experimental results obtained, to identify the benefits that these products can have on the air quality of the indoor space and, implicitly, on the health of the users, also identifying possible weaknesses to draw future research directions.

2. Materials and Methods

2.1. Materials

The experimental testing was carried out for six types of non-woven thermal insulation materials (thermal insulation mattresses), presented in Table 1, identified with codes P1–P6. They were produced by carding-folding technology with thermal consolidation at low temperature (110–180 °C), from a mixture of raw materials. The mixture of fibres used to produce the six heat-insulating mattresses (mass ratio) is characterised by three parts combed sheep wool; 1.5 parts siliconised cellulosic fibre; 2.5 parts heat-sealable bicomponent recycled polyethylene terephthalate (PET) fibre; and 3 parts recycled polyester fibre (PES). Sheep wool yarn was obtained by splitting combed sheep wool, which was purchased in bulk from local traders. The siliconised cellulosic fibre is characterised by an average linear density of 2 dtex and length of 20 mm. Recycled PES fibre is characterised by an average linear density of 7 dtex and a length of 65 mm. Recycled PET fibre is bicomponent, max. 9 dtex and max. 80 mm length.

Table 1. Thermal-insulation mattresses produced using textile waste, recycled PET waste and natural fibres of plant and animal origin.

Identification	Thickness (mm)	Apparent Density (kg/m^3)
P1	19.99	18.56
P2	29.99	29.22
P3	49.98	21.41
P4	49.98	25.23
P5	59.99	16.38
P6	29.99	39.99

The six thermal insulation mattresses, although produced using the same fibre blend, had different bulk densities and thicknesses, characteristics that were controlled by controlling specific parameters on the technological flow. The production of the materials took place in an industrial system, on the technological flow of MINET S.A. Rm.—Vâlcea, Romania.

Given the intended field of use, several categories of measurable indicators have been assessed for each type of thermal insulation mattress according to EAD 040456-00-1201/2017 "In situ formed loose fill thermal and/or acoustic insulation material made

of animal fibres" and EAD 040005-001201/2015 "Factory-made thermal and/or acoustic insulation products made of vegetable or animal fibres". These indicators are: physical–mechanical (heat transfer coefficient, compressive strength, tensile strength, elongation failure, short-term water absorption) and durability, biological resistance and impact on human health (sorption–desorption characteristics of atmospheric moisture, water vapour permeability, resistance to the action of micro-organisms, formaldehyde neutralisation capacity and corrosivity).

2.2. Thermal Insulation Performance

Heat transfer coefficient, $\lambda_{10,ct.}$ (W/mK) was determined using a FOX 314 conductivity meter by the hot plate method at a temperature difference between the plates of 10 °C. Samples were placed between the two plates, and then a temperature gradient was established over the probe thickness. The equipment automatically detects equilibrium conditions and determines the heat transfer resistance R (m^2K/W) and, for the homogenous probes, the equivalent heat transfer coefficient.

2.3. Mechanical Performance

In order to evaluate the compressive strength (universal testing machine, type ZDM-5/91, VEB Leipzig, Germany), a compressive load was applied with uniformly increasing speed, perpendicularly and uniformly distributed over the surface of the specimen, and the degree of indentation of the specimen was recorded. The compressive strength was calculated as the ratio of the applied force to the area of application, for an indentation of 10% of the initial thickness of the specimen.

Tensile behaviour was assessed by recording the maximum tensile strength and elongation at failure of specimens taken in the longitudinal/transverse direction of the material (Shenzhen Wance Testing Machine Co., Ltd., Shenzhen, China). According to the standards in force, short-term water absorption is an indicator of the material behaviour in the situation caused by a 24 h rain period during the construction process. The test specimen was placed with the bottom side in contact with water for 24 h and its mass change in relation to the exposed surface area was measured.

2.4. Behaviour in Water and in the Presence of Water Vapour

Water vapour sorption/desorption capacity was quantified by plotting characteristic curves of specimen mass variation against relative air humidity. Thermal-insulation conditions, 23 °C, controlled by relative air humidity (RH) of 30%, 45%, 60%, 80%, and 95%, were chosen for testing.

Water vapour permeability was evaluated using test specimens sealed over circular cups in which water vapour pressure was kept constant by a saturated potassium nitrate solution under specified conditions (23 ± 2 °C). Moisture transfer was determined as the change in weight of the test system when constant vapour flow was reached.

The samples were constantly weighted using an analytical balance from Kern & Sohn GmbH, Albstadt, Germany, with a precision of 0.0001 g.

2.5. Resistance to the Action of Biological Agents

Mould resistance was determined by exposing the specimens for a defined period of time (4 weeks), at a constant temperature of 23 ± 2 °C, in an environment with high humidity, after which a visual and microscopic evaluation was carried out on the appearance of signs of growth of microorganisms, after which the product was given a certain class indicated in Tables 2 and 3, respectively.

Table 2. Criteria for assessing mould resistance.

Fungal Growth Class	Evaluation of Fungal Growth	Product Category	Product Performance
Class 0	No sign of growth under the microscope.	Category 0	The material is not a nutrient medium for microorganisms (it is inert or fungistatic)
Class 1	Growth invisible to the naked eye but clearly visible under a microscope.		
Class 2	Increase visible to the naked eye, covering up to 25% of the test area.	Category 1	The material contains nutrients or is so poorly contaminated that it allows very little growth
Class 3	Visible growth to the naked eye, covering up to 50% of the test area.		
Class 4	Considerable growth, covering more than 50% of the test area.	Category 2–3	The material is not resistant to fungal attack; it contains nutrients that allow micro-organisms to grow.
Class 5	Strong growth, covering the entire test area		

Table 3. Criteria for assessing insect resistance.

Estimation of Surface Degradation		Hole Estimation	
Symbol	Ruptures-Visibly Degraded Surface	Symbol	
1	No visible damage	A	No visible holes
2	Reduced degradation	B	Partially destroyed yarns and fibres
3	Moderate damage	C	Reduced number of holes; destroyed yarns and fibres
4	Major damage	D	Large holes

Biological resistance to worm and insect attack was assessed by evaluating the viability of the first generation and the development of the second generation of insects, the common moth (*Order lepidoptera*), under conditions of the contact of specimens with eggs, larvae and adult insects for 6 months. The classification into resistance classes by visual assessment of the damage caused by was carried out according to Table 3.

Resistance to soil biological attack was assessed by microscopic analysis to identify signs of microorganism and worm growth and by determining the percentage reduction in tensile strength and elongation at break under conditions of complete burial of the specimens in soil with a water holding capacity of 60% for 4 weeks and 6 months, respectively.

The analysis of the samples in terms of resistance to the action of biological agents was carried out using a Leica DMC2900 microscope (Leica Microsystems GmbH, Wetzlar, Germany) and results/images were obtained using the dedicated image capturing application (Leica Application Suite, Leica Microsystems GmbH, Wetzlar, Germany).

2.6. Metal Corrosion Development Capacity

The metal corrosion development capability provided information on the level of corrosivity of the thermal insulation material on Cu/Zn metal elements (metal parts that may come into contact with the thermal insulation material in place) by allowing the migration of corrosive agents adjacent to the thermal insulation material towards these metal elements. The ability of metal corrosion to develop was assessed by visual and microscopic evaluation of the appearance of signs of corrosion on the surface of metal plates (Cu sheet or galvanised steel sheet) after they had been kept in contact with the surface of specimens of thermal insulation material saturated with water, for 4 weeks. The analysis of the samples in terms of metal corrosion development capacity was carried out using the same equipments as the ones used for the analysis of the action of biological agents.

2.7. Impact on Indoor Air Quality

The formaldehyde neutralisation capacity was assessed by recording the variation in formaldehyde concentration in a sealed enclosure of which the base was completely covered with a heat-insulating mattress. Initially, the atmosphere in the $0.1 \, m^3$ volume enclosure was enriched with formaldehyde to a concentration of more than $25,000 \, \mu g/m^3$, equivalent in terms of health impact to a "toxic level with neurotoxic manifestations". Formaldehyde concentration monitoring was performed using commercial equipment equipped with a

formaldehyde sensor and electronic display (HCHO & TVOC Meter, Shenzhen Everbest Machinery Industry Co., Ltd., Shenzhen, China). When the formaldehyde concentration in the monitored volume fell below the limit level of 200 $\mu g/m^3$, which is equivalent in terms of the health impact on the population to a state of "no signs of discomfort or irritation", a new amount of formaldehyde was introduced into the test enclosure to assess the maintenance of the formaldehyde-neutralising capacity of the heat-insulating mattress over time. The specimen used, with dimensions equal to the base dimensions of the enclosure, 600×450 mm, was covered on the lower face and on the edges with aluminium foil, so that formaldehyde transfer was achieved only through the upper, exposed face.

To ensure repeatability, five determinations were performed for each test, the results being presented as the mean values of the individual values.

The results obtained experimentally were analysed both in comparison with other references in the literature and with existing data in the NIRD URBAN-INCERC databases on the performance of similar thermal insulation products produced by other Romanian manufacturers.

3. Results and Discussions

As is well known, some of the performances analysed are influenced by the material, by its composition, not by its thickness or density. Following the experimental tests carried out, several experimental results were recorded; some expected, others less anticipated. Thus, in terms of thermal insulation performance, the products tested meet the specific requirements of the intended field of use, and the results are in accordance with the specifications in the literature in terms of the heat transfer coefficient, the values recorded being in the ranges 0.034–0.042 W/mK for products tested with their full thickness and 0.030–0.034 W/mK for products tested at half thickness by tamping (Table 4), giving heat transfer resistances, R, in the range 0.55–1.46 mK/W^2 for products tested with their full thickness and 0.33–0.89 mK/W^2 for products tested at halved thickness. Comparing the experimental results obtained with the declared performance of non-woven thermal insulation products made exclusively or predominantly from sheep wool by local producers (Figure 1), it can be said that, in terms of thermal insulation performance, the analysed composite products fall within the general trend, in the higher performance area, with heat transfer coefficient values of 0.032–0.050 W/mK for the comparison products. It should be specified that the comparison values presented in Figure 2 are the results of experimental tests carried out at NIRD URBAN-INCERC Cluj-Napoca Branch Laboratory, on some insulation products present on the local market, with data collected in the past five years. As seen in Figure 1, in terms of thermal insulation performance, analysed on the basis of the measurable indicator λ—heat transfer coefficient, it can be said with certainty that the tested specimens P1–P6 correspond to the intended field of use. The values recorded are comparable with those presented by various types of common thermal insulation materials (expanded polystyrene, extruded polystyrene, mineral wool, etc.) as well as alternative products such as mattresses produced only with sheep wool. It should be noted, however, that under current legislation in the field, this validation in terms of thermal insulation performance is insufficient, and at least a complement is needed in terms of operational safety, durability, and analysis, with regard to environmental and user health impacts.

The density of the material (Table 4) has a significant impact on the thermal conductivity, market acceptance and feasibility when put into operation. When plotted against the density, thermal conductivity first drops as the air cavities between fibres are reduced in volume when increasing in density. An optimum value is reached, the heat transfer through conduction grows as the contact between fibres increases, and the convective part of heat transfer cannot compensate anymore. Generally, a mattress with a higher density (around 30 kg/m^3) has better compressive strength values and is easier to deal with from the workers' perspective. However, we have to keep in mind that market acceptance is of the essence. Therefore, production prices should be kept as low as possible. One should observe and balance all these aspects for a viable product, and material density is the common denominator of all these aspects.

Table 4. Physical-mechanical performance of thermal-insulation mattresses produced using recycled textile and PET waste and natural fibres of plant and animal origin.

Identification Code		P1	P2	P3	P4	P5	P6
Heat transfer coefficient at full thickness (W/mK)		0.0362	0.0358	0.0421	0.0377	0.0412	0.0336
Heat transfer coefficient at 1/2 of thickness (W/mK)		0.0306	0.0308	0.0338	0.0325	0.0337	0.0303
Heat transfer resistance at full thickness (mK/W^2)		0.55	0.84	1.19	1.33	1.46	0.89
Heat transfer resistance at 1/2 of thickness (mK/W^2)		0.33	0.49	0.74	0.77	0.89	0.50
Compressive strength (kPa)		0.17	0.18	0.14	0.20	0.10	0.11
Tensile strength (N/mm^2)	longitudinal direction	0.05	0.11	0.06	0.06	0.04	0.13
	transverse direction	0.03	0.11	0.05	0.08	0.05	0.19
Elongation at break (%)	longitudinal direction	47.60	34.02	34.03	26.62	35.27	22.86
	transverse direction	43.45	37.71	28.64	38.26	31.82	31.24
Short-term water absorption (kg/m^2)		0.069	0.223	0.132	0.121	0.387	0.350
Water vapour resistance (m·h·Pa/mg^2)		0.06	0.06	0.09	0.11	0.09	0.08
Water vapour resistance factor, μ		1.35	1.41	1.26	1.61	0.95	2.32
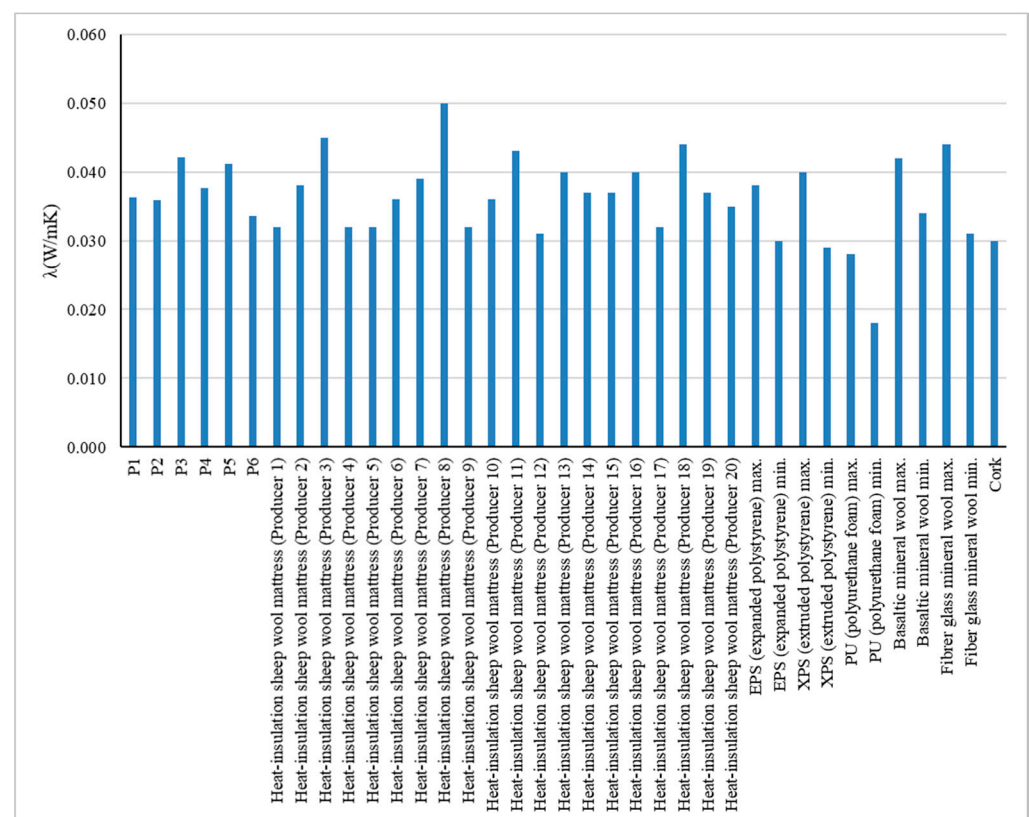
Figure 2. Thermal conductivity coefficient recorded for samples P1–P6 in comparison with the thermal conductivity coefficient of sheep wool mattresses and common thermal insulation materials available on the building materials market.

Additionally, in the same vein, as presented in Table 4, it is not possible to establish a pattern regarding the values of density vs. thickness vs. thermal performance, since for each case there are advantages and disadvantages, thermal insulation performance being influenced by factors other than dimensional ones.

In terms of mechanical strength, as expected due to the non-woven mattress technology used, low values were recorded. Thus, the compressive strengths for an indentation of 10%

of the original thickness (Table 4) was in the range 0.10–0.20 kPa. The tensile strength was in the range 0.05–0.13 N/mm^2 for the specimens cut in the longitudinal direction of the thermal insulation mattress, with a total elongation at break of 22.86–47.60%, and in the range 0.03–0.19 N/mm^2, with a total elongation at break of 28.64–43.45% for the specimens cut in the transverse direction.

The short-term water absorption recorded in the range of 0.07–0.38 kg/m^2 confirmed the sensitivity of this type of thermal insulation material to water and the need for protection both during storage, transport, and commissioning and during the entire service life. However, compared with similar products produced under similar conditions, but exclusively from natural fibres of animal origin (sheep wool), an improvement in the parameter is noted by reducing it even 10 times. This improvement was due to the contribution of the other types of fibres introduced in the raw material mix, in particular recycled PET fibres.

In terms of water vapour sorption/desorption capacity (Figure 3), it is noticeable that the potential regulating character of the indoor air humidity, and therefore its quality, is preserved, a characteristic of similar sheep wool products. The placement of the sorption curve, in all cases, below the desorption curve, means that, although permeable to water vapour, these innovative thermal insulation mattresses, under conditions of increased humidity of the ambient environment, are able to retain a certain amount of water, the results being in agreement with those reported in the literature [2,18–22,25]. As the ambient humidity is reduced, this water will be released to the environment, but at a lower rate than the retention rate, as demonstrated by the slope of the sorption-desorption curves. As a result of this behaviour, it can be seen that this type of product contributes not only to the thermal insulation of the interior space but also to the regulation of its humidity. By analysing the shape of the sorption curves, it can be appreciated that they are in accordance with the specifications of the literature [2,18–22,25], which indicate that water absorption of up to 5% of the dry weight of the fibre takes place at a higher speed, with water binding strongly, after which the phenomenon is influenced by the relative humidity of the environment, the speed stabilising towards the saturation zone, which is also identified by analysing the slope of the sorption–desorption curves. The identification of a slope change zone on each of the desorption curves was considered to delimit a range of relative air humidity in which the activity of regulating atmospheric humidity by releasing water is characterised by a maximum yield. Mathematical modelling of the air moisture sorption/desorption process revealed first-order equations (ax + b), i.e., that these phenomena are influenced by relative air humidity.
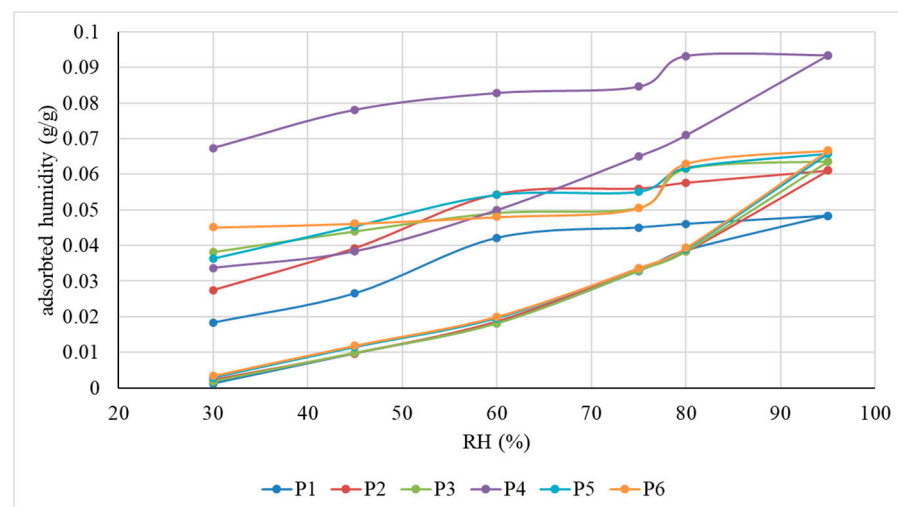
Figure 3. Atmospheric moisture sorption–desorption curves.

Satisfactory results were also obtained in terms of water vapour permeability. These thermal insulation composites have a good water vapour permeability, which will contribute substantially to the air quality of the indoor space, allowing the transfer of moisture

from the inside to the outside and thus making a significant contribution to reducing the risk of mould growth or the development of other types of micro-organisms. Experimental testing showed the following characteristic parameters: water vapour permeance, W, in the range 8.83–18.43 m/mhPa^2; vapour resistance, Z, in the range 0.06–0.11 mPa/mg^2; water vapour permeability, δ, in the range 0.31–0.75 mg/mhPa; water vapour diffusion resistance factor, μ, in the range 0.95–2.32; and water vapour diffusion equivalent air layer thickness, s$_d$, in the range 0.04–0.08 m. Compared with other thermal insulation products, the water vapour diffusion resistance factor, μ, of the tested thermal insulation composite products is similar to that of other non-woven thermal insulation products (sheep wool mattresses) and clearly superior to commonly used thermal insulation products such as mineral wool and, even more so, expanded or extruded polystyrene. In fact, this is one of the great advantages of the composite thermal insulation mattresses tested.

Microscopic analysis of the specimens after testing them under mould growth conditions showed numerous areas where mould develops (Figure 4). However, it was not possible to identify precisely which type of fibre of the four raw materials used was favoured, and to what extent it contributed to mould growth. After the first four weeks of testing, there were already clear signs of mould, visible under the microscope, on the whole surface of the specimen and in its depth, the classification according to Table 2 being class 1 (growth invisible to the naked eye, but clearly visible under the microscope), category 2–3 (material does not resist fungal attack; it contains nutrients that allow microorganisms to grow). Continued testing over the next 4, 8, 16 weeks revealed continued mould growth over time, which indicated an urgent need to identify a treatment solution to reduce mould susceptibility.
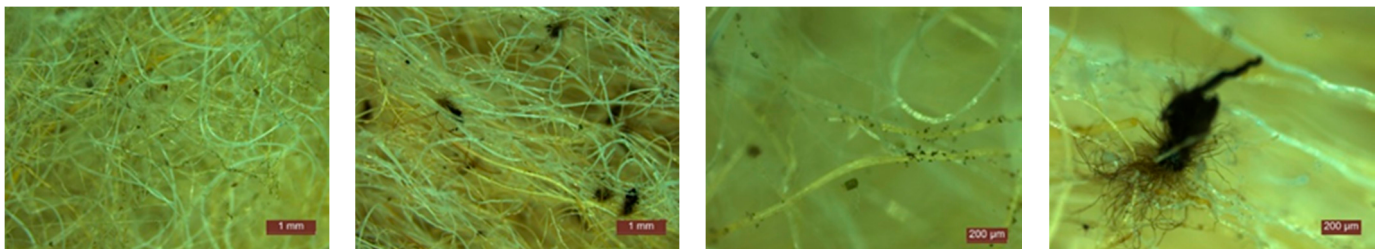
Figure 4. Image captures obtained by microscopic analysis of test specimens for mould resistance.

Biological resistance to attack by worms and insects has highlighted an advantage of these thermal insulation materials compared with similar thermal insulation made exclusively or mainly of sheep wool: visual and, subsequently, microscopic analysis (Figure 5) showed that they fall into category 1A (Table 3) and that the bio-eco-innovative products tested do not represent a viable environment for moths (*Order lepidoptera*), their eggs and larvae. After 7 days of exposure, all adult insects died and there was no evidence of egg laying for the further life cycle. In the case of samples on which moth eggs and larvae were artificially deposited, life cycle interruption was recorded and they did not develop into larvae or adult insects, respectively. Testing continued by follow-up for 56 days with no signs of insect development or the appearance of developmental signs recorded. In contrast to thermal insulation mattresses made exclusively or predominantly of sheep wool, the risk of moth colonies developing, characteristic of products made of wool or various other textile fibres, is minimised in this case. Although clear and proven identification has not been achieved, it is assumed that the introduction of recycled PET and vegetable fibres and their siliconisation has contributed to the insecticidal action of the tested material.

(a)   (b)   (c)
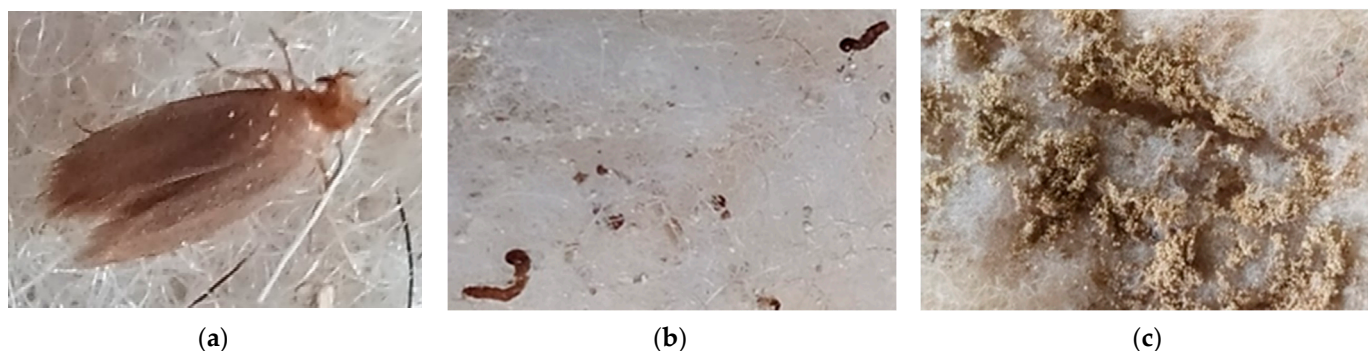
Figure 5. Exposure of heat-insulating mattresses specimens to assess biological resistance to attack by worms and insects: (**a**) in the presence of adult insects; (**b**) in the presence of larvae; (**c**) in the presence of insect eggs.

In terms of resistance to ground action (Figures 6 and 7), after keeping the specimens buried in soil for one month, there were already signs of degradation. Without showing the exact degradation at the level of the fibres, deposits of microorganisms, mould (Figure 6b,e–h), worm colonies, worm eggs (Figure 6a,c,d,g,h), etc., can be observed on the fibres, which leads to the hypothesis that this material is a favourable environment for the development of microorganisms and worms. After six months in the soil, signs of the degradation of the specimens are evident, as well as indications of the development of colonies of microorganisms (Figure 7a,b,e) and worms (Figure 7c–f); the presence of at least two types of moulds (green and black—Figure 7a,b,e), and the presence of at least two types of small organisms, worms (Figure 6e,f), their larvae and eggs (Figure 7c,d) are identified. These results, on the one hand, indicate the need to impose restrictions in terms of use so as not to come into direct contact with the soil, but, on the other hand, they represent the fact that, after the end of the products' life span, they become waste, which could be directed towards the realisation of composite matrices that, in combination with the soil and specific nutrient substrates, allow the development of substrates favourable to plant cultivation; a trend reported in the literature [57–62].

In terms of the measurable parameters evaluated, tensile strength and elongation at break (Figure 8), it can be observed that after one month of keeping the specimens buried in the soil, the tensile strength was little influenced, the loss of strength being at most 1 N/mm^2, which could indicate the maintenance of the thermo-welding effect, but the elongation at break was reduced by 7–30%, depending on the tested composite, which could indicate a degradation in the fibres, becoming more prone to breakage and having less elastic. After six months in the soil, the specimens were more strongly degraded, with measurable parameters indicating a reduction of at least 20% in tensile strength and elongation at break, which could be considered a sign of the degradation of both the degree of thermal welding between fibres and the integrity and performance of the fibres in the matrix of the thermal insulation material.

As can be seen in Figures 9 and 10, in humid conditions, when in contact with the composite thermal insulation mattresses, the Cu or galvanised metal elements undergo slight corrosion, manifested by the loss of gloss and the formation of a small quantity of corrosion products, which are easily removed by washing. It can therefore be said that, in terms of the migration of corrosive agents adjacent to the thermal insulation material towards these metal elements, bio-eco-innovative thermal insulation products do not provide corrosion protection, as atmospheric oxygen, water and other corrosive agents easily reach the metal surface, nor do they accelerate this process.
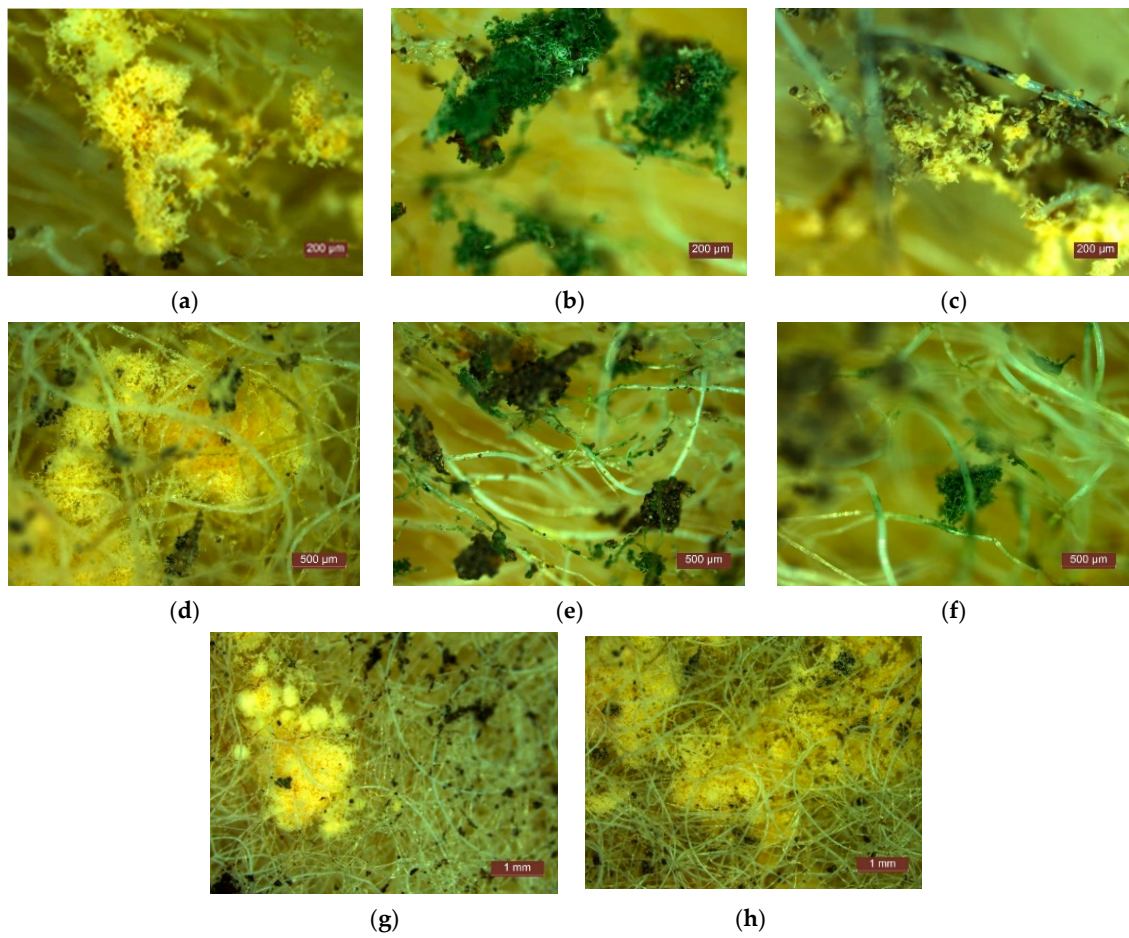
Figure 6. Instances regarding the microscopic analysis of test specimens by holding in soil for one month (**a**–**h**).
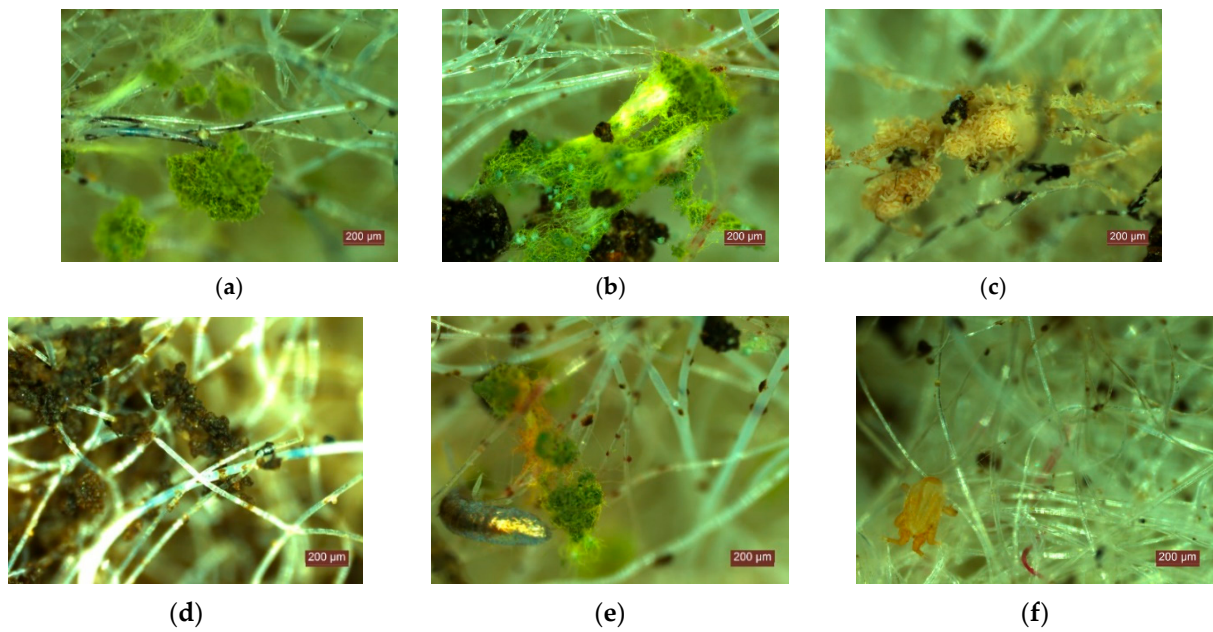
Figure 7. Instances regarding microscopic analysis of test specimens by holding in soil for six months (**a**–**f**).

(a)

(b)
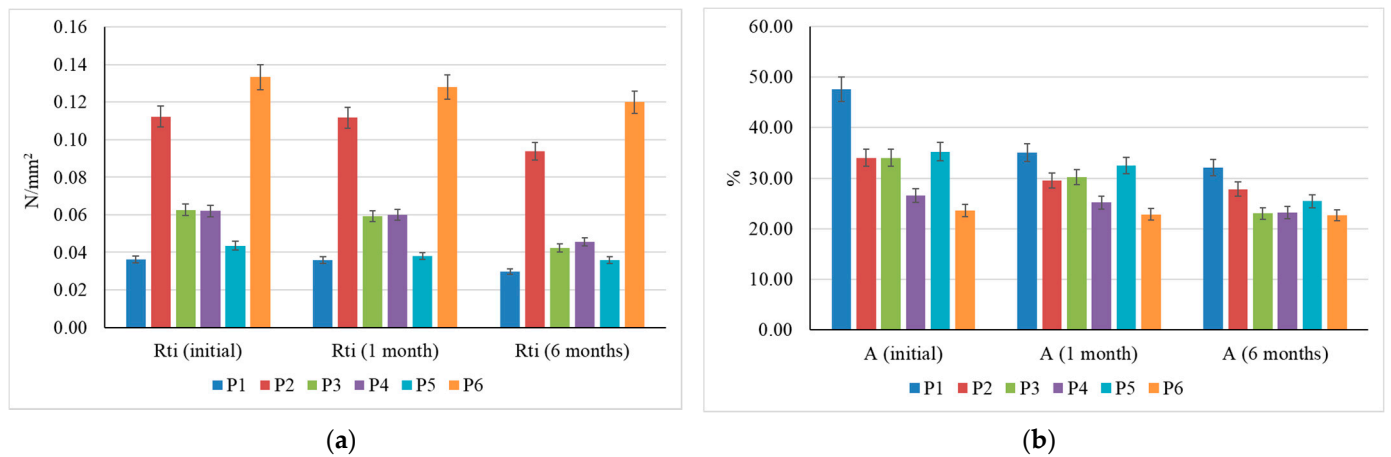
Figure 8. Variation in tensile strength (**a**) and elongation at break (**b**) after soil retention.

(a)

(b)

(c)
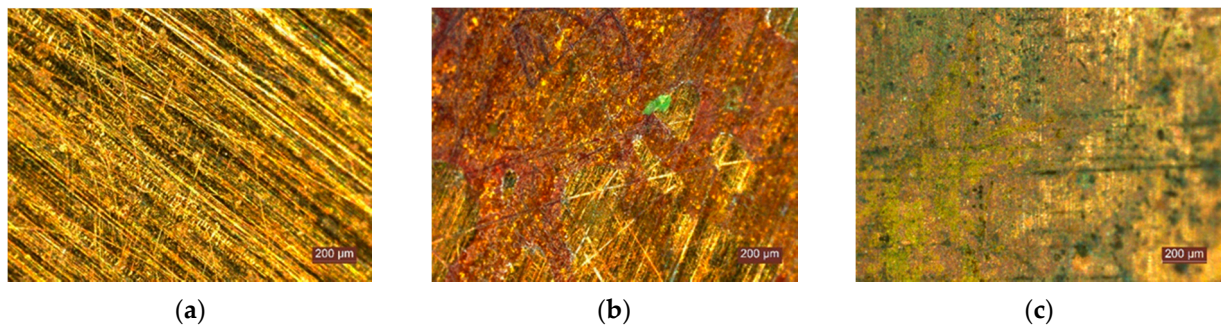
Figure 9. Evolution of the appearance of metallic Cu: (**a**) initial appearance of the metal specimen; (**b**) appearance of the metal specimen after testing; (**c**) appearance of the metal specimen after testing and washing of corrosion products.

(a)

(b)

(c)
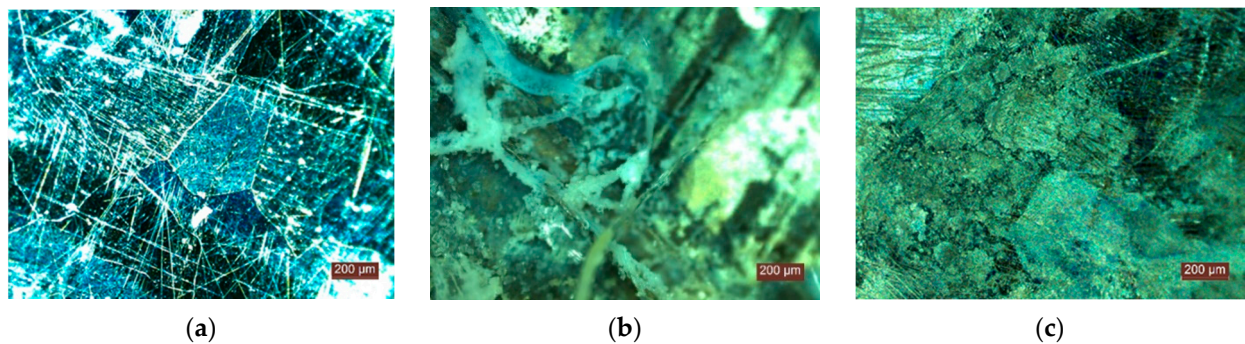
Figure 10. Evolution of the appearance of galvanised steel specimens: (**a**) initial appearance of the metal specimen; (**b**) appearance of the metal specimen after testing; (**c**) appearance of the metal specimen after testing and washing of corrosion products.

The formaldehyde neutralisation capacity (Figure 11) revealed the good ability of the composite thermal insulation matrix in terms of formaldehyde neutralisation. In the first 72 h after the start of the test, the composite matrix succeeded in neutralising a sufficient amount of formaldehyde, to reach, from a concentration in the zone of high risk, high discomfort, headaches, possible skin allergies, sickness and nausea, a zone of moderate risk concentration, and in the following hours this concentration zone is also exceeded, entering a zone of formaldehyde concentration in the air that does not pose a risk to the population. After neutralisation of the first dose of formaldehyde, the replenishment of the air with the chemical agent does not pose a problem for the test product to develop a new neutralisation reaction. In both cases, the neutralisation of formaldehyde

occurs at a high rate initially in the high concentration zone, and then decreases as the concentration of formaldehyde in the air decreases. It should be noted, however, that under normal conditions of use in the living space, it is rare that the formaldehyde concentration reaches concentrations similar to those at which the test started. These concentrations have been chosen precisely to evaluate the behaviour of the product under extreme conditions. It can therefore be said that the composite matrix obtained by recycling and reusing PET and PES waste, together with the use of natural vegetable fibres and sheep wool, successfully copes with and certainly contributes to improving indoor air quality, in fact maintaining the special character of sheep's wool, which, through its keratin structure, is the neutralising agent. Moreover, according to the literature, formaldehyde adsorbed by chemisorption mechanisms, inducing chemical, stable bonds, also has the advantage that it becomes, indirectly but effectively, a passive treatment to increase resistance to attack by microorganisms, insects and their larvae [31,37].
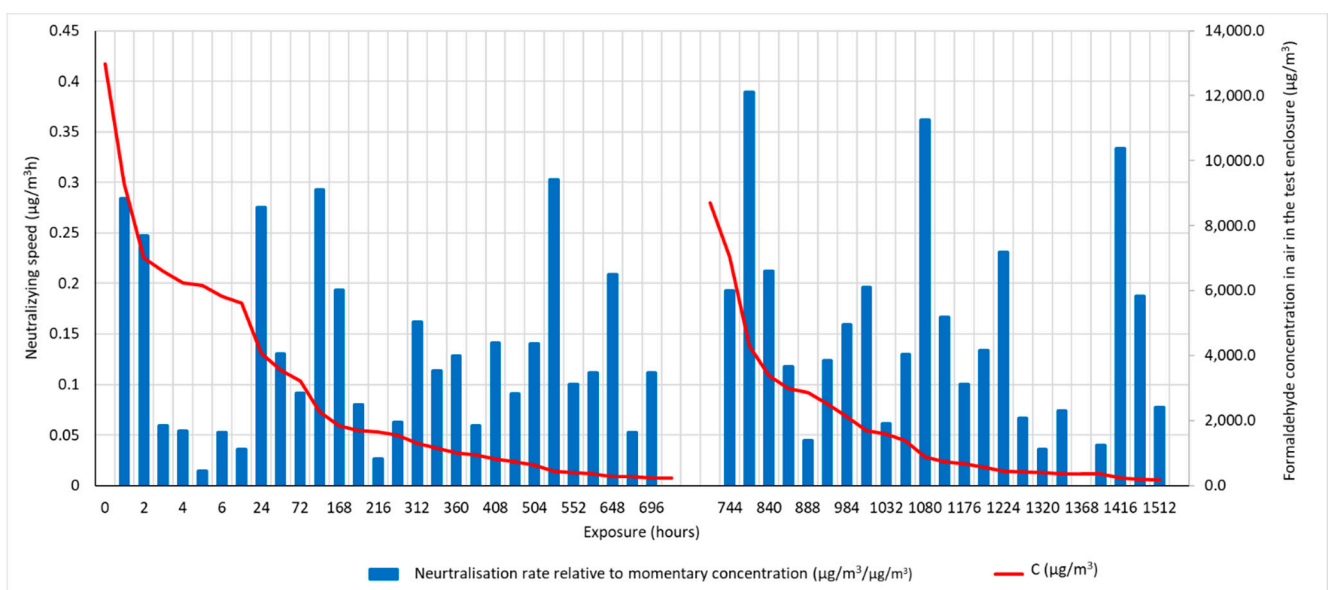
Figure 11. Variation over time in formaldehyde concentration in the air in the room where the heat-insulating mattress was placed and its neutralisation rate (neutralisation rate relative to the momentary concentration represents the amount of formaldehyde neutralised from time t of measurement to time t + 1 of measurement, relative to the formaldehyde concentration existing at time t).

Analysing this neutralisation rate in relation to the momentary concentration, and relating it to the time interval between two consecutive measurements, it can be seen that, as the concentration of formaldehyde in the indoor air decreases, the amount of formaldehyde neutralised per unit time decreases.

4. Conclusions

This work aimed to analyse the possibility and benefits of making composite products based on PET, recycled PES and natural fibres of plant and animal origin, of non-woven type (mattresses), intended for the thermal insulation of buildings, also highlighting the weaknesses, identified as possibilities for improvement through the development of future research.

By design, the analysed thermal insulation products identify clear possibilities to implement the guidelines of the Circular Economy concept, contributing both to waste recycling and to sustainable development through the use of components from renewable sources, with the final result of reducing energy consumption and increasing air quality in the living space.

Therefore, the originality of this work is a result of the approach to the topic of insulating products, combining the need to implement the principles of the Circular Economy

with existing knowledge to date, but limited to the development of alternative insulating products using one or two of the four raw materials used in this research. The article focuses on an original formula for a thermal-insulating product which incorporates 55% recycled materials (25% rPET and 30% rPES), 30% wool by-products or virgin wool with low-quality fibre impossible to use in the textile industry, and 15% siliconised cellulosic fibre. Additionally, in general, the literature is mainly concerned with the analysis of thermal performance and less with compatibility and the influence on indoor environmental quality and user health.

Although in terms of mechanical resistance, these products have low performance, requiring the imposition of limiting conditions of use (mounting in wooden frames, protection of exposed surfaces, protection from prolonged contact with water or soil), they have a number of other significant advantages compared with similar products made of a single type of fibre:

- The thermal insulation performance, evaluated by the two indicators, thermal conductivity coefficient and heat transfer resistance, indicates a good thermal insulation capacity, compared with some thermal insulation products currently used on the construction market and, therefore, a significant contribution to the reduction in energy consumption used to ensure thermal comfort. If the thickness is reduced by half, as a result of an impact load, for the same type of sample, a decrease in the heat transfer coefficient can be observed and therefore an increase in thermal insulation performance by 15.7% (P1), 14.2% (P2), 19.8% (P3), 13.8% (P4), 18.2% (P5) and 10.0% (P6);
- The water absorption, although having values that impose the need for protection in contact with water, is reduced to values up to 10 times lower than the values characteristic of sheep wool mattresses. It is estimated that the improvement of this parameter is due to the inclusion in the composite matrix of recycled PET and vegetable fibre components;
- The composite material retained the specific capacity of natural fibres to sorb/desorb atmospheric humidity, thus contributing to the improvement of air quality in the indoor space. Additionally, the component of animal origin, sheep wool, in the composite matrix, is sufficiently efficient also in terms of formaldehyde neutralisation capacity, thus making another significant contribution to improving indoor air quality;
- The evident water vapour permeability characteristic of the thermal insulation products analysed demonstrates, once again, their benefits in ensuring adequate indoor air quality, contributing significantly to ensuring the breathability of the walls and thus reducing the risk of moisture accumulation and mould growth;
- The recycled waste components, and probably the siliconised component of the fibrous matrix, significantly improved resistance to insect action. This improvement is particularly important as it is known that thermo-sheep wool mattresses are generally very sensitive to insect attack, especially moths;
- From the point of view of the corrosivity on metallic elements with which these products could come into contact, the experimental results obtained allow the assessment that the composite thermal insulation matrix does not contribute to provide corrosion protection, but neither does it accelerate the corrosion phenomenon;
- The reduced resistance to mould attack and contact with the soil, although they could be seen as disadvantages of these thermal insulation materials, are a challenge for the development of future research directions, but, above all, they can be seen as a first step towards the development of new possibilities for waste recycling by developing materials that can be successfully used in the agricultural field, such as growing substrate or protective material.

Therefore, based on the experimental results and in accordance with references in the literature, it can be said that thermal insulation mattresses made of recycled PET and PES fibres, natural plant fibres and sheep wool can be an alternative to commonly used thermal insulation products (expanded polystyrene, extruded polystyrene, mineral wool, etc.), and,

at the same time, can contribute to increasing the quality of life of the population by ensuring better indoor air quality.

Author Contributions: Conceptualisation, A.H., C.P. and C.B.; methodology, A.H., H.V., A.-V.L. and C.P.; validation, H.V. and C.P.; formal analysis, A.H., H.V., A.-V.L., C.P. and C.B.; investigation, A.H., A.-V.L. and C.P.; resources, H.V. and C.B.; data curation, A.H., H.V., A.-V.L., C.P. and C.B.; writing—original draft preparation, A.H.; writing—review and editing, A.H., H.V., A.-V.L., C.P. and C.B.; project administration, A.H.; funding acquisition, A.H., H.V. and C.B. All authors have read and agreed to the published version of the manuscript.

Institutional Review Board Statement: Not applicable.

Informed Consent Statement: Not applicable.

Data Availability Statement: The data presented in this study are available on request from the corresponding authors.

Conflicts of Interest: The authors declare no conflict of interest.

References

1. European Parliament. Directive 2010/31/EU of the European Parliament and of the Council of 19 May 2010 on the energy performance of buildings (recast/consolidated text). *Off. J. Eur. Union* **2010**, *153*, 13–35.
2. Zach, J.; Hroudová, J.; Brožovský, J.; Krejza, Z.; Gailius, A. Development of Thermal Insulating Materials on Natural Base for Thermal Insulation Systems. *Procedia Eng.* **2013**, *57*, 1288–1294. [CrossRef]
3. Ricciu, R.; Besalduch, L.A.; Galatioto, A.; Ciulla, G. Thermal characterization of insulating materials. *Renew. Sustain. Energy Rev.* **2018**, *82*, 1765–1773. [CrossRef]
4. Dodoo, A.; Gustavsson, L.; Sathre, R. Building energy-efficiency standards in a lifecycle primary energy perspective. *Energy Build.* **2011**, *43*, 1589–1597. [CrossRef]
5. IEA. Towards Net Zero Energy Solar Buildings. In *ECBCS/SHC Project Factsheet*; Energy Conservation in Buildings and Community Systems Programme; International Energy Agency: London, UK, 2011; pp. 1–15.
6. Csanády, D.; Fenyvesi, O.; Nagy, B. Heat Transfer in Straw-Based Thermal Insulating Materials. *Materials* **2021**, *14*, 4408. [CrossRef]
7. Maskell, D.; da Silva, C.F.; Mower, K.; Rana, C.; Dengel, A.; Ball, R.J.; Ansell, M.P.; Walker, P.J.; Shea, A. Properties of bio-based insulation materials and their potential impact on indoor air quality. *Am. J. Civ. Eng. AJCE* **2015**, *33*, 156–163.
8. Mølhave, L.; Clausen, G.; Berglund, B.; Ceaurriz, J.D.; Kettrup, A.; Lindvall, T.; Younes, M. Total volatile organic 348 compounds (TVOC) in indoor air quality investigations. *Indoor Air* **1997**, *7*, 225–240. [CrossRef]
9. Curling, S.F.; Loxton, C.; Ormondroyd, G.A. A Rapid Method for Investigating the Absorbtion of Formaldehyde from Air. *J. Mater. Sci.* **2012**, *47*, 3248–3251. [CrossRef]
10. Mansour, E.; Curling, S.; Stéphan, A.; Ormondroyd, G. Absorption of Volatile Organic Compounds by Different Wool Types. *Green Mater.* **2016**, *4*, 1–7. [CrossRef]
11. Mansour, E.; Loxton, C.; Elias, R.M.; Ormondroyd, G.A. Assessment of health implications related to processing and use of natural wool insulation products. *Environ. Int.* **2014**, *73*, 402–412. [CrossRef]
12. Stolwijk, J.A.J. Sick-building syndrome. *Environ. Health Perspect.* **1991**, *5*, 99–108. [CrossRef] [PubMed]
13. Mitchell, C.S.; Zhang, J.; Sigsgaard, T.; Jantunen, M.; Lioy, P.J.; Samson, R.; Karol, M.H. Current State of the Science: Health Effects and Indoor Environmental Quality. *Environ. Health Perspect.* **2007**, *115*, 958–964. [CrossRef] [PubMed]
14. Salthammer, T.; Mentese, S.; Marutzky, R. Formaldehyde in the Indoor Environment. *Chem. Rev.* **2010**, *110*, 2536–2572. [CrossRef] [PubMed]
15. Takeda, M.; Saijo, Y.; Yuasa, M.; Kanazawa, A.; Araki, A.; Kishi, R. Relationship between sick building syndrome and indoor environmental factors in newly built Japanese dwellings. *Int. Arch. Occup. Environ. Health* **2009**, *82*, 583–593. [CrossRef]
16. Ahlberg, J.; Georges, E.; Norlén, M. The Potential of Hemp Buildings in Different Climates. A Comparison between a Common Passive House and the Hempcrete Building System. Bachelor's Thesis, Uppsala University, Uppsala, Sweden, 2014.
17. Stevulova, N.; Cigasova, J.; Sicakova, A.; Junak, J. Lightweight Composites Based on Rapidly Renewable Natural Resource. *Chem. Eng. Trans.* **2013**, *35*, 589–594.
18. Vėjelienė, J.; Gailius, A.; Vėjelis, S.; Vaitkus, S.; Balčiūnas, G. Evaluation of Structure Influence on Thermal Conductivity of Thermal Insulating Materials from Renewable Resources. *Mater. Sci.* **2011**, *17*, 208–212. [CrossRef]
19. Kymalainen, H.R.; Sjoberg, A.M. Flax and Hemp FibreFibres as Raw Materials for Thermal Insulations. *Build. Environ.* **2008**, *43*, 1261–1269. [CrossRef]
20. Murphy, D.P.L.; Behring, H.; Wieland, H. The Use of Flax and Hemp Materials for Insulating. In Proceedings of the Flax and Other Bast Plants Symposium, Poznan, Poland, 30 September–1 October 1997; pp. 79–84.

21. Watt, I.C. Kinetic Study of the Wool-Water System: Part I: The Influence of Water Concentration. *Text. Res. J.* **1960**, *30*, 443–450. [CrossRef]
22. Hill, C.A.S.; Norton, A.; Newman, G. The water vapor sorption behavior of natural fibres. *J. Appl. Polym. Sci.* **2009**, *112*, 1524–1537. [CrossRef]
23. Gellert, R. Natural fibre and fibre composite materials for insulation in buildings. In *Materials for Energy Efficiency and Thermal Comfort in Buildings*; Hall, M.A., Ed.; Woodhead Publishing Series in Energy; Woodhead Publishing: Cambridge, UK, 2010; pp. 229–256.
24. Schiavoni, S.; Bianchi, F.; Asdrubali, F. Insulation materials for the building sector: A review and comparative analysis. *Renew. Sustain. Energy Rev.* **2016**, *62*, 988–1011. [CrossRef]
25. Zach, J.; Korjenic, A.; Petránek, V.; Hroudová, J.; Bednar, T. Performance evaluation and research of alternative thermal insulations based on sheep wool. *Energy Build.* **2012**, *49*, 246–253. [CrossRef]
26. Marques, F.M.; Salgado, M.S. The Building Material Selection. Importance at the Building Design; Process for Its Sustainability. In Proceedings of the CIB World Building Congress, Cape Town, South Africa, 14–17 May 2007; pp. 2384–2396.
27. Korjenic, A.; Klarić, S.; Hadžić, A.; Korjenic, S. Sheep Wool as a Construction Material for Energy Efficiency Improvement. *Energies* **2015**, *8*, 5765–5781. [CrossRef]
28. Wallbaum, H.; Ostermeyer, Y.; Salzer, C.; Escamilla, E.Z. Indicator based sustainability assessment tool for affordable housing construction technologies. *Ecol. Indic.* **2012**, *18*, 353–364. [CrossRef]
29. Patnaik, A.; Mvubu, M.; Muniyasamy, S.; Botha, A.; Anandjiwala, R.D. Thermal and sound insulation materials from waste wool and recycled polyester fibres and their biodegradation studies. *Energy Build.* **2015**, *92*, 161–169. [CrossRef]
30. Asdrubali, F.; D'Alessandro, F.; Schiavoni, S. A review of unconventional sustainable building insulation materials. *Sustain. Mater. Technol.* **2015**, *4*, 1–17. [CrossRef]
31. Bosia, D.; Savio, L.; Thiebat, F.; Patrucco, A.; Fantucci, S.; Piccablotto, G.; Marino, D. Sheep wool for sustainable architecture. *Energy Procedia* **2015**, *78*, 315–320. [CrossRef]
32. Ghosh, A.; Collie, S.R. Keratinous Materials as Novel Absorbent Systems for Toxic Pollutants. *Def. Sci. J.* **2014**, *64*, 209–221. [CrossRef]
33. Crawshaw, G.H. The role of wool carpets in controlling indoor air pollution. *J. Text. Inst.* **1978**, *16*, 12–15.
34. Cieślak, M.; Schmidt, H. Contamination of wool fibre exposed to environmental tobacco smoke. *Fibres Text. East. Eur.* **2004**, *12*, 81–83.
35. Jin, X.; Lu, L.; Wu, H.; Ke, Q.; Wang, H. Duck feather/nonwoven composite fabrics for removing metals present in textile dyeing effluents. *J. Eng. Fibres Fabr.* **2013**, *8*, 89–96. [CrossRef]
36. Hassan, M.M.; Davies-McConchie, J.F. Removal of arsenic and heavy metals from potable water by bauxsol immobilized onto wool fibres. *Ind. Eng. Chem. Res.* **2012**, *51*, 9634–9641. [CrossRef]
37. Ghanbarnejad, P.; Goli, A.; Bayat, B.; Barzkar, H.; Talaiekhozani, A.; Bagheri, M.; Alaee, S. Evaluation of Formaldehyde Adsorbtion by Human Hair and Sheep Wool in Industrial Wastewater with High Concentration. *J. Environ. Treat. Tech.* **2014**, *2*, 12–17.
38. Rajabinejad, H.; Bucişcanu, I.I.; Maier, S.S. Current Approaches for Raw Wool Waste Management and Unconventional Valorization: A Review. *Environ. Eng. Manag. J.* **2019**, *18*, 1439–1456.
39. Cardamone, J.M. Investigating the microstructure of keratin extracted from wool: Peptide sequence (MALDI-TOF/TOF) and protein conformation (FTIR). *J. Mol. Struct.* **2010**, *969*, 97–105. [CrossRef]
40. Cardamone, J.M.; Erazo-Majewicz, P.; Naouli, N. Composition and Methods for Treating a Keratin-Based Substrate. U.S. Patent 8747823, 10 June 2014.
41. European Parliament. Directive 2008/98/EC of the European Parliament and of the Council of 19 November 2008 on waste and repealing certain Directives (consolidated text). *Off. J. Eur. Union* **2008**, *312*, 3.
42. Sinha, V.; Patel, M.R.; Patel, J.V. Pet Waste Management by Chemical Recycling: A Review. *J. Polym. Environ.* **2010**, *18*, 8–25. [CrossRef]
43. Bartolome, L.; Imran, M.; Bong, G.C.; Al-Masry, W.A.; Kim, D.H. *Recent Developments in the Chemical Recycling of PET*; InTech Open: London, UK, 2019; pp. 65–84.
44. Lin, C.C. Recycling Technology of Polyethy1ene Terephthalate Materials. *Macromol. Symp.* **1998**, *135*, 129–135. [CrossRef]
45. Achilias, D.S.; Karayannidis, G.P. The chemical recycling of PET in the framework of sustainabile development. *Water Air Soil Pollut.* **2004**, *4*, 385–396. [CrossRef]
46. Santos, P.; Pezzin, S.H. Mechanical properties of polypropylene reinforced with recycled-pet fibrefibres. *J. Mater. Process. Technol.* **2003**, *143*, 517–520. [CrossRef]
47. Candal, M.V.; Safari, M.; Fernández, M.; Otaegi, I.; Múgica, A.; Zubitur, M.; Müller, A.J. Structure and Properties of Reactively Extruded Opaque Post-Consumer Recycled PET. *Polymers* **2021**, *13*, 3531. [CrossRef]
48. Zeinab, S.; Abdel-Rehim, Z.S.; Saad, M.M.; El-Shakankery, M.; Hanafy, I. Textile fabrics as thermal insulators. *Autex Res. J.* **2016**, *6*, 148–161.
49. Jirsak, O. Thermo-Insulating Properties of Perpendicular-Laid versus Cross-Laid Lofty Nonwoven Fabrics. *Text. Res. J.* **2000**, *20*, 121–128. [CrossRef]
50. Morris, G.J. Thermal Properties of Textile Materials. *Text. Inst. J.* **1953**, *44*, 449–476. [CrossRef]
51. Sukigara, S.; Yokura, H.; Fujimoto, T. Compression and Thermal Properties of Recycled Fibre Assemblies Made from Industrial Waste of Seawater Products. *Text. Res. J.* **2003**, *73*, 310–315. [CrossRef]
52. Drochytka, R.; Dvorakova, M.; Hodn, J. Performance Evaluation and Research of Alternative Thermal Insulation Based on Waste Poliester Fibres. *Procedia Eng.* **2017**, *195*, 236–243. [CrossRef]
53. Briga-Sá, A.; Nascimento, D.; Teixeira, N.; Pinto, J.; Caldeira, F.; Varum, H.; Paiva, A. Textile waste as an alternative thermal insulation building material solution. *Constr. Build. Mater.* **2013**, *38*, 155–160. [CrossRef]

54. Dissanayake, D.G.K.; Weerasinghe, D.U.; Wijesinghe, K.A.P.; Kalpage, K.M.D.M.P. Developing a compression moulded thermal insulation panel using postindustrial textile waste. *J. Waste Manag.* **2018**, *79*, 356–361. [CrossRef]

55. Danihelová, A.; Nemec, M.; Gergel, T.; Gejdoš, M.; Scensný, G.J. Usage of Recycled Technical Textiles as Thermal Insulation and an Acoustic Absorber. *Sustainability* **2019**, *11*, 2968. [CrossRef]

56. Hadded, A.; Benltoufa, S.; Fayala, F.J. Thermo physical characterisation of recycled textile materials used for building insulating. *J. Build. Eng.* **2016**, *5*, 34–40. [CrossRef]

57. Butcaru, A.C.; Stănică, F.; Dobrin, A. Some results on nutritional properties of organic rose petals and related processed products. *Sci. Pap. Ser. B Hortic.* **2018**, *63*, 197–202.

58. Matei, G.M.; Dumitru, S.; Matei, S.; Butcaru, A.C.; Stănică, F. Microbiological aspects in soil microbiome composition and activity under the influence of organic mulches. In Proceedings of the 17th International Multidisciplinary Scientific GeoConference SGEM, Albena, Bulgaria, 29 June–5 July 2017; Volume 17, pp. 813–820.

59. Butcaru, A.C.; Stănică, F.; Matei, G.M.; Matei, S. Alternative methods to improve soil activity before planting an organic edible rose crop. *J. Hortic. Sci. Biotechnol.* **2016**, *20*, 12–17.

60. Mosnegutu, E.F.; Panaite-Lehăduș, M.; Nedeff, F.; Irimia, O.T.; Tomozei, C. Waste management evaluation in the context of sustainable develompment. Case study Vasile Alecsandri University of Bacau. *Int. J. Conserv. Sci. IJCS* **2020**, *11*, 179–188.

61. Rydzewski, P. Between environmental protection and technology: Europeans' ecological attitudes. *Int. J. Conserv. Sci. IJCS* **2020**, *12*, 781–792.

62. Malec, A.; Garbacz, M.; Klimek, B.; Guz, L.; Golianek, P.; Suchorab, Z. Damages caused by microorganisms in historical buildings on the example of a multi-family residential building. *Int. J. Conserv. Sci. IJCS* **2020**, *12*, 805–816.

Improving Indoor Air Quality by Using Sheep Wool Thermal Insulation

Andreea Hegyi [1], Cezar Bulacu [2], Henriette Szilagyi [1], Adrian-Victor Lăzărescu [1,*], Vasile Meiţă [3], Petrică Vizureanu [4,*] and Mihaela Sandu [3]

1. NIRD URBAN-INCERC Cluj-Napoca Branch, 117 Calea Floreşti, 400524 Cluj-Napoca, Romania; andreea.hegyi@incerc-cluj.ro (A.H.); henriette.szilagyi@incerc-cluj.ro (H.S.)
2. MINET S.A., 12 Depozitelor Street, 240426 Râmnicu Vâlcea, Romania; cezar.bulacu@minet.ro
3. NIRD URBAN-INCERC Bucharest, 266 Şoseaua Pantelimon, 021652 Bucharest, Romania; vasile.meita@gmail.com (V.M.); msandu1970@yahoo.com (M.S.)
4. Faculty of Material Science and Engineering, Gheorghe Asachi Technical University of Iaşi, 41 D. Mangeron St., 700050 Iasi, Romania
* Correspondence: adrian.lazarescu@incerc-cluj.ro (A.-V.L.); peviz2002@yahoo.com (P.V.)

Abstract: Currently, the need to ensure adequate quality of air inside the living space but also the thermal efficiency of buildings is pressing. This paper presents the capacity of sheep wool heat-insulating mattresses to simultaneously provide these needs, cumulatively analyzing efficiency indicators for thermal insulation and indicators of improving air quality. Thus, the values obtained for the coefficient of thermal conductivity, and its resistance to heat transfer, demonstrate the suitability of their use for thermal insulation. The results of the permeability to water vapor characteristics on the sorption/desorption of water, air, demonstrate the ability to control the humidity of the indoor air and the results on the reduction of the concentration of formaldehyde, demonstrating their contribution to the growth of the quality of the air, and to reduce the risk of disease in the population.

Keywords: sheep wool thermal-insulating mattresses; air quality; water vapor permeability; formaldehyde

1. Introduction

Currently, the population living in developed countries spends about 87% of their time inside buildings [1–3]. In this context, huge amounts of fuels (wood, oil, coal, natural gas, burned to produce heat during cold weather, or, for the production of electricity used by heating appliances during cold weather or cooling during hot weather) are used worldwide, together with considerable greenhouse gas emissions, to ensure indoor thermal comfort. At the European level, 55–67% of total energy consumption is dedicated to ensure indoor comfort in living spaces, office buildings, or commercial spaces [1,4,5]. According to the communication from the Commission of the European Parliament, the Council, the European Economic and Social Committee, and the Committee of the Regions, COM/2016/051, heating and cooling is the largest energy sector in the EU where 75% of the required energy is provided from fossil fuels and only 18% from renewable sources. In 2012, the report indicated that, 45% of EU heating and cooling energy is used in the residential sector, 37% in industry, and 18% in the service sector, with space heating accounting for more than 80% of energy consumption in colder climates. According to this report, in order to meet heating needs, almost half of EU buildings have individual boilers installed before 1992, with an efficiency of 60% or less. Moreover, at the EU level, the 2016 reporting shows that 22% of individual gas boilers, 34% of electric direct heating appliances, 47% of fuel-oil boilers, and 58% of coal-fired boilers exceeded their technical life, implying low efficiency and high pollutant emissions [6]. Therefore, the current trend is to reduce fuel consumption, to reduce greenhouse emissions, and to ensure the

thermal efficiency of buildings through the use of high-performance insulating materials and systems. However, a thermal-insulating "sealing" which only takes into account the total heat transfer is not desirable because a low rate of ventilation will significantly reduce the quality of the air inside [4,7,8] due to the accumulation of moisture, volatile organic compounds gases—one of which, the most dangerous, classified as a 1B carcinogen is formaldehyde [2,9–11], allergens, gases, radioactive materials (radon gas), pollutant, inorganic, resulting in a decrease in the quality of life and even make people ill. The sources of these emissions are diverse, some acting continuously, others intermittently or occasionally: food preparation activities (cooking), personal hygiene activities of the population, sanitation of space or things for personal use (e.g., washing clothes, cleaning surfaces with chemicals or their maintenance by lacquering, periodic waxing), smoking, the purchase of new products (emissions of organic compounds of a new element of furniture, for example), even harmless activities intended for relaxation (perfuming space, burning fragrant sticks) and, last but not least, radon emissions from the soil (radon being a gas with a lower density than air, will climb through each crack of the construction, accumulating in ventilated rooms rarely). Moreover, the degradation of an indicator of indoor air quality can induce the degradation of other indicators, for example, the excessive increase in humidity will become a catalyst for the development of microorganisms, which will determine the need for sanitization of the space by chemical treatment of the affected surfaces in order to remove the biological film (treatment carried out with chemicals, biocides), which will bring into the interior a new amount of emissions of volatile organic compounds. The World Health Organization [4,12,13] argues that it is impossible to eliminate all exposure to these pollutants, but sets the risk limits [4,14] in relation to the concentration of the emission of volatile organic compounds expressed as total volatile organic compounds (TVOC) (Table 1). Accordingly, at the European level, two directives limit emissions of volatile organic compounds, as follows: the Solvent Emissions Directive (SED) 1999/13/EC (fully implemented since 2007) and the Products Directive (PD or DECO) 2004/42/EC (which introduces VOC limits for 2010 that relate to specific products and materials (such as paints) containing VOCs).

Table 1. Impact of TVOC [4,14].

TVOC ($\mu g/m^3$)	Health Impact
<200	No irritation or discomfort expected
200–3000	Irritation and discomfort may be possible
3000–25,000	Discomfort expected and headache possible
>25,000	Toxic range where other neurotoxic effects may occur

The symptoms of irritation, discomfort, and physical illness such as headaches, irritation of the eyes, diseases of the respiratory system, allergic reactions, and disorders of the skin, insomnia, difficulty in concentrating, fatigue, and illness, more severe, possibly fatal [4], which may occur not only because of the high concentrations of TVOC in the indoor air, but also to the high content of moisture which can cause mold and mildew whose spores in the air are just as dangerous. These symptoms are currently associated with the "sick building syndrome" [15–20]. Therefore, it is necessary and important that, from the point of view of the impact on human health as a result of indoor air quality, at the execution of thermal insulation works, at least three more factors should be analyzed in addition to the thermal performance: water vapor permeability, water adsorption, and the contribution of the thermal-insulating material to the TVOC concentration.

One of the possibilities of achieving a proper thermal insulation without affecting the indoor air quality can be achieved by the use of natural thermal-insulating materials. Therefore, the production of sheep wool thermal-insulation products has a substantial potential as a result of its numerous advantages: it is an abundant renewable raw material resource, it is made from the waste of the wool that cannot be used in the textile industry, the technology of the embodiment is relatively simple and less polluting, the costs of producing

and commissioning work are reduced, presents high durability, low flammability, all of the performances needed for a good thermal insulation material [21–26]. In terms of the availability of raw material resources, research carried out at the Politecnico di Torino, Department of Architecture and Design [27–29] indicated some aspects of the production and processing of sheep products in the Piedmont Region, Italy, which are similar to the situation in Romania. Thus, sheep farms are populated with milk and meat-producing breeds and less with breeds recognized for the fineness of the wool thread. Moreover, for use in the textile industry, the wool is selected and the categories with thick or semi-thick yarn being extremely low in demand, are stored in improper conditions, discarded or burned, thus having a strong pollutant impact. According to the data presented by the National Institute of Statistics, Romania is the fourth country in the EU in terms of the number of sheep and goats and the fourth/fifth place in terms of the number of sheep and goats/100 ha of land, and each sheep shearing operation generates about 2–2.5 kg of wool/sheep's head, wool that is not taken by the textile industry, becomes polluting waste. According to the United States Department of Agriculture (USDA) Sheep and Lambs Inventory, in 2011, there were 5.5 million sheep in the US [30], statistics indicating an abundance of animals at the level of many areas throughout the planet. As a rule, these thermal-insulating mattresses are placed on the surfaces of walls, ceilings, etc., inside the rooms, in wooden frames mounted on the wall surface, and intended to support the thermal-insulating material, due to the need for protection from the action of water, known as the high-water absorption that wool has in general, and the need to ensure the conditions of keeping the shape and dimensions, since they are non-woven products. This location, however, has substantial advantages over the air quality inside the rooms.

Due to the genetic structure, sheep wool yarn has certain peculiarities. It has a natural protein structure, being represented by cuticles whose surface is hydrophobic due to the presence of organic saturated fat, covalently bound to the protein substrate and hydrophilic cortex [21,31] and the medullary canal. Overlapping the cuticles on top of each other determines the roughness and toughness of the thread [21]. The cortex is composed of elongated cells, containing more than 93% by mass, keratin [21,32,33] containing 18 α-amino acids, mainly cysteine, they are responsible for the specific characteristics—gloss, own corrugation, insolubility in water, high resistance to chemicals, low biodegradability, high mechanical strength. The medullary canal is responsible for the characteristic of general hygroscopicity of the wool thread, being known that it absorbs 15–18% of the mass water vapor under normal conditions (20 ± 5 °C, 50–65% RH), but can reach up to 40% under saturated atmosphere conditions (100% RH), absorption that occurs through the expansion of the medullary canal, the diameter of the thread can increase by up to 18% and its length by 1% [21]. According to Downes and Mackay [34], sorption and desorption of moisture under the influence of relative humidity is one of the fundamental properties of wool fibers. Research has shown that, in general, the vapor transfer inside thermal-insulating materials and not only, is influenced by the phenomenon of sorption and the specific resistance to the flow of water vapor, so for two products with equal densities, the water vapor resistance factor, µ, can be much different. On the other hand, it is shown that the action of acidic or basic substances reduces the resistance and increases the castability of the thread, and the increase in temperature and humidity causes the elongation of the wool thread breakage (from 30% for dry thread to 70% for wet thread) because, in accordance with research reported since the 1960s [35–37], in the presence of water, a molecular reorganization of the thread. This phenomenon is also supported by other research reported in the literature [38,39], which shows that under conditions of relative humidity of 100%, the wool thread undergoes a process of swelling of 40% on the transverse direction and 1% on the longitudinal direction, with the water molecules entering the protein structure of the thread breaking some protein bonds. The same research indicated that the kinetics of water adsorption on the wool yarn is influenced by the diameter of the yarn, the amount of water adsorbed being inversely proportional to its thickness [39]. Consequently, it can be said that sheep wool is an "smart material",

with a behavior that adapts according to external conditions: it has the ability to absorb water in conditions of high humidity and give it away in conditions of low humidity, thus regulating the humidity of the environment. The behavior of sheep wool in the presence of volatile organic compounds, especially formaldehyde, can be considered a second reason why it can be called a "smart material". Inside buildings, there are many materials that can emit VOCs, from finishing materials such as paints and varnishes, to treated and processed wood-based composite materials for furniture and finishes, and to elements made of plastics, each of these materials, by their own emissions, variable according to their nature, the time elapsed from installation/use (for example, in the case of a paint, VOC emissions are very high at application, during drying and immediately after drying, decreasing over time), contributing to the accumulation of the VOC (levels indicated in Table 1). Research conducted to date has shown the ability of the wool to adsorb formaldehyde [15,40–46] and, accordingly, reduce the level of formaldehyde in the inhaled air. This research also showed that the maximum adsorption is achieved at the surrounding temperature of 20 °C, the temperature normally encountered in the living space, and the formaldehyde is absorbed by the wool fibers in one of two ways: physisorption, in which case it is adsorbed in the micropores of the structure of the fibers, and the chemosorbtion, when the formaldehyde forms a chemical bond of stable chains on the side of the amino acids lysine and arginine, and with the groups that the amide of glutamine and asparagine [15] in a chemical reaction, resulting in a pattern (Figure 1). These stable chemical bonds formed will definitely contribute to reducing the concentration of formaldehyde in indoor air. Moreover, the specific character of the formaldehyde thread, which has a keratin structure, allows the chemical binding of a large amount of formaldehyde. Compared to human hair, research has shown that sheep wool has a higher rate of formaldehyde adsorption, thus becoming a "protector" of the population [47]. Studies carried out on the adsorption of formaldehyde, both on strands of hair and sheep wool, have pointed to the fact that, after the binding of formaldehyde to the keratin, the reaction was carried out at the level of the amino group to formaldehyde, which results in the formation of an aminomethylol itself, the process proceeds to a chain reaction that leads to the formation of a solid connection with the methylene bridge, and the release of a molecule of water. To date, no reports have been identified in the literature, indicating the attainment of a degree of formaldehyde saturation of mattress products made of sheep wool. This ability of sheep wool is considered particularly important, especially given that 2–5% of cancer cases reported in the US are attributed to the continuous and prolonged exposure of the population to formaldehyde present in the living environment, schools, offices, or commercial spaces. For extreme situations of high formaldehyde concentration, it is estimated that the risk of cancer increases from 42 cases/million people for a concentration of 10 µg/m^3, to 252 cases/million people for a concentration of 60 µg/m^3 [48].
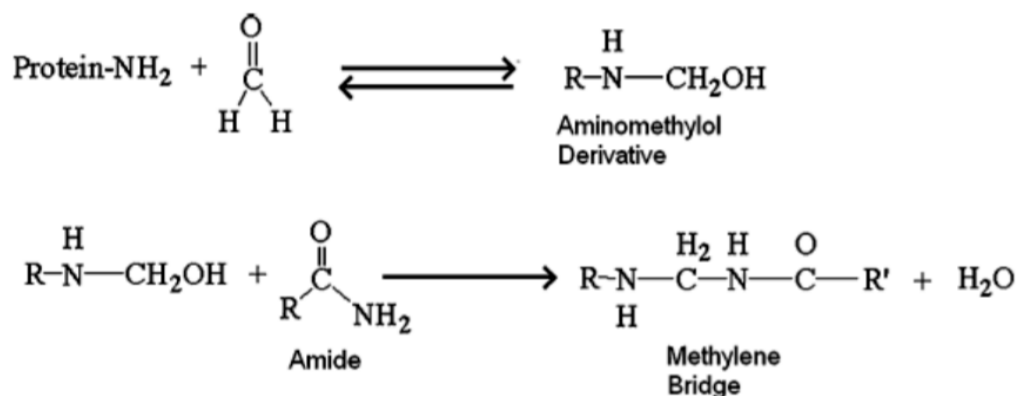
Figure 1. General reaction involving chemisorption of formaldehyde on the wool thread.

Some studies have shown that wool spontaneously absorbs VOCs in the atmosphere, and thus, it was reported that a capacity reduction of more than 89% of the total concentration of formaldehyde in 3 days after exposure to conditions of 20 °C and 65% RH [49], or the placing of a sample in 150 g of wool into a chamber with a volume of 0.158 m^3, in which the formaldehyde concentration is 20 ppm, and resulted in the full absorption of the latter within 4 h and, by increasing the formaldehyde concentration to 400 ppm, and in the same condition it was involved in a 35-min drive [50,51].

Moreover, keratin in the wool thread behaves amphoterically, depending on the pH of the medium: at a basic pH, keratin determines an affinity of the thread for negative ions, and at a lower pH, it will determine an affinity of the thread for positive ions [21,52]. This behavior is essential for interaction with the environment, even with pollutants such as oxides, heavy metals, etc. [49]. Thus, some research has shown that under conditions of 2.32 ppm concentration of sulfur dioxide, its absorption capacity by the wool was initially 0.012 mg/gram wool/minute, reaching 0.003 mg/gram wool/minute after 60 min of exposure [50,53]. Research in this direction has been carried out including on the adsorption of toxic products from cigarette smoke, showing the capacity of 40 mg of cigarette smoke/gram of wool [50,54]. Other research has indicated the ability to reduce the concentration of Cu_2+ by 41% in 1 h, and by 34–53% As_3+ in 1 h, respectively [55,56].

From the point of view of the intended use and way to produce, in the case of non-woven thermal insulation products, mattresses made of sheep wool, there are both advantages and disadvantages compared to classic thermal insulation products, in particular when comparing to expanded or extruded polystyrene. Thus, classic thermal insulation products are intended for placement, especially on the outside of buildings, on the one hand from the desire not to reduce the internal volume of the rooms, and on the other hand because by design, they significantly reduce the water vapor permeability of the wall. Located indoors will substantially contribute to increasing the humidity of indoor air and, accordingly, increase the likelihood of the development of microorganisms. However, there are situations in which thermal insulation on the outside is not only not the best solution and may even be unfeasible (the case of historical buildings where it is forbidden to modify their exterior appearance) or impossible (constructions with buried walls, not accessible for thermal insulation works). Moreover, the placement inside of thermal insulation materials of the classical type, polystyrene in particular, not only does not allow good ventilation of the walls, but also significantly contributes to the degradation of indoor air quality by the emissions of harmful substances that characterize them. Therefore, the use of a natural thermal insulation sheep wool mattress will cause a small reduction in space, but will also bring major benefits, starting with a feasible thermal insulation solution, up to a significant contribution to air quality (humidity regulation, the possibility of preserving the permeability of the walls, etc.). The reduction of space by thermal insulation inside is a result of the fact that this type of product is placed in wooden frames equal to the thickness of the mattress used, over which sheets of gypsum board or wooden slats are applied. Thus, the resulting surface will be smooth, with sufficient mechanical strength for the application of finishes and for current uses. Therefore, the operation of thermal insulation indoors using mattresses made of sheep wool brings more benefits compared to its main drawback, that of reducing the inner volume of space.

The aim of this paper is to analyze the adsorption processes of water vapor and formaldehyde in the air, simultaneously with the evaluation from the point of view of water vapor permeability of four sheep wool thermal-insulating mattress of Romanian origin. This work will thus contribute to the increase of knowledge in the field of bio-insulating materials used in the construction industry; a sector that is still insufficiently documented. It is therefore considered that it will contribute to the development of this still under-exploited area, to increase the possibilities of using sheep wool that is unproperly used in the textile industry to produce new materials and also to increase the confidence of users.

2. Materials and Methods

2.1. Materials

Four types of products, non-woven type sheep wool mattresses, intended for use as thermal-insulating material in construction, produced within the framework of an experimental research project by MINET SA Râmnicu Vâlcea, Romania, were analyzed. Those were produced by thermal-sealing carding technology of a mixture of 90% sheep wool yarn (thickness between 0.020–0.040 mm) and 10% BICO polymer fibers, characterized by nominal density, thickness, and average real thickness (average result of 10 measurements) according to Table 2. Those were also analyzed microscopically in order to inspect their appearance (Figure 2). For an easier analysis, thermal-insulating mattresses with similar density, within the limits of 30–35 kg/m^3, were chosen.

Table 2. Characterization of non-woven type sheep wool thermal-insulating mattresses.

Type	A	B	C	D
Density (kg/m^3)	33.6	34.8	30.8	32.4
Nominal Thickness (mm)	15 ± 10%	25 ± 10%	45 ± 10%	40 ± 10%
Average Real Thickness (mm)	15.6	23.4	44.0	42.2
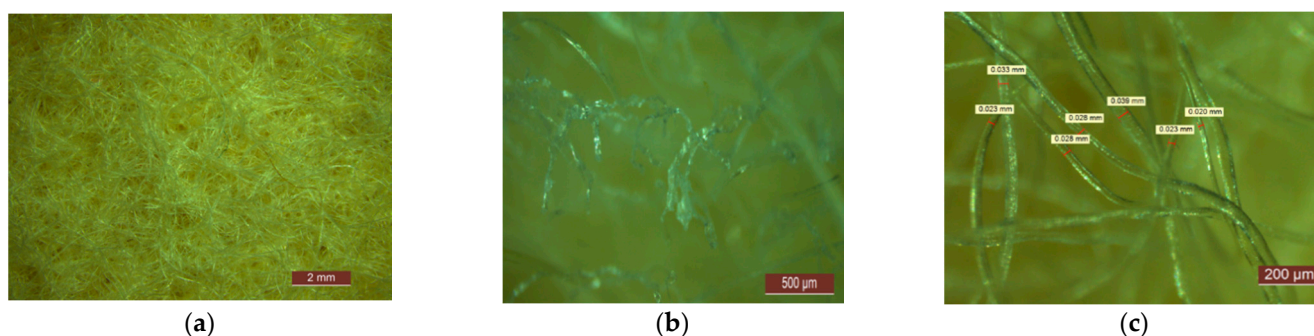
Figure 2. Microscopic analysis of sheep wool thermal-insulating mattresses: (**a**) 1×-overview; (**b**) 5×-identification of the thermal-sealing area; (**c**) 8×-analysis of the thickness of the wool thread.

2.2. Thermal Insulation Efficiency

For the characterization of products from the point of view of thermal insulation efficiency, the coefficient of thermal conductivity, $\lambda_{10,\,ct.}$ was determined (W/mK) and thermal transfer resistance, R (m^2 K/W) by means of a Fox 314 conductivity meter, by the hot plate method, at a temperature difference between turntables of 10 °C, according to EN 12667:2002, using specimens of the size 300 × 300 mm^2, at their natural thickness, after being dried at constant mass in a ventilated oven, the results are presented as the arithmetic mean of five individual measurements for each type of product.

2.3. Analysis of the Interaction Phenomenon between Sheep Wool Mattresses and Humidity

Water vapor permeability was quantified by water vapor transmission rate, G (mg/m^2 h), water vapor resistance, Z (m^2 h Pa/mg), and by water vapor resistance factor, μ, were calculated according to Equations (1)–(3), where G is the flow of moisture crossing the sample in the time interval Δt, A is the exposed area of the sample, Δp is the atmospheric pressure, δair is the vapor permeability of the air, and d is the thickness of the sample. The tests were performed under laboratory conditions, 65 ± 5% RH and 23 ± 1 °C, using the wet cup method.

$$g = G/A \ (mg/m^2h), \tag{1}$$

$$Z = (A \times \Delta p)/G \ (m^2 hPa/mg), \tag{2}$$

$$\mu = (\delta air \times Z)/d. \tag{3}$$

The sorption/desorption capacity of water vapor was quantified by drawing the characteristic curves, by the variation of the sample mass, according to the relative humidity of the air, for 30%, 45%, 60%, 80%, and 95% RH. To stabilize the parameters being followed, the samples were maintained at each RH value for 7 days, after which they were weighed. To ensure repeatability conditions, five determinations were made for each test.

Due to the technology of production of the products, knowing the higher probability of a slight variation in performance, as a result of the specific inhomogeneous structure of the products, it was considered useful to calculate a quadratic mean deviation, as a consequence of a measurement uncertainty, for each set of measurements, the test being conclusively considered if the calculated measurement uncertainty was less than 10% of the average value of the analyzed data.

2.4. Influence on Formaldehyde Concentration

The sorption/reduction capacity of formaldehyde was finally analyzed, according to ISO 16000-3, for the product that achieved the best performance of those previously presented. The working parameters of the test chamber that complied with the conditions according to EN 16000-9 and EN 16516, are presented in Table 3. The specimen used, with dimensions of 300×300 mm^2 (Figure 3), was covered on the lower face and edges with aluminum foil so that the transfer of formaldehyde was carried out only by the exposed upper face. The testing was carried out over 7 days and the atmospheric concentration of formaldehyde was recorded (day 1, 3, and 7).

Table 3. Formaldehyde absorption test parameters.

Parameter	Chamber Volume, V (l)	Air Change Rate, n (h^{-1})	Relative Humidity of Supply Air, RH (%)	Temperature of Supply Air, T (°C)	Average Formaldehyde Injection (µg/m^3)	Area Specific Ventilation Rate, q (m^3/m^2/h)
Value	119	0.5	50 ± 3	23 ± 1	100 ± 20	0.36

Figure 3. Sheep wool mattress sample.

Before loading the test chamber, the indoor air was cleaned and checked according to EN 16,516 and ISO 16000-9. During the test, an artificial atmosphere containing a known concentration of formaldehyde was continuously injected into the test chamber to create the basis for the investigation of the reductive properties of the test product, according to Table 3. The presence of aldehydes was tested by air sampling through DNPH-coated silica gel tubes positioned in the exit area of the test chamber after each specified exposure period. The analysis was carried out using an HPLC detector with UV diodes. The absence

of formaldehyde and other aldehydes is indicated if the detector's response to the specific UV wavelength is missing from the chromatogram. The presence and quantification of formaldehyde in the analyzed atmosphere was achieved by comparing specific UV spectra with standard UV spectra.

Formaldehyde consumption, FC (%), was calculated with Equation (4) and sorption flux, F ($\mu g/m^2 \cdot h$), was calculated with Equation (5), where C_{in} = inlet concentration, $\mu g/m^3$; C_{out} = chamber concentration, $\mu g/m^3$; Q_c = air flow of chamber = 0.06 m^3/h and A = area of the test specimen.

$$FC = (C_{in} - C_{out})/C_{in} \times 100 \ (\%), \tag{4}$$

$$F = [(C_{in} - C_{out}) \times Q_c]/A \ (\mu g/m^2 h). \tag{5}$$

3. Results and Discussion

First of all, in line with the existing literature [1,25,57–59], it can be seen the suitability of this material for thermal insulation and the difference between the quantifiable parameters of performance of the thermal insulation: the coefficient of thermal conductivity, λ, is a factor of the material, depending on its density, as the resistance to heat transfer, R, is an indicator of the product, depending on both the specifics of the material and the thickness of the product (Figure 4). It can be said that in the case of tested materials, the coefficient of thermal conductivity, λ, increases with increasing density, and the heat transfer resistance, R, increases with increasing thickness of the product. It can easily be seen that a higher density product does not necessarily provide a lower heat transfer if it does not satisfy a corresponding thickness, so to obtain a high-performance thermal-insulating product, it is necessary to establish an optimal density–thickness balance.

(a)

(b)
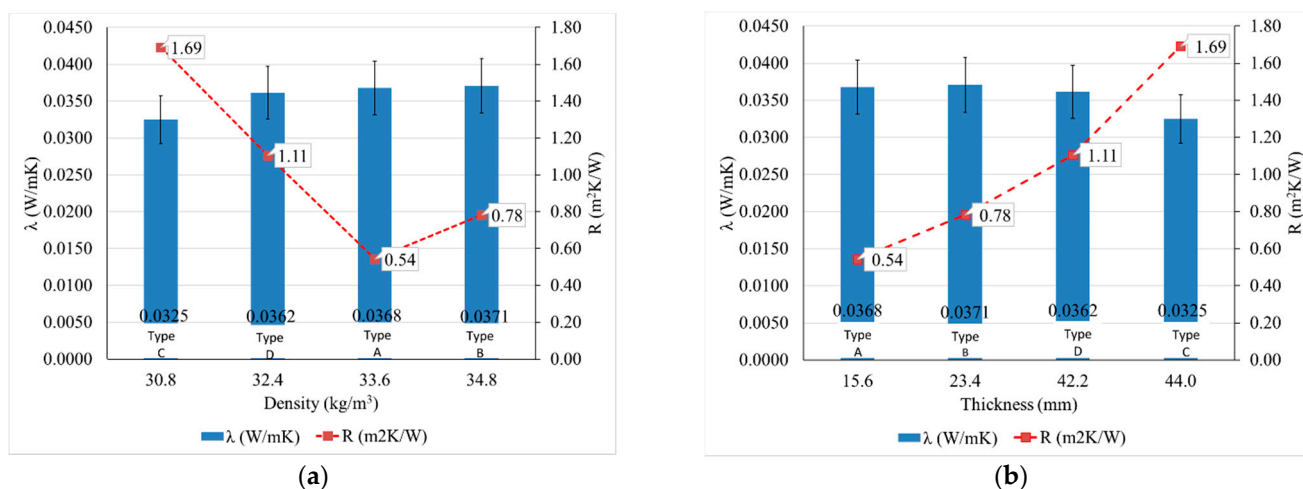
Figure 4. Analysis of thermal insulation performance of thermal insulation sheep wool mattresses: (**a**) influence of material density; (**b**) influence of the thickness of the thermal-insulating mattress (Types A, B, C, D defined according to Table 2).

Water vapor permeability performance was analyzed according to the thickness of the thermal-insulating mattresses and in conjunction with the thermal insulation performance quantified as heat transfer resistance and is presented in Figure 5.

It is noted that, regardless of other characteristics of wool mattresses, the water vapor resistance factor, μ, corresponds to values close, in order of magnitude, to values characteristic of other thermal insulation products—mineral wool (μ = 2), glass wool (μ = 1), rigid polyurethane foam (μ = 10), straw or stabilized chipboard plates (μ = 1.5) and are much more permeable than thermal insulation products made of expanded polystyrene (μ = 30–60) or extruded (μ = 150) or open-pore glass (μ = 28), thus ensuring the "breathing" of the walls on which they are used, results that are consistent with specifications from the literature [1]. As expected, the speed of the water vapor transmission decreases with the increase of the thickness of the specimen, but the resistance to vapor-water is less

influenced by this increase of the thickness, which might imply that these parameters are affected differently by the characteristics of the test specimen, the first one being dependent upon the characteristic of the product (thickness), and the second one is dependent on the characteristic of the material (density).
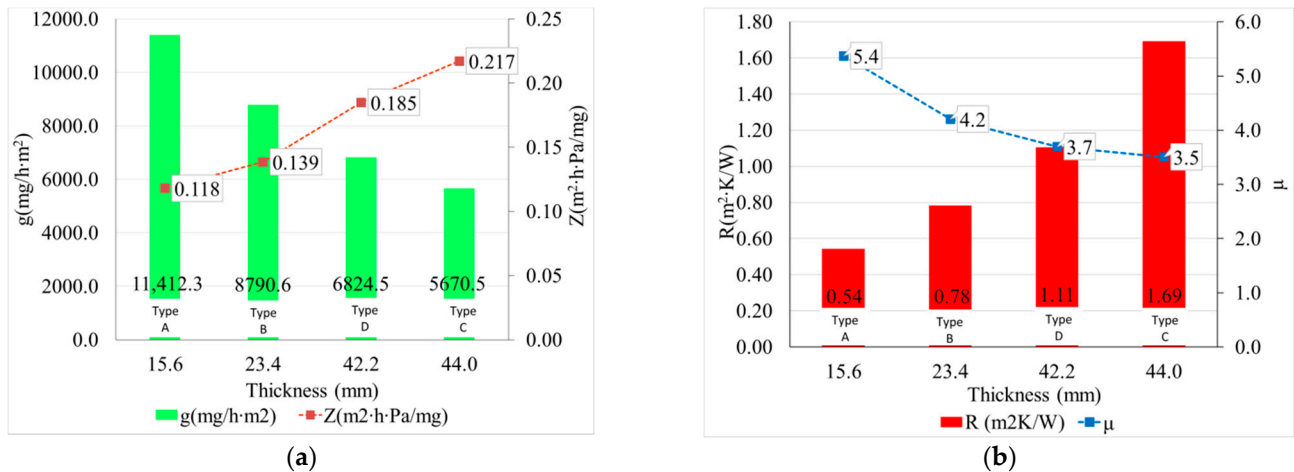
Figure 5. Water vapor permeability quantified by water vapor transmission rate, g (mg/hm^2), water vapor resistance, Z (m^2 h Pa/mg), and water vapor resistance factor, μ: (**a**) presented in order of increase in their thickness, respectively (**b**) in correlation with their thermal transfer resistance (Types A, B, C, D defined according to Table 2).

The sorption/desorption capacity of water vapor determined experimentally for thermal-insulating mattresses was achieved by graphical representation of the sorption/desorption curves constructed on the basis of moisture content according to RH (Figure 6). Since these curves are very close, even superimposed in some areas, for better detail, we chose the broken-down graphic representation, Figure 6a for the phenomenon of sorption, and Figure 6b for the phenomenon of desorption, keeping the same proportions to facilitate comparison.
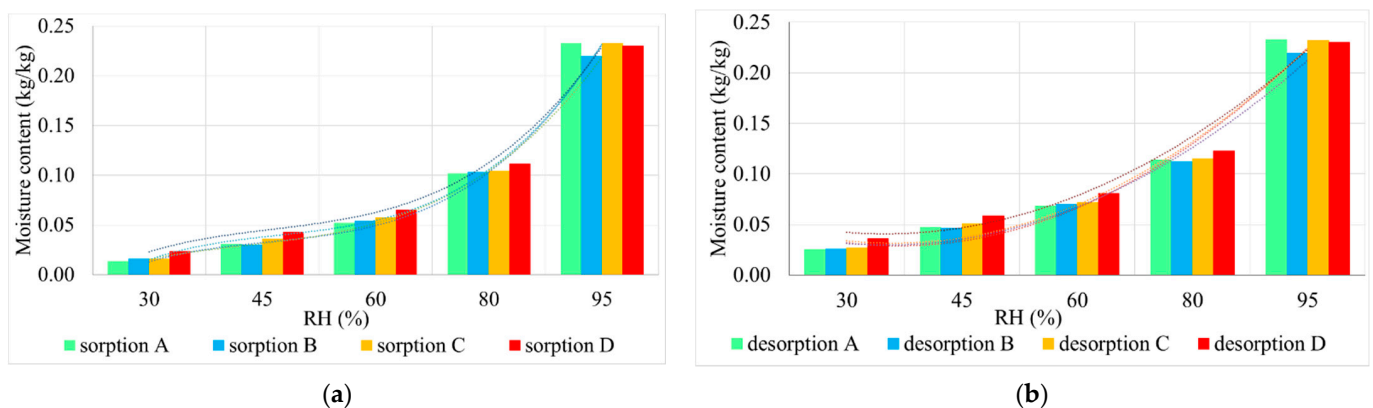
Figure 6. Evolution of the phenomenon of: (**a**) sorption; (**b**) desorption—the sorption/desorption curves obtained by drawing through the points defined as mass variation = f(RH) (Types A, B, C, D defined according to Table 2).

Placing the sorption curve, in all cases, under the desorption curve, signifies that, although permeable to water vapor, the sheep wool thermal-insulating mattresses, under conditions of increased humidity of the environment, are able to retain a certain amount of water, the results being consistent with those reported in the literature [1,25,60]. With the reduction of the humidity of the environment, this water will be released to the environment, but at a lower speed than the retention rate, as demonstrated by the slope of the sorption–desorption curves. As a result of this behavior, it can be appreciated that this

type of products contributes not only to the thermal insulation of the interior space but also to the regulation of its humidity. Analyzing the allure of the sorption curves, it can be seen that they are consistent with previous results obtained in the literature [25,34,60–62], which indicates that the water absorption of up to 5% of the fiber drying weight is carried out with a higher speed, the water binding strongly, after which, the phenomenon is influenced by the relative humidity of the environment, the speed stabilizing towards the saturation zone, a fact also identified by the analysis of the slope of the sorption curves, respectively, desorption. Considering that the thermal insulation of the building, on the inside can be done for walls, floors, and ceilings, and the volume of indoor air is proportional to their surface area, the literature also points to a high probability of meeting the needs of the improving indoor air quality through the use of this type thermal-insulating material [23,25,27,28,49].

As a result of the analysis of the cumulative, it was considered that type-C mattress (30.8 kg/m^3- density, and 44 mm) meets the simultaneous criteria of performance for thermal insulation, water vapor permeability, and the ability to regulate the humidity of indoor air by sorption/desorption of moisture, according to the need. Thus, for this purpose, the test was performed by the performance of reducing the concentration of formaldehyde in the indoor air, respectively. Binding of this compound by chemisorption, the results being presented in Figure 7.

(**a**)   (**b**)
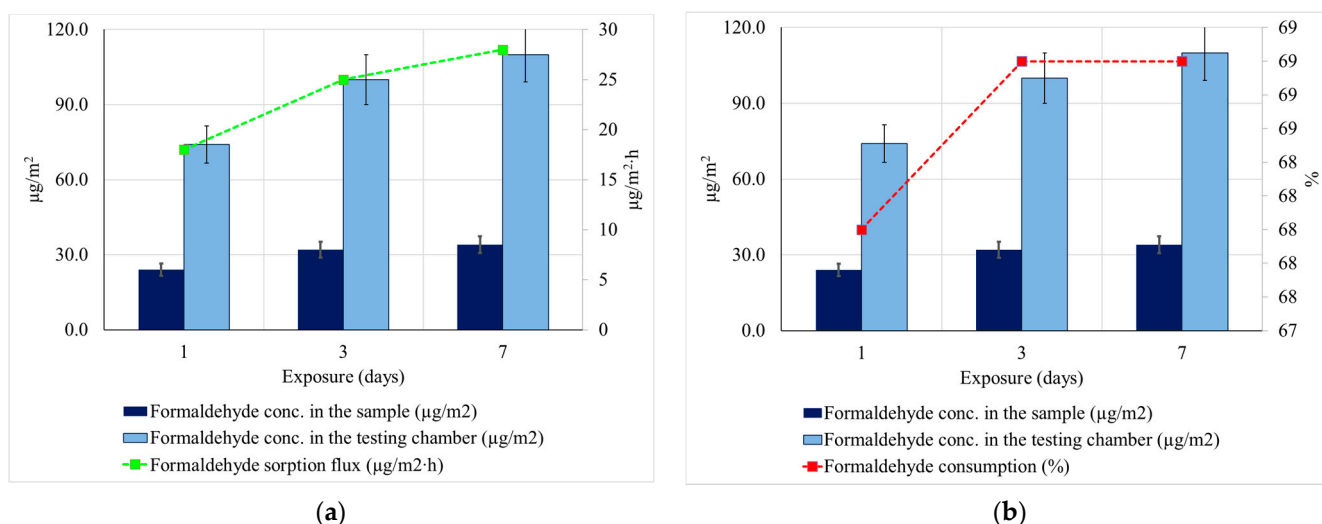
Figure 7. Capacity of the 44 mm thickness sheep wool thermal-insulating mattress on the sorption of formaldehyde. (**a**) Formaldehyde sorption flux (µg/m^2 h); (**b**) Formaldehyde consumption (%).

The results obtained showed that, for equal flows of formaldehyde introduction into the test room, in the situation of the existence of the wool sample, the concentration of formaldehyde recorded in the atmosphere of the enclosure is much lower (24 µg/m^2 per 1 day, 32 µg/m^2 per 3 days, respectively, 34 µg/m^2 per 7 days), compared to the concentration recorded in at 74 µg/m^2 on 1 day at 110 µg/m^2 on 7 days). The calculated flow of formaldehyde sorption in the wool test tube was 18 µg/m^{2}h at 1 day, 25 µg/m^{2}h at 3 days, 28 µg/m^{2}h at 7 days, increasing steadily with the duration of exposure and the amount of formaldehyde introduced into the atmosphere inside the test chamber increased, the consumption of formaldehyde by sorption in the wool mattress, calculated, being 68% after the first day of constant, 69%, in the next test period, up to 7 days. Based on these results, the efficiency of the tested thermal-insulating mattress in terms of improving the air quality inside the rooms by reducing the concentration of formaldehyde was demonstrated. Moreover, by keeping the wool sample in the test chamber for another 24 h after the end of the test, under constant conditions and without further introduction of formaldehyde, an amount of 29.5 µg/m^2 remaining formaldehyde in the sample was determined, which

indicates two aspects: the desorption of formaldehyde at 24 h is very low (only 13% of the adsorbed amount and the probability that chemisorption mechanisms that induce chemical bonds, much more stable, than sorption in micropores of the wool thread by mechanisms of a physical nature (physisorption), in accordance with the references in the literature [15,23,49]. According to the literature, this ability to bind formaldehyde also has the advantage that, according to the specialized literature, it becomes, indirectly but effectively, even a passive treatment to increase resistance to attack by microorganisms, insects and their larvae, a concentration of 0.5% formaldehyde is sufficient to provide an annihilation capacity of microorganisms within 5–6 h of exposure [62].

4. Conclusions

The aim of this work was to analyze the capacity of sheep wool thermal-insulating mattresses to improve indoor air quality by evaluating the performance of ensuring the water vapor permeability of the thermally insulated surface, regulating humidity by sorption/desorption of atmospheric humidity, and reducing the concentration of formaldehyde, the main toxic substance found in indoor air, under conditions of satisfying the needs of thermal insulation.

Based on the experimental results, it can be said that, according to the literature, sheep wool mattresses have characteristics that successfully fit them into the category of thermal-insulating materials, the coefficient of thermal conductivity being a characteristic property of the material, and the resistance to heat transfer being a characteristic property of the product, that is, influenced by the type of material and its thickness. From the point of view of air humidity, the analyzed products ensure a high degree of comfort by maintaining the "breathability" of the surfaces on which they are applied (walls, ceilings, floors) but also by the ability to regulate humidity through processes of sorption/desorption of atmospheric water. At the same time, these sheep wool mattresses contribute to maintaining the safety and health of the population through the ability to reduce the concentration of formaldehyde.

Tests carried out on the four types of sheep wool mattresses indicated that they have good thermal insulation performance, but, at the same time, they have a beneficial influence on the air in the interior space. Depending on the specific characteristics and the intended use of the products, the use of these materials allows the user to choose the thickness of the mattress, so that both the thermal insulation requirements are met, as well as meeting the limitations imposed by the volume and architecture of the rooms or climatic conditions.

Further studies regarding the possibility of using sheep wool mattresses as thermal insulating materials are focused on statistical analysis regarding the influence of specific production technology on the performance of the product and on identifying optimization opportunities.

Author Contributions: Conceptualization, A.H., C.B. and A.-V.L.; methodology, A.H., C.B., H.S. and P.V.; validation, A.H., C.B., H.S., A.-V.L., V.M., P.V. and M.S.; formal analysis, H.S. and P.V.; investigation, A.H., H.S. and A.-V.L.; resources, H.S., V.M. and M.S.; data curation, A.H., H.S. and P.V.; writing—original draft preparation, A.H. and C.B.; writing—review and editing, H.S., A.-V.L. and P.V.; visualization, H.S. and M.S.; supervision, A.H., V.M. and P.V.; project administration, A.H. All authors have read and agreed to the published version of the manuscript.

Institutional Review Board Statement: Not applicable.

Informed Consent Statement: Not applicable.

Data Availability Statement: The data presented in this study are available on request from the corresponding authors.

Conflicts of Interest: The authors declare no conflict of interest.

References

1. Holcroft, N.; Shea, A. Heat of Sorption and Moisture Buffering Properties of Building Insulation Materials. In *InCIEC 2013*; Hassan, R., Yusoff, M., Ismail, Z., Amin, N., Fadzil, M., Eds.; Springer: Singapore, 2014.
2. Mansour, E.; Curling, S.; Stephan, A.; Ormondroyd, G. Absorption of volatile organic compounds by different wool types. *Green Mater.* **2016**, *4*, 1–7. [CrossRef]
3. Klepeis, N.E.; Nelson, W.C.; Ott, W.R.; Robinson, J.P.; Tsang, A.M.; Switzer, P.; Behar, J.V.; Hern, S.C.; Engelmann, W.H. The National Human Activity Pattern Survey (NHAPS): A resource for assessing exposure to environmental pollutants. *J. Expo. Sci. Environ. Epidemiol.* **2001**, *11*, 231–252. [CrossRef]
4. Maskell, D.; da Silva, C.F.; Mower, K.; Rana, C.; Dengel, A.; Ball, R.J.; Ansell, M.P.; Walker, P.J.; Shea, A. Properties of bio-based insulation materials and their potential impact on indoor air quality. *Acad. J. Civ. Eng.* **2015**, *33*, 156–163.
5. BPIE—Buildings Performance Institute Europe. Available online: https://bpie.eu/wp-content/uploads/2015/10/HR_EU_B_under_microscope_study.pdf (accessed on 20 March 2021).
6. EUR-Lex—Communication from the Commission to the European Parliament, the Council, the European Economic and Social Committee and the Committee of the Regions an EU Strategy on Heating and Cooling COM/2016/051. Available online: https://eur-lex.europa.eu/legal-content/EN/TXT/?uri=CELEX%3A52016DC0051 (accessed on 25 April 2021).
7. Crump, D.R.; Yu, C.W.F.; Squire, R.; Atkinson, M. Small Chamber Methods for Characterising Formaldehyde Emission from Particleboard. In *Characterising Sources of Indoor Air Pollution and Related Sink Effects*; ASTM International: West Conshohocken, PA, USA, 1996; pp. 211–224.
8. Klinge, A.; Roswag-Klinge, E.; Ziegert, C.; Fontana, P.; Richter, M.; Hoppe, J. Naturally Ventilated Earth Timber Constructions. In *Expanding Boundaries: Systems Thinking for the Built Environment, Sustainable Built Environment (SBE) Regional Conference*; Habert, G., Schlueter, A., Eds.; VDF Hochschulverlag AG at the ETH Zurich: Zurich, Switzerland, 2016.
9. Formaldehyde—CASRN 50-00-0/DTXSID7020637. Available online: https://cfpub.epa.gov/ncea/iris2/chemicallanding.cfm?substance_nmbr=419 (accessed on 16 March 2021).
10. Nielsen, G.D.; Wolkoff, P. Cancer effects of formaldehyde: A proposal for an indoor air guideline value. *Arch. Toxicol.* **2010**, *84*, 423–446. [CrossRef]
11. EUR—Lex. Available online: https://eur-lex.europa.eu/legal-content/EN/TXT/?uri=celex%3A32008R1272 (accessed on 5 March 2021).
12. WHO Guidelines for Indoor Air Quality. Available online: https://www.euro.who.int/__data/assets/pdf_file/0009/128169/e94535.pdf (accessed on 27 February 2021).
13. Air Quality in Europe. Available online: https://www.eea.europa.eu/publications/air-quality-in-europe-2020-report (accessed on 25 January 2021).
14. Molhave, L.; Clausen, G.; Berglund, B.; De Ceaurriz, J.; Kettrup, A.; Lindvall, T.; Maroni, M.; Pickering, A.C.; Risse, U.; Rothweiler, H.; et al. Total Volatile Organic Compounds (TVOC) in Indoor Air Quality Investigations. *Indoor Air* **1997**, *7*, 225–240. [CrossRef]
15. Curling, S.F.; Loxton, C.; Ormondroyd, G.A. A rapid method for investigating the absorption of formaldehyde from air by wool. *J. Mater. Sci.* **2012**, *47*, 3248–3251. [CrossRef]
16. Mansour, E.; Loxton, C.; Elias, R.; Ormondroyd, G. Assessment of health implications related to processing and use of natural wool insulation products. *Environ. Int.* **2014**, *73*, 402–412. [CrossRef] [PubMed]
17. Stolwijk, J.A.J. Sick-building syndrome. *Environ. Health Perspect.* **1991**, *5*, 99–108. [CrossRef]
18. Mitchell, C.S.; Zhang, J.; Sigsgaard, T.; Jantunen, M.; Lioy, P.J.; Samson, R.; Karol, M.H. Current State of the Science: Health Effects and Indoor Environmental Quality. *Environ. Health Perspect.* **2007**, *115*, 958–964. [CrossRef] [PubMed]
19. Salthammer, T.; Mentese, S.; Marutzky, R. Formaldehyde in the Indoor Environment. *Chem. Rev.* **2010**, *110*, 2536–2572. [CrossRef]
20. Takeda, M.; Saijo, Y.; Yuasa, M.; Kanazawa, A.; Araki, A.; Kishi, R. Relationship between sick building syndrome and indoor environmental factors in newly built Japanese dwellings. *Int. Arch. Occup. Environ. Health* **2009**, *82*, 583–593. [CrossRef]
21. Maier, S.S.; Rajabinejad, H.; Buciscanu, I.-I. Current approaches for raw wool waste management and unconventional valorization: A review. *Environ. Eng. Manag. J.* **2019**, *18*, 1439–1456. [CrossRef]
22. Huang, X.; Wang, Y.-J.; Di, Y.-H. Experimental Study of Wool Fiber on Purification of Indoor Air. *Text. Res. J.* **2007**, *77*, 946–950. [CrossRef]
23. Ormondroyd, G.A.; Curling, S.F.; Mansour, E.; Hill, C.A.S. The water vapour sorption characteristics and kinetics of different wool types. *J. Text. Inst.* **2017**, *108*, 1198–1210. [CrossRef]
24. Ye, Z.; Wells, C.M.; Carrington, C.G.; Hewitt, N.J. Thermal conductivity of wool and wool-hemp insulation. *Int. J. Energy Res.* **2005**, *30*, 37–49. [CrossRef]
25. Zach, J.; Korjenic, A.; Petránek, V.; Hroudová, J.; Bednar, T. Performance evaluation and research of alternative thermal insulations based on sheep wool. *Energy Build.* **2012**, *49*, 246–253. [CrossRef]
26. Corscadden, K.; Biggs, J.; Stiles, D. Sheep's wool insulation: A sustainable alternative use for a renewable resource? *Resour. Conserv. Recycl.* **2014**, *86*, 9–15. [CrossRef]
27. Pennacchio, R.; Savio, L.; Bosia, D.; Thiebat, F.; Piccablotto, G.; Patrucco, A.; Fantucci, S. Fitness: Sheep-wool and Hemp Sustainable Insulation Panels. *Energy Procedia* **2017**, *111*, 287–297. [CrossRef]

28. Bosia, D.; Giordano, R.; Savio, L. A sustainable building product: Advanced insulation panels obtained by recycling regional sheep's wool. *J. Technol. Archit. Environ.* **2011**, *1*, 110–115.

29. Giordano, R.; Savio, L.; Bosia, D. Natural is always Ecological? From a study concerning the environmental impact building insulating wool to the awareness to promote a SLOWTECH approach in architecture. In Proceedings of the International Conference SB11, Helsinki, Finland, 18–21 October 2011; Volume 1, pp. 1–10.

30. USDA—Overview of the United States Sheep and Goat Industry. Available online: https://downloads.usda.library.cornell.edu/usda-esmis/files/sx61dm30x/st74ct34d/xs55mg16m/ShpGtInd-08-09-2011.pdf (accessed on 23 April 2021).

31. Popescu, C.; Höcker, H. Hair—The most sophisticated biological composite material. *Chem. Soc. Rev.* **2007**, *36*, 1282–1291. [CrossRef]

32. Cardamone, J.M. Investigating the microstructure of keratin extracted from wool: Peptide sequence (MALDI-TOF/TOF) and protein conformation (FTIR). *J. Mol. Struct.* **2010**, *969*, 97–105. [CrossRef]

33. Cardamone, J.M.; Erazo-Majewicz, P.; Naouli, N. Composition and Methods for Treating a Keratin Based Substrate. U.S. Patent 8,747,823, 10 June 2014.

34. Hegyi, A.; Dico, C.; Szilagyi, H. Sheep Wool Thermal Insulating Mattresses Behaviour in the Water Vapours Presence. *Procedia Manuf.* **2020**, *46*, 410–417. [CrossRef]

35. Watt, I.C. Kinetic Study of the Wool-Water System: Part I: The Influence of Water Concentration. *Text. Res. J.* **1960**, *30*, 443–450. [CrossRef]

36. Watt, I.C. Kinetic Study of the Wool-Water System: Part II: The Mechanism of Two-Stage Absorption. *Text. Res. J.* **1960**, *30*, 644–651. [CrossRef]

37. Watt, I.C. Kinetic Study of the Wool-Water System: Part III: The Mechanism of Sorption at High Water Concentrations. *Text. Res. J.* **1961**, *31*, 793–799. [CrossRef]

38. Truter, E.V. *Introduction to Natural Protein Fibres: Basic Chemistry*; Barnes & Noble Book: New York, NY, USA, 1973; p. 92.

39. Tuzcu, T.M. Hygro-Thermal Properties of Sheep Wool Insulation. Ph.D. Thesis, Civil Engineering Faculty Delft University of Technology, Delft, The Netherlands, 2007.

40. Kim, D.I.; Park, J.H.; Kim, S.D.; Lee, J.-Y.; Yim, J.-H.; Jeon, J.-K.; Park, S.H.; Park, Y.-K. Comparison of removal ability of indoor formaldehyde over different materials functionalized with various amine groups. *J. Ind. Eng. Chem.* **2011**, *17*, 1–5. [CrossRef]

41. Rong, H.; Ryu, Z.; Zheng, J.; Zhang, Y. Effect of air oxydation of Rayon-based activated carbon fibers on the adsorption behavior for formaldehyde. *Carbon* **2002**, *40*, 2291–2300. [CrossRef]

42. Song, Y.; Qiao, W.; Yoon, S.; Mochida, I.; Guo, Q.; Liu, L. Removal of formaldehyde at low concentration using various activated carbon fibers. *J. Appl. Polym. Sci.* **2007**, *106*, 2151–2157. [CrossRef]

43. Alexander, P.; Carter, D.; Johnson, K.G. Formation by formaldehyde of a cross-link between lysine and tyrosine residues in wool. *Biochem. J.* **1951**, *48*, 435–441. [CrossRef]

44. Middlebrook, W.R. The irreversible combination of formaldehyde with proteins. *Biochem. J.* **1949**, *44*, 17–23. [CrossRef]

45. Hasselaar, B. Vernieuwbare Isolatie Als Duurzaam Alternatief. Master's Thesis, TU Delft, Delft, The Netherlands, 2003.

46. Seo, J.; Kato, S.; Atak, Y.; Chino, S. Performance test for evaluating the reduction of VOCs in rooms and evaluating the lifetime of sorptive building materials. *Build. Environ.* **2009**, *44*, 207–215. [CrossRef]

47. Ghanbarnejad, P.; Goli, A.; Bayat, B.; Barzkar, H.; Talaiekhozani, A.; Bagheri, M.; Alaee, S. Evaluation of Formaldehyde Adsorbtion by Human Hair and Sheep Wool in Industrial Wastewater with High Concentration. *J. Environ. Treat. Tech.* **2014**, *2*, 12–17.

48. Jemal, A.; Siegel, R.; Ward, E.; Hao, Y.; Xu, J.; Murray, T.; Thun, M.J. Cancer Statistics, 2008. *CA Cancer J. Clin.* **2008**, *58*, 71–96. [CrossRef]

49. Bosia, D.; Savio, L.; Thiebat, F.; Patrucco, A.; Fantucci, S.; Piccablotto, G.; Marino, D. Sheep Wool for Sustainable Architecture. *Energy Procedia* **2015**, *78*, 315–320. [CrossRef]

50. Ghosh, A.; Collie, S.R. Keratinous Materials as Novel Absorbent Systems for Toxic Pollutants. *Def. Sci. J.* **2014**, *64*, 209–221. [CrossRef]

51. Causer, S.M.; McMillan, R.C.; Bryson, W.G. The role of wool carpets and furnishings in reducing indoor air pollution. In Proceedings of the 9th International Wool Textile Research Conference, Biella, Italy, 28 June–5 July 1995; Volume 1, p. 155.

52. Coulombe, P.A.; Bernot, K.M.; Lee, C.-H. Keratins and the Skin. In *Encyclopedia of Biological Chemistry*, 2nd ed.; Lennarz, W.J., Lane, M.D., Eds.; Academic Press: New York, NY, USA, 2013; pp. 665–671.

53. Crawshaw, G.H. The role of wool carpets in controlling indoor air pollution. *J. Text. Inst.* **1978**, *16*, 12–15.

54. Cieślak, M.; Schmidt, H. Contamination of wool fibre exposed to environmental tobacco smoke. *Fibres Text. East. Eur.* **2004**, *12*, 81–83.

55. Jin, X.; Lu, L.; Wu, H.; Ke, Q.; Wang, H. Duck Feather/Nonwoven Composite Fabrics for Removing Metals Present in Textile Dyeing Effluents. *J. Eng. Fibers Fabr.* **2013**, *8*, 89–96. [CrossRef]

56. Hassan, M.M.; Davies-McConchie, J.F. Removal of Arsenic and Heavy Metals from Potable Water by Bauxsol Immobilized onto Wool Fibers. *Ind. Eng. Chem. Res.* **2012**, *51*, 9634–9641. [CrossRef]

57. Korjenic, A.; Klarić, S.; Hadžić, A.; Korjenic, S. Sheep Wool as a Construction Material for Energy Efficiency Improvement. *Energies* **2015**, *8*, 5765–5781. [CrossRef]

58. Kehrer, M.; Künzel, H.M.; Sedlbauer, K. Ecological insulation materials. Does sorption moisture affect their insulation performance? *J. Therm. Envel. Build. Sci.* **2003**, *26*, 207–212. [CrossRef]

59. Padfiled, T. *Humidity Buffering of Interieur Spaces by Porous, Absorbent Insulation*; Series R; Technical University of Denmark: Kongens Lyngby, Denmark, 1999; p. 61.

60. Papadopoulos, A. State of the art in thermal insulation materials and aims for future developments. *Energy Build.* **2005**, *37*, 77–86. [CrossRef]

61. Patnaik, A.; Mvubu, M.; Muniyasamy, S.; Botha, A.; Anandjiwala, R.D. Thermal and sound insulation materials from waste wool and recycled polyester fibers and their biodegradation studies. *Energy Build.* **2015**, *92*, 161–169. [CrossRef]

62. Abdou, A.; Budaiwi, I. The variation of thermal conductivity of fibrous insulation materials under different levels of moisture content. *Constr. Build. Mater.* **2013**, *43*, 533–544. [CrossRef]

Article

Extraction of Metals from Polluted Soils by Bioleaching in Relation to Environmental Risk Assessment

Ioana Monica Sur [1,*]**, Valer Micle** [1,*] **, Andreea Hegyi** [2,*] **and Adrian-Victor Lăzărescu** [2]

1   Department of Environment Engineering and Entrepreneurship of Sustainable Development, Faculty of Materials and Environmental Engineering, Technical University of Cluj-Napoca, 103-105 Muncii Avenue, 400641 Cluj-Napoca, Romania
2   NIRD URBAN-INCERC Cluj-Napoca Branch, 117 Calea Floresti, 400524 Cluj-Napoca, Romania; adrian.lazarescu@incerc-cluj.ro
*   Correspondence: ioana.sur@imadd.utcluj.ro (I.M.S.); valer.micle@imadd.utcluj.ro (V.M.); andreea.hegyi@incerc-cluj.ro (A.H.)

Abstract: Environmental pollution has particular implications for the whole geosystem and increases the global risk to human and ecological health. In this regard, investigations were carried out on soil samples to perform the quality status assessment by determining: pH, texture, structure and metal concentration, as well as carrying out an assessment of anthropogenic activity by determining pollution indices: C_f (contamination factor), C_d (degree of contamination), PLI (pollution load index), E_r (ecological risk index) and PERI (potential ecological risk index). Analyses on soil samples showed high concentrations of metals (Cu: 113–2996 mg kg^{-1}; Pb: 665–5466 mg kg^{-1}; Cr: 40–187 mg kg^{-1}; Ni: 221–1708 mg kg^{-1}). The metal extraction experiments were carried out by bioleaching using *Thiobacillus ferrooxidans*, microorganisms at different amounts of bioleaching solution (20 mL and 40 mL 9K medium) and a stirring time of up to 12 h. The results on the degree of contamination, pollution loading index PLI (2.03–57.23) and potential ecological risk index PERI (165–2298) indicate that the soils in the studied area have a very high degree of pollution. The decontamination procedure by bioleaching showed a decrease, but at the end of the test (12 h), the followed indices indicate high values, suggesting that bioleaching should continue. The depollution yield after 12 h of treatment is, however, encouraging: Cu 29–76%, Pb: 10–32%, Cr: 39–72% and Ni 44–68%. The use of yield–time correlation equations allows the identification of the optimal exposure time on the bioleaching extraction process to obtain optimal results. The aim of the research is to determine the soil quality, soil environmental risk, extraction of metals from polluted soils by bioleaching and to identify influencing factors in achieving high remediation yields.

Keywords: 9K medium; bioleaching; *Thiobacillus ferrooxidans*; pollution indices; ecological risk

1. Introduction

The interest in a cleaner and healthier environment has increased in recent years, becoming a pressing need due to the awareness of the negative impact that pollution has on the quality of life and health of the population [1,2].

The presence of metals generates the most widespread chemical pollution of soil, and its adverse effects are particularly strong. Metal concentrations in uncontaminated dry soils in Romania range from: Cu 20–40 mg kg^{-1}; Pb 22 mg kg^{-1}; Cr 10 mg kg^{-1}; Ni 25–40 mg kg^{-1} [3]. Naturally high levels of metals can be found in soil as a result of geological processes. However, concentrations are mostly very high due to anthropogenic influences from excessive agriculture and intensive industrial pollution [4–7].

The accumulation of metals in soil affects the surrounding environment through quantity and toxicity, but also through chemical bonds that influence soil reaction, resulting in degradation or loss of soil functions [6–8]. Soil pollution with metals affects the physical and chemical properties of soil. High concentrations of Cu alter the humus composition,

and Pb inhibits enzymatic processes, reducing the intensity of carbon dioxide removal, both of them reducing the number of microorganisms and nutrient uptake by plants [6,9,10].

These pollutants also affect the health of the population, because copper compounds, through ingestion, can cause digestive and nervous disorders. In high concentrations these copper compounds can even trigger paralysis or cardio-respiratory arrest. Lead is a metal that can cause, even in very low concentrations, serious damage to the brain and nervous system [4,5,10]. Chromium is deposited in the liver, spleen and kidneys, and nickel is carcinogenic and, in some people, can cause allergies [7,10].

The phenomenon of environmental pollution is no longer local or regional, but global, with particular implications for the entire geosystem and leading to an increase in the global risk to human and ecological health [1,2,4,5].

Bioleaching, or bacterial leaching, has gained increased attention as it is innovative, environmentally friendly, and economical [11,12]. The bioleaching process relies on the ability of micro-organisms to transform solid compounds into soluble and extractable elements that can be recovered [13,14]. Acidophile microorganisms (*Sulfolobus acidocaldarius*, *Acidithiobacillus*, *Leptospirillum* and *Thiobacillus ferrooxidans*) live in highly acidic environments (pH 1–3.0) and in the presence of very high concentrations of metals [14–18].

The microorganisms or bacteria that are used in the aerobic bioleaching process directly or indirectly oxidize inorganic compounds. Oxidation and acid-producing activities by sulfo-oxidizing bacteria are essential [13].

In the direct process, bacteria can directly oxidize the sulfur ion from metal sulfide into sulfate. This process is shown in Equations (1) and (2) [13,19,20]:

$$MS \longrightarrow M^{2+} + S^{2-} \tag{1}$$

$$S^{2-} + 2O_2 \xrightarrow{\text{bacteria}} MSO_4^{2-} \tag{2}$$

A general reaction is used to express the biological oxidation of a metal sulfide involved in bioleaching. Metal sulfides can be iron-based (pyrites) or other metal-based (Equation (3)) [13]:

$$MS + 2O_2 \xrightarrow{\text{bacteria}} MSO_4 \tag{3}$$

In the indirect process, the oxidation of metal sulfides is done by microbially generated ferric ions (Equation (4)):

$$MS + 2Fe^{3+} \longrightarrow M^{2+} + 2Fe^{2+} + S^0 \tag{4}$$
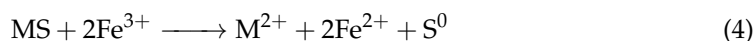
The ferrous iron that is formed is re-oxidized by bacteria. When sulfur is formed, the presence of bacteria is indispensable for its oxidation to sulfuric acid and thus maintaining the solubilized metal (Equation (5)) [13]:

$$S + H_2O + 3/2O_2 \xrightarrow{\text{bacteria}} H_2SO_4 \tag{5}$$

The production of sulfuric acid maintains the acidity of the solution at a favorable pH, and leads to the growth of ferro-oxidizing and sulfo-oxidizing bacteria and the solubilization of metals [14]. The general indirect leaching process involves the ferric–ferric cycle [19] (Equation (6)):

$$4FeSO_4 + O_2 + 2H_2SO_4 \xrightarrow{\text{bacteria}} 2Fe_2(SO_4)_3 + 2H_2O \tag{6}$$
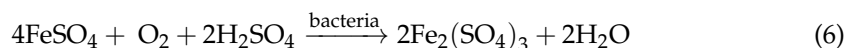
Microorganisms can alter the mobility of metals in the environment through its physical or chemical changes by microbial redox reactions. These microorganisms help in the development of mechanisms that alter solubility, mobility and/or toxicity (Figure 1) and allow soil remediation by separating or dissolving contaminants [21]. Separation or immobilization involves mechanisms of bioabsorption (uptake of contaminants into biomass), as well as changes in the redox state (reduction of oxidized metal to an insoluble form), and

the accumulation, precipitation and/or volatilization of pollutants by phytoremediation. Dissolution or mobilization includes the processes of bioleaching metals and metalloids and changes in the redox state (oxidation of small insoluble metal forms to soluble forms), which favor dissolution or volatilization. The removal of inorganic pollutants can be achieved according to the following principles: (1) after precipitation, the pollutants are immobilized; (2) the concentration of the pollutant reduces the volume of the contaminated matrix; (3) the separation of metals is in an environment with lower risk potential [21].
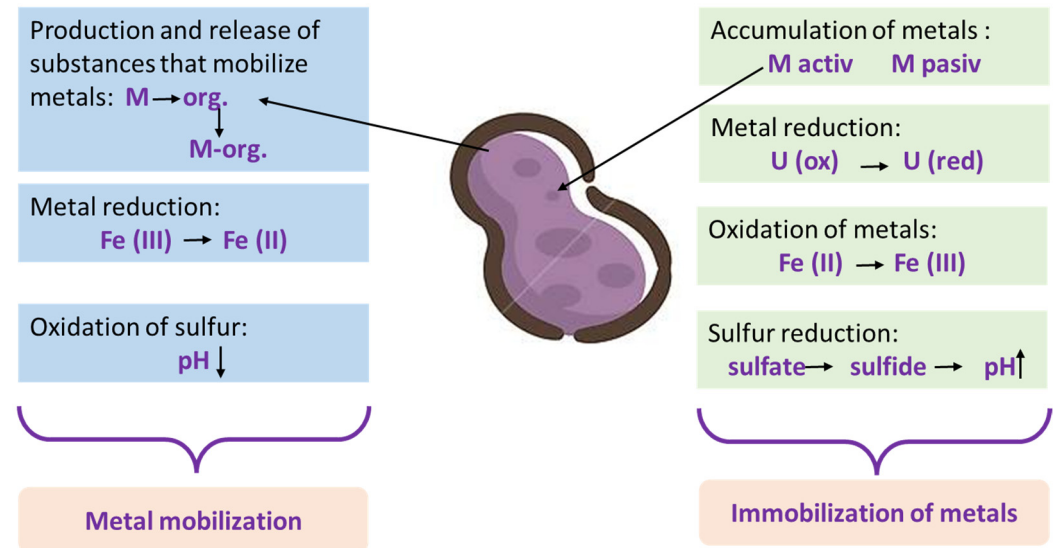
Figure 1. Interactions between metals and microorganisms.

Organisms are exposed to the presence of different types of metals and metalloids in the environment. Interaction between them develops defense mechanisms, which sometimes generates benefits and sometimes is to their detriment [21]. Microorganisms use metals for structural and/or catalytic functions and have the ability to bind metal ions present on the outside of the cell surface or transport them to the cell interior for various intracellular functions (Ca and Mg have structural and catalytic functions, V, Cr, Mn, Fe, Co, Ni, Cu, Zn, Mo and Se in low concentrations can participate in catalytic functions). Some prokaryotic microorganisms can use, during metabolism, metal species that may exist with different valences, such as Cr, Mn, Fe, Co, Cu and Ca, because they act as acceptors or donors of electrons [21].

Having a very rich and mobile enzymatic apparatus, the microorganisms have a true advantage in their use for biotechnological soil depollution processes. This also mainly happens because they have a high biosynthesis capacity and a high adaptability to environmental conditions. Generally, the following microorganism species are used for the bioleaching of metals: *Thiobacillus*, *Leptospirillum* or *Sulfolobus* [10].

Thiobacillus ferrooxidans, are single-celled, rod-shaped microorganisms, 1–2 microns long and 0.5–1.0 microns wide. They are tolerant of high acidity and are found in soils with a pH of 2.2, continuing to live even at pH below 0.6, but these organisms grow best at pH 2–5 and at temperatures between 25–35 °C [22].

Thiobacillus ferrooxidans use Fe^{2+} as an energy source. Equation (7) shows the oxidation relationship of Fe^{2+}:

$$4Fe^{2+} + O_2 + 4H^+ \longrightarrow 4Fe^{3+} + 2H_2O \tag{7}$$
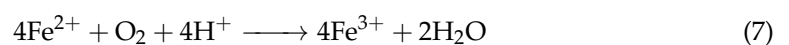
The assessment of soil metal contamination is done by calculating several parameters that indicate the pollution of the soil. These parameters are used to monitor soil quality and ensure future sustainability [23,24] by highlighting the degree of contamination and the potential ecological risk [25,26].

To highlight the influence of anthropogenic activities on soil quality and to assess soil metal pollution, a simultaneous evaluation of the contamination index (C_f), degree of contamination (C_d), pollution index (PLI), ecological risk factor (E_r) and potential ecological risk index (PERI) parameters can be performed [27–29].

The PLI index is used for the overall assessment of the degree of contamination in the soil and provides an easy way to demonstrate the deterioration of soil conditions due to metal accumulation [23]. The PERI index allows the identification of various environmental effects (toxicology, environmental chemistry and ecology) and can assess the environmental risks caused by metals [8,30].

Rouchalova (2020) pointed out that particle size (71–100 μm), pH (1.8) and microorganism density (9K medium) are the most important parameters in achieving high depollution yields [31]. Groudev et al. (2001) pointed out that microbial activity is the most important factor in Cu, Zn, Cd and As bioleaching, the exception being Pb [32].

Studies in the literature have shown that bioleaching is efficient for the extraction of metals from water treatment sludge (Cr 92.6%, Cu 80.6%, Fe 95.6%, Mg 91%, Ni 89.7%, Pb 99.5%, Zn 93% [33–35], Fe 76.5%, Cu 82%, Pb 89.9%, Zn 90%) [31] or from municipal and industrial waste [36]. Pyrotite bioleaching could increase Fe recovery by bacterial adaptation and biological contact oxidation [37], and Fe can be removed (18%) by adding 9K medium [38].

Results obtained in the literature regarding the bioleaching of metals from soils, obtained under similar experimental conditions (use of *Thiobacillus* microorganisms, sample agitation (120–170 rpm), extraction time (5–48 days) and temperature (28–30 °C)) have shown that good extraction yields can be obtained for: Cu: 44% [39], 46% [40], 20–73% [41], 72. 8% [42], 69–92% [43], 95% [44,45], 51–72% [46], 78% [47], 80.6% [33–35], 82% [31], 83% [48], 89–96% [49], 95–96% [50]; Pb: 10–54% [43], 16–60% [50], 18% [40], 33–72% [51], 39.4% [42], 75–84% [49]; Ni: 10–47% [50], 35–65% [51], 69–92% [43], 75–93% [49], 78% [40], 90% [33–35]; and Cr: 14% [40], 10–41% [43], 9–20% [51], 53–92% [49], 64% [39].

As a result, based on the information present in the literature, it can be said that in order to obtain a high yield of soil metal extraction technologies, it is important to know the optimal parameters: pH, texture, structure, type and quantity of microorganisms, temperature and extraction time, used in the extraction process. At the same time, it can be said that there is still a number of controversies worldwide, especially in terms of the effectiveness of the process (i.e., the optimal intervention time needed to obtain a satisfactory degree of depollution) which vary according to the specific characteristics of the soil and the initial concentration of the pollutant and the type of pollutant. It should also be mentioned that, due to the high degree of inhomogeneity of the soils, it is particularly important to accumulate as many experimental results as possible. Accumulating the necessary data generates the possibility to assess, on a case-by-case basis, the parameters necessary to obtain a satisfactory degree of decontamination, such as the duration of intervention, the concentration and quantity of the pollutant, etc.

The aim of the paper is to highlight the factors that influence the yield of the bioleaching process, these being mainly the amount of bioleaching solution and the duration of the extraction process of potentially toxic elements (metals), in relation to the environmental risk assessment. The use of yield–time correlation equations allows the identification of the optimal exposure time on the bioleaching extraction's potentially toxic elements to obtain optimal results.

2. Materials and Methods

2.1. Soil Sampling

In order to study the assesed parameters, soil samples from two different areas in Romania were extracted. These areas are particulary known for generating industrial activities (area P1—Maramureș County and area P2—Alba County). Soil from three different depths was analyzed for each of the two areas: 0–10 cm, 10–20 cm and 20–30 cm. The analysis of the data was performed according to the Romanian standard STAS 7184/1-84

and were processed according to ISO 11464:1998 [52,53]. The investigated areas are specific to mining areas and adjacent to these types of activities, being known as polluted areas in Romania [54–56].

2.2. Soil Analysis

Characterization of the soil samples was carried out in terms of pH, texture, structure and content of metals (Cu, Pb, Cr and Ni). Soil pH was determined in soil/water extract 1/5 (*w/v*) using a HANNA pH meter. Soil texture was determined by gravimetric method with RETSCH AS 200 sieve and soil structure was determined by Sekera method. Soil metal content was determined by atomic absorption spectrometry (AAS) with a SHIMADZU AA-6800 spectrometer (Shimadzu, Tokyo, Japan) using the aqua regia digestion. The soil samples were dried, grounded to a fine powder and sieved through a 100 μm sieve. Three grams of each sample of soil were weighed into a beaker and 7 mL of HCl and 21 mL of HNO_3 were added. The mixture was then refluxed for 2 h. After cooling to room temperature, the supernatant was filtered and diluted to 100 mL.

2.3. Bioleaching Process

The extraction of metals from contaminated soil was achieved by bioleaching using 180 *Thiobacillus ferrooxidans* (TF) microorganisms inoculated in 9K medium in different quantities: 20 mL and 40 mL. The 9K medium contained: $(NH_4)2SO_4$—3.0 g; KCl—0.1 g; K_2HPO_4—0.5 g; $MgSO_4 \cdot 7H_2O$—0.5 g; $Ca(NO_3)_2 \cdot 4H_2O$—0.01 g; $FeSO_4 \cdot 7H_2O$—44.2 g; and distilled water up to 1000 mL [57].

From each soil sample, 10 g of soil (from the 2 mm soil fraction) was weighed and 20 mL and 40 mL of 9K medium was added. Samples were stirred using an orbitally oscillating–rotating platform shaker (200 rpm) for 2 h, 4 h, 6 h, 8 h, 10 h and 12 h. Research was carried out in laboratory conditions under constant temperature, real air humidity and ventilation conditions (T = (27 ± 1) °C, RH = (65 ± 2)%), without forced ventilation of ambient air. At regular time intervals (2 h, 4 h, 6 h, 8 h, 10 h, 12 h) the leachate was filtered and the concentrations of the four metals (Cu, Pb, Cr, Ni) were determined by Atomic Absorption Spectrometry (AAS). To ensure repeatability and reproducibility, the results were recorded as the average of three successive measurements.

2.4. Ecological Risk Assessment Methodology

Based on previous studies and results [8,27,28,58–61], C_f contamination index and E_r ecological risk parameters were calculated for each sample and for each type of pollutant and measurable indices for general assessment of the soil condition were analyzed, i.e., C_d, PLI and PERI.

The calculation of the parameters were performed using background values of: Cu: 25; Pb: 20; Cr: 35; Ni: 20 [62]. The degree of C_d contamination was calculated by summing the contamination indices according to Equation (8):

$$C_f = \frac{C_{Ai}}{C_{Ni}} - 1 \tag{8}$$

where,

C_{Ai}—analyte concentration,
C_{Ni}—background value (in the case of soil).

$$C_d = \sum_{i=1}^{n}(C_f) \tag{9}$$

$$PLI = \sqrt[n]{c_{f1} * c_{f2} * c_{f3} * \dots * c_{fn}} \tag{10}$$

$$Er = C_f * T_r \tag{11}$$

where,

E_r—ecological risk index of the metal i,

C_f—contamination factor of the metal i,

T_r—metal toxicity response coefficient for each metal: Cu: 5, Pb: 5, Cr: 2, Ni: 5 [8,63].

$$PERI = \sum_{i=1}^{n} Er \tag{12}$$

The results obtained from the calculations are interpreted according to the values of the corresponding parameters by comparison with the information available in the literature (Table 1) and presented also in colors, in order to easily asses the degree of pollution and/or ecological risk.

Table 1. Metal pollution indices used for soil quality assessment.

PARAMETERS			
	C_f—**Contamination factor** [8,27,28]		$C_f < 1$—Low contamination factor
			$1 \leq C_f < 3$—Moderate contamination factor
			$3 \leq C_f < 6$—Considerable contamination factor
			$C_f \geq 6$—Very high contamination factor
	C_d—**Degree of Contamination** [8,58]		$C_d < 8$—Low degree of contamination
			$8 \leq C_d \leq 16$—Moderate degree of contamination
			$16 \leq C_d \leq 32$—Considerable degree of contamination
			$C_d > 32$—Very high degree of contamination
	PLI—Pollution Load Index [27,28,59]		$PLI < 1$—Not polluted soil
			$PLI = 1$—Soil with normal background level
			$PLI > 1$—Polluted soil
	Er—Ecological risk index [8,60]		$E_r < 40$—Low ecological risk
			$40 < E_r \leq 80$—Moderate ecological risk
			$80 < E_r \leq 160$—Considerable ecological risk
			$160 < E_r \leq 320$—High ecological risk
			$E_r > 320$—Serious ecological risk
	PERI—Potential Ecological Risk Index [8,61]		$PERI < 150$—Low ecological risk
			$150 \leq PERI < 300$—Moderate ecological risk
			$300 \leq PERI < 600$—High potential ecological risk
			$PERI \geq 600$—Significantly high ecological risk

During the entire experimental program, the evolution of the "soil health status" was monitored. This parameter was expressed as the accumulation of all the factors influencing this aspect, as well as the kinetics of the evolution of each type of pollutant in relation to the duration of exposure to the bioleaching solution, the amount of 9K medium used, the depth of soil sampling and the pH of the soil. The kinetics of the decontamination process was followed by decreasing the concentration of the pollutant in relation to the time of action of each type of solution.

The effectiveness of the extraction process (ER) was determined with Equation (13) [64]:

$$\text{removal efficiency } (\%) = \frac{C_i - C_f}{C_i} \times 100 \tag{13}$$

where:

C_i is the initial metals' concentration (mg kg^{-1}) of soil;

C_f is the final concentration of metals (mg kg^{-1}) in soil, after soil bioleaching treatment.

In order to estimate the time needed to apply the process until a satisfactory degree of depollution is obtained, a series of equations correlating the yield with the time of action were identified on the basis of experimental data. In this respect, the identified correlation relationship was considered acceptable if the condition $R^2 \geq 0.9$ was satisfied.

3. Results and Discussions

3.1. Analysis and Assessment of Ecological Risks for Initial Soil Samples

The results of the pH tests indicate that all soil samples show a low pH (acid reaction) with varying degrees of acidity. Samples P1 show a pH value of 5.2–5.5 (medium acidic reaction), while samples P2 show a pH value of 2.3–2.5 (highly acidic reaction). In both investigated locations, the soil was found to be well structured and has a sandy loam texture with the following composition: 21.8% clay, 40.2% silt and 38% sand, according to the USDA classification [65].

Initial testing of the soil samples indicated that, depending on the location and depth of extraction, metal concentrations vary substantially. As shown in Figure 2, a slight decrease in Pb concentration with an increasing depth of investigation was observed at both investigated locations. On the other hand, the Cu, Ni and Cr content increased with the depth of investigation. This can be explained by the fact that Pb is associated with the acid-soluble and reducible phases, while the other metals studied are mainly associated with the oxidization phase. These metal migration trends in the top layer (up to 30 cm) are in agreement with the literature. Regarding the different concentrations of metals, between the two areas investigated, it can be appreciated that the fact that these areas are part of two different regions, with two different types of exploitation and pollution, lead to the presented results.
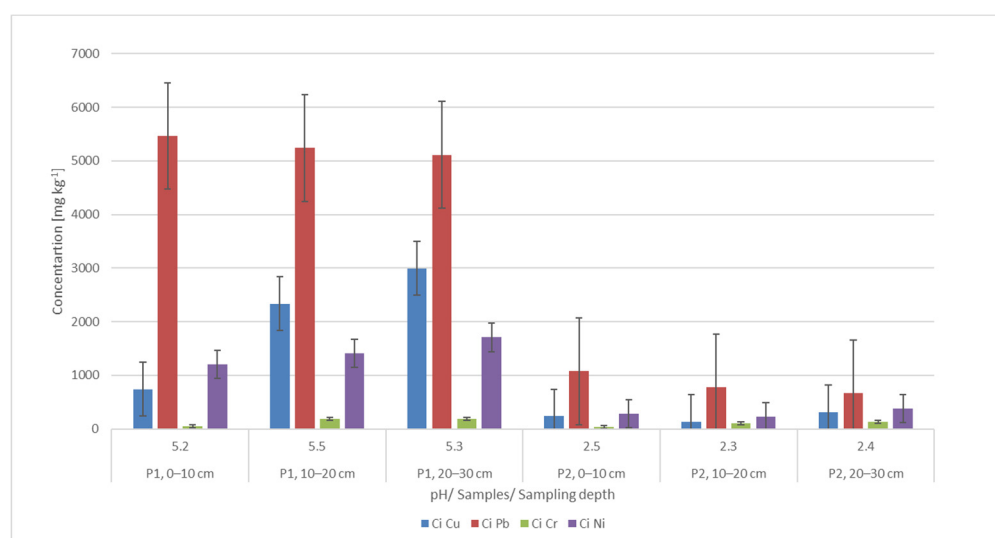
Figure 2. Initial metal concentration and pH of soil samples as a function of sampling location and depth.

The metal concentration values of the investigated samples show that they exceed the normal values: 20 mg kg^{-1} (Cu, Pb and Ni) and 30 mg kg^{-1} (Cr), according to the Romanian legislation (Order no. 756/1997). In the case of sample P1, the concentrations are so high that they even exceed the action threshold: 1000 mg kg^{-1} (Pb), 500 mg kg^{-1} (Cu and Ni) [66]. Comparing the calculated indicators, C_d, E_r, PLI and PERI with the admissibility thresholds (Figure 3), it can be seen that all these indicators indicate the need for decontamination intervention. The sources of the pollution in this area are the mining activities carried out in the area over the years. At the moment, all the mines in the area are closed.

3.2. Environmental Risk Assessment during the Bioleaching Process

After applying the metal extraction treatment by bioleaching, with 20 mL and 40 mL of 9K medium, the results obtained show that the C_d indicator decreases steadily over time (Figure 4), indicating the overall efficiency of the decontamination process. From the shape of the curves, it can be seen that the variation of this indicator is directly influenced by the

duration of the soil being exposed to the bioleaching solution, i.e., a linear dependence of the C_d parameter on time.

(**a**)

(**b**)

(**c**)

(**d**)
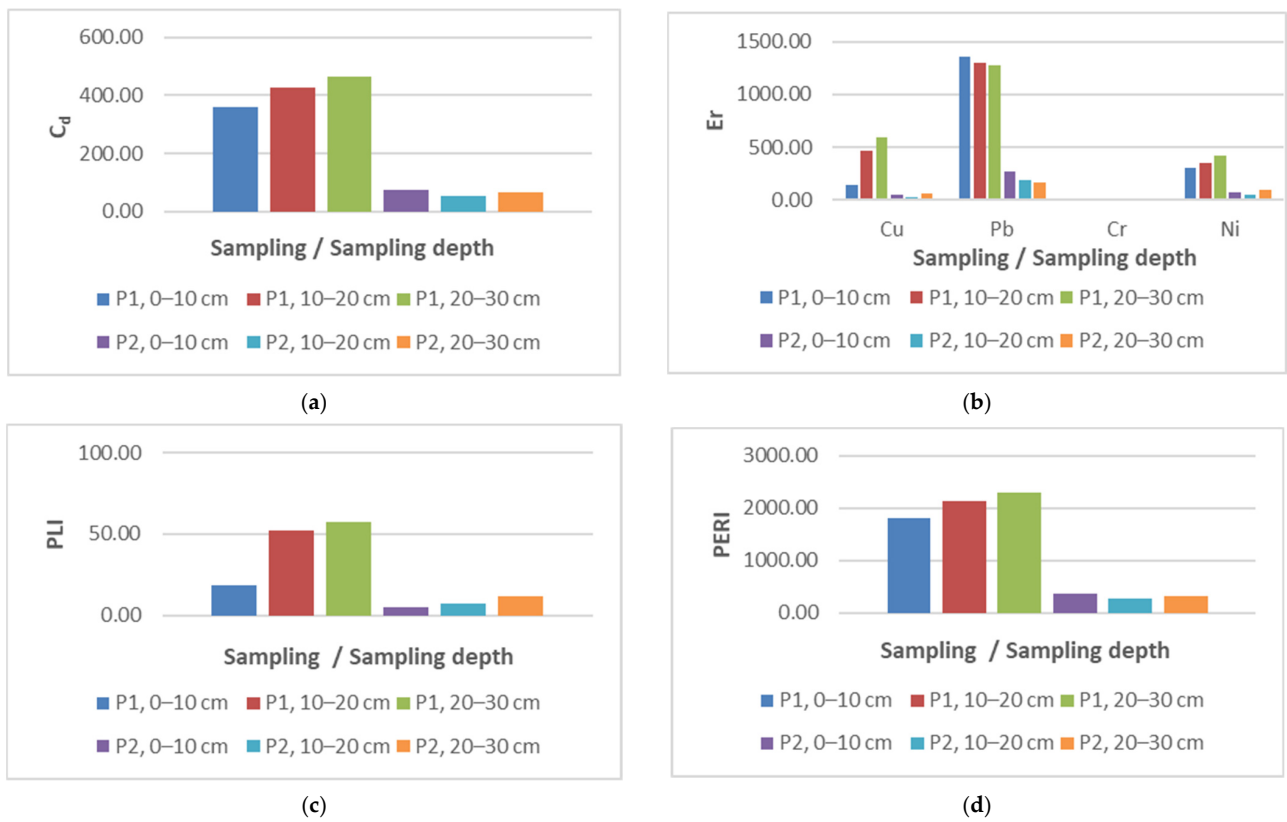
Figure 3. Parameters calculated for the initial concentration: (**a**) C_d—degree of contamination; (**b**) E_r—environmental risk index; (**c**) PLI—pollution loading index; and (**d**) PERI—potential environmental risk index.

Figure 4. C_d—degree of contamination during the extraction process according to admissibility limits and sampling depth using 20 mL 9K medium.

On the other hand, soil with a more acidic pH, but also with an initially lower contaminant content, shows a variation much closer to the ideal situation of linear variation. However, the plot area indicates a slower rate of change of the C_d indicator in this case (compared to the more contaminant-rich soil with a higher pH). These observations suggest that, in addition to the length of time of exposure to the soil decontamination method, the evolution of the C_d indicator is influenced by both the concentration of contaminant metals and soil pH. The positioning of the experimental results, grouped for each soil type, even for the three different sampling depths, may be an indication that the sampling depth is not a factor directly influencing the evolution of the extraction process.

Results obtained for the C_d indicator are also found for the other two indicators, PLI (Figure 5) and PERI (Figure 6). The evolution of these indicators, on the other hand, is influenced by the evolution of the pollutant concentration which is a direct influence in the evolution of the E_r indicator.
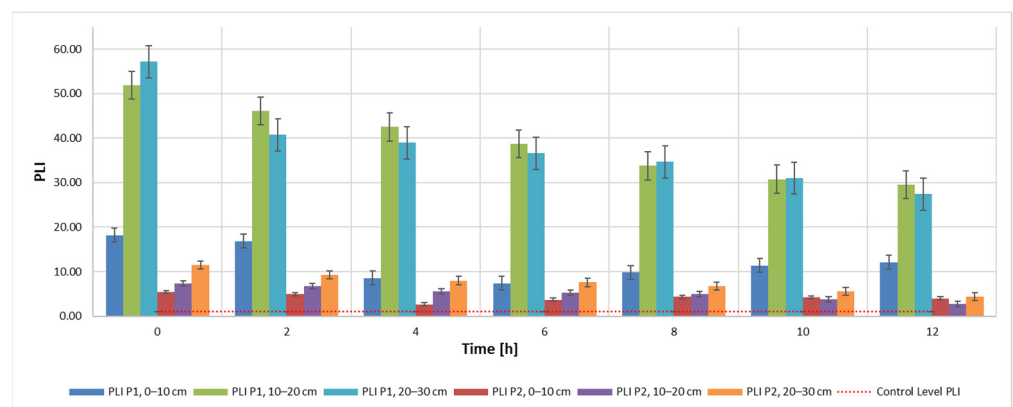
Figure 5. PLI—pollution load index during the extraction process according to admissibility limits and sampling depth using 20 mL 9K medium.

Figure 6. PERI—potential ecological risk index during the extraction process according to admissibility limits and sampling depth using 20 mL 9K medium.

As shown in the figures above, in contradiction to the evolution of the concentrations of the three polyunsaturated metals, Cu, Pb and Ni, the Cr concentration shows a different variation. During the first 4–5 h of treatment, the concentration and its impact on the general soil characterization decreases. Afterwards, a continuous and constant increase of this parameter in terms of pollution is observed.

This can be explained by the specificity of the bioleaching process using TF microorganisms, whose metabolism contributes to the transition from Cr(IV) to Cr(III) [6,11,67]. Bacteria can degrade Cr(VI) to Cr(III) in anaerobic environments, where it uses chromate as

a terminal electron acceptor, and in aerobic environments via cellular depleting agents. The transformation of Cr(VI) to Cr(III) leads to a reduction of toxicity, showing the stabilization of Cr in the soil with little migration of Cr to the plant [6]. It can also be noticed that, although the measuring equipment records this Cr concentration, the advantage of the process is the ability of the element to change from its form which is hazardous to human health to a less hazardous form. In accordance with the specifications in the literature, results show a very high degree of contamination (Cd > 32), a pollution index PLI > 1 and a significant ecological risk for both soil samples that were analyzed in this study (Figures 7–9). Results obtained on both soil samples show that interventions are required for the decontamination and reduction of both the pollution index and the environmental risk. Although the extraction process by bioleaching was applied for 12 h, the aforementioned parameters, at the end of the test, were not positioned in safe zones, which indicates the need for further treatment.
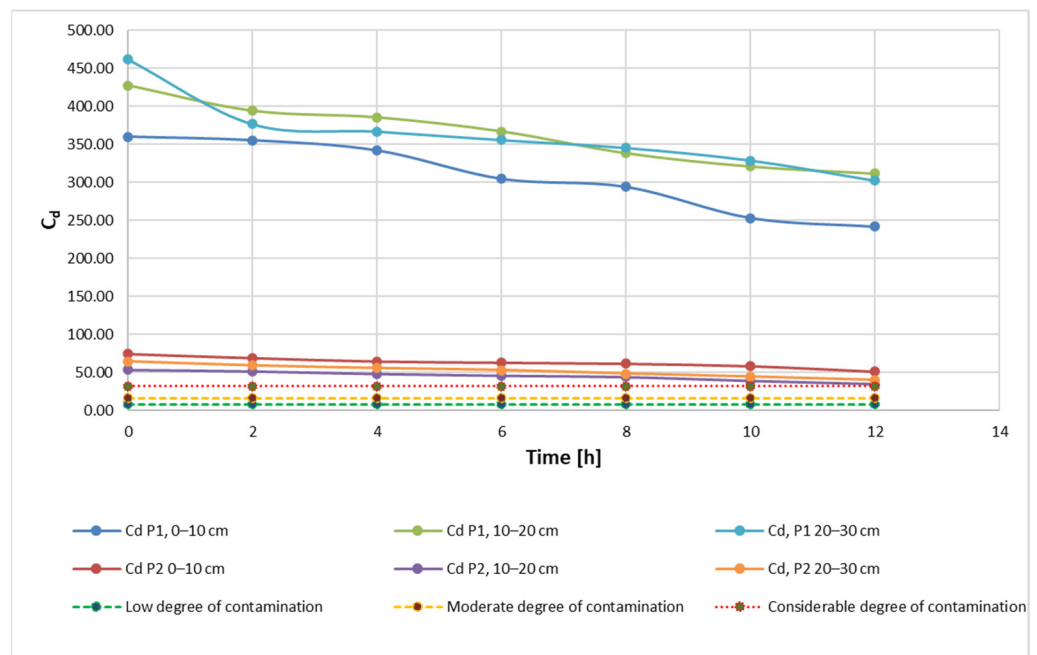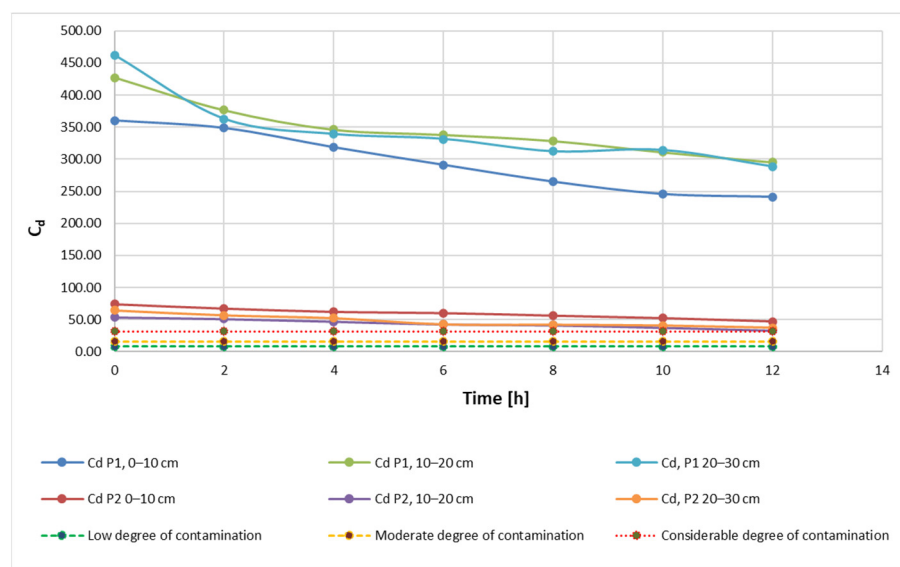

Figure 7. C_d—degree of contamination during the extraction process according to the admissibility limits and sampling depth using 40 mL 9K medium.
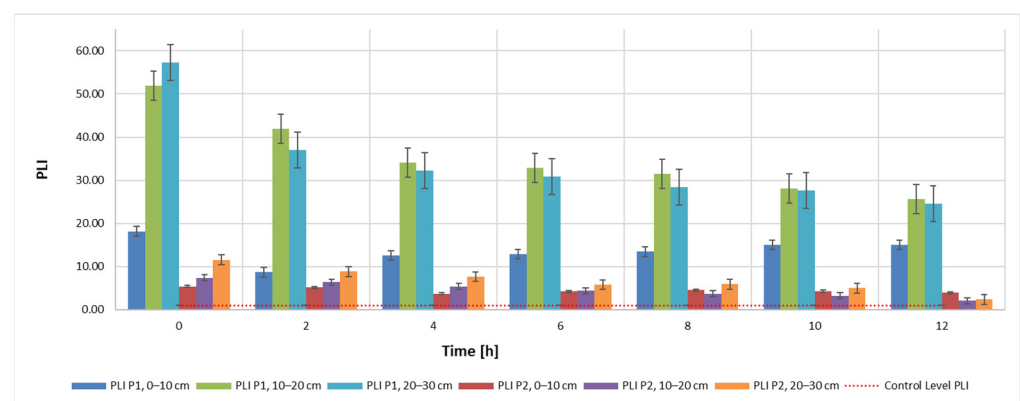
Figure 8. PLI—pollution load index during the extraction process according to admissibility limits and sampling depth using 40 mL 9K medium.

Most of the soil samples presented $C_f \geq$ six values, resulting in a very high degree of pollution (Table 2). Although samples have shown high values in terms of the analyzed parameters, the C_r parameter showed values < one for most samples. A relatively small number of samples (seven samples) had a C_f ranging from three to six, indicating considerable contamination (Cr = Ni < Cu). The C_f contamination index has the following order:

Pb > Cu > Ni > Cr. The soil in the studied areas shows a high degree of contamination, with the PLI pollution index greater than one and the C_d contamination degree greater than 32 at the end of the 12 h of treatment, regardless of the amount of 9K medium used.
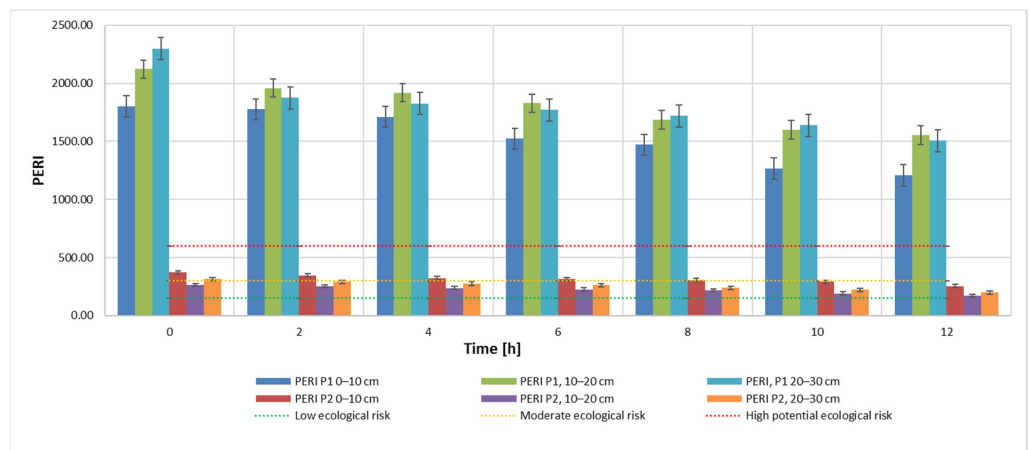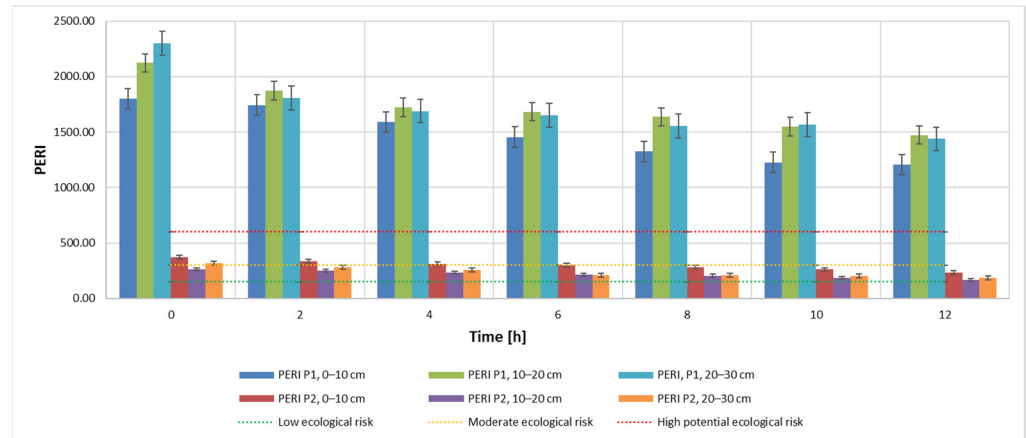

Figure 9. PERI—potential ecological risk index during the extraction process depending on the admissibility limits and sampling depth using 40 mL 9K medium.

Table 2. Calculated values for the C_f (contamination factor), C_d (contamination degree) and PLI (pollution load index).

Sample				C_f					
Code	Sampling Depth [cm]	Time [h]	9K Medium [mL]	Cu	Pb	Cr	Ni	C_d	PLI
P1	0–10	Initial	-	28.44	272.30	0.24	59.30	360.28	18.17
		Final	20	19.92	198.95	0.24	22.65	241.76	12.12
		(after 12 h)	40	18.84	189.10	0.44	32.70	241.08	15.05
	10–20	Initial	-	92.44	261.15	4.34	69.35	427.28	51.93
		Final	20	42.60	229.60	2.07	37.70	311.97	29.56
		(after 12 h)	40	35.52	224.60	1.61	33.70	295.43	25.67
	20–30	Initial	-	118.84	254.65	4.20	84.40	462.09	57.23
		Final	20	36.60	229.00	1.94	34.65	302.19	27.41
		(after 12 h)	40	28.60	224.00	1.66	34.15	288.41	24.54
P2	0–10	Initial	-	8.44	52.75	0.14	13.25	74.58	5.39
		Final	20	5.24	41.80	0.33	3.55	50.92	3.99
		(after 12 h)	40	4.04	39.10	0.44	3.30	46.88	3.89
	10–20	Initial	-	4.32	37.55	1.80	10.05	53.72	7.36
		Final	20	1.68	29.60	0.43	2.80	34.51	2.79
		(after 12 h)	40	1.24	29.10	0.18	2.60	33.12	2.03
	20–30	Initial	-	11.44	32.25	2.66	18.05	64.40	11.53
		Final	20	7.12	25.15	0.26	7.55	40.08	4.32
		(after 12 h)	40	6.80	24.10	0.03	6.50	37.43	2.35
Legend:	C_f < 1—Low contamination factor					$C_f \geq 6$—Very high contamination factor			
	C_f: 1–3—Moderate contamination factor					C_d > 32—Very high degree of contamination			
	C_f: 3–6—Considerable contamination factor					PLI > 1—Polluted soil			

The E_r ecological risk factor values for the studied areas ranged from 0.06 to 1361.50 (Table 3). Samples from the investigation area P1 (ER > 320) show very high values in all studied cases (Pb, Cu and Ni). For samples of P2 (ER < 40), an increase in Pb is observed, which highlights an increased risk or considerable risk of contamination. P2 samples generally show a low or moderate environmental risk for Cu, Cr and Ni. Cr is the only element with a low environmental risk regardless of the location of the soil sample. Analyzing the degree of ecological risk for the samples studied, the following order can be established: Pb > Ni > Cu > Cr.

Table 3. Ecological risk index E_r and PERI potential ecological risk, recorded after 12 h of treatment with 20 mL and 40 mL 9K medium solution, respectively.

	Sample			E_r				PERI
Code	Sampling Depth [cm]	Time [h]	9K Medium [mL]	Cu	Pb	Cr	Ni	
P1	0–10	Initial	-	142.20	1361.50	0.47	296.50	1800.67
		Final	20	99.60	994.75	0.48	113.25	1208.08
		(after 12 h)	40	94.20	945.50	0.88	163.50	1204.08
	10–20	Initial	-	462.20	1305.75	8.69	346.75	2123.39
		Final	20	213.00	1148.00	4.14	188.50	1553.64
		(after 12 h)	40	177.60	1123.00	3.23	168.50	1472.33
	20–30	Initial	-	594.20	1273.25	8.40	422.00	2297.85
		Final	20	183.00	1145.00	3.89	173.25	1505.14
		(after 12 h)	40	143.00	1120.00	3.31	170.75	1437.06
P2	0–10	Initial	-	42.20	263.75	0.29	66.25	372.49
		Final	20	26.20	209.00	0.65	17.75	253.60
		(after 12 h)	40	20.20	195.50	0.88	16.50	233.08
	10–20	Initial	-	21.60	187.75	3.60	50.25	263.20
		Final	20	8.40	148.00	0.87	14.00	171.27
		(after 12 h)	40	6.20	145.50	0.36	13.00	165.06
	20–30	Initial	-	57.20	161.25	5.31	90.25	314.01
		Final	20	35.60	125.75	0.51	37.75	199.61
		(after 12 h)	40	34.00	120.50	0.06	32.50	187.06

Legend:
$E_r < 40$—Low ecological risk
E_r: 40–80—Moderate ecological risk   PERI: 150–300—Moderate ecological risk
E_r: 80–160—Considerable ecological risk   PERI: 300–600—High potential ecological risk
E_r: 160–320—High ecological risk   PERI $\geq$ 600—Significantly high ecological risk
$E_r > 320$—Serious ecological risk

Figure 10 shows the evolution of the E_r parameter for samples P1 and P2 (extracted from a 0–10 cm depth). As seen in the figure, the samples have similar evolutions in terms of the analyzed parameters.

The values obtained for the potential environmental risk index (PERI) for samples extracted from area P1 range from 1204.08 to 2297.85, far exceeding the PERI = 600 value. This indicates a significantly high degree. The PERI values obtained for samples extracted from area P2 indicate a moderate ecological risk, except two initial samples (depth 0–10 cm and 20–30 cm, respectively).

The C_d contamination degree, and the PLI pollution parameters have very high values for all 18 samples investigated. The PERI indicator shows high concentrations for samples extracted from area P1 and a moderate ecological risk for those from area P2. The results of the analyzed indicators suggest that the area has a high level of soil pollution and indicate a strong anthropogenic influence on the soil in the studied area.

From the point of view of the yield of the extraction process (Figures 11 and 12), it can be said that, regardless of whether 20 mL or 40 mL 9K medium was used, the depth of the sample extraction does not directly influence this parameter or the rate of reduction of the pollutant concentration (Figures 13 and 14). Indirectly, through the concentration of the pollutant in the analyzed samples, both the yield and the speed of the pollutant concentration reduction process are influenced, but a direct correlation, expressed by a mathematical dependence function of each of the two measurable indicators with the depth of extraction of the soil samples, cannot be made.
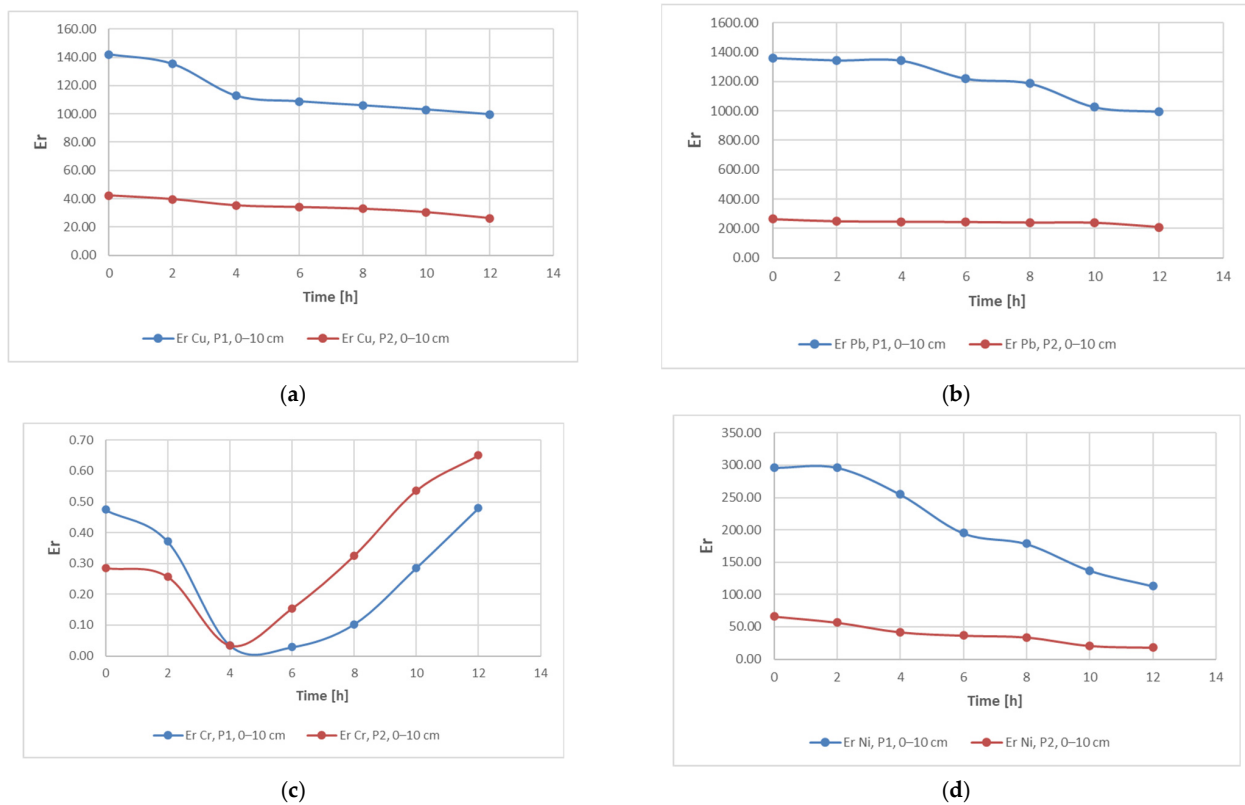
Figure 10. Evolution of the E_r indicator as a function of metal, location and sampling depth: (**a**) Cu, (**b**) Pb, (**c**) Cr and (**d**) Ni.
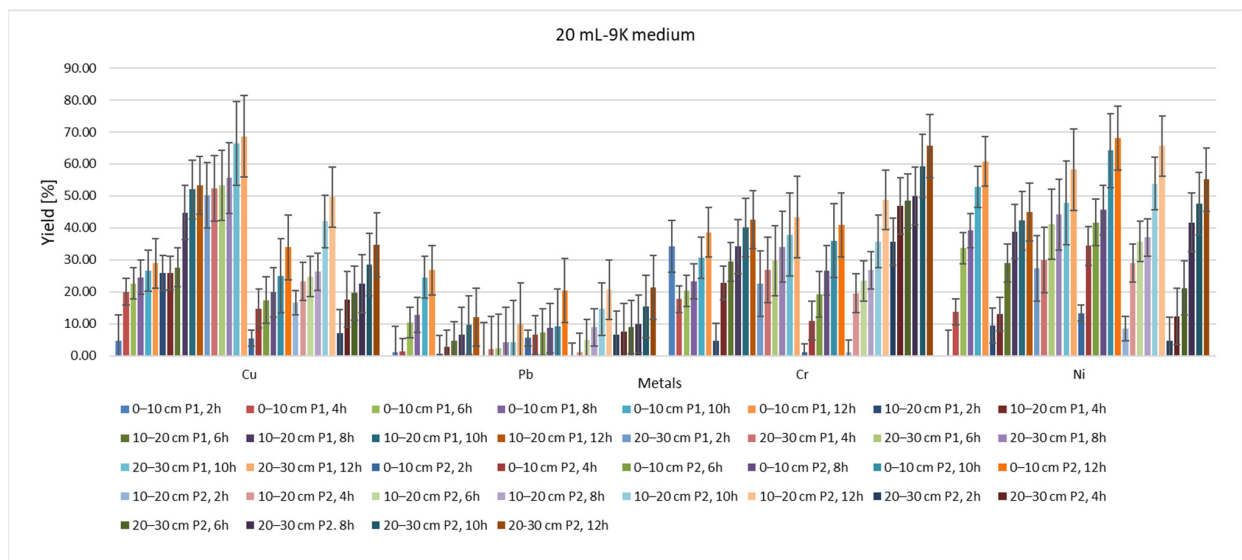
Figure 11. Yield of extraction process with 20 mL of 9K medium.

On the other hand, it can be seen that the type of pollutant directly influences both the speed of the extraction process and its rate of reduction from the soil. Thus, in the case of Pb, the lowest yield is observed for the use of 20 mL of 9K medium, for a soil with a pH of 5.2–5.5. In contrast, in the case of soil with a pH of 2.3–2.5, the lowest yield of the depollution process is observed for Cr. In the two studied areas, the depollution process has a good yield in the case of Cu. In terms of the rate at which the pollutant concentration is reduced, in the case of soil with pH 5, poor results are observed in the case of Cr. All these

observations lead to the appreciation that, in addition to the type of pollutant, the duration of action and the amount of 9K solution used, the initial concentration of the pollutant is of great importance in the mechanism of depollution by this process. A high concentration of pollutant will determine a good yield of the depollution process as well as a good speed of reduction of the concentration of the pollutant. This, however, varies greatly depending on the type of metal pollutant. The results obtained for Pb (10–32%) and Ni (44–68%) using TF are higher compared to the yields obtained using *Aspergillus niger*: Pb: 13% and Ni: 21% [68]. The same can be observed for Cu (39–72%), and when using *Acidithiobacillus*, *Sulfobacillus* and *Ferroplasma*, where Cu amounts to 27% [69], *Pleurotus florida* (18%) and *Pseudomonas* spp. (16.6%) [70].

By analyzing the yield of the extraction process for each type of metal, in relation to the time of action of the 9K medium, and by analyzing the plot area, it can be seen that this process indicator could be modeled based on polynomial equations. Figure 15 shows the identified equations and yield–time correlation indices for the situation of P1 and P2 samples extracted from a 0–10 cm depth and treated with 20 mL of 9K medium. The results indicate that the yield of the extraction process varies, for all the analyzed metals, with respect to time according to polynomial 3-degree equations. Therefore, the evolution of the extraction process could be assessed, in time, with significantly good accuracy (correlation index $R^2 > 0.95$) for each type of polluted metal.
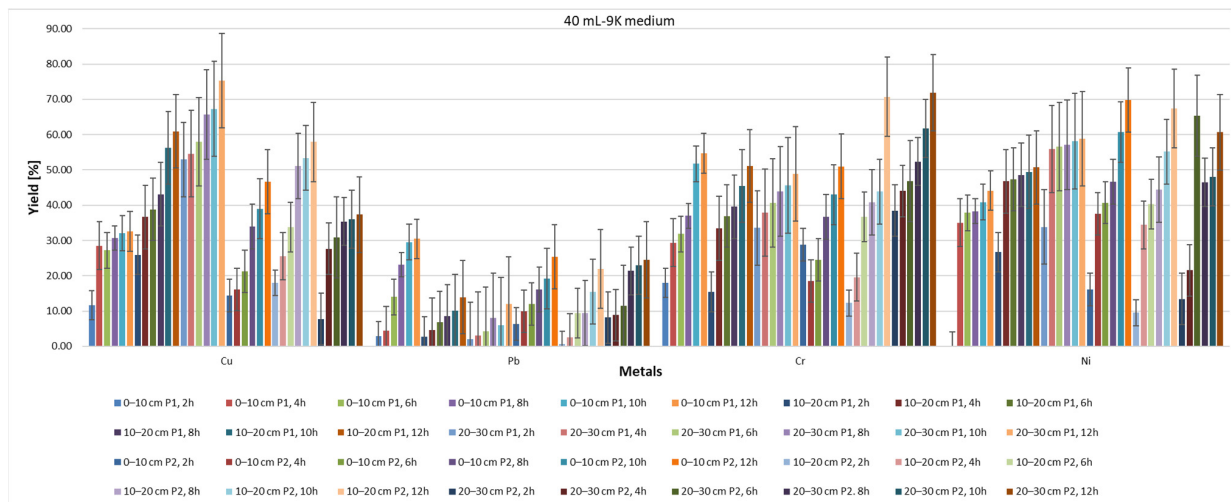
Figure 12. Yield of extraction process with 40 mL of 9K medium.
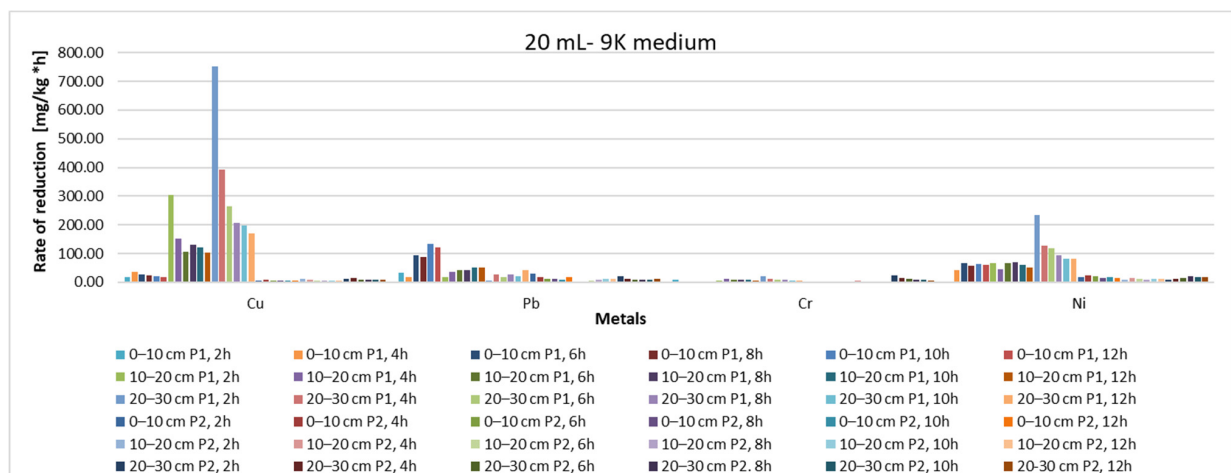
Figure 13. Reduction rate of pollutant concentration, depending on sample, sampling depth, amount of 9K medium and extraction time (20 mL 9K medium).
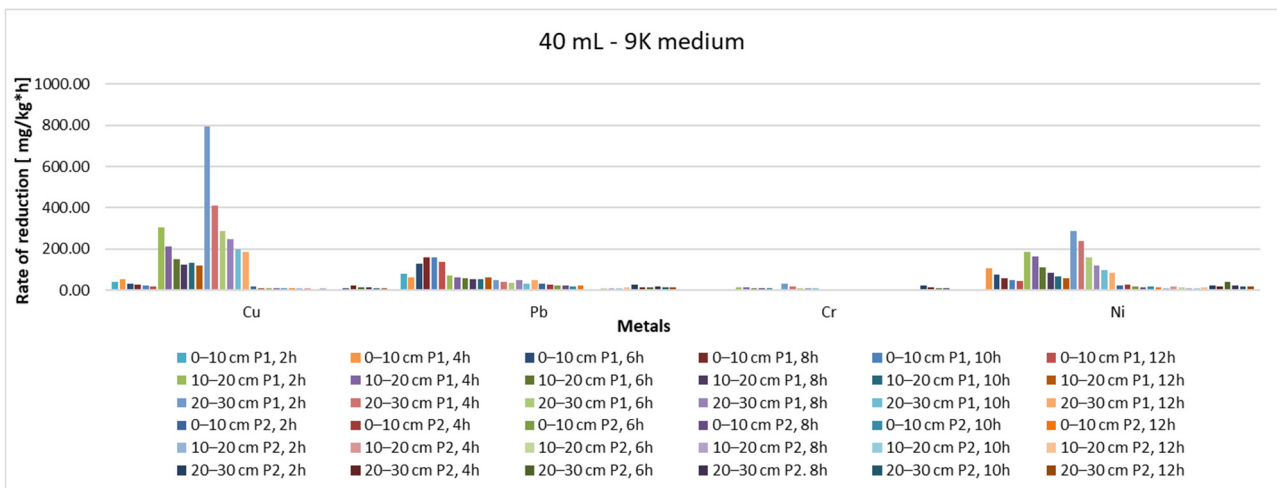
Figure 14. Reduction rate of pollutant concentration, depending on sample, sampling depth, amount of 9K medium and extraction time (40 mL 9K medium).
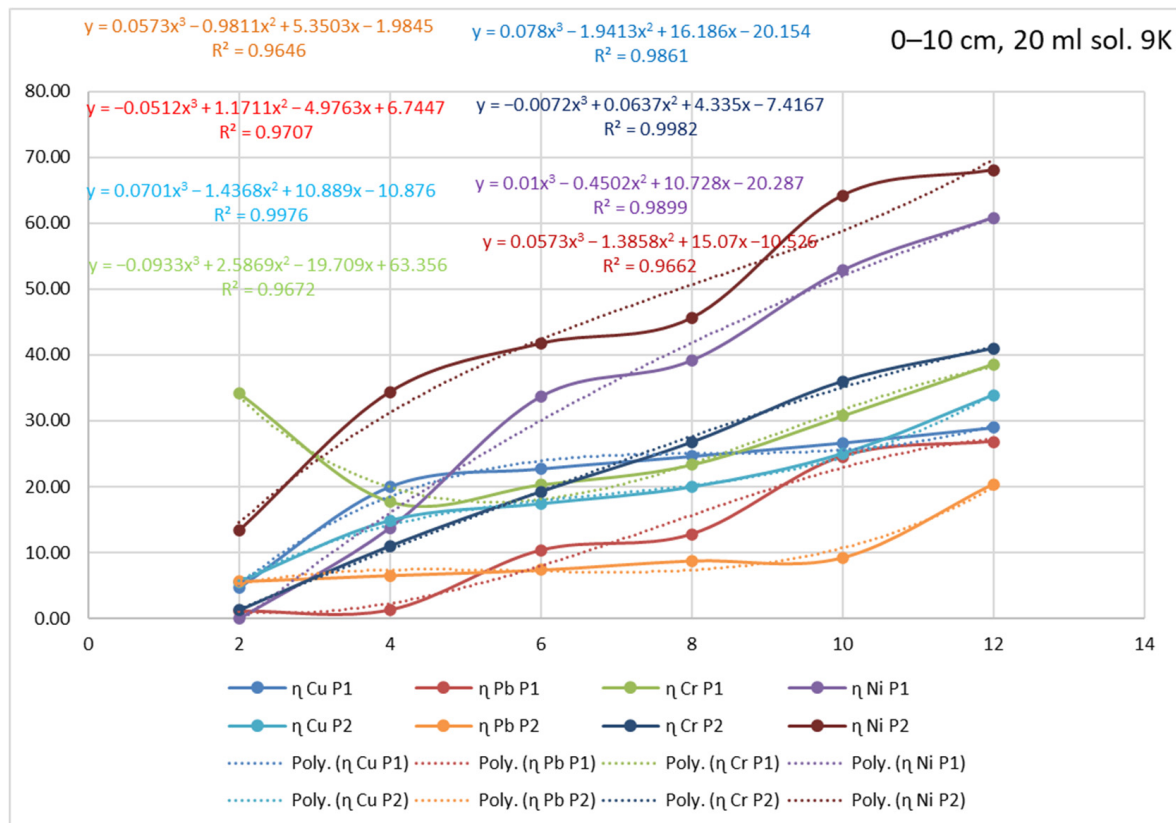
Figure 15. Identification of equations and yield–time correlation indices for P1 and P2 samples taken from 0–10 cm depth and treated with 20 mL of 9K medium.

Table 4 shows the correlation equations of the extraction process yield with time and the correlation factor R^2. However, the fact that the mathematical equations identified are of degree three ($ax^3 + bx^2 + cx + d$) leads to the hypothesis that, although time might be the main determinant of the yield process, there are other influencing factors. Among them, the most important is the type of polluting metal and its concentration. The importance of identifying these yield–time correlation equations lines is the possibility of demonstrating the influence that the exposure time has on the yield of the process, or more precisely, the need to carry out longer tests to demonstrate and quantify the efficiency of this method

of depollution. On the other hand, based on these equations, it is possible to estimate the duration necessary for the process of extraction by bioleaching to obtain the best results, i.e., maximum yield, and to restore the ecological balance of the soil. Analyzing the relationships, two exceptions are observed for Pb ($R^2 = 0.8697$) and Ni ($R^2 = 0.734$). These equations are not considered to be representative for assessing the evolution of the decontamination phenomenon. It is considered that these situations may be due to the high degree of inhomogeneity of the soil sample.

When analyzing the rate of reduction of the pollutant concentration, different results can be observed, as the kinetics of this process can be appreciated, over time, with a significantly good accuracy ($R^2 > 0.95$) for some polluted metals, respectively, with a lower accuracy for other samples analyzed ($0.85 < R^2 < 0.9$). The results show that for samples extracted from area P1 (in terms of Pb) and area P2 (in terms of Cu) the kinetics of the phenomenon cannot be appreciated as having an evolution characterized by an equation as a function of time. Therefore, the rate of depollution is considered to depend on a combination of several factors, not just time.

The results obtained in the research regarding extraction yields for Pb (10–32%) support the claims of Blais J.F. (10–54%) [43], Chen S.Y. (16–60%) [50] and Beolchini F. (18%) [40], but the yields are slightly lower than those obtained by Chen S.Y. (33–72%) [33], Zhou Q. (39%) [42] and Li Q. (75–84%) [49].

The results obtained in the case of Cu and Pb are similar to those obtained by other researchers, while in the case of Cr and Ni, higher yields were obtained than in most of the studies studied. For example, Cr was extracted by 39–72%, while Beolchini F. (14%) [40], Blais J.F. (10–41%) [43] and Chen S.Y (9–20%) [51] obtained lower yields, and at the opposite pole are the results obtained by Li Q. who extracted 53–92% of Cr [49].

The Ni concentrations extracted (44–68%) are comparable to those of Chen S.Y. (35–65%) [51], much lower than those of Blais J.F. (69–92%) [43], Beolchini F. (78%) [40], Kamizela T. (90%) [33], but higher than the yields obtained by Chen S.Y. (10–47%) [51].

The Cu yield (39–72%) falls within the same values as those obtained by Duyusen G. 44% [39] and Beolchini F. 46% [40], but most studies in the literature show higher yields with values above 80% [31,43,47,48] or even above 95% [44,45,49,50].

The investigated samples show very high values for the investigated indices (C_d, PLI and PERI) indicating that the investigated areas have a high level of soil pollution with a strong anthropogenic influence. This demonstrates that the two areas show complex, multi-element contamination, typical of areas with a long history of mining-specific industrial activities, and is comparable with the results of studies reported by other researchers [71–73].

Table 4. Correlation equations of extractive process yield with time and correlation factor R^2.

Code	Sampling Depth [cm]	Pollutant	Correlation Equation of Extraction Yield with Time	Correlation Index, R^2
			20 mL 9K medium	
P1	0–10	Cu	$y = 0.078x^3 - 1.9413x^2 + 16.186x - 20.154$	$R^2 = 0.9861$
		Pb	$y = -0.0512x^3 + 1.1711x^2 - 4.9763x + 6.7447$	$R^2 = 0.9707$
		Cr	$y = -0.0933x^3 + 2.5869x^2 - 19.709x + 63.356$	$R^2 = 0.9672$
		Ni	$y = 0.01x^3 - 0.4502x^2 + 10.728x - 20.287$	$R^2 = 0.9899$
	10–20	Cu	$y = -0.1323x^3 + 2.9061x^2 - 15.246x + 46.49$	$R^2 = 0.9751$
		Pb	$y = -0.0002x^3 + 0.0314x^2 + 0.7325x - 0.8138$	$R^2 = 0.9982$
		Cr	$y = 0.0557x^3 - 1.5327x^2 + 15.658x - 20.428$	$R^2 = 0.9927$
		Ni	$y = -0.0779x^3 + 1.3926x^2 - 2.5333x + 8.6472$	$R^2 = 0.9811$
	20–30	Cu	$y = -0.0195x^3 + 0.5892x^2 - 3.0349x + 54.717$	$R^2 = 0.9442$
		Pb	$y = 0.0309x^3 - 0.5623x^2 + 3.5127x - 4.8439$	$R^2 = 0.9667$
		Cr	$y = 0.0114x^3 - 0.1962x^2 + 2.8585x + 17.582$	$R^2 = 0.9985$
		Ni	$y = 0.0204x^3 - 0.3889x^2 + 5.0498x + 17.721$	$R^2 = 0.9679$

Table 4. *Cont.*

Code	Sampling Depth [cm]	Pollutant	Correlation Equation of Extraction Yield with Time	Correlation Index, R^2
P2	0–10	Cu	$y = 0.0701x^3 - 1.4368x^2 + 10.889x - 10.876$	$R^2 = 0.9976$
		Pb	$y = 0.0573x^3 - 0.9811x^2 + 5.3503x - 1.9845$	$R^2 = 0.9646$
		Cr	$y = -0.0072x^3 + 0.0637x^2 + 4.335x - 7.4167$	$R^2 = 0.9982$
		Ni	$y = 0.0573x^3 - 1.3858x^2 + 15.07x - 10.526$	$R^2 = 0.9662$
	10–20	Cu	$y = 0.0322x^3 - 0.4043x^2 + 3.4665x + 11.779$	$R^2 = 0.9548$
		Pb	$y = -0.0095x^3 + 0.3439x^2 - 1.1457x + 1.1673$	$R^2 = 0.9989$
		Cr	$y = 0.129x^3 - 2.7375x^2 + 20.897x - 30.102$	$R^2 = 0.9934$
		Ni	$y = 0.122x^3 - 2.5767x^2 + 20.829x - 22.926$	$R^2 = 0.9794$
	20–30	Cu	$y = 0.0581x^3 - 1.245x^2 + 10.208x - 8.3601$	$R^2 = 0.9869$
		Pb	$y = 0.019x^3 - 0.2151x^2 + 1.2339x + 4.9123$	$R^2 = 0.9924$
		Cr	$y = 0.0645x^3 - 1.3256x^2 + 10.484x + 20.104$	$R^2 = 0.9706$
		Ni	$y = -0.0881x^3 + 1.7938x^2 - 4.9839x + 8.3115$	$R^2 = 0.9875$
40 mL 9K medium				
P1	0–10	Cu	$y = 0.0761x^3 - 1.9138x^2 + 15.763x - 11.866$	$R^2 = 0.9259$
		Pb	$y = -0.0866x^3 + 1.7478x^2 - 6.8215x + 10.062$	$R^2 = 0.9982$
		Cr	$y = 0.0075x^3 - 0.1242x^2 + 4.1427x + 11.239$	$R^2 = 0.9583$
		Ni	$y = 0.2053x^3 - 5.0242x^2 + 39.427x - 59.204$	$R^2 = 0.9726$
	10–20	Cu	$y = 0.0237x^3 - 0.4359x^2 + 5.534x + 17.352$	$R^2 = 0.9646$
		Pb	$y = 0.0128x^3 - 0.2366x^2 + 2.2303x - 1.0236$	$R^2 = 0.9965$
		Cr	$y = 0.0966x^3 - 2.2616x^2 + 18.62x - 12.941$	$R^2 = 0.986$
		Ni	$y = 0.1115x^3 - 2.7581x^2 + 21.812x - 6.0412$	$R^2 = 0.9615$
	20–30	Cu	$y = -0.0089x^3 + 0.2983x^2 - 0.4406x + 52.492$	$R^2 = 0.9773$
		Pb	$y = 0.0165x^3 - 0.2933x^2 + 2.2293x - 1.6559$	$R^2 = 0.8697$
		Cr	$y = 0.0114x^3 - 0.2845x^2 + 3.5453x + 27.473$	$R^2 = 0.9972$
		Ni	$y = 0.1245x^3 - 3.0828x^2 + 24.233x - 2.42$	$R^2 = 0.9588$
P2	0–10	Cu	$y = -0.0579x^3 + 1.3477x^2 - 5.7293x + 20.904$	$R^2 = 0.9894$
		Pb	$y = 0.0168x^3 - 0.2763x^2 + 2.8752x + 1.5814$	$R^2 = 0.9967$
		Cr	$y = -0.1264x^3 + 3.0672x^2 - 18.985x + 54.917$	$R^2 = 0.982$
		Ni	$y = 0.0954x^3 - 2.084x^2 + 18.132x - 11.345$	$R^2 = 0.9766$
	10–20	Cu	$y = -0.0748x^3 + 1.3971x^2 - 2.7604x + 18.546$	$R^2 = 0.9819$
		Pb	$y = 0.018x^3 - 0.288x^2 + 3.0948x - 4.9287$	$R^2 = 0.9718$
		Cr	$y = 0.1227x^3 - 2.3933x^2 + 18.265x - 17.483$	$R^2 = 0.9607$
		Ni	$y = 0.1477x^3 - 3.2954x^2 + 26.529x - 30.769$	$R^2 = 0.9905$
	20–30	Cu	$y = 0.0826x^3 - 2.1972x^2 + 19.483x - 22.508$	$R^2 = 0.9825$
		Pb	$y = -0.0656x^3 + 1.3786x^2 - 6.4111x + 16.04$	$R^2 = 0.9709$
		Cr	$y = 0.0245x^3 - 0.2959x^2 + 3.2722x + 33.177$	$R^2 = 0.9967$
		Ni	$y = 0.1461x^3 - 3.7235x^2 + 31.939x - 41.032$	$R^2 = 0.734$

4. Conclusions

Results obtained on the analyzed soil samples used in the current study showed that the soil is well structured, has a sandy loam texture, a medium acidic to highly acidic reaction and is highly contaminated with metals, exceeding normal values or even exceeding the alert and intervention thresholds, according to Romanian legislation.

Analyzing the ecological risk (Er) (Pb > Ni > Cu > Cr) and the contamination index (C_f) (Pb > Cu > Ni > Cr) revealed that the greatest danger is posed by Pb, and at the opposite pole is Cr. Analyzing the PERI, we can conclude that the potential ecological risk index differs in the two studied areas, so that the samples from area P1 predict a significantly high risk and those from area P2, a moderate ecological risk. Thus, after analyzing the results of C_d, PLI and PERI, which have very high values for all the samples analyzed, it can be stated that the soils in the studied area have a very high degree of pollution, which is caused by anthropogenic activity in the area.

The results obtained by the extraction of metals by bioleaching allowed us to highlight the factors influencing the yield of the process, these being mainly the amount of bioleaching solution and the duration of the extraction process. It was found, for all metals investigated, that a higher amount of bioleaching solution allows for the obtaining of a higher metal extraction efficiency. It can be appreciated that a longer time duration leads to a higher yield of the extraction process.

The identification of the yield–time correlation equations allows the possibility of demonstrating the influence that the exposure time has on the yield of the process and the appreciation of the necessary duration of the extraction process by bioleaching to obtain the best results, i.e., maximum yield, and to restore the ecological balance at soil level.

References

1. *Healthy Environments for Healthier Populations: Why Do They Matter, and What Can We Do?* Licence: CC BYNC-SA 3.0 IGO., Printed in Geneva, Switzerland (WHO/CED/PHE/DO/19.01); World Health Organization: Geneva, Switzerland, 2019.
2. Manisalidis, I.; Stavropoulou, E.; Stavropoulos, A.; Bezirtzoglou, E. Environmental and Health Impacts of Air Pollution: A Review. *Front. Public Health* **2020**, *8*, 14. [CrossRef] [PubMed]
3. Dumitru, M.; Manea, A.; Ciobanu, C.; Dumitru, S.; Vrînceanu, N.; Calciu, I.; Tănase, V.; Pred, M.; Rîşnoveanu, I.; Mocanu, V.; et al. *Monitoring the Quality of Soils in Romania*; Institute for Soil Science Agro-Chemistry and Environment-ICPA: Bucureşti, Romania; Editura Sitech: Craiova, Romania, 2011; Available online: https://www.icpa.ro/proiecte/Proiecte%20nationale/monitoring/atlasICPA.pdf (accessed on 15 April 2022). (In Romanian)
4. Briffa, J.; Sinagra, E.; Blundell, R. Heavy metal pollution in the environment and their toxicological effects on humans. *Heliyon* **2020**, *6*, e04691. [CrossRef] [PubMed]
5. Akhtar, N.; Syakir Ishak, M.I.; Bhawani, S.A.; Umar, K. Various Natural and Anthropogenic Factors Responsible for Water Quality Degradation: A Review. *Water* **2021**, *13*, 2660. [CrossRef]
6. Kumar, V.; Radziemska, M. Impact of physiochemical properties, microbes and biochar on bioavailability of toxic elements in the soil: A review. *Environ. Geochem. Health* **2021**, 34811628. [CrossRef] [PubMed]
7. Kumar, V.; Sharma, A.; Cerdà, A. *Heavy Metals in the Environment: Impact, Assessment, and Remediation*; Elsevier: Amsterdam, The Netherlands, 2020. [CrossRef]
8. Weissmannová, H.D.; Pavlovský, J. Indices of soil contamination by heavy metals-Methodology of calculation for pollution assessment (minireview). *Environ. Monit. Assess.* **2017**, *189*, 616. [CrossRef] [PubMed]
9. Ludusan, N. The effects of heavy metal accumulation in soils on the biotic component of the Zlatna Depression. *Cadastre Rev.* **2007**, *7*, 189–194. (In Romanian)
10. Micle, V.; Neag, G. *Soil and Groundwater Remediation Processes and Equipment*; UT Press: Cluj-Napoca, Romania, 2009; ISBN 978-973-662-447-6. (In Romanian)
11. Zeng, J.; Gou, M.; Tang, Y.Q.; Li, G.Y.; Sun, Z.Y.; Kida, K.J. Effective bioleaching of chromium in tannery sludge with an enriched sulfur-oxidizing bacterial community. *Bioresour. Technol.* **2016**, *218*, 859–866. [CrossRef]
12. Zheng, C.H.; Huang, Y.J.; Guo, J.S.; Cai, R.Y.; Zheng, H.D.; Lin, C.; Chen, Q.G. Investigation of cleaner sulfide mineral oxidation technology: Simulation and evaluation of stirred bioreactors for gold-bioleaching process. *J. Clean. Prod.* **2018**, *192*, 364–375. [CrossRef]
13. Liu, Y.-G.; Zhou, M.; Zeng, G.-M.; Wang, X.; Li, X.; Fan, T.; Xu, W.-H. Bioleaching of heavy metals from mine tailings by indigenous sulfur-oxidizing bacteria: Effects of substrate concentration. *Bioresour. Technol.* **2008**, *99*, 4124–4129. [CrossRef]

14. Băbuţ, C.S.; Micle, V.; Potra, A.F. Reflection on Remediation of Heavy Metals Contaminated Soils Using Bioleaching. In *Analele Universităţii Constantin Brâncuşi, Seria Inginerie*; Universităţii Constantin Brâncuşi: Târgu Jiu, Romania, 2011; Volume 3, pp. 368–378.

15. Jerez, C.A. Biomining Microorganisms: Molecular Aspects and Applications in Biotechnology and Bioremediation—Soil Biology. In *Advances in Applied Bioremediation*; Springer: Berlin/Heidelberg, Germany, 2009.

16. Chen, X. Thriving at Low pH: Adaptation Mechanisms of Acidophiles. In *Acidophiles—Fundamentals and Applications*; Lin, J., Chen, L., Lin, J., Eds.; IntechOpen: London, UK, 2021; Available online: https://www.intechopen.com/chapters/75730 (accessed on 15 April 2022). [CrossRef]

17. Barrie Johnson, D. Biodiversity and ecology of acidophilic microorganisms. *FEMS Microbiol. Ecol.* **1998**, *27*, 307–317. [CrossRef]

18. Falagán, C.; Barrie Johnson, D. The significance of pH in dictating the relative toxicities of chloride and copper to acidophilic bacteria. *Res. Microbiol.* **2018**, *169*, 552–557. [CrossRef]

19. Jayesh, D.-S.-D.-M. *Bioleaching of Lateritic Nickel Ore Using Chemolithotrophic Microorganisms (Acidithiobacillus ferrooxidans)*; National Institute of Technology Rourkela: Rourkela, India, 2007.

20. Chen, S.-Y.; Lin, J.-G. Bioleaching of heavy metals from contaminated sediment by indigenous sulfur-oxidizing bacteria in an air-lift bioreactor: Effects of sulfur concentration. *Water Res.* **2004**, *38*, 3205–3214. [CrossRef] [PubMed]

21. Volke Sepúlveda, T.; Juan, A.; Velasco Trejo, J.A.; de la Rosa Pérez, D.A. *Suelos Contaminados por Metales y Metaloides: Muestreo y Alternativas Para su Remediación*; Secretaría de Medio Ambiente y Recursos Naturales; Instituto Nacional de Ecología: Mexico City, Mexico, 2005.

22. Rawlings, D.E.; Kusano, T. Molecular genetics of *Thiobacillus ferrooxidans*. *Microbiol. Rev.* **1994**, *58*, 39–55. [CrossRef] [PubMed]

23. Kowalska, J.B.; Mazurek, R.; Gasiorek, M.; Zaleski, T. Pollution indices as useful tools for the comprehensive evaluation of the degree of soil contamination—A review. *Environ. Geochem. Health* **2018**, *40*, 2395–2420. [CrossRef] [PubMed]

24. Golia, E.E.; Papadimou, S.G.; Cavalaris, C.; Tsiropoulos, N.G. Level of Contamination Assessment of Potentially Toxic Elements in the Urban Soils of Volos City (Central Greece). *Sustainability* **2021**, *13*, 2029. [CrossRef]

25. Muller, G. Index of geoaccumulation in sediments of the Rhine River. *GeoJournal* **1969**, *2*, 108–118.

26. Hakanson, L. An ecological risk index for aquatic pollution control a sedimentological approach. *Water Res.* **1980**, *14*, 975–1001. [CrossRef]

27. Islam, M.S.; Ahmed, M.K.; Al-Mamun, M.H. Metal speciation in soil and health risk due to vegetables consumption in Bangladesh. *Environ. Monit. Assess.* **2015**, *187*, 288–303. [CrossRef]

28. Shaheen, S.M.; Shams, M.S.; Khalifa, M.R.; El-Daly, M.A.; Rinklebe, J. Various soil amendments and wastes affect the (im)mobilization and phytoavailability of potentially toxic elements in a sewage effluent irrigated sandy soil. *Ecotoxicol. Environ. Saf.* **2017**, *142*, 375–387. [CrossRef]

29. Setia, R.; Dhaliwal, S.S.; Kumar, V.; Singh, R.; Dhir, N.; Surinder, S.; Kukal, S.S.; Pateriya, B. Assessment of metal contamination in sediments of a perennial river in India using pollution indices and multivariate statistics. *Arab. J. Geosci.* **2021**, *14*, 2190. [CrossRef]

30. Ke, X.; Gui, S.; Huang, H.; Zhang, H.; Wang, C.; Guo, W. Ecological risk assessment and source identification for heavy metals in surface sediment from the Liaohe River protected area, China. *Chemosphere* **2017**, *175*, 473–481. [CrossRef] [PubMed]

31. Rouchalova, D.; Rouchalova, K.; Janakova, I.; Cablik, V.; Janstova, S. Bioleaching of Iron, Copper, Lead, and Zinc from the Sludge Mining Sediment at Different Particle Sizes, pH, and Pulp Density Using *Acidithiobacillus ferrooxidans*. *Minerals* **2020**, *10*, 1013. [CrossRef]

32. Groudev, S.N.; Georgiev, P.S.; Komnitsas, K. In Situ Bioremediation of a Soil Contaminated with Heavy Metals and Arsenic. In Proceedings of the Bioremediation of Inorganic Compounds: The Sixth International in Situ and On-Site Bioremediation Symposium, San Diego, CA, USA, 4–7 June 2001; Leeson, A., Peyton, B.M., Means, J.L., Magar, V.S., Eds.; Volume 6, pp. 97–103.

33. Kamizela, T.; Worwag, M. Processing of Water Treatment Sludge by Bioleaching. *Energies* **2020**, *13*, 6539. [CrossRef]

34. Peng, G.; Tian, G.; Liu, J.; Bao, Q.; Zang, L. Removal of heavy metals from sewage sludge with a combination of bioleaching and electrokinetic remediation technology. *Desalination* **2011**, *271*, 100–104. [CrossRef]

35. Pathak, A.; Dastidar, M.G.; Sreekrishnan, T.R. Bioleaching of heavy metals from sewage sludge: A review. *J. Environ. Manag.* **2009**, *90*, 2343–2353. [CrossRef]

36. Johnson, D.B. Biomining—biotechnologies for extracting and recovering metals from ores and waste materials. *Curr. Opin. Biotechnol.* **2014**, *30*, 24–31. [CrossRef]

37. Kim, B.-J.; Koh, Y.-K.; Kwon, J.-S. Bioleaching of Pyrrhotite with Bacterial Adaptation and Biological Oxidation for Iron Recovery. *Metals* **2021**, *11*, 295. [CrossRef]

38. Podder, P.; Zhang, Z.; Honaker, R.Q.; Free, M.L.; Sarswat, P.K. Evaluating and Enhancing Iron Removal via Filterable Iron Precipitates Formation during Coal-Waste Bioleaching. *Eng* **2021**, *2*, 632–642. [CrossRef]

39. Duyusen, G.; Gorkem, A. Heavy metals partitioning in the sediments of Izmir Inner Bay. *J. Environ. Sci.* **2008**, *20*, 413–418. [CrossRef]

40. Beolchini, F.; Dell'Anno, A.; Fonti, V.; Rocchetti, L.; Ubaldini, S.; Vegliò, F.; Danovaro, R. Bioleaching as a bioremediation strategy for dredged sediments polluted by heavy metals. In Proceedings of the 4th European Bioremediation Conference, Chania, Greece, 3–6 September 2008; pp. 1–5.

41. Couillard, D.; Chartier, M.; Mercier, G. Study of the abduction of Cd, Cu, Mn and Zn by biological solubilization in the lacustrine sediments heavily contaminated. *J. Water Sci.* **1994**, *7*, 251–268.

42. Zhou, Q.; Gao, J.; Li, Y.; Zhu, S.; He, L.; Nie, W.; Zhang, R. Bioleaching in batch tests for improving sludge dewaterability and metal removal using *Acidithiobacillus ferrooxidans* and *Acidithiobacillus thiooxidans* after cold acclimation. *Water Sci. Et Technol.* **2017**, *76*, 1347–1359. [CrossRef] [PubMed]

43. Blais, J.F.; Tyagi, R.D.; Auclair, J.C. Bioleaching of metals from sewage sludge: Microorganisms and growth kinetics. *Water Res.* **1993**, *27*, 101–110. [CrossRef]

44. Ivănuş, R.C.; Bică, G. Economic aspects the bioleaching of polluting waste containing copper. *Studia Univ. "Vasile Goldiş" Ser. Econ. Sci.* **2007**, *12*, 109–117.

45. Ivănuş, R.C. *Bioleaching Solubilization*; Universitaria Press: Craiova, Romania, 2005. (In Romanian)

46. Wang, J.; Qin, W.-Q.; Zhang, Y.-S.; Yang, C.-R.; Zhang, J.-W.; Nai, S.-S.; Shang, H.; Qiu, G.-Z. Bacterial leaching of chalcopyrite and bornite with native bioleaching microorganism. *Trans. Nonferrous Met. Soc. China* **2008**, *18*, 1468–1472. [CrossRef]

47. Nakade, D.B. Biomining of Copper Using Halophilic Thiobacillus ferroxidans N-9. *Adv. Life Sci.* **2013**, *2*, 19–22.

48. Conić, V.T.; Rajčić Vujasinović, M.M.; Trujić, V.K.; Cvetkovski, V.B. Copper, Zinc, and Iron Bioleaching from Polymetallic Sulphide Concentrate. *Trans. Nonferrous Met. Soc. China* **2014**, *24*, 3688–3695. [CrossRef]

49. Li, Q.; Wang, C.; Li, B.; Sun, C.; Deng, F.; Song, C.; Wang, S. Isolation of *Thiobacillus* spp. and its application in the removal of heavy metals from activated sludge. *Afr. J. Biotechnol.* **2012**, *11*, 16336–16341.

50. Chen, S.Y.; Chiu, Y.C.; Chang, P.L.; Lin, J.G. Assessment of recoverable forms of sulphur particles used in bioleaching of contaminated sediments. *Water Res.* **2003**, *37*, 450–458. [CrossRef]

51. Chen, S.Y.; Lin, J.G. Influence of solid content on bioleaching of heavy metals from contaminated sediment by *Thiobacillus* spp. *J. Chem. Technol. Biotechnol.* **2000**, *75*, 649–656. [CrossRef]

52. *STAS 7184/1-84*; Soils. Sampling for Pedological and Agrochemical Studies. ASRO: Bucharest, Romania, 1984. (In Romanian)

53. *SR ISO 11464:1998*; Soil Quality. Pretreatment of Samples for Physico-Chemical Analysis. ASRO: Bucharest, Romania, 1998. (In Romanian)

54. Sur, I.M.; Micle, V.; Polyak, E.T.; Gabor, T. Assessment of Soil Quality Status and the Ecological Risk in the Baia Mare, Romania Area. *Sustainability* **2022**, *14*, 3739. [CrossRef]

55. Babau, A.M.C.; Micle, V.; Damian, G.E.; Sur, I.M. Sustainable Ecological Restoration of Sterile Dumps Using Robinia pseudoacacia. *Sustainability* **2021**, *13*, 14021. [CrossRef]

56. Damian, G.E.; Micle, V.; Sur, I.M.; Chirila Babau, A.M. From environmental ethics to sustainable decision making: Assessment of potential ecological risk in soils around abandoned mining areas-case study "Larga de Sus mine" (Romania). *J. Agric. Environ. Ethics* **2019**, *32*, 27–49. [CrossRef]

57. Silverman, M.P.; Lundgren, D.G. Studies on the chemoautotrophic iron bacterium *Ferrobacillus ferrooxidans*. I. An imnproved medium and a harvesting procedure for securing high cell yields. *J. Bacteriol.* **1959**, *77*, 642–647. [CrossRef] [PubMed]

58. Levei, E.; Frentiu, T.; Ponta, M.; Tanaselia, C.; Borodi, G. Characterization and assessment of potential environmental risk of tailings stored in seven impoundments in the Aries river basin, Western Romania. *Chem. Cent. J.* **2013**, *7*, 5. [CrossRef] [PubMed]

59. Saha, S.; Hazra, G.C.; Saha, B.; Mandal, B. Assessment of heavy metals contamination in different crops grown in long-term sewage-irrigated areas of Kolkata, West Bengal, India. *Environ. Monit. Assess.* **2015**, *187*, 4087. [CrossRef] [PubMed]

60. Kabata-Pendias, A. *Trace Elements in Soils and Plants*, 4th ed.; CRC Press: Boca Raton, FL, USA, 2010. [CrossRef]

61. Kükrer, S.; Şeker, S.S.; Murathan, Z.T.; Kutlu, B. Ecological risk assessment of heavy metals in surface sediments of northern littoral zone of Lake Cildir, Ardahan, Turkey. *Environ. Monit. Assess.* **2014**, *186*, 3847–3857. [CrossRef]

62. Gong, Q.; Deng, J.; Xiang, Y.; Wang, Q.; Yang, L. Calculating Pollution Indices by Heavy Metals in Ecological Geochemistry Assessment and a Case Study in Parks of Beijing. *J. China Univ. Geosci.* **2008**, *19*, 230–241. [CrossRef]

63. Yan, T.; Zhao, W.; Yu, X.; Li, H.; Gao, Z.; Ding, M.; Yue, J. Evaluating heavy metal pollution and potential risk of soil around a coal mining region of Tai'an City, China. *Alex. Eng. J.* **2022**, *61*, 2156–2165. [CrossRef]

64. Bahemmat, M.; Farahbakhsh, M.; Kianirad, M. Humic Substances-enhanced Electroremediation of Heavy Metals Contaminated Soil. *J. Hazard. Mater.* **2016**, *312*, 307. [CrossRef]

65. USEPA. *Treatment Technologies for Site Cleanup*; Annual Status Report; United States Environmental Protection Agency: Washington, DC, USA, 2007.

66. *Order No. 756 of 3 November 1997 for the Approval of the Regulation on Environmental Pollution Assessmen*; Published in: Official Gazette No 303 bis of 6 November 1997; Ministry of Waters, Forests and Environmental Protection: Bucharest, Romania. Available online: http://legislatie.just.ro/Public/DetaliiDocumentAfis/151788 (accessed on 15 April 2022). (In Romanian).

67. Qian, J.; Wei, L.; Liu, R.; Jiang, F.; Hao, X.; Chen, G.H. An exploratory study on the pathways of Cr (VI) reduction in sulfate-reducing up-flow anaerobic sludge bed (UASB) reactor. *Sci. Rep.* **2016**, *6*, 23694. [CrossRef]

68. Chen, S.-Y.; Wang, S.-Y. Effects of Solid Content and Substrate Concentration on Bioleaching of Heavy Metals from Sewage Sludge Using *Aspergillus niger*. *Metals* **2019**, *9*, 994. [CrossRef]

69. Elkina, Y.; Nechaeva, A.; Artykova, A.; Kolosoff, A.; Bugubaeva, A.; Melamud, V.; Mardanov, A.; Bulaev, A. Continuous Bioleaching of Arsenic-Containing Copper-Zinc Concentrate and Shift of Microbial Population under Various Conditions. *Minerals* **2022**, *12*, 592. [CrossRef]

70. Kaur, P.; Sharma, S.; Albarakaty, F.M.; Kalia, A.; Hassan, M.M.; Abd-Elsalam, K.A. Biosorption and Bioleaching of Heavy Metals from Electronic Waste Varied with Microbial Genera. *Sustainability* **2022**, *14*, 935. [CrossRef]

71. Rinklebe, J.; Antoniadis, V.; Shaheen, S.M.; Rosche, O.; Altermann, M. Health risk assessment of potentially toxic elements in soils along the Central Elbe River, Germany. *Environ. Int.* **2019**, *126*, 76–88. [CrossRef] [PubMed]

72. Gabersek, M.; Gosar, M. Geochemistry of urban soil in the industrial town of Maribor, Slovenia. *J. Geochem. Explor.* **2018**, *187*, 141–154. [CrossRef]

73. Antoniadis, V.; Golia, E.E.; Liu, Y.; Wang, S.; Shaheen, S.M.; Rinklebe, J. Soil and maize contamination by trace elements and associated health risk assessment in the industrial area of Volos, Greece. *Environ. Int.* **2019**, *124*, 79–88. [CrossRef]

Investigation of the Effects of Roller Spreading Parameters on Powder Bed Quality in Selective Laser Sintering

Xiangwu Xiao [1],*, Yufeng Jin [1], Yuanqiang Tan [2], Wei Gao [3], Shengqiang Jiang [1], Sisi Liu [1] and Meiliang Chen [1],*

[1]   School of Mechanical Engineering, Xiangtan University, Xiangtan 411105, China; 13669902083@163.com (Y.J.); jsqcx@126.com (S.J.); liusisi@xtu.edu.cn (S.L.)
[2]   Institute of Manufacturing Engineering, Huaqiao University, Xiamen 361021, China; tanyq@hqu.edu.cn
[3]   School of Electro-Mechanical Engineering, Guangdong University of Technology, Guangzhou 510006, China; gaowei@gdut.edu.cn
*   Correspondence: xiaoxiangwu@163.com (X.X.); mlchen18@163.com (M.C.)

Abstract: Powder spreading is one of crucial steps in selective laser sintering (SLS), which controls the quality of the powder bed and affects the quality of the printed parts. It is not advisable to use empirical methods or trial-and-error methods that consume lots of manpower and material resources to match the powder property parameters and powder laying process parameters. In this paper, powder spreading in realistic SLS settings was simulated using a discrete element method (DEM) to investigate the effects of the powder's physical properties and operating conditions on the bed quality, characterized by the density characteristics, density uniformity, and flatness of the powder layer. A regression model of the powdering quality was established based on the response surface methodology (RSM). The relationship between the proposed powdering quality index and the research variables was well expressed. An improved multi-objective optimization algorithm of the non-dominated sorting genetic algorithm II (NSGA-II) was used to optimize the powder laying quality of nylon powder in the SLS process. We provided different optimization schemes according to the different process requirements. The reliability of the multi-objective optimization results for powdering quality was verified via experiments.

Keywords: selective laser sintering; spread the powder quality; parameter optimization; DEM; RSM; NSGA-II

1. Introduction

Selective laser sintering (SLS) is one of the typical additive manufacturing processes, which creates objects via scanning and layer-by-layer sintering. As a novel technology used for the design and manufacturing of complex shapes and structures, SLS is implemented a fast rate for automobile, shipbuilding, aerospace, and medical applications [1,2]. The laying of a flat, uniform, and high-density powder bed is the aim when preparing the molded parts to ensure good performance [3,4]. The size accuracy and mechanical properties of the sintered parts are directly affected by the powder laying quality, which is closely related to the powder flow characteristics and powder laying process parameters [5].

Flowability is an essential powder property for the achievement of uniformly spread powder layers [6]. The powder must have appropriate rheological properties to form thin, dense, and uniform powder layers [7]. The commonly used characterization methods for powder fluidity include the angle of repose method, outflow velocity method, Hausner index method, Carr fluidity index method, and shear method [8,9]. The powder flow characteristics depend on many parameters, such as the particle size distribution [10,11], particle shape [12,13], interparticle interaction force [14], and temperature [15]. For example, Wei et al. [16]'s research suggests that the surface shape affects the stability of the particle stacking structure and the uniformity of the pore distribution. Dai et al.'s research showed

that [14] both the sliding friction and rolling friction hinder the particle flowability, leading to a higher angle of repose and a lower packing fraction in the sandpile.

The technological parameters of the roller spreading process are relatively complex, which include the thickness of the powder layer and the diameter, rotation speed, and displacement speed of drum [17]. It is not advisable to optimize the powder laying process through experience and tedious experiments. Therefore, it is necessary to optimize the technological parameters of the roller powder laying process via numerical simulation to improve the spreading properties of the powder. The discrete element method (DEM) has great advantages in simulating the motion of powder systems [18,19]. The basic idea of the DEM is to divide the system into a number of particles, whereby the response of the whole system is described through the mechanical and kinetic states of each particle in the system [20]. The DEM has been widely used to investigate the flow mode and dynamic behavior of powder particles in additive manufacturing and to reveal the effects of the powder laying process on the powder laying quality [21,22]. For instance, Meier [23] studied the influence of the particle size distribution and adhesion forces between particles on the uniformity of the powder layer in additive manufacturing. Tan et al. [24] established a contact model between powder particles, which took van der Waals forces between particles into account. The parameters of the contact model were calibrated experimentally. The powder laying process was simulated, the density uniformity of powder layer was evaluated, and the fluidity of the new powder and residual powder was compared.

It is of great significance to establish the relationship between powder property parameters, powder laying process parameters, and powder laying quality to expand the raw material range of the powder promotion process. The evaluation index of the powder spreading quality can be divided into powder quality (such as the powder density, powder spreading thickness, coverage rate, and surface uniformity) and powder flow morphology (such as deposition rate and avalanche angle change rate) aspects. More scholars are focusing on the influence of the powder laying process on the powder laying quality. Mussatto et al. [7] systematically studied the effects of the powder morphology, diffusion rate, and layer thickness on the powder bed morphology uniformity. Chen [25] studied the fluidity and powder quality of the powder laying process. The results showed that the continuity and stability of the powder flow decrease with the increase in powder spreading speed and the decrease in powder spreading layer thickness, which lead to the deterioration of the bulk density and uniformity. Yao et al. [26] simulated the powder laying process with a 316L stainless steel powder scraper. The effects of technological parameters, the scraper structure, and the powder particle size on the powder laying quality were studied. The optimum process parameters were determined. Parteli et al. [27] developed a DEM numerical tool for the SLS powder laying process, with which the characteristics of the powder layer deposited on the parts are studied by applying it to the roller powder dispensing system. The results showed that an increase in powder spreading speed and wider particle size distribution will lead to an increase in the surface roughness of the powder layer, and will ultimately affect the quality of the parts.

The powder laying process parameters and physical powder parameters affect each other and affect the quality of the powder laying process. At present, some researchers still use empirical or trial-and-error methods in this process, which consume more manpower and material resources to match the powder property parameters and powder laying process parameters. Although DEM simulation of the SLS powder laying process can monitor the powder laying quality well, this approach requires a lot of time because the powder size is very small, the simulation system is huge, and the computing capacity is limited. In the development of various optimization methods, the response surface methodology (RSM) and genetic algorithm (GA) are used to optimize parameters to solve engineering problems [28–30]. The multi-objective optimization method, which uses polynomials to fit the relationship between factors and responses, can simplify these engineering problems. The influences of the single factor and interaction factor on the response index were analyzed previously and the optimal parameters were obtained [31].

In this paper, powder spreading in realistic SLS settings was simulated using the DEM to investigate the effects of the powder's physical properties and operating conditions on the bed quality, characterized by its density characteristics, density uniformity, and flatness of the powder layer. The central composite design (CCD) approach was used to generate 13 groups of cases and to establish the regression model of the 3 indicators. A regression model of the powdering quality was established based on the response surface methodology. According to the analysis of variance (ANOVA), the influences of single factors and their interactions on the response indicators were determined. Multi-objective optimization was carried out for the drum powder laying parameters and the optimization results were verified via experiments. This study will be helpful to optimize the drum powder laying process parameters and improve the powder laying quality in the SLS process.

2. Methods

2.1. Discrete Element Method

In this model, based on the Hertz–Mindlin model and SLS powder paving process, the particle gravity, collision force between particles (between particles and wall), friction, van der Waals force, and electrostatic force were comprehensively considered to describe the contact dynamic behavior of nylon powder at preheating temperature via DEM. There are two modes of motion, namely translational motion and rotational motion, which describe the motion of particles according to Newton's second law of motion:

$$m_i \frac{dv_i}{dt} = \sum_j F_{ij}^c + \sum_k F_{ik}^{nc} + F_i^g \tag{1}$$

$$I_i \frac{d\omega_i}{dt} = \sum_j M_{ij} \tag{2}$$

where F_{ij}^e is the contact force of particle j to particle i or wall j to particle i, F_{ik}^{nc} is the non-contact force of particle k to particle i or wall k to particle i, and F_i^g is the self-gravity of nylon power i; v_i is the position vector of the particle i, ω_i is the angle vector of the particle i, and M_{ij} is the torque of particle j to particle i or wall j to particle i.

F_{ij}^c can be decomposed into the normal contact force F_{nc} and tangential contact force F_{tc}. The contact force F_{nc} of nylon powder i in the normal direction is composed of the normal elastic force $F_{nc,s}$, normal damping force $F_{nc,d}$, van der Waals F_{nc}^{vdw}, and static force F_{nc}^{ele}:

$$F_{nc} = F_{nc,s} + F_{nc,d} + F_{nc}^{vdw} + F_{nc}^{ele} \tag{3}$$

The Van der Waals forces take into account only the gravitational component based on Hmaker's theory. The normal elastic force $F_{nc,s}$ and normal damping force $F_{nc,d}$ can be obtained according to the Hertz–Mindlin model:

$$F_{n,s}^c = \frac{4}{3} E^* \sqrt{R^*} \delta_n^{3/2} \tag{4}$$

$$F_{n,d}^c = -2\sqrt{\frac{5}{6}} \beta \sqrt{S_n m^*} \overline{v_n^{rel}} \tag{5}$$

where E^* is the equivalent elastic modulus of nylon powder, R^* is the equivalent radius of nylon powder, m^* is the equivalent mass of nylon powder, β is the damping coefficient, and S_n is the normal contact stiffness, the expression of which is as follows:

$$E^* = \frac{E_p}{2(1 - \gamma_p^2)} \tag{6}$$

$$R^* = \left[\frac{1}{R_i} + \frac{1}{R_j} \right]^{-1} \tag{7}$$

$$m^* = \left[\frac{1}{m_i} + \frac{1}{m_j} \right]^{-1} \tag{8}$$

$$\beta = \frac{Ine}{\sqrt{In^2 e + \pi^2}} \tag{9}$$

$$S_n = 2E^* \sqrt{R^* \delta_n} \tag{10}$$

where E_p is the elastic modulus of nylon powder, γ_p is Poisson's ratio of nylon powder, and m_i and m_j are the mass of nylon powder i and j, respectively; e is the recovery coefficient of collision between nylon powders, δ_n is the normal overlap quantity, and $v_n^{\overline{rel}}$ is the normal relative velocity of contacting nylon powder.

Van der Waals forces are inherent in fine particle flows [32]. In the study of fine particle flow, the Hamaker theory is often used to calculate Van der Waals forces between fine particles [33]:

$$F_{PP}^{vdw} = -\frac{\partial U_{PP}^0}{\partial Z_0} = -\frac{A_{pp}}{12Z_0^2} \frac{d_i d_j}{d_i + d_j} \tag{11}$$

$$F_{pw}^{vdw} = -\frac{\partial U_{pw}^0}{\partial Z_0} = -\frac{A_{pw} d_i}{12Z_0^2} \tag{12}$$

where F_{PP}^{vdw} is the Van der Waals force between particles, F_{pw}^{vdw} is the Van der Waals force between particles and walls, d_i and d_j are the diameters of particles i and j, Z_0 is the distance between the particles, A_{pp} is the Hamaker constant between powders, and A_{pw} is the Hamaker constant of the powder and wall.

The friction charge of the powder involves the friction charge between the powder and the wall, as well as between the powders. The electrostatic force between two charged particles is calculated by:

$$F_{pp}^{ele} = \frac{1}{4\pi\varepsilon_0} \frac{q_i q_j}{r_{ij}^2} n_{ij} \tag{13}$$

where q_i and q_j are the charges of particles i and j, respectively; r_{ij} is the distance between the centers of particle i and j, ε_0 is the dielectric constant of vacuum, and n_{ij} is the unit vector from particle i to particle j.

The electrostatic force between the particle and the conducting plane is:

$$F_{pw}^{ele} = \frac{1}{4\pi\varepsilon_0} \frac{q_i^2}{[2(Z_0 + s)]^2} n_{pw} \tag{14}$$

where s is the correction factor and n_{pw} is the unit vector. Refer to the literature for detailed information on static force modeling [34].

2.2. Establishment of Powder Laying Process Model

Nylon powder was selected as the research object in this study. The DEM model of the powder laying process established in this research is based on PA3200 powder. The preheating temperature of the SLS powder laying process is 171 °C. The contact parameters of nylon powder in DEM simulation are calculated according to the inverse parameter results. The DEM simulation results agree well with the experimental results. The reliability and accuracy of the DEM model at preheating temperature were verified.

The above research laid a foundation for the study of the PA3200 SLS powder laying process. Figure 1 shows the SLS powder DEM model established in this study. The construction and verification process of the DEM model are detailed in our previous

work [34,35]. Tables 1 and 2 present the physical parameters and working parameters, respectively, in the SLS powder laying process.
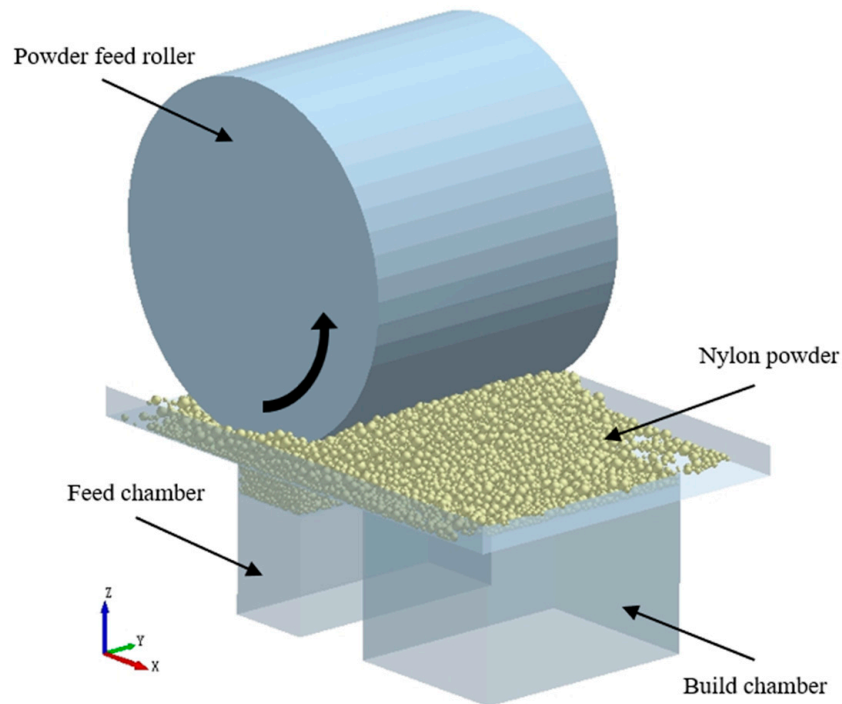
Figure 1. DEM simulation of roller spreading processes.

Table 1. DEM model parameters of PA3200 powder spreading process.

Parameter	Value
Density (kg/m^3)	1000
Shear modulus of powder (MPa)	61
Poisson ratio of power	0.35
Wall density (kg/m^3)	7800
Wall shear modulus (Gpa)	80
Poisson ratio of wall	0.30
Coefficient of sliding friction between powder and wall	0.51
Coefficient of rolling friction between powder and wall	0.15
Hamaker constant between powder and wall	9.72×10^{-20}
Resilience factor between powder and wall	0.52
Coefficient of sliding friction between powders	0.48
Rolling friction coefficient between powder and wall surface	0.24
Springback coefficient between powders	0.11
Hamaker constant between powders (J)	7.21×10^{-20}
Powder charge generation factor	0.03
Power D50 (µm)	50
Number of powder particles	215,000

Table 2. Working parameters of numerical simulation of powder laying process.

Parameter	Value
Drum translational velocity Vs (mm/s)	60, 100, 140, 180, 220, 260, 280, 320
Ratio of drum linear velocity to translational velocity Vr/Vs	0.16, 0.33, 0.50, 0.66, 1.0, 1.31, 2.0, 2.63
Diameter of roller Rg (mm)	4, 12, 20, 24, 28, 32, 36, 40
Powder particle D50 diameter (µm)	30, 40, 50, 60, 70, 80, 90, 100

2.3. Quality Index of Powder Laying

It is necessary to characterize the quality of nylon powder in the molding area before studying the influence of powder laying process parameters and powder property parameters on the quality of nylon powder laying in the molding area. In this study, the quality of powder laying is expressed by the density characteristics, density uniformity, and flatness of the powder layer in the formation area.

A schematic diagram of the area meshing used to measure the apparent density is shown in Figure 2. The density of the powder layer in the formation area is characterized by the ratio of the total particle mass to the particle volume of the layer:

$$\rho = \frac{\sum\limits_{i=1}^{n} m_i}{\sum\limits_{i=1}^{n} v_i} \tag{15}$$

where v_i is the volume of grid i and m_i is the particle mass of grid i.
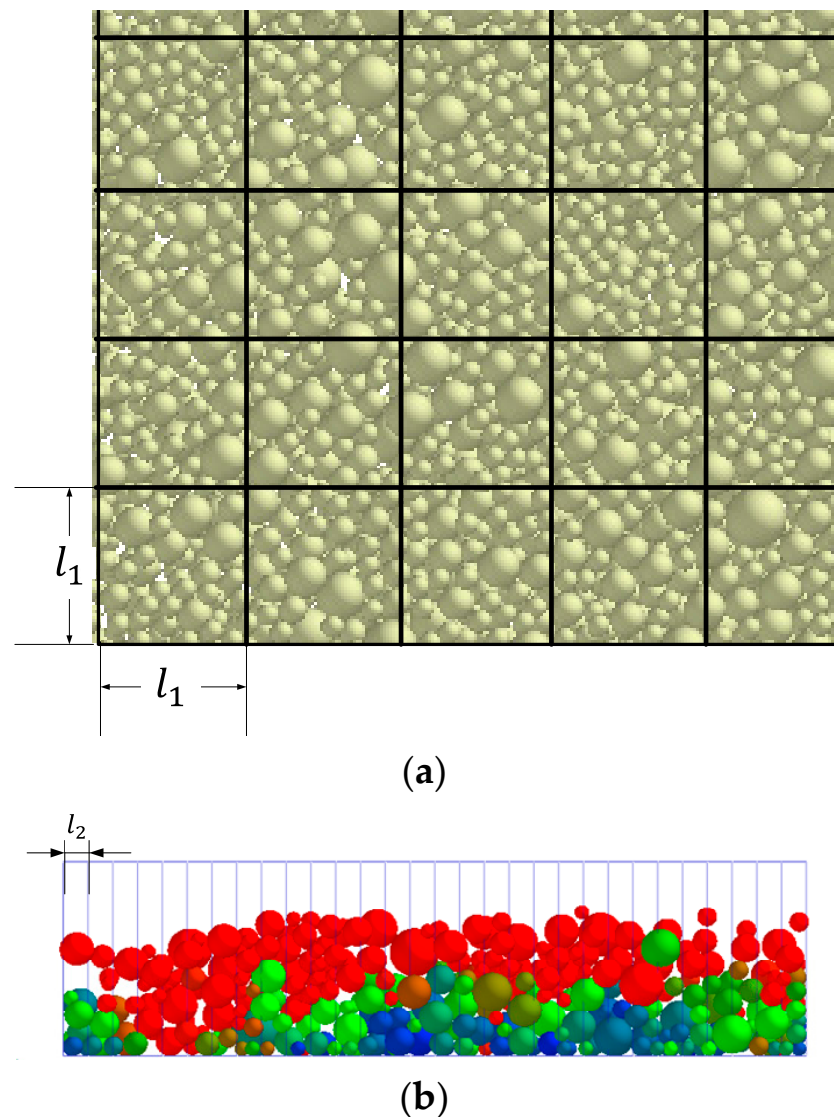

(a)

(b)

Figure 2. Grid division diagram of apparent density statistics: (**a**) meshing of horizontal plane of powder layer in formation area; (**b**) grid division of vertical plane of powder layer in formation area.

The standard deviation of the apparent density of the powder layer in the formation region is denoted by *S*, which can be used to represent the density uniformity of the powder layer. The standard deviation *S* of the apparent density of the powder layer can be expressed as:

$$S = \sqrt{\frac{1}{N-1}\sum_{i=1}^{N}\left(\rho_i' - \overline{\rho'}\right)^2} \qquad (16)$$

where $\overline{\rho'}$ is the average apparent density of particles in the selected box, which is given by:

$$\overline{\rho'} = \frac{\sum_{i=1}^{N}\rho_i'}{N} \qquad (17)$$

Here, R_a is the surface roughness. This can be used to characterize the flatness of the powder layer, which is given by [36]:

$$R_a = \frac{1}{l}\int_0^l |y(x)|dx \qquad (18)$$

where *l* is the sampling length, $y(x)$ is the distance between the contour point and the reference line in the *x* direction, and the reference line is the least squares centerline of the contour.

In order to study the influence of the number of grids on the flatness of the powder layer in the formation area, the sampling lengths on the horizontal and vertical sections are divided by different number of grids. Figure 3 shows the effect of the mesh number on the standard deviation of the apparent density of powder layer $\overline{\rho'}$ in the formation area. It can be seen that $\overline{\rho'}$ increases with the increase in mesh number. When the number of grids increases from 20 to 48, the number of particles in each grid increases, but $\overline{\rho'}$ is less sensitive to the number of grids. The effect of the number of grids on the surface roughness of the powdering layer R_a in the formation area is shown in Figure 4. When the number of grids increases to a certain extent, R_a does not change much. Therefore, the number of grids should not be too large when calculating the surface roughness of the powder layer in the formation area. In order to find out the optimum cell size, the mesh size of the powder layer selection box in the formation area should meet $S_1 \geq 2.5d_{max}$ and $S_2 \leq 0.5d_{min}$. Here, d_{max} is the maximum particle diameter and d_{min} is the minimum particle diameter.
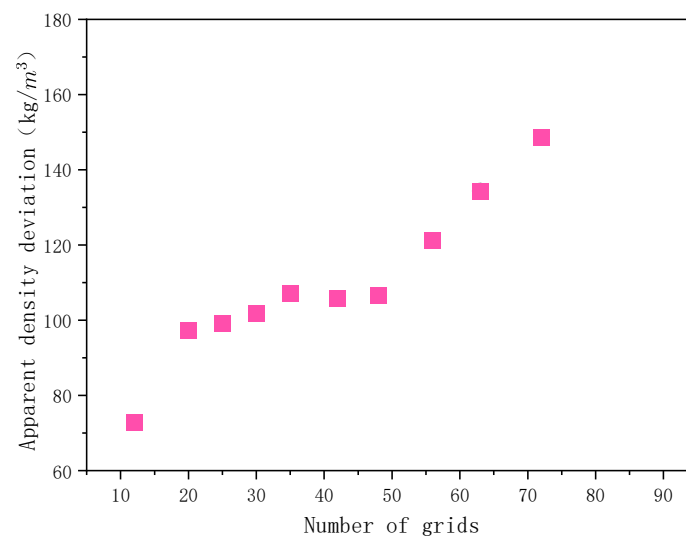

Figure 3. Influence of grid number on standard deviation of the density.
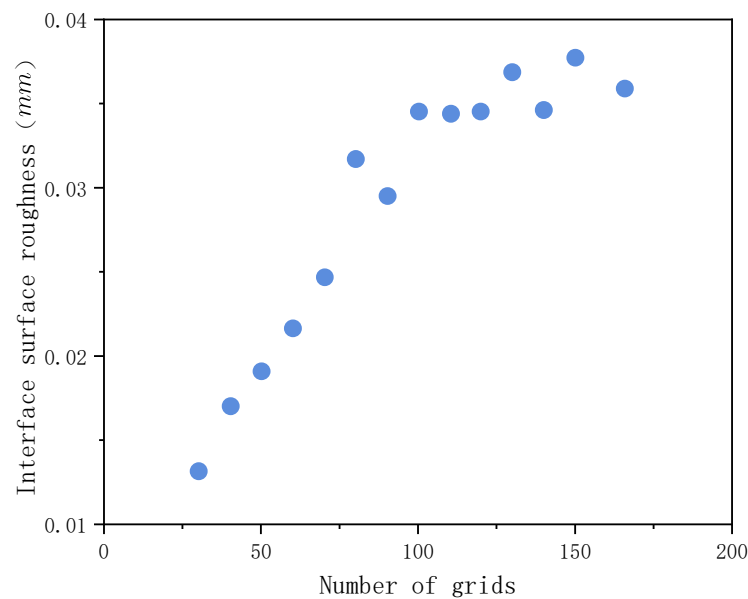
Figure 4. Effect of grid number on surface roughness.

2.4. Response Surface Methodology

The response surface methodology (RSM) proposed by British statisticians Box and Wilson in 1951 [37] is frequently used to approximately fit unknown functions, such as the relationship between variables and responses. In practical applications, RSM establishes mathematical relations through regression analysis of the test results of physical experiments or simulation tests, which can evaluate the relevant factors and their interactions to determine the optimal level range. RSM has been successfully applied to optimize a variety of processes [38–40].

The basic idea of RSM can be summarized as follows:

$$y = f(x_1, x_2, \cdots, x_p) + \varepsilon \tag{19}$$

where y is a variable, $f(x_1, x_2, \cdots, x_p)$ is the response function of factor $x_1, x_2, \cdots, x_p$, and ε is the residual of the construction model.

The second-order response surface model is:

$$y = \beta_0 + \sum_{i=1}^{m} \beta_i x_i + \sum_{i=1}^{m} \beta_{ii} x_i^2 + \sum_{i<j}^{m} \beta_{ij} x_i x_j + \varepsilon \tag{20}$$

where β_0 is the constant term, β_i is the linear effect of x_i, β_{ij} is the interaction effect of x_i and x_j, and β_{ii} is the second-order response of x_i. The second-order response surface method mainly includes the central composite design (CCD), Box–Behnken design, uniform design, and D-optimal design. The most commonly used second-order response surface design method is the central composite design method, which is used to optimize the reaction process parameters or to find the best synthesis conditions [41]. The central composite design method includes the universal rotary composite design, quadratic orthogonal composite design, and others. In this research, the universal rotating combination design is used to design the DEM simulation test scheme.

The general rotating composite design experiment was carried out considering the drum translation speed Vs (mm/s) and particle size d (mm) of D50 as experimental factors. The design factors of the DEM simulation test for the nylon powder laying process are shown in Table 3. The CCD model of RSM was used to generate 13 cases. The response indexes of the apparent density Y_1, standard deviation of the density Y_2, and powder layer roughness Y_3 can be calculated using Equation (18). Table 4 shows the simulation results of the corresponding indicators.

Table 3. Design factor level of DEM simulation test for nylon powder laying process.

Test Factor	−1.414	−1	0	1	1.414
Drum translational velocity *Vs* (mm/s)	68.93	100.00	175.00	250.00	281.07
particle diameter d (μm)	39.46	50.00	75.00	100.00	110.36

Table 4. DEM simulation test scheme and simulation results of powder laying process (*Rg* = 20 mm, *Vr/Vs* = 0.5).

Test No.	Translational Velocity *Vs* (mm/s)	Particle Size D (μm)	Apparent Density (kg/m³)	Standard Deviation of the Density (kg/m³)	Roughness (μm)
1	175.00	75.00	535.00	79.60	42.04
2	100.00	100.00	542.10	113.70	40.60
3	175.00	75.00	535.00	79.60	42.04
4	175.00	39.64	572.20	75.60	43.02
5	250.00	100.00	549.40	124.90	44.21
6	250.00	50.00	558.40	82.50	43.12
7	175.00	75.00	535.00	79.60	42.04
8	175.00	110.36	557.70	133.90	42.14
9	281.07	75.00	535.80	95.10	45.25
10	68.93	75.00	553.30	90.80	44.36
11	100.00	50.00	563.50	67.30	44.37
12	175.00	75.00	535.00	79.60	42.04
13	175.00	75.00	535.00	79.60	42.04

2.5. Multi-Objective Optimization Method Based on Genetic Algorithm

The multi-objective optimization problems (MOP) approach was first proposed by the Italian economist V. Pareto in 1896 [42]. The optimization objective can be expressed as:

$$\min \ Y = F(X) = [F_1(X), F_2(X), \cdots, F_m(X)]$$
$$s.t.g_i(X) \leq 0 \ldots$$
$$h_j(X) = 0, j = 1, 2, \cdots, q$$
(21)

where X is the optimization parameter vector, $X = (x_1, x_2, \cdots, x_m) \in D$, Y is the optimization target vector, and $Y = (f_1, f_2, \cdots f_m) \in F$.

In general, different objectives are in conflict with each other for MOP. There is no single optimal objective solution for MOP, but the Pareto optimal solution is set [43]. The Pareto optimal solution set is defined as $\forall x \in \Omega$; if $x' \in \Omega$ does not exist in the domain Δx, let $(x' + \Delta x) \in \Omega$, when the following conditions are satisfied:

$$F_i(x' + \Delta x) \leq F_i(x')$$
(22)

$$F_j(x' + \Delta x) \leq F_j(x')$$
(23)

We note that $x' \in \Omega$ is the Pareto optimal solution set used for multi-objective optimization.

The non-dominated genetic algorithm II (NSGA-II) is a kind of multi-objective genetic optimization algorithm, which was proposed by Kalyanmoy et al. in 2002 [44]. In this research, the NSGA-II improved algorithm Gamultiobj function provided by MATLAB is used to optimize the powder laying quality.

3. Results and Discussion

3.1. Variance Analysis and Regression Model Establishment

Design-expert 8.0.6 was used to conduct an RSM analysis on the DEM simulation results from the SLS powder laying process shown in Table 4. The response surface equation for the powdering quality can be obtained via regression analysis of the numerical simulation results. The apparent density, standard deviation of the density, and surface roughness formulae of the powder layer in the formation area are as follows:

$$Y_1 = 716.3832 - 0.3129v_s - 3.7645d + 0.0008v_s{}^2 + 0.0234d^2 \tag{24}$$

$$Y_2 = 149.1053 - 0.33340v_s - 2.0568d + 0.0011v_s{}^2 + 0.0194d^2 \tag{25}$$

$$Y_3 = 57.6460 - 0.1181v_s - 0.1330d + 0.0006v_sd + 0.0002dv_s{}^2 \tag{26}$$

where v_s is the translational speed of the drum and d is the diameter of particle D50.

Analysis of variance (ANOVA) is used to test the significance of the fitted second-order regression equation. The drum translation velocity Vs (mm/s) and the particle size D (mm) of the powder D50 are selected as independent variables of the multi-objective optimization model. In the optimization of powder laying process in the formation area, there are three objectives to be optimized, namely the maximum apparent density, the minimum standard deviation of the apparent density, and the minimum surface roughness. The regression model of the powdering quality established by the RSM is the objective function to be optimized, $F_1(x) = -Y_1$, $F_2(x) = -Y_2$, $F_3(x) = -Y_3$.

If the drum speed is too slow, the production efficiency will be affected; if the speed is too fast, the powder laying quality will be reduced. Therefore, the interval constraint is $100 \le Vs \le 300$ (mm/s). The particle size of D50 is mainly controlled by the thickness of the powder layer, and the interval constraint is $50 \le D \le 100$ (μm).

The crossover rate is 0.8, the population size is 100, the maximum evolution algebra is 200, the stop algebra is 200, and the deviation of the fitness function is 10^{-100}. The variation rate is determined by the feasible region adaptation equation. The adaptive feasible mutation method can be used to assess the diversity of the population, which is conducive to the optimization of the results. The tolerance is set to 10^{-4} as the termination condition of the calculation. The other parameters are set to recommended values.

3.2. Effects of Powder Laying Process Parameters on Powder Laying Quality Index

In the formation area, the distribution of the normal residual diagram includes the apparent density of the powder layer, the standard deviation of the apparent density, and the surface roughness, as shown in Figure 5. It can be seen that the distribution of the residual points is almost in a straight line. The results show that the second-order model fitting effect of the nylon powder quality in the SLS process is good.

The response surface diagram of the relationships among the drum translational velocity, particle size, and powder laying quality is shown in Figure 6. Based on the response surface diagram, the influence of a single factor on the process parameters (drum translation speed) and powder property parameters (nylon powder particle size) can be assessed, and the synergistic influence of these parameters on the powder laying quality can be obtained.

The analysis shows that the particle size has a great influence on the apparent density, standard deviation of the density, and roughness of the powder layer in the formation area. The smaller the particles are, the more likely they are to agglomerate under the action of electrostatic and van der Waals forces. Therefore, the pores left by the roller powder are smaller and the densification degree of the powder bed is also increased. The smaller particle size improves the apparent density of the powder layer, reduces the standard deviation of the density, and improves the density uniformity, but is not conducive to reducing the surface roughness. The effects of the roller translation speed on the apparent density and density uniformity of the formation area are relatively small, but the effect on

the roughness is greater. With the increase in drum translation speed, the apparent density of the powder layer in the formation area decreases slowly. When the drum translation speed increases to a certain extent, the apparent density of the powder layer will increase slightly, although the overall change trend will be small. However, this is contrary to the effects of the roller translational velocity on the density uniformity and roughness. If the roller translation speed is too high or too low, this will not be conducive to improving the uniformity of the powder layer density and reducing the roughness of the powder layer surface. The apparent density of the powder layer is in conflict with the standard deviation of the apparent density and the surface roughness in the target formation area. This is also consistent with the previous simulation results. The regression equation for the powdering quality established based on the RSM is reliable and can predict the powdering quality well.

### 3.3. Multi-Objective Optimization Results for the Powder Laying Quality

Based on the Gamultiobj function, 80 Pareto optimal solutions were obtained to assess the nylon powder quality during the SLS process. Partial Pareto optimal solutions are given in Table 5. Here, an optimal compromise solution is selected in the Pareto set according to product preference. The first solution is biased towards the maximum apparent density of the powder layer in the formation region. The second solution is biased towards the best uniformity of the powder layer density in the formation region. The third solution is biased towards the optimal surface flatness of the powder layer in the formation region. If all three are considered, the fourth solution can be selected as the optimal compromise solution. When the particle size of the powder is determined in the actual engineering process, the appropriate drum translation speed can be selected according to Table 5 to optimize the powder laying quality. Through this method, the matching of the physical property parameters and the SLS powder laying process parameters and the prediction of powder laying quality were achieved.

**Table 5.** Partial Pareto optimal solution for multi-objective optimization of powdering quality via DEM simulation.

Test No.	x(1)	x(2)	f(1)	f(2)	f(3)
1	100.000	50.000	−566.332	71.509	44.637
2	145.201	52.547	−555.438	69.179	43.021
3	124.124	100.000	−545.108	113.938	41.099
4	153.701	55.058	−551.242	69.371	42.750
5	122.961	50.120	−562.044	69.813	43.759
6	105.078	50.003	−565.348	71.035	44.424
7	126.765	97.187	−542.746	108.696	41.219
8	151.930	68.351	−539.267	74.025	42.255
9	109.506	50.645	−563.553	70.626	44.202
10	129.048	88.767	−538.274	95.260	41.578
11	120.959	99.525	−544.970	113.299	41.123
12	118.713	98.379	−544.272	111.400	41.182
13	146.365	91.364	−538.048	98.421	41.471
14	139.111	50.677	−558.840	69.282	43.257
15	114.194	87.017	−539.307	93.891	41.798
16	124.878	95.907	−542.035	106.622	41.277
17	104.755	100.000	−546.880	115.748	41.181
18	133.703	50.750	−559.483	69.377	43.396
19	139.166	90.231	−538.007	96.921	41.494
20	152.929	66.994	−540.043	73.241	42.296
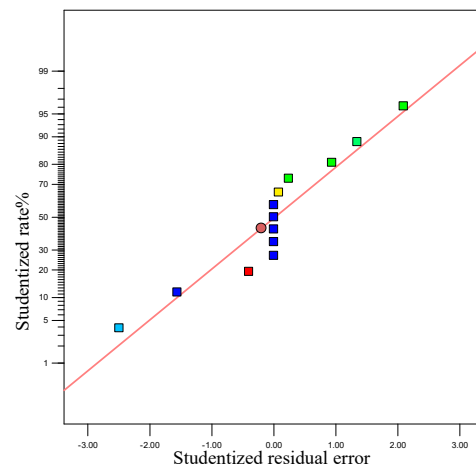
(**a**)
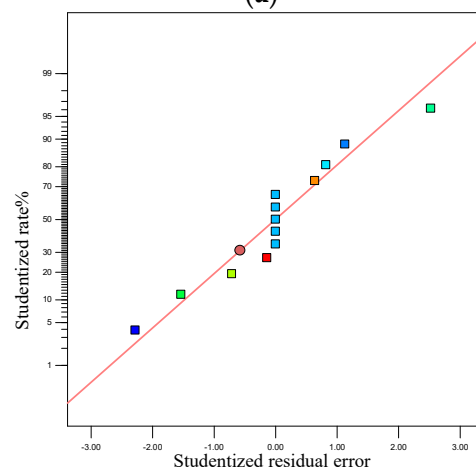
(**b**)
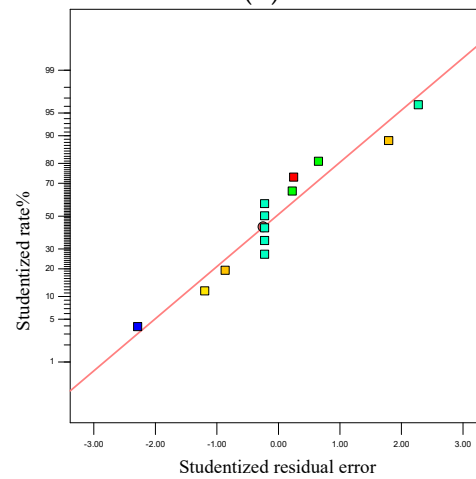
(**c**)

Figure 5. Normal residual diagram of powder quality from DEM simulation: (**a**) normal residual diagram of apparent density; (**b**) normal residuals of standard deviation of the density; (**c**) normal residual diagram of powder surface roughness.
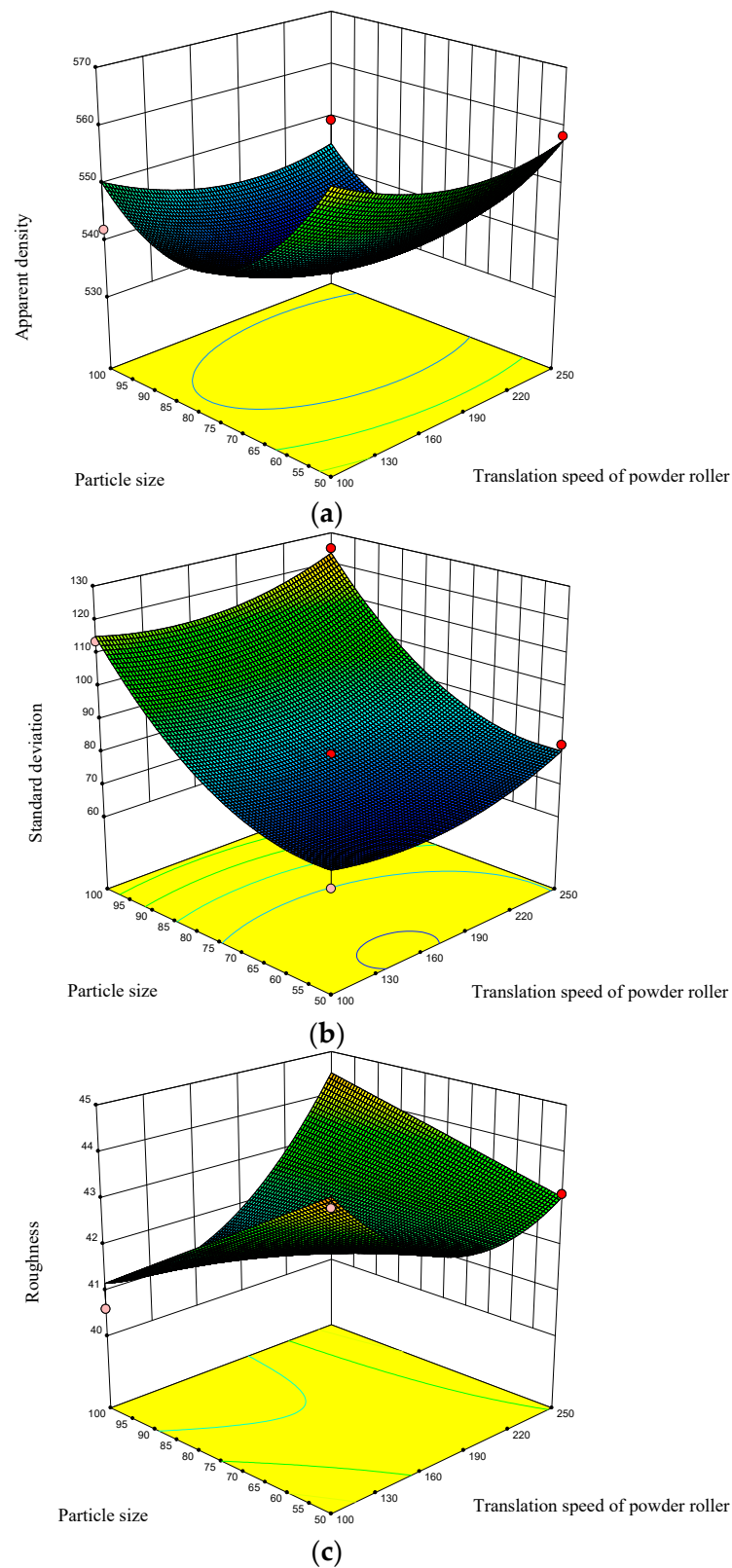
Figure 6. Response surface diagram of powdery mass from DEM simulation: (**a**) performance density; (**b**) standard deviation of the density; (**c**) roughness.

4. Experimental Verification

PA3200 powder with a particle size of 50.02 mm was selected as the experimental material, The polymer powder sintering machine (FS251) designed and manufactured by Hunan Hua Shu Hi-tech co., Ltd., was used for the powder laying experiment. The molding process parameters are shown in Table 6.

Table 6. SLS process parameters used in the experiment.

Parameter	Value
Laser power (W)	21
Scanning interval (mm)	0.15
Drum diameter (mm)	40
Ratio of drum linear velocity to translational velocity	0.5
Preheating temperature of formation cylinder (°C)	171
Preheating temperature of powder feeding cylinder (°C)	132

In order to explore the influence of the powder laying parameters on the SLS powder laying quality and to verify the optimized test results, an experimental method of online sampling was designed to measure the powder laying quality. Figure 7 shows the schematic diagram of the SLS powder laying quality detection process. In the formation area, three experimental package layers can be seen, with each layer containing a powder paving roller working from the bottom up to 100 mm/s, 140 mm/s, and 227 mm/s, respectively. Each layer of the experimental package has the same design, including 13 statistical picker boxes, 1 no-cover statistical picker box, and 1 statistical picker box cover. The size of the outer cavity of the selection box is 20 mm × 20 mm × 10 mm, and the thickness of the cavity wall is 2 mm. The lumen is filled with powder. After sintering, it is cooled for a period of time and then the sintering package is removed. The sintered parts of the statistical selection box are then cleaned and sandblasted. The statistical selection boxes in each layer after cleaning are numbered and distinguished. A high-precision balance (accurate to 0.0001 g) is used to measure the mass m_{pi} of each statistical selection box in each layer. Here, m_{pi} can be expressed as:

$$m_{pi} = m_{1i} - m_2 - m_3 \tag{27}$$

where m_2 is the mass of an open statistical box and m_3 is the mass of the statistical box cover.
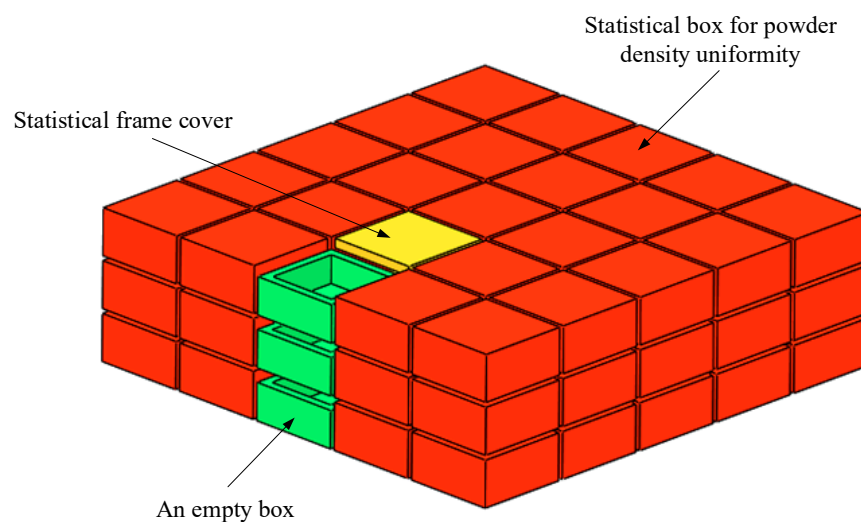

Figure 7. Sketch of the powder quality inspection design in the formation area.

The powder's apparent density ρ'_{pi} in each statistical selection box is:

$$\rho'_{pi} = \frac{m_{pi}}{l_i w_i h_i} \tag{28}$$

where l_i, w_i, and h_i represent the length, width, and height of the sintered parts in the statistical selection box, respectively.

The apparent density of the powder layer in the formation area is:

$$\rho_p = \frac{\sum\limits_{i=1}^{13} m_{pi}}{\sum\limits_{i=1}^{13} l_i w_i h_i} \tag{29}$$

The standard deviation of laminar density in the formation zone is:

$$S_p = \sqrt{\frac{1}{N-1}\sum_{i=1}^{N}\left(\rho'_{pi} - \overline{\rho'_{pi}}\right)^2} \tag{30}$$

where $\overline{\rho'_{pi}}$ is the average value of the apparent density of the powder in the selection box.

According to the above experimental methods, the statistical box was prepared, as shown in Figure 8a. We selected the box to sinter the molded parts for powder cleaning (see Figure 8b). After cooling for a period of time, the size and quality parameters of the sintered parts in the statistical selection box were measured, as shown in Figure 9.
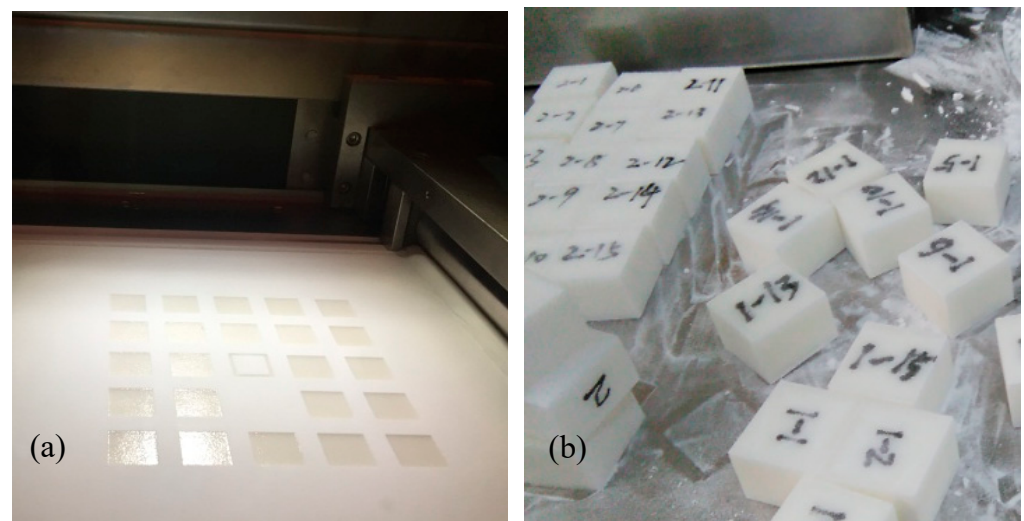

Figure 8. Statistical sintering experiment: (**a**) SLS molding process for the statistical box; (**b**) powder cleaning of sintered parts in the statistics box.

Figure 9. The size and quality parameters of sintered parts in the selection box.

With the increase in drum speed, the apparent density of the powder in the formation area decreases (Figure 10). The reliability of the numerical simulation study on SLS powder laying process of nylon powder was verified. When the PA3200 powder D50 is 50 μm, the diameter of powder spreading drum is 40 mm, the ratio of the linear velocity to translation velocity of the drum is 0.5, the translation velocity of drum is 100 mm/s, the apparent powder density in the formation area is 579.8 kg/m^3 (Figure 10a), and the standard deviation of the apparent powder density in the formation area is 70.3 kg/m^3 (Figure 10b). This is in good agreement with the absolute value of optimization target result no. 1 in Table 5, and the errors are 2.38% and 1.69%, respectively. When the roller translation speed is 140 mm/s, the apparent powder density in the formation area is 543.1 kg/m^3 and the standard deviation of the apparent powder density in the formation area is 66.1 kg/m^3. This is in good agreement with the absolute value of optimization target result no. 14 in Table 5, and the errors are 2.82% and 4.59%, respectively. This shows that the experimental method of online sampling and measurement of the powder laying quality is feasible and that the multi-objective optimization results of the nylon powder laying quality in the SLS process based on the genetic algorithm are reliable.
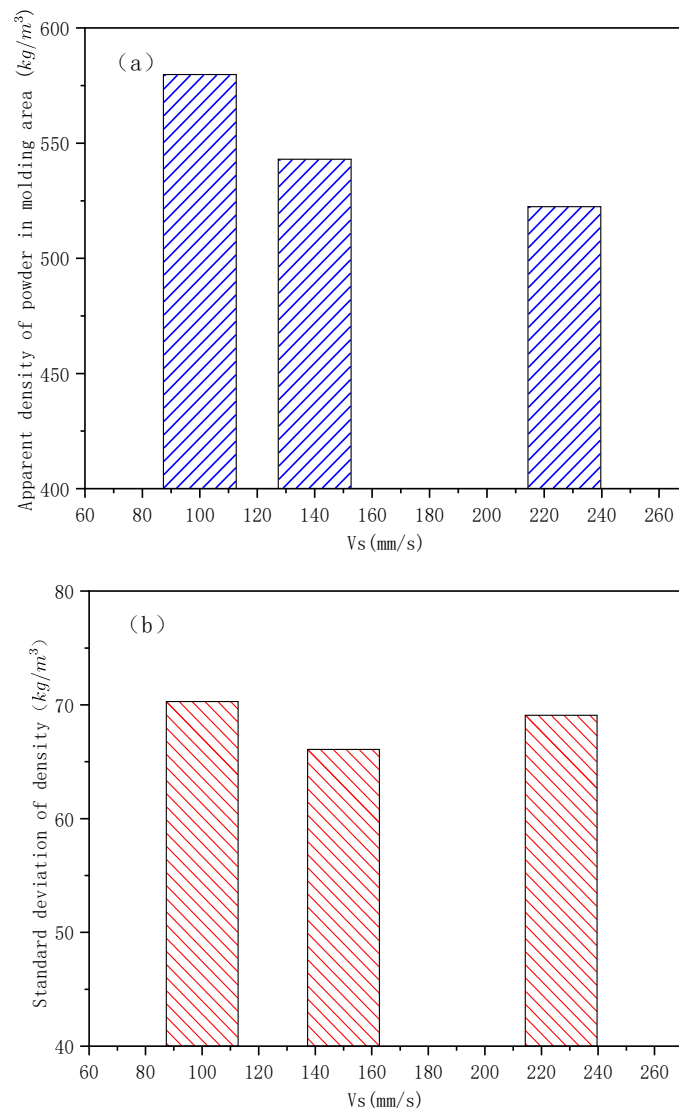
Figure 10. Experimental results of the powder spreading quality in the formation area (V_r/V_s = 0.5, R_g = 20 mm, D50 = 50 μm): (**a**) effect of V_s on the apparent density of powder in the formation zone; (**b**) effect of V_s on the standard deviation of the formation zone density.

5. Conclusions

The SLS powder spreading process was numerically simulated based on the DEM. The effects of the powder's physical properties and operating conditions on the bed quality were investigated, characterized by the density characteristics, density uniformity, and flatness of the powder layer. The main results from the present study are summarized as follows:

(1) Statistical analysis and curve fitting of the DEM simulation data from the powder laying process were conducted based on the central composite experimental design method. ANOVA was used to modify the fitting model. A regression model of the powdering quality was established based on the RSM. The relationship between the proposed powdering quality index and the research variables was expressed well;

(2) An improved multi-objective optimization algorithm based on NSGA-II was used to optimize the powder laying quality of nylon powder in the SLS. The solutions in the optimized Pareto solution set were evenly distributed in the target space. An optimal compromise solution can be selected from Pareto optimal solution set according to the product requirements;

(3) The apparent density and standard deviation of the powder under different conditions were determined experimentally. The translation speed of the roller has a great influence on the powder laying quality, and the apparent powder density in the formation area decreases with the increase in roller speed. The experimental results agreed well with the selected optimization results and the maximum error was less than 4.6%. The reliability of the numerical simulation study on the SLS powder laying process of nylon powder was verified.

At present, it is difficult to accurately measure the force and deformation of the particle contacts using experimental equipment, and the inexact mechanical parameters are not conducive to modeling simulations and for improvement of the adhesion collision model. In addition, on the basis of improving the measurement method used for the particle electrostatic transfer characteristics, the particle band charge and electrification mechanism in this model need to be further refined. The model simulation system is smaller than the actual system, so the parallel calculation of the DEM may increase the simulation system and improve the computational efficiency.

References

1. Yan, C.; Shi, Y.; Li, Z.; Wen, S.; Wei, Q. Chapter 6—Numerical analysis of selective laser sintering key technology. In *Selective Laser Sintering Additive Manufacturing Technology*; Academic Press: New York, NY, USA, 2021; pp. 713–872.
2. Chen, H.; Zhu, W.; Tang, H.; Yan, W. Oriented structure of short fiber reinforced polymer composites processed by selective laser sintering: The role of powder-spreading process. *Int. J. Mach. Tools Manuf.* **2021**, *163*, 103703. [CrossRef]
3. Oropeza, D.; Penny, R.W.; Gilbert, D.; Hart, A.J. Mechanized spreading of ceramic powder layers for additive manufacturing characterized by transmission x-ray imaging: Influence of powder feedstock and spreading parameters on powder layer density. *Powder Technol.* **2022**, *398*, 117053. [CrossRef]
4. Nan, W.; Gu, Y. Experimental investigation on the spreadability of cohesive and frictional powder. *Adv. Powder Technol.* **2022**, *33*, 103466. [CrossRef]
5. Zhang, J.; Tan, Y.; Xiao, X.; Jiang, S. Comparison of roller-spreading and blade-spreading processes in powder-bed additive manufacturing by DEM simulations. *Particuology* **2021**, *66*, 48–58. [CrossRef]
6. Wang, L.; Li, E.; Shen, H.; Zou, R.; Yu, A.; Zhou, Z. Adhesion effects on spreading of metal powders in selective laser melting. *Powder Technol.* **2019**, *363*, 602–610. [CrossRef]
7. Mussatto, A.; Groarke, R.; O'Neill, A.; Obeidi, M.A.; Delaure, Y.; Brabazon, D. Influences of powder morphology and spreading parameters on the powder bed topography uniformity in powder bed fusion metal additive manufacturing. *Addit. Manuf.* **2020**, *38*, 101807. [CrossRef]
8. Peleg, M. Flowability of food powders and methods for its evaluation—A review. *J. Food Process Eng.* **1977**, *1*, 303–328. [CrossRef]
9. Juliano, P.; Muhunthan, B.; Barbosa-Cánovas, G.V. Flow and shear descriptors of preconsolidated food powders. *J. Food Eng.* **2006**, *72*, 157–166. [CrossRef]
10. Wang, W.; Zhang, J.; Yang, S.; Zhang, H.; Yang, H.; Yue, G. Experimental study on the angle of repose of pulverized coal. *Particuology* **2010**, *8*, 482–485. [CrossRef]

11. Vlachos, N.; Chang, I.T. Investigation of flow properties of metal powders from narrow particle size distribution to polydisperse mixtures through an improved Hall-flowmeter. *Powder Technol.* **2011**, *205*, 71–80. [CrossRef]

12. Berretta, S.; Ghita, O.; Evans, K.; Anderson, A.; Newman, C. Size, shape and flow of powders for use in Selective Laser Sintering (SLS). In *High Value Manufacturing: Advanced Research in Virtual and Rapid Prototyping*; CRC Press: Boca Raton, FL, USA, 2013; pp. 49–54. [CrossRef]

13. Wu, C.-Y.; Cocks, A.C. Numerical and experimental investigations of the flow of powder into a confined space. *Mech. Mater.* **2006**, *38*, 304–324. [CrossRef]

14. Dai, L.; Sorkin, V.; Vastola, G.; Zhang, Y. Dynamics calibration of particle sandpile packing characteristics via discrete element method. *Powder Technol.* **2019**, *347*, 220–226. [CrossRef]

15. Amado, A.; Schmid, M.; Wegener, K. Flowability of SLS powders at elevated temperature. *ETH Zurich.* **2014**. [CrossRef]

16. Wei, G.; Zhang, H.; An, X.; Xiong, B.; Jiang, S. CFD-DEM study on heat transfer characteristics and microstructure of the blast furnace raceway with ellipsoidal particles. *Powder Technol.* **2019**, *346*, 350–362. [CrossRef]

17. Zhang, J.; Tan, Y.; Bao, T.; Xu, Y.; Xiao, X.; Jiang, S. Discrete Element Simulation of the Effect of Roller-Spreading Parameters on Powder-Bed Density in Additive Manufacturing. *Materials* **2020**, *13*, 2285. [CrossRef]

18. Kovalev, O.; Gusarov, A.; Belyaev, V. Morphology of random packing of micro-particles and its effect on the absorption of laser radiation during selective melting of powders. *Int. J. Eng. Sci.* **2020**, *157*, 103378. [CrossRef]

19. Hugonnet, B.; Missiaen, J.M.; Martin, C.L.; Rado, C. Effect of contact alignment on shrinkage anisotropy during sintering: Stereological model, discrete element model and experiments on NdFeB compacts. *Mater. Des.* **2020**, *191*, 108575. [CrossRef]

20. Gao, W.; Liu, L.; Liao, Z.; Chen, S.; Zang, M.; Tan, Y. Discrete element analysis of the particle mixing performance in a ribbon mixer with a double U-shaped vessel. *Granul. Matter* **2019**, *21*, 12. [CrossRef]

21. Steuben, J.C.; Iliopoulos, A.P.; Michopoulos, J.G. Discrete element modeling of particle-based additive manufacturing processes. *Comput. Methods Appl. Mech. Eng.* **2016**, *305*, 537–561. [CrossRef]

22. Xin, H.; Sun, W.; Fish, J. Discrete element simulations of powder-bed sintering-based additive manufacturing. *Int. J. Mech. Sci.* **2018**, *149*, 373–392. [CrossRef]

23. Meier, C.; Weissbach, R.; Weinberg, J.; Wall, W.A.; Hart, A.J. Critical influences of particle size and adhesion on the powder layer uniformity in metal additive manufacturing. *J. Mater. Process. Technol.* **2018**, *266*, 484–501. [CrossRef]

24. Tan, Y.-Q.; Zheng, J.-H.; Gao, W.; Jiang, S.-Q.; Feng, Y. The Effect of Powder Flowability in the Selective Laser Sintering Process. In Proceedings of the 7th International Conference on Discrete Element Methods, Dalian, China, 1–4 August 2016; Springer: Singapore, 2016; Volume 188, pp. 629–636. [CrossRef]

25. Chen, H.; Wei, Q.; Wen, S.; Li, Z.; Shi, Y. Flow behavior of powder particles in layering process of selective laser melting: Numerical modeling and experimental verification based on discrete element method. *Int. J. Mach. Tools Manuf.* **2017**, *123*, 146–159. [CrossRef]

26. Yao, D.; An, X.; Fu, H.; Zhang, H.; Yang, X.; Zou, Q.; Dong, K. Dynamic investigation on the powder spreading during selective laser melting additive manufacturing. *Addit. Manuf.* **2020**, *37*, 101707. [CrossRef]

27. Parteli, E.J.R.; Pöschel, T. Particle-based simulation of powder application in additive manufacturing. *Powder Technol.* **2016**, *288*, 96–102. [CrossRef]

28. Dehghani, M.H.; Karri, R.R.; Yeganeh, Z.T.; Mahvi, A.H.; Nourmoradi, H.; Salari, M.; Zarei, A.; Sillanpää, M. Statistical modelling of endocrine disrupting compounds adsorption onto activated carbon prepared from wood using CCD-RSM and DE hybrid evolutionary optimization framework: Comparison of linear vs non-linear isotherm and kinetic parameters. *J. Mol. Liq.* **2020**, *302*, 112526. [CrossRef]

29. Islam, M.; Buijk, A.; Rais-Rohani, M.; Motoyama, K. Process parameter optimization of lap joint fillet weld based on FEM–RSM–GA integration technique. *Adv. Eng. Softw.* **2015**, *79*, 127–136. [CrossRef]

30. Elkelawy, M.; El Shenawy, E.; Bastawissi, H.A.-E.; Shams, M.M.; Panchal, H. A comprehensive review on the effects of diesel/biofuel blends with nanofluid additives on compression ignition engine by response surface methodology. *Energy Convers. Manag. X* **2022**, *14*, 100177. [CrossRef]

31. Zhang, J.; Tan, Y.; Ji, C.; Xiao, X.; Jiang, S. Research on the effects of roller-spreading parameters for nylon powder spreadability in additive manufacturing. *Chin. J. Theor. Appl. Mech.* **2021**, *53*, 11.

32. Gady, B.; Schleef, D.; Reifenberger, R.; Rimai, D.; DeMejo, L.P. Identification of electrostatic and van der Waals interaction forces between a micrometer-size sphere and a flat substrate. *Phys. Rev. B* **1996**, *53*, 8065–8070. [CrossRef]

33. Hamaker, H.C. The London—Van der Waals attraction between spherical particles. *Physica* **1937**, *4*, 1058–1072. [CrossRef]

34. Tan, Y.; Zhang, J.; Jiang, S. Determination of Discrete Element Model Contact Parameters of Nylon Powder at SLS Preheating Temperature and its Flow Charateristics. *Chin. J. Theor. Appl. Mech.* **2019**, *51*, 56.

35. Xiao, X.; Tan, Y.; Zhang, H.; Deng, R.; Jiang, S. Experimental and DEM studies on the particle mixing performance in rotating drums: Effect of area ratio. *Powder Technol.* **2017**, *314*, 182–194. [CrossRef]

36. Haeri, S.; Wang, Y.; Ghita, O.; Sun, J. Discrete element simulation and experimental study of powder spreading process in additive manufacturing. *Powder Technol.* **2017**, *306*, 45–54. [CrossRef]

37. Box, G.E.P.; Wilson, K.B. On the Experimental Attainment of Optimum Conditions. *J. R. Stat. Soc. Ser. B Methodol.* **1951**, *13*, 1–45. [CrossRef]

38. Pezzin, A.P.T.; Capellari, J.B.; Neves, E.; Garcia, M.C.F.; Apati, G.P.; Schneider, A.L.D.S. Application of response surface methodology and central composite rotatable design (CCDR) for modelling the influence of agro-industrial waste in lactic acid biosynthesis. *Acta Biol. Catarin.* **2019**, *6*, 51–60. [CrossRef]

39. Boubakri, A.; Hafiane, A.; Bouguecha, S.A.T. Application of response surface methodology for modeling and optimization of membrane distillation desalination process. *J. Ind. Eng. Chem.* **2014**, *20*, 3163–3169. [CrossRef]

40. Yu, K.; Zhao, Y.; He, Y.; He, D. Response surface methodology for optimizing LIBS testing parameters: A case to conduct the elemental contents analysis in soil. *Chemom. Intell. Lab. Syst.* **2019**, *195*, 103891. [CrossRef]

41. Dixit, P.; Tiwari, R.; Mukherjee, A.K.; Banerjee, P.K. Application of response surface methodology for modeling and optimization of spiral separator for processing of iron ore slime. *Powder Technol.* **2015**, *275*, 105–112. [CrossRef]

42. Pierre, B. Pareto (Vilfredo)—Cours d'économie politique. *Rev. Écon.* **1965**, *16*, 811–812.

43. Goetz-Girey, R.; Marchal, J. Cours d'économie politique. *Rev. Écon.* **1956**, *7*, 490. [CrossRef]

44. Deb, K.; Pratap, A.; Agarwal, S.; Meyarivan, T.A.M.T. A fast and elitist multiobjective genetic algorithm: NSGA-II. *IEEE Trans. Evol. Comput.* **2022**, *6*, 182–197. [CrossRef]

Article

Influence of 1.5 wt.% Bi on the Microstructure, Hardness, and Shear Strength of Sn-0.7Cu Solder Joints after Isothermal Annealing

Mohd Izrul Izwan Ramli [1,2], Mohd Arif Anuar Mohd Salleh [1,2,*], Andrei Victor Sandu [1,3,4,5,*], Siti Farahnabilah Muhd Amli [1,2], Rita Mohd Said [1,2], Norainiza Saud [1,2], Mohd Mustafa Al Bakri Abdullah [1,2], Petrica Vizureanu [1,3], Adam Rylski [6], Jitrin Chaiprapa [7] and Marcin Nabialek [8]

1   Center of Excellence Geopolymer & Green Technology (CEGeoGTech), Universiti Malaysia Perlis (UniMAP), Jalan Kangar-Arau 02600, Perlis, Malaysia; izrulizwan@unimap.edu.my (M.I.I.R.); sitifarahnabilah@outlook.com (S.F.M.A.); rita@unimap.edu.my (R.M.S.); norainiza@unimap.edu.my (N.S.); mustafa_albakri@unimap.edu.my (M.M.A.B.A.); peviz@tuiasi.ro (P.V.)
2   Faculty of Chemical Engineering Technology, Universiti Malaysia Perlis (UniMAP), Jalan Kangar-Arau 02600, Perlis, Malaysia
3   Faculty of Materials Science and Engineering, Gheorghe Asachi Technical University of Iasi, D. Mangeron 41, 700050 Iasi, Romania
4   Romanian Inventors Forum, St. P. Movila 3, 700089 Iasi, Romania
5   National Institute for Research and Development in Environmental Protection INCDPM, Splaiul Independentei 294, 060031 Bucuresti, Romania
6   Institute of Materials Science and Engineering, Faculty of Mechanical Engineering, Lodz University of Technology, Stefanowskiego 1/15, 90-924 Lodz, Poland; adam.rylski@p.lodz.pl
7   Synchrotron Light Research Institute, Muang District, Nakhon Ratchasima 3000, Thailand; jitrin@slri.or.th
8   Department of Physics, Czestochowa University of Technology, 42-201 Czestochowa, Poland; nmarcell@wp.pl
*   Correspondence: arifanuar@unimap.edu.my (M.A.A.M.S.); sav@tuiasi.ro (A.V.S.)

Abstract: This manuscript reports the isothermal annealing effect on the mechanical and microstructure characteristics of Sn-0.7Cu-1.5Bi solder joints. A detailed microstructure observation was carried out, including measuring the activation energy of the intermetallic compound (IMC) layer of the solder joints. Additionally, the synchrotron μX-ray fluorescence (XRF) method was adopted to precisely explore the elemental distribution in the joints. Results indicated that the Cu_6Sn_5 and Cu3Sn intermetallic layers thickness at the solder/Cu interface rises with annealing time at a rate of 0.042 μm/h for Sn-0.7Cu and 0.037 μm/h for Sn-0.7Cu-1.5Bi. The IMC growth's activation energy during annealing is 48.96 kJ mol-1 for Sn-0.7Cu, while adding Bi into Sn-0.7Cu solder increased the activation energy to 55.76 kJ mol^{-1}. The μ-XRF shows a lower Cu concentration level in Sn-0.7Cu-1.5Bi, where the Bi element was well dispersed in the β-Sn area as a result of the solid solution mechanism. The shape of the IMC layer also reconstructs from a scallop shape to a planar shape after the annealing process. The Sn-0.7Cu hardness and shear strength increased significantly with 1.5 wt.% Bi addition in reflowed and after isothermal annealing conditions.

Keywords: bismuth; intermetallic compound; IMC thickness; mechanical properties; isothermal annealing

1. Introduction

Eutectic lead-tin solder has a significant impact on interconnecting an electronic packaging in a variety of electronic systems and assembly. However, lead-tin solder has disadvantages in terms of its harmfulness. This is due to the fact that the lead contained in the solder of discarded electronic components is melted by contaminated groundwater and acid rain. Thus, the European Union's recommendation on the Waste Electrical and Electronic Equipment (WEEE) Directive and the Directive Restricting the Use of Certain Hazardous Substances quickly triggered the electronic packaging's use of lead [1,2]. Therefore, the Sn-0.7Cu solder alloy is an outstanding choice rather than the classical

Sn-Pb solder alloy in electronic devices [3]. However, in electronic devices, the long-term electronic component usage and the on-off rotations of the power supply could affect the solder joint strength. The IMC in the soldered joint will rise up by solid-state diffusion as a result of the thermal condition under this case. Many scholars have conducted experimental studies utilising isothermal annealing to replicate the actual thermal conditions.

An intermetallic compound denotes a solid phase that forms when two or more molten metallic elements are combined and cooled, where the resultant phase possesses a fixed chemical composition. Primary and interfacial IMC are the two kinds of IMC. The main intermetallic compound is found in the solder joint's bulk microstructure, whereas the interfacial IMC compound is found at the solder-to-copper substrate interface. The most common intermetallic in Sn-0.7Cu solder alloy is Cu_6Sn_5 and Cu_3Sn. In interfacial IMC, a thin and planar of Cu_3Sn IMC is formed below the Cu_6Sn_5 IMC phase since the Cu_3Sn IMC acquired greater activation energy than the Cu_6Sn_5 IMC phase. Hence, it is recommended that adjustments in microstructure can have a big impact on solder joint strength.

Consequently, the information regarding the microstructure changes in solders and joints is essential. In order to construct dependable lead-free solder joints, it is essential to measure the growth behaviour of the IMC during thermal annealing. Here, the IMC layers grow gradually, leading to decreased ductility and defects-like voids forming at the interface. The presence of defects could cause the failure of the solder interconnection. Recently, Bismuth (Bi) elements were reported that might help boost the intensity of the characteristics in the solder joint [1]. During the soldering and annealing process, the Bi influence on the IMC layer in Sn-Ag-Cu/Cu solder joints was investigated [4,5]. Here, it was discovered that the Bi addition could slow the growth tendency of the IMC layer. It was also shown that Bi's microstructure of the IMCs and precipitates happened due to supersaturation [6]. As discovered by Teoh et al. [2], the Bi addition on Sn-0.7Cu could increase the solder joint's mechanical strength. The extension of that study regarding the growth of activation energy of Sn-0.7Cu-1.5Bi in various temperature ranges will be discussed in this manuscript. It is noteworthy to investigate the value of activation energy since it can estimate the expansion of the IMC layer. In our previous study [1], the effect of Bi and Ni addition to the microstructure focusing on the primary intermetallic compound (IMC) growth rate during soldering using the in situ imaging technique were investigated. Basic properties of the solder joint after soldering (without thermal annealing) such as wettability and mechanical properties were also investigated.

Since the interfacial IMC growth is normally known to influence the solder joint strength, this study investigates the microstructure, hardness, and shear strength of Sn-0.7Cu and Sn-0.7Cu-1.5Bi after isothermal annealing. Focusing more on the growth rate and activation energy of the interfacial IMC after isothermal annealing, the interfacial IMC growth mechanism and its relation to the hardness and shear strength of the solder joint were investigated. As discovered in our previous study [1], the limit of Bi solubility in Sn is around 1.8 wt.% maximum, which is why only the 1.5 wt.% Bi is chosen for this study. This is due to the fact that high Bi addition may lead to the brittle properties of solder joint.

2. Materials and Methods

In this work, the mixture of Sn-0.7Cu alloy with 1.5 wt.% of Bismuth was fabricated. Sn-0.7Cu ingot was purchased from Nihon Superior, Osaka, Japan, while Bi was gained from Sigma-Aldrich (M) Sdn. Bhd, Selangor, Malaysia. The Sn-0.7Cu solder ingot and Bi were suspended in a furnace at 350 °C for 1 h. Then, the molten solder was stirred and pour into treated steel moulds and cooled to room temperature. With a diameter of 600 μm, the solder balls were formed with a diameter of 2.0 mm puncher from the alloy foils using 30 μm thickness. These solder balls were reflowed in an oven at 250 °C and eventually went through a sieving process to get a uniform solder size. Then, the solder ball was reflowed on the printed circuit board to form a solder joint. After that, these soldered solder joints were aged at 120, 150, and 180 °C for 24, 120, and 240 h, respectively.

The cross-sectional microstructure was imaged and analysed at the solder joints interfacial. Here, the influence of Bi addition on Sn-0.7Cu solder alloy at three different temperatures was measured. The IMC layer's average thickness across the joint was ascertained by analysing the thickness of the IMC layer for each subject from three photographs in three separate places. In addition, the element's distribution was investigated using a μ-XRF experiment at BL6B beamline at Synchrotron Light Research Institute (SLRI), Nakhon Ratchasima, Thailand. The sample was located at a 90° level between the charge-couple device camera and the X-ray camera. The sample was then scanned at a fast rate in the air atmosphere with a step size of 0.05 mm for 30 s exposure time, which was then examined with the PyMca software (5.0.0, European Synchrotron Radiation Facility (ESRF), France).

The microhardness test was investigated via a Vickers microhardness (FV-700, Future-Tech Corp, Osaka, Japan) followed by the ASTM B933-09 standard test. With a 1 kg indenting load for a 10 s dwell time of the consistency, the results will be calculated using five points for each combination. The shear test was performed to investigate the solder's joint strength after the annealing process. An Instron machine with a strain rate of 2 mm.min^{-1} was used for shear testing. The specification of shear strength was based on the ASTM D1002. For each annealing condition, five samples were examined, and the average shear strength has been measured. The fractography for the fracture surface was also imaged using an SEM (JEOL, Peabody, MA, USA).

3. Results

3.1. Primary Intermetallic Compound

The microstructure of the primary intermetallic compound of Sn-0.7Cu-1.5Bi as well as Sn-0.7Cu after being aged at 180 °C at various annealing times was portrayed in Figure 1. β-Sn and primary Cu_6Sn_5 were found in the Sn-0.7Cu's bulk solder. In Sn-0.7Cu-1.5Bi solder alloy, the primary IMC did not cause a significant change after the reflowed process. However, after the annealing process at a certain period, it was observed that the hallowed Cu_6Sn_5 were formed lesser in comparison to Sn-0.7Cu solder alloy. It is recommended that the dissolution of the Cu atoms in the interfacial reaction solute forms a hallowed Cu_6Sn_5 intermetallic during the annealing process [7,8]. In the Sn-0.7Cu-1.5Bi sample, the existing Bi dissolved in the β-Sn phase due to the solid solution mechanism, making the Cu_6Sn_5 in Sn-0.7Cu-1.5Bi difficult to be formed.
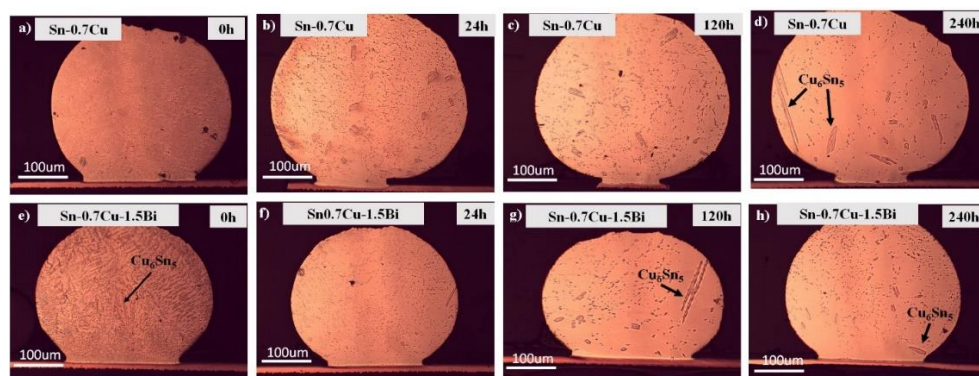
Figure 1. The microstructure of primary intermetallic for (**a**–**d**) Sn-0.7Cu and (**e**–**h**) Sn-0.7Cu-1.5Bi after isothermal annealing at 180 °C.

The distribution of the elements as reflowed and after the annealing were analysed using synchrotron μ-XRF mapping. Figure 2 shows the image of an μ-XRF in Sn-0.7Cu solder ball. Here, the elemental map of Sn and Cu as reflowed and after the annealing process are presented. The higher concentration of the element represents the higher intensities. It shows the Sn and Cu dispersion through the Sn-grain. On the contrary, Figure 3 shows the distribution of Sn-0.7Cu-1.5Bi solder balls, indicating the existence of the mapping area of Sn, Cu, and Bi as reflowed and after the annealing process. It shows

the lower Cu concentration level in Sn-0.7Cu-1.5Bi compared to Sn-0.7Cu solder alloy, where the Bi element was also found well dispersed in the β-Sn area.
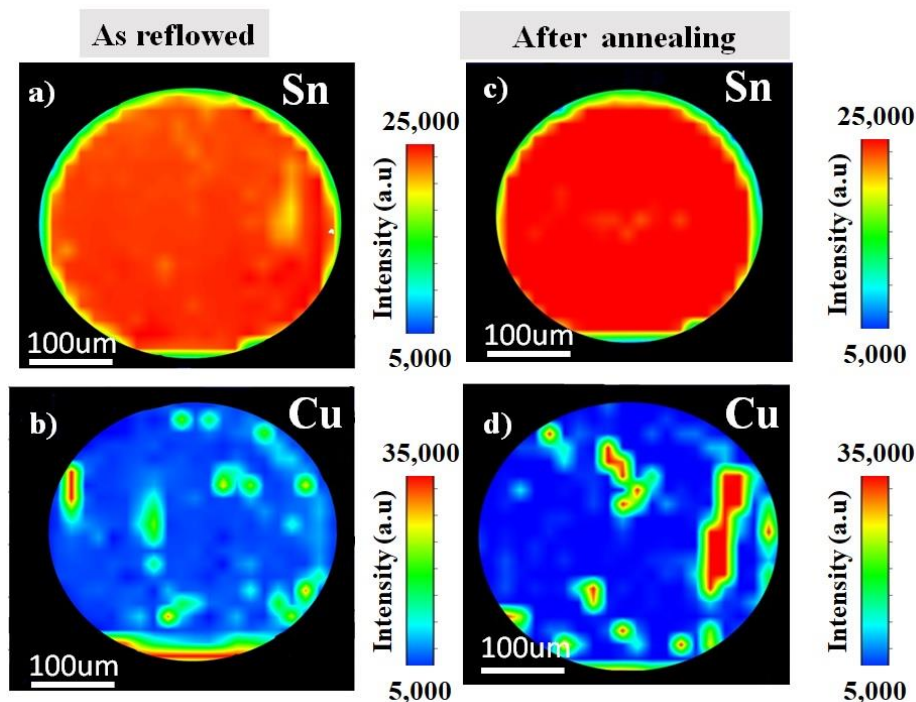
Figure 2. The μ-XRF area mapping of Sn-0.7Cu (**a**,**b**) as reflowed and (**c**,**d**) after isothermal annealing at 180 °C.

3.2. Interfacial Intermetallic Compound and Activation Energy

Figure 4 portrays the interfacial microstructures' evolution of the Sn-0.7Cu/Cu-substrate and Sn-0.7Cu-1.5Bi/Cu-substrate solder joint samples after being aged at 180 °C. It can be seen that the interfacial intermetallic layers constitute Cu_6Sn_5 with a round scallop-type morphology and that the Cu_3Sn layers are too fine to be viewed objectively. In the Sn-0.7Cu system, the interfacial layer commonly consists of two similar layers, which are Cu_3Sn intermetallic and Cu_6Sn_5 intermetallic. The Cu_6Sn_5 is normally formed during soldering and grew via diffusion of Cu and Sn reactions, meanwhile Cu_3Sn grows via diffusion between the Cu-substrate and the Cu_6Sn_5 IMC layer. After the reflow process, the interfacial Cu_6Sn_5 layers exist in the solder joints in the scallop-like morphology. After the annealing process, this shape gradually changed to planar-like morphology. This total IMC layer thickness also increases significantly, as revealed in Figure 4a–h.

The interfacial intermetallic compound can be divided into two types: The Cu_6Sn_5 phase that would grow initially at the soldering interface, then during the Cu_3Sn phase that grows after the solder joint's diffusion process [9]. The diffusivity and solubility of Cu in Sn during solid-state annealing are substantially lower than in molten solder. As a result, the IMC growth is substantially gradual, which is amplified when the IMC layer acts as a diffusion barrier [10]. The improvement rate for different phases is distinct, relying on the service requirement. For example, Chen et al. [9] pointed out that the Cu_6Sn_5 has a slower rate of growth than Cu_3Sn under isothermal annealing conditions. Simultaneously, the exaggerated IMC layer's growth may also deteriorate the solder joints' reliability [11]. Shen et al. [12] also posited that the IMC layer rises with annealing time due to the solid-state diffusion taking place between Cu atoms from the Cu-pad and Sn from the bulk solder. The average thicknesses of Cu_3Sn and Cu_6Sn_5 at 180 °C are plotted as shown in Figure 5. When the annealing time increases, the Cu_6Sn_5 and Cu_3Sn IMC grows. For Sn-0.7Cu-1.5Bi, the thickness of Cu_6Sn_5 and Cu_3Sn becomes lower relative to the Sn-0.7Cu solder, confirming the fact that the Bi addition effectively retarded the Sn

diffusion and prevented the spread of Cu_6Sn_5 and Cu_3Sn. The growth of interfacial IMC thickness (Cu_6Sn_5 + Cu_3Sn) increases with the annealing process at a rate of 0.042 μm/h for Sn-0.7Cu and 0.037 μm/h for Sn-0.7Cu-1.5Bi. The implication also encompasses the fact that the intermetallic compound layer grows gradually and is compacted with the Bi addition.
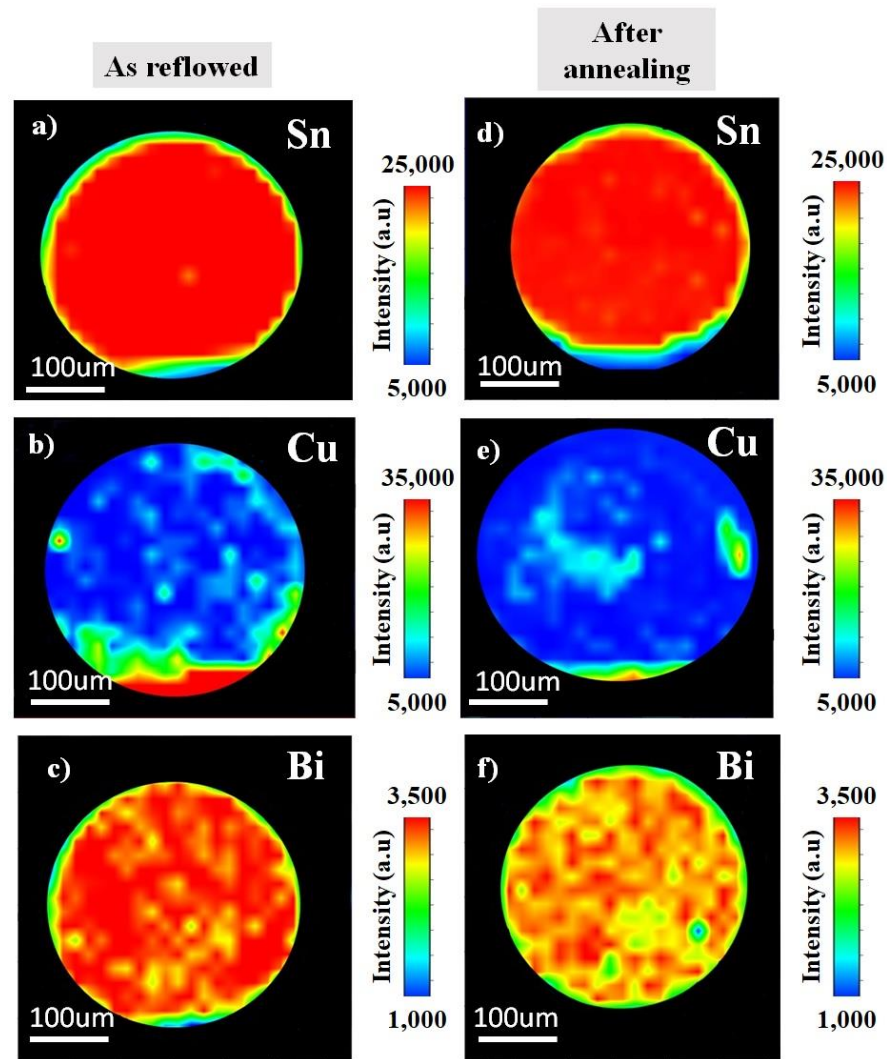
Figure 3. The μ-XRF area mapping of Sn-0.7Cu-1.5Bi (**a–c**) as reflowed and (**d–f**) after isothermal annealing.

A cross-section view of the Sn-0.7Cu/Cu-substrate and Sn-0.7Cu-1.5Bi/Cu-substrate solder joints as a reflowed and annealed sample at 180 °C for 240 h is shown in Figure 6. Two types of the interfacial intermetallic compound layer, which is Cu_6Sn_5 and Cu_3Sn was found in the Sn-0.7Cu/Cu-substrate and Sn-0.7Cu-1.5Bi/Cu-substrate solder joints. As compared with the interfacial intermetallic compound of the Sn-0.7Cu-1.5Bi/Cu-substrate solder joints, some cracks were detected in the interfacial intermetallic compound layer of the solder joints at the Sn-0.7Cu/Cu-substrate. This implies that the Bi inclusion could reduce the crack formation at the interfacial intermetallic compound layer. This observation can be clarified with these cracks, which might happen in a thicker intermetallic compound layer formed by higher annealing temperatures due to the inherent brittle behaviour of the intermetallic compound. Impressively, some voids that existed at Cu_3Sn/Cu and Cu_6Sn_5/Cu_3Sn have an interaction.
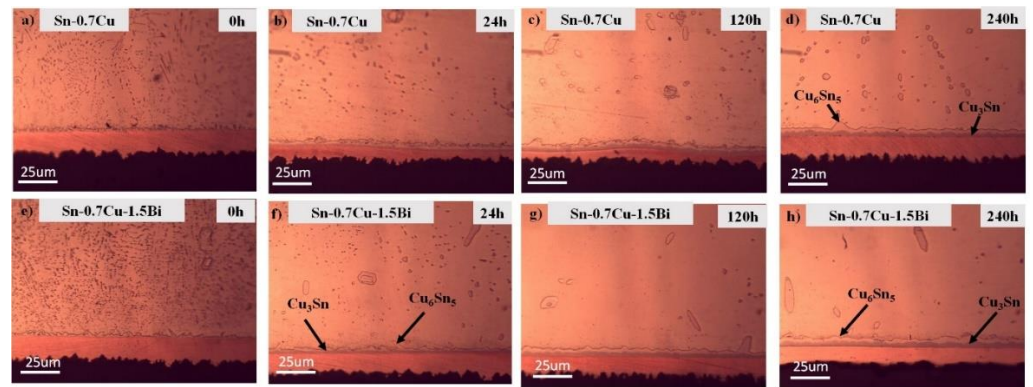
Figure 4. The microstructure of interfacial intermetallic for (**a**–**d**) Sn-0.7Cu and (**e**–**h**) Sn-0.7Cu-1.5Bi after isothermal annealing at 180 °C.
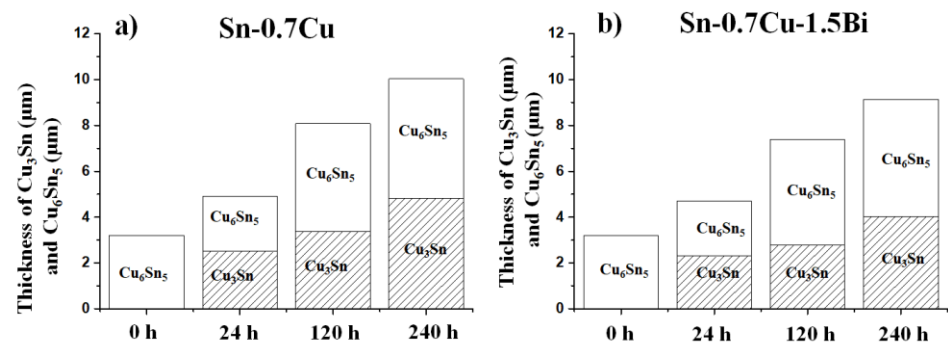
Figure 5. Average thickness of IMC (**a**) Sn-0.7Cu and (**b**) Sn-0.7Cu-1.5Bi during isothermal annealing at 180 °C.
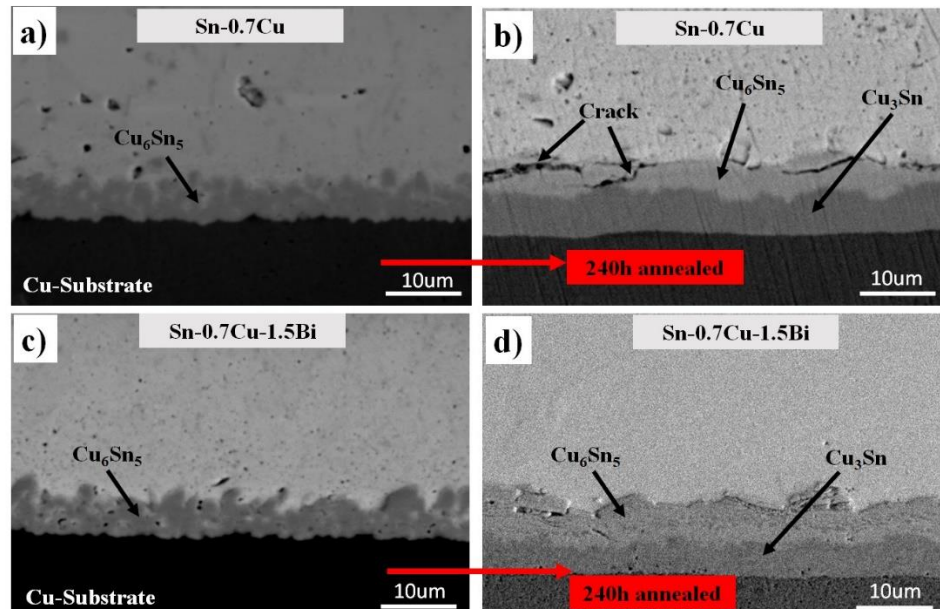
Figure 6. Cross-sectional microstructure of interfacial IMC (**a**,**c**) as reflowed and (**b**,**d**) isothermal annealing at 180 °C.

In this study, the Cu_6Sn_5 and Cu_3Sn were produced when annealed at 180 °C. The Cu_6Sn_5 thickness was increased with the increment of the annealing duration. The 1.5Bi addition, on the other hand, had only a little effect on the development rate of the Cu_6Sn_5 intermetallic layer. These values propose that the expansion of the interfacial Cu_6Sn_5 layers

has been suppressed due to the Bi addition into the solder alloy. It may be surmised that the Bi addition reduced the Sn flux in the Cu_6Sn_5 layer due to the diffusion of Sn at that temperature [5]. Therefore, the interfacial IMC thickness for both solders improves as the annealing temperature and duration are increased. The connection between the total interfacial intermetallic compound thickness and annealing period with the Bi inclusion into Sn-0.7Cu is revealed in Figure 7.
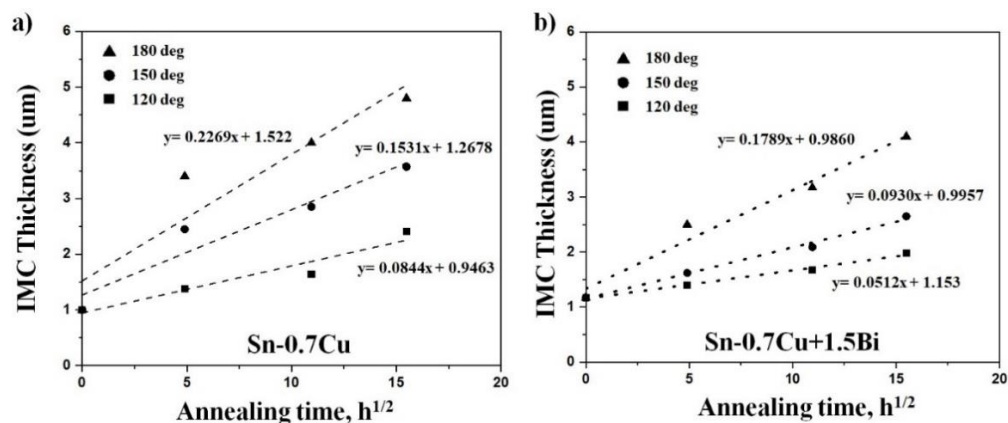
Figure 7. Relationship between the total interfacial intermetallic layer thickness (Cu_6Sn_5 and Cu_3Sn) with annealing time for (**a**) Sn-0.7Cu and (**b**) Sn-0.7Cu-1.5Bi.

A reflowed intermetallic compound in the solder joint will continue to grow via solid-state diffusion. The growth kinetics after isothermal annealing of the intermetallic layer can be calculated using:

$$X = \sqrt{Dt}. \tag{1}$$

Here, X denotes the intermetallic compound thickness at t, while D and t indicate the constant growth rate and annealing time, respectively. The straight-line slope is $\sqrt{D}$ and the growth rate was discovered from a linear regression model of X vs $\sqrt{t}$.

The activation energy was measured using the Arrhenius relationship from the layer growth, given by:

$$k = k0\exp\left(\frac{-Q}{RT}\right), \tag{2}$$

where the diffusion coefficient is k, the constant temperature is k_0, the activation energy is Q, the gas constant is R, and the absolute temperature value is T. The activation energy could be determined by taking the plot's slope as shown in Figure 8, as per Equation (3).

$$\ln k = \ln k0 - \left(\frac{-Q}{R}\right)\frac{1}{T}. \tag{3}$$

The Arrhenius plots of the Sn-0.7Cu and Sn-0.7Cu-1.5Bi of two distinct types of Sn solder joints are portrayed in Figure 8. The activation energy of the intermetallic compound growth during annealing in Sn-0.7Cu is approximated to be 48.96 kJ mol^{-1}, while adding Bi into the Sn-0.7Cu solder increased the activation energy to 55.76 kJ mol^{-1}. With higher activation energy, it implies that the intermetallic compound needs higher energy to grow. The higher activation energy could be attributed to bulk diffusion via the intermetallic compound layer. The inhibition effect due to the addition of Bi can be interpreted via the following considerations. First, the addition of Bi influences the Sn diffusion's driving mechanism by the Cu_6Sn_5 layer and the formation's driving force of the Cu_6Sn_5 intermetallic [5]. Second, the solid-solution effect with Bi addition causes the lattice distortion of the Sn-rich phase, thus retarding the Sn dispersion from the solder to the intermetallic compound. A mechanism is suggested to elucidate why Bi gathered together to the joint. Regarding the Sn-Bi phase diagram, the Sn-rich phase could dissolve large amounts of Bi at higher temperatures. Through the annealing process, the firstly

produced intermetallic compound layers regularly grew to the bulk solder side. The Sn and Cu reactions typically form the Cu_6Sn_5 intermetallic compound. The Bi element does not dissipate in the Cu_6Sn_5 intermetallic compound. It is initially dispersed in the bulk solder area with an apparent gathering near the intermetallic compound layer. It showed that Bi dissolves typically in the Sn matrix in the Sn-0.7Cu solders. Consequently, Bi gathers in the Sn matrix nearby the joint, precipitating from the Sn-rich phase. It is assumed that the suppression of the IMC layer's growth rate is due to the precipitation and accumulation of Bi. Generally, the solder alloys with higher activation energies can grow faster at high temperatures and slower at low temperatures. The Cu_6Sn_5 phase is typically formed after the reflow process, while the Cu_3Sn phase is formed via diffusion between Cu and Cu_6Sn_5 [13]. This finding focused on the sample that aged at 120, 150, and 180 °C for 24, 120, and 240 h, respectively. However, to better understand the growth behaviour of interfacial IMC, higher temperature and longer time is suggested to investigate.
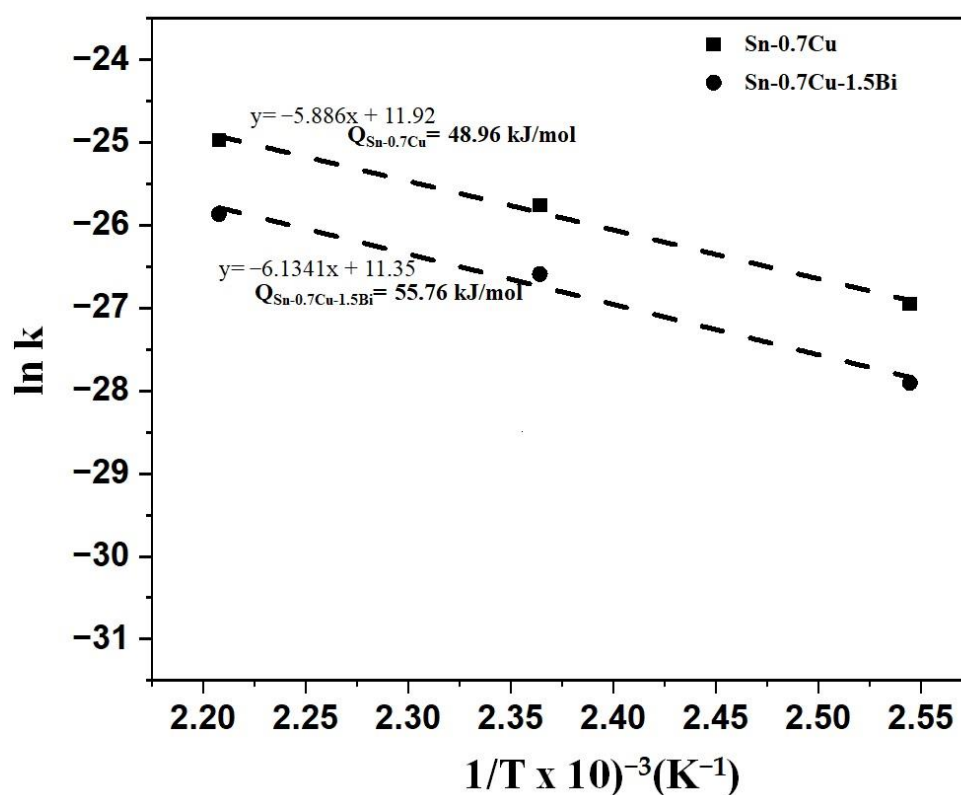
Figure 8. ln k vs. 1/T for the interfacial intermetallic compound growth kinetics for the Sn-0.7Cu-1.5Bi and Sn-0.7Cu solder joints using Arrhenius plots.

3.3. Mechanical Properties

Figure 9 displays the hardness of Sn-0.7Cu and Sn-0.7Cu-1.5Bi solder alloys as reflowed and after the annealing process at 180 °C. The hardness of bulk solder Sn-0.7Cu decreased with the increasing annealing time. Meanwhile, with the inclusion of Bi, the hardness was enhanced by 40.1%. The hardness continues to increase after 24 h annealing. However, it then starts to decrease with 120 and 240 h of annealing time. The hardness was increased due to the Bi addition mainly caused by the coarsening of the microstructure resulting from the IMC's growth [14]. Bi also strengthened the solder alloy via a solid solution [15]. Due to isothermal annealing, the IMC grew in size. The IMCs are hard but quite brittle, and the formation of a large number of the IMCs in a bulk solder hardened it further. This is caused by the Bi atom addition that can efficiently impede the movement of dislocations, which strengthens the Sn-0.7Cu solder by limiting strain due to the solid-solution effect. The existence of the distributed Bi increased the rate of recrystallisation during the annealing process owing to the increased number of potential

sites for nucleation. Contrarily, the distributed Bi acted as the holding agent that retards the grain growth, which resulted in increased hardness.
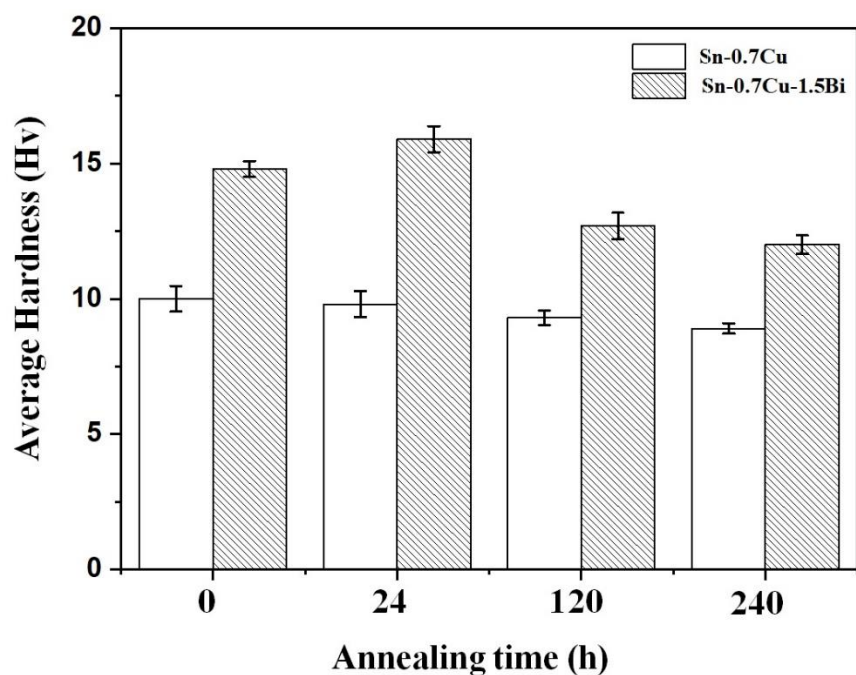
Figure 9. The Sn-0.7Cu and Sn-0.7Cu-1.5Bi hardness after isothermal annealing at 180 °C.

The shear strength results of Sn-0.7Cu-1.5Bi and Sn-0.7Cu as reflowed and after annealing are shown in Figure 10. The shear test was performed at 180 °C for 24, 120, and 240 h. The results illustrate that the Sn-0.7Cu alloy's shear strength reduced with an extended annealing time. However, on the Bi addition in Sn-0.7Cu, it showed an improvement of the shear strength of the solder joint by 37%. After annealing samples for 24 h, the Sn-0.7Cu-1.5Bi alloys' strength increased. However, after annealing for 120 and 240 h, the strength of the Sn-0.7Cu-1.5Bi alloy decreased. This increment in the shear strength of solder alloy was improved with Bi inclusion. This increment via the addition of a metallic element could be ascribed to solid solution hardening. Tateyama et al. [16] pointed out that the addition of 2–3% of Bi renders the solid-solution hardening dominant, which in turn upsurges the shear strength.

The strength of Sn-0.7Cu after annealing was decreased, which can be attributed to two significant facts. First, annealing coarsens the Cu_6Sn_5 intermetallic compounds, which can reduce the capability to prevent the dislocation movement. Second, the β-Sn phase also toughens due to annealing, which decreases the strength. Bi has a solubility limit in Sn at room temperature, and any extra Bi forms a secondary precipitate phase. With the rising temperature, the amount of Bi to enter Sn increased due to the solid solution. Once in the solid solution and at a higher temperature, Bi could diffuse throughout the Sn, which increases the homogeneousness of the alloy. Decreasing the temperature to room temperature forces the precipitation of homogeneously spaced Bi precipitates, contributing to stabilising the strength [17]. Additionally, 1.8% of Bi is considered to have good solubility in Sn at room temperature and can contribute some improvement in strength before the annealing process [18].

However, Bi travels into the solution in the β-Sn during the Sn-0.7Cu-1.5Bi alloy's annealing process. As a result, the solid solution solubility of Bi increases from only 1.8% at 25 °C, to 14% at 100 °C. This suggested that Bi exists in the solidified Sn-0.7Cu alloy's microstructure as a separate Bi-phase and goes into the β-Sn matrix during annealing, which leads to additional solid-solution strengthening in the Sn-0.7Cu-Bi alloy. We hypothesised that the improvement of Sn-0.7Cu strength through annealing is owing to the

improvement in strength from solid-solution strengthening, superseding any decreases in strength due to the intermetallic compound and β-Sn phase coarsening. Ahmed et al. [18] also reported mitigating the annealing effect in SAC-Bi alloys. They reported that Bi atoms are wholly dissolved into the β-Sn induced solid-solution strengthening, thus increasing the shear strength.
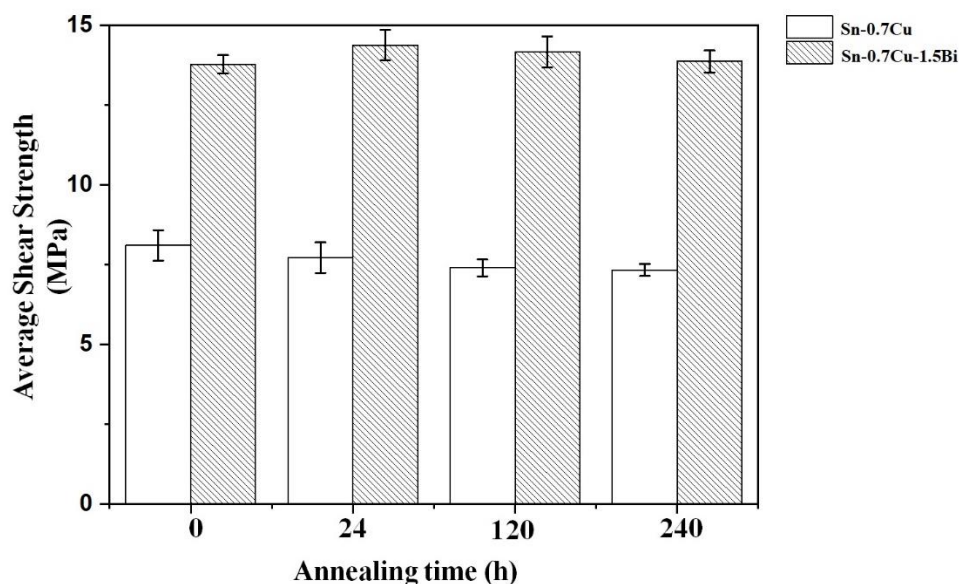
Figure 10. The Sn-0.7Cu and Sn-0.7Cu-1.5Bi shear strength after isothermal annealing at 180 °C.

3.4. Fracture Morphology

The fractography of sheared samples was imaged using the SEM to further elucidate the shear behaviours of the Sn-0.7Cu-1.5Bi solder joint. Figure 11 shows the shear fracture morphology of Sn-0.7Cu and Sn-0.7Cu-1.5Bi alloys before and after the annealing process at 180 °C. Figure 11a shows a typical ductile mode on the fracture surface aged at 0 h.
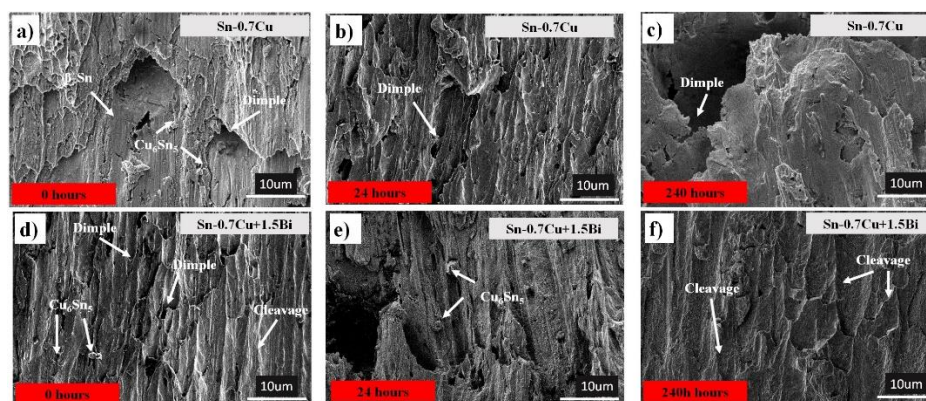
Figure 11. Fractographies of Sn-0.7Cu (**a**) 0 h, (**b**) 24 h, (**c**) 240 h and Sn-0.7Cu-1.5Bi (**d**) 0 h, (**e**) 24 h, (**f**) 240 h.

Nevertheless, after Sn-0.7Cu was annealed up to 240 h, the fracture surface changed to a mixture of brittle fracture, as displayed in Figure 11b. Bi (1.5 wt.%) was added to the mix, which showed a ductile fracture mode with a small dimple. After the sample was annealed up to 240 h, it showed a cleaved pattern and brittle failure mode. It also can be seen that the joint break happens at the interfacial IMC when a thicker IMC forms due to the annealing process. Another reason is the existence of an initial crack at the interfacial IMC, as shown in Figure 6b,d. This can be related to the reduced activation energy of IMC in the Sn-0.7Cu solder joint, which increased the IMC's growth thickness during the annealing process.

However, with the Bi inclusion in Sn-0.7Cu, the IMC needs higher energy to grow, which could reduce the IMC thickness growth.

Thus, it was concluded that if the fracture happens at the bulk region, it is ductile [19]. Moreover, if the fracture occurs in the region near the solder and intermetallic interface, it is a mixture of brittle and ductile fractures [20]. As a result, the strength near the solder and intermetallic interface is a weak point for the fracture, resulting in decreased shear strength with time.

4. Conclusions

This study presents the mechanical characteristics of Sn-0.7Cu-1.5Bi, which are examined on the primary and interfacial intermetallic after isothermal annealing. Some conclusions were drawn from the results of this work:

1. The 1.5 wt.% Bi addition did not lead to a significant change in the primary Cu_6Sn_5, as was observed in the bulk solder Sn-0.7Cu. The μ-XRF analysis shows the lower Cu concentration level of Cu_6Sn_5 primary intermetallic with the addition of Bi after the annealing process. It can also be seen that the Bi element is well dispersed in the β-Sn region.

2. The growth of interfacial IMC thickness ($Cu_6Sn_5 + Cu_3Sn$) increases with the annealing process at a rate of 0.042 μm/h for Sn-0.7Cu and 0.037 μm/h for Sn-0.7Cu-1.5Bi. The shape shifted from the scallop shape to the planar shape after the annealing process with a small microcrack form. Bi also inhibited the growth of Cu_3Sn interfacial intermetallic compound after the annealing process.

3. The activation energy for the formation of intermetallic layers of Sn-0.7Cu was set to 48.96 kJ mol^{-1}, and the activation energy of the Sn-0.7Cu-1.5Bi system was measured at 55.76 kJ mol^{-1}. It is obvious that the intermetallic compound thickness of the Sn-0.7Cu-1.5Bi system is difficult to grow when matched to the Sn-0.7Cu system due to the high activation energy.

4. Compared to Sn-0.7Cu, adding Bi improves hardness by 40.3% and shear strength by 37.1%. After 24 h of annealing, the shear strength of Sn-0.7Cu-1.5Bi was increased. This is due to the fact that with the addition of Bi, it can be that the dissolution of the Bi element in the matrix improved the shear performance of the solder joint. However, a longer annealing time could reduce the shear strength. The fracture of the annealing sample shows a mixture of brittle fractures in the area near the solder/intermetallic interface due to a thicker intermetallic compound layer during the annealing process.

Author Contributions: Conceptualization, methodology, and writing, M.I.I.R.; supervision and resources, M.A.A.M.S.; methodology, formal analysis, and investigation, S.F.M.A., R.M.S., P.V. and N.S.; interpretation, review and editing, A.V.S., M.M.A.B.A., J.C., A.R. and M.N. All authors have read and agreed to the published version of the manuscript.

Institutional Review Board Statement: Not applicable.

Informed Consent Statement: Not applicable.

Data Availability Statement: The data presented in this study are available on request from the corresponding author.

Conflicts of Interest: The authors declare no conflict of interest.

References

1. Ramli, M.I.I.; Salleh, M.A.A.M.; Yasuda, H.; Chaiprapa, J.; Nogita, K. The effect of Bi on the Microstructure, Electrical, Wettability and Mechanical Properties of Sn-0.7Cu-0.05Ni alloys for High Strength Soldering. *Mater. Des.* **2019**, *186*, 108281. [CrossRef]
2. Teoh, A.; Salleh, M.M.; Halin, D.; Foo, K.; Razak, N.A.; Yasuda, H.; Nogita, K. Microstructure, thermal behavior and joint strength of Sn-0.7 Cu-1.5 B[1]i/electroless nickel immersion gold (ENIG). *J. Mater. Res. Technol.* **2021**, *12*, 1700–1714. [CrossRef]
3. Bogno, A.-A.; Spinelli, J.E.; Afonso, C.R.M.; Henein, H. Microstructural and mechanical properties analysis of extruded Sn–0.7 Cu solder alloy. *J. Mater. Res. Technol.* **2015**, *4*, 84–92. [CrossRef]
4. Rizvi, M.J.; Chan, Y.C.; Bailey, C.; Lu, H.; Islam, M.N. Effect of adding 1 wt% Bi into the Sn-2.8Ag-0.5Cu solder alloy on the intermetallic formations with Cu-substrate during soldering and isothermal aging. *J. Alloy. Compd.* **2006**, *407*, 208–214. [CrossRef]
5. Zhao, J.; Cheng, C.-Q.; Qi, L.; Chi, C.-Y. Kinetics of intermetallic compound layers and shear strength in Bi-bearing SnAgCu/Cu soldering couples. *J. Alloy. Compd.* **2009**, *473*, 382–388. [CrossRef]
6. Zhao, J.; Qi, L.; Wang, X.M.; Wang, L. Influence of Bi on microstructures evolution and mechanical properties in Sn-Ag-Cu lead-free solder. *J. Alloy. Compd.* **2004**, *375*, 196–201. [CrossRef]
7. Wang, K.K.; Gan, D.; Hsieh, K.C. Orientation relationships, interfaces, and microstructure of η-Cu6Sn5 formed in the early-stage reaction between Cu and molten Sn. *Thin Solid Film.* **2010**, *519*, 1380–1386. [CrossRef]
8. Sayyadi, R.; Khodabakhshi, F.; Javid, N.S.; Khatibi, G. Influence of graphene content and nickel decoration on the microstructural and mechanical characteristics of the Cu/Sn–Ag–Cu/Cu soldered joint. *J. Mater. Res. Technol.* **2020**, *9*, 8953–8970. [CrossRef]
9. Shen, J.; Zhao, M.; He, P.; Pu, Y. Growth behaviors of intermetallic compounds at Sn-3Ag-0.5Cu/Cu interface during isothermal and non-isothermal aging. *J. Alloy. Compd.* **2013**, *574*, 451–458. [CrossRef]
10. Zhang, L.; Xue, S.B.; Zeng, G.; Gao, L.L.; Ye, H. Interface reaction between SnAgCu/SnAgCuCe solders and Cu substrate subjected to thermal cycling and isothermal aging. *J. Alloy. Compd.* **2012**, *510*, 38–45. [CrossRef]
11. Nergis, D.D.B.; Vizureanu, P.; Ardelean, I.; Sandu, A.V.; Corbu, O.; Matei, E. Revealing the Influence of Microparticles on Geopolymers' Synthesis and Porosity. *Materials* **2020**, *13*, 3211. [CrossRef] [PubMed]
12. Shen, J.; Cao, Z.; Zhai, D.; Zhao, M.; He, P. Effect of isothermal aging and low density current on intermetallic compound growth rate in lead-free solder interface. *Microelectron. Reliab.* **2014**, *54*, 252–258. [CrossRef]
13. Deng, X.; Sidhu, R.S.; Johnson, P.; Chawla, N. Influence of reflow and thermal aging on the shear strength and fracture behavior of Sn-3.5 Ag solder/Cu joints. *Metall. Mater. Trans. A* **2005**, *36*, 55–64. [CrossRef]
14. Aamir, M.; Muhammad, R.; Ahmed, N.; Sadiq, M.; Waqas, M. Izhar, Mechanical Properties of Lead Free Solder Alloy for Green Electronics under High Strain Rate and Thermal Aging. *J. Eng. Appl. Sci.* **2017**. [CrossRef]
15. Mahdavifarda, M.H.; Sabria, M.F.M.; Saidb, S.M.; Rozalia, S. High stability and aging resistance Sn-1Ag-0.5Cu solder alloy by Fe and Bi minor alloying. *Microelectron. Eng.* **2019**, *208*, 29–38. [CrossRef]
16. Tateyama, H.U.K.; Yamaoka, Y.; Takahashi, K.; Yamada, H.; Saito, M. Effects of Bi Content on Mechanical Properties and Bump Interconnection Reliability of Sn-Ag Solder Alloys. *Int. J. Microcircuits Electron. Packag.* **2000**, *23*, 1063–1674.
17. Delhaise, A.M.; Chen, Z.; Perovic, D.D. Solid-State Diffusion of Bi in Sn: Effects of b-Sn Grain Orientation. *J. Electron. Mater.* **2019**, *48*, 32–43. [CrossRef]
18. Ahmed, S.; Basit, M.; Suhling, J.C.; Lall, P. Effects of aging on SAC-Bi solder materials. In Proceedings of the 2016 15th IEEE Intersociety Conference on Thermal and Thermomechanical Phenomena in Electronic Systems (ITherm), Las Vegas, NV, USA, 31 May–3 June 2016; IEEE: Piscataway, NJ, USA, 2016; pp. 746–754.
19. Mohd Said, R.; Mohd Salleh, M.A.A.; Saud, N.; Ramli, M.I.I.; Yasuda, H.; Nogita, K. Microstructure and growth kinetic study in Sn–Cu transient liquid phase sintering solder paste. *J. Mater. Sci-Mater. El.* **2020**, *31*, 11077–11094. [CrossRef]
20. Muhd Amli, S.F.N.; Mohd Salleh, M.A.A.; Ramli, M.I.I.; Yasuda, H.; Chaiprapa, J.; Somidin, F.; Shayfull, Z.; Nogita, K. Origin of Primary Cu$_6$Sn$_5$ in Hypoeutectic Solder Alloys and a Method of Suppression to Improve Mechanical Properties. *J. Electron. Mater.* **2021**, *50*, 710–722. [CrossRef]

The Influence of UV Radiation Aging on Degradation of Shear Thickening Fluids

Radosław Żurowski [1], Mariusz Tryznowski [2,*], Selim Gürgen [3], Mikołaj Szafran [1] and Aleksandra Świderska [1]

[1] Faculty of Chemistry, Warsaw University of Technology, Noakowskiego 3, 00-664 Warsaw, Poland; rzurowski@ch.pw.edu.pl (R.Ż.); szafran@ch.pw.edu.pl (M.S.); aswiderska23@wp.pl (A.Ś.)
[2] Faculty of Mechanical and Industrial Engineering, Warsaw University of Technology, Narbutta 85, 02-524 Warsaw, Poland
[3] Department of Aeronautical Engineering, Eskişehir Osmangazi University, 26040 Eskişehir, Turkey; sgurgen@ogu.edu.tr
* Correspondence: mariusz.tryznowski@pw.edu.pl

Abstract: Shear thickening fluids (STFs) are innovative materials that can find applications in smart body armor. However, the usage of STFs is limited by the aging of these materials. This work aims to analyze the influence of UV radiation on the aging process of STFs. The investigation was done experimentally, and artificial aging was applied to investigate the impact of UV radiation on the properties of STFs. The shear-thickening properties of obtained STFs were confirmed by viscosity measurements. The STFs based on PPG425, PPG2700, and KE-P10 exhibited a very high maximum viscosity of up to 580.7 Pa·s and 3313 Pa·s for the STF425 and STF2700, respectively. The aging of the obtained STFs caused the liquid matrix degradation, causing damage to the STFs and their change from liquid into solid. Furthermore, the FT-IR, ^{1}H NMR, and ^{13}C NMR spectroscopies were used for the confirmation of the breakdown of STFs. The FT-IR spectroscopy revealed the appearance of carbonyl groups in STFs after aging. Moreover, ^{1}H NMR and ^{13}C NMR spectroscopy confirmed the formation of the typical groups containing carbonyl groups. Our results demonstrate that STFs are UV light-sensitive and may lose their properties during storage.

Keywords: shear thickening fluids; aging; lightfastness; product degradation

1. Introduction

The need for innovative and intelligent materials is encouraging the search for and development of novel materials and applications. An example of such materials is shear thickening fluids (STFs). These are non-Newtonian fluids, and their viscosity increases with either increasing shear rate or applied stress [1]. STFs are ceramic-polymer composites, wherein a ceramic powder is dispersed in an organic matrix such as glycerin, poly(ethylene oxide), or poly(propylene glycol). These are technically not new materials; STFs have been known for many years [2]. One of the material properties of STFs is the logarithmic increase of viscosity as a function of shear rate, known as the dilatation jump and observed as the liquid-to-solid transition. The viscosity of STFs can increase rapidly, and they can appear as solid-like suspensions. This behavior may be utilized in many applications, such as in body armor or various other elements of human protection [3].

The STFs can be used to impregnate the ballistic fabrics, improving the fiber fabric's friction and energy absorption [3]. For this purpose, high-performance fabrics can be used, for example Kevlar® [4,5] or UHMWPE (Ultra High Molecular Weight Polyethylene) [6]. Arora et al. have reported the usage of panels made from up to five layers impregnated with STFs [5]. In this work, it was discovered that the angular orientation of fabrics highlights the synergic effect of impregnating fabrics with STFs. Other researchers proposed hybrid composite materials and novel composite materials based on natural fibers and cornstarch with STFs layers [7]. Finally, aramid fabrics may be impregnated with STFs and combined

with a thermoplastic polyurethane coating, resulting in sandwich-structured composite panels [8]. Chang et al. have reported the usage of polyurea elastomer/Kevlar fabric composites enriched with STFs as protective materials [9]. Despite of the type of STFs, the studies on the topic of STFs confirm the bullet resistance of Kevlar® fabrics reinforced with STFs [6,7]. Unfortunately, the resistance of fabrics impregnated with STFs declines when the fabrics contain too many STFs [4]. Aside from the application of STFs in human protection, other applications have been reported in the literature. For example, Gürgen et al. reported using STFs in cutting tools to prevent vibration dumping [10]. Additionally, Liu et al. proposed using STFs with magneto-sensitive properties as shock absorbers for high-end vehicles [11]. Furthermore, STFs can be used in multilayer composites for energy-absorbing purposes [12].

STFs can be composed of various liquid matrices, which include PEGs, PPGs, and even ionic liquids. The most popular materials for the STFs preparation, due to their good properties and low price, are various PPGs. In our research team, STFs were prepared from PPGs characterized by different molecular masses and silica (see for example in [13–15]). Qin et al. have proposed novel STFs based on various imidazolium and pyridinium ILs characterized by a maximum viscosity of up to 1000 Pa·s [16].

There are some disadvantages of introducing STFs into mass-scale use. Despite several literature reports, the effect of shear thickening is not fully understood nor clearly defined. However, several researchers have presented modeling of the shear thickening effect in STFs [17–21]. Furthermore, STFs, like other materials, exhibit certain stability and lifetime. The stability and shear thickening properties of STFs strongly limit the manufacturing of products such as protective devices [22]. According to the literature, STFs seem to exhibit excellent stability [13]. However, the conditions of storage and usage may influence the lifetime of the material. For example, the presence of water in the environment where STFs are stored decreases their viscosity [23]. Finally, there is a technological barrier to obtaining STFs in large amounts for mass-scale adoption.

The application of STFs is strongly limited by their lifetime and the nature of their usage and storage before usage. Apart from the aging of the STFs, the aging of fabrics in the body armor can be observed [24]. Those two effects strongly limit the expiration date of body armor. To the best of our knowledge, the aging of STFs has not been previously reported in the literature. Nakonieczna et al. have reported excellent stability after 8 days of STFs based on PPG and amorphous silica [13]. Furthermore, Żurawski et al. have compared the rheological behaviors of STFs after different periods of time and discovered that STFs demonstrated no changes in dilatant effect [25]. This work aims to analyze the influence of UV radiation on the aging process of STFs. The STFs can be stored prior to usage in various conditions, whereas they can be exposed to external factors, for example light. Additionally, the high-performance fabric panels used in body armors have a warranty period and use-by date (approximately 5–10 years depending on the producer), and after that they should not be used. The method and intensity of bulletproof vest usage also affects the quality of the panels based on high-performance fabrics. The aging with UV light gives an overview of the stability of STFs and their shelf life, especially when the accelerated aging process is used. For this work, STFs with high maximum viscosity were prepared. Next, the aging process was performed on the obtained samples. Comprehensive analyses of STF aging products were performed, including FT-IR, ^{1}H NMR, and ^{13}C NMR spectroscopies. For the first time, we demonstrate the limitations of the wide usage of innovative and smart materials like STFs.

2. Materials and Methods

2.1. Materials

For STF preparation, poly(propylene glycol) PPG425 and PPG2700 (CAS 25322-69-4, Sigma-Aldrich, St. Louis, MO, USA) and spherical silica powder KE-P10 (Nippon Shokubai, Tokyo, Japan), with a particle size within the range of 100–200 nm, specific surface area of

132.2 m^2 g^{-1}, and density of 1.96 g cm^{-3} [26], were used. The properties of poly(propylene glycol) types used in this work are summarized in Table 1.

Table 1. Properties of poly(propylene glycol) [1].

Abbreviation	M_n (g mol^{-1})	Density (g cm^{-3})
PPG425	~425	1.01
PPG2700	~2700	1.01

[1] According to the Safety Data Sheet provided by the supplier.

2.2. STF Preparation

The STFs were produced by mixing poly(propylene glycol) with silica powder. The Computer Aided Design, CAD, scheme of the mixer is displayed in Figure 1. The laboratory stand was specially built for the STF preparation. The mixer is equipped with a glass 250 mL reactor and a mechanical stirrer (R50D, Ingenieurbüro CAT, Ballrechten-Gottingen, Germany) equipped with a stainless-steel propeller-mixing geometry. The silica powder was added stepwise. The applied mixing speed was within the range of 150–200 rpm. The solid-phase concentration of the fluid was 50 vol. %. Table 2 displays the composition of STFs.
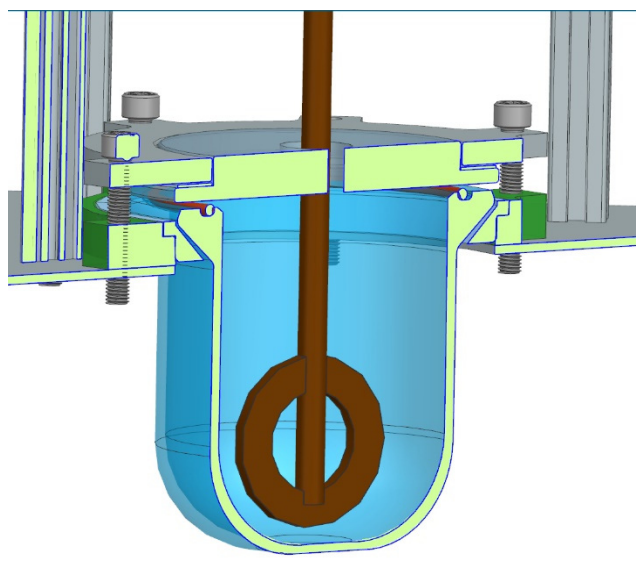
Figure 1. Scheme of the mixer used for the STF preparation.

Table 2. Properties of spherical silica powders.

Abbreviation	Ceramic Powder	Carrier Fluid
STF425		PPG425
STF2700	KE-P10	PPG2700

2.3. Rheology Measurements

The rheological behavior of STFs was studied using a rational KinexusPro rheometer (Malvern Panalytical, Malvern, Worcestershire, UK) with parallel plate geometry (top plate φ 20 mm; bottom plate φ 100 mm; spacing gap 0.7 mm) with applied shear stress in the range of 10^{-2} up to 10^3 s^{-1}. The measurements were repeated twice with fresh samples.

2.4. Artificial Aging

Artificial aging was carried out using a Suntest CPS+ (Atlas, Mount Prospect, IL, USA). The device was equipped with an optical filter which is a UV external light filter

that eliminates UV radiation with wavelengths shorter than 290 nm. The applied light intensity was 580 W m^{-2}. The Black Standard Thermometer (BST) was set at 35 °C. A small amount (approximately 10 g) of each STF was placed in a glass Petri dish (φ 80 mm) covered with a quartz lid. The samples subjected to artificial aging are displayed in Figure 2. Blue Wool Scale samples (approximately 1 cm^2) were exposed together with STF samples. The contrast between exposed and unexposed Blue Wool Scales stripes was measured after the aging cycle using greyscale, according to ISO 105-A02:1993 standard. The procedure is described elsewhere [27]. The tests were performed for a total of 167 h, which corresponds to approximately 15.5 weeks (108 days) of natural aging. Every 1 h spent under aging conditions corresponds to a 1980 kJ m^{-2} dose absorbed by the samples.
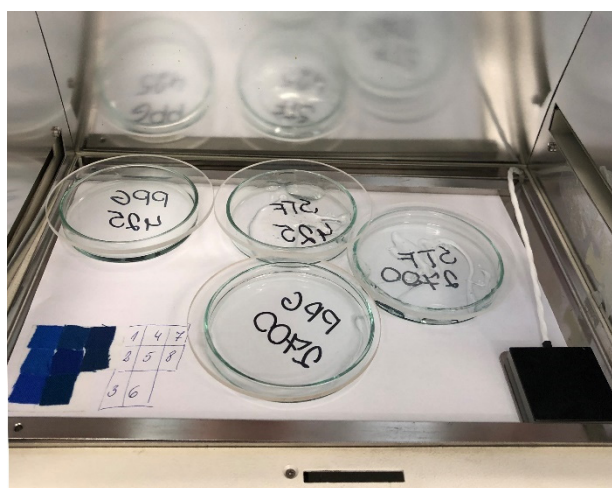
Figure 2. PPG and STF samples together with Blue Wool Scale prepared for aging.

2.5. Product Analyses

FT-IR, ^{1}H NMR, and ^{13}C NMR spectroscopies were used to characterize the emerging products during aging. The analyses were performed both prior to and after aging.

The attenuated total reflectance ATR FT-IR spectra were recorded within the wavelength range of 400–4000 cm^{-1}, with a resolution of 4 cm^{-1} using a Nicolet iS5 (Thermo Fisher Scientific, Waltham, MA, USA) spectrometer. The FT-IR spectra were analyzed with OMNIC Specta™ software (series 9.12.968, Thermo Fisher Scientific, Waltham, MA, USA).

^{1}H NMR and ^{13}C NMR spectra were recorded using a Varian VXR 400 MHz spectrometer (Varian, Palo Alto, CA, USA) with tetramethylsilane as an internal standard and deuterated solvents (CDCl$_3$). The results were analyzed with MestReNova v.6.2.0 (Mestrelab Research S.L, Santiago de Compostela, Spain) software.

3. Results and Discussion

3.1. Flow Fluid Properties

Figure 3 demonstrates the viscosity curves of the STFs. The results confirm the typical shear thickening behavior of the obtained STFs. The maximum viscosity of STF2700 is five times higher than for STF425. The STF2700 exhibited a dilatant effect at 4.4 s^{-1} with a maximum viscosity of 3313 Pa·s, and STF425 exhibited a dilatant effect at 12.7 s^{-1} with a maximum viscosity of 580.7 Pa·s.

The dilatant effect observed for STF2700 is much higher than for those previously reported in the literature. For example, Głuszek et al. reported the maximum viscosity for STFs based on KE-P10 and poly(propylene glycol) (molar mass 1000 g mol^{-1}) to be above 350 Pa·s [26]. In this work, the maximum viscosity reaches up to 1000 Pa·s [5,16,26,28]. The maximum viscosities reported by Arora et al. and Bajya et al. exceeded 170 Pa·s [5,28]. However, Qin et al. reported STFs with higher solid contents than STFs obtained by us, with maximum viscosities above 800 Pa·s [4]. Furthermore, modification of carrier liquid

does not reflect much higher values of maximum viscosity. For example, Ghosh et al. have reported a simple modification of polyglycols with citric acid, and maximum viscosity increased 76 times with the peak viscosity up to 800 Pa·s [29].
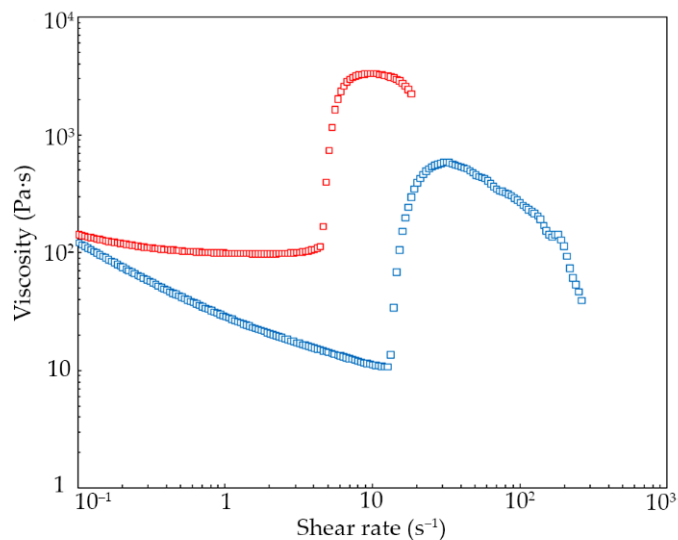
Figure 3. Viscosity vs. shear rate for the investigated STFs: blue squares STF425, red squares STF2700.

3.2. Influence of Artificial Aging

The total aging time together with an absorbed dosage of 1980 kJ m^{-2} h^{-1} corresponds to about approximately 15.5 weeks under natural conditions. Additionally, the fading of Blue Wool Scale #5 was observed, corresponding to approximately three months of exposure to light under natural conditions [30].

The samples after aging are displayed in Figure 4. The total degradation of STFs was observed, hence the product analyses (FT-IR, ^{1}HNMR, and ^{13}CNMR) were performed without viscosity measurements. The condition of the STF samples after aging enables the viscosity measurement. During the aging of STFs, the change from liquid- to solid-state was observed. It is related to the degradation and breakdowns of the PPGs macromolecules, which are liquid-phase forming a solvation layer on the surface of the silica granules. Therefore, depending on the degree of PPG degradation during aging, liquid STFs changed into solid-state. The product analyses with FT-IR, ^{1}HNMR, and ^{13}CNMR confirmed the degradation of the PPGs during aging.
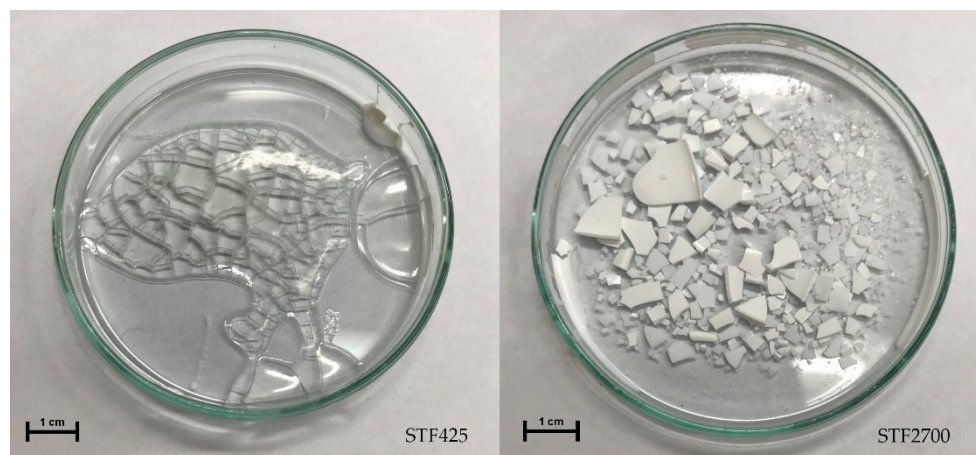
Figure 4. Samples of STFs after aging.

The FT-IR spectra of STF2700 before and after aging are displayed in Figure 5. The FT-IR spectra were measured with the ATR technique and transferred to KBr using Omnic software. In the FT-IR spectra, characteristic changes within the range of 3000–3600 cm^{-1} and 1700–1800 cm^{-1} are observed after aging. Peak broadening within the range of 3000–3600 cm^{-1} is related to the presence of –OH groups, which appear with the degradation of the carrier fluid into macromolecules with shorter chains. Finally, a new peak appears at 1720 cm^{-1}, related to the presence of carbonyl groups (–C=O).
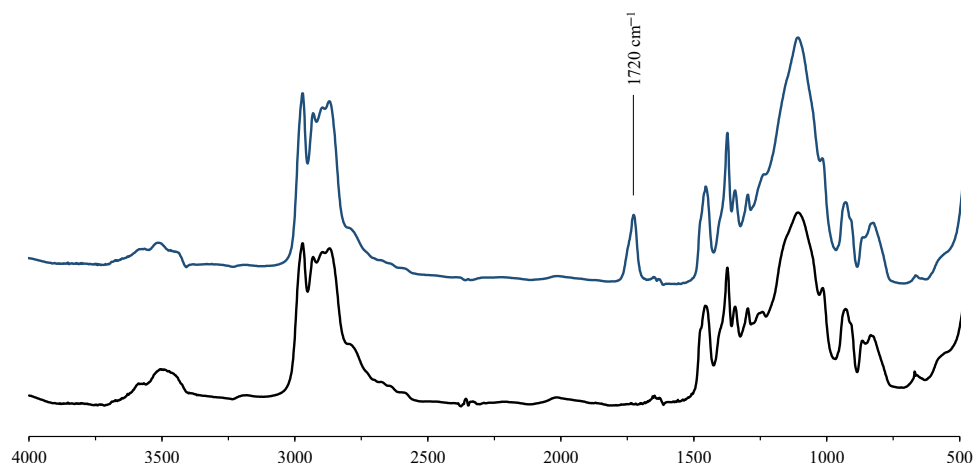
Figure 5. FT-IR spectra of STF2700 before (black line) and after (dark blue line) aging.
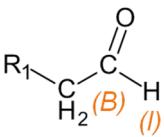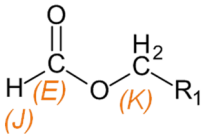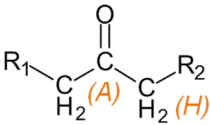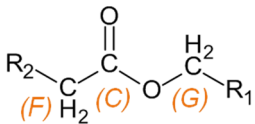
PPG2700 and PPG425 were analyzed after exposure to UV radiation, using ^{1}H NMR and ^{13}C NMR spectroscopies to identify the degradation products.

In the ^{1}H NMR spectrum of raw PPG2700 there are peaks between 3–4 ppm corresponding to the chemical shift range of methine and methylene groups bound to the oxygen atom, and a broadened peak at 1.1 ppm corresponding to methyl groups. The integrals of both signals are equal. In the ^{13}C NMR spectrum there are peaks between 71–77 ppm corresponding to methine and methylene groups; peaks at 66.9, 65.3, and 65.0 ppm corresponding to CH$_x$–OH; and peaks between 17–18 ppm corresponding to methyl groups. Additional signals appeared in the ^{1}H and ^{13}C NMR spectra of PPG2700 after UV exposure. Analysis and interpretation of the spectra displayed that the new peaks are characteristic of the formic ester and other esters, consistent with the results presented in previous reports on the thermal degradation of PEG or PPG as a result of oxidation [31–35]. Peaks appeared in the ^{13}C NMR spectrum at 207.4, 200.0, 172.8, 170.4, 162.0, and 160.5 ppm, characteristic of carbonyl atoms from ketones, aldehydes, and esters, including formic esters, respectively. In the ^{1}H NMR spectrum, signals appeared that are characteristic of aldehydes (9.6 ppm) and formic esters (7.9 ppm). Additionally, signals between 3.5–5.0 ppm and 1.9–2.1 ppm verify the formation of esters. The assignment of signals to their appropriate groups is displayed in Table 3, and in Figures 6 and 7.

Table 3. Chemical structures and assignment of characteristic groups to signals in ^{1}H and ^{13}C NMR spectra.

Chemical Structure	Chemical Shift (^{1}H NMR)	Chemical Shift (^{13}C NMR)
	P, *R*: 3–4 ppm *S*: 1.1 ppm	*P*, *R*: 71–77 ppm *S*: 17–18 ppm

Table 3. *Cont.*

Chemical Structure	Chemical Shift (^{1}H NMR)	Chemical Shift (^{13}C NMR)
	I: 9.6 ppm	*B*: 200.0 ppm
	J: 7.9 ppm *K*: 5.0 ppm	*E*: 160–162 ppm
	H: 1.8–2.2 ppm	*A*: 207.4 ppm *H*: 25.8 ppm
	G: 3.7–4.3 ppm *F*: 1.8–2.2 ppm	*C*: 170–173 ppm *G*: 63.5–68.0 ppm *F*: 18–20 ppm
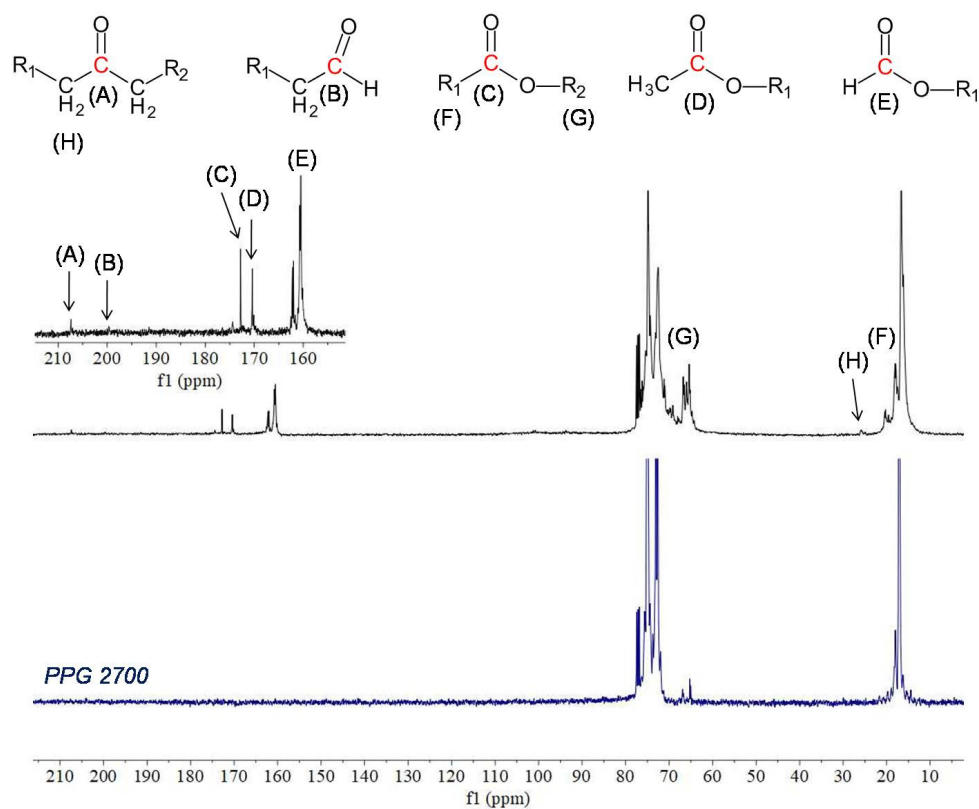
Figure 6. ^{13}C NMR spectra (CDCl$_3$, 100 MHz) of raw PPG2700 (blue) and PPG2700 exposed to UV radiation (black). Inset: enlarged region within the 150–210 ppm spectral range after UV exposure.
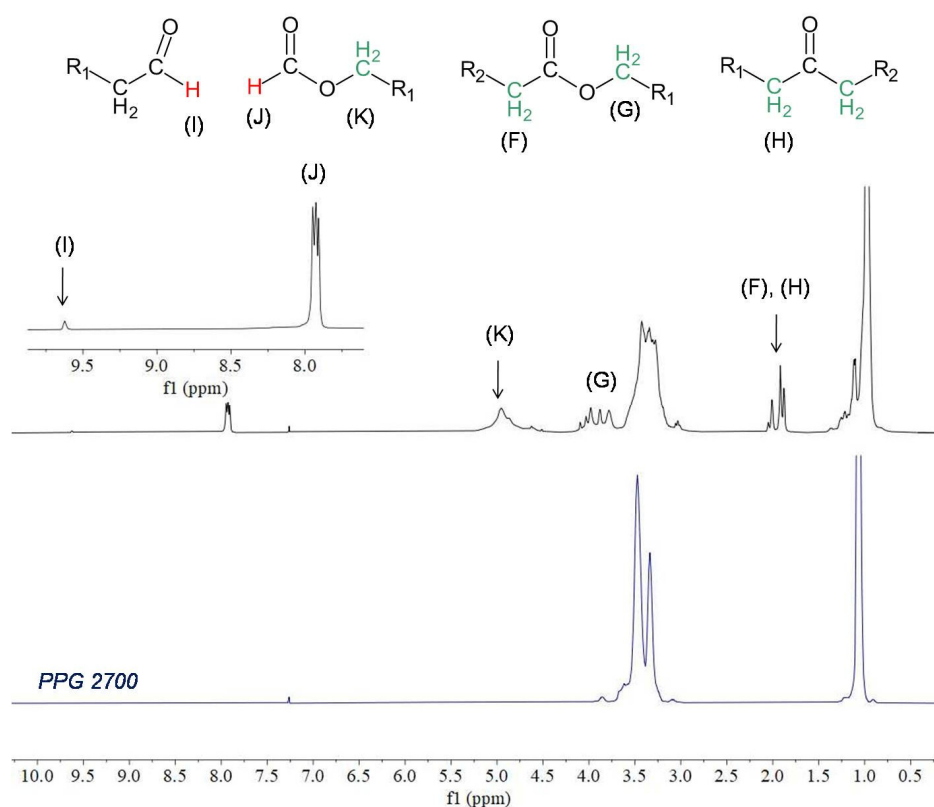
Figure 7. ^{1}H NMR spectra (CDCl$_3$, 400 MHz) of raw PPG2700 (blue) and PPG2700 exposed to UV radiation (black). Inset: enlarged region within the 7.5–10 ppm spectral range after UV exposure.

4. Conclusions

For the first time, the influence of UV exposure time on the properties of STFs was measured after artificial aging. The STFs obtained in this work exhibited a shear thickening effect up to a maximum of 3313 Pa·s, exhibiting a much more significant shear thickening effect than previously observed in the literature.

The aging time of STF samples corresponds to approximately three months of natural aging indoors, and the aging causes visible changes in their appearance. FT-IR spectroscopy and ^{1}H NMR and ^{13}C NMR spectroscopies confirm the degradation of the obtained STFs. The spectrometric analyses confirm the appearance of carbonyl groups during aging. Therefore, the degradation causes the shortening of the oligomer macromolecule chains, related to the change of STFs during UV aging from a liquid into a solid, making it impossible to perform repeated rheological tests.

Our results reveal the necessity of preparation and storage of fluids under reduced UV radiation conditions to prevent the degradation of STFs and the significant deterioration of their properties.

Our results can be summarized in a few points:

- We have obtained STFs with a very high dilatant effect (the shear thickening effect of up to a maximum of 3313 Pa·s) not previously reported in the literature.
- The UV radiation causes the damage of the STFs and the change of the STFs from the liquid to solid.
- The results indicate the need for appropriate storage of STFs in the UV-free environment prior to and during usage.

References

1. Yu, K.; Cao, H.; Qian, K.; Sha, X.; Chen, Y. Shear-Thickening Behavior of Modified Silica Nanoparticles in Polyethylene Glycol. *J. Nanoparticle Res.* **2012**, *14*, 747. [CrossRef]
2. Zarei, M.; Aalaie, J. Application of Shear Thickening Fluids in Material Development. *J. Mater. Res. Technol.* **2020**, *9*, 10411–10433. [CrossRef]
3. Czech, K.; Oliwa, R.; Krajewski, D.; Bulanda, K.; Oleksy, M.; Budzik, G.; Mazurkow, A. Hybrid Polymer Composites Used in the Arms Industry: A Review. *Materials* **2021**, *14*, 3047. [CrossRef]
4. Shih, C.-H.; Chang, C.-P.; Liu, Y.-M.; Chen, Y.-L.; Ger, M.-D. Ballistic Performance of Shear Thickening Fluids (STFs) Filled Paper Honeycomb Panel: Effects of Laminating Sequence and Rheological Property of STFs. *Appl. Compos. Mater.* **2021**, *28*, 201–218. [CrossRef]
5. Arora, S.; Majumdar, A.; Butola, B.S. Soft Armour Design by Angular Stacking of Shear Thickening Fluid Impregnated High-Performance Fabrics for Quasi-Isotropic Ballistic Response. *Compos. Struct.* **2020**, *233*, 111720. [CrossRef]
6. Mishra, V.D.; Mishra, A.; Singh, A.; Verma, L.; Rajesh, G. Ballistic Impact Performance of UHMWP Fabric Impregnated with Shear Thickening Fluid Nanocomposite. *Compos. Struct.* **2022**, *281*, 114991. [CrossRef]
7. Cho, H.; Lee, J.; Hong, S.; Kim, S. Bulletproof Performance of Composite Plate Fabricated Using Shear Thickening Fluid and Natural Fiber Paper. *Appl. Sci.* **2020**, *10*, 88. [CrossRef]
8. Zhang, X.; Li, T.T.; Peng, H.K.; Lou, C.W.; Lin, J.H. Enhanced Sandwich Structure Composite with Shear Thickening Fluid and Thermoplastic Polyurethanes for High-Performance Stab Resistance. *Compos. Struct.* **2022**, *280*, 114930. [CrossRef]
9. Chang, C.P.; Shih, C.H.; You, J.L.; Youh, M.J.; Liu, Y.M.; Ger, M. der Preparation and Ballistic Performance of a Multi-Layer Armor System Composed of Kevlar/Polyurea Composites and Shear Thickening Fluid (Stf)-Filled Paper Honeycomb Panels. *Polymers* **2021**, *13*, 3080. [CrossRef]
10. Gürgen, S.; Sofuoğlu, M.A. Integration of Shear Thickening Fluid into Cutting Tools for Improved Turning Operations. *J. Manuf. Processes* **2020**, *56*, 1146–1154. [CrossRef]
11. Liu, B.; Du, C.; Deng, H.; Fan, Z.; Zhang, J.; Zeng, F.; Fu, Y.; Gong, X. Mechanical Properties of Magneto-Sensitive Shear Thickening Fluid Absorber and Application Potential in a Vehicle. *Compos. Part A Appl. Sci. Manuf.* **2022**, *154*, 106782. [CrossRef]
12. Sheikhi, M.R.; Gürgen, S. Anti-Impact Design of Multi-Layer Composites Enhanced by Shear Thickening Fluid. *Compos. Struct.* **2022**, *279*, 114797. [CrossRef]
13. Nakonieczna, P.; Wojnarowicz, J.; Wierzbicki, Ł.; Leonowicz, M. Rheological Properties and Stability of Shear Thickening Fluids Based on Silica and Polypropylene Glycol. *Mater. Res. Express* **2019**, *6*, 115702. [CrossRef]
14. Nakonieczna-Dąbrowska, P.; Wróblewski, R.; Płocińska, M.; Leonowicz, M. Impact of the Carbon Nanofillers Addition on Rheology and Absorption Ability of Composite Shear Thickening Fluids. *Materials* **2020**, *13*, 3870. [CrossRef] [PubMed]
15. Wierzbicki, Ł.; Danelska, A.; Chrońska, K.; Tryznowski, M.; Zielińska, D.; Kucińska, I.; Szafran, M.; Leonowicz, M. Shear thickening fluids based on nanosized silica suspensions for advanced body armour. *Compos. Theory Pract.* **2013**, *13*, 241–244.
16. Qin, J.; Guo, B.; Zhang, L.; Wang, T.; Zhang, G.; Shi, X. Soft Armor Materials Constructed with Kevlar Fabric and a Novel Shear Thickening Fluid. *Compos. Part B Eng.* **2020**, *183*, 107686. [CrossRef]
17. Shende, T.; Niasar, V.J.; Babaei, M. An Empirical Equation for Shear Viscosity of Shear Thickening Fluids. *J. Mol. Liq.* **2021**, *325*, 115220. [CrossRef]
18. Gürgen, S. Numerical Modeling of Fabrics Treated with Multi-Phase Shear Thickening Fluids under High Velocity Impacts. *Thin-Walled Struct.* **2020**, *148*, 106573. [CrossRef]

19. Lam, L.; Chen, W.; Hao, H.; Li, Z.; Ha, N.S.; Pham, T.M. Numerical Study of Bio-Inspired Energy-Absorbing Device Using Shear Thickening Fluid (STF). *Int. J. Impact Eng.* **2022**, *162*, 104158. [CrossRef]

20. Zhang, X.; Yan, R.; Zhang, Q.; Jia, L. The Numerical Simulation of the Mechanical Failure Behavior of Shear Thickening Fluid/Fiber Composites: A Review. *Polym. Adv. Technol.* **2022**, *33*, 20–33. [CrossRef]

21. Salehin, R.; Xu, R.-G.; Papanikolaou, S. Colloidal Shear-Thickening Fluids Using Variable Functional Star-Shaped Particles: A Molecular Dynamics Study. *Materials* **2021**, *14*, 6867. [CrossRef] [PubMed]

22. Singh, M.; Mehta, R.; Verma, S.K.; Biswas, I. Effect of Addition of Different Nano-Clays on the Fumed Silica-Polyethylene Glycol Based Shear-Thickening Fluids. *Mater. Res. Express* **2018**, *5*, 014001. [CrossRef]

23. Heinze, D.A.; Carastan, D.J. The Influence of Fumed Silica Content, Dispersion Energy, and Humidity on the Stability of Shear Thickening Fluids. *Rheol. Acta* **2020**, *59*, 455–468. [CrossRef]

24. Tsinas, Z.; Orski, S.V.; Bentley, V.R.C.; Gonzalez Lopez, L.; Al-Sheikhly, M.; Forster, A.L. Effects of Thermal Aging on Molar Mass of Ultra-High Molar Mass Polyethylene Fibers. *Polymers* **2022**, *14*, 1324. [CrossRef]

25. Żurowski, R.; Antosik, A.; Głuszek, M.; Szafran, M. Shear Thickening Ceramic-Polymer Composite. *Compos. Theory Prac.* **2015**, *15*, 255–258.

26. Głuszek, M.; Kubiś, M.; Żurowski, R.; Wiśniewski, T.; Szafran, M. Enhancement of Thermo-Rheological Properties of Smart Materials Based on SiO2 and PPG Modified with Expanded Graphite. *Int. J. Appl. Ceram. Technol.* **2018**, *15*, 538–545. [CrossRef]

27. Izdebska-Podsiadły, J.; Żołek-Tryznowska, Z.; Annusik, T.; Tryznowski, M. Improvement of Light Fastness of Water-Based Printing Inks with Addition of Glycerol Derivative Containing Thiol Groups. *Coloration Technol.* **2018**, *134*, 100–105. [CrossRef]

28. Bajya, M.; Majumdar, A.; Butola, B.S.; Verma, S.K.; Bhattacharjee, D. Design Strategy for Optimising Weight and Ballistic Performance of Soft Body Armour Reinforced with Shear Thickening Fluid. *Compos. Part B Eng.* **2020**, *183*, 107721. [CrossRef]

29. Ghosh, A.; Majumdar, A.; Butola, B.S. Rheometry of Novel Shear Thickening Fluid and Its Application for Improving the Impact Energy Absorption of P-Aramid Fabric. *Thin-Walled Struct.* **2020**, *155*, 106954. [CrossRef]

30. Aydemir, C.; Yenidoğan, S. Light Fastness of Printing Inks: A Review. *J. Graph. Eng. Des.* **2018**, *9*, 37–43. [CrossRef]

31. Choe, S.; Kim, M.J.; Kim, H.C.; Lim, T.; Park, K.J.; Kim, K.H.; Ahn, S.H.; Lee, A.; Kim, S.K.; Kim, J.J. Degradation of Poly(Ethylene Glycol–Propylene Glycol) Copolymer and Its Influences on Copper Electrodeposition. *J. Electroanal. Chem.* **2014**, *714–715*, 85–91. [CrossRef]

32. Han, S.; Kim, C.; Kwon, D. Thermal/Oxidative Degradation and Stabilization of Polyethylene Glycol. *Polymer* **1997**, *38*, 317–323. [CrossRef]

33. Morlat, S.; Gardette, J.L. Phototransformation of Water-Soluble Polymers. I: Photo- and Thermooxidation of Poly(Ethylene Oxide) in Solid State. *Polymer* **2001**, *42*, 6071–6079. [CrossRef]

34. Guo, X.; Minakata, D.; Crittenden, J. Computer-Based First-Principles Kinetic Monte Carlo Simulation of Polyethylene Glycol Degradation in Aqueous Phase UV/H$_2$O$_2$ Advanced Oxidation Process. *Environ. Sci. Technol.* **2014**, *48*, 10813–10820. [CrossRef] [PubMed]

35. Camós Noguer, A.; Olsen, S.M.; Hvilsted, S.; Kiil, S. Long-Term Stability of PEG-Based Antifouling Surfaces in Seawater. *J. Coat. Technol. Res.* **2016**, *13*, 567–575. [CrossRef]

Article

Hydroxyapatite/L-Lysine Composite Coating as Glassy Carbon Electrode Modifier for the Analysis and Detection of Nile Blue A

Jimmy Julio Kouanang Ngouoko [1], Kevin Yemele Tajeu [1], Ranil Clément Tonleu Temgoua [1,2], Giscard Doungmo [3], Ingo Doench [4,5,6], Arnaud Kamdem Tamo [4,5,6,*], Théophile Kamgaing [1], Anayancy Osorio-Madrazo [4,5,6,*] and Ignas Kenfack Tonle [1,*]

[1] Department of Chemistry, Faculty of Science, University of Dschang, Dschang P.O. Box 67, Cameroon; ngouoalex@yahoo.com (J.J.K.N.); tasergekev@yahoo.fr (K.Y.T.); raniltemgoua@yahoo.fr (R.C.T.T.); theokamgaing@yahoo.fr (T.K.)

[2] Higher Teacher Training College, University of Yaoundé 1, Yaoundé P.O. Box 47, Cameroon

[3] Institute of Inorganic Chemistry, Christian-Albrechts-Universität zu Kiel, Max-Eyth-Straβe 2, 24118 Kiel, Germany; gdoungmo@ac.uni-kiel.de

[4] Laboratory for Bioinspired Materials BMBT, Institute of Microsystems Engineering IMTEK-Sensors, University of Freiburg, 79110 Freiburg, Germany; ingo.doench@imtek.uni-freiburg.de

[5] Freiburg Center for Interactive Materials and Bioinspired Technologies FIT, University of Freiburg, 79110 Freiburg, Germany

[6] Freiburg Materials Research Center FMF, University of Freiburg, 79104 Freiburg, Germany

* Correspondence: arnaud.kamdem@imtek.uni-freiburg.de (A.K.T.); anayancy.osorio@imtek.uni-freiburg.de (A.O.-M.); ignas.tonle@univ-dschang.org (I.K.T.); Tel.: +49-761-203-95096 (A.K.T.); +49-761-203-67363 (A.O.-M.); +237-696-141-545 (I.K.T.)

Abstract: An amperometric sensor was developed by depositing a film coating of hydroxyapatite (HA)/L-lysine (Lys) composite material on a glassy carbon electrode (GCE). It was applied for the detection of Nile blue A (NBA). Hydroxyapatite was obtained from snail shells and its structural properties before and after its combination with Lys were characterized using X-ray diffraction (XRD), Fourier-transform infrared (FTIR) spectroscopy, scanning electron microscopy (SEM), and Brunauer–Emmett–Teller (BET) surface area analyses. The coupling of Lys to HA was attributed to favorable interaction between negatively charged -COO$^-$ groups of Lys and divalent ions Ca^{2+} of HA. Electrochemical investigations pointed out the improvement in sensitivity of the GCE/Lys/HA sensor towards the detection of NBA in solution. The dependence of the peak current and potential on the pH, scan rate, and NBA concentration was also investigated. Under optimal conditions, the GCE/Lys/HA sensor showed a good reproducibility, selectivity, and a NBA low detection limit of 5.07×10^{-8} mol L^{-1}. The developed HA/Lys-modified electrode was successfully applied for the detection of NBA in various water samples.

Keywords: hydroxyapatite; lysine; inorganic–organic composite; glassy carbon electrode; electrode coating; electrochemical analysis; Nile blue A

1. Introduction

Nile blue A (bis [5-Amino-9-(diethylamino)benzo[a]phenoxazin-7-ium] sulphate) is an azo dye of the phenoxazine family [1]. It finds applications in histology and medicine for the detection of micro-organisms [2], as well as in photodynamic therapy for the treatment of malignant tumors [3,4]. It is also applied in dye-sensitized solar cells [5]. However, it is a mutagen [6] and carcinogen [7], and for these reasons, prohibited as a food additive. The presence of this dye in water is harmful to microbial life [8]. Due to the risks presented by this dye, its elimination in water and in various matrices is an active field of research. For that purpose, various techniques have been used, including adsorption [9], chemical degradation [10], and absorption [11,12]. Furthermore, the quantification of NBA at trace level is relevant in analytical and environmental sciences. In these fields,

solid electrodes chemically modified by convenient inorganic materials, likely to display great affinity for a target species, are usually used. Some common examples of such materials are silica [13,14], clay minerals [15,16], various carbon derivatives [17–20], and metal oxides [21,22]. Furthermore, additional studies also have highlighted the use of conjugated organic polymers (conductive polymers) as electrode modifiers in the fabrication of modified electrodes for the electroanalysis of various analytes [23,24]. Conducting polymers are organic compounds with considerable flexibility and an extended π-orbital system, through which electrons can move from one end of the polymer to the other. They are among the most relevant and widely used materials for sensor modification due to their unique physical and chemical properties, such as tunable architecture and versatility, good stability, and sensitivity [25–28]. The resort to these materials aims at improving either the sensitivity or the selectivity of the bare solid electrode. In recent years, the scientific community in analytical electrochemistry has shown great interest in the development of hydroxyapatite-based sensors [29–31]. Hydroxyapatite is a low-cost material that can be produced from high calcium phosphate biominerals present, for example, in seashells and animal bones [32,33]. It is a phosphate mineral with the formula $Ca_5(PO_4)_3(OH)$, usually written $Ca_{10}(PO_4)_6(OH)_2$ to underline the fact that a dimer is present in one unit cell [34]. The acid-base properties, ion-exchange capability, and adsorption ability capacity of hydroxyapatite (HA) have boosted the development of electrochemical sensors wherein HA serves as adequate electrode material. Thus, El-Mhammedi et al. [35] used it to modify a carbon paste electrode, which was then applied for the detection of para-nitrophenol. Yin et al. [36] also detected 4-nitrophenol, using a glassy carbon electrode modified with HA nanopowder. Kanchana and Sekar [37] reported the exploitation of the same material as the GCE modifier for the determination of folic acid. Although these works have been relevant, the poor electron transfer capacity associated with insufficient selectivity are known as the drawbacks of sensors based on pure HA. This has further prompted the search for additional compounds to be combined with HA to yield more efficient sensing devices. Along these lines, Kanchana and Sekar [38] proposed an electrochemical sensor of uric acid, based on EDTA/HA nanoparticles. The electroanalysis of both diquat and lead ions was successfully achieved by Tchoffo and coworkers [31,39], using a glassy carbon electrode modified with a hybrid material from HA and β-cyclodextrin.

The present work focused on the synthesis of HA powder from snail shells and the further preparation of HA/L-lysine composite material useful as electrode coating for the detection of Nile blue A (NBA) in solution by electrochemical analysis. L-lysine bears amine groups, which are expected to display, upon protonation, strong affinity with NBA. After its preparation, the Lys/HA composite material was characterized by several physicochemistry techniques. Then, the HA/Lys composite was deposited as a thin film on the active surface of a glassy carbon electrode (GCE) for the voltammetric analysis of NBA by means of cyclic voltammetry (CV), followed by the detection of the same analyte by differential pulse voltammetry (DPV). Key parameters affecting the amperometric response of the sensor were investigated to obtain the best NBA analysis conditions, which were successfully applied for the quantification of NBA in a spring water sample. Scheme 1 below highlights the chemical structure of hydroxyapatite (HA) and that of L-lysine (Lys), as well as a simplified schematic representation of the structure of the Lys/HA complex, including the different functional groups available for interactions with the target analyte (Nile blue A).
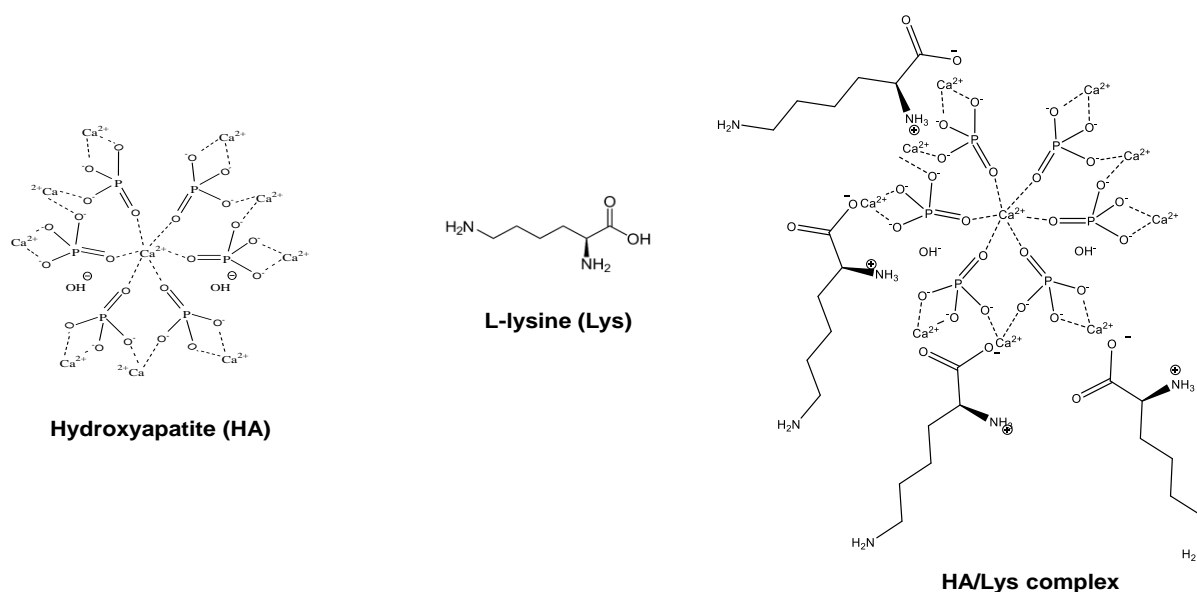
Scheme 1. Chemical structures of hydroxyapatite (HA) and L−lysine (Lys), as well as a simplified schematic representation of the hydroxyapatite/L−lysine (HA/Lys) complex.

2. Materials and Methods

2.1. Reagents and Chemicals

All chemicals were used without further purification. Na_2HPO_4 (98%) and KH_2PO_4 (99%) were obtained from BDH. NaOH, EDTA, Nile blue A (98%), L-lysine, and methyl orange were purchased from International Fisher Scientific. Caffeine (99%), toluidine blue, $Ni(NO_3)_2.6H_2O$ (98%), $Cd(NO_3)_2.4H_2O$ (98%), and ascorbic acid were obtained from Sigma-Aldrich. $Pb(NO_3)_2$ (99%) was purchased from VWR Chemicals BDH and $Cu(HCO_2)_2.2H_2O$ (99%) from Merck Chemicals GmbH. Citric acid monohydrate and HCl (36%) were purchased from J.T. Baker and Pronalys AR, respectively. The phosphate buffer solutions used in this work consisted of a mixture of monobasic dihydrogen phosphate and dibasic monohydrogen phosphate. By varying the amount of each salt, we prepared a range of phosphate buffers with pHs between 5.0 and 9.0. Analytical solutions of NBA at various concentrations were obtained by dilution from a standard solution of a concentration of 0.01 M, using doubly distilled water.

Specimens of snail shells were collected from a local market in downtown Nkongsamba (Cameroon). The raw snail shells were washed with water, rinsed with distilled water, and dried at room temperature for two weeks. They were exploited to yield hydroxyapatite, as described in the next section.

2.2. Preparation of Hydroxyapatite Powder

The preparation was performed according to a method published by Shavandi et al. [40], with slight modifications. Thus, the calcination of the snail shells was achieved at 1000 °C for 90 min, in an electrical furnace at a heating rate of 5 °C min^{-1}. The calcinated product was then crushed using a mortar, then sieved to obtain a white powder (with a particle diameter less than 25 μm). To 2.8 g of calcinated shell, 50 mL of 0.1 M EDTA was added to yield a solution of 0.1 M Ca-EDTA complex. To that solution and under stirring, 50 mL of 0.06 M Na_2HPO_4 was added (4 mL min^{-1}). The obtained mixture was stirred for 120 min, maintained at a pH around 13. Upon drying in an oven for 12 h, a milky white powder was obtained.

2.3. Preparation of Hydroxyapatite/L-Lysine (HA/Lys) Modified Working Electrode

Before modification, the surface of the glassy carbon electrode (GCE) (3 mm in Ø) was polished with alumina slurries of different sizes (1, then 0.5 μm) on billiard cloth and placed

in a sonicator for 5 min to eliminate remaining alumina particles. The thin hydroxyapatite (HA) film working electrode was prepared by the drop-coating of 5 μL of a dispersion obtained by sonication for 30 min, and of 5 mg L-lysine with various amounts of HA (0, 1, 2, 3, and 4 mg), in 1 mL of double distilled water. The modified electrodes were dried in an oven at 80 °C for 5 min. In this manuscript, they are denoted: GCE/HA, GCE/Lys, and GCE/Lys/HA, for the GCEs modified with HA, Lys, and Lys/HA composite, respectively.

2.4. Material Characterization

The synthesized hydroxyapatite (HA), L-lysine (Lys), and the Lys/HA composite materials were characterized by various physicochemical techniques.

2.4.1. X-ray Diffraction (XRD)

X-ray diffraction patterns were collected using a Stoe Stadi-P X-ray powder diffractometer, with Cu Kα1 radiation (λ = 1.54056 Å, gemonochromator, flat sample). The data were collected in the 2θ angle ranging from 5° to 70°, with a scanning speed of 1.5° min^{-1}.

2.4.2. Fourier-Transform Infrared (FTIR) Spectroscopy

FTIR spectra were registered on a genesis FTIRM spectrometer (ATI Mattson), equipped with a DTGS (deuterated triglycine sulfate).

2.4.3. Brunauer–Emmett–Teller (BET) Analysis

Nitrogen adsorption–desorption isotherms were collected for selected samples using Thermo Electron Corporation, Sorptomatic Advanced Data Processing. Before N_2 adsorption, the samples were degassed at 307.13 K under a vacuum.

2.4.4. Scanning Electron Microscopy (SEM)

The surface morphology of the L-lysine (Lys), hydroxyapatite (HA), and Lys/HA materials was characterized with a scanning electron microscope (FEI Scios FIB-SEM) at an accelerating voltage of 10 kV. For SEM measurements, the samples were deposited on conductive carbon tabs and coated with gold under a vacuum, using a sputter coater.

2.5. Electrochemical Measurements

Electrochemical measurements were carried out at room temperature with μ-Autolab potentiostat (Ecochimie, Holland), employing a conventional three-electrode cell compartment containing the film-modified GCE as the working electrode, the Ag/AgCl (3 M KCl) as the reference electrode (Metrohm), and a steel auxiliary electrode.

Cyclic voltammetry was carried out in a 0.1 M phosphate buffer solution (pH 5.5) containing NBA, in the potential range of −0.9 V to +0.1 V. For stripping analysis of NBA, differential pulse voltammetry in anodic mode was performed at closed circuit in the potential scan range from −0.7 V to 0 V, using the following optimized parameters: pulse amplitude: 95 mV; step potential: 7.5 mV; and equilibrium time: 5 s.

3. Results and Discussion

3.1. Characterization of Hydroxyapatite (HA) and L-Lysine/Hydroxyapatite (Lys/HA) Hybrid Materials

Figure 1a presents the X-ray diffraction (XRD) patterns of the synthesized HA, pure L-lysine (Lys), and Lys/HA composite materials. On the curve of HA (curve 1), the main diffraction peaks usually observed for pure hydroxyapatite ((101), (002), (300), (310), (222), and (213)) were identified. This was proof that the prepared HA was well-synthesized and constituted a single phase material. However, a broaden background indicates a relatively low crystallinity of the HA. After the addition of lysine to HA, the diffractogram of the Lys/HA hybrid material (curve 3) matched with that of HA, while the intensity of the peaks related to L-lysine were negligible. This could be due to the low amount of the amino acid on the inorganic–organic composite structure. The pattern of pure L-lysine was given in curve 2, for comparison.
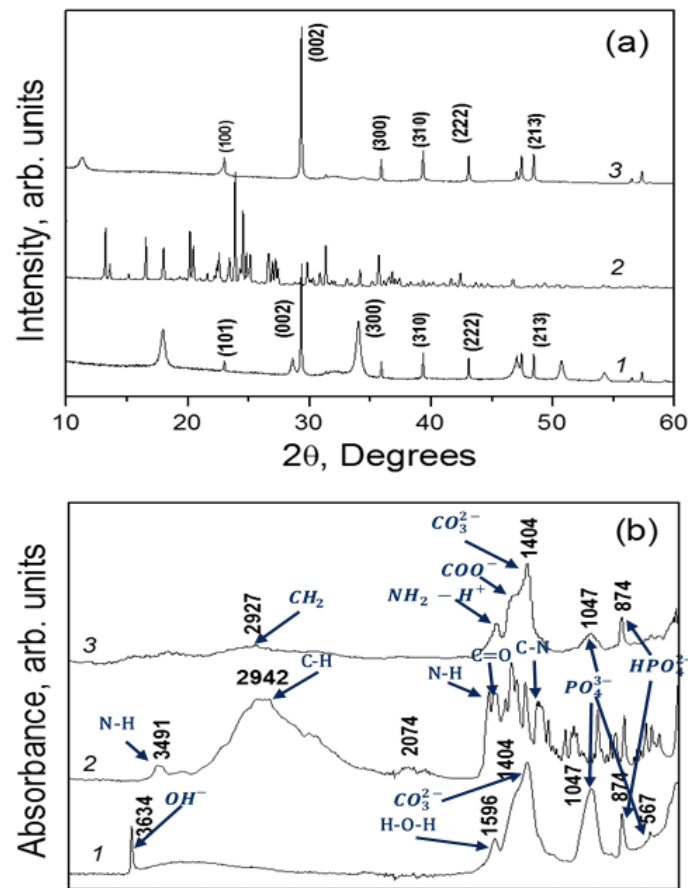
Figure 1. (**a**) Powder X-ray diffraction patterns, and (**b**) FTIR spectra of (1) hydroxyapatite (HA), (2) L-lysine (Lys), and (3) Lys/HA hybrid material.

This observation led us to estimate the crystallite size and lattice strain [41] of HA before and after its hybridization with L-lysine. Thus, the Williamson–Hall (W-H) equation given by Equation (1) was used [42,43];

$$\beta \cos \theta = \frac{k\lambda}{\tau} + 4\varepsilon \sin \theta \qquad (1)$$

where λ is the wavelength of the CuKα X-ray radiation (λ = 1.54178Å), θ is the Bragg angle, ε is the value of the lattice strain, τ is the crystallite size, β the full width at half maximum (FWHM) corresponding to (hkl) Bragg's peak, and k is the Scherrer constant usually equal to 0.9.

The W-H plots ($\beta\cos\theta$ vs. $4\sin\theta$) for Lys/HA and HA are given in Figure S1 (Supplementary Materials). The crystallite size was determined through the y-intercept, while the lattice strain was derived through the slope of the fitted straight line shown in Figure S1 (Supplementary Materials). The obtained results are given in Table 1.

Table 1. Crystallite size, lattice strain, and crystallinity index of HA and Lys/Ha from W-H method.

Sample	Crystallite Size (nm)	Lattice Strain (10^{-3})	Crystallinity Index (%)
HA	21.68	3.2	42.4
Lys/HA	40.81	1.6	42.01

The observed decrease in lattice strain and increase in crystallite size from HA to Lys/HA were due to an increase in the lattice side after the addition of L-lysine. The degree of crystallization (crystallinity index) was determined based on Equation (2), where *C* is

the area of the peaks in the diffraction pattern (crystalline area), and A is the area between the peaks and the background (amorphous area).

$$Crystallinity\ index = \frac{C}{C + A} \times 100 \qquad (2)$$

The values of *C* and *A* were calculated using Powder X software (version 2017, Germany). From Table 1, crystallinity index values were less than 50%, showing that HA crystallites were practically not affected by the addition of Lys.

Although XRD data did not show the presence of L-lysine on HA, FTIR spectroscopy characterizations were performed to check whether the absorption of amino acid on the surface of HA was effective. The FTIR results are shown in Figure 1b. On the infrared spectrum of synthesized HA (curve 1, Figure 1b), fundamental vibrational modes of the phosphate group were observed: the band at 1047 cm^{-1} was attributed to the phosphate stretching, and the bands at 608, 561, and 476 cm^{-1} were due to the phosphate bending [44,45]. The bands at 3434 and 567 cm^{-1} were attributed to the stretching vibration of OH$^-$. The peaks at 1625 and 3334 cm^{-1} were due to absorbed water. The peaks at 1404 and 874 cm^{-1} were attributed to the deformation vibration of CO$_3{}^{2-}$ incorporated in the PO$_4{}^{3-}$ site and OH$^-$ site, respectively; the presence of the peak at 874 cm^{-1} could also have been due to the incorporation of HPO$_4{}^{2-}$, characteristic of non-stoichiometric HA [35,36]. These observations confirmed that the synthesized material was pure hydroxyapatite, as revealed by the XRD results. Upon addition of lysine to HA, a comparison between the spectra of pure lysine (curve 2, Figure 1b) and Lys/HA composite (curve 3, Figure 1b) showed bands attributed to the stretching of phosphate (1047 cm^{-1}) and the deformation vibration of carbonate ions (1404 and 874 cm^{-1}), as well as bands at 1550 cm^{-1} and 1430 cm^{-1} attributed to the symmetric stretching of NH$_2$–H$^+$ and COO$^-$, respectively [46,47]. Furthermore, the band attributed to the stretching of methylene (-CH$_2{}^-$) was observed (2927 cm^{-1}) [37,38]. All these observations suggested the adsorption of lysine on the surface of synthesized HA.

The specific surface area and pore volume of pristine HA, L-lysine, and Lys/HA materials were calculated from the nitrogen adsorption–desorption isotherms, via the Brunauer–Emmett–Teller (BET) and the Barrett–Joyner–Halenda (BJH) methods. The measured specific surface and the pore volume of pristine HA were 46.69 m^2 g^{-1} and 0.1266 cm^3 g^{-1}, respectively (Table 2). These data decreased to 9.63 m^2 g^{-1} and 0.0258 cm^3 g^{-1} when L-lysine was bounded to the surface of the inorganic backbone, meaning that the coupling of L-lysine resulted in the reduction of the porosity of HA. Similar results were already reported by previous works from the literature [48,49], which support the successful adsorption of L-lysine on the surface of HA.

Table 2. Specific surfaces and pore volume of studied materials.

Sample	Surface Area (m$^2 \cdot$g^{-1})	Pore Volume (cm$^3 \cdot$g^{-1})
HA	46.69	0.1266
L-Lysine	0.23	-
Lys/HA	9.63	0.0258

The surface morphologies of the coating materials L-lysine (Lys), hydroxyapatite (HA), and HA/Lys composite, as investigated by scanning electron microscopy (SEM), are shown in Figure 2. The SEM image of the L-lysine material (Figure 2a) showed a smooth surface of low porosity, typical for protein-based materials, with some platelet-like agglomerates. In contrast, the hydroxyapatite surface (Figure 2b) showed micro-sized particles clumped together with interconnected pores. The surface grains were homogeneously small, and the porous sizes were uniform. The addition of lysine to the hydroxyapatite to form the Lys/HA composite (Figure 2c) changed the material morphology compared to that of pure lysine. The surface of the Lys/HA composite (Figure 2c) showed a structure more or less similar to that of the naked hydroxyapatite (as expected for a low lysine content) with a

rough surface morphology, a slightly reduced porosity compared to that of HA alone, and foam-like grains with some agglomerated nanocrystals. As for these SEM observations and the above discussed X-ray diffractograms, the HA/Lys might have a relatively low content of organic material, this is, low lysine content. Nevertheless, the addition of lysine slightly decreased the specific surface area and the diameter of the pores (Figure 2), as previously revealed by the absorption and desorption experiments of N_2 (BET and BJH measurements). Besides, this addition provided new chemical functions and additional active sites, as observed in the FTIR analyses, capable to interact with the target analyte (Nile blue A) in the electrochemical and sorption processes.
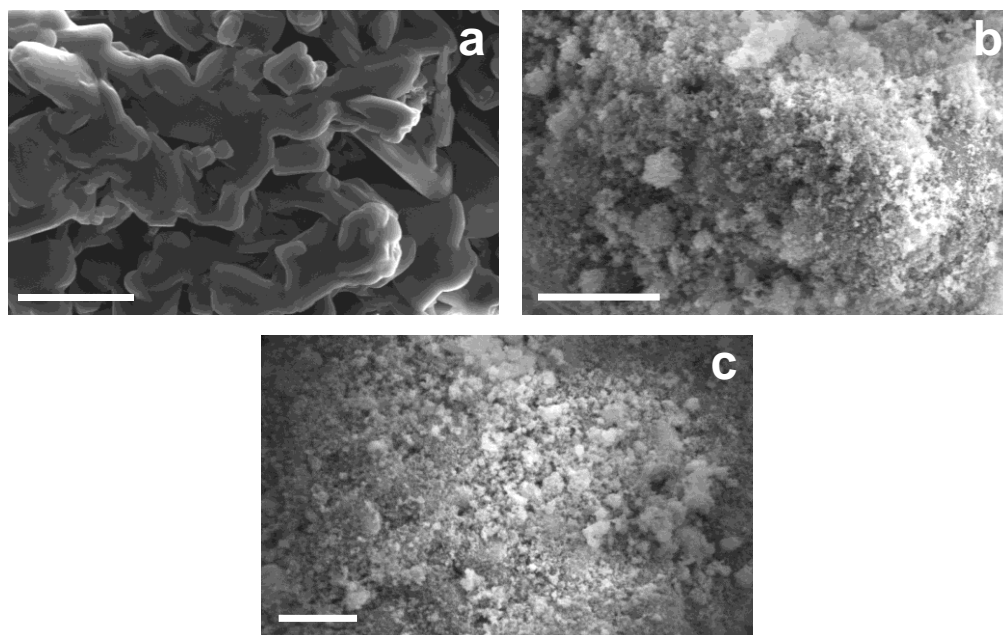
Figure 2. Scanning electron micrographs (SEM) of coating materials: (**a**) L-lysine (Lys); (**b**) hydroxyapatite (HA); and (**c**) hydroxyapatite/L-lysine (HA/Lys) composite. Scale bars: (**a**) 10 μm; (**b**,**c**) 5 μm.

3.2. Electroanalytical Applications of Lys/HA Composite for Nile Blue A Sensing

3.2.1. Preliminary Study on the Effect of the Working Electrode Modification

Preliminary experiments were performed to establish the possibility of using Lys/HA composite as an electrode modifier for the electroanalysis of NBA. Thus, the performance of the GCE/HA, GCE/Lys, and GCE/Lys/HA towards the detection of NBA was compared. The results obtained are shown in Figure 3. Each electrode gave rise to a well-defined peak in the potential range from −0.6 to −0.1 V. On the bare GCE, a peak current of 6.4 μA was recorded, proving that NBA was electroactive on the GCE. Then, the presence of each modifier improved the performance of the GCE, according to the following ability order: GCE/HA < GCE/Lys < GCE/Lys/HA, with peak currents of 8.8; 12.2, and 13.2 μA, respectively. The presence of HA, on one hand, and Lys, on another hand, on the GCE significantly increased the electrochemical signal of the electrode due to the pre-concentration of NBA dye. By combining HA and Lys on the GCE, the highest current was obtained, meaning that the composite material was more efficient towards the fixation of NBA at the working electrode. To explain these observations, one could reasonably evoke the adsorption of NBA cations on the HA surface and the uptake by lysine through electrostatic attraction between the negative carboxylate ions and protonated NH_2 groups of NBA. The $-NH_3^+$ groups of lysine can also interact with NH or the aromatic ring of NBA. Explicitly, the Ca^{2+} site of HA can easily bind to negatively charged anionic groups, such as the COO^- carboxyl groups carried by lysine. This thus offers the possibility of incorporating biological molecules such as amino acids on the surface of HA. Ozhukil Kollath et al. [50]

provided qualitative and quantitative analyses of the L-lysine molecules incorporated on the HA surface and the mechanism of interaction, which demonstrated that the carboxyl group of lysine lends itself well to Coulomb interactions with the Ca^{2+} of hydroxyapatite, which leaves the amino group of lysine available for other reactions, such as interactions with the chemical functions of NBA (for the case of the present work).
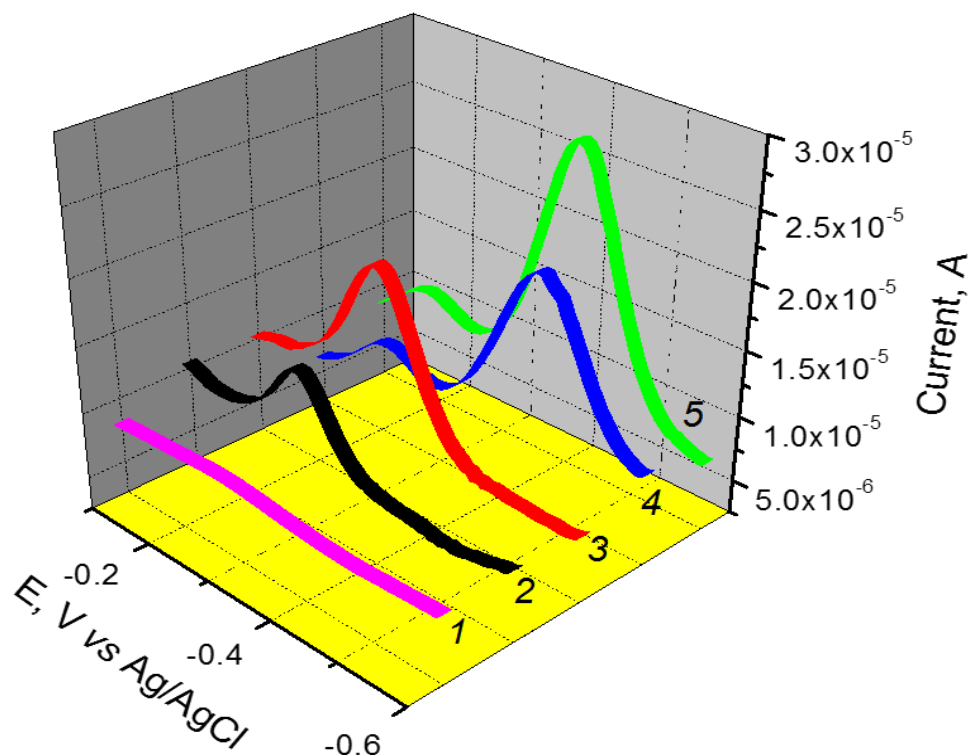
Figure 3. Differential pulse voltammetry (DPV) curves recorded in 0.1 M PBS (pH 5.5) containing 1 µM of NBA on (2) bare GCE, (3) GCE/HA, (4) GCE/Lys, and (5) GCE/Lys/HA. (1) represents the curve recorded in blank electrolyte using GCE/Lys/HA.

In addition, other studies [35,37,51–53] also demonstrated that there is a special affinity between HA and amino acids and proteins. This can be explained by the electrostatic attraction forces existing between the carboxylate groups of the amino acids and the Ca^{2+} cations on the surface of HA. Such interactions have also been highlighted in various published works [47,54–58]. Besides, the intermolecular H bonds existing between the N-containing group and the phosphate on the HA surface, as well as the cooperation of several protein functions, Ca^{2+} cations, and phosphate groups on the surface of HA, could explain this affinity. Therefore, amino acids are adsorbed on HA surfaces and maintain their activity due to the good biocompatibility of HA. The good stability and the biocompatibility of HA allow, without ambiguity, to easily incorporate additional chemical functions and physicochemical properties in their structure (in our case, through the incorporation of lysine in the structure of HA), allowing its use as an electrode material for the improvement of the sensitivity and selectivity of resulting electrodes in the electroanalysis of analytes in solution. Moreover, HA is an inexpensive material with high stability, low toxicity, and high abundance. Thanks to these advantages, we fabricated a Lys/HA electrode for the detection of NBA in solution, which improved the electrochemical parameters, such as sensitivity, stability, and selectivity, of the fabricated electrode with respect to the detection electrochemistry of the target analyte (NBA). It is also important to point out the electrocatalytic effect of the modifier, observed through the shift in potential towards negative values compared to the bare GCE electrode. The observations evolved from this section's conclusion revealed that the GCE modified by a combination of Lys and HA is a prominent tool that can be exploited for the electrochemical analysis and detection of NBA

in an aqueous solution. However, it seemed useful to analyze some kinetics aspects taking place at the GCE/Lys/HA, in order to gain insight into the phenomenon occurring in the bulk of this electrode.

3.2.2. Kinetics Studies of GCE/Lys/HA Sensor by Cyclic Voltammetry

To determine the heterogeneous electron transfer rate constant and the number of electrons transferred during the oxidation–reduction reaction of NBA at the surface of the GCE/Lys/HA, the effect of scan rate (v) on both the oxidation and reduction peak current of NBA was investigated for v, varied between 15 and 150 mV·s^{-1}. The voltammograms obtained in 0.1 M PBS (pH 5.5) containing 1 mM of NBA are shown in Figure 4a.
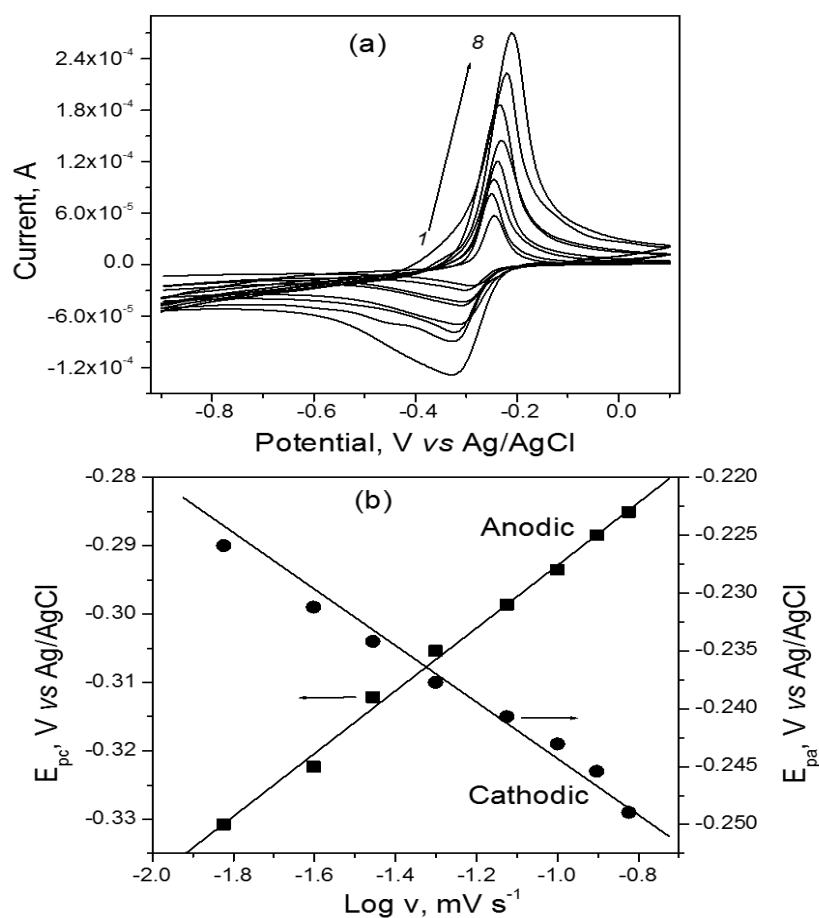
Figure 4. (**a**) Cyclic voltammograms recorded in 0.1 M PBS (at pH 5.5) +1 mM NBA at various scan rates: (1) 15, (2) 25, (3) 35, (4) 50, (5) 75, (6) 100, (7) 125, and (8) 150 mV·s^{-1}. The cyclic voltammograms recorded from lowest to highest intensity are those obtained at increasing scan rates between 15 and 150 mV.s^{-1} respectively. (**b**) Plot scan rate potential as a function of the logarithm of scan rate, from the cyclic voltammograms in (**a**).

The electrode exhibited a quasi-reversible system, with peak currents increasing with scan rate. The plot of the peak intensity as a function of scan rate (see Supplementary Materials, Figure S2) was linear, and the regression equations of the straight line obtained in oxidation and reduction directions were, respectively:

$$\text{Iox(A)} = 1.354 \times 10^{-6} \text{ v(V/s)} + 5.163 \times 10^{-5} \text{ (R}^2 = 0.991) \tag{3}$$

$$\text{Ired(A)} = -5.969 \times 10^{-7} \text{ v(V/s)} - 1.819 \times 10^{-5} \text{ (R}^2 = 0.985) \tag{4}$$

The values of R^2 close to one showed that both the oxidation and reduction of NBA at the GCE/Lys/HA are adsorption-controlled processes. Such behavior was obtained by

Dilek et al. during the electrosynthesis of poly (Nile blue) films on the surface of a glassy carbon disc electrode [59].

The number of electron(s) exchanged and the heterogeneous electron transfer rate constant were determined based on the graph Ep(V) vs. Logv (Figure 4b), and on Laviron Equations (5) and (6) for the quasi-reversible system [60].

$$E_{pa} = E° + \left(\frac{2.303RT}{(1 - \alpha)nF} \right) \log v + \left(\frac{2.303RT}{(1 - \alpha)nF} \right) \log \left(\frac{nF(1 - \alpha)}{RTK_s} \right) \tag{5}$$

$$E_{pc} = E° + \left(\frac{2.303RT}{\alpha nF} \right) \log v + \left(\frac{2.303RT}{\alpha nF} \right) \log \left(\frac{nF\alpha}{RTK_s} \right) \tag{6}$$

where R = 8.314 J.mol^{-1}.k^{-1}, T = 298 K, and F = 96,487 C.mol^{-1}.

The value of the transfer coefficient α was obtained from Equation (7), which represents the ratio of the slope of Equations (5) and (6).

$$\frac{\alpha}{1-\alpha} = \frac{0.0271}{0.03656} = 0.741 \tag{7}$$

The obtained value of α was 0.426. By reporting this in the slope of either Equation (5) or Equation (6), the number of electrons transferred was found to be n = 1.65, smaller than 2 as in the literature [45]. The heterogeneous electron transfer rate constant Ks was calculated at a scan rate of 50 mV s^{-1} from Equation (8):

$$\log K_s = \alpha \log(1 - \alpha) + (1 - \alpha) \log \alpha - \log \left(\frac{RT}{nFv} \right) - \frac{\alpha(1 - \alpha)nF\Delta E}{2.303RT} \tag{8}$$

A value of Ks = 0.511 s^{-1} was obtained, indicating that the electron-transfer kinetics are quite fast, despite the process at the electrode being quasi-reversible.

3.2.3. Effect of the Amount of Hydroxyapatite (HA) in the L-Lysine/HA Composite on the Detection of Nile Blue A (NBA)

The amount of hydroxyapatite in the modifier film was expected to affect the response of the electrode. Thus, the variation of the mass of HA in the Lys/HA composite was evaluated and the results are presented in Figure S3 (Supplementary Materials). It was observed that the peak current of NBA increased when the mass of HA in the film was increased between 1 and 3 mg; then it decreased. The observed increase in the peak current with an HA mass between 1 and 3 mg was associated with the presence of more absorption sites in the bulk of the working electrode, arising with the increase in HA. Above 3 mg, the presence of the huge amount of HA in the film reduced the conductivity of the electrode, as the inorganic material behaves like a physical barrier. The mass of 3 mg was therefore adopted for further experiments.

3.2.4. Effect of pH on the Peak Current and Potential

To elucidate the oxidation mechanism of NBA at the GCE/Lys/HA, the variation of peak potential with the pH was studied. For this purpose, DPV experiments at different pH values were carried out in the PBS, and the graphs of the peak current and peak potential vs. pH were plotted (Figure 5). As noticed, the peak current decreased slightly when the pH was raised from 5 to 6.5. Then, it significantly increased to reach a maximum value at pH 8; it then decreased for pH values set between 8 and 9. Regarding the plot of the peak potential vs. pH, a linear decreasing dependent relation was obtained, according to the equation Ep(V) = −0.074 − 0.053 pH (R^2 = 0.995). The slope of −0.053 V/pH, obtained close to the theoretical value of −0.059 V/pH, showed that an equal number of protons and electrons were exchanged during this process [61–63].
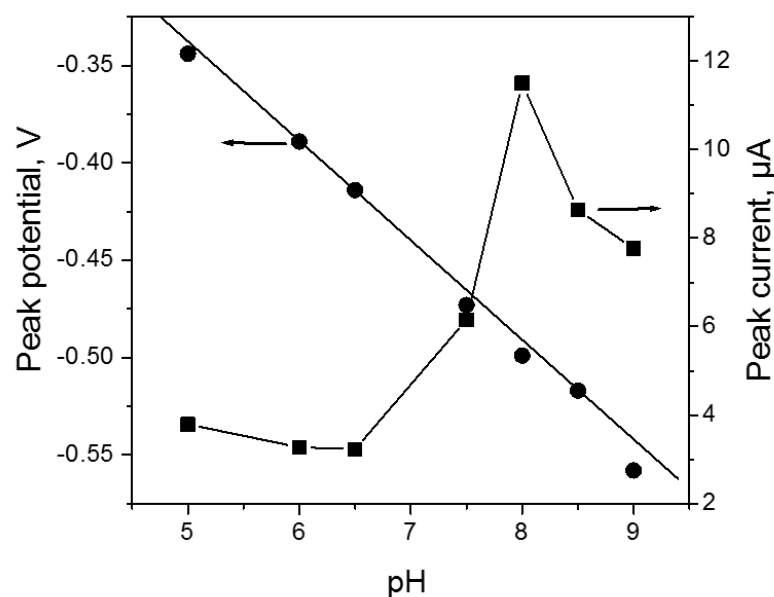
Figure 5. Effect of PBS solution pH on the peak current and peak potential of 10^{-6} M NBA at GCE/Lys/HA.

According to the structure of NBA and to the number of electrons and protons transferred, the following redox mechanism was proposed [59]. The chemical equation representing the electro-oxidation mechanism of NBA is highlighted in Scheme 2.
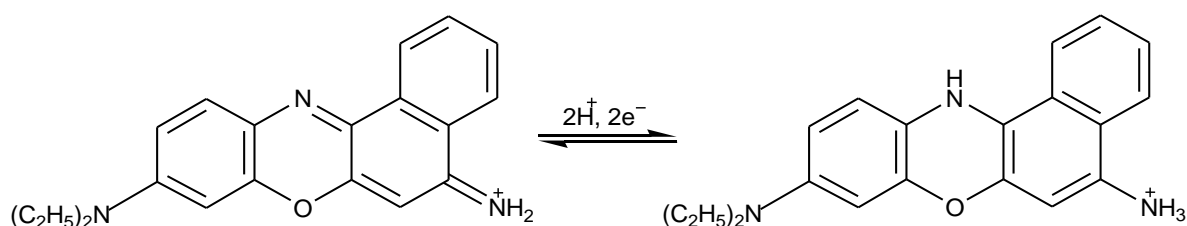
Scheme 2. Mechanism of the electro-oxidation of NBA.

3.2.5. Validation and Analytical Application of Lys/HA-Coated GCE Electrode Sensor—Calibration Curve and Interference Studies

DPV analysis of NBA at various concentrations between 0.1 and 1 μM was performed using the GCE/Lys/HA under optimized conditions. The result is presented in Figure 6. As expected, the DPV peak current Ipa increased with NBA concentration (inset in Figure 6). The calibration equation and its correlation coefficient were Ipa(A) = 12.18022 [NBA] (mol L^{-1}) + 5.3736 × 10^{-8} and R^2 = 0.992, respectively. A limit of detection of 5.07 × 10^{-8} mol L^{-1} was determined, calculated as three times the standard deviation of the intercept divided by the slope of the calibration curve [64].

Table 3 gives a comparison with the values obtained in other articles for the detection of similar analytes, in particular methylene blue (MB), since to our knowledge, the electroanalysis of Nile blue A had not yet been carried out. The results displayed in this table highlight the fact that the developed sensor in this work highlighted a detection limit value comparable to those recorded in previous publications using modified electrodes for the detection of analytes similar to Nile blue A, in particular dyes.
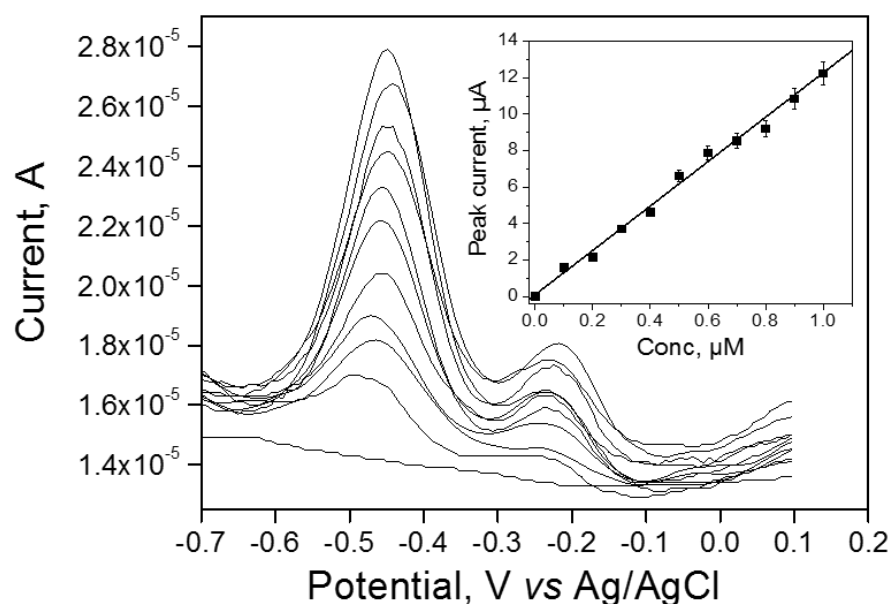
Figure 6. Differential pulse voltammetry (DPV) curves obtained on GCE/Lys/HA in PBS (pH 8) at various concentrations (0, 0.1, 0.2, 0.3, 0.4, 0.5, 0.6, 0.7, 0.8, 0.9, and 1 μM (DPV curves are ordered from bottom to top, respectively)) of NBA. The first peak, which is the most intense, was used to plot the concentration dependency. (The inset shows the corresponding calibration curve).

Table 3. Comparison of the performances of the developed sensor GCE/Lys/HA with respect to the electroanalysis of Nile blue A, with those of other modified electrodes applied to the electroanalysis of similar analytes.

Electrode	Modifier	DLR (μM)	LOD (μM)	Method	Analyte	Reference
CPE [a]	Thiol-functionalized clay	1–14	0.4000	CV [b]	MB [c]	[65]
CPE	Ibuprofen-coated gold	0.01–1	0.0039	DPV [d]	MB	[66]
CPE	Coffee husks	1–125	3.0000	SWV [e]	MB	[67]
GCE	CMTN [f]	0.01–10	0.0030	DPV	MB	[68]
GCE [g]	Lys/HA	0.1–1	0.0507	DPV	NBA	This work

[a] Carbon paste electrode, CPE; [b] cyclic voltammetry, CV; [c] methylene blue, MB; [d] differential pulse voltammetry, DPV; [e] square wave voltammetry, SWV; [f] carbon-modified titanium dioxide nanostructured, CMTN; [g] glassy carbon electrode, GCE.

The detection limit recorded was lower than those obtained by other authors for similar analytes. This showed that the Lys/HA composite made from less expensive, locally available and abundant materials is part of the efficient and stable electrode matrices allowing the simple and rapid modification of the electrode surface in order to improve its sensitivity and selectivity with respect to the electrochemical detection of dyes.

The selectivity of the GCE/Lys/HA was evaluated in the presence of some interfering molecules, such as toluidine blue (TB), methyl orange (MO), caffeine (CAF), citric acid (CA), and ascorbic acid (AA), as well as some metal cations (Ni^{2+}, Pb^{2+}, Cu^{2+}, and Cd^{2+}). Among its multiple applications, Nile blue A is a stain generally used in biology and histology. As examples, Nile blue A is mainly used with living cells, which fix it and give a blue color to cell nuclei [1]. It has also been applied to textiles and other products, such as leather, cosmetics, pulp and paper, pharmaceuticals, plastics, and foods [2–5]. In view of what was said previously, Nile blue A is very often used for various purposes and is therefore likely to be found in addition to other classes of chemical compounds in various types of liquid effluents, for example, biological, pharmaceutical, agro-food, and textile effluents. Concerning the study of the effect of interferents on the response of the Lys/HA fabricated electrode to the detection of Nile blue A, we attempted to reconstitute a physiobiological or

industrial effluent by including a wide range of chemicals likely to be found in the effluents with Nile blue A at the same time. For this, we used as interference species other dyes (such as toluidine blue and methyl orange), compounds of pharmaceutical interest and also present in some foods consumed daily (caffeine, citric acid, and ascorbic acid), as well as metal ions (nickel, cadmium, copper, and lead ions). Thus, in the electrochemical cell containing a 10^{-6} M NBA solution, the previously mentioned species were added in a concentration equivalent to 0.5, 1, 5, and 10-fold that of NBA. The peak current of NBA was then recorded in optimized conditions, and its variation was noticed as shown in Table 4.

Table 4. Effect of some potential interference species on the response of the GCE/Lys/HA to 10^{-6} mol·L^{-1} NBA in 0.1 M PBS (at pH 8).

Interference Species	Added Amount over NBA Concentration	Percentual Variation in the Anodic Peak Current (I_{pa}) for NBA
Toludine blue	0.5	−3.45
	1	−24.48
	5	−44.15
	10	−68.49
Methyl orange	0.5	−1.68
	1	0
	5	−7.95
	10	−3.9
Caffeine	0.5	0.72
	1	−4.08
	5	−7.59
	10	−55.75
Citric acid	0.5	−6.34
	1	−2.21
	5	0
	10	18.03
Ascorbic acid	0.5	−1.45
	1	8.13
	5	13.44
	10	18.78
Pb^{2+}	0.5	1.69
	1	1.37
	5	−2.23
	10	−8.8
Cu^{2+}	0.5	1.12
	1	2.34
	5	−4.3
	10	−6.48
Ni^{2+}	0.5	0.32
	1	1.31
	5	4.09
	10	5.16
Cd^{2+}	0.5	−0.28
	1	−2.86
	5	−3.67
	10	−7.5

Globally, when added in a concentration 0.5-fold of NBA, all species did not interfere on the signal of the NBA analyte. At a concentration equivalent to that of NBA, the TB and AA significantly affected the response of NBA, as a variation in the target analyte signal for more than ±5% was recorded. Finally, when the concentration of the investigated species was more than five-fold that of NBA, then CAF, TB, and AA induced more deviation (≥7%)

in the response of NBA, somewhat limiting the selectivity of the proposed sensor. For all the cationic species studied, the presence of these species more or less influenced the electrochemical signal of Nile blue A, when their concentration was 10 times higher than that of NBA in the reaction medium, with a recorded variation of more or less 5 % of the NBA target analyte signal. The obtained results suggest that a GCE/Lys/HA sensor could be efficiently applied for media less concentrated in NBA dye.

The practical application of the proposed sensor was evaluated through the analysis of NBA in a spring water sample collected in Dschang (Cameroon). The water was filtered using a filter paper, and then 50 mL was added in the electrochemical cell. The corresponding amounts of Na_2HPO_4 and KH_2PO_4 salts were added to reach a concentration of 0.1 M. A preliminary electrochemical experiment was performed to check the presence of NBA in spring water by using the procedure applied for calibration curve experiments. Under established optimized conditions, no NBA peak was found. By spiking the sample with 1 µM of NBA, recovery rates above 95% were achieved for experiments conducted in triplicate. This implies that the methodology herein proposed can be successfully used in the electroanalytical determination of NBA in water and other aqueous media expected to contain such a compound.

4. Conclusions

In this work, a composite material consisting of hydroxyapatite and L-lysine (Lys/HA) was prepared and tested as electrode material for the electroanalysis of Nile blue A (NBA). Before proposing the use of this composite for sensing purposes, its physicochemical properties were determined. The deposition of a thin coating of Lys/HA material on a glassy carbon electrode led to a sensitive and selective method for the detection of NBA based on differential pulse voltammetry (DPV). The proposed sensor electrode showed practical application in the detection of NBA in spring water.

Conflicts of Interest: The authors declare no conflict of interest.

References

1. Sabnis, R.W. *Handbook of Biological Dyes and Stains: Synthesis and Industrial Applications*; Wiley: Oxford, UK, 2010; ISBN 9780470407530.
2. Martinez, V.; Henary, M. Nile Red and Nile Blue: Applications and Syntheses of Structural Analogues. *Chemistry* **2016**, *22*, 13764–13782. [CrossRef] [PubMed]
3. Masood, M.A.; Wu, Y.; Chen, Y.; Yuan, H.; Sher, N.; Faiz, F.; Yao, S.; Qi, F.; Khan, M.I.; Ahmed, M.; et al. Optimizing the photodynamic therapeutic effect of BODIPY-based photosensitizers against cancer and bacterial cells. *Dye. Pigment.* **2022**, *202*, 110255. [CrossRef]
4. Zhao, X.; Liu, J.; Fan, J.; Chao, H.; Peng, X. Recent progress in photosensitizers for overcoming the challenges of photodynamic therapy: From molecular design to application. *Chem. Soc. Rev.* **2021**, *50*, 4185–4219. [CrossRef] [PubMed]
5. Siami, E.; Sabzi, R.E.; Rasouli, F.; Kheiri, F. Nile Blue and Nickel Organometallic Dyes Applied in Dye-sensitized Solar Cells. *Port. Electrochim. Acta* **2015**, *33*, 23–33. [CrossRef]
6. Kassa, B.A. Cytotoxicity and Genotoxicity evaluation of municipal wastewater discharged into the head of Blue Nile River using the Allium Cepa test. *Sci. Afr.* **2021**, *13*, e00911. [CrossRef]
7. Tong, Z.; Singh, G.; Rainbow, A.J. Extreme Dark Cytotoxicity of Nile Blue A in Normal Human Fibroblasts. *Photochem. Photobiol.* **2001**, *74*, 707. [CrossRef]
8. Oros, G.; Cserháti, T.; Forgács, E. Separation of the strength and selectivity of the microbiological effect of synthetic dyes by spectral mapping technique. *Chemosphere* **2003**, *52*, 185–193. [CrossRef]
9. Aazami, J.; Taban, P. Monitoring of Heavy Metals in Water, Sediment and Phragmites australis of Aras River along the Iranian-Armenian Border. *IJT* **2018**, *12*, 1–6. [CrossRef]
10. Kushwaha, R.; Garg, S.; Bajpai, S.; Giri, A.S. Degradation of Nile blue sulphate dye onto iron oxide nanoparticles: Kinetic study, identification of reaction intermediates, and proposed mechanistic pathways. *Asia Pac. J. Chem. Eng.* **2018**, *13*, e2200. [CrossRef]
11. Wang, X.-L.; Sun, R.; Zhu, W.-J.; Sha, X.-L.; Ge, J.-F. Reversible Absorption and Emission Responses of Nile Blue and Azure A Derivatives in Extreme Acidic and Basic Conditions. *J. Fluoresc.* **2017**, *27*, 819–827. [CrossRef]
12. Nayak, A.K.; Pal, A. Statistical modeling and performance evaluation of biosorptive removal of Nile blue A by lignocellulosic agricultural waste under the application of high-strength dye concentrations. *J. Environ. Chem. Eng.* **2020**, *8*, 103677. [CrossRef]
13. Herzog, G.; Sibottier, E.; Etienne, M.; Walcarius, A. Electrochemically assisted self-assembly of ordered and functionalized mesoporous silica films: Impact of the electrode geometry and size on film formation and properties. *Faraday Discuss.* **2013**, *164*, 259–273. [CrossRef] [PubMed]
14. Maheshwari, H.; Vilà, N.; Herzog, G.; Walcarius, A. Selective Detection of Cysteine at a Mesoporous Silica Film Electrode Functionalized with Ferrocene in the Presence of Glutathione. *ChemElectroChem* **2020**, *7*, 2095–2101. [CrossRef]
15. Guo, Q.; Yang, X.; Chen, Z.; Wang, G.; Yao, L.; Lin, Z. Low-cost electrochemical sensor based on montmorillonite for antibiotic tetracycline hydrochloride detection. *J. Mater. Sci. Mater. Electron.* **2022**, *33*, 427–442. [CrossRef]
16. Dongmo, L.M.; Guenang, L.S.; Jiokeng, S.L.Z.; Kamdem, A.T.; Doungmo, G.; Victor, B.C.; Jović, M.; Lesch, A.; Tonlé, I.K.; Girault, H. A new sensor based on an amino-montmorillonite-modified inkjet-printed graphene electrode for the voltammetric determination of gentisic acid. *Mikrochim. Acta* **2021**, *188*, 36. [CrossRef] [PubMed]
17. Teadoum, D.N.; Noumbo, S.K.; Arnaud, K.T.; Ranil, T.T.; Mvondo Zé, A.D.; Tonle, I.K. Square Wave Voltammetric Determination of Residues of Carbendazim Using a Fullerene/Multiwalled Carbon Nanotubes/Nafion ®/Coated Glassy Carbon Electrode. *Int. J. Electrochem.* **2016**, *2016*, 1–9. [CrossRef]
18. Tajik, S.; Beitollahi, H.; Hosseinzadeh, R.; Aghaei Afshar, A.; Varma, R.S.; Jang, H.W.; Shokouhimehr, M. Electrochemical Detection of Hydrazine by Carbon Paste Electrode Modified with Ferrocene Derivatives, Ionic Liquid, and CoS$_2$-Carbon Nanotube Nanocomposite. *ACS Omega* **2021**, *6*, 4641–4648. [CrossRef]
19. Ngaha, M.C.; Tchieda, V.; Kamdem, A.; Doungmo, G.; Njanja, E.; Tonle, I. Aminoalcohol-Functionalization of Alkali Palm Oil Fiber and Application as Electrochemical Sensor for 2-Nitrophenol Determination. *Electroanalysis* **2022**, *34*, 1–14. [CrossRef]
20. Boonkaew, S.; Chaiyo, S.; Jampasa, S.; Rengpipat, S.; Siangproh, W.; Chailapakul, O. An origami paper-based electrochemical immunoassay for the C-reactive protein using a screen-printed carbon electrode modified with graphene and gold nanoparticles. *Mikrochim. Acta* **2019**, *186*, 153. [CrossRef]
21. Fazl, F.; Gholivand, M.B. High performance electrochemical method for simultaneous determination dopamine, serotonin, and tryptophan by ZrO$_2$-CuO co-doped CeO$_2$ modified carbon paste electrode. *Talanta* **2022**, *239*, 122982. [CrossRef]
22. Kumar, R.; Thangappan, R. Electrode material based on reduced graphene oxide (rGO)/transition metal oxide composites for supercapacitor applications: A review. *Emergent Mater.* **2022**, *96*, 416. [CrossRef]
23. Terán-Alcocer, Á.; Bravo-Plascencia, F.; Cevallos-Morillo, C.; Palma-Cando, A. Electrochemical Sensors Based on Conducting Polymers for the Aqueous Detection of Biologically Relevant Molecules. *Nanomaterials* **2021**, *11*, 252. [CrossRef] [PubMed]
24. Song, N.-N.; Wang, Y.-Z.; Yang, X.-Y.; Zong, H.-L.; Chen, Y.-X.; Ma, Z.; Chen, C.-X. A novel electrochemical biosensor for the determination of dopamine and ascorbic acid based on graphene oxide /poly(aniline-co-thionine) nanocomposite. *J. Electroanal. Chem.* **2020**, *873*, 114352. [CrossRef]
25. Rahman, M.A.; Kumar, P.; Park, D.-S.; Shim, Y.-B. Electrochemical Sensors Based on Organic Conjugated Polymers. *Sensors* **2008**, *8*, 118–141. [CrossRef] [PubMed]

26. Pan, H.M.; Gonuguntla, S.; Li, S.; Trau, D. 3.33 Conjugated Polymers for Biosensor Devices. In *Comprehensive Biomaterials II*; Elsevier: Amsterdam, The Netherlands, 2017; pp. 716–754. ISBN 9780081006924.

27. Moon, J.-M.; Thapliyal, N.; Hussain, K.K.; Goyal, R.N.; Shim, Y.-B. Conducting polymer-based electrochemical biosensors for neurotransmitters: A review. *Biosens. Bioelectron.* **2018**, *102*, 540–552. [CrossRef] [PubMed]

28. Tajik, S.; Beitollahi, H.; Nejad, F.G.; Shoaie, I.S.; Khalilzadeh, M.A.; Asl, M.S.; van Le, Q.; Zhang, K.; Jang, H.W.; Shokouhimehr, M. Recent developments in conducting polymers: Applications for electrochemistry. *RSC Adv.* **2020**, *10*, 37834–37856. [CrossRef]

29. Gopal, T.V.; Reddy, T.M.; Shaikshavali, P.; Venkataprasad, G. Eco-friendly and bio-waste based hydroxyapatite/reduced graphene oxide hybrid material for synergic electrocatalytic detection of dopamine and study of its simultaneous performance with acetaminophen and uric acid. *Surf. Interfaces* **2021**, *24*, 101145. [CrossRef]

30. Chen, F.-F.; Zhu, Y.-J.; Chen, F.; Dong, L.-Y.; Yang, R.-L.; Xiong, Z.-C. Fire Alarm Wallpaper Based on Fire-Resistant Hydroxyapatite Nanowire Inorganic Paper and Graphene Oxide Thermosensitive Sensor. *ACS Nano* **2018**, *12*, 3159–3171. [CrossRef]

31. Tchoffo, R.; Ngassa, G.B.P.; Doungmo, G.; Kamdem, A.T.; Tonlé, I.K.; Ngameni, E. Surface functionalization of natural hydroxyapatite by polymerization of β-cyclodextrin: Application as electrode material for the electrochemical detection of Pb(II). *Environ. Sci. Pollut. Res. Int.* **2022**, *29*, 222–235. [CrossRef]

32. Agbeboh, N.I.; Oladele, I.O.; Daramola, O.O.; Adediran, A.A.; Olasukanmi, O.O.; Tanimola, M.O. Environmentally sustainable processes for the synthesis of hydroxyapatite. *Heliyon* **2020**, *6*, e03765. [CrossRef]

33. Mohd Pu'ad, N.A.S.; Koshy, P.; Abdullah, H.Z.; Idris, M.I.; Lee, T.C. Syntheses of hydroxyapatite from natural sources. *Heliyon* **2019**, *5*, e01588. [CrossRef] [PubMed]

34. Antoniac, I.V. (Ed.) *Handbook of Bioceramics and Biocomposites*, 1st ed.; Springer International Publishing: Cham, Switzerland, 2016; ISBN 978-3-319-12460-5.

35. El Mhammedi, M.A.; Achak, M.; Bakasse, M.; Chtaini, A. Electrochemical determination of para-nitrophenol at apatite-modified carbon paste electrode: Application in river water samples. *J. Hazard. Mater.* **2009**, *163*, 323–328. [CrossRef] [PubMed]

36. Yin, H.; Zhou, Y.; Ai, S.; Liu, X.; Zhu, L.; Lu, L. Electrochemical oxidative determination of 4-nitrophenol based on a glassy carbon electrode modified with a hydroxyapatite nanopowder. *Microchim Acta* **2010**, *169*, 87–92. [CrossRef]

37. Kanchana, P.; Sekar, C. Development of electrochemical folic acid sensor based on hydroxyapatite nanoparticles. *Spectrochim. Acta A Mol. Biomol. Spectrosc.* **2015**, *137*, 58–65. [CrossRef] [PubMed]

38. Kanchana, P.; Sekar, C. EDTA assisted synthesis of hydroxyapatite nanoparticles for electrochemical sensing of uric acid. *Mater. Sci. Eng. C Mater. Biol. Appl.* **2014**, *42*, 601–607. [CrossRef]

39. Tchoffo, R.; Ngassa, G.B.P.; Tonlé, I.K.; Ngameni, E. Electroanalysis of diquat using a glassy carbon electrode modified with natural hydroxyapatite and β-cyclodextrin composite. *Talanta* **2021**, *222*, 121550. [CrossRef]

40. Shavandi, A.; Bekhit, A.E.-D.A.; Ali, A.; Sun, Z. Synthesis of nano-hydroxyapatite (nHA) from waste mussel shells using a rapid microwave method. *Mater. Chem. Phys.* **2015**, *149–150*, 607–616. [CrossRef]

41. Khtaoui, L.; Laghrouche, M.; Fernane, F.; Chaouchi, A. High-sensitivity humidity sensor based on natural hydroxyapatite. *J. Mater. Sci. Mater. Electron.* **2021**, *32*, 8668–8686. [CrossRef]

42. Zeng, Y.; Yu, D.; Yu, Y.; Zhou, T.; Shi, G. Differential pulse voltammetric determination of methyl parathion based on multiwalled carbon nanotubes-poly(acrylamide) nanocomposite film modified electrode. *J. Hazard. Mater.* **2012**, *217–218*, 315–322. [CrossRef]

43. Sudhan, N.; Sekar, C. Nanostructured β-tricalcium Phosphate (Ca₃(PO₄)₂) Based Electrochemical Sensor for Detection of Methyl Parathion and Mercury (II) Ions. *Front. Nanotechnol.* **2021**, *3*, 49. [CrossRef]

44. Gheisari, H.; Karamian, E.; Abdellahi, M. A novel hydroxyapatite—Hardystonite nanocomposite ceramic. *Ceram. Int.* **2015**, *41*, 5967–5975. [CrossRef]

45. Chappard, C.; André, G.; Daudon, M.; Bazin, D. Analysis of hydroxyapatite crystallites in subchondral bone by Fourier transform infrared spectroscopy and powder neutron diffraction methods. *Comptes. Rendus. Chim.* **2016**, *19*, 1625–1630. [CrossRef]

46. Marquez-Bravo, S.; Doench, I.; Molina, P.; Bentley, F.E.; Tamo, A.K.; Passieux, R.; Lossada, F.; David, L.; Osorio-Madrazo, A. Functional Bionanocomposite Fibers of Chitosan Filled with Cellulose Nanofibers Obtained by Gel Spinning. *Polymers* **2021**, *13*, 1563. [CrossRef] [PubMed]

47. Lall, A.; Kamdem Tamo, A.; Doench, I.; David, L.; Nunes de Oliveira, P.; Gorzelanny, C.; Osorio-Madrazo, A. Nanoparticles and Colloidal Hydrogels of Chitosan-Caseinate Polyelectrolyte Complexes for Drug-Controlled Release Applications. *Int. J. Mol. Sci.* **2020**, *21*, 5602. [CrossRef]

48. Jahromi, M.T.; Yao, G.; Cerruti, M. The importance of amino acid interactions in the crystallization of hydroxyapatite. *J. R. Soc. Interface* **2013**, *10*, 20120906. [CrossRef]

49. Kojima, S.; Nagata, F.; Inagaki, M.; Kugimiya, S.; Kato, K. Enzyme immobilisation on poly- l -lysine-containing calcium phosphate particles for highly sensitive glucose detection. *RSC Adv.* **2019**, *9*, 10832–10841. [CrossRef]

50. Ozhukil Kollath, V.; van den Broeck, F.; Fehér, K.; Martins, J.C.; Luyten, J.; Traina, K.; Mullens, S.; Cloots, R. A Modular Approach to Study Protein Adsorption on Surface Modified Hydroxyapatite. *Chemistry* **2015**, *21*, 10497–10505. [CrossRef]

51. Gao, F.; Chen, X.; Tanaka, H.; Nishitani, A.; Wang, Q. Alkaline phosphatase mediated synthesis of carbon nanotube–hydroxyapatite nanocomposite and its application for electrochemical determination of luteolin. *Adv. Powder Technol.* **2016**, *27*, 921–928. [CrossRef]

52. Liu, J.; Weng, W.; Xie, H.; Luo, G.; Li, G.; Sun, W.; Ruan, C.; Wang, X. Myoglobin- and Hydroxyapatite-Doped Carbon Nanofiber-Modified Electrodes for Electrochemistry and Electrocatalysis. *ACS Omega* **2019**, *4*, 15653–15659. [CrossRef]

53. Gao, F.; Wang, Q.; Gao, N.; Yang, Y.; Cai, F.; Yamane, M.; Gao, F.; Tanaka, H. Hydroxyapatite/chemically reduced graphene oxide composite: Environment-friendly synthesis and high-performance electrochemical sensing for hydrazine. *Biosens. Bioelectron.* **2017**, *97*, 238–245. [CrossRef]

54. Amine, S.; Montembault, A.; Fumagalli, M.; Osorio-Madrazo, A.; David, L. Controlled Polyelectrolyte Association of Chitosan and Carboxylated Nano-Fibrillated Cellulose by Desalting. *Polymers* **2021**, *13*, 2023. [CrossRef] [PubMed]

55. Doench, I.; Torres-Ramos, M.E.W.; Montembault, A.; Nunes de Oliveira, P.; Halimi, C.; Viguier, E.; Heux, L.; Siadous, R.; Thiré, R.M.S.M.; Osorio-Madrazo, A. Injectable and Gellable Chitosan Formulations Filled with Cellulose Nanofibers for Intervertebral Disc Tissue Engineering. *Polymers* **2018**, *10*, 1202. [CrossRef] [PubMed]

56. Kamdem Tamo, A.; Doench, I.; Morales Helguera, A.; Hoenders, D.; Walther, A.; Madrazo, A.O. Biodegradation of Crystalline Cellulose Nanofibers by Means of Enzyme Immobilized-Alginate Beads and Microparticles. *Polymers* **2020**, *12*, 1522. [CrossRef] [PubMed]

57. Kamdem Tamo, A.; Doench, I.; Walter, L.; Montembault, A.; Sudre, G.; David, L.; Morales-Helguera, A.; Selig, M.; Rolauffs, B.; Bernstein, A.; et al. Development of Bioinspired Functional Chitosan/Cellulose Nanofiber 3D Hydrogel Constructs by 3D Printing for Application in the Engineering of Mechanically Demanding Tissues. *Polymers* **2021**, *13*, 1663. [CrossRef] [PubMed]

58. Samyn, P.; Osorio-Madrazo, A. Native crystalline polysaccharide nanofibers: Processing and properties. In *Handbook of Nanofibers*; Barhoum, A., Bechelany, M., Makhlouf, A., Eds.; Springer International Publishing: Cham, Germany, 2018; pp. 1–36.

59. Kul, D.; Pauliukaite, R.; Brett, C.M.A. Electrosynthesis and characterisation of poly(Nile blue) films. *J. Electroanal. Chem.* **2011**, *662*, 328–333. [CrossRef]

60. Laviron, E. General expression of the linear potential sweep voltammogram in the case of diffusionless electrochemical systems. *J. Electroanal. Chem. Interfacial Electrochem.* **1979**, *101*, 19–28. [CrossRef]

61. Ju, H.; Shen, C. Electrocatalytic Reduction and Determination of Dissolved Oxygen at a Poly(nile blue) Modified Electrode. *Electroanalysis* **2001**, *13*, 789–793. [CrossRef]

62. Ju, H.; Ye, Y.; Zhu, Y. Interaction between nile blue and immobilized single- or double-stranded DNA and its application in electrochemical recognition. *Electrochim. Acta* **2005**, *50*, 1361–1367. [CrossRef]

63. Kul, D.; Brett, C.M.A. Electrochemical Investigation and Determination of Levodopa on Poly(Nile Blue-A)/Multiwalled Carbon Nanotube Modified Glassy Carbon Electrodes. *Electroanalysis* **2014**, *26*, 1320–1325. [CrossRef]

64. Tcheumi, H.L.; Babu, B.R. Surfactant-intercalated smectite modified electrode: Sensitive electrochemical detection of methyl orange dye. *Int. J. Environ. Anal. Chem.* **2017**, *97*, 1207–1222. [CrossRef]

65. Tonlé, I.K.; Ngameni, E.; Tcheumi, H.L.; Tchiéda, V.; Carteret, C.; Walcarius, A. Sorption of methylene blue on an organoclay bearing thiol groups and application to electrochemical sensing of the dye. *Talanta* **2008**, *74*, 489–497. [CrossRef] [PubMed]

66. Hassan, S.S.; Nafady, A.; Sirajuddin; Solangi, A.R.; Kalhoro, M.S.; Abro, M.I.; Sherazi, S.T.H. Ultra-trace level electrochemical sensor for methylene blue dye based on nafion stabilized ibuprofen derived gold nanoparticles. *Sens. Actuators B Chem.* **2015**, *208*, 320–326. [CrossRef]

67. Njanja, E.; Mbokou, S.F.; Pontie, M.; Nacef, M.; Tonle, I.K. Comparative assessment of methylene blue biosorption using coffee husks and corn cobs: Towards the elaboration of a lignocellulosic-based amperometric sensor. *SN Appl. Sci.* **2019**, *1*, 233. [CrossRef]

68. Nekoueian, K.; Jafari, S.; Amiri, M.; Sillanpaa, M. Pre-Adsorbed Methylene Blue at Carbon-Modified TiO_2 Electrode: Application for Lead Sensing in Water. *IEEE Sens. J.* **2018**, *18*, 9477–9485. [CrossRef]

Article

Physicochemical Characterization of Novel Epoxidized Vegetable Oil from Chia Seed Oil

Ivan Dominguez-Candela [1], Alejandro Lerma-Canto [2], Salvador Cayetano Cardona [1], Jaime Lora [1] and Vicent Fombuena [2,*]

1   Instituto de Seguridad Industrial, Radiofísica y Medioambiental (ISIRYM), Universitat Politècnica de València (UPV), Plaza Ferrándiz y Carbonell, s/n, 03801 Alcoy, Spain; ivdocan@doctor.upv.es (I.D.-C.); scardona@iqn.upv.es (S.C.C.); jlora@iqn.upv.es (J.L.)
2   Technological Institute of Materials (ITM), Universitat Politècnica de València (UPV), Plaza Ferrándiz y Carbonell 1, 03801 Alcoy, Spain; allercan@epsa.upv.es
*   Correspondence: vifombor@upv.es

Abstract: In this study, a novel epoxidized vegetable oil (EVO) from chia seed oil (CSO) has been obtained, with the aim to be employed in a great variety of green products related to the polymeric industry, as plasticizers and compatibilizers. Previous to the epoxidation process characterization, the fatty acid (FA) composition of CSO was analyzed using gas chromatography (GC). Epoxidation of CSO has been performed using peracetic acid formed in situ with hydrogen peroxide and acetic acid, applying sulfuric acid as catalyst. The effects of key parameters as temperature (60, 70, and 75 °C), the molar ratio of hydrogen peroxide:double bond (H_2O_2:DB) (0.75:1.0 and 1.50:1.0), and reaction time (0–8 h) were evaluated to obtain the highest relative oxirane oxygen yield (Y_{oo}). The evaluation of the epoxidation process was carried out through iodine value (IV), oxirane oxygen content (O_o), epoxy equivalent weight (EEW), and selectivity (S). The main functional groups were identified by means of FTIR and ^{1}H NMR spectroscopy. Physical properties were compared in the different assays. The study of different parameters showed that the best epoxidation conditions were carried out at 75 °C and H_2O_2:DB (1.50:1), obtaining an O_o value of 8.26% and an EEW of 193 (g·eq^{-1}). These high values, even higher than those obtained for commercial epoxidized oils such as soybean or linseed oil, show the potential of the chemical modification of chia seed oil to be used in the development of biopolymers.

Keywords: chia seed oil; fatty acids composition; epoxidized vegetable oil; epoxy equivalent weight

1. Introduction

Nowadays, fossil-based materials use is increasing greenhouse gas emissions, wastes in landfills, and the exhaustion of non-renewable resources [1]. This situation leads to the need to find new alternatives in order to decrease the elevated production of fossil-based materials. One of the most promising renewables resources is vegetable oils (VO) because of their availability, relatively low cost, and non-toxicity [2]. According to the latest data of European Bioplastics Association, the land used to produce the renewable feedstock is approximately 0.0013% in 2021 and is estimated to increase up to 0.058% in 2026 [3]. This increase continues to be a very low value compared with food and feed land used (25% in 2021), indicating that there is not competition between the renewable feedstock for feed, food, and the production of bioplastics. In case of VO production, it increases each year where approximately 20% is used for industrial applications due to the concern of environmental problems [4]. VO is mainly formed by triglycerides, which are composed of three fatty acids (FAs) connected to glycerol molecules. In their structure, carbon-carbon double bonds enable VO to be easily transformed, increasing their reactivity. One of the several ways to take advantage of these double bonds in VO is through the epoxidation reaction, which introduces oxirane oxygen in double bonds [5].

Epoxidized vegetable oils (EVOs) are used as reagents and intermediates in the manufacture of polymers and are commonly used as plasticizers, compatibilizers, stabilizers, reactive diluents, or epoxy matrices for composites [6–9]. Several EVOs have been reported in the literature, highlighting studies of linseed [10], cottonseed [11], soybean [12], karanja [13] or castor oil [14], among others [15–18].

Notwithstanding, one of the VO with the most significant potential, due to its high amount of double bonds present in the FA chains, is the chia seed oil (CSO) (*Salvia hispanica,* L.). As it is possible to observe in Table 1, the iodine value (*IV*) of CSO, which is a parameter used to determine the number of unsaturation in fats, oils, and waxes, is above 190 g I_2/100 g. For this reason, CSO is one of the VO with the greatest potential for use in different sectors. Nowadays, CSO presents a market share of 20% of chia market with an expected increase of 23.4% from 2019 to 2025 in order to use it for food and non-food applications [19]. Regarding food applications, although is not widely used as others edible VOs, it is employed as food complements and cooking oil [20]. Some authors have also suggested the addition of CSO in food applications due to its high benefits [21,22]. On the other hand, as non-food applications, CSO has been epoxidized and employed as environmentally friendly plasticizer in one of the most promising industrial applications [23]. However, this study showed a lack of assessed parameters such as temperature and reagents concentration that can enhanced the epoxidation yield and no physico-chemical characterizations were carried out. Therefore, CSO could be one of the best VO candidates to be epoxidized, due to its high availability of double bonds, which can lead to obtain one of the highest theoretical oxirane oxygen content (O_o) even higher than EVOs of greater industrial use (linseed and soybean). CSO has the potential to obtain more O_o using fewer amounts of reagents (sulphuric and acetic acid or hydrogen peroxide e.g.), resulting in a low-cost process and a more environmentally friendly EVO [24–26].

Table 1. Iodine value and theoretical oxirane oxygen content of different vegetable oils.

Vegetable Oil	Initial Iodine Value (IV_0, g I_2/100 g)	Theoretical Oxirane Oxygen Content (O_o, %)	References
Castor	84	5.03	[14]
Soybean	126	7.36	[27]
Rubber	156	8.95	[28]
Cottonseed	107	6.32	[11]
Linseed	188	10.6	[29]
Canola	112	6.60	[5]
Sunflower	130	7.57	[30]
Palm	62	3.76	[12]
Olive	127	7.41	[31]
Corn	115	6.76	[32]
Chia seed	197	11.05	Present study

Regarding the epoxidation process, selectivity (*S*) and O_o vary depending on the catalyst used to obtain epoxides. Different methods have been studied, each with its advantages and disadvantages. For example, Guenter et al. employed molecular oxygen to carry out the epoxidation process [33]. This method could be low-cost and ecological using silver as the catalyst, but it is restricted to precursors like ethylene or butadiene and is not very efficient. The same authors studied the possibility of using halohydrins through hypohalous acids and their respective salts, but this route was not environmentally friendly [33]. The most employed route to synthesize EVOs is the use of hydrogen peroxide with in situ formed peroxyacid, as can be observed in Figure 1. This route presents some benefits compared to preformed peroxyacids, such as safer processing and handling, as well as requiring a minimum quantity of reagents to produce EVOs [34]. However, this route can lead to thermal runaway due to the exothermic reaction [35]. In order to reduce this risk, several actions can be considered such as comprehensive temperature control with adequate cooling capacity or dosing rate [36]. In this regard, this issue is taking into account

industrially due to this route is the most employed [37]. Moreover, it is commonly known that, in many epoxidation processes, the excess of molar ratio reagents and/or higher temperatures can lead to side-reactions, being the most common the oxirane ring cleavage. The ring-opening has been studied for the purpose of comprehending the influence of factors in these side-reactions. For instance, Cai et al. [38] have studied the ring-opening for the epoxidation of cottonseed oil, where evaluated the effect of reagents taking into account the kinetic model. Furthermore, in the recent literature, the use of different epoxidation methods such as chemoenzymatic, polyoxometalates or heterogeneous catalytic systems in the presence of titanium silicate or ion exchange resin has been reported to overcome this drawback [4]. However, homogeneous catalysts have been proved to be more effective for industrial-scale plants to produce EVOs in batch reaction over 8 h [39,40]. In this regard, the use of strong mineral acid with acetic acid leads to a higher reaction rate [41].
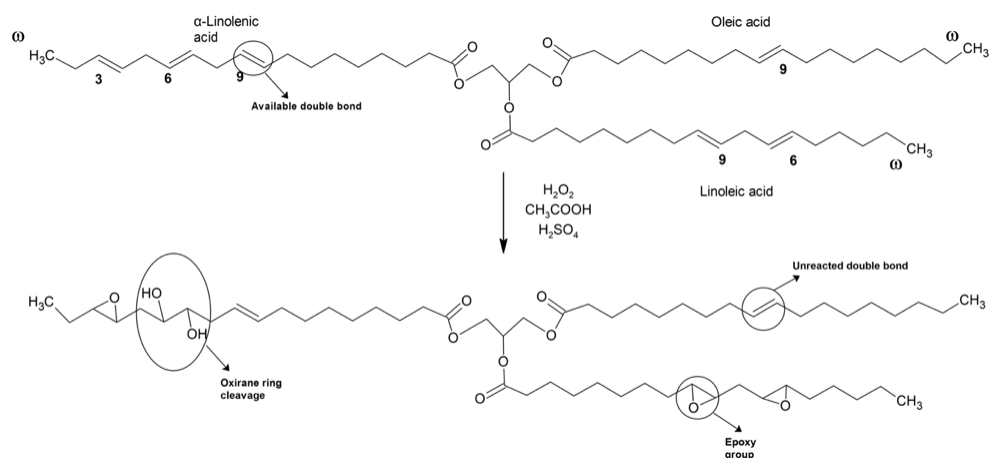
Figure 1. Schematic representation of epoxidation by means of in situ formed peroxyacids.

The main purpose of this study was to develop a new EVO from chia seed oil (ECSO) as a raw material due to its great potential, determined by the high IV. This new EVO was carried out by in situ epoxidation process with acetic acid and hydrogen peroxide. In this way, a new reagent for use in the polymeric industry can be obtained through a naturally renewable resource as an alternative to the current petrochemical compounds or commercially available EVOs. After the analysis by GC of the composition of the fatty acids of chia oil obtained by cold mechanical extrusion, the epoxidation process was carried out, optimizing key parameters such as temperature, the molar ratio of H_2O_2:DB, and reaction time. The oxirane oxygen content (O_o) was analyzed by titration method and the functional groups were confirmed using FTIR as well as ^{1}H NMR spectroscopy. Further characterization was performed to evaluate the changes in physical-chemical parameters such as specific gravity, dynamic viscosity, and colorimetric coordinates.

2. Materials and Methods

2.1. Materials

Chia seed (Salvia hispanica, L.) was supplied by Frutoseco (Bigastro, Alicante, Spain) and CSO was obtained by cold extraction using a CZR-309 press machine (Changyouxin Trading Co., Zhucheng, China). Aqueous hydrogen peroxide (30 wt.%), glacial acetic acid (99.7 wt.%), and sulphuric acid (96 wt.%) were purchased from Sigma Aldrich (Sigma Aldrich, Madrid, Spain). Reagents required for *IV* characterization such as Wijs solution (ICl), 0.1 N sodium thiosulphate solution ($Na_2S_2O_3$), potassium iodide (KI), and cyclohexane (C_6H_{12}), were supplied from Sigma Aldrich (Sigma Aldrich, Madrid, Spain). To determine oxirane oxygen content, chlorobenzene (C_6H_5Cl), crystal violet indicator, potassium acid phthalate ($KHC_8H_4O_4$), and 0.1 N HBr solution in glacial acetic acid were supplied from Panreac Química S.L.U. (Castellar del Vallés, Barcelona, Spain).

2.2. Epoxidation Process

Epoxidation reaction was performed in a three-necked round-bottom flask (1000 mL capacity). The flask, equipped with a two-bladed stirrer, was immersed in a thermostatic water bath where the temperature could be controlled to ± 0.1 °C of the desired temperature. A propeller mechanical stirrer was connected to the central neck, a drop-wise device was introduced in one of the side necks, and a thermometer was connected to the third neck.

Epoxidation of CSO was carried out using a peroxyacid generated in situ from an organic acid. The most widely used in this process are formic ($HCOOH$) and acetic (CH_3COOH) acids due to their high reactivity. The efficiency of these oxidants depends on the operating temperature, taking into account that according to literature, acetic acid is the most effective above 60 °C [42]. Furthermore, acting as the catalyst, sulphuric (H_2SO_4) and nitric acid (HNO_3) are the most employed. In this regard, sulphuric acid with an optimal value of 3 wt.% with respect to the sum of the masses of hydrogen peroxide and acetic acid, was the most effective inorganic acid in order to obtain the highest conversion to oxirane oxygen, as was reported [43]. Therefore, the procedure is summarized as follows: firstly, 232 g of CSO (0.776 mol double bond for each 100 g of oil) and 25.3 g of glacial acetic acid were maintained at a constant temperature (60 °C) and stirring rate (220 rpm), which allowed a sufficient agitation to ensure proper mass transfer. After 10 min, sulphuric acid and hydrogen peroxide were mixed and added dropwise. The addition was completed within half an hour, at a constant rate following the method reported by Dinda et al. [44]. Two different H_2O_2:DB molar ratios (MR) mentioned previously (MR 0.75 and MR 1.50) at 60 °C were studied. MR 1.50 has been selected as the optimal amount of peroxide, which means 1.50 moles of H_2O_2 for one mole of double blonds [45]. It should be noted that CSO contains a higher iodine value compared to other VOs and, thus, a higher O_o can be obtained. Therefore, MR 0.75 (half of the MR 1.50) has also been tested in this epoxidation process in order to study the effect of hydrogen peroxide and the possibility to achieve a reduction of the chemical compounds used. With respect to the temperature, different tests have been carried out at 60, 70, and 75 °C ± 1 °C, studying the reaction from 0 to 8 h considering the ranges reported in previous literature [46]. Samples were extracted at 0.5, 1.0, 1.5, 2.0, 4.0, 6.0 and 8.0 h, after adding the peroxide and sulphuric acid to monitor the reaction process. The collected samples were cooled at room temperature and then washed with water until they were acid-free up to pH neutral. To purify and remove the excess of water, samples were centrifuged 10 min at 7000 rpm.

2.3. Characterization

2.3.1. Fatty Acid Composition

Prior to quantitative determination, FAs of oils have been transformed into methyl esters (FAMEs) following the standard method ISO 12966. The FAs profile was determined using HP/Agilent 6890 N gas chromatograph (Palo Alto, CA, USA) with Agilent 5973 N mass spectrometer detector (GC-MS). Equipment is provided with a splitless injector, ionization detector mode (70 eV), and integrator. The GC-MS method applied was according to ISO 12966. A DB-5MS capillary column (30 m length, 0.25 mm inner diameter, and 0.25 mm film thickness) from Teknokroma (Barcelona, Spain) was used using a temperature program from 140 to 300 °C at 20 °C/min. The injector and detector temperatures used were 280 and 300 °C, respectively. The sample injection volume was 1 μL using a splitless injector. Helium was used as carrier gas at a flow rate of 1 μL/min. Each FA was identified through the retention time comparison between pure commercial standard and the studied sample. FA results were expressed as percentages of the total regarding FAMEs.

2.3.2. Iodine Value (IV)

The iodine value is referred to the mass of Iodine (I_2 in grams) absorbed by 100 g of oil. It is an index used to determine the amount of unsaturation (double bonds) in FAs. This value was determined using Wijs solution (ICl) that reacted with double bonds and it was

possible to detect the evolution by using sodium thiosulfate solution. *IV* was determined according to ISO 3961 using Equation (1):

$$IV = \frac{12.69 \times c \times (V_1 - V_2)}{m} \tag{1}$$

where *IV* refers to the mass of Iodine per 100 g of oil (g I_2/100 g oil), *c* to the normality of sodium thiosulfate solution 0.1 N ($Na_2S_2O_3$), V_1 to the volume of $Na_2S_2O_3$ needed for titration of the blank (mL), V_2 to the volume of $Na_2S_2O_3$ needed for titration of the sample (CSO) (mL), and m refers to the amount of sample used (g). Moreover, it is possible to determine the conversion of double bond (X_{IV}) using Equation (2) [10]:

$$X_{IV}(\%) = \left(\frac{IV_0 - IV_f}{IV_0} \right) \times 100 \tag{2}$$

where IV_0 is the initial iodine value of the VO sample and IV_f is the final iodine value of the EVO after the epoxidation process. At least five measurements were made for each sample and the average values were reported.

2.3.3. Oxirane Oxygen Content (O_o)

The number of epoxy groups was determined using the direct method of titration with hydrobromic acid (HBr) solution in glacial acetic acid, using ASTM D1652. The sample was dissolved in chlorobenzene, followed by the addition of drops of crystal violet and titration using 0.1 N HBr in glacial acetic acid. The oxirane oxygen content (O_o) was calculated with Equation (3):

$$O_o(\text{wt. }\%) = 1.6 \times N_i \times \frac{(V - B)}{W} \tag{3}$$

where N_i refers to the normality of HBr in glacial acetic acid, *V* to the volume of HBr solution for titration of the sample (mL), *B* to the volume of HBr solution for titration of the blank (mL), and *W* refers to the amount of sample used (g). At least five measurements were made for each sample and the average values were reported.

To determine the percentage conversion to oxirane (Y_{OO}) Equation (4) has been employed:

$$Y_{OO}(\%) = \left(\frac{O_o}{O_{the}} \right) \times 100 \tag{4}$$

where, O_o is the oxirane oxygen content experimentally obtained and O_{the} is the theoretical maximum oxirane oxygen content that was calculated using Equation (5) [43]:

$$O_{the}(\text{wt. }\%) = \left(\frac{\frac{IV_o}{2AM_i}}{\left\lceil 100 + \left(\frac{IV_o}{2AM_i} \right) \times AM_o \right\rceil} \right) \times AM_o \times 100 \tag{5}$$

Regarding Equation (5), IV_o is the initial iodine value of the sample, AM_i is the atomic mass of Iodine (126.9 g/mol), and AM_o is the atomic mass of oxygen (16 g/mol). Moreover, the selectivity for oxirane oxygen (*S*) can be determined using Equation (6) [47].

$$S = \left(\frac{O}{O_{the}} \right) \times \left(\frac{IV_o}{IV_o - IV_f} \right) \tag{6}$$

2.3.4. Epoxy Equivalent Weight (EEW)

The epoxy equivalent weight (*EEW*) is defined as the mass, expressed in grams, of the epoxy resin which contains one equivalent of the epoxy group (g·eq^{-1}). It is one of the most important features of epoxy resins, which is related to the crosslinking density and allows

the calculation of the required amount of crosslinking agent for the curing process [48]. The *EEW* of ECSO was obtained following ASTM D1652 via titration using Equation (7):

$$EEW \left(\text{g·eq}^{-1} \right) = \left(\frac{1000 \times W}{(V - B) \times N_i} \right) \tag{7}$$

2.3.5. Fourier Transform InfraRed (FTIR) Spectroscopy

The substitution of double bonds and changes in functional groups was identified by Fourier Transform Infrared (FTIR) spectroscopy equipped with a horizontal attenuated total reflection modulus (ATR). Both CSO and ECSO were analyzed using a Bruker Vector 22 (Bruker Española, S. A, Madrid, España), averaging 20 scans at 4000–400 cm^{-1} and 4 cm^{-1} of resolution. It must be remarked that this method is immediate and straightforward to evaluate the possible change of the main functional groups, allowing to correlate the progress of epoxidations from infrared studies. However, the titration method obtains a better accuracy than the FTIR spectroscopy method, as has been reported by [15,49]. Thus, the FTIR method was used to verify the evolution of the main functional groups.

2.3.6. Nuclear Magnetic Resonance (NMR) Spectroscopy

^{1}H NMR spectroscopy was employed to compare and confirm the chemical structure of CSO and ECSO. Samples were analyzed using a Bruker AMX 500 unit (Bruker BioSpin GmbH, Rheinstetten, Germany) at 25 °C. Samples of 40 mg were dissolved in 0.6 mL of deuterated chloroform (CDCl$_3$), mixed for 10 s and transferred to 5 mm NMR tubes for data acquisition.

2.3.7. Physico-Chemical Properties

The method used to determine changes in specific gravity was a pycnometer, according to ASTM D1963. This method uses a 25 mL pycnometer maintaining a constant temperature of 25 °C. All densities of liquids were obtained against water. The specific gravities of untreated CSO and epoxidized were measured using Equation (8):

$$\rho_r = \frac{W_s - W_e}{W_w - W_e} \tag{8}$$

where W_s is the weight (g) of the sample in the pycnometer, W_e is the weight (g) of the empty pycnometer, and W_w is the weight (g) of water in the pycnometer. At least five measurements were obtained with a maximum deviation of 3×10^{-3}.

Dynamic viscosities were obtained using two Cannon-Fenske viscosimeters of 300 and 450 mm with flow ranges from 5×10^{-5} to 2.5×10^{-4} m^2·s^{-1} and from 5×10^{-4} to 2.5×10^{-2} m^2·s^{-1}, respectively, at 20 °C. The assay has been carried out following the guidelines of the ASTM D-445. Viscosimeter was introduced in a water bath monitoring the temperature with a precision of $\pm$ 0.1 °C. At least five measurements were measured with a maximum dynamic viscosity deviation of 1.02 mPa·s.

The colorimetric coordinates of CSO and ECSO were measured using a Hunter Lab Colorimeter (Colour Flex, Hunter Associates Inc., Reston, VA, USA). The instrument (45°/0° geometry, D45 optical sensor, 10° observer) was calibrated before the experiments with Black and White reference tiles, and Green tiles were used to verify the correct operation. The values of luminance (L*) (0–100) represent lightness, parameters a* and b* indicate the approach from green (negative) to red (positive), and from blue (negative) to yellow (positive), respectively. At least five measurements were made for each sample and the average values were reported. Color variation was evaluated by using Equation (9):

$$\Delta E = \sqrt{\Delta L^2 + \Delta a^2 + \Delta b^2} \tag{9}$$

3. Results

3.1. CSO Extraction and Fatty Acid Composition

CSO was extracted by double cold extraction in a press machine to avoid chemical changes in the FA composition caused by high temperatures and the use of chemical solvents. Firstly, whole seeds were pressed to obtain oil and cake. Then, the residual cake was pressed again in order to obtain a higher yield of oil extraction. At the end of the pressing process, oil was filtered and centrifuged at 4000 rpm to be cleaned, and then it was stored in a cold dark room. The yield of extracted CSO was increased from 20.4% for the first process to 24.5% adding up the oil obtained from the second press of the chia cake. This slow increase of extraction yield with the second press shows that no longer than two presses are considered economically feasible, as reported by Kasote et al. [50]. This total yield is in the same range that was reported by Ixtaina et al. [51], in which the production yield of CSO was 24.8%.

The FA composition obtained by GC and the comparison with results published by other authors are shown in Table 2. As it can be observed, CSO presents a low proportion of saturated fatty acids (SFAs), with a value of 10.7%, integrated by myristic (0.06%), palmitic (7.2%), stearic (2.88%), and arachidic (0.55%) acids. With respect to monounsaturated fatty acids (MUFAs), it is observed even a lower proportion (4.41%), with palmitoleic (0.09%) and oleic (4.32%) acids. The higher content is found in polyunsaturated fatty acids (PUFAs) with 84.9%, which provides the most CSO double bonds: Linoleic (15.8%), γ-Linolenic (0.41%), and α-Linolenic (68.6%). The main difference between γ-Linolenic and α- Linolenic is the position of the double bond, where α-Linolenic contains the double bond in the 3rd, 6th, and 9th carbon position with respect to methyl terminus, whereas γ-Linolenic in 6th, 9th and 12th position. The high amount of α-Linolenic acid in the FAs profile provides better reactivity due to the position of double bonds in the carbon chain. The double bonds closer to the methyl terminus in the 3rd position present more reactivity than the 6th and 9th as has been reported by Scala and Wool [52], where the kinetics of the epoxidation process of vegetable oil was studied. Furthermore, CSO is the seed oil with the highest α-Linolenic content known compared to other studies of vegetable oils [53]. The results of the FAs of CSO are in concordance with the results reported by other authors, as is gathered in Table 2. The slight difference is probably due to the seed origin that has influenced FA composition. Some authors have reported that the FA profile and its quantity depend on several environmental factors such as temperature, light, or soil type [54].

Table 2. Content of fatty acids presents in chia seeds (expressed as g of fatty acid/100 g of oil) and comparison with other studies.

	Fatty Acids (FAs)	**In This STUDY**	**Demin et al. [53]**	**Kulczyński et al. [55]**
SFAs	Myristic (C14:0)	0.06	0.04	0.06
	Palmitic (C16:0)	7.20	6.84	7.04
	Stearic (C18:0)	2.88	2.71	2.84
	Arachidic (C20:0)	0.55	0.28	0.02
	Total SFAs	**10.7**	**9.87**	**9.96**
MUFAs	Palmitoleic (C16:1)	0.09	0.24	0.03
	Oleic (C18:1)	4.32	6.17	7.3
	Total MUFAs	**4.41**	**6.41**	**7.33**
PUFAs	Linoleic (C18:2)	15.8	18.6	18.9
	γ-Linolenic (C18:3)	0.41	n.m [1]	n.m [1]
	α-Linolenic (C18:3)	68.6	64.4	63.8
	Total PUFAs	**84.9**	**83**	**82.7**

[1] Where n.m means not mentioned.

3.2. Effect of Molar Ratio H_2O_2:Double Bond in the Epoxidation Process

To investigate the effect of molar ratio H_2O_2:DB, two experiments were made at MR 0.75 and 1.50 applying a constant temperature of 60 °C. In these conditions, both *IV* and O_o analyses were obtained to monitor the epoxidation reaction. As it is possible to observe in Figure 2, IV_0 was 197 g I_2/100 g of oil for CSO, which is in accordance with Imran et al. [56] and Timilsena et al. [57], where both obtained values of 193 and 204 g I_2/100 g of oil, respectively. The plot representation shows that once the epoxidation process takes place, the *IV* decreases due to the reaction of double bonds, as reported by Campanella et al. [58] with soybean oil. In the assay carried out at MR 1.50, the *IV* decreases more sharply, showing a greater rate yield in the process of double bonds substitution. However, although the results using MR 1.5 have been better than those with MR 0.75, the authors do not consider it appropriate to increase the MR above 1.5, due to an excess of reagents can cause side-reactions as the oxirane ring cleavage. In addition, the slope of the *IV* curve changes at the first 4 h, being less pronounced with MR 0.75 due to less initial oxygen active donor in the reaction for the lower hydrogen peroxide ratio, which is strongly related to the reduction of IV. Therefore, using MR 1.50 at 60 °C, *IV* is reduced up to 80.1 g I_2/100 g of oil after 8 h of reaction, reaching almost a value of 60% for X_{IV}. However, lower values were obtained using MR 0.75, with 42.2% for X_{IV} and 114 g I_2/100 g of oil for *IV*.
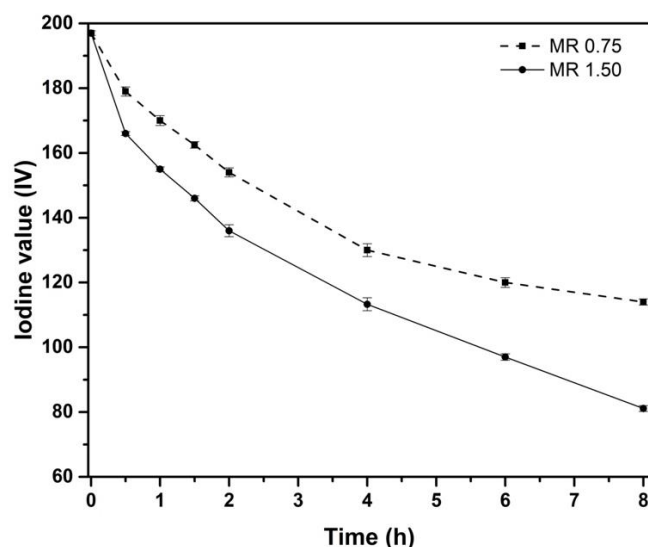
Figure 2. Effect on Iodine value (*IV*) of the MR 0.75 and 1.50 during the epoxidation process.

Figure 3 shows the plot evolution of O_o and *EEW*. Inversely proportional to *IV*, when MR increases, the presence of O_o increases as well. As reaction time proceeds, significant differences were observed comparing both MR. It is known that hydrogen peroxide is an active oxygen donor in the reaction [27]. Thus, when MR is increased from 0.75 to 1.50, an increase of O_o can be noticed. The reason for this result is the increase in peracetic acid formation due to a higher amount of hydrogen peroxide [10]. Peracetic acid acts as a vector of oxygen, causing a conversion improvement. Then, doubling the amount of hydrogen peroxide, an increase of 36.8% in O_o from 4.48 wt.% to 6.13 wt.% was obtained at the end of the reaction. Taking Equation (5) into account, a theoretical maximum oxirane oxygen content (O_{the}) of 11.05% was obtained, thus achieving a Y_{oo} value of 55.6% for MR 1.50. This epoxidation yield value can be ascribed to the lower efficiency of acetic acid at 60 °C, when the most effective temperature is observed above 60 °C [42]. Results are gathered in Table 3.
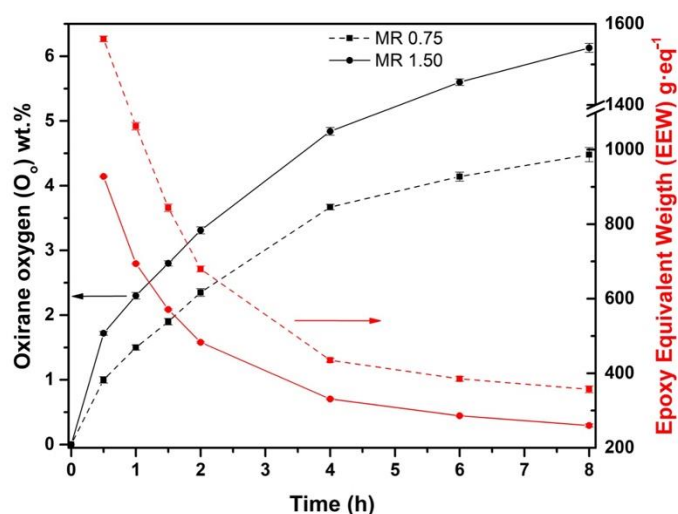
Figure 3. Effect on oxirane oxygen (O_o) of the MR 0.75 and 1.50 at 60°C during the epoxidation process.

Table 3. Main parameters used to characterize the epoxidation process of the chia seed oil (CSO) at different molar ratios and temperatures.

Epoxidation	Temperature (°C)	MR [1]	IV_f [2]	X_{IV} [3]	O_o [4]	EEW [5] (g·eq⁻¹)	Y_{OO} [6]	S [7]
1	60	0.75	114 ± 0.94	42.2 ± 0.48	4.48 ± 0.11	357 ± 8.9	39.9 ± 1.02	0.946 ± 1.88
2	60	1.50	80.1 ± 0.87	59.4 ± 0.41	6.13 ± 0.12	260 ± 4.94	55.6 ± 1.07	0.935 ± 1.92
3	70	1.50	37.9 ± 0.62	80.8 ± 0.32	7.61 ± 0.10	210 ± 3.10	68.9 ± 0.98	0.853 ± 1.70
4	75	1.50	13.1 ± 1.52	93.4 ± 0.75	8.26 ± 0.11	193 ± 2.39	74.8 ± 0.78	0.801 ± 1.79

[1] Hydrogen peroxide to double bond (H_2O_2:DB); [2] Final iodine value (g I_2/100 g oil); [3] Conversion iodine value; [4] Oxirane oxygen content; [5] Epoxy equivalent weight; [6] Conversion to oxirane; [7] Selectivity.

Related to selectivity (*S*) (values also summarized in Table 3), it is possible to appreciate that this value slightly decreases at MR 1.50 compared to MR 0.75. These results demonstrate that there are double bonds that were not replaced by epoxy groups. Although X_{IV} and Y_{oo} for MR 1.50 are higher than for MR 0.75, the opposite occurs with *S*. It is known that higher MR leads to an increment of Y_{oo} and the presence of hydrolysis reactions, i.e., epoxy ring cleavage [28]. For that reason, *S* for MR 1.50 is slightly lesser than for MR 0.75 due to more presence of side-reactions caused by a higher amount of hydrogen peroxide. This is another reason why the use of higher reagent ratios is not technically feasible, as the high reactivity of the fatty acids present in chia oil causes unwanted side reactions. Therefore, the highest O_o and lowest *EEW* values were obtained for MR 1.50 with values of 6.13 wt.% and 260 g·eq⁻¹, respectively.

3.3. Effect of the Temperature in the Epoxidation Process

The influence of temperature on the epoxidation process was studied at 60 °C, 70 °C, and 75 °C with the best MR (1.50) previously detailed. In Figure 4, it is possible to observe an increase in *IV* conversion at higher temperatures. As happened previously, the slope of *IV* showed a sharper change at the first 4 h. This behavior can be ascribed to the higher reactivity of double bonds present in the 3rd position of methyl terminus of fatty acid in α-Linolenic acid [52], which react faster at the initial time of the experiments. In contrast, the less reactive double bonds (6th and 9th) present in α-Linolenic acid, Linoleic, and Oleic acid take a longer time to react. Then, increasing the temperature from 60 °C to 75 °C, an *IV* of 13.1 g I_2/100 g of oil was obtained with regard to 80.1 g I_2/100 g of oil at 60 °C. Therefore, the temperature is shown as the key factor to increase the conversion of *IV*.
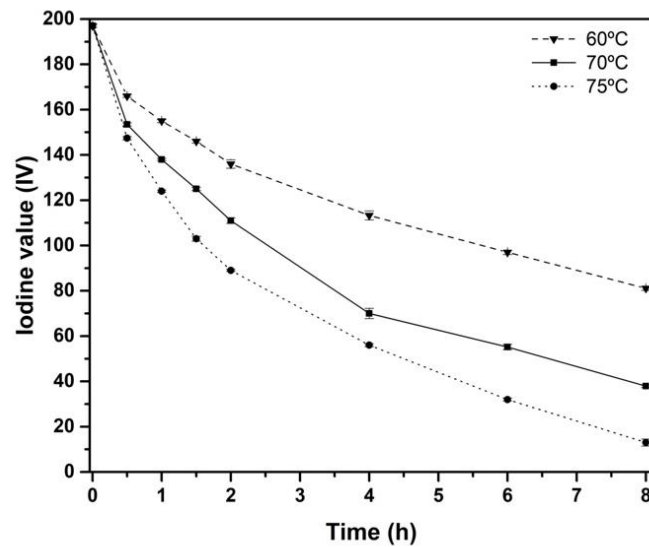
Figure 4. Effect on Iodine value (*IV*) of the temperature (60 °C, 70 °C, and 75 °C) with MR 1.50 during the epoxidation process.

Regarding the formation of epoxy groups plotted in Figure 5, it increases as temperature increases, accelerating the kinetic of epoxidation to form oxirane oxygen [46]. In the same way as with *IV*, the O_o slope is higher at the first 4 h of reaction whereas, after that time, this trend decreases. This reduction in reaction rate can be related to the decomposition of peracetic acid, acetic acid, and hydrogen peroxide along the time [59]. With the higher temperature (75 °C) studied, it is possible to obtain the highest value of O_o, 8.26 wt.%, or lowest *EEW*, 193 g·eq^{-1}, obtaining a Y_{oo} of 74.8%. An increase of 15°C from 60 °C to 75 °C contributes to an improvement of 25.7% for O_o. It should be noted that higher temperatures and extended time, increase the O_o but can also cause a greater oxirane cleavage rate [44]. As Campanella et al. [60] and Gan et al. [61] studied for temperatures higher than 75 °C in soybean and palm oil, respectively, the oxirane ring was destabilized, which slowed the growth of the conversion to epoxy groups, even reducing the oxirane oxygen formed. In this sense, all temperatures studied showed almost no conversion to epoxy groups from 6 h onwards, being more pronounced with the temperature of 75 °C. For this reason, the authors did not consider it appropriate to carry out the epoxidation process at higher temperatures.
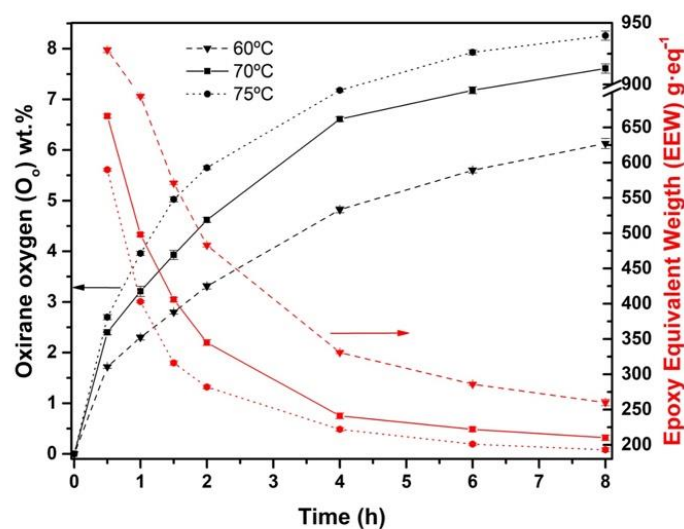
Figure 5. Effect on oxirane oxygen (*O_o*) of the temperature (60 °C, 70 °C, and 75 °C) using MR 1.50 during the epoxidation process.

Regarding the selectivity, *S*, gathered in Table 3, it is possible to compare that it decreases substantially as temperature increases. At 70 °C and 75 °C the best O_o have been obtained, as well as the lowest *S*. Thus, *S* decreases as higher is the temperature, which indicates an increase in oxirane cleavage. Although Y_{oo} was 74.8% with these conditions, an interesting wt.% of O_o or *EEW* have obtained if they are compared to other reports. Dinda et al. [44] used the same epoxidation method with cottonseed oil, reaching 4.96 wt.% for O_o with 80% for Y_{oo}. Furthermore, Mungroo et al. [5] studied the epoxidation of Canola oil using ion exchange resin as the catalyst, where 6.13 wt.% for O_o and 90% for Y_{oo} could be obtained. With the current values obtained with ECSO (8.26 wt.% for O_o or *EEW* 193 g·eq^{-1}), it is possible to forecast that it could be an excellent EVO as an alternative to the commercially available VO. A comparative example is found in the study carried out by Samper et al. [62], where epoxidized soybean oil with *EWW* of 238 g·eq^{-1}, is used to manufacture a composite laminate with engineering applications. In addition, another example is reported by Fombuena et al. [63], where green composites are manufactured using commercial epoxidized linseed oil with 8 wt.% as epoxy matrix. Therefore, the present ECSO contains equal or even higher wt.% of O_o or lower *EEW* than the most commercially available EVOs.

3.4. FTIR Analysis

As an alternative to evaluating the characterization of the epoxidation reaction through titration, FTIR spectroscopy is shown as an efficient tool for determining the representative peaks. Figure 6 shows the spectrum of untreated CSO, taken as reference. The characteristic peaks of double bonds are associated with 3010 cm^{-1} (=CH$_{(v)}$) due to stretching of cis-olefinic bonds, 1652 cm^{-1} (C=C$_{(v)}$) caused by stretching of disubstituted cis-olefins, and 723 cm^{-1} (C=C$_{(cis-\delta)}$) due to the combination of out-of-plane deformation and rocking vibration in cis-disubstituted olefins. Other characteristics peaks associated to methyl and methylene groups are obtained from 2961 to 2851 cm^{-1} (-CH$_{3(asym-v)}$ and -CH$_{2(sym \text{ and } asym-v)}$) and from 1462 to 1375 cm^{-1} (-CH$_{2(asym-\delta)}$ and –CH$_{3(sym-\delta)}$). Finally, the peak at 1743 cm^{-1} represents a carbonyl stretching (C=O$_{(v)}$) of ester groups, and also the peak obtained at 821 cm^{-1} (C-O-C$_{(v)}$) should be noted, barely visible in the untreated CSO but indicative of oxirane oxygen. Compared to the characteristic peaks of untreated CSO described in the literature, such as Timilsena et al. [64], a slight difference is shown due to the origin of seed and climate conditions, which can influence the fatty acid composition.
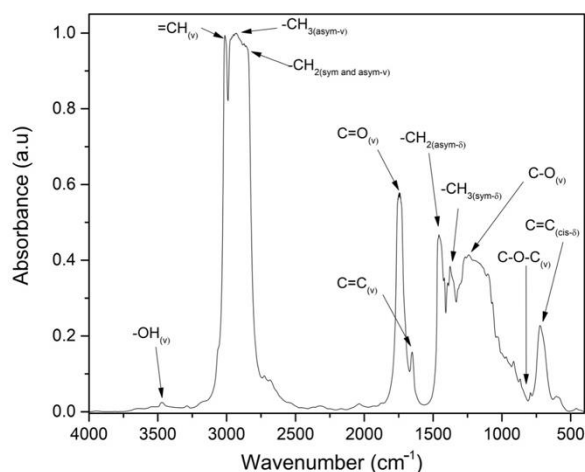
Figure 6. FTIR spectrum of CSO.

The monitoring of the epoxidation reaction by FTIR spectroscopy at different MR and temperatures has been focused on the characteristic peaks corresponding to double bonds (Figure 7) and the plot evolution of the oxirane oxygen content (O_o) (Figure 8). All spectra are obtained after 8 h of epoxidation reaction time. Figure 7a represents the

plot evolution of the peak at 3010 cm^{-1} (=CH$_{(v)}$). It is possible to observe that the peak decreases drastically using MR 1.50 at 75 °C, which is in concordance with the analysis done by titration. This indicates the low quantity of available doubles bonds after the epoxidation reaction. Figure 7b,c show the graphical evolution of the peaks at 1652 (C=C$_{(v)}$) and 723 cm^{-1} (C=C$_{(cis-\delta)}$), respectively, with the same trend mentioned previously. In general, the characteristic peaks of double bonds decrease when MR increase from 0.75 to 1.50 and the temperature reaches 75 °C, obtaining fewer available double bonds.
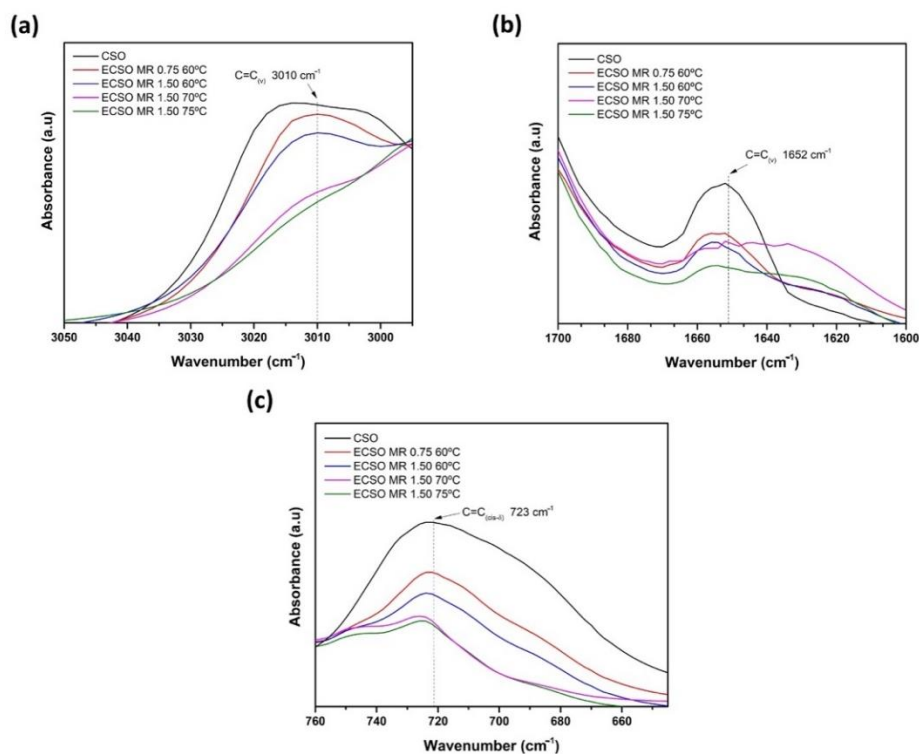
Figure 7. FTIR spectra of ECSO obtained with different epoxidation conditions by the analysis of characteristic peaks of the double bonds (**a**) 3010 cm^{-1} (=CH$_{(v)}$), (**b**) 1652 cm^{-1} (C=C$_{(v)}$) and (**c**) 723 cm^{-1} (C=C$_{(cis-\delta)}$).
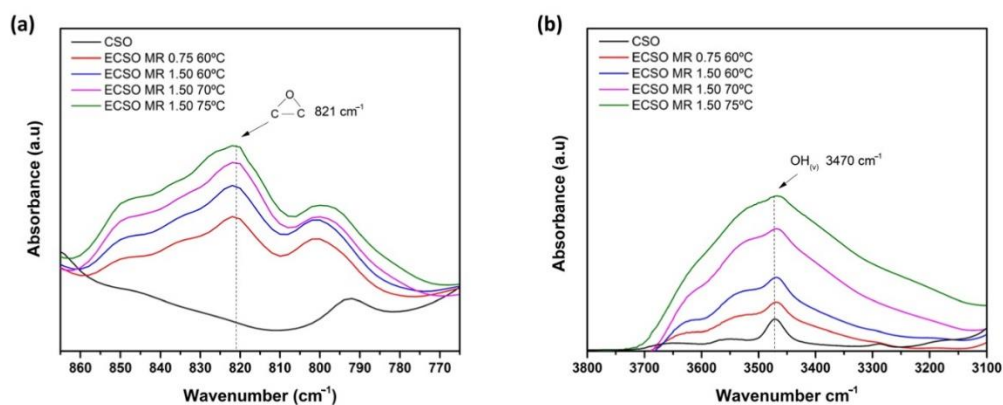
Figure 8. FTIR spectra of ECSO obtained with different epoxidation conditions by the analysis of characteristics peaks of (**a**) oxirane oxygen, and (**b**) hydroxyl groups.

On the other hand, the increase of MR from 0.75 to 1.50, leads to a higher intensity of the oxirane oxygen group peak, (C-O-C$_{(v)}$), located at 821 cm^{-1}, following the same trend as the titration method as it is observed in Figure 8a. This new molecular group, not detectable in CSO, increases due to the insertion of oxygen into the double bonds through peracetic acid formed by the epoxidation reaction process. In parallel form, in Figure 8b,

the same trend for the hydroxyl group (-OH$_{(v)}$) can be observed at 3470 cm^{-1}. In this case, greater MR accelerates the presence of hydroxyl groups by oxirane ring decomposition in the ECSO structure, as has been reported by Goud et al. [65]. The main reason is that the great amount of hydrogen peroxide employed contributes to the epoxy group formation, whereas another quantity is led to opening the oxirane ring obtaining hydroxyl groups [45].

With regard to the temperature effect, the temperature at 75 °C increases the intensity of the peaks corresponding to the hydroxyl group, compared with the MR effect. It indicates that the opening of the oxirane ring is more pronounced at higher temperatures than the MR ranges studied. This behavior has also been reported by Dinda et al. [44] during cottonseed epoxidation, where the highest content of hydroxyl groups was obtained at 75 °C. In addition, this effect is increased with VOs with higher initial IV, which contributes to obtaining a greater epoxy conversion as well as hydroxyl groups formation in a simultaneous process [66].

3.5. ^{1}H NMR Analysis

^{1}H NMR spectra were obtained to confirm the change of functional groups in ECSO synthesized with the best conditions in the epoxidation process, i.e., MR 1.50 at 75 °C. In Figure 9 the ^{1}H NMR spectra of CSO and ECSO are plotted, showing a signal intensity (A) at 5.3–5.5 ppm for CSO. This characteristic peak corresponds to vinyl hydrogens from double bonds, which almost disappeared for the ECSO sample due to the conversion of *IV*. This peak was split into two signals: on the one hand, a small signal of vinyl hydrogen from double bonds located at 5.6 ppm, indicating that few double bonds remain after epoxidation reaction as was corroborated by *IV* and FTIR; on the other hand, a signal at 5.3 ppm for the central hydrogen of the glyceride moiety [67]. In addition, two more signals were observed at 2.02 ppm (C), associated with hydrogen adjacent to double bonds, and at 2.8 ppm (B), corresponding to allyl hydrogen between double bonds. After the epoxidation process, the peak at 2.8 ppm disappeared completely to show a displacement to 1.5 ppm (F) assigned to methylene hydrogens adjacent to oxirane groups in ECSO. The newly formed group was also registered in two new peaks between 2.85–3.00 (E) and 3.00–3.25 ppm (D) in ECSO. The first one corresponds to methylene hydrogens between two oxirane oxygen groups, whereas the second is related to hydrogens of the carbons of the new oxirane oxygen group. The evidence of hydroxyl groups formed by the opening of the oxirane ring was observed in the 4–3.4 ppm region as was described by M. Farias et al. [68], who evaluated the epoxidation of soybean oil using a homogeneous catalyst such as molybdenum (IV) complex. In that study a lower conversion to oxirane oxygen and selectivity at 80 °C was reported compared to this paper. The ^{1}H NMR spectra obtained were consistent with the previous analysis, confirming the formation of oxirane oxygen in double bonds of the ECSO sample as well as hydroxyl groups as a result of side-reactions.

3.6. Physico-Chemical Properties

Physico-chemical properties such as specific gravity, dynamic viscosity, and colorimetric coordinates have been measured before and after the epoxidation reaction process of the CSO at different MR and temperatures. These parameters can be taken as a quick and easy methodology to monitor the epoxidation process. Results obtained after 8 h of reaction time are gathered in Table 4. With respect to specific gravity, low values in VO could be associated with the presence of cis double bonds present in FA structure, which difficult the packaging of the molecular chains [69]. The specific gravity value obtained in CSO, 0.9285, is in concordance with previous studies performed by Uzunova et al. [70] with values reported of 0.9288. As the epoxidation reaction advances and greater MR and temperatures are employed to improve the reaction yield, the insertion of oxirane oxygen in the FA structural chain increases the specific gravity of ECSO. Values reach up to 1.026, which is 10.5% higher than untreated CSO. The epoxy groups contribute to increase molecular mass without significant change in its volume due to the variation from sp^2 hybridization of double bond (C=C) to sp^3 hybridization of a single bond. This change improved chain

packing, even though the stress on the chains was increased by the insertion of epoxy groups [69].
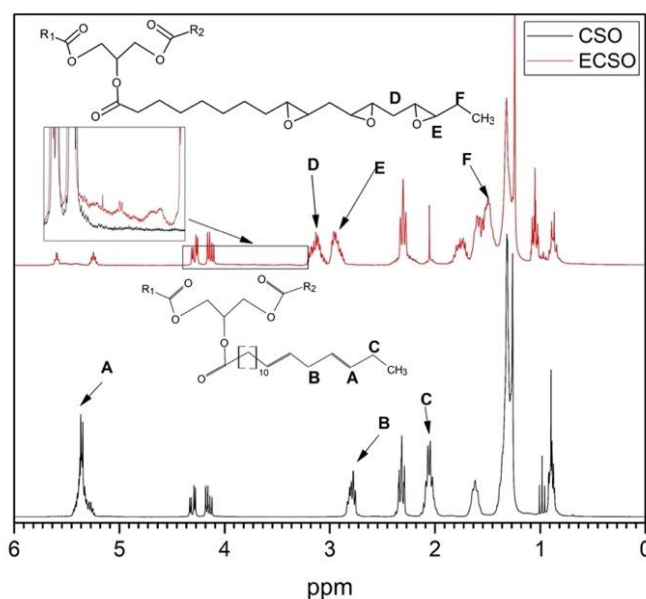
Figure 9. Comparison of CSO and ECSO by ^{1}H NMR spectra.

Table 4. Comparative of physico-chemical properties of chia seed oil (CSO) and epoxidized chia seed oil (ECSO).

Sample	Specific Gravity (ρ_r)	Dynamic Viscosity (mPa·s)	Colourimetric Coordinates			Colour Variation (ΔE)
			L*	a*	b*	
CSO	$0.9285 \pm 2.2 \cdot 10^{-3}$	32 ± 0.45	75.4 ± 0.21	-6.27 ± 0.30	31.5 ± 0.35	0
ECSO MR 0.75 60 °C	$0.9745 \pm 1.2 \cdot 10^{-3}$	109 ± 0.78	77.1 ± 0.28	6.73 ± 0.21	18.6 ± 0.21	18.4 ± 0.25
ECSO MR 1.50 60 °C	$0.9901 \pm 2.3 \cdot 10^{-3}$	163 ± 0.73	76.5 ± 0.23	2.91 ± 0.17	13.8 ± 0.49	19.9 ± 0.19
ECSO MR 1.50 70 °C	$1.0175 \pm 1.7 \cdot 10^{-3}$	420 ± 0.87	76.4 ± 0.28	-3.69 ± 0.35	4.47 ± 0.16	27.1 ± 0.44
ECSO MR 1.50 75 °C	$1.0260 \pm 2.9 \cdot 10^{-3}$	558 ± 1.02	79.6 ± 0.42	-2.85 ± 0.36	4.50 ± 0.21	27.5 ± 0.42

Regarding the dynamic viscosity of untreated CSO, it depends on the presence of unsaturations in the FA molecular chains. The presence of carbon-carbon double bonds kinks the fatty acid chains, increasing the average distance between them [71]. Therefore, an oil such as untreated CSO with high proportions of linolenic acid, i.e., a high amount of double bonds, results in lower dynamic viscosity compared to more saturated vegetable oils with an average value of 32 mPa·s. In epoxidized samples, dynamic viscosity is substantially higher as the performance of the epoxidation reaction progresses, reaching values of 558 mPa·s. These higher dynamic viscosities are ascribed to the increase of molecular weight and polarity in the structure compared to CSO, thus becoming stronger the interaction between molecules [72]. In addition, this property could also be increased, especially at high temperatures, due to the opening of the oxirane ring to form hydroxyl, ketone, and carboxylic groups that increase the intermolecular bonding and, consequently, increase the viscosity [73].

Finally, the variation of the color as a consequence of the epoxidation process can be observed in Figure 10. The untreated CSO is characterized by a yellow color, attributed to the high value of b* and L* (31.5 and 75.4 respectively), which are in concordance with values reported by Timilsena et al. [57]. As the yield of the reaction progresses by increasing the MR and the temperature, the greater presence of epoxy groups and lower *IV* in ECSO leads to decrease the yellow color, as it is possible to quantify by analyzing the b* parameter (decrease from 31.5 in CSO to 4.50 in ECSO). Regarding a*, a slightly reddish color (a* > 0) was observed in epoxidized samples with lesser epoxy groups (<6.3 wt.%) and

higher *IV* (>80 g I$_2$/100 g of oil) such as MR 0.75 and 1.50 at 60 °C. As the epoxidation yield increases, a* decreases from 6.73 for ECSO MR 0.75 at 60 °C up to negative values such as −3.69 and −2.85 for MR 1.50 at 70 °C and 75 °C, respectively, characterized by a lightly green color. Alarcon et al. [74] reported pale-yellow color in both epoxidized Baru and Macaw vegetable oils with epoxy content of 5.98 wt.% and 5.39 wt.%, respectively, but with low *IV* content (<15 g I$_2$/100 g of oil) regardless the initial color of virgin oil. Therefore, the change of color observed from yellow (CSO) to reddish or to pale-yellow of different epoxidized samples can be attributed to the final *IV* change, regardless of the epoxy content of the epoxidized sample. Besides, the brightness (L*) of ECSO slightly increases after each epoxidation process, where the highest value was obtained for MR 1.50 at 75 °C. The noticeable color change can be quantified by analysing the color change (ΔE). Aguero et al. [75] reported that a value greater than 5 implies a change visible to the naked eye. In this case, an increase of noticeable color change has been observed for all epoxidation conditions (Δ*E* > 5) compared to CSO, where no significant changes were observed between 70 °C and 75 °C.
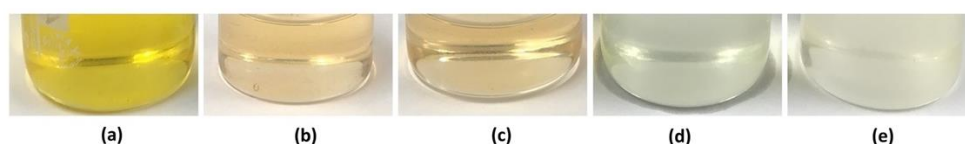
Figure 10. Influence of the MR and temperature on the color during the epoxidation process of the chia seed oil (CSO). (**a**) Untreated chia seed oil (CSO), (**b**) ECSO MR 0.75 at 60 °C, (**c**) ECSO MR 1.50 at 60 °C, (**d**) ECSO MR 1.50:1 at 70 °C and (**e**) ECSO MR 1.50 at 75 °C.

4. Conclusions

This research work assesses the development of a novel EVO obtained from chia seed oil (CSO). Previously to the epoxidation process, the fatty acid profile of CSO analyzed by GC showed polyunsaturated fatty acids (PUFAs) up to 84.9%, highlighting a proportion of α-Linolenic acid higher than 68.6%. These results make CSO an excellent candidate to be an alternative to the current commercial epoxidized oils. Variables such as MR and temperature have been studied in the epoxidation process. Results obtained with a MR 1.50 provide more *O$_o$* caused by more peracetic acid formed that contributes to epoxy group formation. In a second step, the effect of the temperature was evaluated at 60, 70, and 75 °C. Epoxidation reaction at 75 °C provided the highest *O$_o$* (8.26 wt.%) and lowest *EEW* (193 g·eq^{-1}) with conversion to oxirane of 74.8%, and the reduction of the iodine value from 197 g I$_2$/100 g oil up to 13.1 g I$_2$/100 g oil, with a conversion for double bonds of 93.4%. Although the conversion to oxirane is less than 90%, *O$_o$* obtained is similar to or even higher than available commercial epoxidized vegetable oils. The use of higher ratios of reactants and temperatures has not been carried out due to the problems provided by side-reactions as the oxirane ring cleavage, which reduces the efficiency of the process. The main functional groups formed by the epoxidation process have been confirmed by FTIR and ^{1}H NMR spectroscopy, where both were in concordance with tendencies observed in the titration method. The influence of the epoxidation process in physico-chemical parameters such as specific gravity, dynamic viscosity, and color measurement has been reported, demonstrating that these parameters, as well as FTIR studies, can be used for rapid monitoring of the reaction. Results indicate that the epoxidation process implied a substantial increase in specific gravity and dynamic viscosity. All epoxidized samples showed an evident color variation (Δ*E* > 5) from yellow (CSO) to light reddish for samples with higher *IV* (>80 g I$_2$/100 g of oil) or to pale-yellow for samples with lower *IV* (<35 g I$_2$/100 g of oil), that can be ascribed to the final *IV* change of epoxidized samples. Therefore, it is possible to conclude that ECSO is a highly potential EVO considered an alternative to the current epoxidized oils on the market, from an environmental point of view, and with high interest to be used in the manufacture of polymers and biopolymers.

Nomenclature

FTIR	Fourier Transform InfraRed spectroscopy	PUFA	polyunsaturated fatty acid
AM_i	atomic mass iodine (126.9 g/mol)	S	selectivity
AM_o	atomic mass oxygen (16 g/mol)	SFA	saturated fatty acid
B	volume HBr for titration of blank (mL)	T	temperature (K)
c	normality thiosulfate (N)	V	volume HBr for titration of sample (mL)
CSO	chia seed oil	V_1	volume thiosulfate for titration blank (mL)
EEW	epoxy equivalent weight (g·eq^{-1})	V_2	volume thiosulfate for titration of sample (mL)
EVO	epoxidized vegetable oil	VO	vegetable oil
ECSO	epoxidized chia seed oil	W	amount of sample for epoxy content (g)
FA	fatty acids	W_e	weight of empty pycnometer (g)
FAME	fatty acids methyl esters	W_s	weight of the sample in pycnometer (g)
GC	gas chromatography	W_w	weight of water in pycnometer (g)
IV	iodine value	X_{IV}	conversion of iodine value (%)
IV_0	initial iodine value (g I$_2$/100 g oil)	Y_{OO}	oxirane oxygen yield (%)
IV_f	final iodine value (g I$_2$/100 g oil)		
m	amount of sample in iodine value (g)	Greek letters	
MR	molar ratio H$_2$O$_2$ to double bond	Δa	difference of green to red (a*)
MUFA	monounsaturated fatty acid	Δb	difference of blue to yellow (b*)
N_i	normality of HBr (N)	ΔE	color variation
O_o	oxirane oxygen content (wt.%)	ΔL	difference of luminance (L*)
O_{the}	theorical maximum oxirane oxygen (%)	ρ_r	specific gravity

References

1. Biermann, U.; Bornscheuer, U.; Meier, M.A.R.; Metzger, J.O.; Schäfer, H.J. Oils and Fats as Renewable Raw Materials in Chemistry. *Angew. Chem. Int. Ed.* **2011**, *50*, 3854–3871. [CrossRef] [PubMed]
2. Corma, A.; Iborra, S.; Velty, A. Chemical Routes for the Transformation of Biomass into Chemicals. *Chem. Rev.* **2007**, *107*, 2411–2502. [CrossRef] [PubMed]
3. Bioplastics, E. Bioplastics Market Data. Available online: https://www.european-bioplastics.org/ (accessed on 19 April 2022).
4. Danov, S.M.; Kazantsev, O.A.; Esipovich, A.L.; Belousov, A.S.; Rogozhin, A.E.; Kanakov, E.A. Recent advances in the field of selective epoxidation of vegetable oils and their derivatives: A review and perspective. *Catal. Sci. Technol.* **2017**, *7*, 3659–3675. [CrossRef]
5. Mungroo, R.; Pradhan, N.C.; Goud, V.V.; Dalai, A.K. Epoxidation of Canola Oil with Hydrogen Peroxide Catalyzed by Acidic Ion Exchange Resin. *J. Am. Oil Chem. Soc.* **2008**, *85*, 887–896. [CrossRef]
6. Chieng, B.; Ibrahim, N.; Then, Y.; Loo, Y. Epoxidized Vegetable Oils Plasticized Poly (lactic acid) Biocomposites: Mechanical, Thermal and Morphology Properties. *Molecules* **2014**, *19*, 16024–16038. [CrossRef]
7. Sahoo, S.K.; Khandelwal, V.; Manik, G. Development of toughened bio-based epoxy with epoxidized linseed oil as reactive diluent and cured with bio-renewable crosslinker. *Polym. Adv. Technol.* **2018**, *29*, 565–574. [CrossRef]
8. Tee, Y.B.; Talib, R.A.; Abdan, K.; Chin, N.L.; Kadir Basha, R.; Md Yunos, K.F. Comparative Study of Chemical, Mechanical, Thermal, and Barrier Properties of Poly (Lactic Acid) Plasticized with Epoxidized Soybean Oil and Epoxidized Palm Oil. *Bioresources* **2015**, *11*, 1518–1540. [CrossRef]

9. Xiong, Z.; Yang, Y.; Feng, J.; Zhang, X.; Zhang, C.; Tang, Z.; Zhu, J. Preparation and characterization of poly (lactic acid)/starch composites toughened with epoxidized soybean oil. *Carbohydr. Polym.* **2013**, *92*, 810–816. [CrossRef]

10. Janković, M.R.; Govedarica, O.M.; Sinadinović-Fišer, S.V. The epoxidation of linseed oil with in situ formed peracetic acid: A model with included influence of the oil fatty acid composition. *Ind. Crops Prod.* **2020**, *143*, 111881. [CrossRef]

11. Carbonell-Verdu, A.; Bernardi, L.; Garcia-Garcia, D.; Sanchez-Nacher, L.; Balart, R. Development of environmentally friendly composite matrices from epoxidized cottonseed oil. *Eur. Polym. J.* **2015**, *63*, 1–10. [CrossRef]

12. Derawi, D.; Salimon, J. Optimization on Epoxidation of Palm Olein by Using Performic Acid. *Eur. J. Chem.* **2010**, *7*, 1440–1448. [CrossRef]

13. Garcia-Garcia, D.; Carbonell-Verdu, A.; Arrieta, M.P.; Loppez-Martinez, J.; Samper, M.D. Improvement of PLA film ductility by plasticization with epoxidized karanja oil. *Polym. Degrad. Stab.* **2020**, *179*, 109259. [CrossRef]

14. Sahoo, S.K.; Khandelwal, V.; Manik, G. Development of completely bio-based epoxy networks derived from epoxidized linseed and castor oil cured with citric acid. *Polym. Adv. Technol.* **2018**, *29*, 2080–2090. [CrossRef]

15. Vianello, C.; Piccolo, D.; Lorenzetti, A.; Salzano, E.; Maschio, G. Study of Soybean Oil Epoxidation: Effects of Sulfuric Acid and the Mixing Program. *Ind. Eng. Chem. Res.* **2018**, *57*, 11517–11525. [CrossRef]

16. Zheng, J.L.; Wärnå, J.; Salmi, T.; Burel, F.; Taouk, B.; Leveneur, S. Kinetic modeling strategy for an exothermic multiphase reactor system: Application to vegetable oils epoxidation using P rileschajew method. *AIChE J.* **2016**, *62*, 726–741. [CrossRef]

17. Cai, X.; Ait Aissa, K.; Estel, L.; Leveneur, S. Investigation of the physicochemical properties for vegetable oils and their epoxidized and carbonated derivatives. *J. Chem. Eng. Data* **2018**, *63*, 1524–1533. [CrossRef]

18. Shuttleworth, P.S.; Díez-Pascual, A.M.; Marco, C.; Ellis, G. Flexible bionanocomposites from epoxidized hemp seed oil thermosetting resin reinforced with halloysite nanotubes. *J. Phys. Chem. B* **2017**, *121*, 2454–2467. [CrossRef]

19. Chia Seeds Market Size Worth \$4.7 Billion by 2025. Available online: https://www.grandviewresearch.com/press-release/global-chia-seeds-market (accessed on 15 April 2022).

20. Shen, Y.; Zheng, L.; Jin, J.; Li, X.; Fu, J.; Wang, M.; Guan, Y.; Song, X. Phytochemical and biological characteristics of mexican chia seed oil. *Molecules* **2018**, *23*, 3219. [CrossRef]

21. Ullah, R.; Nadeem, M.; Imran, M.; Taj Khan, I.; Shahbaz, M.; Mahmud, A.; Tayyab, M. Omega fatty acids, phenolic compounds, and lipolysis of cheddar cheese supplemented with chia (*Salvia hispanica* L.) oil. *J. Food Process. Preserv.* **2018**, *42*, e13566. [CrossRef]

22. Nadeem, M.; Imran, M.; Taj, I.; Ajmal, M.; Junaid, M. Omega-3 fatty acids, phenolic compounds and antioxidant characteristics of chia oil supplemented margarine. *Lipids Health Dis.* **2017**, *16*, 1–12. [CrossRef]

23. Dominguez-Candela, I.; Ferri, J.M.; Cardona, S.C.; Lora, J.; Fombuena, V. Dual plasticizer/thermal stabilizer effect of epoxidized chia seed oil (*Salvia hispanica* L.) to improve ductility and thermal properties of poly (lactic acid). *Polymers* **2021**, *13*, 1283. [CrossRef]

24. Warwel, S. Complete and partial epoxidation of plant oils by lipase-catalyzed perhydrolysis. *Ind. Crops Prod.* **1999**, *9*, 125–132.

25. Biermann, U.; Friedt, W.; Lang, S.; Lühs, W.; Machmüller, G.; Metzger, J.O.; Rüsch gen. Klaas, M.; Schäfer, H.J.; Schneider, M.P. New syntheses with oils and fats as renewable raw materials for the chemical industry. *Angew. Chem. Int. Ed.* **2000**, *39*, 2206–2224. [CrossRef]

26. Wallace, J.C. *Encyclopedia of Chemical Technology*, 3rd ed.; John Wiley and Sons: New York, NY, USA, 1978; Volume 9.

27. de Quadros, J.V.; Giudici, R. Epoxidation of soybean oil at maximum heat removal and single addition of all reactants. *Chem. Eng. Process. Process Intensif.* **2016**, *100*, 87–93. [CrossRef]

28. Okieimen, F.E.; Bakare, O.I.; Okieimen, C.O. Studies on the epoxidation of rubber seed oil. *Ind. Crops Prod.* **2002**, *15*, 139–144. [CrossRef]

29. Otabor, G.O.; Ifijen, I.H.; Mohammed, F.U.; Aigbodion, A.I.; Ikhuoria, E.U. Alkyd resin from rubber seed oil/linseed oil blend: A comparative study of the physiochemical properties. *Heliyon* **2019**, *5*, e01621. [CrossRef]

30. Benaniba, M.; Belhaneche-Bensemra, N.; Gelbard, G. Epoxidation of sunflower oil with peroxoacetic acid in presence of ion exchange resin by various processes. *Energ. Educ. Sci. Technol.* **2008**, *21*, 71.

31. Huang, Y.B.; Yao, M.Y.; Xin, P.P.; Zhou, M.C.; Yang, T.; Pan, H. Influence of alkenyl structures on the epoxidation of unsaturated fatty acid methyl esters and vegetable oils. *RSC Adv.* **2015**, *5*, 74783–74789, (restar uno a todo a partir de aquí). [CrossRef]

32. Sun, S.; Yang, G.; Bi, Y.; Liang, H. Enzymatic epoxidation of corn oil by perstearic acid. *J. Am. Oil Chem. Soc.* **2011**, *88*, 1567–1571. [CrossRef]

33. Sienel, G.; Rieth, R.; Rowbottom, K.T. Epoxides. In *Ullmann's Encyclopedia of Industrial Chemistry*, 6th ed.; Wiley & Sons: Hoboken, NJ, USA, 2003; Volume 12, pp. 269–284.

34. Yadav, G.; Satoskar, D. Kinetics of epoxidation of alkyl esters of undecylenic acid: Comparison of traditional routes vs. Ishii-Venturello chemistry. *J. Am. Oil Chem. Soc.* **1997**, *74*, 397–407. [CrossRef]

35. Leveneur, S. Thermal safety assessment through the concept of structure–reactivity: Application to vegetable oil valorization. *Org. Process Res. Dev.* **2017**, *21*, 543–550. [CrossRef]

36. Moreno, V.C.; Russo, V.; Tesser, R.; Di Serio, M.; Salzano, E. Thermal risk in semi-batch reactors: The epoxidation of soybean oil. *Process Saf. Environ. Prot.* **2017**, *109*, 529–537. [CrossRef]

37. Tan, S.; Chow, W. Biobased epoxidized vegetable oils and its greener epoxy blends: A review. *Polym.-Plast. Technol. Eng.* **2010**, *49*, 1581–1590. [CrossRef]

38. Cai, X.; Zheng, J.L.; Aguilera, A.F.; Vernières–Hassimi, L.; Tolvanen, P.; Salmi, T.; Leveneur, S. Influence of ring-opening reactions on the kinetics of cottonseed oil epoxidation. *Int. J. Chem. Kinet.* **2018**, *50*, 726–741. [CrossRef]

39. Jadhav, P.D.; Patwardhan, A.V.; Kulkarni, R.D. Kinetic study of in situ epoxidation of mustard oil. *Mol. Catal.* **2021**, *511*, 111748. [CrossRef]

40. Sienkiewicz, A.M.; Czub, P. The unique activity of catalyst in the epoxidation of soybean oil and following reaction of epoxidized product with bisphenol A. *Ind. Crops Prod.* **2016**, *83*, 755–773. [CrossRef]

41. Di Serio, M.; Russo, V.; Santacesaria, E.; Tesser, R.; Turco, R.; Vitiello, R. Liquid–liquid–solid model for the epoxidation of soybean oil catalyzed by Amberlyst-16. *Ind. Eng. Chem. Res.* **2017**, *56*, 12963–12971. [CrossRef]

42. Wai, P.T.; Jiang, P.; Shen, Y.; Zhang, P.; Gu, Q.; Leng, Y. Catalytic developments in the epoxidation of vegetable oils and the analysis methods of epoxidized products. *RSC Adv.* **2019**, *9*, 38119–38136. [CrossRef]

43. Goud, V.V.; Patwardhan, A.V.; Pradhan, N.C. Studies on the epoxidation of mahua oil (Madhumica indica) by hydrogen peroxide. *Bioresour. Technol.* **2006**, *97*, 1365–1371. [CrossRef]

44. Dinda, S.; Patwardhan, A.V.; Goud, V.V.; Pradhan, N.C. Epoxidation of cottonseed oil by aqueous hydrogen peroxide catalysed by liquid inorganic acids. *Bioresour. Technol.* **2008**, *99*, 3737–3744. [CrossRef]

45. Omonov, T.S.; Kharraz, E.; Curtis, J.M. The epoxidation of canola oil and its derivatives. *RSC Adv.* **2016**, *6*, 92874–92886. [CrossRef]

46. Cai, C.; Dai, H.; Chen, R.; Su, C.; Xu, X.; Zhang, S.; Yang, L. Studies on the kinetics of in situ epoxidation of vegetable oils. *Eur. J. Lipid Sci. Technol.* **2008**, *110*, 341–346. [CrossRef]

47. Pérez, J.E.; Haagenson, D.; Pryor, S.; Ulven, C.; Wiesenborn, D. Production and characterization of epoxidized canola oil. *Trans. ASABE* **2009**, *52*, 1289–1297. [CrossRef]

48. Garea, S.-A.; Corbu, A.-C.; Deleanu, C.; Iovu, H. Determination of the epoxide equivalent weight (EEW) of epoxy resins with different chemical structure and functionality using GPC and 1H-NMR. *Polym. Test.* **2006**, *25*, 107–113. [CrossRef]

49. Durbetaki, A.J. Direct Titration of Oxirane Oxygen with Hydrogen Bromide in Acetic Acid. *Anal. Chem.* **1956**, *28*, 2000–2001. [CrossRef]

50. Kasote, D.M.; Badhe, Y.S.; Hegde, M.V. Effect of mechanical press oil extraction processing on quality of linseed oil. *Ind. Crops Prod.* **2013**, *42*, 10–13. [CrossRef]

51. Ixtaina, V.Y.; Martinez, M.L.; Spotorno, V.; Mateo, C.M.; Maestri, D.n.M.; Diehl, B.W.K.; Nolasco, S.M.; Tomas, M.C. Characterization of chia seed oils obtained by pressing and solvent extraction. *J. Food Compos. Anal.* **2011**, *24*, 166–174. [CrossRef]

52. La Scala, J.; Wool, R.P. Effect of FA composition on epoxidation kinetics of TAG. *J. Am. Oil Chem. Soc.* **2002**, *79*, 373–378. [CrossRef]

53. Demin, M.; Rabrenovic, B.; Pezo, L.; Lalicic-Petronijevic, J. Influence of chia seeds (*Salvia hispanica* L.) and extra virgin olive oil addition on nutritional properties of salty crackers. *J. Food Meas. Charact.* **2020**, *14*, 378–387. [CrossRef]

54. Ayerza, R. Oil content and fatty acid composition of chia (*Salvia hispanica* L.) from five northwestern locations in Argentina. *J. Am. Oil Chem. Soc.* **1995**, *72*, 1079–1081. [CrossRef]

55. Kulczyński, B.; Kobus-Cisowska, J.; Taczanowski, M.; Kmiecik, D.; Gramza-Michalowska, A. The Chemical Composition and Nutritional Value of Chia Seeds-Current State of Knowledge. *Nutrients* **2019**, *11*, 1242. [CrossRef]

56. Imran, M.; Nadeem, M.; Manzoor, M.F.; Javed, A.; Ali, Z.; Akhtar, M.N.; Ali, M.; Hussain, Y. Fatty acids characterization, oxidative perspectives and consumer acceptability of oil extracted from pre-treated chia (*Salvia hispanica* L.) seeds. *Lipids Health Dis.* **2016**, *15*, 162. [CrossRef] [PubMed]

57. Timilsena, Y.P.; Vongsvivut, J.; Adhikari, R.; Adhikari, B. Physicochemical and thermal characteristics of Australian chia seed oil. *Food Chem.* **2017**, *228*, 394–402. [CrossRef]

58. Campanella, A.; Baltanás, M.A.; Capel-Sanchez, M.; Campos-Martin, J.; Fierro, J. Soybean oil epoxidation with hydrogen peroxide using an amorphous Ti/SiO$_2$ catalyst. *Green Chem.* **2004**, *6*, 330–334. [CrossRef]

59. Santacesaria, E.; Russo, V.; Tesser, R.; Turco, R.; Di Serio, M. Kinetics of performic acid synthesis and decomposition. *Ind. Eng. Chem. Res.* **2017**, *56*, 12940–12952, ((restar uno a partir de aquí). [CrossRef]

60. Campanella, A.; Baltanás, M.A. Degradation of the oxirane ring of epoxidized vegetable oils in liquid–liquid heterogeneous reaction systems. *Chem. Eng. J.* **2006**, *118*, 141–152. [CrossRef]

61. Gan, L.; Goh, S.; Ooi, K. Kinetic studies of epoxidation and oxirane cleavage of palm olein methyl esters. *J. Am. Oil Chem. Soc.* **1992**, *69*, 347–351. [CrossRef]

62. Samper, M.D.; Petrucci, R.; Sanchez-Nacher, L.; Balart, R.; Kenny, J.M. Properties of composite laminates based on basalt fibers with epoxidized vegetable oils. *Mater. Eng.* **2015**, *72*, 9–15. [CrossRef]

63. Fombuena, V.; Petrucci, R.; Dominici, F.; Jordá-Vilaplana, A.; Montanes, N.; Torre, L. Maleinized Linseed Oil as Epoxy Resin Hardener for Composites with High Bio Content Obtained from Linen Byproducts. *Polymers* **2019**, *11*, 301. [CrossRef]

64. Timilsena, Y.P.; Vongsvivut, J.; Tobin, M.J.; Adhikari, R.; Barrow, C.; Adhikari, B. Investigation of oil distribution in spray-dried chia seed oil microcapsules using synchrotron-FTIR microspectroscopy. *Food Chem.* **2019**, *275*, 457–466. [CrossRef]

65. Goud, V.V.; Dinda, S.; Patwardhan, A.V.; Pradhan, N.C. Epoxidation of Jatropha (*Jatropha curcas*) oil by peroxyacids. *Asia Pac. J. Chem. Eng.* **2010**, *5*, 346–354. [CrossRef]

66. Kim, J.R.; Sharma, S. The development and comparison of bio-thermoset plastics from epoxidized plant oils. *Ind. Crops Prod.* **2012**, *36*, 485–499. [CrossRef]

67. DeHonor-Marquez, E.; Nieto Alarcón, J.F.; Vigueras Santiago, E.; Hernández López, S. Effective and Fast Epoxidation Reaction of Linseed Oil Using 50 wt% Hydrogen Peroxyde. *Am. J. Chem.* **2018**, *8*, 99–106.

68. Farias, M.; Martinelli, M.; Bottega, D.P. Epoxidation of soybean oil using a homogeneous catalytic system based on a molybdenum (VI) complex. *Appl. Catal. A Gen.* **2010**, *384*, 213–219. [CrossRef]

69. Harry-O'kuru, R.E.; Biresaw, G.; Tisserat, B.; Evangelista, R. Synthesis of Polyformate Esters of Vegetable Oils: Milkweed, Pennycress, and Soy. *J. Lipids* **2016**, *2016*, 3128604. [CrossRef]

70. Uzunova, G.; Nikolova, K.; Perifanova, M.; Gentscheva, G.; Marudova, M.; Antova, G. Physicochemical characterization of chia (*Salvia hispanica*) seed oil from Argentina. *Bulg. Chem. Commun.* **2016**, *48*, 131–135.

71. Wool, R.; Sun, X.S. *Bio-Based Polymers and Composites*; Elsevier: Amsterdam, The Netherlands, 2011.

72. Wu, X.; Zhang, X.; Yang, S.; Chen, H.; Wang, D. The study of epoxidized rapeseed oil used as a potential biodegradable lubricant. *J. Am. Oil Chem. Soc.* **2000**, *77*, 561–563. [CrossRef]

73. Monono, E.M.; Haagenson, D.M.; Wiesenborn, D.P. Characterizing the epoxidation process conditions of canola oil for reactor scale-up. *Ind. Crops Prod.* **2015**, *67*, 364–372. [CrossRef]

74. Alarcon, R.T.; Gaglieri, C.; Lamb, K.J.; North, M.; Bannach, G. Spectroscopic characterization and thermal behavior of baru nut and macaw palm vegetable oils and their epoxidized derivatives. *Ind. Crops Prod.* **2020**, *154*, 112585. [CrossRef]

75. Agüero, A.; Morcillo, M.d.C.; Quiles-Carrillo, L.; Balart, R.; Boronat, T.; Lascano, D.; Torres-Giner, S.; Fenollar, O. Study of the Influence of the Reprocessing Cycles on the Final Properties of Polylactide Pieces Obtained by Injection Molding. *Polymers* **2019**, *11*, 1908. [CrossRef]

Article

The Influence of Abrasive and Acidic Aggressions on the Surface Condition of Flowable Composite Resin

Ionuț Tărăboanță [1], **Simona Stoleriu** [1,*], **Silviu Gurlui** [2], **Irina Nica** [1], **Andra Claudia Tărăboanță-Gamen** [1,*], **Alexandru Iovan** [1] and **Sorin Andrian** [1]

[1] Faculty of Dental Medicine, Grigore T. Popa University of Medicine and Pharmacy, 16 Universitatii Str., 700115 Iași, Romania; ionut-taraboanta@umfiasi.ro (I.T.); irina.nica@umfiasi.ro (I.N.); alexandru.iovan@umfiasi.ro (A.I.); sorin.andrian@umfiasi.ro (S.A.)

[2] Faculty of Physics, Atmosphere, Optics, Spectroscopy and Lasers Laboratory (LOA-SL), Alexandru Ioan Cuza University, 11 Carol I Str., 700506 Iași, Romania; sgurlui@uaic.ro

* Correspondence: simona.stoleriu@umfiasi.ro (S.S.); andra-claudia.gamen@umfiasi.ro (A.C.T.-G.); Tel.: +40-745-106-066 (S.S.); +40-726-270-772 (A.C.T.-G.)

Abstract: The aim of this in vitro study was to evaluate the effect of hydrochloric acid associated with the abrasive effect of toothbrushing on the surface condition of three flowable composite resins used for direct restoration. Seventy samples of each composite resin: Grandio Flow (VOCO, Germany)—group A, Filtek Ultimate Flow (3M-ESPE, MN, USA)—group B, G-aenial Flo X (GC Europe)—group C were prepared, submersed in hydrochloric acid 30% for 60 min and then submitted to simulated toothbrushing procedure using 5000 cycles with toothbrushes with medium and hard bristles, immediately after the chemical attack, after 30 min or without any chemical attack. The sample's surface roughness was analyzed using a noncontact profilometer (Dektak XT, Bruker, USA). ANOVA and post hoc Bonferroni tests, with a $p < 0.05$, were used to analyze the values. Hydrochloric acid action for 60 min and six months of toothbrushing using toothbrushes having medium hardness or firm bristles affects the surface roughness of tested flowable composite resins. Toothbrushing with firm bristles immediately after acidic challenge determines increased surface roughness for two of the three flowable composite resins (Grandio Flow and Filtek Ultimate Flow). Toothbrushing with medium or firm bristles thirty minutes after the acidic aggression determine no effect on surface condition of flowable composite resins.

Keywords: flowable composite resin; hydrochloric acid; surface roughness; toothbrush

1. Introduction

Direct dental restorations should meet two goals: aesthetics and functionality [1]. Therefore, resin-based materials have become the most preferred materials for direct anterior and posterior restorations. Since their introduction on the market until now, these materials have undergone many changes regarding the organic matrix or the type of polymerization, but the changes have mainly focused on their filling technology [2]. The reduction in the volume of inorganic phase of composite resins has led to the appearance of low viscosity or flowable composite resins. Although originally intended as restorative materials for V Black Class cavities, flowable composite resins have been accepted for a variety of applications due to their simple maneuverability and their fluidity, which allow the material to reach difficult cavity areas regarding the access or low modulus of elasticity for a uniform distribution and attenuation of occlusal forces [2,3].

The durability of composite resin restorations in oral cavity depends on different factors such as marginal adaptation or surface wear, which can be influenced by the conditions provided by the oral environment such as the erosion process, for instance [1]. Oral acidity is produced by extrinsic or intrinsic acids such as gastric acid in gastroesophageal reflux disease or acids resulting from the degradation of polysaccharides into acids [1,4].

Therefore, the chemical characteristics of the oral environment can negatively influence the restorative materials condition as a result of dissolution and disintegration process [1,5].

Wear was defined by Jones et al. as a progressive loss of substance from the surface of a body as a result of mechanical action [6]. Just like erosion, wear can cause changes in the surface condition of materials or can compromise marginal adaptation [3]. Although toothbrushing is the most effective method to control bacterial biofilm, its action can cause degradation of dental tissues and restorative materials [3,5]. Previous studies have shown that toothbrushing increases the surface roughness of composite resins resulting in material degradation and impairs clinical performance of the restorations. Composite resins are composed of inorganic fillers and an organic matrix bound together by a coupling agent, and the stress created by the brushing procedure can weaken this bond and degrade the polymer matrix, exposing the filler particles [7]. Along with the percentage of volume and weight of inorganic particles, the wear degree of a composite resin depends on the type of polymeric matrix and the degree of its polymerization [7,8].

A rough surface can negatively influence the optical properties of the material, causing changes in the degree of light absorption and reflection [2], can determine bacterial biofilm accumulation and can increase the risk for secondary caries onset. Bollen et al. concluded that the critical value of surface roughness for bacterial adhesion is 0.2 μm [9]. A smooth surface of the restoration maintains the aesthetic properties, reduces the accumulation of bacterial biofilm and is durable [10]. For these reasons, it is important to evaluate the effect of acid challenging in association with mechanical process of toothbrushing, as this is the most common habit of oral hygiene [5].

The aim of this study was to evaluate the surface roughness of three flowable composite resins after the acid attack of hydrochloric acid followed by brushing immediately after or 30 min after the chemical attack using toothbrushes with different hardness of the bristles.

2. Materials and Methods

The study design is presented in Figure 1. The details regarding the materials used in the study are shown in Table 1.
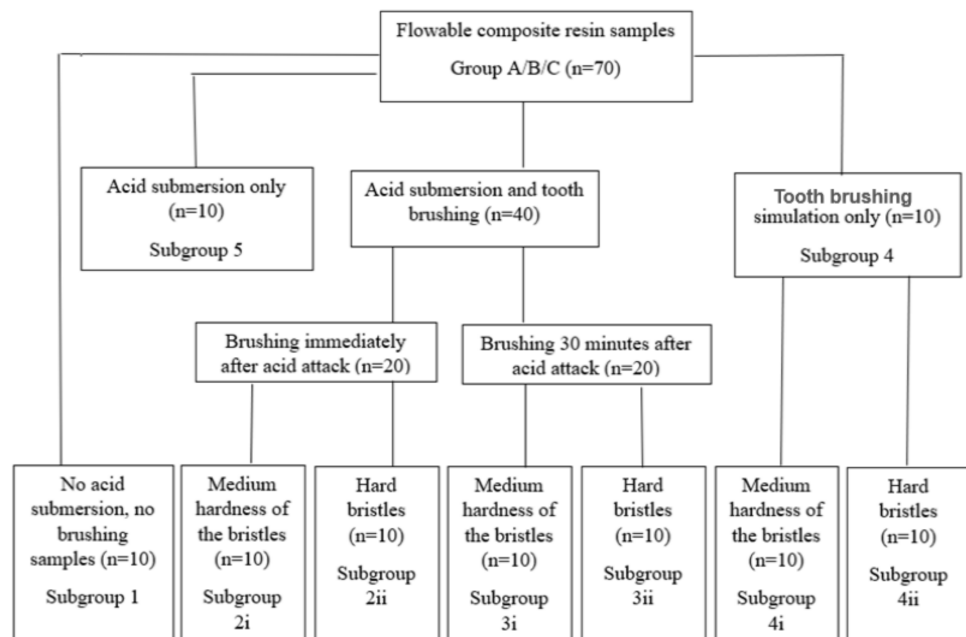

Figure 1. Study design.

Table 1. Detailed presentation of the materials used in the study.

The Name of Flowable Composite Resin	Manufacturer	Batch No.	Composition	Filler wt%/vol%
Grandio Flow	VOCO GmbH, Cuxhaven, Germany	2036127	Bis-GMA, TEGDMA, HEDMA, glass ceramic, nanoparticle	65.6 wt%/ 80 vol%
Filtek Ultimate Flow	3M-ESPE, St. Paul, MN, USA	3930A2	Bis-GMA, UDMA, Bis-EMA, Zirconia/silica, zirconia, silica	78.5 wt%/ 63.3 vol%
G-aenial Flo X	GC Europe	1910162	UDMA, Bis-MEPP, TEGDMA, silicon, dioxide, strontium glass	69 wt%/ 50 vol%

Bis-GMA—Bisphenol A diglycidyl ether methacrylate; Bis-MEPP—Bisphenol 4-methacryloxypolyethoxyphenil propane; Bis-EMA—Bisphenol-A ethoxylated dimethacrylate; TEGDMA—Triethylenglycol dimethacrylate; UDMA—Urethane dimethacrylate; HEMA—Hydroxyethyl methacrylate.

2.1. Sample Preparation

Seventy cylindrical samples of each material were prepared and included in three groups: group A (Grandio Flow, VOCO GmbH, Cuxhaven, Germany), group B (Filtek Ultimate Flow, 3M-ESPE, St. Paul, MN, USA) and group C (G-aenial Flo X, GC Europe, Alcobendas, Spain). The distribution of the samples and the study stages are detailed in Table 2. The samples having 2 mm height and 6 mm diameter were obtained using acrylic molds. The mold was placed on a glass plate, and then it was filled with the restoration material and covered with another glass plate. A transparent matrix was placed between the material and the glass plates in order to create smooth surfaces. A constant pressure was applied to the glass plate for 30 s, using a weight of 500 g, in order to remove the excess material and the air voids. Then the composite resin was light-cured for 40 s through the thickness of the glass plate using a LED light-curing lamp (Woodpecker LED.E, Guilin, Guangxi, China) with a light intensity of 1000 mW/cm^2 and a wavelength range from 420 to 480 nm.

Table 2. Characteristics of the toothbrushes.

Toothbrush Name	Bristle Hardness	Bristle Material	Bristle Length	Bristle Thickness
R.O.C.S. "Professional" Medium	medium	nylon	0.8/1.3	0.18/0.2
R.O.C.S. "Professional" Firm	hard	nylon	Not provided by the producer	Not provided by the producer

2.2. Finishing and Polishing Procedure

After removal from the acrylic molds, all the samples were finished using a Sof-Lex finishing and polishing system (Batch No. NC11342, 3M ESPE, MN, USA). This system is composed of two disposable wheels made of a thermoplastic elastomer impregnated with aluminum oxide particles. The beige spiral wheel is recommended for finishing, smoothing and removing the scratches produced during the restoration stages, while the white wheel is recommended for final polishing. During the finishing and polishing stage, each spiral wheel was used only once for each sample, and the procedure was performed for 1 min per sample (30 s for each wheel). The wheels were activated by a contra-angle handpiece at a speed of 20,000 revolutions per minute, according to the recommendations offered by the manufacturer.

After that, forty samples from each group were subjected to submersion in hydrochloric acid. Ten samples from groups A, B and C were maintained as they resulted after finishing and polishing procedure (subgroup 1) and twenty samples were exposed to a toothbrushing simulation process (subgroups 4i and 4ii).

2.3. Simulation of Acid Attack

A solution of hydrochloric acid with a concentration of 30% and a pH of 2.12 was used to simulate the acid attack produced by gastric acid. The pH value was established with a portable pH meter (Thermo Scientific Eutech pH 5+, Vernon Hills, IL, USA) The submersion of the samples in acid was carried out in a single cycle of 60 min, in an incubator, at a constant temperature of 37 °C. After this stage, the samples were stored in distilled water at 37 °C. Ten samples from each group were not further submitted to toothbrushing simulation process (subgroup 5).

2.4. Brushing Simulation

This stage was performed immediately after acid submersion for twenty samples in each group (subgroups 2i and 2ii) and 30 min after acid submersion for another twenty samples in each group (subgroups 3i and 3ii). A brushing simulation device was used at a frequency of 5000 brushing cycles with an intensity of 100 cycles/minute and a constant load of 200 g. Brushing was performed for a half of the samples in each group using toothbrushes with medium bristle hardness (Toothbrush R.O.C.S. Professional Medium, Tallinn, Estonia) (subgroups 2i, 3i, 4i) and for the other half of the samples using hard bristle hardness (Toothbrush R.O.C.S. Professional Firm, Tallinn, Estonia) (subgroups 2ii, 3ii, 4ii) and a tooth paste slurry obtained by mixing a toothpaste (Sensodyne, GSK, Middlesex, UK) and distilled water in 1:3 ratio. The characteristics of the toothbrushes are presented in Table 2. After performing this step, the samples were rinsed under running water and dried for 2 min using the air spray from the dental unit.

2.5. Profilometry

Surface characteristics of all the samples after finishing and polishing procedure, acid challenge and toothbrushing cycles were evaluated using profilometry. The arithmetic deviation of the evaluated profile values (Pa) were recorded using a noncontact profilometer Dektak XT (Bruker, Tuscon, AZ, USA). For each sample, we reported the mean (Pa) as a result of three determinations. Pa is the arithmetic mean deviation of the primary profile (P).

2.6. Statistical Analysis

The data were stored in a Microsoft Office Excel document. IBM SPSS 26 software was used for statistical analysis of the values between and within the groups and subgroups. Parametric ANOVA and Bonferroni post hoc tests were used at a $p < 0,05$ significance level.

3. Results

Mean surface roughness values (Pa) and standard deviation in groups and subgroups are presented in Figure 2. Aspects of some profilometric measurements of three samples from groups A, B and C in subgroup 2i are presented in Figure 3. There were no statistically significant differences between groups A, B and C in any of the study subgroups (Table 3).

Table 3. Differences between the study subgroups of each study group.

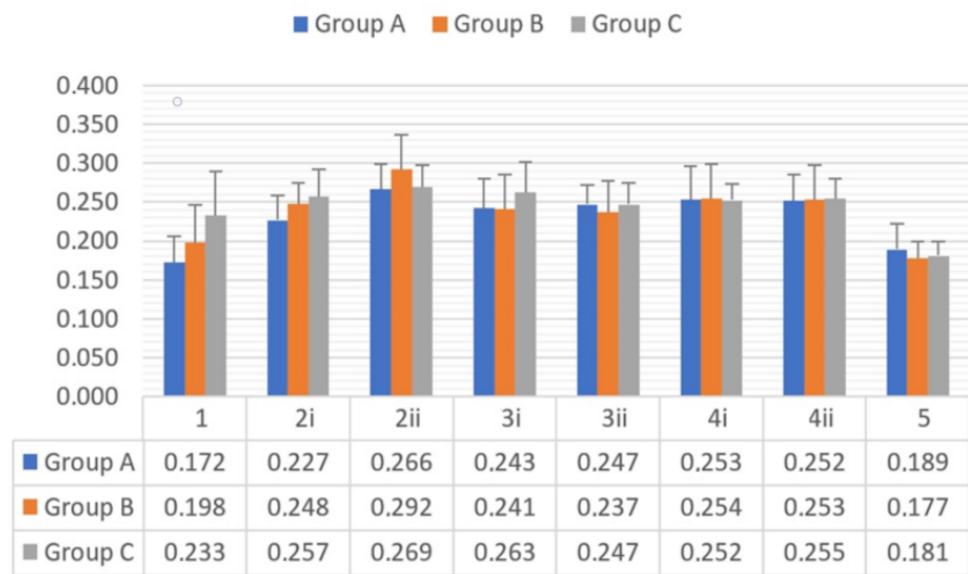| Subgroups	1			2i			2ii			3i			3ii			4i			4ii			5		
Groups	A	B	C	A	B	C	A	B	C	A	B	C	A	B	C	A	B	C	A	B	C	A	B	C
A	-	*	*	-	*	*	-	*	*	-	*	*	-	*	*	-	*	*	-	*	*	-	*	*
B	*	-	*	*	-	*	*	-	*	*	-	*	*	-	*	*	-	*	*	-	*	*	-	*
C	*	*	-	*	*	-	*	*	-	*	*	-	*	*	-	*	*	-	*	*	-	*	*	-

* Statistically not significant ($p < 0.05$).

Figure 2. Mean Pa values and standard deviation of each study subgroup by the end of each stage.
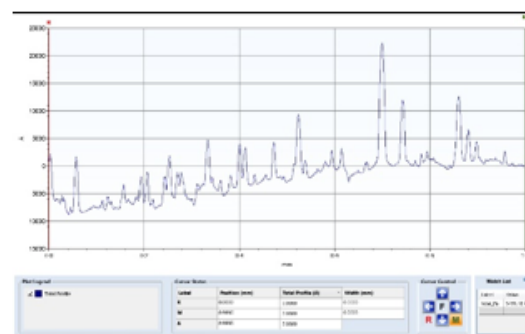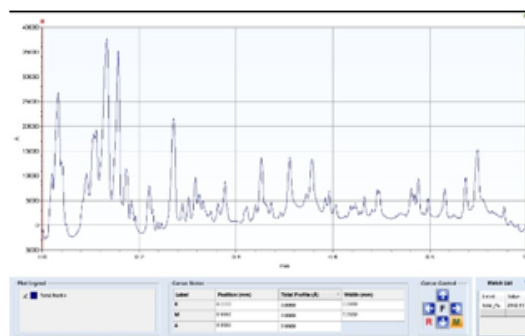

Figure 3. Representative profilometry scan aspect of three samples from groups (**A**–**C**) in subgroup 2ii.

Within the study groups, significant differences were found between the same sub-groups by the end of the stages (Table 4).

Table 4. Differences between the study subgroups in groups A, B and C.

	Group A								Group B								Group C							
	1	2i	2ii	3i	3ii	4i	4ii	5	1	2i	2ii	3i	3ii	4i	4ii	5	1	2i	2ii	3i	3ii	4i	4ii	5
1	-	*	**	*	**	**	**	*	_	*	**	*	*	*	*	*	_	*	*	*	*	*	*	*
2i	*	-	*	*	*	*	*	*	*	_	*	*	*	*	*	*	*	_	*	*	*	*	*	**
2ii	**	*	-	*	*	*	*	**	**	*	_	*	*	*	*	**	*	*	_	*	*	*	*	**
3i	*	*	*	-	*	*	*	*	*	*	*	_	*	*	*	*	*	*	*	_	*	*	*	**
3ii	**	*	*	*	-	*	*	*	*	*	*	*	_	*	*	*	*	*	*	*	_	*	*	*
4i	**	*	*	*	*	-	*	*	*	*	*	*	*	_	*	*	*	*	*	*	*	_	*	*
4ii	**	*	*	*	*		-	*	*	*	*	*	*	_	*	**	*	*	*	*	*	*	_	**
5	*	*	**	*	*	*	*	-	*	*	**	*	*	*	*	_	*	**	**	**	*	*	**	-

** Statistically significant ($p < 0{,}05$); * Not significant.

No significant differences were found between groups A, B and C when comparing the results in each subgroup (Table 3).

Statistical test results regarding the differences between the subgroups in groups A, B and C are presented in Table 4. In group A, significantly higher Pa values were recorded between subgroup 1 and 2ii ($p = 0.003 < 0.05$), between subgroups 1 and 3ii ($p = 0.039$), subgroups 1 and T4i ($p = 0.019$), subgroups 1 and 4ii ($p = 0.021$) and between subgroups 5 and 2ii ($p = 0.033$). In group B, significantly higher Pa values were recorded between subgroups 1 and 2ii ($p = 0.024$) and subgroups 2ii and 5 ($p = 0.002$). In group C, significantly higher differences were recorded between subgroups 5 and 2i ($p = 0.031$), subgroups 5 and 2ii ($p = 0.006$), subgroups 5 and 3i ($p = 0.014$) and subgroups 5 and 4ii ($p = 0.04$).

4. Discussion

The present study investigated the surface roughness of three types of flowable composite resins after exposure to acid attack with hydrochloric acid and after toothbrushing simulation with toothbrushes with bristles of different hardness and toothpaste with a medium abrasive value performed immediately after submersion to acid, 30 min after acid attack or without prior chemical challenge.

The samples were subjected to finishing and polishing procedure using Sof-Lex system, and the results showed that the average surface roughness values were less than 0.2μm for two of the three flowable composite resins used in the study (Grandio Flow and Filtek Ultimate Flow), in accordance with the results of a study conducted by Somacal et al. [5,11]. Yuan et al. noted that bacterial adhesion is also influenced by surface energy, not only by surface roughness [12]. An example of this would be that S mutans have a higher tendency to adhere to substrates with high surface energy, the latter being influenced by the composition of composite resin fillers [5,12,13]. Other studies have shown that composite resins with an organic matrix based on high molecular weight monomers such as Bis-GMA are more resistant and harder to remove by abrasive procedures, exfoliating a smaller number of inorganic particles [14,15].

The wear resistance of composite resins depends on the type of material and is influenced by the particularities of the organic matrix; the filler particles; respectively, the volume and weight in percent; their size, shape and distribution; and the matrix–filler interaction [16]. A number of studies have concluded that flowable composite resins have a higher wear resistance due to the shorter distance between the particles and the presence of small filler particles [16,17]. This idea is also supported by the results of other studies, Condon et al., Sulong et al. and Suzuki et al., which argue that small particles give the matrix greater wear resistance [18–20]. Another study concluded that both flowable and higher viscosity resins have a relatively low wear rate, and there are no statistically significant differences between the two types of composite resins [16]. On the other hand,

Hashemikamangar argues that flowable composite resins are less resistant to wear compared to higher viscosity resins [21]. In the present study, it was observed that there were no statistically significant differences between the three types of fluid composite resins tested (Grandio Flow, Filtek Ultimate Flow and G-aenial Flo X) at any stage of the study, although the percentage of the weight and volume of filler particles are different for all materials used in the study. In another study, it was reported that there was no correlation between the surface roughness obtained after the finishing and polishing procedures and the final wear of resin-based materials [5,22].

Data from the literature considered that the degradation of composite resins is caused by the chemical degradation of polymers following the penetration of water into its structure and the consequent release of oligomers and monomers through the pores created by mechanical wear [5]. It was found that, initially, there is a superficial degradation of the polymer, and later the surface roughness increases by the appearance of cracks due to increased osmotic pressure at the interface between the organic matrix and filler particles, respectively, due to hydrolytic degradation of silane [23–27].

In the present study, hydrochloric acid determined changes in surface roughness of all three flowable composite resins, the results being in agreement with the results of other studies [24,28].

The methodology for simulating toothbrushing is well established in the literature. Thus, Sexson and Phillips claimed that a patient performs about 15 cycles for each brushing session [29]. Thus, two brushing sessions per day will lead to a total number of 10,000 brushing cycles in a year [5,30,31]. In the present study, we subjected the study samples to a session of 5000 brushing cycles, equivalent to 6 months of toothbrushing. In a study conducted by AlAli et al., it was demonstrated that after a toothbrushing procedure of 5000 cycles, the surface polished with Sof-Lex system had been removed, and the exposed layers were more resistant to the following toothbrushing cycles [14].

In our study, we recorded higher Pa values of surface roughness for the subgroups subjected to the abrasive action of hard bristles. These results are inconsistent with those obtained in the study conducted by Carvahlo et al. in which soft bristles created a rougher surface due to the ability of soft bristles to hold toothpaste better and the flexibility of the filaments, which ensures a larger contact area between toothbrushes or toothpaste and restorative materials [32]. From a clinical point of view, the increase of the surface roughness of restoration materials will reduce wear resistance and increase the accumulation of bacterial biofilm, leading to secondary caries or impaired aesthetics [2,32].

The differences in composition of organic and inorganic content of flowable composite resins influence their behavior in acid attack. In the case of the tested composite resins, there are differences both in terms of organic and inorganic components so that it is difficult to specify what contributed to the similar behavior of the materials.

Gaining a better understanding of how surface roughness is affected by the characteristics of filler particles, the resin matrix and the connection between the matrix and the filler material could help to choose the ideal toothbrushes, toothpastes or the proper moment to perform toothbrushing [5,33].

5. Conclusions

Hydrochloric acid action for 60 min and six months of toothbrushing using toothbrushes having medium hardness or firm bristles have no effect on the surface roughness of the tested flowable composite resins. Toothbrushing with firm bristles immediately after acidic challenge determines increased surface roughness for two of the three flowable composite resins (Grandio Flow and Filtek Ultimate Flow). Toothbrushing with medium or firm bristles thirty minutes after the acidic aggression determines no effect on surface condition of flowable composite resins. The results obtained open new perspectives regarding the dental restorative treatment with flowable composite resins in patients with gastroesophageal reflux disease.

References

1. Han, L.; Okamoto, A.; Fukushima, M.; Okiji, T. Evaluation of Flowable Resin Composite Surfaces Eroded by Acidic and Alcoholic Drinks. *Dent. Mater. J.* **2008**, *27*, 455–465. [CrossRef] [PubMed]
2. Lai, G.; Zhao, L.; Wang, J.; Kunzelmann, K.-H. Surface properties and color stability of dental flowable composites influenced by simulated toothbrushing. *Dent. Mater. J.* **2018**, *37*, 717–724. [CrossRef] [PubMed]
3. Garcia, F.C.P.; Wang, L.; D'Alpino, P.H.P.; De Souza, J.B.; De Araújo, P.A.; Mondelli, R.F.D.L. Evaluation of the roughness and mass loss of the flowable composites after simulated toothbrushing abrasion. *Braz. Oral Res.* **2004**, *18*, 156–161. [CrossRef] [PubMed]
4. Ferracane, J.; Moser, J.; Greener, E. Rheology of Composite Restoratives. *J. Dent. Res.* **1981**, *60*, 1678–1685. [CrossRef] [PubMed]
5. Somacal, D.C.; Manfroi, F.B.; Monteiro, M.; Oliveira, S.D.; Bittencourt, H.R.; Borges, A.G.; Spohr, A.M. Effect of pH Cycling Followed by Simulated Toothbrushing on the Surface Roughness and Bacterial Adhesion of Bulk-fill Composite Resins. *Oper. Dent.* **2020**, *45*, 209–218. [CrossRef]
6. Jones, D.W.; Jones, P.; Wilson, H. A simple abrasion test for composites. *J. Dent.* **1972**, *1*, 28–34. [CrossRef]
7. Al Khuraif, A.A. Anin vitroevaluation of wear and surface roughness of particulate filler composite resin after tooth brushing. *Acta Odontol. Scand.* **2014**, *72*, 977–983. [CrossRef]
8. De Oliveira, G.U.; Mondelli, R.; Rodrigues, M.C.; Franco, E.B.; Ishikiriama, S.; Wang, L. Impact of filler size and distribution on roughness and wear of composite resin after simulated toothbrushing. *J. Appl. Oral Sci.* **2012**, *20*, 510–516. [CrossRef]
9. Bollenl, C.M.; Lambrechts, P.; Quirynen, M. Comparison of surface roughness of oral hard materials to the threshold surface roughness for bacterial plaque retention: A review of the literature. *Dent. Mater.* **1997**, *13*, 258–269. [CrossRef]
10. Komandla, D.R.; Acharya, S.R.; Pentapati, K.C. Comparative Evaluation of Surface Roughness of Resin- Modified Glass Ionomer and Glass Hybrid Restorative Materials Simulated by Tooth Brushing: An in-Vitro Study. *Pesqui. Bras. Odontopediatria Clínica Integr.* **2021**, *21*, 1–8. [CrossRef]
11. Walter, R. Bulk-Fill Flowable Composite Resins. *J. Esthet. Restor. Dent.* **2013**, *25*, 72–76. [CrossRef] [PubMed]
12. Yuan, C.; Wang, X.; Gao, X.; Chen, F.; Liang, X.; Li, D. Effects of surface properties of polymer-based restorative materials on early adhesion of *Streptococcus mutans* in vitro. *J. Dent.* **2016**, *54*, 33–40. [CrossRef] [PubMed]
13. Ionescu, A.; Wutscher, E.; Brambilla, E.; Schneider-Feyrer, S.; Giessibl, F.J.; Hahnel, S. Influence of surface properties of resin-based composites on in vitro *Streptococcus mutans* biofilm development. *Eur. J. Oral Sci.* **2012**, *120*, 458–465. [CrossRef] [PubMed]
14. Alali, M.; Silikas, N.; Satterthwaite, J. The Effects of Toothbrush Wear on the Surface Roughness and Gloss of Resin Composites with Various Types of Matrices. *Dent. J.* **2021**, *9*, 8. [CrossRef] [PubMed]
15. Vasudeva, G. Monomer systems for dental composites and their future: A review. *J. Calif. Dent. Assoc.* **2009**, *37*, 389–398. [PubMed]
16. Chimello, D.; Dibb, R.; Corona, S.; Lara, E. Assessing wear and surface roughness of different composite resins after toothbrushing. *Mater. Res.* **2001**, *4*, 285–289. [CrossRef]
17. Rada, E.R. The versatility of flowable composites. *Dent. Today* **1998**, *17*, 78–82.
18. Condon, J.R.; Ferracane, J.L. Evaluation of composite wear with a new multi-mode oral wear simulator. *Dent. Mater.* **1996**, *12*, 218–226. [CrossRef]
19. Sulong, M.Z.A.M.; Aziz, R.A. Wear of materials used in dentistry: A review of the literature. *J. Prosthet. Dent.* **1990**, *63*, 342–349. [CrossRef]
20. Suzuki, S.; Leinfelder, K.F.; Kawai, K.; Tsuchitani, Y. Effect of particle variation on wear rates of posterior composites. *Am. J. Dent.* **1995**, *8*, 173–178.
21. Hashemikamangar, S.S.; Meymand, M.Z.; Kharazifard, M.-J.; Valizadeh, S. Surface microhardness of a self-adhesive composite in comparison with conventional composite resins. *Dent. Med. Probl.* **2020**, *57*, 247–253. [CrossRef] [PubMed]
22. Salama, F.; Abdelmegid, F.; Alhomaidhi, L.; Alswayyed, S.; Alfarraj, S. Effect of Whitening Toothpastes and Brushing on Microhardness of Esthetic Restorative Materials. *J. Clin. Pediatr. Dent.* **2020**, *44*, 296–301. [CrossRef] [PubMed]

23. Göpferich, A. Mechanisms of polymer degradation and erosion. *Biomaterials* **1996**, *17*, 103–114. [CrossRef]

24. Lepri, C.P.; Ribeiro, M.V.M.; Dibb, A.; Palma-Dibb, R.G. Influence of mouth rinse solutions on the color stability and microhardness of a composite resin. *Int. J. Esthet. Dent.* **2014**, *9*, 238–246.

25. Lee, E.-H.; Ahn, J.-S.; Lim, Y.-J.; Kwon, H.-B.; Kim, M.-J. Effect of post-curing time on the color stability and related properties of a tooth-colored 3D-printed resin material. *J. Mech. Behav. Biomed. Mater.* **2021**, *126*, 104993. [CrossRef]

26. Chin, A.; Ikeda, M.; Takagaki, T.; Nikaido, T.; Sadr, A.; Shimada, Y.; Tagami, J. Effects of Immediate and Delayed Cementations for CAD/CAM Resin Block after Alumina Air Abrasion on Adhesion to Newly Developed Resin Cement. *Materials* **2021**, *14*, 7058. [CrossRef]

27. Li, Y.; Guan, H.; Bao, Y.; Guo, S.; Lei, D.; Zhao, T.; Zhong, B.; Li, Z. $Ni0.6Zn0.4Fe_2O_4/Ti_3C_2Tx$ nanocomposite modified epoxy resin coating for improved microwave absorption and impermeability on cement mortar. *Constr. Build. Mater.* **2021**, *310*, 125213. [CrossRef]

28. Carvalho, F.; Sampaio, C.; Fucio, S.; Carlo, H.; Correr-Sobrinho, L.; Puppin-Rontani, R. Effect of Chemical and Mechanical Degradation on Surface Roughness of Three Glass Ionomers and a Nanofilled Resin Composite. *Oper. Dent.* **2012**, *37*, 509–517. [CrossRef]

29. Sexson, J.C.; Phillips, R.W. Studies on the effects of abrasives on acrylic resins. *J. Prosthet. Dent.* **1951**, *1*, 454–471. [CrossRef]

30. Barbieri, G.M.; Mota, E.G.; Rodrigues-Junior, S.A.; Burnett, L.H.B., Jr. Effect of Whitening Dentifrices on the Surface Roughness of Commercial Composites. *J. Esthet. Restor. Dent.* **2011**, *23*, 338–345. [CrossRef]

31. Monteiro, B.; Spohr, A.M. Surface Roughness of Composite Resins after Simulated Toothbrushing with Different Dentifrices. *J. Int. Oral Heal.* **2015**, *7*, 1–5.

32. Carvalho, F.G.; Fucio, S.B.P.; Paula, A.B.; Correr, G.M.; Sinhoreti, M.A.C.; Puppin-Rontani, R.M. Child toothbrush abrasion effect on ionomeric materials. *J. Dent. Child.* **2008**, *75*, 112–116.

33. Barucci-Pfister, N.; Göhring, T.N. Subjective and objective perceptions of specular gloss and surface roughness of esthetic resin composites before and after artificial aging. *Am. J. Dent.* **2009**, *22*, 102–110. [CrossRef] [PubMed]